Transactions of the ASME®

Journal of Fluids Engineering

Published Quarterly by The American Society of Mechanical Engineers

VOLUME 118 • NUMBER 3 • SEPTEMBER 1996

(Contents continued on p. 436)

FLUIDS ENGINEERING DIVISION
Technical Editor
DEMETRI P. TELIONIS (1999)

Executive Secretary
PAT WHITE (1999)
Assistants to the Editor
N. W. SCHAEFFLER
J. E. POWELL
Calendar Editor
M. F. ACKERSON

Associate Technical Editors
P. R. BANDYOPADHYAY (1997)
P. W. BEARMAN (1998)
F. GIRALT (1997)
H. HASHIMOTO (1996)
J. A. C. HUMPHREY (1997)
F. HUSSAIN (1998)
J. KATZ (1998)
J. KIM (1996)
O. JONES (1996)
L. NELIK (1996)
M. W. REEKS (1996)
O. SIMONIN (1998)
P. M. SOCKOL (1998)
M. W. SINDIR (1997)
D. E. STOCK (1996)
M. S. TRIANTAFYLLOU (1998)
S. P. VANKA (1996)

BOARD ON COMMUNICATIONS
Chairman and Vice-President
R. MATES

OFFICERS OF THE ASME
President, **R. J. GOLDSTEIN**

Exec. Director
D. L. BELDEN

Treasurer
J. A. MASON

PUBLISHING STAFF
Managing Director, Engineering
CHARLES W. BEARDSLEY

Director, Technical Publishing
PHILIP DI VIETRO

Managing Editor, Technical Publishing
CYNTHIA B. CLARK

Managing Editor, Transactions
CORNELIA MONAHAN

Production Assistant
MARISOL ANDINO

Transactions of the ASME, Journal of Fluids Engineering (ISSN 0098-2202) is published quarterly (Mar., June, Sept., Dec.) for $185.00 per year by The American Society of Mechanical Engineers, 345 East 47th Street, New York, NY 10017. Periodicals postage paid at New York, NY and additional mailing offices. POSTMASTER: Send address changes to Transactions of the ASME, Journal of Fluids Engineering, c/o THE AMERICAN SOCIETY OF MECHANICAL ENGINEERS, 22 Law Drive, Box 2300, Fairfield, NJ 07007-2300.

CHANGES OF ADDRESS must be received at Society headquarters seven weeks before they are to be effective. Please send old label and new address.

PRICES: To members, $40.00, annually: to nonmembers, $185.00. Add $30.00 for postage to countries outside the United States and Canada.

STATEMENT from By-Laws. The Society shall not be responsible for statements or opinions advanced in papers or . . . printed in its publications (B7.1, Par. 3).

COPYRIGHT © 1996 by The American Society of Mechanical Engineers. Authorization to photocopy material for internal or personal use under circumstances not falling within the fair use provisions of the Copyright Act is granted by ASME to libraries and other users registered with the Copyright Clearance Center (CCC). Transactional Reporting Service provided that the base fee of $3.00 per article is paid directly to CCC, 27 Congress St., Salem, MA 01970. Request for special permission or bulk copying should be addressed to Reprints/Permission Department.

INDEXED by Applied Mechanics Reviews and Engineering Information, Inc. Canadian Goods & Services Tax Registration #126148048.

Downloaded 03 Jun 2010 to 171.66.16.159. Redistribution subject to ASME license or copyright; see http://www.asme.org/terms/Terms_Use.cfm

(Contents continued)

Technical Briefs

Announcements and Special Notices

Journal of Fluids Engineering

Editorial

Micro-Electromechanical Systems Pose Big Challenges in Fluid Dynamics

Less than a decade ago, successful demonstration of the first micro-fabricated motors at the University of California at Berkeley and at MIT captured the imagination of technologists around the world. The tiny motors, roughly the width of a human hair, sparked wide speculation about applications ranging from micro-surgery to miniscule robots. Today, research on MEMS (Micro-Electromechanical Systems) is exploring diverse applications which intimately involve the dynamics of fluid flow in microscale geometries. In fact, many processing steps used in micromachining also involve complex microscale fluid dynamics, and learning to control microscale flows may lead to entirely new avenues for materials processing.

Typical scales for micro-mechanical devices range from microns to millimeters, spanning the range of scales that also includes microelectronics, ultrasonics, visible and infrared radiation, and biological cells and tissues. So applications in diverse technical fields like micro-optics, medicine and biology, arise quite naturally.

Perhaps more important than small size is the fact that micromachining also allows batch fabrication of large numbers of components, providing complex functionality from the integration and control of large arrays of simple elements. This may even allow coupling of MEMS to macro-scale flow systems. Integration of micro-sensors and processors with micromechanical actuators should enable integrated systems not only to acquire and process information from their surroundings, but also to perform mechanical functions designed to alter or control their environment. An example of this would be the use of MEMS for active boundary layer control.

A great deal of research remains to be done for MEMS technology to realize its full potential. The integration of electronic and mechanical components is a major challenge. It requires reasonable compatability between the two sets of fabrication processes, compatability that is increasingly hard to achieve as the variety of materials (e.g., metals and polymers) used for mechanical components expands to meet specialized application requirements. In addition, the design of advanced MEMS requires more powerful computer-aided design tools. Better understanding of microscale flows and transport processes will help to assess the combined influences of mechanical, electromagnetic, thermal, optical, and fluid properties and processes. Basic engineering research on design integration, multidisciplinary design optimization, and distributed, adaptive controls is also important.

This issue of the Journal has micro-fluid mechanics as its theme. A few papers in this area are collected and highlighted. These papers illustrate current research efforts directed towards MEMS applications to sensing and measurement of fluid flows, the prediction and control of flow in microfluidic systems, and the control of macroscale fluid flows using MEMS.

The paper by Ho introduces MEMS, outlining common micromachining processes and summarizing several applications of MEMS technology to sensors and actuators. It also outlines recent progress on the use of MEMS for active flow control, including perhaps the most ambitious project to date, namely, active control of a turbulent boundary layer to reduce surface skin friction. This research tackles a full spectrum of basic research issues, including new materials and processes for micro-actuators and sensors, integration of electronic and mechanical components, and active control of large arrays of sensors and actuators using on-board, embedded, adaptive controls. The practical application of such systems for drag reduction remains a distant goal, one that will require more robust actuators, proven reliability and cost effectiveness. But it is important to begin to develop an understanding of the limits and possibilities for active turbulence control. It is also important to advance flow sensor and actuator capabilities and to develop integrated MEMS processing techniques. Understanding how to design and explore complex system architectures for locally adaptive control assumes greater importance as we continue to evolve ever more complex, distributed, autonomous electromechanical systems.

Microfabrication techniques have been used to develop flow sensors with extraordinary spatial resolution and frequency response. The application of microfabrication technology to turbulence research using silicon pressure transducers is discussed in the paper by Lofdahl et al.

On the micro-scale, fluid flow in small spaces is strongly affected by surface phenomena, and it is further compounded by Knudsen number effects, compressibility and viscous heating. The paper by Beshok et al. addresses the simulation of gas microflows in the slip-flow regime with emphasis on rarefaction effects due to compressibility. The dominance of surface forces in microscale flows is illustrated for the case of a novel low Reynolds number pump in the paper by Sen et al.

Rashidi et al. report on the chemical flow and transport at the microscale in an experimental porous medium. They developed a new, nonintrusive fluorescence imaging technique to measure velocity and concentration within the porous medium. Some fundamental unanswered question on microscale porous media are posed in the short communication that appears in the Technical Forum. Finally, Piekos and Breuer present results obtained via a Monte Carlo direct numerical simulation. They examine the effects of rarefaction for a micro-nozzle which produces a maximum Mach number of 2.4 with a pressure ratio of 24.

MEMS technology is here to stay. Its progress toward useful applications hinges in part on our understanding of microscale fluid dynamics and its role in both the fabrication and performance of microelectromechanical systems. Broadening our understanding to include the full spectrum of multidisciplinary science and engineering issues for MEMS will be the biggest challenge of all.

James M. McMichael
Air Force Office of Scientific Research

Journal of
Fluids
Engineering

Technical Forum

Questions in Fluid Mechanics

Tortuous Micro-Flow in Large Disordered Packed Beds

By John G. Georgiadis,[1] David R. Noble,[1] Michael R. Uchanski,[1] and Richard O. Buckius[1]

The need to study flow through porous media with structural disorder first arose in soil science (fluid transport in soils) and chemical engineering (mass transport in filters and packed bed reactors). Currently, the characterization of flow in tortuous micro-channels is of importance in many industrial convective heat transfer areas that interest the fluid engineer (McEligot and McEligot, 1994; Rosenfeld and North, 1995). With the recent improvement of micro-fabrication methods and increased functionality of engineered media with complex micro-structures, a whole class of low Reynolds number flows needs to be revisited. Examples include flows in Micro-Electro-Mechanical Systems (MEMS) fabricated on silicon substrates (Udell et al., 1990), polymer injection through fiber matrices during resin transfer molding (Coulter and Güçeri, 1988), and emerging technologies mimicking biomechanical processes (biomimetics). Methodologically, the most severe obstacle towards modeling the microscopic hydrodynamic field is the need to account for the intrinsic complexity of pore structure. If linear superposition is not allowed (as in the case when nonlinear effects are included), the coupling between structure and flow is severe. Since it is not obvious what the size of the elementary flow domain should be (in order to contain all characteristic hydrodynamic scales), it is desirable to maintain as large a domain as possible in the model.

Stokesian pore-level hydrodynamics is well understood. There are several open issues regarding the modeling of flow in rigid porous media (Kaviany, 1991; Adler, 1992), particularly involving geometrical disorder and non-linear (inertial) effects. By modeling the full Navier-Stokes equations with an accurate scheme (cf. Noble et al., 1995; Noble et al., 1996), we performed extensive numerical experiments on pore-level flow in 2-D analogs of randomly packed beds. The simulation is based on the Lattice Boltzmann method (LBM) and involves two stages. Since realistic porous media can be most economically described by statistics (Torquato, 1991), one needs to first "manufacture" statistically-valid samples of the pore structure. For each value of the solid fraction (ratio of solid to total volume), M "realizations" of disordered configurations are generated by repeatedly distributing N cylinders in a square domain randomly. M and N of $O(100)$ are required in order to ensure that the ensemble of configurations is statistically homogeneous and isotropic. Second, the steady-state flow driven by a constant macroscopic pressure gradient is computed with the LBM code for each realization. An example of the computed streamwise velocity component (parallel to the pressure gradient) in a single realization is given in Fig. 1. The most dramatic feature of the flow is that the monotony of slow viscous wakes is interrupted by the appearance of "break-through jets," which are narrow bands of high speed flow. This is of great significance in enhancing advective transport and mixing in packed bed reactors. Note that these jets involve speeds up to twenty times the mean velocity. The creation of such severe flow heterogeneity in domains which are statistically (i.e., "on average") homogeneous and isotropic is—to our knowledge—unprecedented in slow flows. The break-through jets form robust patterns; they appear consistently throughout the high solid fraction simulations.

Although we are only dealing with laminar and steady flow, it is useful to reintroduce (following Buyevich et al., 1969) the concept of "pseudo-turbulence" to characterize the flow through disordered beds. By repeating the simulation of flow through an ensemble of configurations, a spatially "random" velocity field is essentially created, which is parameterized by the solid fraction, the cylinder shape, and the packing algorithm. A standard statistical formulation can now be introduced. Figure 2 summarizes the LBM results for the probability density function of the microscopic (interstitial) velocity component along the pressure gradient. The results for the highest solid fraction reported here (62 percent) agree with the regular exponential decay first reported by Shattuck et al. (1991; 1996), who used Magnetic Resonance Imaging (MRI) to measure the axial velocity in Poiseuille flow through randomly packed beds made of sphere-filled tubes. The numerical predictions reported here were obtained by averaging over the ensemble (many realizations), while the experimental result was obtained by volume averaging in a single realization (involving a single 3-D packing with solid fraction approaching 60 percent). It is clear that the predicted exponential tail in the 62 and 50 percent histograms for positive values of velocity is consistent with the presence of a small number of high-speed areas in the flow field (break-through jets of Fig. 1). Recent systematic MRI studies in packed beds by Lebon et al. (1996) and Kutsovsky et al. (1996) verified the existence of long exponential tails in the streamwise velocity

---

[1] Department of Mechanical and Industrial Engineering, University of Illinois, Urbana, IL 61801.

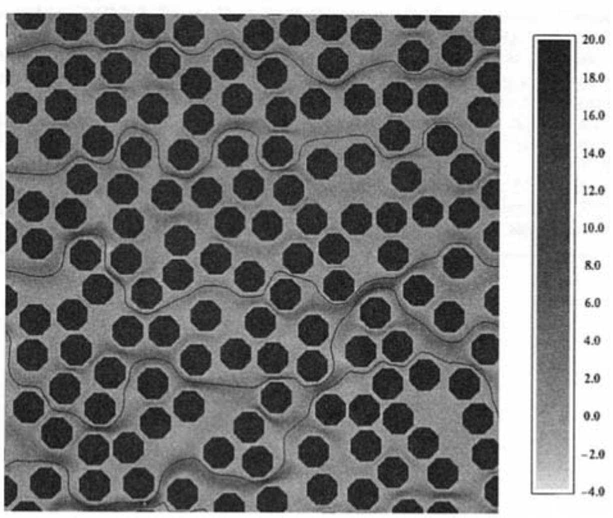

Fig. 1 LBM simulation of steady flow driven by a uniform pressure gradient (from left to right), 50 percent solid fraction, Re = 8 (based on particle size and average streamwise velocity). Periodic boundary conditions are imposed on the domain boundaries. Greyscale indicates magnitude of streamwise velocity normalized by the average. Solid lines represent streamlines. The bar gives the greyscale value of the normalized velocity.

histograms. LBM calculations show that similar behavior is exhibited by the transverse (normal to the mean pressure gradient) component of interstitial velocity. We know of no other flow with such a velocity distribution. For example, the histogram for 10 percent solid fraction (dilute packing) is flat and unremarkable (Fig. 2), and this corresponds to a velocity distribution in flow over an isolated cylinder. As Fig. 3 demonstrates, the transverse velocity reaches values comparable to those of the streamwise component, and this implies that transverse advection of scalars (and therefore the effective dispersion) is enhanced.

In the inertial regime, the macroscopic pressure drop versus flow rate results obtained via ensemble averaging demonstrate a large scale divergence with respect to solid fraction if the Reynolds number is based on a single length scale. In fact, our simulations show that the flow is characterized by a wide range of length scales when the solid fraction is high. In the past, much of the development of models in the nonlinear regime was facilitated by the study of prototypical (limiting or simplified) analogs, or by performing experiments in a single realization.

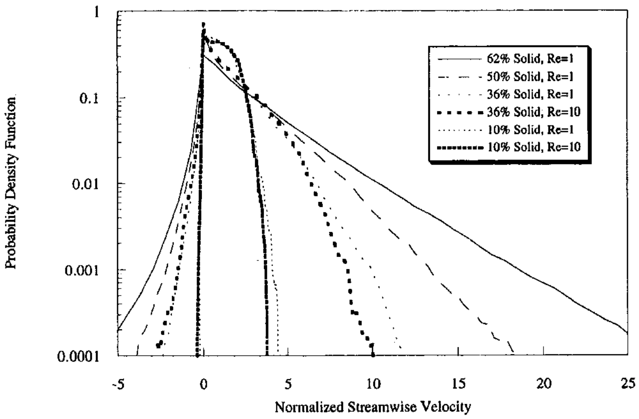

Fig. 2 Velocity histogram (compiled from the flow ensembles) indicating probability of finding a given streamwise velocity normalized by the (streamwise) average. Notice the long exponential tail for the 50 and 62 percent solid fraction.

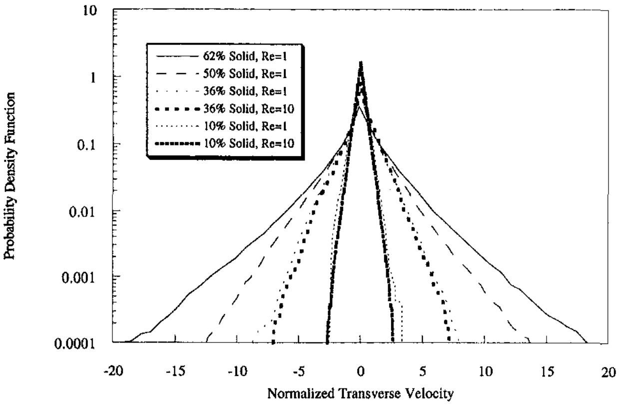

Fig. 3 Histogram of the transverse velocity component normalized by the (streamwise) average. Notice the long exponential tail for the 50 and 62 percent solid fraction (analogous to Fig. 2) and the symmetry about zero.

Given the intrinsic complexity of structure and flow, it is obvious that only measurement or direct simulation of the microscopic flow can improve the macroscopic (or average) models. By using more realistic pore space models and considering ensemble statistics, we can now begin to pose new questions, such as:

(1) Why the breakthrough jets in flow through densely packed arrays? Equivalently, why (when) does the geometrical homogeneity of the domain cause flow heterogeneity?

(2) Why the approximately exponential distribution of pore velocity at high solid fractions, as observed in Figs. 2 and 3? The histograms presented here (and corroborated by MRI results available in the literature) pertain to random (equilibrium) packings of mono-disperse disks. Is the exponential tail also a universal characteristic of micro-flows through polydisperse random packed beds or other classes of disordered porous media?

Such questions can not only aid in the modeling of flow through disordered packed beds (which is an approximately 100 year-old problem) but may also inspire some innovative closures in the plethora of problems that the former flow exemplifies (i.e., flow through natural or engineered micro-structures).

References

Adler, P., 1992, *Porous Media: Geometry and Transports,* Butterworth-Heinemann, Boston.

Buyevich, Yu. A., Leonov, A. I., and Safrai, V. M., 1969, "Variations in Filtration Velocity Due to Random Large-Scale Fluctuations of Porosity," *Journal of Fluid Mechanics,* Vol. 37(2), pp. 371–381.

Coulter, J. P., and Güçeri, S. I., 1988, "Resin Transfer Molding: Process Review, Modeling and Research Opportunities," *The Manufacturing Science of Composites,* Gutowski, T. G. ed., ASME Book No. H00415, pp. 79–86.

Kaviany, M., 1991, *Principles of Heat Transfer in Porous Media,* Sect. 2.9, Springer, New York.

Kutsovsky, Y. E., Scriven, L. E., Davis, H. T., and Hammer, B. E., 1996, "NMR Image of Velocity Profiles and Velocity Distributions in Bead Packs," *Phys. Fluids,* Vol. 8(4), pp. 863–871.

Lebon, L., Oger, L., Leblond, J., Hulin, J. P., Martys, N. S., and Schwartz, L. M., 1996, "Pulsed Gradient NMR Measurements and Numerical Simulation of Flow Velocity Distribution in Sphere Packings," *Phys. Fluids,* Vol. 8(2), pp. 293–301.

McEligot, J., and McEligot, D. M., 1994, "Perspective: Some Research Needs in Convective Heat Transfer for Industry," ASME Journal of Fluids Engineering, Vol. 116, pp. 398–404.

Noble, D., Georgiadis, J. G., and Buckius, R. O., 1995, "Direct Assessment of Lattice-Boltzmann Simulations of Recirculating Flow," *J. Stat. Physics,* Vol. 81(1/2), pp. 17–33.

Noble, D., Georgiadis, J. G., and Buckius, R. O., 1996, "Comparison of Accuracy and Performance for Lattice Boltzmann and Finite Difference Simulations of Steady Viscous Flow," *Int. J. Numerical Methods Fluids,* Vol. 23, pp. 1–18.

Rosenfeld, J. H., and North, M. T., (1995) "Porous Media Heat Exchangers for Cooling of High-Power Optical Components," *Optical Engineering (SPIE),* Vol. 34(2), pp. 335–341.

Shattuck, M., Behringer, R., Georgiadis, J. G., and Johnson, G. A., 1991, "Magnetic Resonance Imaging of Interstitial Velocity Distributions in Porous Media," *Experimental Techniques in Multiphase Flows,* (T. J. O'Hern and R. A. Gore, eds.), ASME FED-Vol. 125, pp. 39–46.

Shattuck, M., Behringer, R. P., Johnson, G. A., and Georgiadis, J. G., 1996, "Convection and Flow in Porous Media, I: Visualization by Magnetic Resonance Imaging," *Journal of Fluid Mechanics,* in the press.

Torquato, S., 1991, "Random Heterogeneous Media: Microstructure and Improved Bounds on Effective Properties," *Applied Mechanics Reviews,* Vol. 44, pp. 37–76.

Udell, K. S., Pisano, A. P., Howe, R. T., Muller, R. S., and White, R. M., 1990, "Microsensors for Heat Transfer and Fluid Flow Measurements," *Exp. Thermal Fluid Sci.,* Vol. 3, pp. 52–59.

Chih-Ming Ho
Mechanical and Aerospace
Engineering Department,
University of California, Los Angeles,
Los Angeles, CA 90095

Yu-Chong Tai
Division of Engineering
and Applied Science,
California Institute of Technology,
Pasadena, CA 91125

REVIEW: MEMS and Its Applications for Flow Control

Emerging micromachining technology enables us to fabricate mechanical parts on the order of micron size. It provides us with micro-sensors and micro-actuators which facilitate the exploration of all areas of science. Furthermore, these miniature transducers can be integrated with microelectronics. With an integrated system, it then becomes possible to complete the loop of sensing, information processing, and actuation. This type of system enables us to perform real-time control of time varying events which are common in fluid dynamics. In this review paper, we will first briefly introduce Micro-Electro-Mechanical-Systems (MEMS) technology. Then, the applications of MEMS to flow control will be discussed.

Introduction

During the last three decades, the field of solid-state electronics kept improving the manufacturing technology involved in the miniaturization of electronic elements. At present, it is possible to make electronic feature sizes on a sub-micron scale. The integrated circuit (IC) evolved from a small number of transistors on a chip to several million transistors on a chip. The range of applications increased dramatically with time such that the IC has changed our lives. However, an IC cannot interact with the environment. The interaction between a system and the external world has to rely on sensors and actuators which are usually mechanical devices. In the past, almost all of the mechanical parts had sizes much larger than the electronic elements because traditional manufacturing technology had difficulty in fabricating small mechanical parts, say less than a mm. Interestingly enough, Feynman did raise the question of making miniature things in his inspiring paper entitled "There is plenty of room at the bottom" (1956). He even proposed a prize to the first person who could make a motor of $\frac{1}{64}$ in. cube. Though the prize was claimed a few years after 1959, it was accomplished by delicate handicraft not by a mass production technology. In the 1980s, a new manufacturing process, the surface micromachining technology (Howe and Muller, 1983), became available. It could be used to manufacture micron sized mechanical devices with sophisticated geometry. An example is the micro motor (Fan, et al., 1988a), which is shown in Fig. 1. A piece of human hair is also shown in the figure to indicate the size of the motor. These achievements signified the beginning of the era of micromachinery, which will be as valuable as the emergence of microelectronics thirty years ago.

The significance of micromachine technology is that it makes it possible to provide us with mechanical parts

1. of micron size,
2. batch fabricated in large quantities and
3. integrateble with electronics.

Length scale matching between transducers and investigated phenomena is essential so that enough spatial resolution can be achieved for sensing, and efficient momentum and energy transfers from the actuator to the controlled subject can happen. Our scientific knowledge spans the length scales from light years to the sub-atomic domain. Natural phenomena with length scales much larger than the size of human beings, such as the weather, are understood mainly through sensing. No actuation of that scale is possible. At the other extreme is the atomic scale which we can explore both by sensing and actuation. Accelerated particles are used as actuators, because these particles match the size of the sub-atomic world. When we deal with natural phenomena of human size, there are abundant transducers for both sensing and actuation. However, a gap exists in the spectrum of our knowledge for scales on the order of microns. We do not know very much about the nature of physics in this range due mainly to the lack of transducers of this size. The miniature mechanical parts fabricated by micromachining technology are going to fill this gap.

Micromachining is a batch production process which employs lithographic processes. Since the micromachining technology is derived from the IC technology, it is possible to monolithically integrate the mechanical and electronic elements. The micro-electro-mechanical-systems (MEMS), with its integrated micron-size mechanical parts and IC, will be able to sense the physical world, to process the information, and to then manipulate the physical phenomena through actuators.

There are numerous opportunities for applying MEMS to flow control. It is known for example that shear flows are sensitive to perturbations. If these perturbations are exerted at the origin of the shear layer and are within the instability band, the streamwise development of the flow can be significantly modified (Ho and Huang, 1982 and Ho and Huerre, 1984). This type of flow control scheme has been demonstrated to be very effective on free shear flow because it takes advantage of the flow instability, which is a powerful flow amplifier. This point is especially important for micro actuators because these actuators cannot deliver large forces or high power.

For turbulent wall-bounded shear flow, we face different types of challenges. The flow structures responsible for viscous drag increase in turbulent flow are very small in size, typically several hundred microns in width and several mm in length. Their life time is short, in the millisecond range or less. Great difficulties arise from the fact that they are randomly distributed in time and space. In the past, direct manipulation of these structures was very difficult. The matching in length scale between the micro transducers and the structures makes this task possible.

In this review paper, several examples of micromachines will first be presented. Then, the manufacturing technology will be briefly summarized. Finally, we will discuss the science issues unique to the micron dimension and flow control using MEMS based transducers.

Micromachined Devices

MEMS technology provides transducers to enable us to perform sensing and actuation in various engineering applications.

Contributed by the Fluids Engineering Division for publication in the JOURNAL OF FLUIDS ENGINEERING. Manuscript received by the Fluids Engineering Division October 25, 1995; revised manuscript received June 10, 1996. Technical Editor: D. P. Telionis.

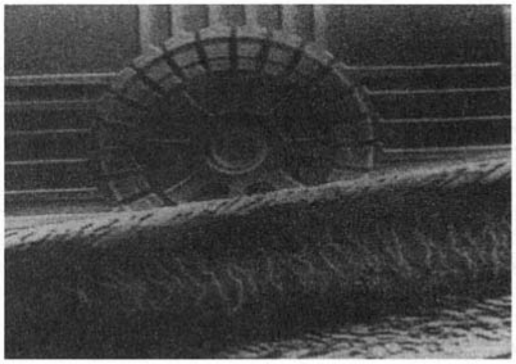

Fig. 1 Micro motor (Fan et al., 1988b)

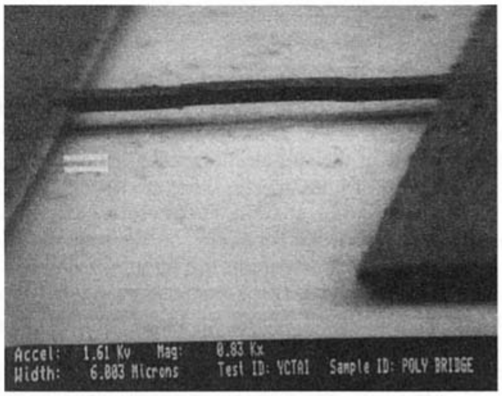

Fig. 2 A micro beam (Tai and Muller, 1988)

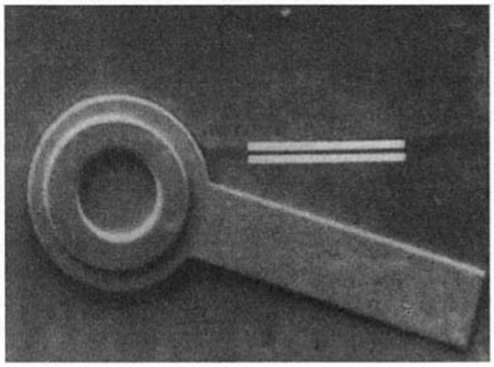

Fig. 3 Micro pin-joint (Fan et al., 1988)

Figures 2 and 3 are two fundamental micro mechanical elements, a beam and a pin joint, from which many micromachines can be derived. For example, the micro motor (Fig. 1) is a combination of a pin joint (rotor) and several short cantilever beams (stators).

Micro transducers also contribute to the advancement of science by enabling us to study the natural phenomena that occur in the order of microns in all branches of science; fluid dynamics, solid mechanics, materials science, biology, etc. The push-pull relationship between science and technology further enriches this field. Most biological cell sizes are in the order of microns which match the scale of micromachines. The micro gripper in Fig. 4 (Kim et al., 1992) shows that is possible to hold a single cell of 7 μm in diameter by a micro device. With some imagination, we can now see a new world through the picture.

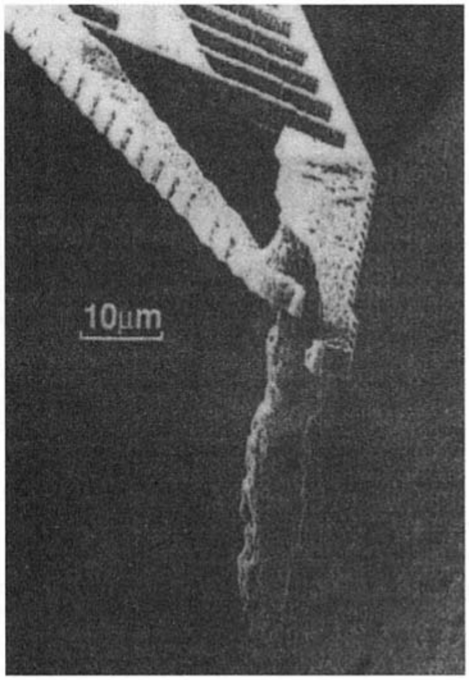

Fig. 4 Micro gripper (Kim et al., 1992)

In the near future, it should also be possible to sense and to manipulate the function of a cell through transducers (Najafi and Wise, 1986). It is interesting for us to understand the functions of neurons which facilitate our cognitive ability, our body's motion and sensing. Micromachines makes it possible to capture a single neuron in a micro cavity and to obtain the electrical signal between neurons (Fig. 5, Tatic-Lucic et al., 1993). It is even possible to receive the neuron signal in vivo by inserting micro neuron probes into the brain without disturbing much the neuron due to the probe's miniature size (Fig. 6, Tatic-Lucic et al., 1994).

In the field of material science, it is known that micron-sized subjects are much stronger than large subjects. The fracture strength can be an order of magnitude larger than the bulk fracture strength. Furthermore, silicon material at room temperature experiences only elastic deformation until fracture. Plastic deformation is not obvious. These two features provide a new design concept for micro parts. The buckled state, in a large deformed subject, has seldom been used in the engineering design of macro subjects because it poses the risk of experiencing plastic deformation and even the possibility of fracture. Buckled micro parts are much less prone to these problems. As

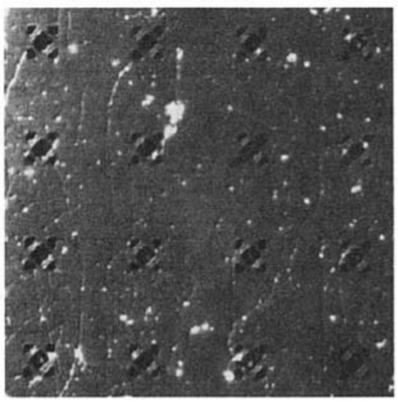

Fig. 5 Neurons in micro cavities (Tatic-Lucic et al., 1993)

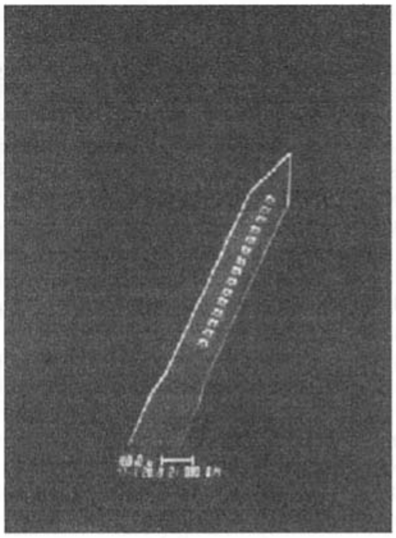

Fig. 6 Neuron probe (Tatic-Lucic et al., 1994)

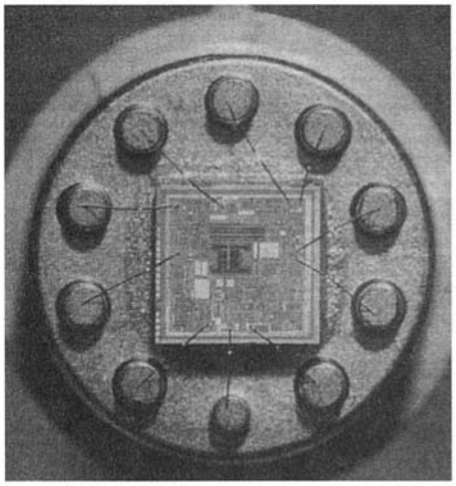

Fig. 8 Air bag sensor (Analog Devices)

a matter of fact, several designers have already created devices that utilize these advantages (Ataka, et al., 1994; Matoba, et al., 1994).

In the fluid mechanics arena, turbulence research can benefit from the micro transducers. The spread of the length scales is a function of Reynolds number. The fine dissipation scale in very high Reynolds number flows requires a time response in the order of μs and a spatial resolution in the order of μm. The traditional hot-wire has a spatial resolution of about one mm which is three orders of magnitude larger than the requirement. Its time constant is about one order of magnitude away from the requirement. Transducers made by micromachining technology make it possible to meet these requirements. Using the surface micromachining technique, a micron-sized hot-wire anemometer was made from doped polysilicon (Jiang et al., 1994a and 1994b). When operated in constant temperature mode, a one mega-Hertz bandwidth is possible. Due to the flexibility of the geometric design by lithographic techniques, manufacturing a multiple sensor array is not a painstaking process anymore (Fig. 7).

Micro transducers are already available for industrial applications. The automobile air-bag sensor (Fig. 8) developed by Analog Devices is used to sense the deceleration during an automobile accident to activate the air-bag. Monolithically integrated sensor-microelectronics (Fig. 8) are used for the detection of the capacitance variation of the comb structure (Fig. 9) due to impact, signal conditioner, calibration and many other functions. The integrability between sensor and electronics simplify the packaging process. The lithographic process can reproduce large numbers of integrated micro-sensors and decision circuits on a wafer and therefore greatly reduce the unit cost. The micro optical mirror (Fig. 10) developed by Texas Instrument illustrates a new concept for light beam steering. In a fairly small area, 2.3 cm^2, about 400 thousand individually addressable mirrors are used to reflect images onto a large screen for a high definition television projection. These mirrors have high optical efficiency and at least a 15 year life span. This is an example of using a large number of distributed actuators to accomplish a complicated light steering task.

The above mentioned examples are a very small fraction of the available micromachines. Intensive research efforts in the last few years have brought forth many new devices as well as new processing techniques. Three basic manufacturing techniques are introduced in the following sections.

Micromachining Technology

Micromachining is the use of a sequence of microfabrication processes to make micromechanical components. As a result, the fundamentals of micromachining are very different from conventional machining. In fact, because of the use of microfabrication processes, micromachining has generally been regarded as being derived from integrated-circuit (IC) technology. There is no doubt that micromachining and IC technology do have many similarities. As an example, micromachining also relies heavily on the use of lithographic methods to first form

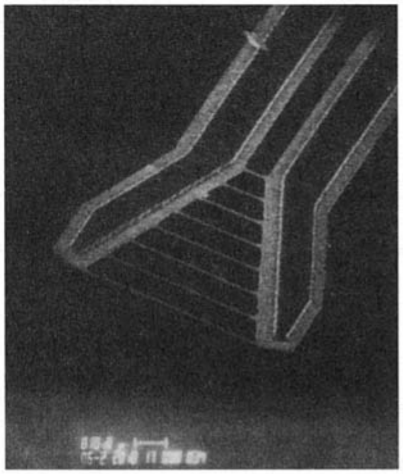

Fig. 7 Hot-wire rake (Jiang et al., 1994)

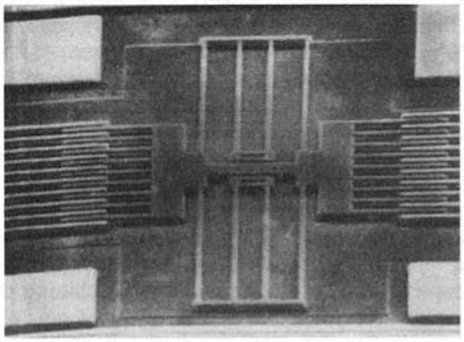

Fig. 9 Microcomb (Tang et al., 1990)

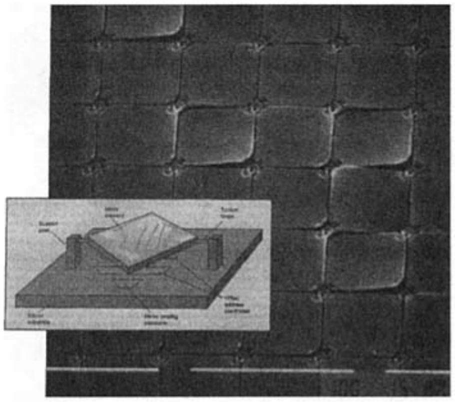

Fig. 10 Micro optic mirror (Texas Instrument)

pre-designed resist patterns (or masks) and then selectively etch the undesirable part away. Nevertheless, they still have many differences and one important difference is that in micromachining, selective etching is used purposely to create 3-D structures while in IC fabrication, distinctively 3-D structures must be avoided so as to facilitate the process of making smaller and smaller feature sizes on a planar wafer surface. Interestingly, it is then these 3-D or even free-standing structures that make micromachining useful as they have numerous micromechanical applications.

Since its beginning, micromachining has already developed into many branch technologies. Among them, bulk micromachining, surface micromachining, and LIGA technology are the most important ones. We will discuss them in the following section, but only briefly. For more information, the readers are referred to some excellent review papers. (Petersen, 1982; Seidel, 1987; O'Connor, 1992; Bryzek et al., 1994)

Bulk Micromachining. A general definition of bulk micromachining is to microfabricate microstructures from a starting substrate by removing the unwanted portion of it. Accordingly, there are many possible combinations of choosing the starting substrate materials and the means of material removal. The main stream of bulk micromachining, however, usually implies that the substrate is a single-crystalline silicon wafer and the material removal is done by selective wet-chemical etching, either isotropically or anisotropically. Moreover, the selective etching of silicon is often through the use of photolithographic masking in conjunction with etch-stop techniques such as using a heavily-doped boron layer (Raley, 1984) or a silicon p-n junction (Jackson, 1981). Altogether, many silicon microstructures can be made including cantilevers, beams, diaphragms, channels, nozzles, etc. These microstructures have formed the building blocks of many MEMS devices.

Chronologically, the development of silicon chemical etchants has been documented since the 1950's as researchers tried to find a precise way of etching silicon (Robbins, 1959). The developed aqueous silicon etchants were mainly isotropic and based on the mixture of hydrofluoric acid, nitric acid, and acetic acid (HNA). Anisotropic etchants for silicon started in the 1960's. The most studied etchants were potassium hydroxide (KOH) (Times, 1967), ethylene-diamine-pyrocatechol with water (EDP or EPW) (Finne, 1967), and hydrazine solutions (Lee, 1969). The anisotropic feature of these etchants is that they etch in the (100) and (110) silicon crystallographic directions much faster than in the (111) direction, which allows the design of microstructures to be naturally bounded by {111} crystalline planes. Figure 11 then shows the typical cases of both isotropic and anisotropic bulk micromachining. Note that etching happens only when the surface is not covered by the patterned mask. For the case of anisotropic etching, different surface orientations, either ⟨100⟩ or ⟨110⟩, will give totally different geometeries although the saturating walls are all {111} planes.

This feature was broadly used and these anisotropic etchants were further refined in 1970s and 1980s (Kern, 1978; Bassous, 1978; Bean, 1978; Reisman, 1979; Kendall, 1985). Recently, even metal-exclusive anisotropic etchants of ammonium hydroxide (Schnakenberg, 1991a) and tetramethyl ammonium hydroxide (TMAH) (Schnakenberg, 1991b, Tabata, 1991) have been developed. As more and more MEMS devices are integrated with electronics, these etchants have become more important. Today, it is generally agreed that bulk micromachining using wet chemical etching is a mature technology and many MEMS devices are fabricated using it.

In addition to wet chemical etching, recently people also started to look at dry etching processes that can replace or even outperform it. For example, laser etching (Bloomstein, 1994), plasma etching (Miu, 1993), gas etching, reactive-ion etching (Linder, 1991), ion beam etching and even micro electro-discharge-machining (EDM) all have been demonstrated. Bulk micromachining using dry etching is not limited to special crystalline orientations and there will be no surface-tension problems as often encountered in wet etching. However, in order for dry bulk micromachining to become practical, a lot of research still needs to be done.

Surface Micromachining. As the name suggests, surface micromachining is performed on the surface of a substrate, which can be a piece of silicon, glass, alumina, or even metal. This substrate, however, only functions as a mechanical support and it does not participate in the processing. The micromachining then involves combinations of thin-film deposition and patterning. In the end, a selective etch will take away certain layers (called sacrificial layers) and leave other layers (called structural layers) standing free. Figure 12 demonstrates a simplified process of surface micromachining.

According to literature, this concept of surface micromachining was readily demonstrated in the 1950's [US Patent 1956].

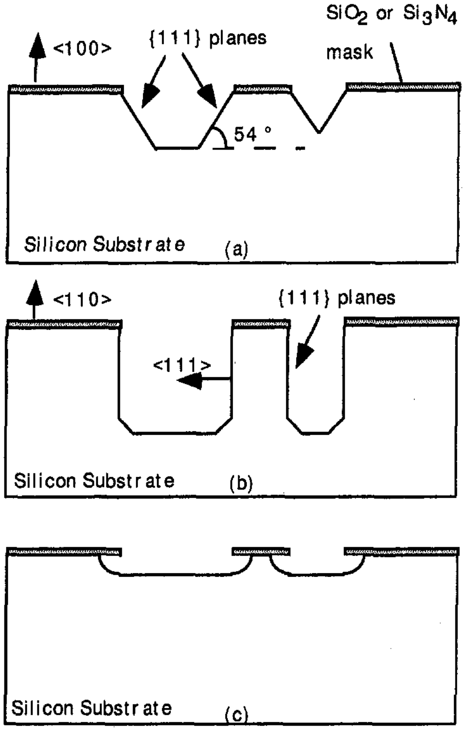

Fig. 11 Typical cases of silicon bulk micromachining (a) anisotropic etching of (100) Si wafer, (b) anisotropic etching of (110) wafer, (c) isotropic etching

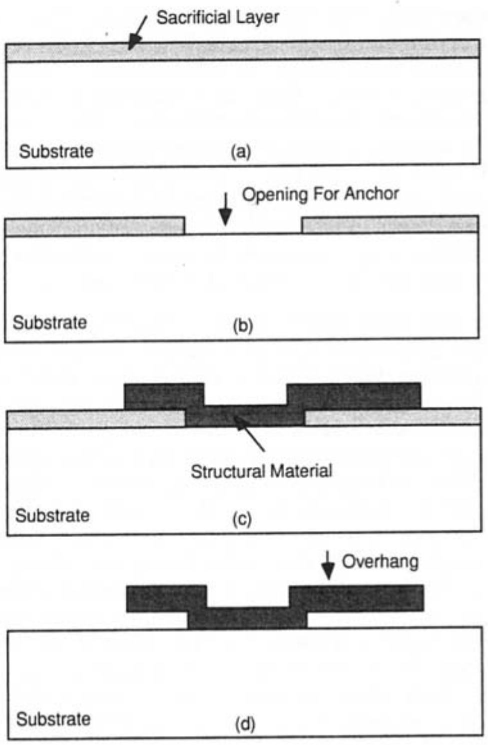

Fig. 12 A schematic process to demonstrate the surface micromachining technology. Note that the overhang structure in (d) can be part of a cantilever beam, a bridge, a plate, or even a diaphragm.

However, the use of it to make a complete MEMS resonant-gate transistor was done much later by Nathanson (1967). After this paper, a series of surface-micromachined devices were published including the early work of the digital mirror display (Preston, 1972). But, it was not until 1982 that Howe (1982) used LPCVD polycrystalline silicon to make micro cantilevers and bridges. The significance of this polysilicon surface micromachining process is that it is compatible with IC technology. The following work at Berkeley in the late 1980s (Fan, 1988; Tai, 1989; Tang, 1989; Kim, 1992) then demonstrated the broad use of polysilicon micromachining for various devices such as micro beams (Fig. 2), pin-joints (Fig. 3), sliders, resonators, tweezers (Fig. 4), and micromotors (Fig. 1). Today, polysilicon micromachining has established itself as one of the most important branches of surface micromachining. In addition to polysilicon surface micromachining, researchers have also explored many other materials such as aluminum (Sampsell, 1993) and silicon nitride (Tabata, 1991). Surface micromachining continues to flourish as MEMS devices become smaller, lighter, faster and cheaper.

LIGA Technology. Finally, there also is the LIGA technology (a German acronym for LIthographie Galvanoformung Anformung) (Becker, 1986; Ehrfeld, 1988). Basically, the LIGA process uses X-ray lithography to generate a deep pattern on a conductive substrate. The empty space in the X-ray resist then is electroplated from the bottom of the substrate to the top of the resist (Fig. 13), which generates a negative replica of the resist mold. This allows structures with submicron resolution from the capability of X-ray lithography. The microstructures can actually be one millimeter thick, and with a submicron precision, there is no other micromachining technique that can match up with it. However, the drawback is the cost for the X-ray source which requires a high-energy synchrotron. Because of this, LIGA may not be a popular technology but it is useful for some special applications which require a fine spatial resolution and a high aspect ratio. Otherwise, the rarity of the X-ray source and the cost of the technique made others develop similar techniques but with ultraviolet (UV) light sources (Frazier, 1992), available in any IC manufacturing laboratory. Lightheartedly termed as "poor-man's LIGA" or simply "cheap LIGA," this UV-based micro-electroplating gained popularity in many areas and is used to fabricate motors, flaps, and channels (Frazier, 1991; Miu, 1993; Joo, 1995).

Design of Micromachines

A machine consists of several basic requirements: configuration, motion, function and efficiency. Each machine part has its specific geometry and moves in a required manner. The combination of configuration and motion makes the machine capable of carrying out its function. The efficiency or performance of the machine depends on its design.

A micromachine also has to satisfy the same requirements. However, the design is much more challenging because the governing physical mechanism might change in the micro scale. The drastic size reduction in the micro world results in the breakdown of the scaling laws used in traditional engineering fields because the large length scale change is significant enough such that the equations governing the momentum and energy balances need to be re-examined. In addition, the inter-link among these fields becomes important in micron scales, such that the surface physics and chemistry may significantly affect the boundary conditions in fluid and solid mechanics. The changes in the governing equations and boundary conditions prevent us from using the traditional approaches which were well developed in the past. Scaling from the macro to the micro world is questionable. Design rules developed for the macro

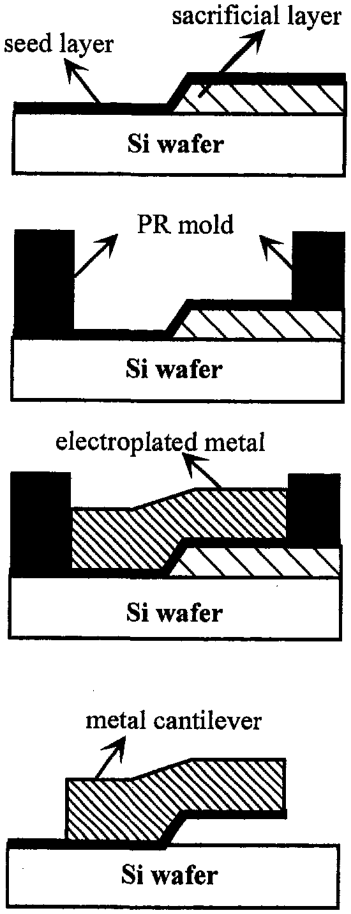

Fig. 13 Micro electro-plating

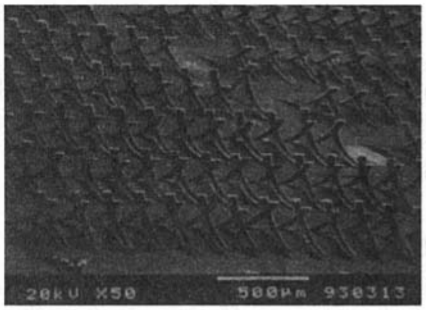

Fig. 14 Micro cilia (Ataka et al., 1994)

scale will not be valid for the micro scale. We need to develop new intuition to design micromachinery.

Relative motion between parts is essential for most machines. However, two micromachine parts designed to have a certain type of motion might not perform according to the desired way due to the large friction between two solid surfaces. A well-known example (Tai and Muller, 1989) is that the rotor of a micro motor will not rotate if the rotor is in full contact with the substrate. If dimples are placed between the rotor and the substrate to reduce the contact area, rotation becomes possible. This result leads to the conclusion that the friction force depends on the contact area which should not be a critical parameter in the conventional physics. It suggests that friction force in the micron scale has undergone a fundamental change. In general, the frictional force is a sum of the surface force and the contribution from the body force. In the macro scale, the body force is much larger than the surface force. Therefore, the frictional coefficient is a function of the body force normal to the contact surface and not a function of the contact area. In the force balance equation, the frictional force therefore has a simple expression. For surface micromachined subjects, the dimension normal to the wafer surface is typically two orders of magnitude smaller than the transverse length scale. This results in the volume per unit contact area of the micro subjects being much smaller than that of the macro subjects. Hence, surface force dominates in the frictional force in the motion of micro subjects. However, the scientific nature of various surface forces which contribute to the frictional force are largely unknown so the analytical form of the frictional force cannot be expressed explicitly or implicitly in writing. This fact leaves an unknown term in the equation of motion of the micro rigid body. The role switch between the body force and the surface force certainly poses a significant burden in designing a micromachine.

Due to the difference in governing mechanisms, we might also have to change the basic design principle. Most of the geometry used in the micromachines, e.g. gear and rotor, are still a size-reduced emulation from the macro world. It is not obvious that the direct emulation is the most appropriate design, especially the ones involving relative motion between large surfaces. Due to the large friction force, the efficiency of micromachines involving sliding motion cannot have high efficiency. Therefore, a new design is needed when a subject is to be transported from one place to another. Simulating the transport mechanism of the cilia, Ataka et al (1994) made an array of flexible silicon cilia (Fig. 14). By thermal actuation, the extension-contraction cycle can move a solid subject sitting on the top of the array. This design can transport a subject without encountering the large friction problem in the micro sliding surface.

Micro Transducers for Flow Control

The small physical size associated with the miniature transducers improves the spatial resolution. The temporal response can easily be increased to a large extent because of the low inertia of the transducer. These transducers have obvious advantages for flow control problems (McMichael, 1996). Jacobson and Reynolds (1993) used resonant beam actuators to examined the effect on the surface shear stress produced by a stationary vortex pair. Smith and Glezer (1995) have demonstrated the concept of applying a micro jet to achieve thrust vectoring. On the other hand, the capability of providing large quantities of sensors and actuators allows us to perform distributed control. This potential opens a new horizon in many engineering applications and remains to be explored. Its impact could even be more profound than the size reduction of transducers.

Micro Hot-Wire Anemometer. Since the spatial resolution of the anemometers for flow measurement is determined by their physical dimensions, it is advantageous if the wire size can be reduced. In addition, miniature hot-wires also reduce power consumption and thermal interference to the flow. In the past, many anemometer designs have been demonstrated using either surface or bulk-micromachining. However, they are all in the form of a wire adjacent to the surface of a chip. None of them consists of a wire free-standing in space without any nearby structure so that undisturbed free space velocity can be measured. We have developed a micromachined anemometer that has the configuration of a conventional hot-wire anemometer but with a greatly reduced wire size (Jiang et al., 1994a and 1994b). Not only are the spatial resolution and device sensitivity better, the frequency response is also improved by at least one order of magnitude over the conventional hot-wire anemometers.

The micromachined hot-wire anemometer is made of a polysilicon wire. The typical sensor wires are about 0.5 μm thick, 1 μm wide, 10–160 μm long. The dynamic performance and sensitivity of the micromachined hot-wire were tested. A heating time of 2 μs and a cooling time of 8 μs for the 30 μm long probe in constant current mode have been obtained. For constant temperature operation, a time constant of 0.5 μs for the 10 μm long probe can be reached. The corresponding cut-off frequency is 1.4 MHz. A calibration curve of the 20 μm long micromachined hot-wire is shown in Fig. 15. The average sensitivity is 20 mV/m/s at a heating current of 0.5 mA.

Micro Surface Shear Stress Sensor. Conventional hot-film type surface shear stress sensors have been used for several decades but the heat transfer to the substrate has always been a handicap in their operation. For measurements in air, the sensitivity is close to zero because of the low heat capacity of air. By using surface micromachining technology, a vacuum chamber is placed under the heating element, as shown schemat-

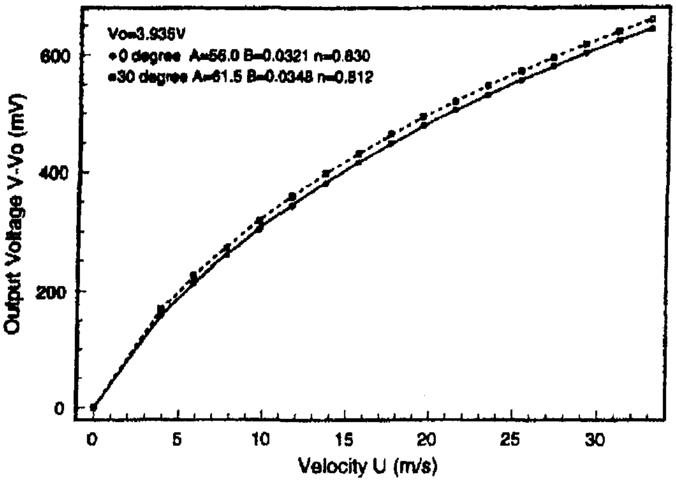

Fig. 15 Calibration of a 20 μm long micromachine hot-wire sensor at two different angles

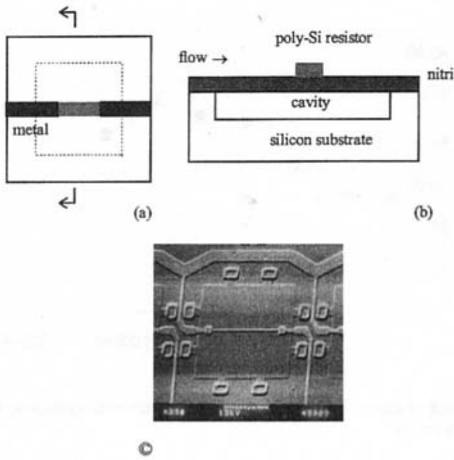

Fig. 16 Schematic of the top (*a*) and cross-sectional, (*b*) views of the micro shear-stress sensor, (c) SEM picture of the micro shear-stress sensor

ically in Fig. 16. This cavity significantly decreases the heat loss to the substrate and increases the shear stress sensitivity (Liu et al., 1994, Huang et al., 1995 and 1996).

A silicon nitride film is used as the diaphragm material which supports the heating element. The chamber is formed by etching away a sacrificial layer underneath the diaphragm. The heating element is made of a uniformly doped polysilicon resistor. The aluminum metalization forms the metal leads.

The typical sensitivity of the sensor with a cavity underneath is 15 mV/Pa, which is about one order of magnitude higher than that without a cavity. Figure 17 is a calibration curve of the shear stress sensor, which is plotted with the square of the output voltage versus the $\frac{1}{3}$ power of the shear stress. A linear relationship is obtained. The typical cut-off frequency of the sensor is 10 kHz when operating in the constant temperature mode. Another approach is to directly measure the shear stress by sensing the force on a micro floating element flush mounted on the wall (Shajji et al., 1992, Pan et al., 1995).

Micro Pressure Sensor. The pressure sensor can be designed and fabricated by a similar technology as the aforementioned shear stress sensor. A deposited polysilicon film is patterned as the piezoresistor for strain measurement (Liu et al., 1993). On a 250 × 250 μm^2 silicon nitride diaphragm, there are four polysilicon resistors placed around the center and another four on the edge of the diaphragm. The total thickness of the diaphragm is 1.5 μm. Polysilicon resistors are buried inside the diaphragm. The thickness of the polysilicon resistors is 500 nm. The polysilicon resistors are connected to form a Wheatstone bridge for temperature compensation although the heavily doped polysilicon shows a very small temperature coefficient. The output of the Wheatstone bridge is proportional to the pressure exerted on the diaphragm. Figure 18 shows a micromachined pressure sensor.

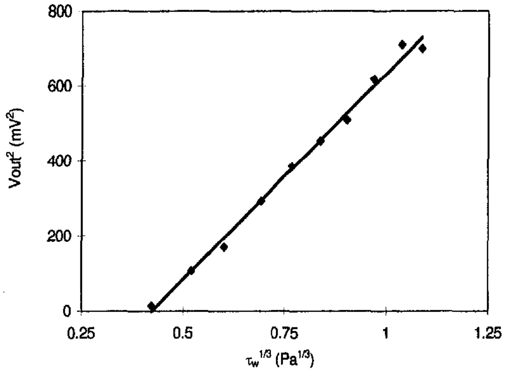

Fig. 17 Micro surface shear stress sensor output versus shear stress at constant temperature mode

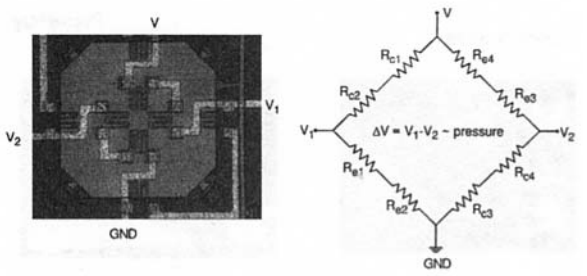

Fig. 18 A micromachined pressure sensor

The pressure sensors are fabricated by surfacing micromachining which is compatible with other MEMS devices. We have already integrated this kind of pressure sensor into a microflow measurement system (Pong et al., 1994; Shih et al., 1995). The sensitivity of this sensor is about 245 μV/V-psi.

Micro Actuator. In flow control problems, we need actuators which are able to provide about one mm off-plane motion and about milli-Newton force per mm^2 for sustaining the wind loading. These requirements are several orders of magnitude higher than that available from existing micro actuators. In order to accomplish these stringent performances, we first select an actuator which has simple configuration so that we at least will not be overburdened by fabrication difficulties. A flap type actuator was chosen for the design. It obviously is fragile, sensitive to the wind load direction as well as has many other deficiencies. However, it does serve the purpose for concept demonstration in laboratory tests (Liu et al., 1994; Tsao et al., 1994; Liu et al., 1995a and 1995b). On the other hand, these flap actuators have many other applications, such as large angle light steering and heat transfer enhancement.

The integration of permalloy with surface-micromachined polysilicon flaps has been completed (Fig. 19). Such a flap uses polysilicon as a structural material for both its beam supports and plate. Permalloy (5 μm thick) is electrodeposited on the top of the plate to provide the actuation mechanism.

Two size flaps, 1 × 1 mm^2 and 2 × 2 mm^2, have been made and bending angles up to 80 deg have been achieved with a magnetic flux density of about 800 Gauss. Such a large bending angle equals a point force of 0.2 mN acting on the edge of the flap. These flaps have been mounted on the leading edge of a delta wing and have been proven to be useful for aerodynamic control of the wing.

In addition to the permalloy flaps, we have also developed a bulk-micromachined flap with both copper coils and permalloy (Fig. 20) so the control of the device has more alternatives. The active flap is fabricated by the integration of bulk microma-

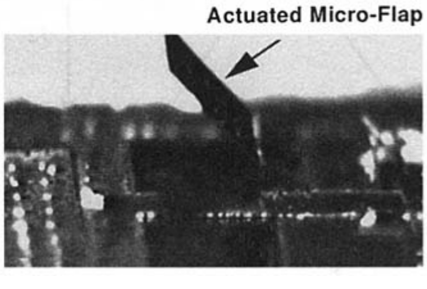

Fig. 19 A magnetically actuated surface-micromachined permalloy flap in a B-field of 400 Gauss

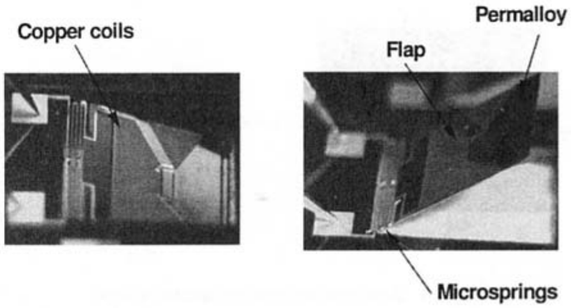

Fig. 20 An active flap integrated with both coil and permalloy. Both up and down positioning are achieved.

chining techniques with magnetic thin film processes. The mechanical structure consists of a 40 μm thick, 4 mm by 4 mm single crystal silicon plate, attached to bulk silicon through two 50 μm wide S-shaped springs. The electromagnetic component of the actuator sits on the plate surface and consists of a 30-turn planar copper coil, on top of which is a 10 μm triangular permalloy ($Ni_{80}Fe_{20}$) layer. Controllable deflection of the flap up to ±60° has been achieved by both external fields and coil current.

Control of Macro Aerodynamic Device by Micro Transducers

In flow control problems, it is desirable to be able to globally alter the flow by applying minute amounts of energy. We are interested in exploring the possibility of manipulating a macro aerodynamic device by using microactuators. The key point is finding a coupling between the macro physical world and the micro actuation. For a delta wing at high angle of attack, a large fraction of the lift is contributed by the vortices originated from boundary layers around the two leading edges. The coupling here is in the thin boundary layer before separation. If the off-plane displacement of the micro actuator matches the boundary layer thickness before flow separation, we will be able to either change the separation location or vary the vorticity of the delta wing's leading edge vortices. Once the symmetry of the two vortices is broken, it is possible to obtain a rolling torque or even other components of torque and force.

A delta wing model with a sweep angle of 56.5 deg was employed for the test (Fig. 21). The delta wing model had rounded leading edges. Micromachined actuators and micro shear stress sensors were placed on a cylindrical rod located at the leading edge. The rod can be rotated such that the positions of these transducers could be changed to cover the leading edge area. Microactuators with a flap size on the order of mm have been distributed from the apex to the trailing edge. An open-type wind tunnel was used for aerodynamic tests. The test-section was 100 cm × 100 cm and 730 cm long. The speed of this wind tunnel was from 10 m/s to 45 m/s. A six component force/moment transducer was used to measure aerodynamic forces and moments. However, only rolling moment was investigated at present.

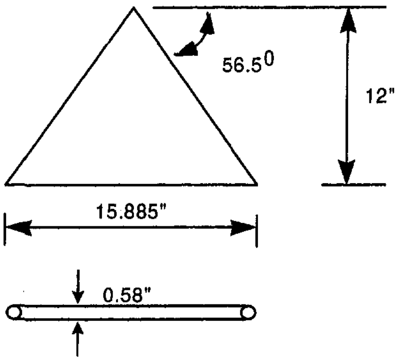

Fig. 21 Schematic of the delta wing

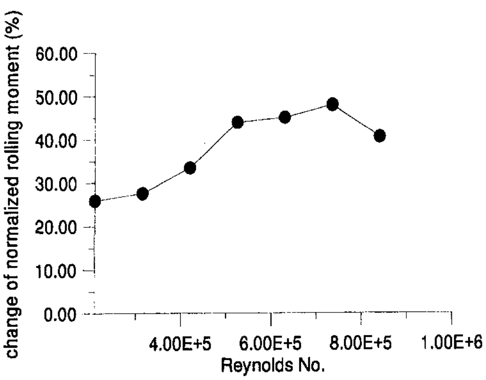

Fig. 22 Effect of micro actuators (both sides) on rolling moment of delta wing at AOA of 25°

After a detailed survey of the surface shear stress, we can correlate the effective actuation region with the flow separation region around the leading edge. The most exciting finding is that the rolling torque obtained by the actuation of the micro flaps can be a very significant amount compared with the toque contributed by the leading edge vortices. We use the pressure (suction) produced by one of the leading edge vortices multiplied by the distance between the pressure center and the center chord as the reference torque, T_r. Based on our recent experimental data, the amount of the torque produced by the microactuators can be on the order of 50 percent of T_r (Fig. 22).

Large Scale Integrated System for Distributed Control

For a phenomenon with a wide spread of length scales, e.g., turbulence, a large scale integrated transducer system can facilitate communication of the local information measured by individual sensors as well as identify the global characteristics through a collection of the sensors. The actuators then can, based on the local and global information, execute the proper control strategy.

This concept is best illustrated by research in turbulence control. Surface shear stress reduction in the turbulent boundary layer is the grand challenge in fluid mechanics research. Many randomly distributed small flow structures in the boundary layer are responsible for drag production. The width of these structures at high Reynolds number is only about several hundred microns, much smaller than conventional sensors and actuators. Furthermore, a large number of sensors spread around the surface are necessary to detect these random features and then the actuators can interactively manipulate these vortices. Micromachine based transducers are small in size as well as capable of forming large scale integrated systems. Direct control of individual structures to understand the response to actuation and its underlying physics now becomes possible. However, only matching of the length scales between the micro transducers and the flow features will not be enough to accomplish the task because detection and control logic need to be implemented. Furthermore, the amount of data associated with a large number of transducers is tremendous. The bandwidth needed is currently beyond the capability of the existing data transmission instrumentation to handle the transmission between the transducer assembly and a computer. A more stringent requirement is that the detection-decision-actuation process needs to be accomplished in the life time of the wall structures. That means real-time operation in a necessity. In other words, on-board

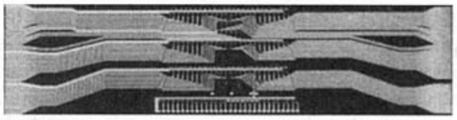

Fig. 23 A surface shear stress imaging chip

signal processing is required. A micro-electro-mechanical-system with large scale integrated microsensors, microelectronics and microactuators offers an opportunity to solve these types of engineering problems which require distributed real-time control.

The Surface Shear Stress Reduction Experiment. The surface shear stress reduction experiment was carried out in a two-dimensional channel flow facility. The channel has a cross section of 2.54 cm × 61 cm. The channel is 488 cm long. The mean velocity can be varied from 5 m/s to 30 m/s. The background turbulence level is about 0.1 percent.

The detection of the high shear stress streaks was performed in the fully developed turbulent portion of the channel. An understanding of the interaction between the actuator and the wall structure is a crucial part of controlling the shear stress. Since the integrated sensing-decision-actuation is still under development, a stationary streamwise vortex embedded in the laminar part of the channel flow was used as a model to study the actuator-vortex interaction (Tung et al., 1995).

Detection of High Shear Stress Streaks. A surface shear stress imaging chip was developed for mapping the instantaneous shear stress (Jiang et al., 1996). The imaging chip contains eighty-five micro sensors (Fig. 23). Each of the three long rows contains twenty-five sensors and the two short rows have five sensors. By placing the imaging chip in the turbulent flow, the voltage outputs from twenty five sensors in the same row were sampled and processed against the calibration curve to convert into stress. The signals are displayed as 2-D shear stress contours in Fig. 24. The time axis is converted to a pseudo streamwise coordinate by multiplying by the convection speed. This surface stress map shows the long streaky pattern of the high stress region (light regions). When the Reynolds number is reduced, the mean width of the streaks increases (Fig. 24(*b*)). These data demonstrate the capability of distributed sensors in capturing random events.

In order to activate the actuator only in the high stress region, we first need to determine the transverse dimension of the high stress region. Then, the actuator located downstream will be moved. A single sensor which is much smaller than the size of the flow feature is not able to know whether itself is experiencing high stress or not. A detection logic circuit (Fig. 25) was design for this purpose (Gupta et al., 1996). Basically, the signal output of a sensor is compared with its neighboring sensors through a filter-threshold combination. Whenever a sudden change is found, the edge of the high shear stress region is determined (Fig. 26). This chip can provide real-time decisions and also delivers current to energize the electro-magnetically driven actuator.

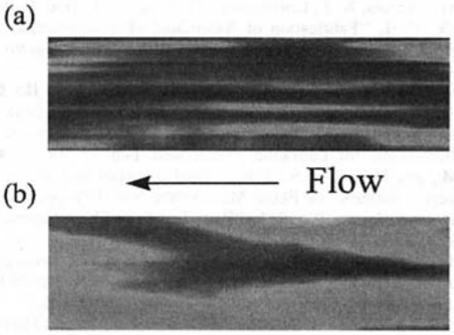

Fig. 24 Instantaneous surface shear stress measured by the imaging chip. (*a*) Re = 17,517; (*b*) Re = 8,758. Re is based on the half width and centerline velocity of the a turbulent channel flow.

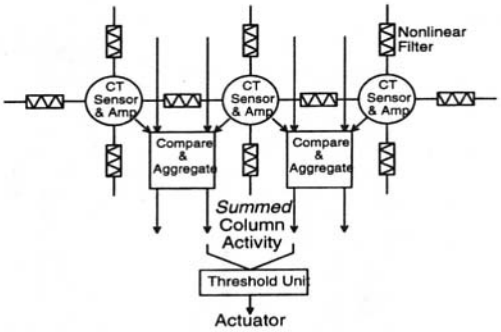

Fig. 25 Block diagram of the control circuits

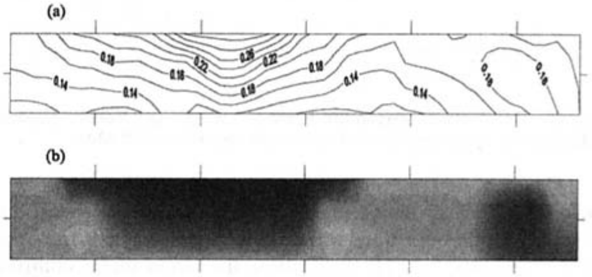

Fig. 26 Contours of (*a*) the instantaneous surface shear stress and (*b*) the output of the control circuits

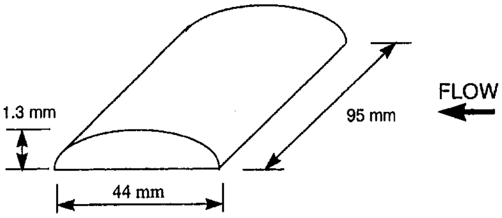

Fig. 27 Schematic of the vortex generator

Interaction between Micromachined Actuator and Streamwise Vortices. A crucial part of shear stress control is to determine the efficient control scheme which needs to be developed with an in-depth understanding of the interaction between actuator and flow structures. As a first step, an actuator interacting with a stationary vortex embedded in a laminar flow is used to explore this phenomenon. A 1.3 mm thick vortex generator with a curved surface (Fig. 27) is placed on the surface of the channel. At the end of the vortex generator, a longitudinal vortex pair is produced. Between the two vortices, high speed fluid is brought toward the wall. It generates a high shear stress streak (Fig. 28(*a*)). The micromachined actuator is a silicon nitride flap with 30 turns of copper coil and matches the size of the longitudinal vortex pair. A permanent magnet is located under the actuator. When an a.c. current passes through the coils at a constant frequency, the flap oscillates at that frequency (Miller et al., 1996). The surface shear stress is measured and phase averaged (Fig. 28(*b*)). The surface shear stress map shows an appreciable reduction. We integrate the shear stress along the spanwise direction and plot the integrated stress as a function of the phase angle of the actuator motion (Fig. 29). Throughout the whole cycle, the surface shear stress is

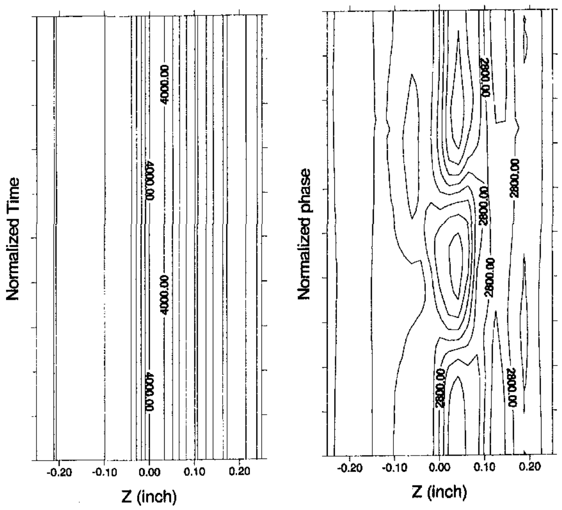

Fig. 28 Contours of ensemble-average *dU/dy*. (*a*) Vortex generator only; (*b*) Vortex generator and an oscillating micro actuator.

lower than that of the stationary vortex alone. The lowest duration is at around the time when the actuator stays at the uppermost location. At 20 Hz oscillation, the stress under controlled conditions can be lower than that of a Blasius velocity profile. This suggests that the flap type actuator can effectively transport the low speed fluid into the high speed stream. At frequencies higher than 20 Hz, the efficiency decreases. However, frequency should not to be the proper operating parameter to characterize the actuation. We believe that the frequency multiplied by the oscillation amplitude of the flap is a more appropriate parameter because it is related to the perpendicular speed needed to transport the high speed fluid away from the surface in the high shear stress region. More experiments are underway to clarify the actuator-vortex interaction phenomenon.

Concluding Remarks

The emerging Micro-Electro-Mechanical-Systems (MEMS) technology deals with phenomena in a very distinct length scale, the micron size. In this range, the surface to volume ratio is much larger than that in the macro scale. Hence, the surface effects, e.g. force and chemistry, become a dominating factor. On the other hand, MEMS technology provides us with sensors and actuators in the micron size. These micro transducers enable us to explore and control the natural phenomena in a length scale regime in which we have not had much experience. The integrated micro-electro-mechanical system can execute in real-time a sensing-decision-actuation process which enables us to control randomly distributed events in intricate turbulence control problems. MEMS is a field which is rich in scientific challenges as well as an enabling technology for broad engineering applications.

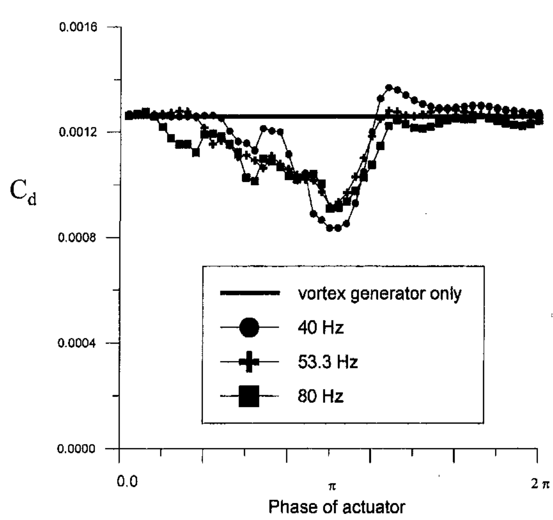

Fig. 29 Variation of the drag coefficient with actuator phase angles for different actuator oscillating frequencies

Acknowledgment

The authors appreciate the help from R. Goodman, B. Gupta, J.B. Huang, F.K. Jiang, G.B. Lee, C. Liu, R. Miller, T. Tsao, and S. Tung. This work is supported by Air Force Office of Scientific Research and Defense Advanced Research Project Agency.

References

Allen M. G., 1993, "Polyimide-based Processes for the Fabrication of Thick Electroplated Microstructures," *Transducers '93,* pp. 60–65.

Arkillic, E., and Breuer, K. S., 1993, "Gaseous Flow in Small Channels," AIAA Paper No. 93-3270.

Ataka, M., Omodaka, A., and Fujita, H., 1994, "A Biomimetic Micro Motion System—A Ciliary Motion System," *Transducer 93,* pp. 38–41.

Bandyopadhyay, P. R. and Gad-el-Hak, M., 1994, "Reynolds Number Effects in Wall-bounded Turbulent Flows," to appear in *Applied Mechanics Reviews.*

Bassous, E., 1978, "Fabrication of Novel Three-Dimensional Microstructures by the Anisotropic Etching of (100) and (110) silicon," *IEEE Trans. on Electron Devices,* Vol. ED-25, No. 10, Oct., pp. 1178–1185.

Bean, K., "Anisotropic Etching of Silicon, 1978," *IEEE Trans. on Electron Devices,* Vol. ED-25, No. 10, Oct., pp. 1185–1193.

Becker, E. W., Ehrfeld, W., Hagmann, P., Maner, A., and Munchmeyer, D., 1986, "Fabrication of Microstructures With High-aspect Ratios and Great Structural Heights by Synchrotron Radiation Lithography, Galvanoformung, and Plastic Moulding (LIGA Process)," *Microelectronic Engineering,* Vol. 4, pp. 35–36.

Beskok, A., and Karniadakis, G. E., 1993, "Simulation of Heat and Momentum Transfer in Complex Micro-Geometries," AIAA Paper No. 93-3269.

Bloomstein, T. M., and Ehrlich, D. J., 1994, "Laser Stereo Micromachining at One-Half Million Cubic Micrometers per Second," *Solid-State Sensors and Actuators Workshop,* Technical Digest, June 13–16, Hilton Head, North Carolina, U.S.A., pp. 142–144.

Brysek, J., Petersen, K., Mallon, J., Christel, L., and Pourahmadi, F., 1990, *Silicon Sensors and Microstructures,* NovaSensors.

Bryzek, J., Petersen, K., and McCulley, W., 1994, "Micromachines on the March," *IEEE Spectrum,* pp. 20–31.

Ehrfeld, W., Gotz, F., Munchmeyer, D., Schelb, W., and Schmidt, D., 1988, "LIGA Process: Sensor Construction Techniques Via X-ray Lithography," Technical Digest, Solid-State Sensor and Actuator Workshop, Hilton Head, SC, June 6–9, pp. 1–4.

Fan, L. S., Tai, Y. C., and Muller, R. S., 1988a, "Integrated Movable Micromechanical Structures for Sensors and Actuators," *IEEE Trans. on Electronic Devices,* Vol. 35, No. 6, pp. 724–730.

Fan, L. S., Tai, Y. C., and Muller, R. S., 1988b, "IC-processed Electrostatic Micromotors," *Technical Digest,* IEDM, pp. 666–669.

Feynman, R. P., 1959, "There's Plenty of Room at the Bottom," Annual Meeting of the APS, Caltech.

Finne, R. M., and Klein, D. L., 1967, "A Water-Amine-Completing Agent System for Etching Silicon," *J. Electrochem. Soc.,* Vol. 114, No. 9, Sept., pp. 965–970.

Frazier, A. B., and Allen, M. G., 1992, "High Aspect Ratio Electroplated Microstructures Using a Photosentive Polyimide Process," *Proc. of Micro Electro Mechanical Systems Workshop,* Travemunde, Germany, Feb. pp. 87–92.

Guckel, H., Skrobis, K. J., Christenson, T. R., Klein, J., Han, S., Choi, B., and Lovell, E. G., 1991, "Fabrication of Assembled Micromechanical Components via Deep X-ray Lithography," *Proc. of 1991 IEEE Micro Electro Mechanical System Conf.,* pp. 74–79.

Gupta, B., Goodman, R., Jiang, F., Tai, Y. C., Tung, S., and Ho, C. M., 1996, "Analog VLSI System for Active Drag Reduction," *Proceedings of the Fifth International Conference on Microelectronics for Neural Networks and Fuzzy Systems,* MicroNeuro '96, Lausanne, Switzerland, Feb. 12–14, pp. 45–52.

Ho, C. M., and Huang, L. S., 1982, "Subharmonics and Vortex Merging in Mixing Layers," JOURNAL OF FLUID MECHANICS, Vol. 119, pp. 443–473.

Ho, C. M., and Huerre, P., 1984, "Perturbed Free Shear Layers," *Ann. Rev. of Fluid Mech.,* Vol. 16, pp. 365–424.

Ho, C. M., and Tai, Y. C., 1994, "MEMS: Science and Technology," Application of Microfabriation to Fluid Mechanics, *Proceedings of the 1994 International Mechanical Engineering Congress and Exposition,* Chicago, IL.

Howe, R. T., and Muller, R. S., 1983, "Polycrystalline silicon Micromechanical Beams," *J. Electrochemical Soc.,* Vol. 130, pp. 1420–1423.

Huang, J., Ho, C. M., Tung, S., Liu, C., and Tai, Y. C., 1995, "Micro Thermal Shear Stress Sensor With and Without Cavity Underneath," *Proceedings, IEEE Instrumentation and Measurement Technology Conference,* Waltham, MA.

Huang, J., Tung, S., Ho, C. M., Liu, C., and Tai, Y. C., 1996, "Improved Micro Thermal Shear-Stress Sensor," *IEEE Transactions on Instrumentation and Measurement,* Vol. 45, No. 2, Apr.

Jackson, T. N., Tischler, M. A., and Wise, K. D., 1981, "An Electrochemical P-N Junction Etch-Stop for the formation of Silicon Microstructures," *IEEE Electron Device Letters,* Vol. EDL-2, No. 2, Feb., pp. 44–45.

Jacobson, S. A., and Reynolds, W. C., 1993, "Active Boundary Layer Control Using Mounted Surface Actuators," *Bulletin of American Physical Society,* Vol. 38, pp. 2197.

Jiang, F., Tai, Y. C., Ho, C. M., and Li, W., 1994a, "A Micromachined Polysilicon Hot-wire Anemometer," 1994 Solid-State Sensor and Actuator Workshop, Hilton Head Island, SC.

Jiang, F., Tai, Y. C., Ho, C. M., Karan, R., and Garstenauer, M., 1994b, "A Theoretical and Experimental Studies of Micromachined Hot-Wire Anemometers," *Technical Digest, IEDM,* San Francisco, CA, pp. 264–267.

Jiang, F., Tai, Y. C., Gupta, B., Goodman, R., Tung, S., Huang, J., and Ho, C. M., 1996, "A Surface-Micromachined Shear Stress Imager," *Proceedings of the 9th International IEEE Workshop on MEMS,* pp. 110–115, San Diego.

Joo, Y., Dieu, K., and Kim, C.-J., 1995, "Fabrication of Monolithic Microchannels for IC Chip Cooling," *Proc. of IEEE Micro Electro Mechanical Systems Workshop,* Amsterdam, The Netherlands, Jan.–Feb., pp. 362–367.

Kern, W., 1978, "Chemical Etching of Silicon, Germanium, Gallium Arsenide, and Gallium Phosphide," *RCA Review,* Vol. 39, No. 6, June, pp. 278–308.

Kendall, D. L., and De Guel, G. R., 1985, "Orientations of The Third Kind: The Coming of The Age of (110) Silicon," *Micromachining and Micropackaging of Transducers, edited by* C. D. Fung, P. W. Cheung, W. H. Ko, and D. G. Fleming, eds., Elsevier Science Publishers B. V., Amsterdam, The Netherlands.

Kim, C. J., Pisano, A. P., and Muller, R. S., 1992, "Silicon-Processed Overhanging Microgripper," *J. Microelectromechanical Systems,* Vol. 1, No. 1, pp. 31–36.

Lee, D. B., 1969, "Anisotropic Etching of Silicon," *J. Appl. Phys.,* Vol. 40, No. 11, Oct., pp. 4569–4574.

Linder, C., Tschan, T., Rooij, N. F., 1991, "Deep Dry Etching Techniques As a New IC Compatible Tools For Silicon Micromachining," Technical Digest, *Transducers '91,* San Francisco, pp. 54–57.

Liu, C., Tai, Y. C. Huang, J., and Ho, C. M., 1994, "Surface-Micromachined Thermal Shear Stress Sensor," *Application of Microfabrication to Fluid Mechanics,* FED-Vol. 197, pp. 9–16, ASME.

Liu, C., Tsao, T., Tai, Y. C., and Ho, C. M., 1994, "Surface Micromachined Magnetic Actuators," *Proceed. IEEE International Workshop on MEMS,* MEMS '94, Oiso, Japan.

Liu, C., Tsao, T., Tai, Y. C., Leu, J., Ho, C. M., Tang, W. L., and Miu, D., 1995a, "Out-Of-Plane Permanent Magnetic Actuators for delta Wing Control," *Proceedings, IEEE Micro Electro Mechanical Systems,* Amsterdam, the Netherlands, Jan. 29, pp. 7–12.

Liu, C., Tsao, T., Tai, Y. C., Liu, W., Will, P., and Ho, C. M., 1995b, "A Micromachined Permalloy Magnetic Actuator Array for Micro Robotics Assembly Systems," *Technical Digest, Transducers '95,* pp. 328–331.

Matoba, H., Ishikawa, T., Kim, C. J., and Muller, R. S., 1994, "A Bistable Snapping Microactuator," *IEEE Micro Electro Mechanical System Workshop,* Oiso, Japan, pp. 45–50.

McMichael, J. M., 1996, "Progress and Prospects for Active Flow Control Using Microfabricated Electro-Mechanical Systems (MEMS)," AIAA paper 96-0306.

Miller, R., Burr, G., Tai, Y. C., Psaltis, D., Ho, C. M., and Katti, R., 1996, "Electromagnetic MEMS Scanning Mirrors for Holographic Data Storage," *Technical Digest, Solid-State Sensor and Actuator Workshop,* Hilton Head Island, SC.

Miu, D., Wu, S., Tatic, S., and Tai, Y. C., 1993, "Silicon Micromachined Microstructures for Super-Compact Magnetic Recording Rigid Disk Drives," *Technical Digest,* Yokohama, Japan, *Transducers '93,* pp. 771–773.

Nathanson, H. C., Newell, W. E., Wickstrom, R. A., and Davis, J. R., 1967, "Resonant Gate Transistors," *IEEE Trans. on Electron Devices,* Vol. 14, pp. 117.

Najafi, K., and Wise, K. D., 1986, "An Implantable Multielectrode Array with On-chip Processing," *IEEE Trans. on Biomed. Eng.,* Vol. 35, pp. 1035–1044.

Nature-Times News Service, 1967, *The London Times,* 23, Nov.

O'Connor, L., 1992, "MEMS: Microelectromechanical Systems," *Mechanical Engineering,* Vol. 114, pp. 40–47.

Pan, T., Hyman, D., Mehregany, M., Reshotko, E., and Willis, B., 1995, "Calibration of microfabricated shear stress sensors," Digest of Technical Papers, *TRANSDUCERS '95, Stockholm, Sweden, June, pp. 443–446.*

Petersen, K., 1982, "Silicon as a Mechanical Material," Proceedings of the IEEE, Vol. 70, No. 5, pp. 420–456.

Preston, K., 1972, *Coherent Optical Computers,* McGraw-Hill, New York.

Raley, N. F., Sugiyama, Y., and Van Duzer, T., 1984, "(100) Silicon Etch-Rate Dependence on Boron Concentration in Ethylenediamine Pyrocatechol Water Solutions," *J. Electrochem. Soc.,* Vol. 131, No. 1, Jan., pp. 161–171.

Reisman, A., Berkenblit, M., Chan, S. A., Kaufman, F. B., and Green, D. C., 1979, "The Controlled Etching of Silicon in Catalyzed Ethylenediamine-Pyrocatechol-Water Solutions," *J. Electrochem. Soc.,* Vol. 126, No. 8, Aug., pp. 1406–1415.

Robbins, H., and Schwartz, B., 1959, "Chemical Etching of Silicon," *J. Electrochem. Soc.,* Vol. 106, No. 6, June, pp. 505–508.

Sampsell, J. B., 1993, "The Digital Micromirror Device and Its Application to Projection Display," *Technical Digest, Transducers '93,* Yokohama, Japan, pp. 24–27.

Schnakenberg, U., Benecke, W., Lochel, B., Ullerich, S., and Lange, P., 1991, "NH4OH-based Etchants for Silicon Micromachining: Influence of Additives and Stability of Passivation Layers," *Sensors and Actuators,* A, 25–27, pp. 1–7.

Schnakenberg, U., Benecke, W., and Lange, P., 1991, "TMAHW Etchants for Silicon Micromachining," *Technical Digest, Transducers '91,* pp. 815–818.

Seidel, H., 1987, "The Mechanism of Anisotropic Silicon Etching and Its Relevance for Micromachining," *Technical Digest, Transducers '87,* Tokyo, Japan, pp. 120–125.

Shajii, J., Ng, K.-Y., and Schmidt, M. A., 1992, "A microfabricated floating-element shear stress sensor using wafer-bonding technology," *IEEE/ASME J. of Microelectromechanical Systems,* Vol. 1, No. 2, pp. 89–94.

Shulman, M. A., Ramaswamy, M., Heytens, M. L., and Senturai, S. D., 1991, "An Object-Oriented Material-Property Database Architecture for Microelectromechanical CAD," *Transducers '91,* pp. 486–489.

Smith, B. L., and Glezer, A., 1995, "Jet Vectoring by Synthetic Jet Actuators," *Bulletin of American Physical Society.,* Vol. 40, pp. 2025.

Tabata, O., Asahi, R., Funabashi, H., and Sugiyama, S., 1991, "Anisotropic Etching of Silicon in (CH3)4NOH Solutions," *Technical Digest, Transducers '91,* pp. 811–814.

Tai, Y. C., and Muller, R. S., 1988, "Polysilicon Bridge as a Flow Meter," *Sensors and Actuators,* Vol. 15, pp. 63–75.

Tai, Y. C., and Muller, R. S., 1989, "IC-Processed Electrostatic Synchronous Micromotors," *Sensors and Actuators,* Vol. 20, pp. 49–55.

Tang, W. C., Nguyen, T. H., and Howe, R. T., 1989, "Laterally Driven Polysilicon Resonant Microstructures," *Sensors and Actuators,* Vol. 20, pp. 25–32.

Tang, W. C., Nguyen, T. C. H., Judy, M. W., and Howe, R. T., 1990, "Electro-static-Comb Drive of Lateral Polysilicon Resonators," *Sensors and Actuators A Physical,* Vol. 21(1–3), pp. 328–331.

Tatic-Lucic, S., Tai, Y. C., Wright, J., Pine, J., and Deunison, T., 1993, "Silicon-micromachined Cultured Neurochip for in vitro Studies of Cultured Neural Networks," *Transducer '93,* pp. 943–945, Japan.

Tatic-Lucic, S., Tai, Y. C., Wright, J., and Pine, J., 1994, "Silicon-micromachined Cultured Neuron Probes for in vivo Studies of Neural Networks," to be published in ASME Winter Meeting, Chicago.

Tsao, T., Liu, C., Tai, Y. C., and Ho, C. M., 1994, "Micromachined Magnetic Actuator for Active Fluid Control," *Application of Microfabrication to Fluid Mechanics,* FED-Vol. 197, pp. 31–38, ASME.

Tung, S., Hong, W., Huang, J., Ho, C. M., Liu, C., and Tai, Y. C., 1995, "Control of a Streamwise Vortex by a Mechanical Actuator," *Tenth Symposium on Turbulent Shear Flows,* Pennsylvania State University, University Park. U.S. Patent 2,749,598 (1956).

Rarefaction and Compressibility Effects in Gas Microflows

Ali Beskok
Research Associate.

George Em Karniadakis
Professor.

Center for Fluid Mechanics,
Brown University,
Providence, RI 02912

William Trimmer
President of Belle Mead Research, Inc.,
Belle Mead, NJ 08502

Gas microflows are encountered in many applications of Micro-Electro-Mechanical Systems (MEMS). Computational modeling and simulation can provide an effective predictive capability for heat and momentum transfer in microscales as well as means of evaluating the performance of a new microdevice before hardware fabrication. In this article, we present models and a computational methodology for simulating gas microflows in the slip-flow regime for which the Knudsen number is less than 0.3. The formulation is based on the classical Maxwell/Smoluchowski boundary conditions that allow partial slip at the wall. We first modify a high-order slip boundary condition we developed in previous work so that it can be easily implemented to provide enhanced numerical stability. We also extend a previous formulation for incompressible flows to include compressibility effects which are primarily responsible for the nonlinear pressure distribution in microchannel flows. The focus of the paper is on the competing effects of compressibility and rarefaction in internal flows in long channels. Several simulation results are presented and comparisons are provided with available experimental data. A specific set of benchmark experiments is proposed to systematically study compressibility, rarefaction and viscous heating in microscales in order to provide validation to the numerical models and the slip-flow theory in general as well as to establish absolute standards in this relatively young field of fluid mechanics.

1 Introduction

Micron size mechanical devices are becoming more prevalent, both in commercial applications and in scientific inquiry. Small accelerometers, with dimensions measured in microns, are being used to deploy air bag systems in automobiles. Tiny pressure sensors for the tip of a catheter are smaller than the head of a pin. Micro actuators are moving scanning electron microscope tips to image single atoms. New fabrication techniques, such as surface silicon micromachining, bulk silicon micromachining, LIGA (Lithographie Galvanoformung Abformung), and EDM (Electro Discharge Machining) are making these microdevices possible. The capability to batch fabricate and automate these fabrication technologies makes these microdevices inexpensive (Howe et al., 1990; Bryzek et al., 1994; Reed, 1993). Inherent with these new technologies is the need to develop fundamental science and engineering of small devices. Microdevices tend to behave differently than the objects we are used to handling in our daily life. The inertial forces, for example, tend to be quite small and surface effects tend to dominate their behavior. Friction, electrostatic forces, and viscous effects due to the surrounding air or liquid become increasingly important as the devices become smaller.

This paper focuses on the fundamental laws and the metrology of gas microflows, i.e., gas flows in devices with characteristic dimension of the order of a micron (μm). They are encountered in many applications of Micro-Electro-Mechanical Systems (MEMS) such as instrumentation, microelectronics, bioengineering, and advanced energy systems (Gabriel et al., 1988; O'Connor, 1992). An example of such a device is a polysilicon, surface-micromachined side-drive micromotor. The fabrication, operation, and performance of such a motor have been studied extensively in recent years by Tai et al. (1989), and Mehregany et al. (1990). Figure 1 shows a sketch of such a motor along with the characteristic dimensions. Typical operating conditions for an angular speed of $\omega = 5000$ rad/sec show that the Reynolds number $\text{Re} \simeq 1$ for the flow in the gap and that the Mach number $M < 0.01$ based on the rotor tip speed. In this small gap, a gas flow cannot be modeled based on the continuum hypothesis. The deviation of the state of the gas from continuum is measured by the Knudsen number (Kn), which is defined as $\text{Kn} = \lambda/L$, where λ is the mean free path of the molecules and L is representative of the domain length. For this micromotor, using the rotor base dimensions ($L = 3$ μm) and assuming that operation conditions are atmospheric, we obtain the value $\text{Kn} = 0.022$.

While the nominal Knudsen number is relatively small for the above example, there are other applications of microflows where the Knudsen number is significantly larger. For example, in magnetic disk storage, the gap between the magnetic head and the recording medium varies from 0.2 to 0.05 μm with the smaller dimension corresponding to an increase in recording capacity. The Knudsen number in this case is above one. Similarly, other microflows such as flows in helium leak detection microdevices and mass spectrometers correspond to a Knudsen number that may achieve values up to 200 (Tison, 1993).

As the value of Knudsen number increases, rarefaction effects become more important and thus pressure drop, shear stress, heat flux and corresponding mass flowrate cannot be predicted from flow and heat transfer models based on the continuum hypothesis. On the other hand, simple models based on kinetic gas theory concepts are not appropriate either. An exception is the very high Knudsen number regime corresponding to near vacuum conditions in finite size devices or at atmospheric conditions but at device dimensions of the order of nanometer (nm). The appropriate flow and heat transfer models depend on the range of the Knudsen number. A classification of the different flow regimes is as follows (Schaaf and Chambre, 1961): For $\text{Kn} \leq 10^{-3}$ the fluid can be considered as a continuum, while for $\text{Kn} \geq 10$ it is considered a free molecular flow. A rarefied gas can neither be considered an absolutely continuous medium nor a free-molecule flow in the Knudsen number range between 10^{-3} and 10. In that region, a further classification is needed, i.e., slip-flow ($10^{-3} < \text{Kn} < 0.1$) and transition flow ($0.1 < \text{Kn} < 10$). This classification is based on empirical

---

Contributed by the Fluids Engineering Division for publication in the JOURNAL OF FLUIDS ENGINEERING. Manuscript received by the Fluids Engineering Division March 17, 1995; revised manuscript received March 26, 1996. Associate Technical Editor: D. P. Telionis.

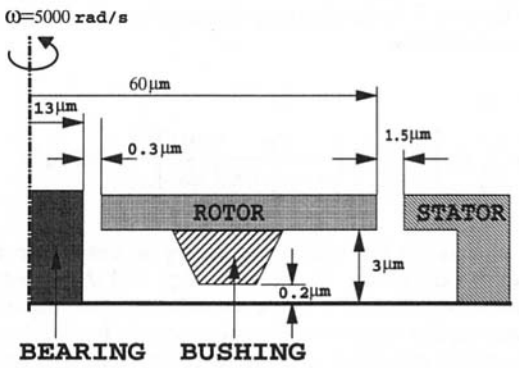

Fig. 1 Diagram of a side-driven micromotor with typical dimensions

information and thus the limits between the different flow regimes may depend on the problem geometry and special conditions. A comprehensive review on the theory of internal flows at low pressures is given by Thompson and Owens (1975); a general review on rarefied gas dynamics is given by Muntz (1989).

A verification of this taxonomy is provided in Fig. 2 where we plot the experimental data by S. Tison obtained at the National Institute of Standards (NIST) at very low pressures in a pipe of diameter $d = 2$ mm (Tison, 1994). Both inlet and outlet pressures were varied in the experiment while the corresponding Knudsen number varied from almost 0 to 200. In this log-log plot, we can easily identify three distinct flow regimes, although the corresponding values at the boundaries between the different regimes is somewhat different than the aforementioned ones (Schaaf and Chambre, 1961). In particular, the slip flow regime extends up to Kn = 0.6 and the transition regime up to Kn = 17. It is interesting to notice the very slow variation of mass flowrate in terms of the pressure difference in the transition regime. In that range of Knudsen number a minimum occurs in the mass flowrate divided by the difference of inlet and exit pressures ($\dot{M}/\Delta P$) if the data are replotted in terms of the average pressure between inlet and outlet. This minimum was first identified by Knudsen (1909) and has been observed in many experimental and analytical studies (Tison, 1993; Loyalka and Hamoodi, 1990; (see Kennard, 1938 p. 309). The form of the plot in Figure 2 also suggests that a nonlinear pressure drop takes place in this rarefied pipe flow. Scaling of the mass flowrate with the difference of pressure squares is characteristic of low Reynolds number, *compressible* flows in long channels.

The first experimental study of microflows using micro-machined channels was conducted for both gases and liquids by Pfahler et al. (1991) in a Reynolds number range $0.50 \leq \mathrm{Re} \leq 20$ and Knudsen number $0.001 \leq \mathrm{Kn} \leq 0.363$ for a hydraulic channel diameter $D_h = 8$ µm and channel length 11 mm. The corresponding Mach number at the inlet was very small but at the exit high subsonic values were achieved. For example, for an inlet to exit pressure ratio of 10, exit Mach numbers as high as 0.7 are reported by Pfahler et al. (1991) and Harley et al. (1995). The reported skin friction reduction due to apparent slip of the flow has been confirmed in other similar experimental studies (Arkilic et al., 1994) using different microfabrication techniques to fabricate the microchannels. In particular, in the work of Liu et al. (1993) and Pong et al. (1994) the pressure distribution along the microchannel was measured by using a surface micromachined system with a number of sensors as part of the surface. A nonlinear pressure distribution was clearly demonstrated in these experiments; however more data are needed to adequately describe its origin. Other recent work focusing on measuring and modeling microflows is presented in Shoji and Esashi (1994), Wilding et al. (1994), and Zengerle and Richter (1994).

In our studies we have identified four important effects in microflows. These are: *compressibility, rarefaction, viscous heating, and thermal creep effects.* The current paper emphasizes compressibility and rarefaction effects for shear and pressure driven microflows. Viscous heating is due to the work done by viscous stresses, and it is important for microflows, especially in creating temperature gradients within the domain even for isothermal boundary conditions. The thermal creep (transpiration) phenomenon is a rarefaction effect. For rarefied gas flows it is possible to start the motion with tangential temperature gradients along the channel surface. In such a case the gas molecules start creeping from cold to hot direction (Kennard, 1938, Kruger et al., 1970). Thermal creep can be important in causing variation of pressure along tubes in the presence of tangential temperature gradients. Thermal creep effects are also included in our model; the importance of these effects for incompressible flows has been documented in Beskok and Karniadakis (1994). A systematic study of thermal creep for compressible flows will be presented in a future publication.

Numerical simulation studies are well suited for microflows, however the breakdown of continuum at microscales leads to uncertainties regarding the governing constitutive laws. In the slip-flow regime, it is reasonable to employ the Navier-Stokes equations modified at the surface with appropriate velocity-slip conditions (Thompson and Owens, 1975). In previous work, in a series of papers (Beskok and Karniadakis, 1992, 1993, 1994) we developed an incompressible flow model with high-order velocity-slip boundary conditions. This approach essentially extends the governing equations used in modeling high-altitude slightly rarefied aerodynamic flows (Kennard, 1938; Schaaf and Chambre, 1961). In the current work, we use a numerical formulation we have developed for *compressible* no-slip as well as slip-flows in order to quantify the compressibility and rarefaction effects in the slip-flow regime. The results we present are consistent with experimental studies and agree very well in nondimensional form both for flows in microdomains where the Knudsen number is finite, due to the micron-size characteristic length, as well as in flows in domains of large size at near vacuum conditions. A fundamental question concerns the validity of the *dynamical similarity* between these two types of flows. In other words, are microflows at atmospheric conditions dynamically similar to rarefied (i.e., low pressure) flows in macro-domains. In conjunction with such questions we propose a set of benchmark experiments which, we believe, will aid in our fundamental understanding of the flow physics

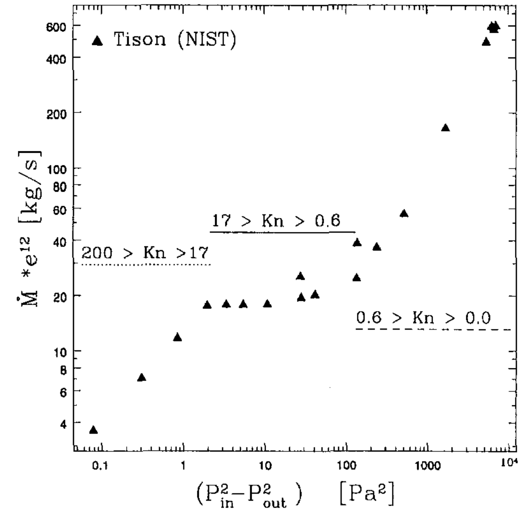

Fig. 2 Variation of mass flowrate as a function of ($P_{in}^2 - P_{out}^2$). The data are for rarefied gas flow experiments conducted by S. Tison at NIST (Kn is based on the pipe exit pressures which are very close to vacuum, and pipe radius).

and will validate the computational models we develop in this work.

The paper is organized as follows: In Section 2 we summarize the mathematical and numerical formulation and develop a high-order velocity slip boundary condition. In Section 3 we present typical results in shear-driven flows and compare with analytical models. In Section 4 we include results for pressure-driven flows and compare with experimental results. In Section 5 we propose a set of benchmark experiments motivated by the simulation results. Finally, in Section 6 we summarize our findings.

2 Models and Formulation

2.1 Compressible Navier-Stokes Algorithm. We consider here the slip-flow regime where we assume that gas microflows are governed by the Navier-Stokes equations and appropriate velocity-slip boundary conditions. In a previous study (Beskok and Karniadakis, 1994), we developed an incompressible flow formulation; however, the experimental results reported by Liu et al. (1993) show nonlinear pressure distribution in microchannel experiments suggestive of strong compressibility effects. For this reason, we have developed a new algorithm that solves the compressible Navier-Stokes equations using a spectral element/time-splitting algorithm. The algorithm treats the inviscid part (Euler equations) first using the characteristic decomposition procedure and a Gauss-Lobatto-Legendre collocation algorithm. Subsequently, the viscous part is discretized using a Galerkin formulation that enforces interelemental continuity conditions. Details of the algorithm including the treatment of element interface boundary conditions as well as validation of the spectral element algorithm for subsonic compressible flows in complex geometries is presented elsewhere (Beskok and Karniadakis, 1996).

In the results that follow, a systematic study of discretization errors has been performed by p-type grid refinements (increasing the order of polynomial expansions). The discretization errors are estimated by using the global mass and momentum balances. A maximum error of 1 percent in global conservation laws is taken as an acceptable norm. It was found that continuity is satisfied with 0.05 percent error and momentum is conserved with less than 1 percent error in all cases.

2.2 Velocity-Slip and Temperature-Jump Conditions. In previous studies (Beskok and Karniadakis, 1992, 1993, 1994) with incompressible flow models we employed the velocity-slip and temperature-jump boundary conditions given in the following non-dimensional form:

$$U_g - U_w = \frac{2-\sigma_v}{\sigma_v}\,\frac{\mathrm{Kn}}{1-b\,\mathrm{Kn}}\,\frac{\partial U_s}{\partial n} + \frac{3}{2\pi}(\gamma-1)\,\mathrm{Kn}^2\,\mathrm{Re}\,\frac{\partial T}{\partial s}, \qquad (1a)$$

$$T_g - T_w = \frac{2-\sigma_T}{\sigma_T}\left[\frac{2\gamma}{\gamma+1}\right]\frac{\mathrm{Kn}}{\mathrm{Pr}}\,\frac{\partial T}{\partial n}, \qquad (1b)$$

where U_g and T_g refer to the gas velocity and temperature, respectively, and U_w and T_w are the corresponding wall quantities. Also $\partial/\partial n$ and $\partial/\partial s$ denote the normal and tangential derivatives evaluated at the surface, respectively. Here σ_v and σ_T are the accommodation coefficients of the solid surface (Saxena and Joshi, 1981), and b is a high-order slip coefficient (see Beskok and Karniadakis, 1994). The case $b = 0$ corresponds to classical Maxwell (first-order) slip boundary condition.

The numerical implementation of Eqs. (1*a*) and (1*b*) are somewhat complicated due to the mixed-type (Robin) boundary conditions. An explicit (in time) implementation of Eq. (1*a*) at time level $(n+1)\Delta t$ (ignoring for simplicity the temperature term) is as follows:

$$U_g^{n+1} - U_w = \sum_{i=0}^{J-1} \alpha_i \left[\frac{2-\sigma_v}{\sigma_v}\left(\frac{\mathrm{Kn}}{1-b\,\mathrm{Kn}}\right)\frac{\partial U}{\partial n}\right]_s^{n-i} + \mathcal{O}(\Delta t^J), \qquad (2)$$

where α_i denotes the weights necessary to obtain the time-accuracy $\mathcal{O}(\Delta t^J)$ with Δt the time step, and J the order of integration rule (e.g., $J = 2$ for second-order time accuracy). However, explicit treatment of boundary conditions is an extrapolation process and thus it is numerically unstable, e.g., for high values of Knudsen number.

Through numerical experimentation, we have determined that the overall Navier-Stokes solution, with explicitly implemented velocity-slip boundary conditions, becomes unstable when the calculated slip amount $(U_g - U_w)$ at a certain time step is sufficiently large to cause a sudden change of the sign of wall vorticity, in the next time step. This empirical finding can be readily justified by considering the following argument. For a linear Couette flow (see Section 3) with driving velocity U_0 and local gas velocity U_1 at a distance (Δy) away from the wall, it is possible to approximate (to a first-order accuracy and for $\sigma_v = 1$) the slip velocity U_g as:

$$U_g - U_0 = \mathrm{Kn}\,\frac{U_1 - U_0}{\Delta y}. \qquad (3)$$

For no-change in the sign of vorticity at the wall, we require that $(U_0 - U_1) > (U_0 - U_g) = -\mathrm{Kn}\,(U_1 - U_0)/\Delta y$; this is satisfied if $\Delta y > \mathrm{Kn}$ (in nondimensional form). This limit is a significant restriction, especially for spectral-based methods as the one we use in our discretization, where collocation points are clustered very rapidly close to the boundaries. Therefore, spectral and high-order methods that typically provide high-order accuracy are amenable to numerical instabilities of this form.

To circumvent this difficulty and model high-order rarefaction effects accurately, we present here a reformulation of the velocity-slip boundary condition. This will be obtained by an approximate analysis of the motion of a monatomic gas near an isothermal surface. To this end, we consider the tangential momentum flux near the surface. We then assume that approximately half of the molecules are coming from the layer of gas one mean free path (λ) away from the surface with an average tangential velocity of U_λ, while the other half of the molecules are reflected from the wall. Furthermore, we assume that σ_v of the molecules are reflected from the wall diffusively (i.e., with average tangential velocity corresponding to that of the wall), and that $(1 - \sigma_v)$ of the molecules are reflected from the wall specularly (i.e., conserving their average incoming tangential velocity U_λ). Following Schaaf and Chambre (1961), the slip velocity for isothermal surfaces is then

$$U_g = \tfrac{1}{2}[U_\lambda + (1-\sigma_v)U_\lambda + \sigma_v U_w]. \qquad (4)$$

This was also our starting point in the derivation of Eq. (1*a*) including second-order effects (Beskok and Karniadakis, 1994). In this new approach, we first find all locations at a distance (λ) away from the surface. We then perform spectrally accurate interpolations to find the local flow variables (U_λ, T_λ) at these locations, and subsequently evaluate the slip velocity using Eq. (4).

Next we show that Eq. (4) corresponds to a high-order slip boundary condition by simply expanding U_λ in (4) in terms of U_g, using Taylor series expansion. This results in:

$$U_g - U_w = \frac{2-\sigma_v}{\sigma_v}\left[\mathrm{Kn}\left(\frac{\partial U}{\partial n}\right)_s + \frac{\mathrm{Kn}^2}{2}\left(\frac{\partial^2 U}{\partial n^2}\right)_s + \frac{\mathrm{Kn}^3}{6}\left(\frac{\partial^3 U}{\partial n^3}\right)_s + \ldots\right], \quad (5)$$

where the subscript s denotes the surface where slip occurs and n is the normal coordinate.

For the temperature-jump boundary condition, a derivation based on kinetic theory of gases is given in (Kennard, 1938). We propose the following form for the high-order temperature-jump condition by analogy with Eq. (5):

$$T_g - T_w = \frac{2-\sigma_T}{\sigma_T}\left[\frac{2\gamma}{\gamma+1}\right]\frac{1}{\mathrm{Pr}}\left[\mathrm{Kn}\left(\frac{\partial T}{\partial n}\right)_s + \frac{\mathrm{Kn}^2}{2}\left(\frac{\partial^2 T}{\partial n^2}\right)_s + \frac{\mathrm{Kn}^3}{6}\left(\frac{\partial^3 T}{\partial n^3}\right)_s + \ldots\right], \quad (6)$$

which can be re-arranged by recognizing the Taylor series expansion of T_λ about T_g to give a temperature-jump boundary condition similar to Eq. (4) as:

$$T_g = \frac{\dfrac{(2-\sigma_T)}{\mathrm{Pr}}\dfrac{\gamma}{(\gamma+1)}T_\lambda + \sigma_T T_w}{\sigma_T + \dfrac{(2-\sigma_T)}{\mathrm{Pr}}}. \quad (7)$$

If temperature gradients are present along the surface, the velocity slip is modified to include thermal creep (Kennard, 1938). Equation (4) should then include the term $(3\sigma_v/8)(\mu R/P)(\partial T/\partial s)$, where s denotes the direction along the surface.

We have found that these new boundary conditions (Eqs. (4) and (7) are numerically stable for values of Knudsen number up to 0.5, covering essentially the entire slip-flow regime. The previous boundary condition developed in (Beskok and Karniadakis, 1994) caused numerical instabilities for typical flows above $\mathrm{Kn} > 0.1$.

As regards accuracy of the two velocity-slip boundary conditions, i.e., Eq. (1*a*) versus Eq. (4) we can analyze the differences for the two-dimensional pressure-driven incompressible flow between parallel plates separated by a distance h in the slip-flow regime. Assuming isothermal conditions and that the slip is given by Eq. (4), the corresponding velocity distribution is

$$U(y) = \frac{h^2}{2\mu}\frac{dP}{dx}\left[\frac{y^2}{h^2} - \frac{y}{h} + \frac{2-\sigma_v}{\sigma_v}(\mathrm{Kn}^2 - \mathrm{Kn})\right], \quad (8)$$

which is identical to the results obtained using the Eq. (1*a*) up to second-order terms in Kn given below:

$$U(y) = \frac{h^2}{2\mu}\frac{dP}{dx}\left[\frac{y^2}{h^2} - \frac{y}{h} - \frac{2-\sigma_v}{\sigma_v}\frac{\mathrm{Kn}}{1+\mathrm{Kn}}\right)\right]. \quad (9)$$

This can be easily seen by expanding the last term in Eq. (9) as a geometric series expansion in terms of powers of Kn. However, it still contains nonphysical third- and higher-order corrections whereas the new approach gives exact results (within the physical model assumptions). The leading error in Eq. (9) is therefore proportional to $(h^2/2\mu)|(\partial P/\partial x)|\,\mathrm{Kn}^3$.

2.3 Summary of Computational Models. We summarize here, for convenience, all the computational models we have developed which are implemented in the spectral element code μFlow. This code can be used to analyze rarefaction, compressibility, viscous heating, and thermal creep effects and their relative importance. The current capabilities of these codes are summarized in Table 1.

Our incompressible models incorporate both the new (Eq. (4)) and the old boundary conditions (Eq. (1*a*)). There are no fundamental limitations in implementing the new boundary conditions for three-dimensional flows. The new boundary conditions have also been implemented in the version of incompressible flow solver, which solves the momentum equation only. In the following sections, we use the code μFlow to study in detail rarefaction and compressibility effects in gas microflows.

3 Shear-Driven Microflows

Shear-driven flows are encountered in micromotors and microbearings. In the simplest form, the linear Couette flow can be used as a prototype flow to model such flows driven by a moving plate. An analytical solution is easy to obtain given the simplicity of the geometry consisting of two plates separated by a distance h. The flow is driven by moving the upper plate at a constant velocity U_∞; the upper plate temperature is at T_∞ while the bottom plate is assumed to be adiabatic. Also for simplification, viscosity and thermal conductivity are assumed to vary linearly with temperature (i.e., $\kappa \sim \mu \sim T$), and the Prandtl number is fixed (for air $\mathrm{Pr} = 0.72$). For a no-slip Couette flow it is possible to obtain the friction coefficient ($C_f = \tau_w/(0.5\rho U_\infty^2)$) (Liepmann and Roshko, 1957; p. 313):

$$C_f = 2\,\frac{1 + \mathrm{Pr}\,\dfrac{\gamma-1}{3}\,\mathrm{M}_\infty^2}{\mathrm{Re}}, \quad (10)$$

where M_∞ is the Mach number based on the upper plate velocity and temperature, and Re is the Reynolds number based on the channel height h.

To validate the developed code μFlow, we have performed a series of simulations corresponding to top plate temperature $T_\infty = 300$ K and Reynolds number $\mathrm{Re} = 5$. The simulations are performed by using 9 elements with 6th order polynomial expansions per direction in each element. The Mach number M_∞ is specified by varying the driving velocity of the top plate U_∞. Correspondingly, rarefaction effects are specified through the Knudsen number, since

$$\mathrm{Kn}_\infty = \frac{\sqrt{\pi\gamma/2}\,\mathrm{M}_\infty}{\mathrm{Re}}. \quad (11)$$

The variation of friction coefficient as a function of Mach number and corresponding Knudsen number is shown in Fig. 3. The friction coefficient of no-slip compressible flow increases quadratically in agreement with Eq. (10), well above the constant value of the corresponding incompressible flow. The no-slip compressible flow simulations match the theoretical results exactly. For rarefied flows, slip effects change the friction coefficient significantly. Compressible slip-flow results are denoted by open circles in Fig. 3; for the specified conditions they correspond to small deviations from the incompressible slip-flow results obtained from

$$C_f = \frac{2}{\mathrm{Re}}\left[\frac{1}{1 + 2\,\dfrac{2-\sigma_v}{\sigma_v}\,\mathrm{Kn}}\right]. \quad (12)$$

In linear Couette flow the pressure is constant and therefore compressibility effects are due to temperature changes only. As M_∞ increases the temperature difference between the two plates gets larger (due to the viscous heating). Correspondingly, compressibility effects become significant. It is seen in Fig. 3 that significant deviations from incompressible flows (slip/no-slip) are obtained for $\mathrm{M}_\infty > 0.3$. In particular, we investigated a case where the bottom plate is kept at $T_w = 350$ K while the top

Table 1 Flow models and boundary conditions implemented in the μFlow code

Flow type	B.C. type	2-D/3-D	V. Slip	T. Creep	T. Jump	Kn limit
Incomp 1	$\mathcal{O}(\mathrm{Kn}, \mathrm{Kn}^2)$	2-D/3-D	Yes	Yes	Yes	<0.1
Incomp 2	$\mathcal{O}(\mathrm{Kn}^n)$	2-D	Yes	assigned	No	>0.1
Comp	$\mathcal{O}(\mathrm{Kn}^n)$	2-D	Yes	Yes	Yes	<0.5

plate is kept at $T_\infty = 300$ K. The friction coefficient of this case is also given in Fig. 3 (indicated as $\Delta T = 50$ K). The simulation results are shown by solid and open triangles for the no-slip and the slip cases, respectively. The trend is different than the adiabatic bottom plate case. No-slip results show small variation of C_f as a function of M, while for slip flows C_f is reduced significantly as Kn is increased.

The density variation across the channel for compressible no-slip as well as slip flows is shown in Fig. 4 for the case with adiabatic bottom wall. Here, we have normalized the density variation by the top plate density of the no-slip case (solid line). The no-slip cases exhibit large density variations for relatively large values of M_∞. Since the pressure is constant, density variation across the channel is due to the drastic change in temperature, which is attributed to viscous heating effects. However, density variations are reduced in slip flows. There are two reasons for this behavior: First, the shear stress is reduced due to slip, reducing the viscous heating (work done by viscous stresses in the energy equation). Second, a temperature jump exists at the driving (top) plate; there is no temperature-jump on the bottom plate since it is adiabatic.

The flow in a micromotor or a microbearing is more complicated than the linear Couette flow. We therefore consider a shear-driven grooved channel flow in order to model the geometric complexity of these microdevices. A segment of the domain is shown in Fig. 6. The flow separates and starts to recirculate in the grooves even for small Reynolds number flows. In our numerical model we have assumed that the top wall is moving with speed U_∞, and both surfaces are kept at the same temperature (300 K). We also assumed that the geometry repeats itself along the flow direction. Therefore the flow is periodic, and only a section of the channel is simulated. In our simulations the Reynolds number is fixed (Re = 5.0), and the Knudsen number is increased by decreasing the channel gap (and correspondingly the entire geometry is reduced by the same scale to ensure dynamic similarity of channels). Therefore the top wall speed U_∞ is increased to keep the Reynolds number constant, resulting in an increase of flow Mach number according to Eq. (11). The domain is discretized with 12 elements of 6th order polynomial expansions in each direction per element. The accuracy of the results was tested by increasing the order of polynomial expansions (p-refinement), and no significant changes in the results were observed.

In order to identify the accuracy of an incompressible model we compare the results of the incompressible model with the compressible model for the same Reynolds and Knudsen number. In Fig. 5 we present the variation of mass flow rate in the channel versus the drag on the top channel wall normalized with its no-slip incompressible counterpart. Drag reduction due to rarefaction is clearly seen. For example, for Kn = 0.128, about 30 percent drag reduction is observed. Both models predict a reduction in mass flow rate for slip flow. This is due to

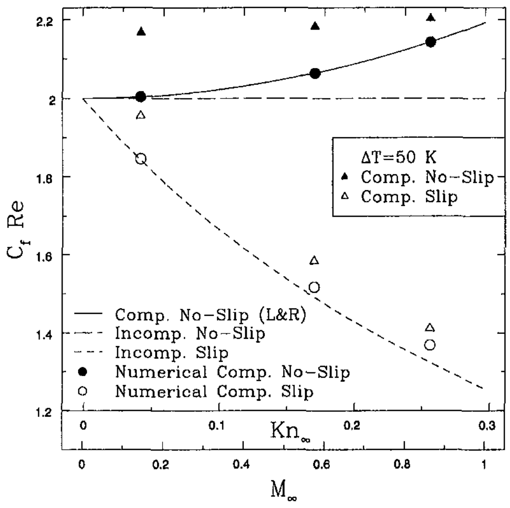

Fig. 3 Variation of skin friction as a function of M and Kn for Couette flow (Re = 5, T_∞ = 300 K)

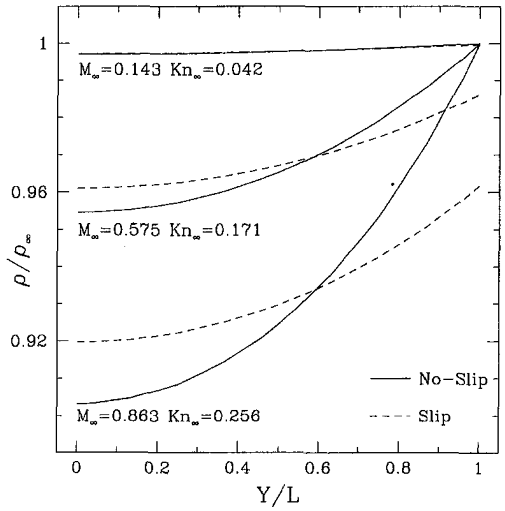

Fig. 4 Couette flow density variation across the channel for various values of M and Kn (Re = 5, T_∞ = 300 K)

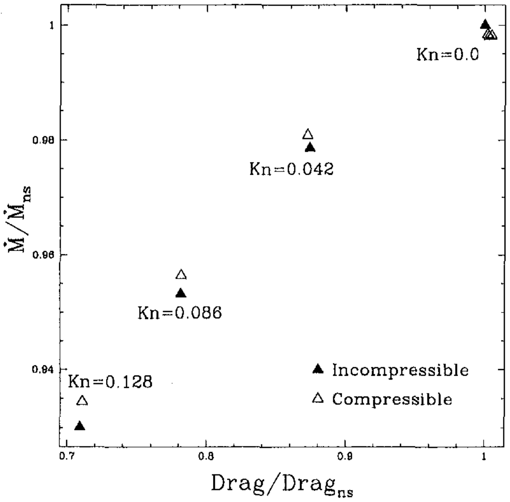

Fig. 5 Variation of mass flow rate versus drag force for the grooved channel, normalized with values of corresponding incompressible no-slip model

the reduction in the volumetric flow rate. The mass flow rate predicted by the incompressible model is less than that of the compressible one due to the inability of the incompressible model to predict variations in density.

The temperature contours for no-slip and slip (Kn = 0.086) flows are given in Fig. 6. The increase in temperature in the middle of the channel is due to viscous heating resulted from large shear stresses in this low Reynolds number flow. The viscous heating for slip flow is less than that of no-slip flow due to the reduction in shear stresses caused by the velocity slip. Also, the temperature of the gas near the walls is not the same with the prescribed wall temperature due to the temperature jump effects. This may create a problem for micro-gas-flow temperature measurements. Finally, the change in the temperature due to the viscous heating seems to be small in magnitude. However, in microflows the *gradients* in temperature can be quite large due to the small length scales even for one degree temperature difference.

4 Pressure-Driven Microflows

We consider here two-dimensional flow between parallel plates at a distance h, with L being the channel length, where $L/h \gg 1$. The flow is sustained by a pressure gradient dP/dx. We also assume that the Reynolds number is relatively low and that the Knudsen number $\mathrm{Kn} < 0.5$. It is therefore possible to simplify the Navier-Stokes equations for a uni-directional, isothermal flow by neglecting the inertial terms $(\rho u_j\,(\partial u_i/\partial x_j))$ in the governing equations. This results in the following analytical solution for the streamwise velocity profile,

$$U(y) = \frac{h^2}{2\mu}\frac{dP}{dx}\left[\frac{y^2}{h^2} - \frac{y}{h} + \frac{2-\sigma_v}{\sigma_v}(\mathrm{Kn}^2 - \mathrm{Kn})\right], \quad (13)$$

where we have used the new high-order boundary conditions (Eq. (4)). Notice that the second-order correction, which is typically omitted in other works (Arkilic et al., 1994), has the opposite sign compared to the first-order term; its contribution may be significant, especially for surfaces for which $\sigma_v < 1$.

The corresponding mass flow rate is computed from $\dot{M} = \rho \int_0^h U(y)dy$, where $\rho = P/RT$, assuming we can still treat the rarefied gas as an ideal gas. Expressing the Knudsen number at a location x as a function of the local pressure, i.e., $\mathrm{Kn} = \mathrm{Kn}_0\, P_0/P$, where the subscript "0" refers to exit conditions, we obtain:

$$\dot{M} = \frac{h^3P_0^2}{24\mu RTL}\,[(\Pi_i^2 - 1) + 12\,\frac{2-\sigma_v}{\sigma_v}(\mathrm{Kn}_0\,(\Pi_i - 1) - \mathrm{Kn}_0^2 \ln \Pi_i)], \quad (14)$$

where we have defined $\Pi_i \equiv P_i/P_0$ as the pressure ratio between inlet and exit. The corresponding flowrate without rarefaction is given by

$$\dot{M}_{ns} = \frac{h^3P_0^2}{24\mu RTL}(\Pi_i^2 - 1). \quad (15)$$

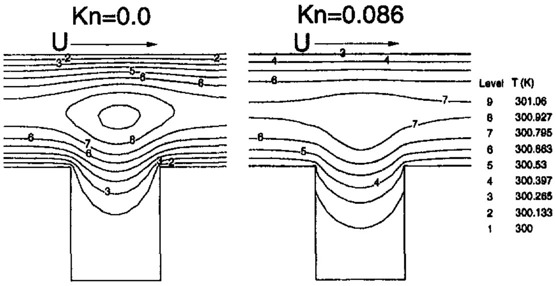

Fig. 6 Temperature contours in no-slip and slip grooved channel

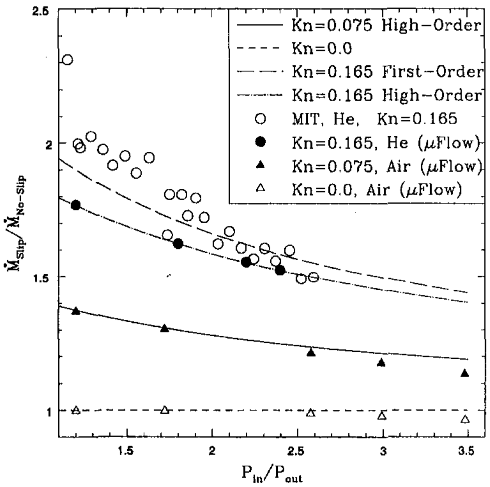

Fig. 7 Variation of mass flow rate normalized with the corresponding no-slip mass flow rate as a function of pressure ratio

Therefore, the increase in mass flow rate due to rarefaction can be expressed as

$$\frac{\dot{M}}{\dot{M}_{ns}} = 1 + 12\,\frac{2-\sigma_v}{\sigma_v}\,\frac{\mathrm{Kn}_0}{\Pi_i + 1} - 12\,\frac{2-\sigma_v}{\sigma_v}\,\mathrm{Kn}_0^2\,\frac{\ln \Pi_i}{\Pi_i^2 - 1}. \quad (16)$$

It is seen from this formula that the effect of the second-order correction is to reduce the increase in mass flow rate due to first-order slip. In other words, the often-used first-order velocity-slip boundary condition over-predicts the mass flowrate for a given pressure ratio Π_i.

Having obtained the mass flowrate, the corresponding pressure distribution along the channel can be easily obtained as

$$1 - \Pi^2 + 12\,\frac{1-\sigma_v}{\sigma_v}\,\mathrm{Kn}_0\,(1 - \Pi) + 12\,\frac{2-\sigma_v}{\sigma_v}\,\mathrm{Kn}_0^2 \ln(\Pi) = B(L - x), \quad (17)$$

where B is a constant such that $\Pi(0) = \Pi_i$. Here we have defined $\Pi(x) = P/P_0$, i.e., the pressure at a station x normalized with the exit pressure. The above equation provides an implicit relation for $\Pi(x)$; the pressure distribution for a first-order boundary condition is obtained explicitly by neglecting the second-order terms $(\mathcal{O}(\mathrm{Kn}^2))$ in Eq. (17).

The formula for the flow rate has been tested directly using experimental data reported by Arkilic et al. (1994) as well as simulation results obtained using our code μFlow. The results are plotted in Fig. 7 in terms of ratio of slip mass flow rate to the corresponding no-slip flow rate predicted by Eq. (16) as a function of pressure ratio. Microchannel helium flow experiments of Arkilic et al. (1994) show a maximum of 10 percent deviation from the first-order theoretical curve. The deviations are more significant especially for low pressure ratio cases. The gain in the mass flow rate due to slip effects is very significant but it is reduced as the pressure ratio is increased. Comparison of the high-order formula with the first-order formula shows about 8 percent deviations for small pressure ratios; the deviations are reduced for higher pressure ratio cases. The numerical predictions for helium flow are consistent with the high-order formula, validating the accuracy of Eq. (16) for helium flows up to the pressure ratios studied in this paper. Both the rarefied air flow (Kn = 0.075) and the no-slip air flow show deviations from the high-order formula especially for high pressure ratios.

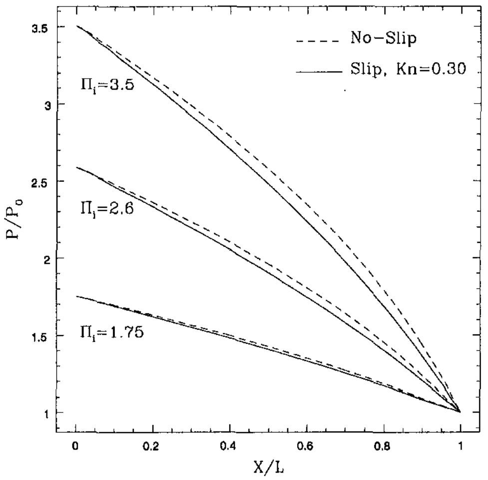

Fig. 8 Computed pressure distribution along the channel center for air flow (results are due to μFlow)

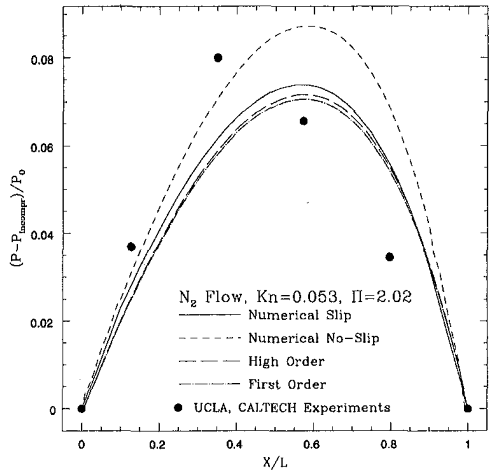

Fig. 10 Deviation from linear pressure drop for Π_i = 2.02, nitrogen flow, (h = 1.25 μm); circles correspond to experimental data by Liu et al. (1993)

The numerical predictions show less mass flow rate than the values predicted by the formula. The reason for this is the pronounced compressibility effects caused by the inertial terms in the Navier-Stokes equations, which were neglected in the derivation of Eq. (16).

Next we examine the pressure distribution along the channel; the experimental results by Liu et al. (1993) and Pong et al. (1994) show a nonlinear pressure distribution. In Fig. 8 we plot the pressure distribution for air flow for different values of pressure ratios (Π_i) obtained from simulation. Also included is the pressure distribution for the corresponding compressible, no-slip flows. The curvature in the pressure distribution is more pronounced for the no-slip compressible flows than the rarefied flows, and this effect gets more dominant as the pressure ratio (Π_i) is increased. For cases with $\Pi_i \leq 1.75$, the pressure drop is practically linear, resembling an incompressible flow.

To investigate the compressibility and rarefaction effects further, deviations from linear pressure distribution for helium and air flows for pressure ratio $\Pi_i = 3.5$ is given in Fig. 9. Here we see that unlike the experimental findings of Liu et al. (1993) and Pong et al. (1994) the curvature in the pressure distribution for helium is less pronounced compared to the air microflow. This trend should be expected since for the same pressure ratio and exit pressure, the local Mach number for helium flow is smaller than the Mach number for air flow. Also the rarefaction effects for helium flow is larger than that of the air flow due to the relatively large mean free-path of helium molecules compared to air. Our simulation results indicated that rarefaction causes the opposite effect than compressibility, which is also evident from the analytical expression (Eq. (17)). This is shown in Fig. 10 where we plot the analytical predictions taking into account first- and second-order Knudsen number effects. The simulation results for nitrogen flow of Kn = 0.156, corresponding to the experiments of Liu et al. (1993), are also included. We see that pressure distribution agrees with the high-order curve. The discrepancies are due to the neglected inertial terms in Eq. (17). The trends of experimental data and the simulations are qualitatively the same. They both predict smaller deviations from linear pressure drop than the corresponding no-slip flow. There are, however, quantitative differences such as the maximum deviation location from linear pressure drop, which is at $X/L \simeq 0.4$ for the experiments, and $X/L \simeq 0.55$ for the simulation. We observed a larger disagreement with the "second generation" experimental data obtained by Pong et al. (1994). Because of current uncertainties in these measurements (a different pressure distribution is measured if the flow direction is reversed) we have not included this comparison in the present paper.

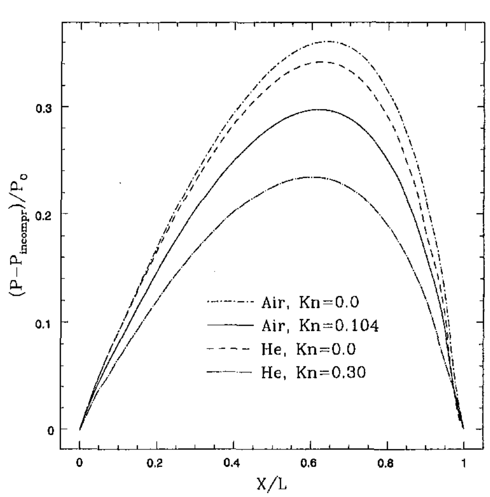

Fig. 9 Deviation from linear pressure drop for air and helium flows (h = 0.65 μm, Π_i = 3.5, P_{out} = 1 atm). Results are due to μFlow)

Before we end this section, we would like to comment on the limitations of the analytic formulas given in (14) and (15). The derivation of these formulas is based on the additional assumptions that density and pressure across the channel at any given location are constant. Thermal effects are also neglected. Due to these limitations the analytic formulas can be applied to low Mach number flows (typically $M_0 \leq 0.10$). In our simulations we have computed non-negligible density variations across the channel, especially for large pressure drop of nitrogen and air flows. The importance of inertial terms compared to the cross flow diffusion terms ($\simeq \mathrm{Re}(h/L)$) is estimated by using the aspect ratio $L/h = 20$, and the Reynolds number obtained by μFlow. The difference between the analytic predictions and the solution of full Navier-Stokes equations is expected to be less than 20% for the most severe cases simulated in this paper. Equation (15) is indeed similar to an incompressible model where $(dP/dx) = (P_{in} - P_{out})/L$, and density is evaluated at average pressure in the channel (i.e., $\rho_{av} = ((P_{in} + P_{out})/2)/RT$).

5 Proposed Benchmark Experiments

There are several difficulties in performing microflow experiments. First, the mass flow rate is quite small ($10^{-13} \sim 10^{-12}$

kg/s) and therefore difficult to measure. Second, pointwise measurements of pressure and temperature are difficult to make; the only pressure distribution obtained experimentally so far is due to Liu et al. (1993). Finally, the size and shape of microchannels are difficult to characterize. In the following, we introduce ideas for specific experiments that can alleviate some of these difficulties. The primary objective is the generation of accurate data bases for validating predictive computational models for gas microflows, and developing absolute standards for measurements.

Pressure-Driven Microflow. The purpose of this experiment is to measure and correlate the mass flowrate and pressure drop in microchannel flows. The pressure distribution in the channels should also be measured to identify compressibility effects. A critical aspect of this benchmark experiment is the ability to modify and characterize the microchannels. Many different channel cross-sections, such as rectangular as well as triangular (in the shape of V-grooves) should be etched. Before the final assembly of the channels, surface characteristics, shape and dimensions of the channels should be accurately measured. The purpose of using various channel cross-sections in these benchmark experiments is to develop the concept of the equivalent "hydraulic diameter" for unified pressure drop predictive models like the Moody diagram in large diameter pipes (Schlichting, 1979).

We propose to perform pointwise pressure measurements by connecting the tap holes on microchannels to a micro-measurement system. The micro-measurement system we propose consists of two volumes separated by a thin, flexible diaphragm, which provides a sensitive measure of the pressure difference between the pressure of two chambers it separates. This provides comparison of pressure in a micro-volume (connected to the microchannels), with a large, and hence easily measured volume of fluid (measurement chamber). The curvature and deflection of the diaphragm will be measured optically, the pressure in the measurement chamber will be adjusted till the deflection of the diaphragm vanishes (i.e., the pressure on both sides of the diaphragm are identical), and the pressure at the measurement chamber will be directly recorded. Our approach of measuring point wise pressure in microchannels differs from that of Liu et al. (1993), where micro-pressure sensors are manufactured adjacent to the microchannels. The proposed measurement system here, is based on pressure measurements of much larger volume of fluids, and therefore it is expected to be more accurate than the measurement system used by Liu et al. (1993) and Pong et al. (1994).

Shear-Driven Microflow. The purpose of this experiment is to study the rarefaction effects without the adverse effects of compressibility, which are present in pressure-driven microchannel flows. Here we consider a device similar to the Taylor-Couette device. The flow is driven by one of the surfaces of the channels which is moving along the flow direction. The inner cylinder is rotated at a prescribed rate; the corresponding torque balancing the shear stress on the inner surface is measured. The gap between two cylinders should be kept in the order of a micron. The cylinder radius and height should be a few centimeters; this is necessary for the validity of "thin gap" approximation. Maximizing the flow surface has several advantages, e.g., more reliable data can be obtained as the magnitude of the torque will be large, and the end-effects can be neglected. The micro-Taylor-Couette device is conceptually a large-scale device with micron-scale flow gap. Therefore, making such a device does not require fabrication techniques used in MEMS.

Compressibility can be neglected for moderate rotational speeds. However, increase in the rotational speed results in significant compressibility and viscous heating effects. The experiments should be performed in a temperature and pressure controlled environment. Preferably one of the cylinder surface should be insulated, and cylinder surface temperature and pressure should also be measured. This way, compressibility and viscous heating effects can be identified. One other advantage of performing the experiments in a pressure-controlled environment is the ability to vary the Knudsen number by either adjusting the pressure in the apparatus or changing the gas.

6 Summary

In this paper, we have investigated the combined effects of compressibility and rarefaction in gas microflows. The flow regime we have considered corresponds to slip-flow, with the Knudsen number $\mathrm{Kn} \leq 0.3$. The geometry we have primarily considered is a flat channel in order to compare with available experimental results and approximate theoretical models. However, the numerical models we have developed are appropriate for complex geometries such as the grooved microchannel flow that we modeled in Section 3. Complex geometries are of great interest due to their practical use in fabricating channel networks in micro-scales consisting of sudden expansions and contractions, bends, branches, etc. (Zohar, 1994).

For pressure-driven channel flows, we have found that a nonlinear pressure distribution is established in microchannels in accordance with the experimental results of Liu et al. (1993). In particular, for large pressure drop in air or nitrogen flow, compressibility effects are dominant and the curvature in the pressure distribution plot is very pronounced. However, in more rarefied flows such as helium flow, a pressure distribution with smaller curvature is obtained. In other words, our simulation results as well as approximate analytical models suggest that *rarefaction negates compressibility,* in contrast with experimental findings of Pong et al. (1994).

We have demonstrated that compressibility for shear-driven flows is negligible, and thus rarefaction dominates the momentum and energy transport. In particular, drag-reduction experienced in micro-devices can be clearly explained by rarefaction effects. Also, viscous heating effects is observed to create considerable temperature gradients in micron-sized domains even for iso-thermal boundary conditions.

Based on the studies presented here we have proposed a set of benchmark experiments designed to validate the slip-flow theory in modeling microflows. In particular, we focus on the combined rarefaction and compressibility effects and suggest specific pressure distribution and mass flowrate measurements in microchannels of various crossections. In addition, we propose a new experiment isolating rarefaction effects only by measuring the shear stress (torque) in a micro-Taylor-Couette device. These experiments are also intended for the experimentalists to perform metrology experiments and establish secondary standards. Moreover, the results of these experiments will be valuable to groups developing CAD systems for micromechanical research and development.

Acknowledgments

We are very grateful to S. A. Tison of NIST, C. M. Ho of UCLA and K. Breuer of MIT for making their experimental data available to us. This work was supported by NSF grant ECS-90-23760 under the supervision of Dr. George Lea.

References

Arkilic, E., Breuer, K. S., and Schmidt, M. A., 1994, "Gaseous Flow in Microchannels," ASME, FED-Vol. 197, *Application of Microfabrication to Fluid Mechanics,* pp. 57–66, ASME.

Beskok, A., and Karniadakis, G. E., 1992, "Simulation of Slip-Flows in Complex Micro-Geometries," ASME, DSC-Vol. 40, pp. 355–370.

Beskok, A., and Karniadakis, G. E., 1993, "Simulation of Heat and Momentum Transfer in Complex Micro-Geometries," AIAA Shear Flow Conference July 6–9, Florida, AIAA 93-3269.

Beskok, A., and Karniadakis, G. E., 1994, "Simulation of Heat and Momentum Transfer in Complex Microgeometries," *AIAA J. Thermophysics & Heat Transfer,* Vol. 8 (4), pp. 647–655.

Beskok, A., and Karniadakis, G. E., 1996, "A Spectral Element Method for Subsonic Viscous Flows," in progress.

Bryzek, J., Petersen, K., and McCulley, W., 1994, "Micromachines on the March," *IEEE Spectrum*, pp. 20–31.

Gabriel, K., Javris J., and Trimmer W., 1988, "Small Machines, Large Opportunities," Technical report, NSF.

Harley, J. C., Huang, Y., Bau, H. H., and Zemel, J. N., 1995, "Gas Flow in Micro-Channels," *Journal of Fluid Mechanics*. Vol. 284, pp. 257–274.

Howe, R. T., Muller R. S., Gabriel, K. J., and Trimmer W. S., 1990, "Silicon Micromechanics: Sensors and Actuators on a Chip," *IEEE Spectrum*, pp. 29–35.

Kennard, E. H., 1938, *Kinetic Theory of Gasses*, McGraw-Hill, New York.

Knudsen, M., 1909, "Die gesetze der molekularströmung und der inneren riebungsströmung der gase durch röhnen," *Ann. Phys*, Vol. 33, pp. 75–130.

Kruger, A. J., Larmit, A. J. F., and de Wit, M. H., 1970, "Flow of a Rarefied Gas Through a Long Capillary (Cylindrical or Bounded by Planes) Generated by a Temperature Gradient," Proc. 7th *Int. Symp. on Rarefied Gas Dynamics*, pp. 1015–1022.

Liepmann, H. W., and Roshko, A., 1957, *Elements of Gas Dynamics*, Wiley.

Liu, J. Q., Tai, Y. C., Pong, K. C., and Ho, C. M., 1993, "Micromachined Channel/Pressure Sensor Systems for Micro Flow Studies," 7th Int. Conf. on Solid-State Sensors and Actuators, pp. 995–998, Transducers '93.

Loyalka, S. K., and Hamoodi, S. A., 1990, "Poiseuille Flow of a Rarefied Gas in a Cylindrical Tube: Solution of Linearized Boltzmann Equation," *Phys. Fluids A*, Vol. 2 (11), pp. 2061–2065.

Mehregany, M., Nagarkar, P., Senturia, S. D., and Lang, J. H., 1990, "Operation of Microfabricated Harmonic and Ordinary Side-Drive Motor," IEEE Micro Electro Mechanical System Workshop, Napa Valley, CA.

Muntz, E. P., 1989, "Rarefied Gas Dynamics" *Ann. Rev. Fluid Mech.* Vol. 21, pp. 387–417.

O'Connor, L., 1992, "MEMS: Microelectromechanical Systems," *Mechanical Engineering*, Vol. 114, No. 2, pp. 40–47.

Pfahler, J., Harley, J., Bau, H. H., and Zemel, J., 1991, "Gas and Liquid Flow in Small Channels," ASME, Vol. 32, pp. 49–59.

Pong, K. C., Ho, C. M., Liu, J., and Tai, Y. C., 1994, "Non-linear Pressure Distribution in Uniform Microchannels," ASME, FED-Vol. 197, *Application of Microfabrication to Fluid Mechanics*, pp. 51–56, ASME.

Reed, M. L., 1993, "Near Term Applications of Microelectromechanical Systems," *4th International Symposium on Micro Machine and Human Science*, Nagoya, Japan, pp. 77.

Saxena, S. C., and Joshi, R. K., 1981, "Thermal Accommodation and Adsorption Coefficients of Gasses," Vol. 1, 2, Series Editors Y. S. Touloukian, C. Y. Ho, McGraw-Hill/CINDAS Data Series On Material Properties, McGraw-Hill, New York.

Schaaf, S. A., and Chambre, P. L., 1961, *Flow of Rarefied Gases*, Princeton University Press, Princeton, NJ.

Schlichting, H., 1979, *Boundary-Layer Theory*, 7th ed., McGraw-Hill, New York.

Shoji, S., and Esashi, M., 1994, "Microflow Devices and Systems," *Journal of Micromechanics and Microengineering*, Vol. 4 no 4, pp. 157–171.

Tai, Y. C., Fan, L. S., and Muller, R. S., 1989, "IC-processed micro-motors: design, technology, and testing," *IEEE Micro Electro Mechanical System Workshop*, Salt Lake City, Utah.

Thompson, S. L., and Owens, W. R., 1975, "A Survey of Flow at Low Pressures," *Vacuum*, Vol. 25, pp. 151–156.

Tison, S. A., 1993, "Experimental Data and Theoretical Modeling of Gas Flows Through Metal Capillary Leaks," *Vacuum*, Vol. 44, pp. 1171–1175.

Tison, S. A., 1994, Private communications.

Wilding, P., Pfahler, J., Zemel, J. N., Bau, H. H., and Kricka, L. J., 1994, "Manipulation and Flow of Biological Fluids in Straight Channels Micromachined in Silicon," *Clinical Chemistry*, Vol. 40, No. 1, pp. 43–47.

Zengerle, R., and Richter, M., 1994, "Simulation of Microfluid Systems," *Journal of Micromechanics and Microengineering*, Vol. 4, No. 4, pp. 192–204.

Zohar, Y., 1995, Private communications.

Small Silicon Pressure Transducers for Space-Time Correlation Measurements in a Flat Plate Boundary Layer

L. Löfdahl
Professor,
Thermo and Fluid Dynamics,
Chalmers University of Technology,
412 96 Göteborg, Sweden

E. Kälvesten
Research Assistant.

G. Stemme
Professor.

Department of Signals, Sensors
and Systems,
Royal Institute of Technology,
100 44 Stockholm, Sweden

Silicon based pressure sensors have been used to measure turbulent wall-pressure fluctuations in a two-dimensional flat plate boundary layer, $Re_\theta = 5072$. The side lengths of the diaphragms were 100 μm ($d^+ = 7.2$) and 300 μm ($d^+ = 21.6$), giving a ratio of the boundary layer thickness to the diaphragm side length of the order of 240 and a resolution of eddies with wave numbers less than ten viscous units. Power spectra were measured for the frequency range 13 Hz $< f <$ 13 kHz. Scaled in outer and inner variables a clear overlap region between the mid and high frequency parts of the spectrum is shown. In this overlap region the slope was found to be ω^{-1}, while in the high frequency part it was ω^{-5}. Correlation measurements in both the longitudinal and transversal directions were performed and compared to other investigations. Longitudinal space time correlations, including the high frequency range, indicated an advection velocity of the order of half the freestream velocity. A broad band filtering of the longitudinal correlation showed that the high frequency part of the spectrum is associated with the smaller eddies from the inner part of the boundary layer, resulting in a reduction of the correlation.

1 Introduction

To increase our knowledge of boundary-layer dynamics, it is important to understand the physics of the fluctuating wall pressure that develops beneath a turbulent boundary layer. From the transport equations for the Reynolds stresses, it is evident that these pressure fluctuations are coupled, via complex interactions, to the mean shear as well as to velocity fluctuations. From an engineering point of view, interest in fluctuating pressure fields arises because the unsteady surface pressures are sources of undesired noise and vibrations. To this end, the characteristics of the fluctuating pressure have been extensively studied in analytical and experimental investigations. Reviews of earlier works may be found in e.g., Blake (1986), Eckelmann (1990), and Keith et al. (1992).

Theoretically the problem has been addressed by Panton and Linebarger (1974) who performed numerical calculations of pressure spectra and examined the contributions from turbulent sources in various regions of the boundary layer. Also direct numerical simulations (DNS) have been used; and Spalart (1988), Kim (1989), and Choi and Moin (1990) examined turbulent channel flows for statistical and spectral features of fluctuating wall pressures. From an experimental point of view, the knowledge of the pressure fluctuations in turbulent flows is far from being as comprehensive as that of the velocity fluctuations. However, in the case of wall-pressure fluctuations, some general facts have been presented, like the order of magnitude of the root mean square (rms) value, the general shape of the power spectra, and the space-time correlation characteristics, see, Harrison (1958), Willmarth and Wooldridge (1962), Bull (1967), Bull and Thomas (1976), Lauchle and Daniels (1987), Schewe (1983), Blake (1986), and Farabee and Casarella (1991). A shortcoming in many of these experiments is the quality of the data. In the low frequency range the data may be contaminated by facility-related noise, while in the high frequency range the spatial resolution of the transducers limits the accuracy. Usually the former difficulty is circumvented by noise cancellation techniques, e.g., Lauchle and Daniels (1987), or measurements on a free-flight glider. The spatial resolution problem, at the other end of the spectrum, is more difficult to handle; small pressure sensors are of course the ultimate solution, but also highly viscous fluids and pinhole microphones have been used. The latter type of sensor has been questioned by e.g., Bull and Thomas (1976), who concluded that the use of pinhole sensors in air may lead to errors in the measured spectra. On the other hand, Farabee (1986), Gedney and Leehey (1989), and Farabee and Casarella (1991) have concluded that the pinhole sensors are effective for wall pressure measurements. Hence, the validity of pinhole microphone measurements is an open question. According to Keith et al. (1992), the spatial extension of the transducer is a key feature in studies of pressure fluctuations, since the pressure sensors must be sufficiently small to resolve turbulent scales of the order of ten viscous lengths. It is also necessary that the sensor frequency response is clearly established. Today silicon micro fabrication technology offers a unique opportunity to overcome these difficulties, since it is possible to fabricate small and fast responding sensors fulfilling the requirements on spatial and temporal resolution.

The purpose of the current experiment was to use silicon based pressure transducers for studies focused on the high-frequency portion of the wall pressure spectrum. Our aim was a large value of the ratio between the boundary-layer thickness, δ, and the transducer diaphragm side length. This was obtained using transducers with diaphragm side lengths, a, of 100 and 300 μm, which in turn correspond to δ/a of 240 and 80, respectively. Our small sensors resolved the high frequency range down to wave numbers less than ten viscous units. In the experiment, all sensor characteristics were established using static as well as dynamic calibrations. Measurements in the turbulent boundary layer yielded rms values and power spectra; and from space-time correlation analysis advection velocities of the pressure fluctuations were determined. (In this paper, we use the

---

Contributed by the Fluids Engineering Division for publication in the JOURNAL OF FLUIDS ENGINEERING. Manuscript received by the Fluids Engineering Division March 27, 1995; revised manuscript received October 24, 1995. Associate Technical Editor: P. R. Bandyopadhyay.

definition of advection given by Webster's New Collegiate Dictionary, viz. "the horizontal movement of a mass of air that causes changes in temperature or in other physical properties of the air".) All our data were compared to other works e.g., Schewe (1983), Choi and Moin (1990) and Farabee and Casarella (1991), and as a guideline for the scaling the results of Keith et al. (1992) was used.

2 Silicon Based Pressure Transducers

The introduction of silicon technology into fluid dynamics offers new possibilities in the design of extremely small sensors for the study of turbulent phenomena. Silicon based sensors for determining fluctuating velocity and pressure have been developed, fabricated and tested by Löfdahl et al. (1992) and (1994).

The first generation of small silicon based pressure transducers, with a diaphragm side length of 1000 μm, was developed and tested by Löfdahl et al. (1993). The important issues were to find a reliable method of detecting the diaphragm deflection, to determine the resolution, and to manage the operation of a sensor with a diaphragm thickness less than one micron. Further improvements of these sensors were reported by Löfdahl et al. (1994). In this work, the emphasis was on reducing the size of the diaphragm area. This second generation of pressure transducers was fabricated with the sensing area consisting of a small (100 × 100 μm and 300 × 300 μm) and thin (0.4 μm) diaphragm, as shown in Fig. 1. The pressure-induced diaphragm deflection is detected using two active piezoresistive polysilicon strain gauges located on the diaphragm. Two other passive gauges are integrated close to the diaphragm, making it possible to connect the four gauges in a temperature insensitive Wheatstone bridge. The requirement that the diaphragm deflection be independent of the ambient pressure leads to the inclusion of a vent channel in order to equalize the static air pressure difference between the cavity and the ambient.

The pressure transducer is fabricated using the same processes as in the fabrication of integrated circuits including batch fabrication, photolithographical techniques, film deposition and different etch procedures. In the fabrication of the silicon sensors the surface micromachining technique is employed, implying that all processing is made from the front side of the silicon wafer giving extremely high precision in the sensor dimensions. The free-standing diaphragm and vent channel are created by the lateral removal of a sacrificial oxide, which is accessible through a number of etch channels connected to the sides of the cavity and the vent channel. As shown in Fig. 1, the vent outlet for each sensor is in the end of the chip opposite the pressure sensor diaphragm, about 3 mm distant, in Kälvesten et al. (1996) a model developed for sensor modeling shows that this vent channel length is more than sufficient. For the multi-sensor array, each pressure sensor has its own vent channels with separate outlets with a spacing of 2 mm.

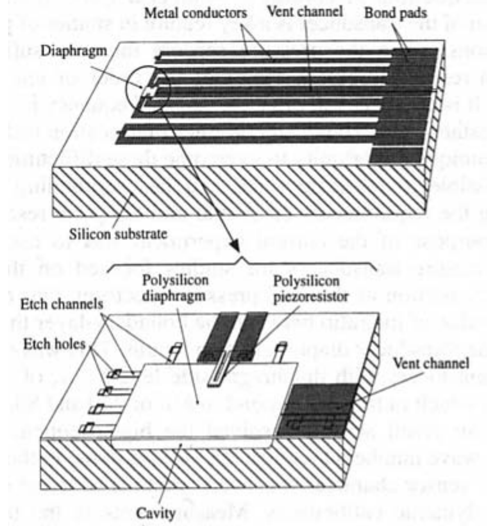

Fig. 1 The sensor and a close-up of the pressure sensitive diaphragm. The silicon chip is 4 × 2 × 0.5 mm and the diaphragm area is 100 × 100 μm and 300 × 300 μm.

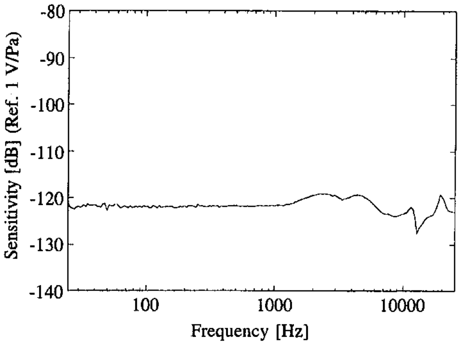

Fig. 2 Frequency response of the pressure sensor with diaphragm side length 100 μm

The frequency characteristics of the transducer were measured using a Brüel and Kjaer Type 4226 closed coupler with a built-in reference microphone at a sound pressure level of 114 dB. As shown in Fig. 2, the frequency response is flat within ±3 dB in the range 10 Hz to 10 kHz. The deviations for high frequencies are due to interference in the coupler and are not a characteristic of the microphone. This conclusion is supported by the fact that the larger similarly fabricated 300 μm diaphragm transducer reveals the same deviations. The acoustical sensitivity of the 100 μm sensor is 0.9 μV/Pa for a bridge supply voltage of 10 V. A low temperature sensitivity of about 1000 ppm/°C is noted. Table 1 summarizes some characteristics of the pressure transducers. Further details of the calibration procedure and the fabrication may be found in Löfdahl et al. (1994) or Kälvesten et al. (1994).

3 Experimental Arrangement

All measurements were conducted in a closed low-speed wind tunnel. To generate the turbulent boundary layer, a flat plate of 2.5 m in length was positioned in the horizontal symmetry plane of the test section (1.25 × 1.80 × 3.00 m). Velocity data were obtained using standard hot-wires mounted on a traverse system. All boundary-layer parameters were calculated from these data. A freestream velocity of $U_\infty = 30$ m/s, corresponding to $\mathrm{Re}_\theta = 5072$ was studied. At the measuring position this corresponds approximately to a boundary-layer thickness, δ, of 24 mm, a displacement thickness, δ^*, of 3.79 mm, and a friction velocity, u_τ, of 1.10 m/s. For the current transducers, a dimensionless diaphragm size, d^+, would be 7.2 and 21.6, respectively. (Here d^+ is defined as $d^+ = u_\tau a/\nu$, where a is a characteristic length, in our case the side length of the diaphragm.) Table 2 summarizes some data and gives a comparison to corresponding measurements of Schewe (1983), Choi and Moin (1990), and Farabee and Casarella (1991). The friction velocity was obtained by fitting the data to the log-law. These

Table 1 Some measured characteristics of the pressure sensor

Frequency response	:10-10000 Hz (±3 dB)
Pressure sensitivity at 10 V	:0.9 μV/Pa (α = 100 μm)
Temperature sensitivity (TCS)	:1000 ppm/°C
Noise (A-weighted)	:90 dB(A)

Table 2 Typical boundary layer and sensor characteristics for different investigations

Investigation	U_∞ [m/s]	u_τ [m/s]	τ_w [Pa]	δ [cm]	δ^* [cm]	Re_θ	Re_τ	d [mm]	$d^+ = du_\tau/\nu$	d/δ^*
Present (1994)	30	1.10	1.43	2.4	0.38	5072	1737	0.1, 0.3 (*a*)	7.2, 21.7	0.026 (0.079)
Schewe (1983)	6.3	0.28	0.09	3.0	0.46	1400	553	1 (*d*)	19	0.22
Choi and Moin (1990)	1.8	0.11	0.014	2.54	0.36	285	184	2.5 (Δx)	17.6	0.696
Farabee and Casarella (1991)	28.3	1.07	1.36	2.78	0.43	6025	2010	0.79 (pinhole)	56	0.18

data agreed very well with an empirical formula for the current Reynolds number. To remove facility related noise the signal of the pressure fluctuations was filtered, so that the measurements include only frequencies in the range 13 Hz $< f <$ 13 kHz, ($9.6 \times 10^{-3} < \omega\delta^*/U_\infty < 9.6$). For the correlation measurements, two other narrower frequency bands have been investigated; one high band of 300 Hz $< f <$ 13 kHz ($0.22 < \omega\delta^*/U_\infty < 9.6$) and one low band of 30 Hz $< f <$ 1000 Hz ($0.022 < \omega\delta^*/U_\infty < 0.74$).

The pressure transducers were flush mounted on the flat plate. To obtain a smooth surface the following mounting procedure was performed; first, a square hole, slightly larger than the silicon chip, was made through the circuit card. A tape was then mounted on the front of the card hanging over the edges with the adhesive side down. Second, from the back of the circuit card the silicon chip was carefully placed on the adhesive side of the tape. Epoxy was then poured from the backside to fill up the air gap between the chip and the edges of the hole. After drying, the tape was removed and a perfectly flat and smooth surface was achieved. In the final step, the circuit card was lowered and glued into the flat plate.

To obtain minimum aerodynamic disturbances all electrical connections were led through the circuit card and soldered on the front. This produces a very smooth surface with the largest irregularities of the order of 30 μm, which is less than the estimated Kolmogorov length scale of 50 μm, see Löfdahl et al. (1994). Errors due to bonding wires were judged to be negligible since the wires were located downstream of the diaphragm and the normal extension was less than the Kolmogorov length. To minimize electrical disturbances the circuit card was equipped with a ground plane on the back and all electrical wires to the amplifier were shielded. For the silicon pressure sensors, disturbances due to internal noise as well as external influences were shown to be less than a corresponding pressure level of 0.6 Pa (see also Fig. 5). To confirm that vibrations of the plate did not affect the measurements, spectral measurements were conducted for a free stream velocity of 30 m/s with the sensor mounted on the plate but shielded acoustically from the flow. The result showed a negligible difference as compared with the results obtained with the sensor unshielded and for zero free stream velocity. All standard velocity and pressure measurements were quite straightforward. The uncertainty in the results was estimated to be much less than 1 percent.

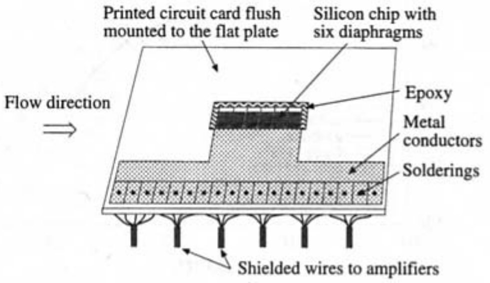

Fig. 3 The six-diaphragm microphone glued with epoxy into the printed circuit card to obtain a smooth surface

For the space and space-time correlation measurements, a silicon chip with a longitudinal array of six diaphragms with a spacing in the streamwise direction, x_1, of 2.000 mm, corresponding to x_1/δ^* of 0.53, between each diaphragm was employed (see Fig. 3). For the transverse correlations, the six diaphragm chip was rotated in the plane. This was accomplished by rotating the printed circuit card in a special revolving section of the plate.

4 Results and Discussion

In this section measured wall pressure fluctuations beneath a fully developed two-dimensional flat plate turbulent boundary layer are presented. The quantities studied are the rms amplitude, the power spectra and the space-time correlations, the latter giving the advection velocities. The definition of a double-sided power spectrum is

$$p_{\rm rms}^2 = 2\int_0^\infty \phi(\omega)d\omega,$$

where $p_{\rm rms}$ is the rms fluctuating wall-pressure, $\phi(\omega)$ the double-sided wall pressure spectral density, and ω the angular frequency. Noteworthy is that the definition of $\phi(f) = 2\pi\phi(\omega)$ is used, and that some data of other authors (included in the figures) are divided by a factor of 2 for consistency.

4.1 Rms Pressure Fluctuation. The rms values of the wall pressure fluctuations, $p_{\rm rms}/\tau_w$, are shown as functions of the Reynolds number, Re_θ, in Fig. 4, where we have included measurements of Bull (1967), Schewe (1983), Blake (1986), Lauchle and Daniels (1987), and Farabee and Casarella (1991) and DNS of Spalart (1988), and Choi and Moin (1990). (The numbers indicated in the figure correspond to the transducer sizes expressed in terms of d^+ units as given by the author in context.) A general increase in $p_{\rm rms}/\tau_w$ can be seen as the diaphragm size decreases, see e.g., Schewe (1986). Our measurements underline that a smaller d^+ implies higher rms pressures due to better spatial resolution. In our work the d^+ range, 7.2

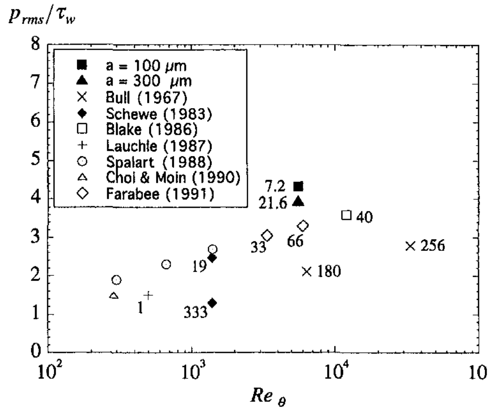

Fig. 4 Dependence of normalized rms pressure fluctuation on Reynolds number, Re_θ (uncertainty less than 10 percent)

Table 3 List of contributions to p^2_{rms}/τ^2_w for the presence fluctuations for different spectral regions

Frequency range	Inner variable scaling	Present investigation for $a = 100\ \mu m$.	Farabee and Casarella (1991)
Low		—	0
Mid	$\omega\nu/u_\tau^2 < 100/\mathrm{Re}_\tau$	9.6	1.7
Overlap	$100/\mathrm{Re}_\tau < \omega\nu/u_\tau^2 < 0.30$	13.9	3.3
High	$0.30 < \omega\nu/u_\tau^2$	0.7	4.8[a]

[a] This contribution is derived from Bull (1967).

$\le d^+ \le 21.6$, was considerably smaller than in the other works, where d^+ varied from 19 to 330. However, Lauchle and Daniels (1987) reported measurements in the range $0.7 \le d^+ \le 1.5$ but their data were taken in a pipe flow with glycerine as working fluid and it is therefore difficult to make a direct comparison to the other data in Fig. 4. Our rms values were obtained in two ways: by direct measurement with a true rms voltmeter and an integration of the pressure spectrum. A comparison of the two methods yielded the same value. Noteworthy in Fig. 4 is that the pinhole measurements of Farabee and Casarella (1991) are lower than ours, in spite of the fact that these measurements were taken in approximately the same Reynolds number range. We divided the frequency range into four subdomains: low, mid, overlap and high. It can be shown (see Farabee and Casarella, 1991) that the low frequency region of the pressure spectra contributes very little to the rms value, and hence, this part may be neglected. In our direct integrations of the different subdomains we obtained for the mid-frequency region, $\omega\nu/u_\tau^2 < 100/\mathrm{Re}_\tau$, $p^2_{\mathrm{rms}}/\tau^2_w = 9.6$, for the overlap region, $100/\mathrm{Re}_\tau < \omega\nu/u_\tau^2 < 0.30$, $p^2_{\mathrm{rms}}/\tau^2_w = 13.9$, and for the high frequency region, $\omega\delta^*/u_\tau^2 \gtrsim 0.3$, $p^2_{\mathrm{rms}}/\tau^2_w = 0.7$. Comparing these data to corresponding calculations of Farabee and Casarella (1991), see Table 3, some deviations may be noted. However, it is important to be aware of the different assumptions made in the two calculations. Farabee and Casarella (1991) assumed that the spectra follow an ω^{-1} scaling for the overlap region and in order to ensure that sensor resolution limitations did not artificially decrease the contribution in the high frequency region, an empirical equation given by Bull (1979) was used. Comparisons to the DNS of Choi and Moin (1990) are difficult to make since these were conducted at far too low Reynolds numbers implying a relatively narrow spectrum with a limited high frequency region. The channel flow simulations of Spalart (1988) reach slightly higher Reynolds numbers and reveal the expected increase in magnitude as the Reynolds number grows, fully in agreement with the measurements. Our smallest transducer has a d^+ value of about seven viscous units, i.e., less than the ten viscous units which are required for measurements of the high frequency components, see Keith et al. (1992). This small d^+ value corresponds to a spatial extension of about two Kolmogorov lengths of the flow in context and this sensor should resolve the smallest eddies of the current flow field. For our larger transducer the spatial extension is about twenty wall units and a certain attenuation of the high frequency eddies must be expected. This is very well reflected in Fig. 4, where our smaller transducer gives about 8 percent larger rms values than the larger one.

4.2 Power Spectra of the Pressure Fluctuations. Figure 5 shows the power spectra for the two different diaphragm side lengths. The noise level is well below the signal levels for the interesting frequency range. As found in Blake (1986) and Choi and Moin (1990), the present silicon sensors show a f^{-1} dependence in the intermediate frequency range and a f^{-5} dependence in the high frequency range. Moreover, the noise spectrum exhibit a f^{-1} dependence as should be expected in polysilicon resistors, according to Jang (1990). (The noise level was obtained for the 100 μm sensor mounted in situ inside the wind tunnel and at zero flow.) The slope of the power spectrum will be discussed further later in this section.

Farabee (1986) concluded that the spectral contributions at high frequencies result from turbulent velocity fluctuations in the wall region and that the low frequency contributions were generated by fluctuations across the entire boundary layer. Based on this, separate scaling laws were suggested for the low and high frequency portions of the spectra. Keith et al. (1992) made a comparison of wall pressure spectra using the nondimensional forms of three commonly used scaling laws. For the low frequency portion of the spectra they suggested an outer scaling in the form $10 \log [\phi(\omega)/\rho^2\delta^*U_\infty^3]$ versus $\omega\delta^*/U_\infty$. For the high frequency portion they proposed a scaling with the inner wall variable $10 \log [\phi(\omega)u_\tau^2/\tau_w^2\nu]$ versus $\omega\nu/u_\tau^2$.

Our wall pressure spectra, scaled in outer variables, are shown in Fig. 6. The data of Carey (1967), Schewe (1983), Farabee and Casarella (1991) and Choi and Moin (1991) are included in the figure for comparison. Due to limitations in the spatial

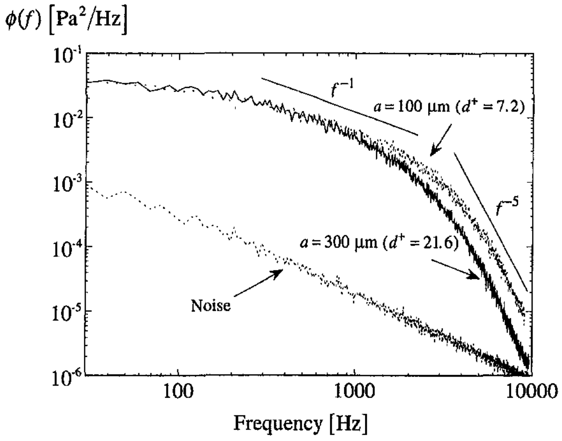

Fig. 5 Power spectra of the pressure fluctuations for sensor diaphragm side lengths of $a = 100$ and $300\ \mu m$ ($d^+ = 7.7$ and 23.1), $\mathrm{Re}_\theta = 5072$ (uncertainty less than 1 dB)

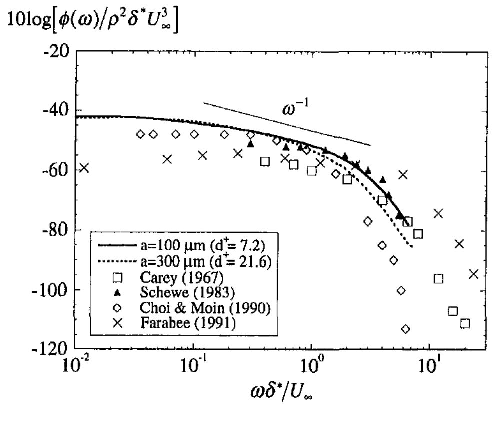

Fig. 6 Nondimensional wall pressure spectra scaled on outer variables, $\mathrm{Re}_\theta = 5072$ (uncertainty less than 1 dB)

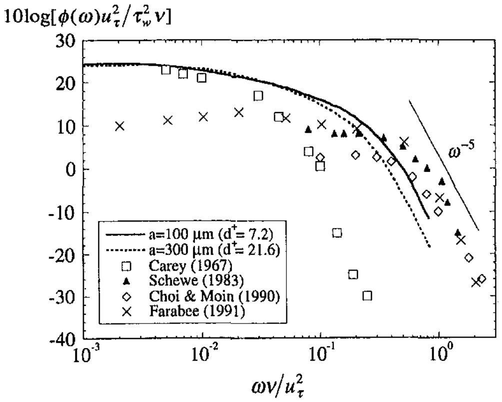

Fig. 7 Nondimensional wall pressure spectra scaled on inner variables, $Re_\theta = 5072$ (uncertainty less than 1 dB)

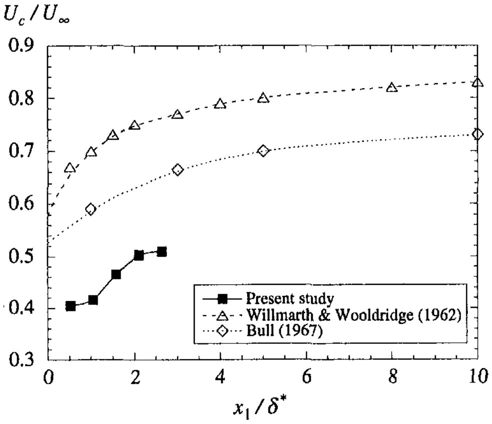

Fig. 9 Local advection velocity of the pressure producing eddies for various frequency ranges, $Re_\theta = 5072$ (uncertainty less than 10 percent)

resolution, the 300 μm diaphragm yields accordingly lower values than the 100 μm for the high frequency part of the spectrum, as expected because of the spatial attenuation.

It has been pointed out by Bradshaw (1967), Panton and Linebarger (1974) and Farabee and Casarella (1991) that if an overlap region exists between the mid- and high frequency regions then the spectrum for this region should exhibit an ω^{-1} dependence. This overlap region is assumed to be associated with the turbulence activity in the log-law region of the boundary layer, and according to Panton and Linebarger (1974) should be strongly dependent on the Reynolds number of the flow. In this region, $0.6 \leq \omega\delta^*/U_\infty \leq 3.5$, agreement between our data and the experiments of Schewe (1983) seems to be good. The slope is approximately ω^{-1} and the spectra scales well with the outer parameters, as was also found by both Farabee and Casarella (1991) and Keith et al. (1992). The DNS of Choi and Moin (1991) agree well with our data in the mid-frequency region, but due to the lower Re_θ the slope in the overlap region differs considerably.

The wall pressure spectra scaled with inner parameters are shown in Fig. 7. Comparisons are made to the same experiments and DNS as in Fig. 6. In the literature, different correction methods for the spatial resolution of the sensor have been suggested (see e.g., Corcos, 1962) but in Fig. 7 no corrections have been used because we want to compare uncorrected data. For the higher frequencies, the same attenuation for the 300 μm diaphragm as in Fig. 6 is noted. The slope of the spectra for the two silicon sensors in the high frequency region, $\omega\nu/u_\tau^2 \geq 0.3$, is ω^{-5}. Agreement with the results of Schewe (1983) as well as these of Farabee and Casarella (1991) is good. In this region there seems to be larger difference in spectral amplitudes between our data and the measurements of both Schewe (1986) and Farabee and Casarella (1991). In the former work a significantly lower Re_θ was used, while in the latter the data were obtained using a pinhole microphone. The higher amplitude of the data obtained by Farabee and Casarella (1991) is supported by the conclusions made by Bull and Thomas (1976) that for this frequency range pinhole microphones yield higher values. The data of Carey (1967) deviates considerably from the other measurements shown in Fig. 7, indicating a strong attenuation in the high frequency range.

From Figs. 6 and 7 it is possible to locate where in the boundary layer the turbulence sources contribute to the different spectral regions of the wall pressure field. Figure 6 shows that the overlap region scales fairly well on outer flow variables implying that the location of these sources is mainly in the outer region of the boundary layer. In Fig. 7 it is shown that the small high frequency scales fluctuations merge together and scale with the inner variables indicating that the activity from these eddies may be derived from the innermost part of the boundary layer, i.e., the inner part of the log region and the buffer layer. These observations are in accordance with the findings of Farabee and Casarella (1991), who also concluded that these statements are consistent with the spectral solution to the Poisson equation for the wall pressure.

From the spectral amplitudes and the power spectra of the wall pressure fluctuations it is possible to observe some characteristic features. First, there is a general increase in p_{rms}/τ_w as

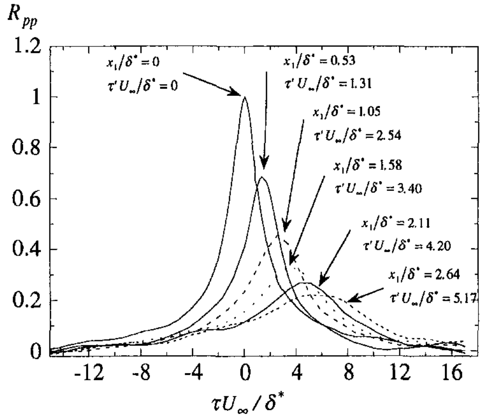

Fig. 8 Measured values of the longitudinal space time correlation in the frequency range 13 Hz < f < 13 kHz, $Re_\theta = 5072$ (uncertainty less than 10 percent)

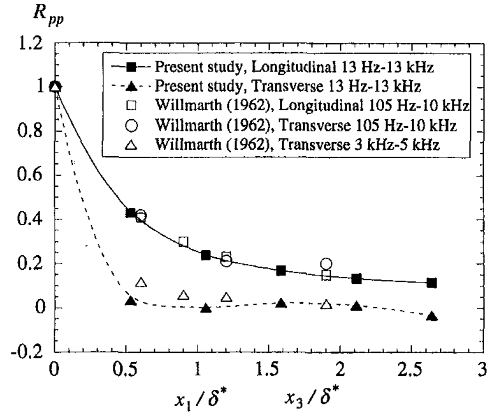

Fig. 10 Transverse and longitudinal spatial correlation of the pressure fluctuations in the frequency range 13 Hz < f < 13 kHz, $Re_\theta = 5072$ (uncertainty less than 10 percent)

Table 4 The asymptotic value of the advection velocity when $x_1/\delta^* \Rightarrow 0$. Also indicated in the table are the corresponding nondimensionalized distances from the wall, where the mean flow velocity is the same as the advection velocity for the pressure structures

Investigation	U_c/U_∞	U_c/u_τ	$y^+ = yu_\tau/V$	y/δ	Boundary layer region
Present	0.40	10.9	36	0.02	inner-wall
Willmarth (1962)	0.56	17.2	100	0.07	log-law
Bull (1967)	0.53	14.3	24	0.008	inner-wall
Schewe (1983)	0.53^(a)^	19.9^a^	21	0.02	inner-wall
Farabee and Casarella (1991)	0.65	17	391	0.2	log-law

(a) This advection velocity is obtained for visually analyzed characteristic pressure structures.

the diaphragm size decreases. However, a limiting value should be reached as the diaphragm size nears ten viscous units. Second, there is a limited ω^{-1} scaling overlap region between the mid- and high frequency ranges, clearly visible in Fig. 6. A third feature is the rapidly decreasing amplitude in the high frequency range, decaying with a slope of ω^{-5}, as shown in Fig. 7.

4.3 Space-Time Correlations and Advection Velocities. Information on the spectral characteristics of the wall pressure fluctuations can be obtained from space-time correlation analysis. We define the space-time pressure correlation coefficient as

$$R_{pp}(x_1, x_3, \tau) = \frac{\overline{p(x, z, t)p(x + x_1, z + x_3, t + \tau)}}{\sqrt{p^2(x, z, t)p^2(x + x_1, z + x_3, t + \tau)}}$$

where $p(x, z, t)$ and $p(x + x_1, z + x_3, t + \tau)$ are the fluctuating pressure signals at two points, separated in the longitudinal (x_1) and the lateral (x_3) directions, for a time delay τ. In our work all correlation measurements are conducted at $\mathrm{Re}_\theta = 5072$. Figure 8 shows the longitudinal correlation in terms of the nondimensional spacing, x_1/δ^* and time delay $\tau U_\infty/\delta^*$. As is evident from the figure, the characteristic feature of this correlation is typically an advected pressure field losing its coherence as the advection proceeds.

The streamwise advection velocity of the wall pressure fluctuations can be computed if we assume the validity of Taylor's hypothesis of "frozen turbulence," viz. we assume that all eddies are advected downstream with a fixed velocity. As pointed out by Farabee and Casarella (1991), this hypothesis does not hold strictly for a turbulent boundary layer. However, as a first approximation it is plausible to assume that the advection velocity is a function of only one single variable, $U_c = U_c(x_1/\delta^*)$. Hence, using the time delay for maximum correlation τ' the advection velocity is calculated as x_1/τ' and is shown in Fig. 9 for the frequency band 13 Hz $< f <$ 13 kHz. In our case, the advection velocity is 40–45 percent of the freestream velocity when x_1/δ^* is small and it increases for larger separations. A low magnitude is expected when the high frequency part of the spectrum is resolved since these frequencies are associated with the innermost regions of the boundary layer where the mean velocity is low. Resolving only eddies in the mid and overlap region results in higher velocities since these eddies are due to activity in the outer part of the boundary layer. In our case, the calculated advection velocities vary from $U_c/U_\infty = 0.41$ for $x_1/\delta^* = 0.53$ to $U_c/U_\infty = 0.51$ for $x_1/\delta^* = 2.63$, while corresponding data from Bull (1967) and Willmarth and Wooldridge (1962), are $U_c/U_\infty \approx 0.6$ for $x_1/\delta^* \approx 2$ and $U_c/U_\infty = 0.65$ for $x_1/\delta^* \approx 1$. Both Bull (1967) and Willmarth and Wooldridge (1962) used transducers in which the value of the ratio of boundary layer thickness to transducer diameter was small, and were hence not able to resolve the small, high frequency eddies. For larger diaphragm separations, $x_1/\delta^* > 5$, it might be expected that the advection velocity data of our work would reach the same asymptotic values as those of Bull (1967) and Willmarth and Wooldridge (1962).

In Table 4, the asymptotic values of the advection velocity when $x_1/\delta^* \Rightarrow 5$ for different investigations are listed. Turbulent sources for different parts of the spectrum can be identified by assuming that the velocity scale of the advecting turbulent structures at a spatial location matches that of the pressure structures. Hence, if the turbulent pressure sources are located a distance y from the wall, the advection velocity can be written as $U_c(x_1/\delta^*) = U(y)$. For our data the asymptotic value when $x_1/\delta^* \Rightarrow 0$ is $U_c/U_\infty = 0.4$ corresponding to $y^+ = yu_\tau/\nu = 36$, a value associated with the innermost region of the boundary layer. For larger distances, $x_1/\delta^* = 2.63$ and the advection velocity of $U_c/U_\infty = 0.51$ corresponds to $y^+ = 54$ or $y/\delta = 0.03$, a value corresponding to the log-law region.

4.4 Broad Band Filtering of Longitudinal and Transversal Correlations. The longitudinal, x_1/δ^*, and the transverse, x_3/δ^*, correlation in the frequency bands 13 Hz $< f <$ 13 kHz were measured and are shown, with zero time delay in Fig. 10 where the measurements of Willmart and Wooldridge (1962) are also included. It is evident that the correlations of the longitudinal pressure fluctuations are in very good agreement with the earlier data where approximately the same frequency range was covered. Comparing our transverse correlations to the data of Willmarth and Woolridge (1962) show that the correlations of their wide band, 105 Hz $< f <$ 10 kHz, yield higher correlation values than we have obtained. However, the transverse correlations of their high frequency band, 3 kHz $< f <$ 5 kHz, are in good agreement with our wide frequency band data.

Some broad band filtering of the pressure fluctuations for the longitudinal correlations was conducted for two frequency bands, one low band, 30 Hz $< f <$ 1000 Hz and one high band, 300 Hz $< f <$ 13 kHz. The results are shown in Fig. 11, where for comparison the regular range 13 Hz $< f <$ 13 kHz is also included. It turns out that the broad frequency range typically gives an average correlation for all pressure fluctuations. The low frequency band gives the highest correlations because the small scale structures are omitted with the result that the large eddies associated with the outer part of the bound-

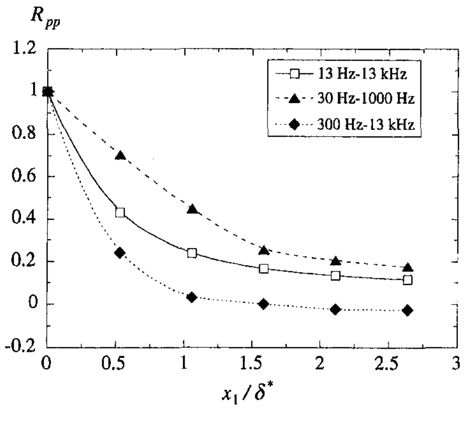

Fig. 11 Longitudinal spatial correlation of the pressure fluctuations in three frequency ranges, 30 Hz $< f <$ 1000 Hz, 300 Hz $< f <$ 13 kHz and 13 Hz $< f <$ 13 kHz, $\mathrm{Re}_\theta = 5072$ (uncertainty less than 10 percent)

ary layer dominate. When part of the low frequencies are omitted, as in the high frequency band, the large eddies are of secondary importance and the smaller eddies associated with the inner part of the boundary layer are more dominating implying a lower correlation.

5 Conclusions

The fluctuating wall pressure beneath a turbulent flat plate boundary layer was measured using small sensitive silicon based pressure transducers. The diaphragms of these sensors were less than ten wall units on a side, thus giving good spatial resolution of the high frequency part of the spectrum. The sensors were used singly as well as arranged in a line for longitudinal and transverse correlation measurements. Measurements were conducted yielding rms pressure fluctuations, space-time correlations, advection velocities and longitudinal and transverse correlations. From these measurements several conclusions may be drawn.

- Our smallest pressure transducer, with a diaphragm with side length of less than ten viscous units, seems to resolve the smallest high frequency eddies of the current flow case. This sensor accordingly shows 8% larger pressure fluctuations than our larger sensor where a certain spatial attenuation is expected.
- The power spectra, scaled in outer and inner variables, show a clear overlap region between the mid and high frequency parts of the spectra. In this region the frequency dependence was found to be ω^{-1} and in the high frequency part it was ω^{-5}.
- The longitudinal space time correlations, including the high frequency range and assuming the validity of Taylor's hypothesis, show smaller values of the advection velocity, about half the free-stream velocity, than earlier reported.
- The longitudinal correlation measurements for the frequency range 13 Hz $< f <$ 13 kHz show good agreement with other experiments. A broad band filtering indicated that the high frequency part is associated with the smaller eddies with an associated reduction of the correlation.

Acknowledgment

Support from the Swedish Research Council for Engineering Sciences (TFR) is gratefully acknowledged.

References

Blake, W. K., 1986, "Mechanics of Flow-Induced Sound and Vibration," *Applied Mathematics and Mechanics,* Vol. 17-1, Academic Press, New York.

Bradshaw, P., 1967, "Irrotational Flow Near a Turbulent Boundary Layer," *Journal of Fluid Mechanics,* Vol. 27, pp. 209–230.

Bull, M. K., 1967, "Wall-Pressure Fluctuations Associated with Subsonic Turbulent Boundary Layer Flow," *Journal of Fluid Mechanics,* Vol. 29, pp. 719–754.

Bull, M. K., and Thomas, A. S. W., 1976, "High Frequency Wall-Pressure Fluctuations in Turbulent Boundary Layers," *Physis of Fluids,* Vol. 19, pp. 597–599.

Carey, G. F., Chlupsa, J. E., and Schloemer, H. H., 1967, "Acoustic Turbulent Water-Flow Tunnel," *Journal of Acoustics Society,* America, Vol. 41, No. 2, pp. 373–379.

Choi, H., and Moin P., 1990, "On the Space-Time Characteristics of Wall-Pressure Fluctuations," *Physics of Fluids,* Vol. 2, pp. 1450–1460.

Corcos, G. M., 1964, "Resolution of Pressure in Turbulence," *Journal of Acoustics Society,* America, Vol. 35, No. 2, pp. 192–199.

Eckelmann, H., 1989, "A Review of Knowledge on Pressure Fluctuations," *Near-Wall Turbulence,* S. J. Klein and N. H. Afgan, eds., Hemisphere, New York, pp. 328–347.

Farabee, T. M., 1986, "An Experimental Investigations of Wall Pressure Fluctuations Beneath Non-Equilibrium Turbulent Flows," DTNSRDC Technical Report No. 86/047, Bethesda, MD.

Farabee, T. M., and Casarella, M., 1991, "Spectral features of wall pressure fluctuations beneath turbulent boundary layers," *Physics of Fluids A,* Vol. 3, No. 10, pp. 2410–2419.

Gedney, C. J., and Leehey, P., 1989, "Wall Pressure Fluctuations During Transition on a Flat Plate," ASME *Procs., Symposium on Flow Induced Noise Due to Laminar-Turbulent Transition Process,* NCA Vol. 5.

Harrison, M., 1958, "Pressure Fluctuations on the Wall Adjacent to Turbulent Boundary Layers," US Navy David Taylor Model Basin, Rep. No. 1260.

Jang, S-L., 1990, "A Model of $1/f$ Noise in Polysilicon Resistors," *Solid State Electronics,* Vol. 33, No. 9, pp. 1155–1162.

Kim, J., 1989, "On the Structure of Pressure Fluctuations in Simulated Turbulent Channel Flow," *Journal of Fluid Mechanics,* Vol. 205, pp. 421–451.

Keith, W., Hurdis, D., and Abraham, B., 1992, "A Comparison of Turbulent Boundary Layer Wall-Pressure Spectra," ASME JOURNAL OF FLUIDS ENGINEERING, Vol. 114, pp. 338–347.

Kälvesten, E., Löfdahl, L., and Stemme, G., 1994, "A small-size silicon microphone for measurements in turbulent gas flows," *Sensors and Actuators A,* Vol. 45, pp. 103–108.

Lauchle, G. C., and Daniels, M. A., 1984, "Wall-Pressure Fluctuations in Turbulent Pipe Flow," *Physics of Fluids,* Vol. 30, (10), pp. 3019–3024.

Löfdahl, L., Stemme, G., and Johansson, B., 1992, "Silicon Based Flow Sensors Used for Mean Velocity and Turbulence Measurements," *Experiments in Fluids,* Vol. 12, pp. 270–276.

Löfdahl, L., Stemme, G., and Johansson, B., 1993, "A Silicon Transducer for the Determination of Wall-Pressure Fluctuations in Turbulent Boundary Layers," *Applied Scientific Research,* Vol. 51, pp. 203–207.

Löfdahl, L., Kälvesten, E., and Stemme, G., 1994, "Small Silicon Based Pressure Transducers for Measurements in Turbulent Boundary Layers," *Experiments in Fluids,* Vol. 17, pp. 24–31.

Panton, R. L., and Linebarger, J. H., 1974, "Wall Pressure Spectra Calculations for Equilibrium Boundary Layers," *Journal of Fluid Mechanics,* Vol. 30, pp. 261–287.

Schewe, G., 1983, "On the Structure and Resolution of Wall-Pressure Fluctuations Associated with Turbulent Boundary-Layer Flow," *Journal of Fluid Mechanics,* Vol. 134, pp. 311–328.

Spalart, P., 1988, "Direct Simulation of a Turbulent Boundary Layer up to $R_\theta = 1410$," *Journal of Fluid Mechanics,* Vol. 187, pp. 61–98.

Willmarth, W. W., and Wooldridge, C. E., 1962, "Measurements of the Fluctuating Pressure at the Wall Beneath a Thick Turbulent Boundary Layer," *Journal of Fluid Mechanics,* Vol. 14, pp. 187–210.

E. S. Piekos

K. S. Breuer

Department of Aeronautics and
Astronautics,
MIT,
77 Massachusetts Avenue,
Cambridge, MA 02139

Numerical Modeling of Micromechanical Devices Using the Direct Simulation Monte Carlo Method

A direct simulation Monte Carlo (DSMC) investigation of flows related to microelectromechanical systems (MEMS) is detailed. This effort is intended to provide tools to facilitate the design and optimization of micro-devices as well as to probe the effects of rarefaction, especially in regimes not amenable to other means of analysis. The code written for this purpose employs an unstructured grid, a trajectory-tracing particle movement scheme, and an "infinite channel" boundary formulation. Its results for slip-flow and transition regime micro-channels and a micro-nozzle are presented to demonstrate its capabilities.

Introduction

Microelectromechanical systems (MEMS) are the subject of increasingly active research in a widening field of disciplines. These are very small (micron-scale) sensors and actuators manufactured with photolithographic techniques similar to those used for integrated circuit (IC) chips. MEMS applications range from consumer products (air-bag triggers, micro-mirror displays), to industrial and medical tools (micro-valves, micromotors), to instrumentation (micro pressure sensors, micro shear-stress sensors) (Scott, 1993).

The small size of MEMS poses unique challenges in the design phase, however. While the mechanical properties of micromachined materials are reasonably well-studied, fluid effects at micron scales are not. These effects, such as film damping of resonant structures, heat transfer in mass flow sensors, and unsteady pressure fields around microvalves, for example, must be understood if these devices are to be effectively designed and optimized.

Unfortunately, Navier-Stokes-based computational fluid dynamics (CFD) techniques are often inaccurate when applied to MEMS. This inaccuracy stems from their calculation of molecular transport effects, such as viscous dissipation and thermal conduction, from bulk flow quantities, such as mean velocity and temperature. This approximation of micro-scale phenomena with macro-scale information fails as the characteristic length of the flow gradients ($\mathcal{L}$) approaches the average distance traveled by molecules between collisions (the mean free path, λ). The ratio of these quantities is known as the Knudsen number ($Kn = \lambda/\mathcal{L}$) and is used to indicate the degree of flow rarefaction. For $Kn < 0.01$, the flow is considered to be in the 'continuum' regime and the Navier-Stokes equations are applicable in their common form. As Kn increases, the flow moves through the "slip-flow" ($0.01 < Kn < 0.1$) and "transition" ($0.1 < Kn < 3$) regimes and finally enters the "free-molecular" ($Kn > 3$) regime, each suggesting a particular type of analysis (Schaff and Chambre, 1958).

The Knudsen number of many MEMS-related flows is driven from the continuum regime by an extremely small feature size, which is often comparable to λ, even for air at standard conditions. Noncontinuum effects, neglected in traditional analyses, may therefore significantly affect device performance. As a result, new models and analysis techniques must be developed to correctly predict the fluid behavior in and around MEMS.

For numerical analyses, the direct simulation Monte Carlo (DSMC) method (Bird, 1994) offers an alternative to traditional CFD that retains its validity at high Knudsen numbers. Commonly applied to reentry vehicles, this technique makes no continuum assumption. Instead, it models the flow as it physically exists: a collection of discrete particles, each with a position, a velocity, an internal energy, a species identity, etc. These particles are moved and allowed to interact with the domain boundaries in small time steps during the calculation. Intermolecular collisions are all performed on a probabilistic basis at the end of each time step to minimize computational work. Macroscopic quantities, such as flow speed and temperature, are then obtained by sampling the microscopic state of all particles in the region of interest.

Algorithm

The DSMC code developed for this investigation is written for unstructured grids to provide flexibility for complex geometries. Particle information is stored locally with each cell, following Dietrich and Boyd (1994), to take advantage of the cache hardware of workstation-class computers and to prepare for a planned transition to parallel machines. Bird's No Time Counter (NTC) scheme (1989) governs collision pair selection, with collision cross-sections calculated according to his Variable Hard Sphere (VHS) model (1981).

Particle movement and current-cell identification are performed simultaneously with a trajectory-tracing scheme similar to that proposed by Dietrich (1991). In this scheme, a particle is moved along its trajectory until it contacts a face of its current cell. It is then passed to another cell, reflected from a solid surface, or allowed to leave the calculation, as appropriate.

Particles impinging on solid walls are reflected diffusely with full thermal and momentum accommodation. Those encountering inflow/outflow faces are simply allowed to leave the domain. The cell-based storage of particle information simplifies the latter operation; impinging particles are simply transferred out of their current cells without passing them to adjacent cells.

At I/O faces, particles must be introduced to represent the influence of fluid outside the domain. In accord with standard CFD practice, their quantity and velocity distribution is determined by considering the flow "characteristics" (cf. Hirsch, 1990), or lines along which certain variables remain constant;

Contributed by the Fluids Engineering Division for publication in the JOURNAL OF FLUIDS ENGINEERING. Manuscript received by the Fluids Engineering Division June 3, 1996; revised manuscript received June 10, 1996. Associate Technical Editor: D. P. Telionis.

namely the entropy, the transverse speed, and the Riemann invariants, which are given (for isentropic flow) by:

$$J_{\pm} = u \pm \frac{2a}{\gamma - 1}, \qquad (1)$$

where u is the streamwise speed, a is the speed of sound, and γ is the ratio of specific heats.

The paths of these characteristics dictate how much information may be specified at the boundary a priori, with the remainder obtained from the instantaneous state inside the domain. In a supersonic flow, all characteristics point downstream. In a subsonic flow, the J_- characteristic points upstream and all others point downstream.

Most DSMC applications to date have involved high speed flows. This greatly simplifies I/O boundary treatment because all variables at the inlet may be specified by the user. At the outlet, where it would be necessary to determine all variables from the flowfield, no treatment is required because an insignificant number of particles travel upstream into the domain, making it possible to neglect the particle introduction step altogether.

Most MEMS, however, involve low speed flows. It is therefore necessary to determine some variables at both inlet and outlet faces from inside the flowfield. All cases discussed in this article are intended to represent portions of long devices far from their pressure reservoirs. To accomplish this, the pressure, temperature, and transverse speed are specified at the inlet, leaving the streamwise velocity to be obtained from inside the domain. Only the pressure is specified at the outlet and the remaining variables are determined from inside the domain.

In a continuum code, this operation is straightforward; the node just inside the boundary is simply queried for the necessary information. Unfortunately, DSMC's statistical nature complicates this step because there may be as few as 20 particles in a given cell at a given time. Determining its macroscopic state from an instantaneous sample therefore yields unacceptable statistical scatter. Two immediate options exist for a steady flow: neighboring cells may be included in the instantaneous sample or it may be replaced with a time average. The proper application of the former option requires identifying neighboring cells with states "close-enough" to the cell in question to yield a meaningful spatial average. The latter option involves choosing a time averaging method that yields a sufficiently accurate estimate but still allows a boundary to be reasonably responsive to changes in the flow as it seeks its steady state.

The latter option is implemented in the current code. An inflow/outflow cell's particles are sampled after a movement step is completed, incoming particles are introduced at boundaries, and collisions are performed. A weighted average is then taken between this result and a running value collected from previous time steps. The weighting of the instantaneous state may be varied to balance the speed of convergence with the accuracy of the running estimate. A weight of $\frac{1}{20}$ was chosen for the cases presented in this article.

Results

Slip Flow Regime Micro-Channel. The first case explored with this code was a steady, low-speed, 2-D flow through a micro-channel with an outlet Knudsen number of 0.05, placing it in the slip flow regime. This geometry is similar to those investigated experimentally by Harley et al. (1995), Pong et al. (1994), and Arkilic et al. (1994) and numerically (with spectral element methods) by Beskok and Karniadakis (1994). This is, historically, an important canonical case for determining the effect of rarefaction on the transport terms in the Navier-Stokes equations. It is also representative of flows along the narrow passages often found in MEMS devices, such as the space under the floating plate of a shear stress sensor or accelerometer, which is typically only one micron high but hundreds of microns in breadth and depth (Padmanabhan et al., 1995). In addition, it serves as a convenient calibration case to assess the accuracy of the numerical algorithm because analytical solutions have been developed for this geometry.

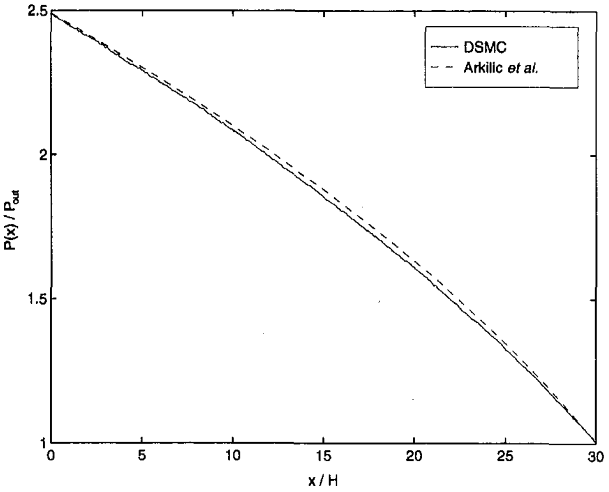

Fig. 1 Comparison of computed and analytical pressure distributions for a micro-channel in the slip flow regime. Excellent agreement is obtained between code and theory including the nonlinear pressure distribution resulting from compressibility.

In one such effort, Arkilic et al. show that the Navier-Stokes equations may be solved analytically for a long, high aspect-ratio, isothermal channel in the slip flow regime if the boundary conditions are modified to include a Kn-dependent streamwise velocity (slip) at the wall, given (for diffuse reflection) by:

$$u_{wall} = \lambda \left.\frac{du}{dy}\right|_{wall} \qquad (2)$$

where u is the streamwise velocity, Kn is the local Knudsen number and y is the transverse coordinate, which has its zero at the channel centerline.

Through this analysis, an expression may be obtained for the pressure distribution as a function of streamwise channel location and overall pressure ratio:

$$\mathcal{P}(x) = -6\ \mathrm{Kn}_o + \sqrt{(6\ \mathrm{Kn}_o + \mathcal{P}_i)^2 - \frac{x}{L}\left[(\mathcal{P}_i^2 - 1) + 12\ \mathrm{Kn}_o(\mathcal{P}_i - 1)\right]} \qquad (3)$$

where $\mathcal{P}(x)$ and $\mathcal{P}_i$ are the local and inlet pressures, respectively, normalized by the outlet value, Kn_o is the outlet Knudsen number, x is the streamwise coordinate, and L is the channel length.

The distribution predicted by Eq. (3) may be compared to a DSMC result as a test of both theory and code. Such a comparison is presented in Fig. 1 for a 31.14×1.04 μm channel filled with nitrogen at a pressure ratio of 2.47. A good agreement is obtained (max error = 1.5 percent), including the pressure curve non-linearity. This nonlinearity is a result of the large down-channel pressure drop, which causes a significant density variation (the flow is essentially isothermal). This was observed experimentally by Pong et al. in silicon microchannels with integral pressure taps and the nonlinearity was found to become more pronounced as the pressure ratio increased. Interestingly, the form of disagreement between the analytic results and DSMC presented here mirrors that found by Beskok et al. (1996) between their spectral code (with modified wall boundary conditions) and a DSMC code of Bird (1994).

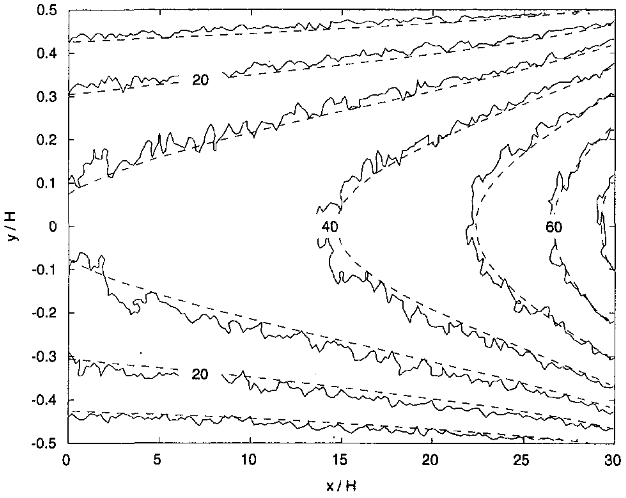

Fig. 2 Theoretical (--) and computed (—) streamwise velocity distributions (in m/s) for a micro-channel in the slip-flow regime. A good agreement is obtained, including the flow acceleration due to compressibility and the non-zero velocity at the wall due to rarefaction.

A theoretical expression for the streamwise velocity distribution was also developed by Arkilic et al.:

$$u = \frac{1}{2\mu}\frac{dp}{dx}\left(y^2 - \frac{H^2}{4} - H^2\,\mathrm{Kn}\right), \tag{4}$$

where μ is the coefficient of viscosity, p is the pressure, and H is the channel height.

This equation is plotted in Fig. 2, along with the DSMC result, for the geometry and conditions used above. An excellent agreement between theory and code is apparent, despite the statistical fluctuation present in the DSMC contours. Unfortunately, this fluctuation is an inherent feature of low-speed DSMC output because the macroscopic flow speed is small compared to the mean particle thermal speed. Calculating the flow speed is therefore a matter of isolating a small-amplitude signal superimposed on large-amplitude noise; an operation which requires an enormous number of samples.

Several interesting features common in micro-channel flows are visible in this figure. First, the fluid accelerates as it moves down the channel, unlike in the familiar Poiseuille result. This is another consequence of the density drop caused by the decreasing pressure in the streamwise direction; the mean streamwise velocity must increase to maintain a constant mass flow. Second, the velocity at the walls is nonzero and increases with increasing x-coordinate. This is the aforementioned "slip flow," which, by Eq. (2), is negligible for continuum flows due to their very small Knudsen numbers. The increase in slip velocity down the channel is caused by growth in both Kn (from the decreasing pressure) and velocity gradient at the wall (from the accelerating flow). This is contrary to the behavior very close to the entrance observed by Beskok and Karniadakis (1994) and Oh et al. (1995), which is absent from this work because the boundary conditions were formulated to eliminate entrance effects.

A further comparison to the theoretical analysis of Arkilic et al. may be obtained by normalizing the velocity distribution of Eq. (4) by the average velocity at a given x-location, u_{ave}, obtained by integrating u from the lower wall to the upper wall and dividing by H. After some rearrangement, this yields:

$$-\mathrm{Kn} + \left(\frac{1}{6} + \mathrm{Kn}\right)\frac{u}{u_{ave}} = \frac{1}{4} - \left(\frac{y}{H}\right)^2 \tag{5}$$

The left side of this equation, which will be referred to as the "similarity speed," u_s, is a function of x and y, while the right is a function of y alone. Consequently, if the slip-flow analysis holds, calculating the similarity speed using the local Kn(x) and $u(x, y)$ will eliminate the x-dependence of the velocity distribution shown in Fig. 2, collapsing the profile at each x-location to a single parabola given by the right side of Eq. (5).

This assertion was tested by computing a similarity speed distribution from the DSMC output. As predicted by the analysis, it was found that the down-channel variation of the streamwise velocity profile seen in Fig. 2 collapsed to a constant similarity speed profile. It was therefore concluded that the similarity assertion expressed in Eq. (5) indeed holds for the slip-flow channel.

Overall, excellent agreement was obtained between the analytical solution of Arkilic et al. and the DSMC results. This supports the accuracy of both techniques. For the DSMC code, however, this a just a convenient validation case; many more interesting flows, for which there are no reliable analytical solutions, may be easily treated with this method. The remaining cases presented in this article are intended to demonstrate this capability.

Transition Regime Micro-Channel. One of DSMC's greatest strengths is its validity for dilute gases in all Knudsen number regimes. By far, the most unexplored of these is the transition regime, $0.1 < \mathrm{Kn} < 3$. Obtaining solutions at these Knudsen numbers is very difficult because the approximation of transport terms based on macroscopic quantities becomes unacceptably inaccurate, precluding the use of the Navier-Stokes equations, even with the slip-flow boundary condition of Eq. (2). Collisions are still important, however, so the collisionless Boltzmann equation is not yet an option.

Because DSMC is a direct method, rather than a numerical solution of a discretized system of equations, it is a very attractive tool for investigating the transition regime. This direct nature also makes it one of the few tractable techniques which is uniformly valid in mixed Kn-regime flows. These are very useful features because, due to the aforementioned problems, relatively little is known about these cases. Such knowledge is critical to MEMS designers, however, because many devices contain flows characterized by these difficulties.

To highlight the changes that occur as Kn enters the transition regime, a micro-channel is again used as the sample case. This time, however, the analytical solution of Arkilic et al. serves only as a convenient reference, allowing transition regime results to be compared to continuum ($\mathrm{Kn} = 0.0$) and slip-flow predictions; significant disagreement is expected. The channel treated was 6.61×0.11 μm, with a pressure ratio of 4.2 and an outlet Knudsen number of 0.44. The working fluid was, again, nitrogen.

Proceeding along the same path of comparison used in the previous case, the computed pressure distribution is plotted with the analytical prediction in Fig. 3. The continuum curve ($\mathrm{Kn} = 0.0$) is also shown for reference. As expected, the excellent agreement between DSMC and theory obtained for the slip-flow case (Fig. 1) is no longer present. The error between the curves has grown from less than 2 to almost 5 percent. The form of this disagreement is also significant: the computed curve is more linear than its analytical counterpart. A trend of increasing pressure curve linearity with increasing rarefaction is therefore established by the relative shape of the continuum, slip-flow, and transition curves.

This trend is contrary to the experimental observations of Pong et al. (1994) (Fig. 7), which were obtained by running a channel with nitrogen and then with helium at the same pressure ratio. It agrees, however, with the conclusions of Beskok et al. (1995). The source of this discrepancy between analytical, DSMC, and spectral results with this experimental data has yet to be identified.

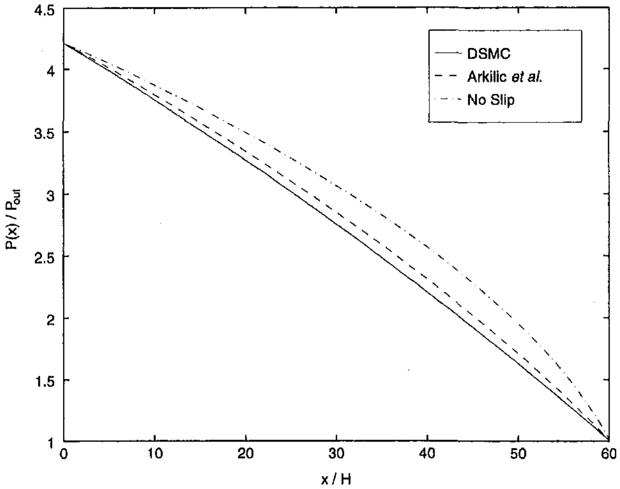

Fig. 3 DSMC-computed pressure distribution for a transition regime micro-channel compared to analytical (slip-flow) solutions for the same Kn and for continuum flow (Kn = 0.0). A trend of increasing pressure curve linearity with increasing rarefaction is apparent.

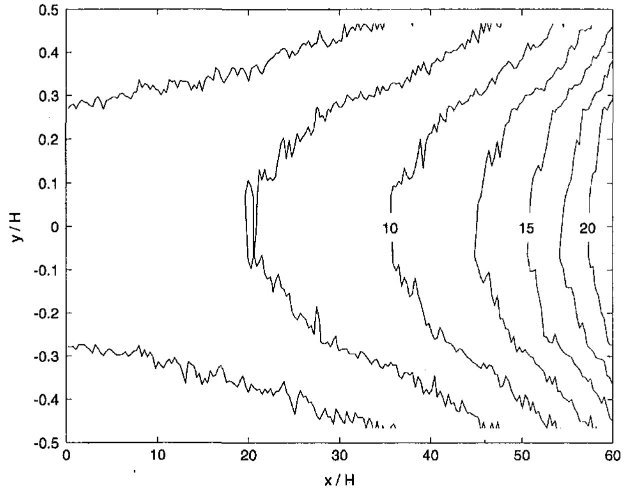

Fig. 5 Computed streamwise velocity distribution for the channel of Figure 4. The magnitude of both the slip and the local maximum velocity are greater than the analytical prediction by as much as 40%.

The streamwise velocity distribution predicted by Eq. (4) for this channel is presented in Fig. 4. Comparing this to Fig. 2, it is evident that Eq. (4) yields a much flatter profile for the higher Kn case. This may be attributed to the last term in Eq. (4), which is constant across the channel and proportional to Kn. The Knudsen number is an order of magnitude larger in this case, so the constant term has a much stronger influence on the shape of the distribution.

Upon plotting the DSMC result for comparison in Fig. 5, it again becomes evident that the assumptions supporting Eq. (4) are beginning to fail. Both the slip flow and maximum speeds at a given x-location are higher than predicted by as much as 40 percent. This allows the channel to support a much larger mass flow than predicted by the slip-flow solution, which is, in turn, a larger mass flow than predicted by the no-slip solution.

Using the similarity expression developed in the previous section, the DSMC result may be used to determine the Kn limit for the slip-flow solution, commonly given as Kn < 0.1. Because each x-location has both a similarity profile and a Knudsen number associated with it, the Kn at which the slip-flow analysis fails may be determined by finding the point where the DSMC and analytical profiles begin to disagree. Toward this end, Fig. 6 contains the computed maximum and minimum similarity speeds at each x-location, plotted with the analytical predictions (which form, by definition, straight lines). The Kn distribution was then overlaid to facilitate determining its value when the slip-flow analysis fails.

It is evident from this figure that the slip flow analysis begins to fail at approximately Kn = 0.15. This limit may be understood if the boundary condition of Eq. (2) is viewed as an expansion of the wall velocity in powers of Kn. The no-slip condition and Eq. (2) are then the zeroth and first order approximations, respectively. It is therefore logical that the neglected second and higher-order terms would begin to significantly affect the result when Kn exceeds approximately 0.1. A second-order accurate boundary condition in terms of the continuum variables is presented in Beskok et al. (1994). It should be remembered, however, that the Navier-Stokes equations themselves are only strictly valid to first order in Kn.

Supersonic Micro-Nozzle. The final case presented in this article is a supersonic micro-nozzle. In relation to the previous cases, this geometry may be viewed as a channel whose upper and lower walls form a parabolic contraction/expansion. The expansion region of similar nozzles was treated with DSMC by Zelesnik et al. (1994) with application to satellite station-keeping rocket motor design. The nozzle treated here is much smaller

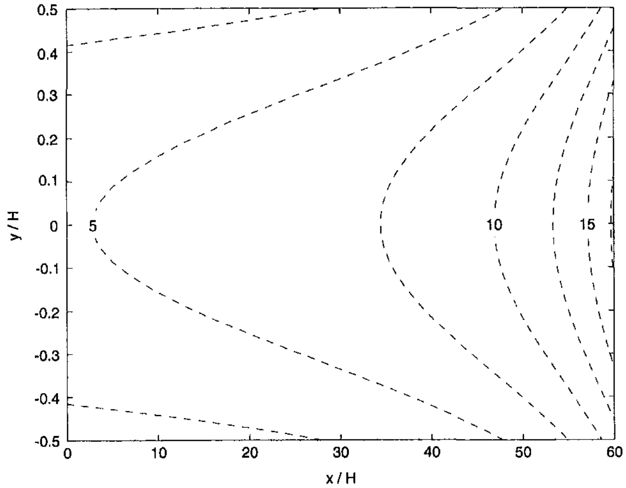

Fig. 4 Theoretical streamwise velocity distribution for a transition-regime micro channel calculated using the slip-flow analysis

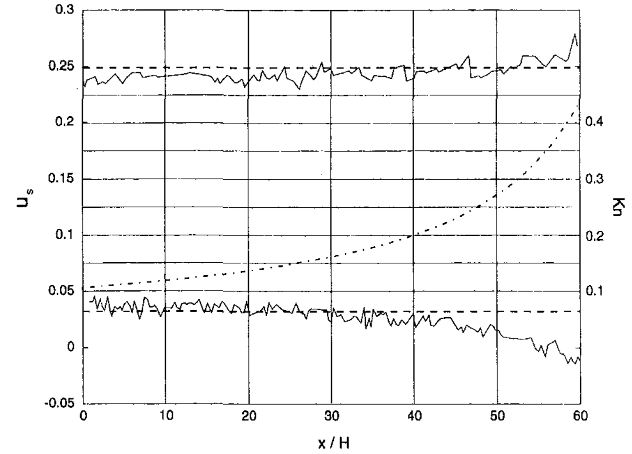

Fig. 6 DSMC (—) and analytical (--) similarity speeds with a Knudsen number (-··-) overlay. The point at which the computed curve begins to diverge from the prediction corresponds well with the commonly-stated Kn for the onset of the transition regime (0.1).

however—only 15.4 μm high at the throat and 92.6 μm long. It is also 2-D, rather than axisymmetric, which is a more attractive configuration for a MEMS device due to the inherently planar nature of photolithographic manufacturing techniques.

Such a nozzle may be considered quasi-1D if its area change is sufficiently gradual. The analytical solution of Arkilic et al. could then be used, with appropriate modifications for the x-dependent area. In the case discussed here, however, the total length is only six times the throat height. In addition, the large density variations brought about by the rapid expansion may cause the Kn-regime to change at one or more streamwise positions.

These factors make both analytical and continuum-based numerical treatment of this geometry prohibitively difficult. Nonetheless, nozzles such as these may play important roles in MEMS devices like micro-rocket thrusters and micro-gas turbine generators, for example. Investigating their behavior is therefore a valuable task for which DSMC is well-suited.

Due to the large pressure variation across the nozzle and DSMC's requirement that a cell's linear dimensions be proportional to the local mean free path, 26,758 cells were required to properly discretize the domain. The inlet was charged with helium at 1 atmosphere and a 'vacuum' outlet condition was enforced. This condition was implemented by simply removing from the simulation any particle crossing the outlet boundary and refraining from introducing new particles at these faces. The resulting pressure at the outlet plane was approximately 0.04 atmospheres, yielding an outlet Knudsen number, based on passage height, of 0.03 and a pressure ratio of 24. Approximately 550,000 particles were present on the grid at steady state.

The Mach number distribution for this nozzle is shown in Fig. 7. Qualitatively, the contours agree quite well with the results of Zelesnik et al. In addition, a number of interesting features are visible. First, contrary to the inviscid, quasi-1D result, the sonic point is actually slightly downstream of the throat. This is possible because the viscous effects are strong enough to overcome the deceleration due to the diverging shape. Second, a Mach number of 2.4 is reached; a considerable speed for such a short, narrow nozzle. Finally, the slip flow speed is substantial, exceeding Mach 0.5 near the outlet.

The temperature distribution for this micro-nozzle is shown in Fig. 8. Again, a good qualitative agreement with the results of Zelesnik et al. is obtained. Clearly, unlike in the previous two cases, this flow cannot be considered isothermal. A strong temperature gradient exists in both the streamwise and transverse directions, creating yet another obstacle to analytical treatment. The presence of such strong temperature variation is a striking feature when the diminutive dimensions of the nozzle are considered. Though the walls are isothermal with full energy accomodation and only approximately 30 local mean free paths apart at the exit, the fluid is still able to realize a substantial reduction in temperature. The effect of rarefaction has therefore been to significantly reduce the thermal communication between the wall and the fluid. This assertion is further supported by noting the large thermal slip at the wall.

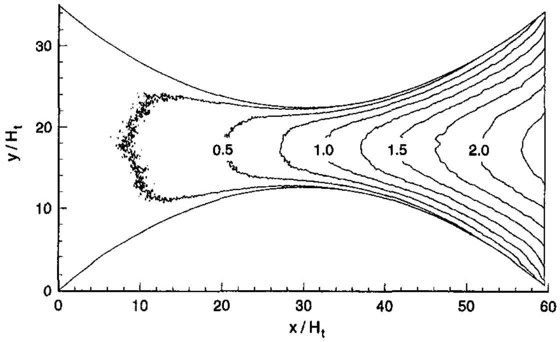

Fig. 7 **Mach number distribution for a supersonic micro-nozzle. A maximum Mach number of 2.4 is obtained from a pressure ratio of 24. The slip speed exceeds Mach 0.5 near the outlet.**

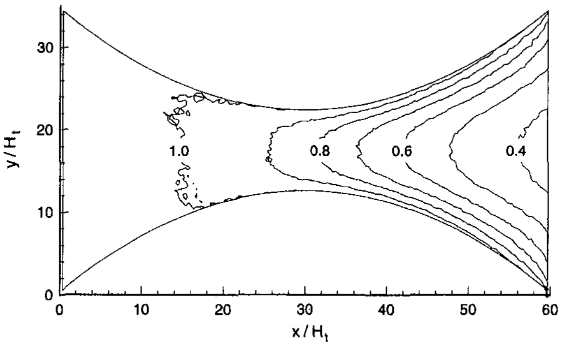

Fig. 8 **Temperature contours for a supersonic micro-nozzle, normalized by the inlet value. Significant temperature gradients are present, despite the fact that the walls are isothermal (at the inlet temp) with full thermal accommodation.**

Conclusion

The direct simulation Monte Carlo method has proven to be a valuable tool for investigating the behavior of flows which are considered 'rarefied' due to miniaturization. This article has presented only a small subset of the many cases of interest to both the fluid-dynamicist and the MEMS designer which are easily treated with this method.

The unique features of rarefied gas flows can significantly affect MEMS operation. The larger mass flow rate for a given geometry and inlet conditions must be considered when designing control systems for micro-chemical reactors and the decreased thermal communication between the fluid and its surroundings must be considered for applications involving temperature measuring devices or heaters, for example. Unfortunately, these effects are neglected in many common design tools.

DSMC, therefore, has great promise for improving the design and optimization of MEMS. Its ability to calculate in any of the four Knudsen number regimes without modification is an important feature for this task. This is especially valuable for flows with regions in different regimes. The addition of an unstructured grid capability and a trajectory-tracing movement scheme enables the code to handle arbitrary geometries. This is a valuable asset when analyzing the complex structures found in many devices. In addition, it is quite straightforward to include flow features such as chemical reactions, multi-species mixing and particle transport in the code due to its modular nature. Finally, its cell-based structure makes it well-suited for parallel computation, which is an increasingly-important attribute for a large-scale numerical scheme.

Acknowledgment

This work was supported by AFOSR grant number F49620-93-1-0376, monitored by Dr. J. McMichael.

References

Arkilic, E., Schmidt, M., and Breuer, K., 1994, "Slip Flow in Microchannels," *Proceedings of the 19th Rarefied Gas Dynamics Symposium,* July, Washington, DC AIAA.

Beskok, A., and Karniadakis, G., 1994, "Simulation of Heat and Momentum Transfer in Complex Microgeometries," *Journal of Thermophysics and Heat Transfer,* Vol. 8 (4), pp. 647–655.

Beskok, A., and Karniadakis, G., 1996, "Models and Scaling Laws for Rarefied Internal Gas Flows Including Separation," Center for Fluid Mechanics #96-4, Brown University, Center for Fluid Mechanics Turbulence and Computation, Providence, RI.

Beskok, A., Karniadakis, G., and Trimmer, W., 1995, "Rarefaction, Compressibility and Thermal Creep Effects in Gas Microflows," *IMECE 95, Proceedings of the ASME Dynamic Systems and Control Division,* DSC-Vol. 57-2, pp. 877–892.

Bird, G., 1981, "Monte Carlo Simulation in an Engineering Context," *Proceedings, 12th International Symposium on Rarefied Gas Dynamics,* Charlottesville, VA, 1980, Vol. 74 of *Progress in Aeronautics and Astronautics,* AIAA, Washington, DC.

Bird, G., 1989, "Perception of Numerical Methods in Rarefied Gas Dynamics," in *Rarefied Gas Dynamics: Theoretical and Computational Techniques,* Vol. 118 of *Progress in Aeronautics and Astronautics,* AIAA, Washington, DC.

Bird, G., 1994, *Molecular Gas Dynamics and the Direct Simulation of Gas Flows,* Oxford Engineering Science, Oxford University Press, New York, NY.

Dietrich, S., 1991, "Efficient Computation of Particle Movement in 3-D DSMC Calculations on Structured Body-Fitted Grids," *Proceedings, 17th International Symposium on Rarefied Gas Dynamics,* Auchen, Germany, 1990, Weinheim VCH.

Dietrich, S., and Boyd, I., 1994, "A Scalar Optimized Parallel Implementation of the DSMC Method," AIAA-94-0355, AIAA, Washington, DC.

Harley, J., Huang, Y., Bau, H., and Zemel, J., Feb. 1995, "Gas Flow in Micro-Channels," *Journal of Fluid Mechanics,* Vol. 284, pp. 257–274.

Hirsch, C., 1990, *Numerical Computation of Internal and External Flows,* Vol. 2, Wiley, New York.

Oh, C. K., Oran, E. S., Cybyk, B. Z., 1995, "Microchannel Flows Computed with the DSMC-MLG" in *30th AIAA Thermophysics Conference,* June, AIAA-95-2090, San Diego.

Padmanabhan, A., Goldberg, H., Breuer, K., and Schmidt, M., 1995, "A Silicon Micromachined Floating-Element Shear Stress Sensor with Optical Position Sensing by Photodiodes," *Proceedings of Transducers '95 and Eurosensors IX—8th International Conference on Solid State Sensors and Actuators.*

Pong, K., Ho, C., Liu, J., and Tai, Y., 1994, "Non-Linear Pressure Distribution in Microchannels," in *ASME Winter Annual Meeting,* Chicago.

Schaff, S., and Chambre, P., 1958, *Fundamentals of Gas Dynamics,* Chapter H, Princeton University Press, Princeton, NJ.

Scott, W., 1993, "Micro Machines Hold Promise for Aerospace," *Aviation Week and Space Technology,* Vol. 138 (9), Mar.

Zelesnik, D., Micci, M., and Long, L., 1994, "Direct Simulation Monte Carlo Model of Low Reynolds Number Nozzle Flows," *Journal of Propulsion and Power,* Vol. 10 (4), July, pp. 546–553.

3-D Microscopic Measurement and Analysis of Chemical Flow and Transport in Porous Media

Mehdi Rashidi
Deputy Director & Principal Scientist,
Laboratories for Cooperative
Applied Physics.

Andrew Tompson
Scientist.

Tom Kulp[1]
Scientist.

Loni Peurrung[2]
Research Fellow.

Environmental Programs Directorate,
Lawrence Livermore National Laboratory,
University of California, Livermore,
CA 94550

Chemical flow and transport have been studied at the pore-scale in an experimental porous medium. Measurements have been taken using a novel nonintrusive fluorescence imaging technique. The experimental setup consists of a cylindrical column carved out of a clear plastic block, packed with clear beads of the same material. A refractive index-matched fluid was pumped under laminar, slow-flow conditions through the column. The fluid was seeded with tracer particles or a solute organic dye for flow and chemical transport measurements, respectively. The system is automated to image through the porous medium for collecting microscopic values of velocity, concentration, and pore geometry at high-accuracy and high-resolution. Various geometric, flow, and transport quantities have been obtained in a full three-dimensional volume within the porous medium. These include microscopic (pore-scale) medium geometry, velocity and concentration fields, dispersive solute fluxes, and reasonable estimates of a representative elementary volume (REV) for the porous medium. The results indicate that the range of allowable REV sizes, as measured from averaged velocity, concentration, and pore volume data, varies among the different quantities, however, a common overlapping range, valid for all quantities, can be determined. For our system, this common REV has been estimated to be about two orders of magnitude larger than the medium's particle volume. Furthermore, correlation results show an increase in correlation of mean-removed velocity and concentration values near the concentration front in our experiments. These results have been confirmed via 3-D plots of concentration, velocity, pore geometry, and microscopic flux distributions in these regions.

Introduction

The physical understanding of chemical flow and transport in porous media is essential to many scientists and engineers. It is of great importance due to its applications in such diversified fields as chemical and petroleum engineering, environmental monitoring and restoration, and microbiological research.

There have been many attempts to study transport phenomena in porous media. Early experimental work dates back to the research of Graham (1833). He studied the process of diffusion of gases through a porous medium. His experiments resulted in what is known now as Graham's law describing the binary, one-dimensional, counter diffusion of gases. His work was followed by studies of Fick (1855), Darcy (1856), Maxwell (1860), and Stefan (1871). Experiments of Darcy on the flow of water through beds of sand resulted in an empirical momentum balance equation or Darcy's law. It relates the flow velocity of liquid in a porous medium linearly to the pressure gradient across the medium. Around the same years, theoretical studies of Fick (1855), Maxwell (1860), and Stefan (1871) resulted in development of Fick's diffusion laws and Stefan-Maxwell equations for multicomponent diffusion in porous media.

Recent experimental studies have provided some macroscopic results and limited microscopic data on the chemical flow and transport in porous media. Experiments of Schwartz and Smith (1953), Rhodes (1963), Murphy (1967), Musser (1971) in packed beds have shown the development of a peak in velocity profile very close to the wall. However, these results were not characterized conclusively as a function of the flow Reynolds number and the pore geometry. Flow visualization and transport studies of Hanratty and coworkers (Joll and Hanratty, 1966; Joll and Hanratty, 1969; Wegner et al., 1971) revealed some flow and mass transfer information near spherical particles. Joll and Hanratty (1966) examined the path line of flow through a packed bed of spherical particles using dye visualization. They observed a transition from laminar to turbulent flow at Reynolds numbers of 268 to 366 (based on pore velocity and particle diameter). Furthermore, they observed a smooth transition from steady to unsteady mass transfer at approximately the same Reynold numbers.

Experimental studies of Harleman and Rumer (1963), Hassinger and Von Rosenberg (1968), Klotz et al. (1980), and Han et al. (1985) have provided some macroscopic estimates of longitudinal and lateral dispersion coefficients. Han et al. (1985) studied the effect of column length and particle size distribution on the two components of the dispersion coefficients. They showed that for the case of uniform size particles, the longitudinal dispersion coefficients were a strong function of axial position in the bed unless the dispersion length satisfied a constraint dependent on the value of the Peclet number. Furthermore, it was seen that for the case of the wide size particle distribution, longitudinal dispersion coefficients were larger (up to 3 times) than in the uniform size particle distribution case, and a longer dispersion length was required in order to obtain a constant dispersion coefficient. However, due to the limited amount of data, they could not provide a quantitative measure of the size of this length scale.

Laser anemometry and flow visualization study of Dybbs and Edwards (1984) for liquid flows in several porous structures has shown the existence of four flow regimes as a function of flow Reynold number (based on particle diameter and pore velocity). These include a Darcy flow regime ($Re < 1$), an inertial flow regime ($1 < Re < 150$), an unsteady laminar flow regime ($150 < Re < 300$), and a turbulent flow regime ($Re > 350$). Their results also showed an increase in velocity profile

---

[1] Present address: Sandia National Laboratories, Livermore, CA 94550.

[2] Present address: Battelle, Pacific Northwest Laboratories, Richland, WA 99352.

Contributed by the Fluids Engineering Division for publication in the JOURNAL OF FLUIDS ENGINEERING. Manuscript received by the Fluids Engineering Division January 16, 1995; revised manuscript received April 15, 1996. Associate Technical Editor: J. A. C. Humphrey.

in about one to two particle diameters from the wall similar to the findings of Schwartz and Smith (1953).

Although, these experimental efforts have provided some valuable information on the macroscopic behavior of the flow and transport in porous media, until recently, little work has been done on the microscopic characterization of processes at the pore-scale. This can be attributed to the experimental difficulty of nonintrusively measuring flow and transport at high resolutions within the solid matrix. Recent experimental improvements have allowed some renewed investigation of pore-scale processes. These include studies using certain forms of noninvasive imaging techniques (i.e., PIV, PVI, and MRI) in and above packed beds for velocity, porosity, and phase distribution measurements (Stephenson and Stewart, 1986; Bories et al., 1991; Shattuck et al., 1991; Saleh et al., 1993; Givler and Altobelli, 1994; Li et al., 1994; Derbyshire et al., 1994; Montemagno and Gray, 1995; and Shattuck et al., 1995) and studies in surrogate media composed of etched glass or capillary network micromodels (Soll et al., 1993; Soll and Celia, 1993; and Wan and Wilson, 1994).

Theoretical descriptions of flow and transport in porous media have been generally derived from simpler ''bulk'' equations of mass and momentum balance or from more systematic approaches in which pore-scale behavior is rigorously averaged over representative elementary volume (REV) of the medium. The works of Whitaker (1967, 1969), Slattery (1967, 1972), Bear (1972), Gray (1975), Hassanizadeh and Gray (1979), Gray et al. (1993), and Rashidi (1996) are representative of the current approach in this field. While each model presents a slightly different point of view, all require some assumptions about a specific medium behavior that must be confirmed and parameterized by detailed experimental work.

The present work is part of an extensive research in our laboratories to understand the nature of the microscopic flow and transport processes within porous media under slow flow, laminar conditions. A novel nonintrusive imaging technique has been used to observe the pore-scale flow and transport behavior at high resolution and high accuracy. Our first paper (Peurrung et al., 1995) described measurement of porous medium velocity fields using particle tracking velocimetry technique. Our second paper (Rashidi et al., 1996) concentrated on the measurement of both solute concentration and velocity at pore-scale in order to derive microscopically the dispersion coefficient of the medium. It compared these results with the macroscopic estimates of dispersion coefficients based upon traditional length scale arguments, mean breakthrough analyses, and curve fits with numerical simulation. This paper reports on further analysis of the data in order to obtain:

(*a*) estimates of the representative elementary volume (REV),
(*b*) correlations between velocity and concentration within the porous medium, and
(*c*) 3-D representation of results to gain insights to the pore-scale flow and transport processes.

The overall objective is to use these findings toward gaining an understanding of chemical flow and transport in a porous medium and as a result provide the basis for improved modeling of these processes.

Experimental Facilities and Measurement Techniques

The detail of experimental setup and measurement techniques is shown in Fig. 1. Experiments were performed in a cylindrical volume of radius, $R = 4.5$ cm, carved out of a clear polymethylmethacrylate (PMMA) block of length, $L = 23.5$ cm in length. The cylindrical volume was filled uniformly with PMMA spherical beads of diameter, $l_d = 0.31$ cm. A mixture of silicone oils (Dow Corning 550 and 556) was chosen as the fluid which matched the beads' refractive index of 1.4885 at 19.8°C and a wavelength of 514.5 nm (see Rashidi and Dickenson, 1996, for experiments in aqueous heterogeneous porous media). The column was maintained at this temperature throughout all runs by being immersed in a circulating constant temperature bath to avoid density and viscosity variations. A syringe pump was used to provide a constant volumetric flow rate of above fluid at 1.15 cm^3/min and Reynolds number ($\mathrm{Re} = \bar{v} l_d / \nu$) of about 10^{-3} (Reynolds number is based on average pore velocity, $\bar{v}$, average particle diameter, l_d, and kinematic viscosity, ν).

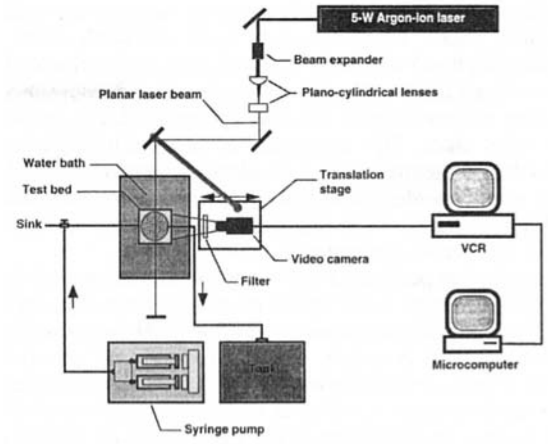

Fig. 1 Experimental setup and measurement apparatus

The experiments were done with the refractive matched fluid seeded with neutrally buoyant fluorescent latex microspheres of 6.5 μm in diameter (for velocity measurements) or an organic dye (for concentration measurements). The column was illuminated by an Argon-ion laser (coherent) operated at 475 nm to record the experimental runs. Since the dye emission peaks around 514.5 nm, a band pass filter was used on the video camera to pass a narrow range of 514.5 nm ± 5 nm wavelength associated with the dye excitation. The video camera was placed perpendicular to the laser propagation beam on a remotely operated platform such that it moved with the beam in order to scan various cross-sections of the column.

The index-matched system yielded a transparent porous medium, free from any scattering and refraction at the solid-liquid interfaces, thus allowing direct optical probing at various vertical planes within the porous system (see Fig. 2). Experimental data were collected in the observation volume on 23 illumination planes parallel with the x and z axes, uniformly separated along the y axis by 2 mm (here, z axis is the axial coordinate in the flow direction along the columnlength and x and y axes are in the transverse directions). The data included (*i*) demarcation of the pore and solid-phase geometry on each plane, (*ii*) the x-z velocity components of the moving fluorescent particles in the fluid phase, and (*iii*) measurements of the normalized (dimensionless) solute concentration within the pore spaces. The microscopic pore geometry and velocity field were assumed to be constant in time. Although concentration measurements had to be made on sequential planes at separate times, the plane-to-plane time delay was significantly shorter than the time between complete sweeps through the volume so that the set of concentration images on all vertical planes in one sweep could be considered to be made simultaneously.

In our experiments, first velocity measurements were taken by sequentially scanning the flow field in vertical cross-sections. Velocity measurements were obtained by tracking the seeded microspheres (particle density ≈ 10 particles/mm^3) in the fluid. This provided velocity measurements of the axial (z) and one transverse (x) velocity components at a large number of microscopic locations within the cylindrical test section. Then, a neutrally buoyant dye (molecular diffusivity, $D_m \approx 10^{-5}$ cm^2/s and Peclet number, $\mathrm{Pe} = \bar{v} l_d / D_m \approx 75$) was steadily introduced into the column and its concentration was imaged within the same segment of the column, where the velocity field was determined.

The video camera recorded fluorescence images on a series of vertical planes while sweeping back and forth (with the illumination plane) across the column once every minute. This allowed interstitial chemical concentrations to be determined as a function of time in the same planes where velocity measurements were taken. Dye concentration measurements also allowed the pore geometry on each plane to be measured. These images were recorded through a high resolution video camera by a frame accurate VCR and then analyzed rigorously using an IBM compatible computer.

A test run was performed to evaluate measurement uncertainties. The uncertainty in the values of average axial velocity was about 3% at 95 percent confidence level for 200 frames analyzed (see Rashidi and Banerjee, 1988, for details on uncertainty analysis of particle tracking techniques). Similarly, the concentration measurements revealed an uncertainty estimate of about 5% at 95 percent confidence level. Peurrung et al. (1995) and Rashidi et al. (1996) provide more details on the image analysis techniques. In particular, the three velocimetry techniques of Particle Imaging Velocimetry (PIV), Particle Streak Velocimetry (PSV), and Particle Tracking Velocimetry (PTV) have been compared in details. It is shown that because of the desire for rapid, automated, and dynamic data collection, the present technique (PTV) is more advantageous in studying the flow and transport in porous media. The present technique also provides an order of magnitude improvement in measurement uncertainties over our previous technique (Northrup et al., 1993).

Results and Analysis

A complete flow experiment was carried out, in which fluid was seeded with microspheres for velocity measurements and a dye front was injected into the porous system for concentration measurements. Experimental data were collected over a three-dimensional volume within the column by scanning the illumination plane across that region. As previously described, the camera and laser illumination sheet were placed on a platform that moved back and forth at a controlled speed for scanning the column. Microscopic values of velocity, concentration, and pore-space geometry were obtained at a 96 by 28 cell resolution per slice. During the experiment which lasted about 120 minute, up to 60,000 individual measurement points were collected each minute. This resulted in an enormous amount of experimental data within our porous medium. The collected data were later placed in three dimensional arrays that could be presented as vertical slices, horizontal disks, or cylindrical pucks of varying radius or height.

(A) Representative Elementary Volume. In the following paragraphs, we will attempt to measure the size of the representative elementary volume (REV) of the porous medium by averaging the microscopic velocity, concentration, and pore geometry data over cross-sectional cylindrical volumes of varying radius and height.

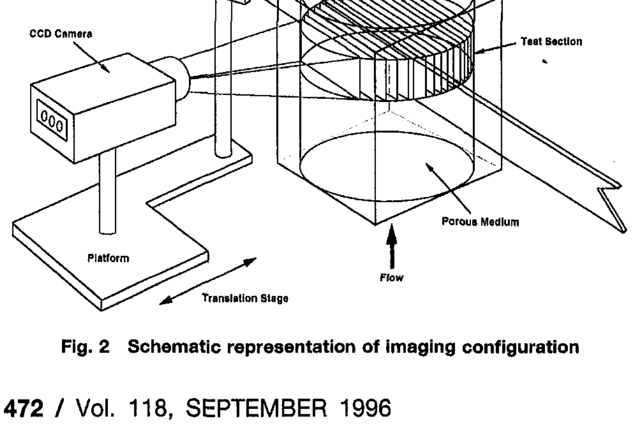

Fig. 2 Schematic representation of imaging configuration

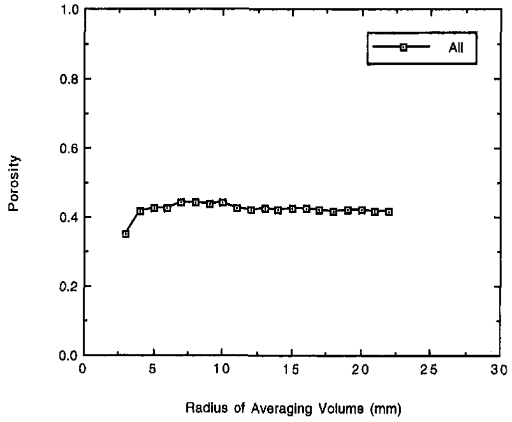

Fig. 3 Distributions of average porosity as a function of a cylindrical REV of varying radius with full height of the test section. Here, the test section is 14 mm long in height. The uncertainty in porosity values is about 5% at 95% confidence level.

The notion of an REV is traditionally defined in terms of a bulk volume element in the porous medium over which representative averages of pore-scale quantities are defined. For example, the porosity, $\phi(z)$, at an axial location z along the experimental column may be defined as

$$\phi(z) = \frac{1}{\pi r_0^2 \Delta z}\int_{-\Delta z/2}^{\Delta z/2}\int_0^{r_0}\gamma(r, z+\zeta)\cdot 2\pi r\cdot dr d\zeta \quad (1)$$

where γ is an indicator function equal to 1 if $z + \zeta$ lies inside a pore, and 0 otherwise. The integration volume is a subcylinder of radius $r_0 < R$, thickness Δz, centered on the main axis of the experimental column. In theory, the averaged quantity will fluctuate rapidly as a function of the integration volume when the volume is small. If the volume is allowed to grow, the average is ultimately assumed to become insensitive to small changes in volume, and the volume of integration is then considered to be "representative" (Hassanizadeh and Gray, 1979). Ultimately, slower variations in the average may be observed for ever-increasing integration volumes if bigger features of the medium are encountered.

Averages of other microscopic quantities (such as velocity or concentration) can be found similarly:

$$v(z) = \frac{1}{\phi(z)}\cdot\frac{1}{\pi r_0^2 \Delta z}\int_{-\Delta z/2}^{\Delta z/2}\int_0^{r_0} v(r, z+\zeta) \times \gamma(r, z+\zeta)\cdot 2\pi r\cdot dr d\zeta \quad (2)$$

$$c(z, t) = \frac{1}{\phi(z)}\cdot\frac{1}{\pi r_0^2 \Delta z}\int_{-\Delta z/2}^{\Delta z/2}\int_0^{r_0} c(r, z+\zeta, t) \times \gamma(r, z+\zeta)\cdot 2\pi r\cdot dr d\zeta \quad (3)$$

Notice that Eqs. (2) and (3) are normalized by $\phi(z)$ to yield more useful, "intrinsic" averages (Hassanizadeh and Gray, 1979).

Ideally, a common REV can be found for all macroscopic quantities of interest, and that this volume is compatible with the volumes associated with macroscopic measurement or observation in porous media. Nevertheless, some differences may occur (Baveye and Sposito, 1984). Formal measurement of macroscopic averages from pore-scale data as a function of integration volume has never been done extensively, and we wish to illustrate some of these types of measurements here with respect to averages of porosity, velocity, and concentration in our experimental system.

We will construct averages as a function of the integration volume radius $r_0 < R$ for volumes extending over the entire length (or height) of the observation section (Δz = 14 mm) or over four separate quarter-lengths of the section. Figure 3 shows the values of porosity computed from equation (1) averaged over cylindrical volumes of varying radius, r_0, and full height (the entire height of the test section, 14 mm). As seen from this figure, the variation of porosity becomes small (under 5% from average porosity of 0.43) after r_0 reaches 10 to 15 mm. Figure 4 shows the porosity values averaged over cylindrical volumes of varying radius, but at 1/4 heights. It illustrates the results averaged over first, second, third, and fourth segment of the column length with varying radius. Each segment (or plot) corresponds to a height of 3.5 mm of the test section. As seen here, once again the variation of porosity values smoothes out as the radius of averaging volumes increases. These plots show that after a radius of about 15 mm the variations of porosity become small (under 5%) with respect to the average values in that segment. Here, it should also be noted that even though the column packing materials are uniform, the average value of porosity is not uniform as a function of axial direction. In other words, the column is packed with uniform size particles but it is not packed uniformly. Therefore, porosity varies axially depending on packing orientation of the particles in various cross sections. This is the reason for the differences in the magnitude of average porosity in the plots of Fig. 4.

Similarly, mean values of the lateral and longitudinal velocity components can be evaluated using Eq. (2) and plotted for averaging volumes of varying radius and length. Figure 5 shows velocity components averaged over cylindrical volumes of varying radius r_0 and the full height of the test section. As seen here, variations in the average velocities are still evident for small radii and they diminish after r_0 increases above 10 to 15 mm. Figure 6 shows the same results as averaged over smaller volumes of 1/4 height and varying radius. Once again, the variations of averaged velocity components become small (under about 5% from average) as r_0 increases above 15 mm.

Figures 7 and 8 show similar plots for averaged concentrations determined from Eq. (3) as a function of time. These results indicate reasonably stable values (within a 5% range) are obtained for r_0 above 5 to 10 mm. Variation in the concentration averages are more subdued than the velocity averages for small r_0, and much more subdued than the porosity averages. This is due to the fact that Eqs. (2) and (3) are intrinsic averages that essentially exclude variability arising from pore geometry or structure. Fluctuations in these results arises only from fluctuations in velocity and concentration within the pore volume alone. Variability in concentration averages are most subdued because molecular diffusion tends to smooth concentration variability within the pores.

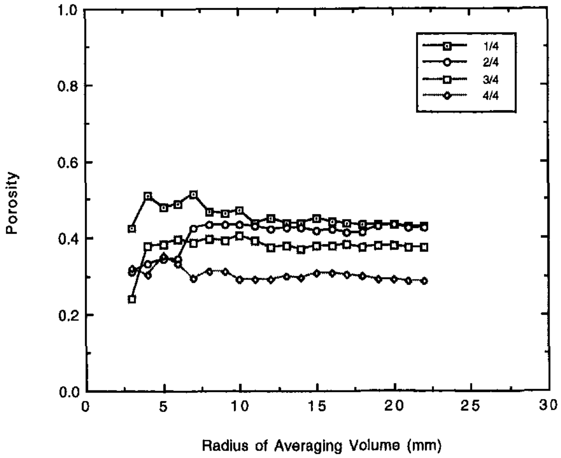

Fig. 4 **Distributions of average porosity as a function of a cylindrical REV of varying radius with 1/4th height of the test section. Here, the averaging is done over four sections of the test section each having a length of 3.5 mm in height. The 1/4, 2/4, 3/4, 4/4 symbols refer to first, second, third, fourth section of the test section from bottom to the top, respectively. The uncertainty in porosity values is about 5% at 95% confidence level.**

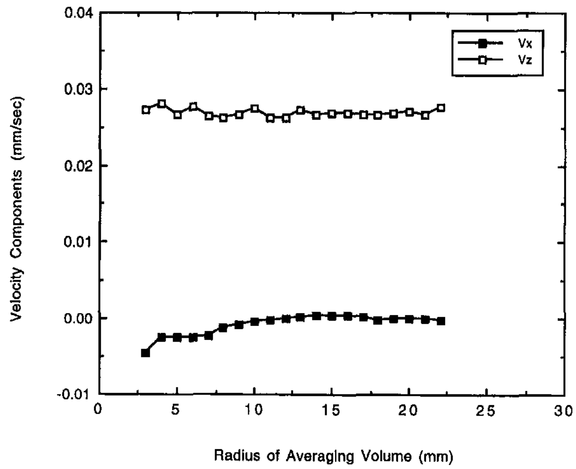

Fig. 5 **Distributions of longitudinal and lateral component of velocities averaged as a function of a cylindrical REV of varying radius with full height of the test section. Here, the test section is 14 mm long in height. The uncertainty in velocity values is about 3% at 95% confidence level.**

The above results provide some perspective on the appropriate REV size for our porous medium. They also bring up an interesting finding that the range of appropriate REV sizes may not necessarily be the same for velocity, porosity, and concentration values (Baveye and Sposito, 1984). It is seen that the insensitivity to increased volume size begins at smaller volume radii for concentration average ($r \approx 5-10$ mm) than for velocity and porosity averages ($r \approx 10-15$ mm), and that this may be dependent on the magnitude of diffusion. Nevertheless, a common range of REV sizes ($r \approx 10-15$ mm) can be found for averaged concentrations, velocities, and porosities. In terms of bead or particle volume in the column, the REV estimation of the system appears to be about two orders of magnitude larger than the particle volume.

(B) Velocity and Concentration Correlations. In order to gain an understanding of the physics of chemical flow and transport, the correlation of mean-removed velocity and concentration values throughout the experimental run was examined. Mean-removed (deviation) values of concentration and axial-velocity (c' and v') were first determined at all pore locations

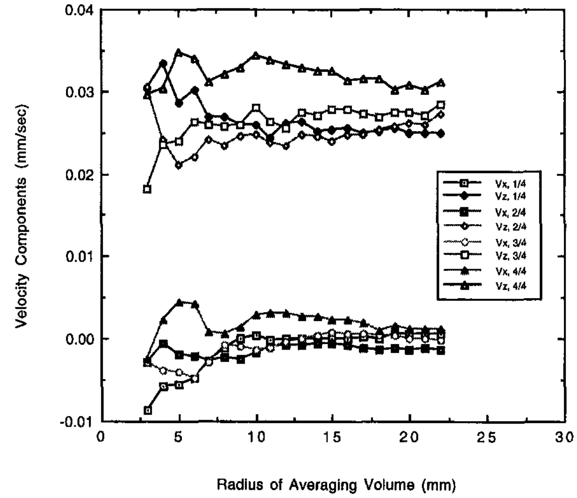

Fig. 6 **Distributions of longitudinal and lateral component of velocities averaged as a function of a cylindrical REV of varying radius with 1/4th height of the test section. Here, the averaging is done over four sections of the test section each having a length of 3.5 mm in height. The 1/4, 2/4, 3/4, 4/4 symbols refer to first, second, third, fourth section of the test section from bottom to the top, respectively. The uncertainty in velocity values is about 3% at 95% confidence level.**

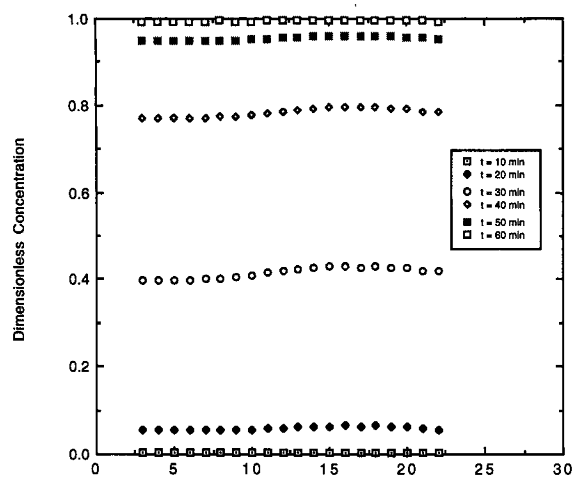

Fig. 7 Distributions of dimensionless concentration values at different times averaged as a function of a cylindrical REV of varying radius with full height of the test section. Here, concentration values are non-dimensionalized by their saturated values. The test section is 14 mm long in height. The uncertainty in concentration values is about 5% at 95% confidence level.

in an REV of the entire test section by subtracting the pore value from the corresponding mean value, as averaged over the REV. Then, the percent occurrence based on four possible combinations of c' and v' were computed as a function of time. These four combinations are as described below:

(*i*) $c' = +, v' = +$
(*ii*) $c' = -, v' = -$
(*iii*) $c' = +, v' = -$
(*iv*) $c' = -, v' = +$

Figure 9 shows the plots of percent occurrence for c' and v' correlations as a function of time throughout the experimental run. As seen from this figure, at the beginning of the run, high occurrence of negative concentration deviations is observed. This is because there are small areas of very high concentration that contribute to a higher number of c''s that are negative or less than average. In other words, it attributes to the channeling of the high concentration fluid in few regions at the beginning of the run when most regions are at very low concentrations. At the end of the run, there are large areas of saturated or high concentration regions that contribute to a higher number of positive c''s (concentration regions that have greater magnitude than the average concentration). Therefore, a high occurrence of positive c' and high noncorrelated regions are observed at the end of the run.

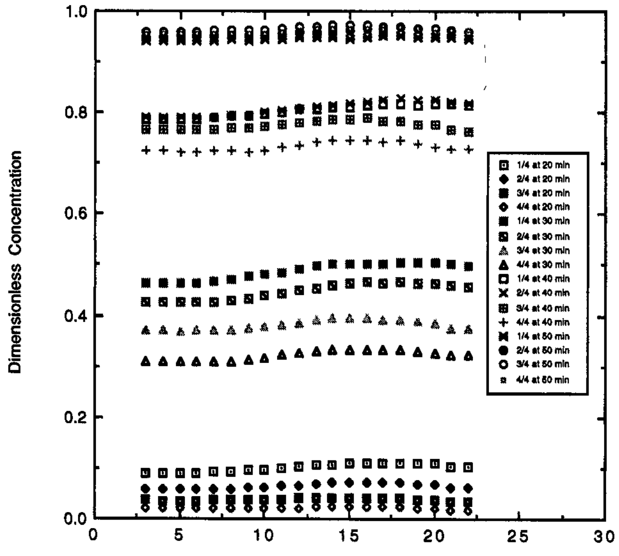

Fig. 8 Distributions of dimensionless concentration values at different times averaged as a function of a cylindrical REV of varying radius with 1/4th height of the test section. Here, concentration values are non-dimensionalized by their saturated values. The averaging is done over four sections of the test section each having a length of 3.5 mm in height. The 1/4, 2/4, 3/4, 4/4 symbols refer to first, second, third, fourth section of the test section from bottom to the top, respectively. The uncertainty in concentration values is about 5% at 95% confidence level.

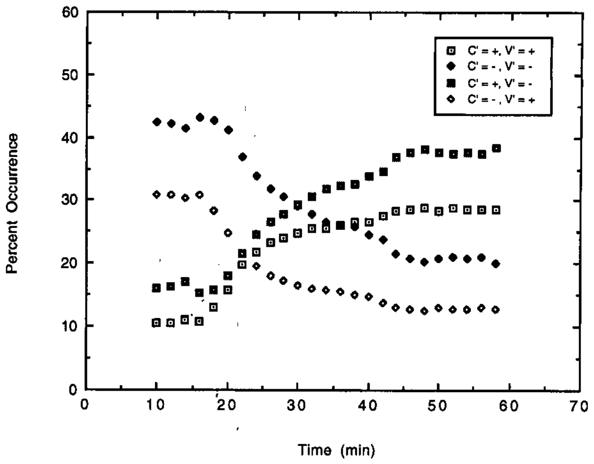

Fig. 9 Correlations of concentration and velocity deviations, c' and v', as a function of time throughout the experimental run. The uncertainty in correlation values is about 6% at 95% confidence level.

Figure 10 simplifies these results by showing the overall correlations of c' and v' as a function of time. Here, using Figure 9, the curves with $c' \cdot v' = +$ (first two curves in Fig. 9 legend) and the ones with $c' \cdot v' = -$ (last two curves in Fig. 9 legend) are simply added together in order to show the overall percent correlation of v' and c' as a function of time for the entire test section. As seen from this figure, at the beginning of the run, high occurrence of negative concentration deviations is observed. It appears that the overall correlations of c' and v' increases and peaks for the time = 10 to 45 minute. It is seen that in general, the values of c' and v' are more often correlated in this experiment. In other words, the flow of fluid and chemical

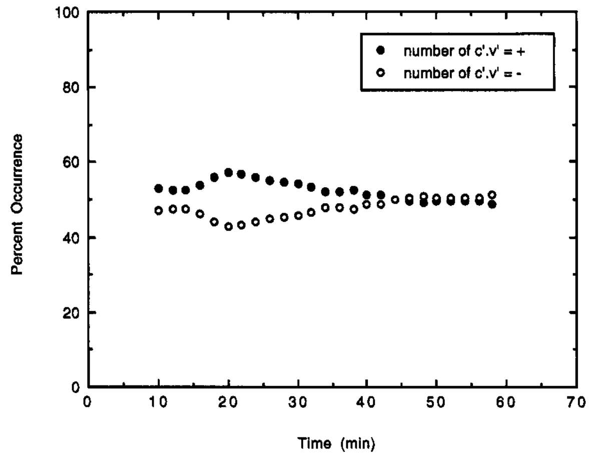

Fig. 10 Overall correlations of concentration and velocity deviations, c' and v', as a function of time throughout the experimental run. $c' \cdot v' = +$ corresponds to correlated c' and v' results while $c' \cdot v' = -$ corresponds to noncorrelated c' and v' values. The uncertainty in correlation values is about 6% at 95% confidence level.

transport are generally correlated in the porous medium. To examine this further, let us look at the overall correlation of c' and v' at a given middle horizontal cross-section of the column and observe the changes in correlations as the concentration front passes through. Figure 11 shows the overall correlations of c' and v' measured as in Fig. 10 (with an REV of the entire test section) at the middle horizontal cross section of the test section (center cross section in the measurement volume) as a function of time throughout the experimental run. As seen from this figure, the concentration front is indeed a slightly more correlated region of flow and chemical transport as indicated by the peak around time = 10 to 45 minute. This is consistent with the fact that the volume average of $c' \cdot v'$, the so-called dispersive flux, also takes on extreme values at solute fronts (Rashidi et al., 1996 and Whitaker, 1967).

(C) Microscopic Plots of Velocity, Concentration, Pore Geometry, and Flux. To investigate the detail of the microscopic processes of flow and transport in the porous medium, pore-scale values of velocity, concentration, microscopic deviatoric-solute flux, and overall medium geometry were evaluated and plotted. The data were put in three-dimensional arrays that could be displayed at different cross-sections or orientations as needed. The following figures provide plots of these microscopic information at various regions within the porous medium. The data are plotted at the same corresponding cross-sections and orientations in order to do cross comparison and analysis. In addition, the color bar at the bottom of each plot represents the magnitude of each quantity.

Figure 12 shows the mean-removed axial velocity (velocity deviation) distribution, v', on three different horizontal cross-sections within the porous medium. In this figure, the bead, outer column, and zero velocity regions are shown with blue color. As it is seen here, although the average velocity of the flow is about 0.0028 cm/s one observes substantial (almost an order of magnitude) increase in velocities in some areas. Looking at the high and low velocity spots, the flow increase is also seen to form a region of high flow in an approximate shape of a ring or donut with the central region having lower velocities than the rest. It is interesting to note that the velocities do not follow at all the typical velocity distributions observed in flow through tubes or pipes. In other words, the introduction of beads or particles in our porous system has caused more of a decrease in velocities in the central region of the column near z-axis (longitudinal or streamwise axis). This is in contrast to flows through unpacked cylindrical pipes or columns.

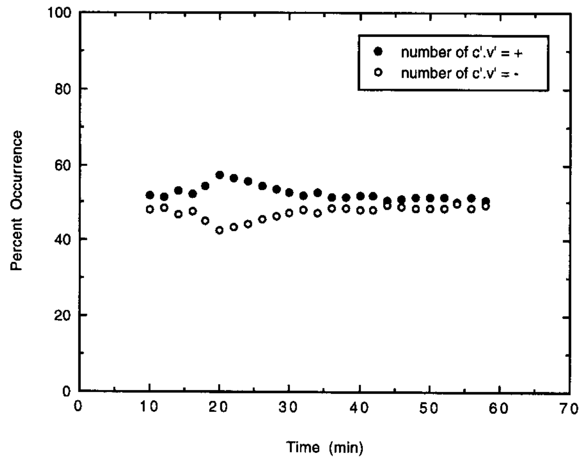

Fig. 11 **Overall correlations of concentration and velocity deviations, c' and v', at a middle horizontal cross section of the column as a function of time throughout the experimental run. $c' \cdot v' = +$ corresponds to correlated c' and v' results while $c' \cdot v' = -$ corresponds to noncorrelated c' and v' values. The uncertainty in correlation values is about 6% at 95% confidence level.**

Turning to concentration distribution plots, Fig. 13 shows the plots of concentration values at three different horizontal cross-sections in the column at time = 30 minute. In this figure and the following concentration and pore geometry figures, the bead, outer column, and zero concentration regions are shown with pink color. These plots show concentration values are much smaller near the wall and in the central region of the column. They show a similar pattern of an approximately donut shape for the high region of concentration. This is also observed to some extent from Figure 14 where concentration values are plotted for four different times of 20, 30, 40, and 50 minutes. Comparison of these plots with the previous velocity plots shows a correlation between regions of high velocities and the regions of high concentrations. As seen in the previous section, often the concentrated regions of the flow are the regions that actually move the fastest through the porous medium and in these experiments they form a ring shape. Indeed, our observations are confirmed by the plots of Fig. 15. This figure shows the regions of high concentration fluid for three different times of 20, 30, and 40 minutes. As seen, these plots show a donut or ring shape region where concentrations are higher.

Due to the presence of the beads in the column, these plots reaffirm that there is no such thing as a uniform concentration front. As seen in Fig. 13, there are regions of saturated spots near the top of the column in as early as minute 30. Figure 16 also confirms the observations that the flow is moving rather nonuniformly with high concentration regions forming a ring shape. Of course, as the experiment continues the porous regions become completely saturated. This is seen in Fig. 17, for the 3-D concentration distribution at time = 50 minute, where most regions of the porous column are saturated.

Let us now look at the microscopic deviatoric solute flux at different regions within the column. This flux describes the mechanical dispersion of chemicals as they move through the medium. The axial component of this flux is defined by

$$j = v'c' \tag{4}$$

where, v' and c' are the mean-removed axial velocity and concentration, respectively, as introduced earlier (Whitaker, 1967 and Rashidi et al., 1996). The macroscopic average of this flux is the traditional macroscopic dispersive flux. Figure 18 shows the values of the unaveraged deviatoric product plotted at the same horizontal cross-section for four different times of 20, 30, 40, and 50 minute. In this and the following figure, the bead, outer column, and zero flux regions are represented by green color. These plots are expected to follow a similar trend as to the velocity and concentration distributions shown above. As seen from these plots, one observes positive fluxes forming a ring shape region corresponding to the regions of high velocity and high concentration. It is also noted that the microscopic fluxes increase up to time = 30 minute and then decrease slowly as the system gets saturated. This corresponds to a peak in average value of dispersive flux at about 30 minute into the experimental run (as shown by Rashidi et al. 1996). Figure 19 shows a 3-D plot of microscopic fluxes at time = 20, 30, and 40 minutes. It is interesting to note from this figure that even at a time of 20 minutes from the start of the experimental run one can observe regions of very high microscopic fluxes reaching to the top of the column. This indeed shows the nature of the chemical transport in porous media to be very complicated due to the complexity of pore structures which results in flow channelings throughout the medium.

Looking at similar plots of pore geometry within the column, Fig. 20 shows the plots of the medium's pore geometry at several corresponding horizontal cross-sections within the column. In these plots, value of 1.0 corresponds to the porous regions and value of 0.0 represents the solid beads area. Comparison of these plots with the previous figures of velocity, concentration, and microscopic fluxes reveals that the ring-shaped region of high transport seems to correspond to the areas of high porosity in the column. In other words, as ex-

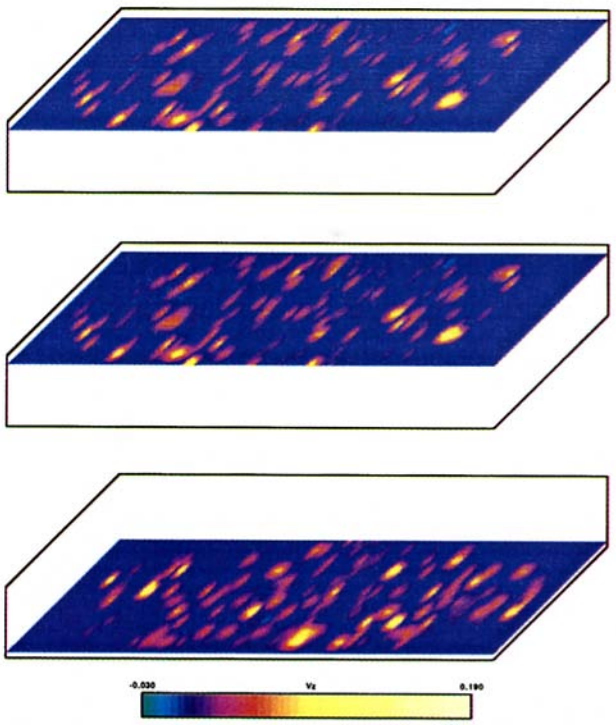

Figure 12. Distributions of axial velocity deviations (mm/sec) at 3 different horizontal cross sections within the porous medium. Here, flow direction is from bottom to top and the velocity values are deviations from the average velocity. The cross sections are representative of the beginning, middle and end sections of the test section from the bottom to the top and are at the same locations in all the following plots. The uncertainty in velocity values is about 3% at 95% confidence level.

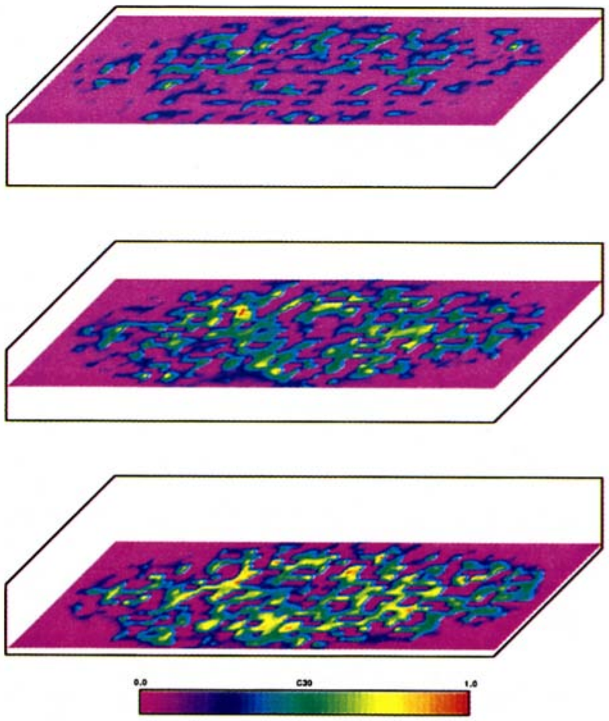

Figure 13. Distributions of non-dimensionalized concentration as a function of the same horizontal cross sections as in Figure 12 at the time of 30 minute from the start of the experiment (t = 30 minute). Here, flow direction is from bottom to top and concentrations are non-dimensionalized by saturated concentration values. C30 refers to concentration values at t = 30 minute. The uncertainty in concentration values is about 5% at 95% confidence level.

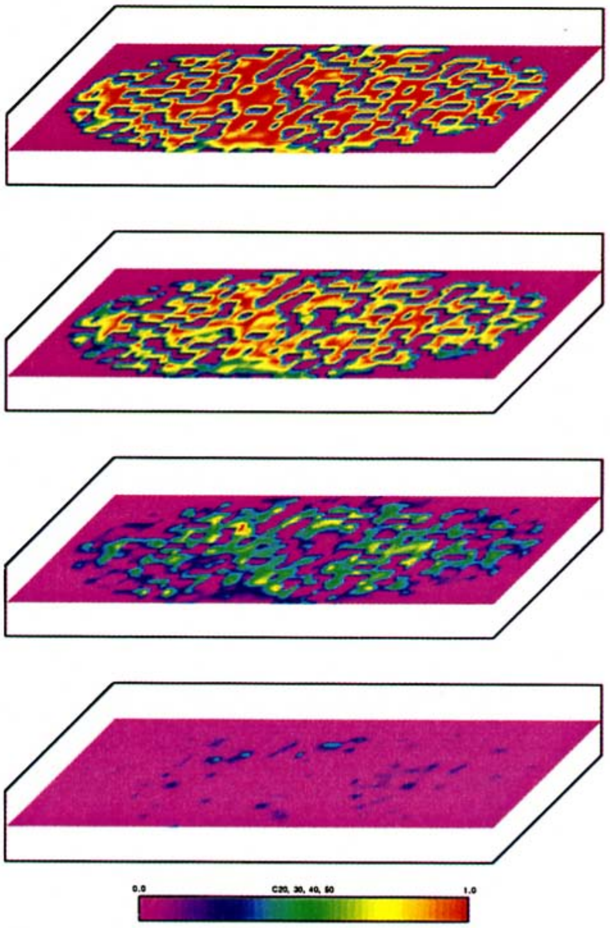

Figure 14. Distributions of non-dimensionalized concentration as a function of time for the middle horizontal cross section in the porous medium. Here, flow direction is from bottom to top and concentrations are non-dimensionalized by saturated concentration values. C20,30,40,50 refer to concentration values at 20, 30, 40, and 50 minute. The uncertainty in concentration values is about 5% at 95% confidence level.

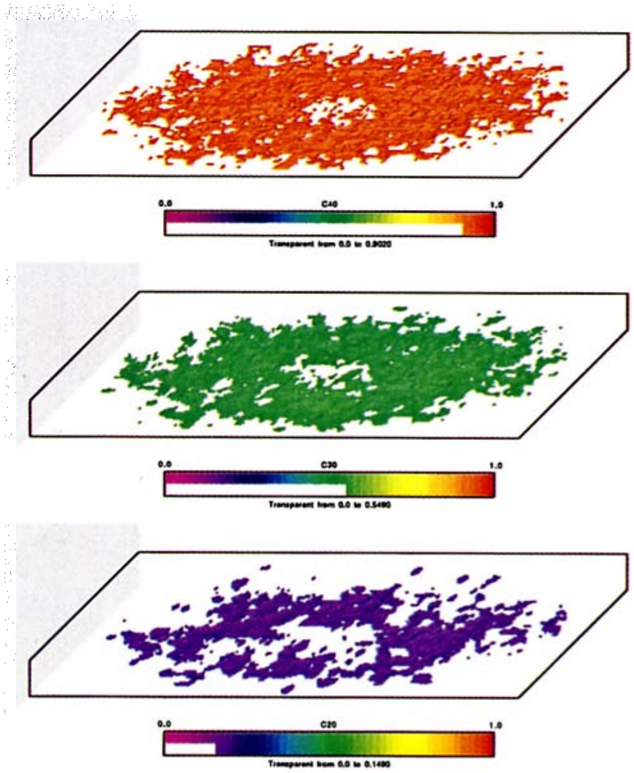

Figure 15. Distributions of non-dimensionalized concentration as a function of time for the entire porous medium. Here, only the large values of concentrations are plotted at each time. As before, flow direction is from bottom to top and concentrations are non-dimensionalized by saturated concentration values. C20, C30, and C40 refer to concentration values at 20, 30, and 40 minute. The uncertainty in concentration values is about 5% at 95% confidence level.

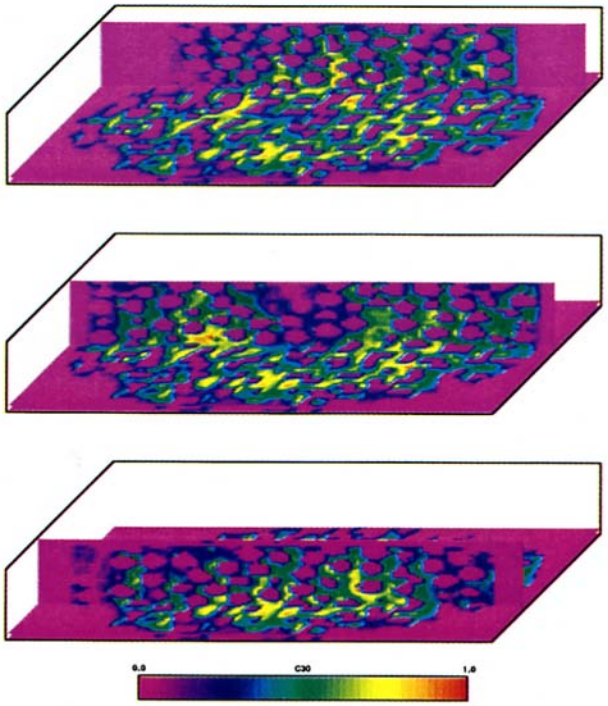

Figure 16. 3D plots of non-dimensionalized concentration distributions for t = 30 minute at a horizontal and three different vertical cross sections within the test section. Here, flow direction is from bottom to top and concentrations are non-dimensionalized by saturated concentration values. C30 refers to concentration values at t = 30 minute. The uncertainty in concentration values is about 5% at 95% confidence level.

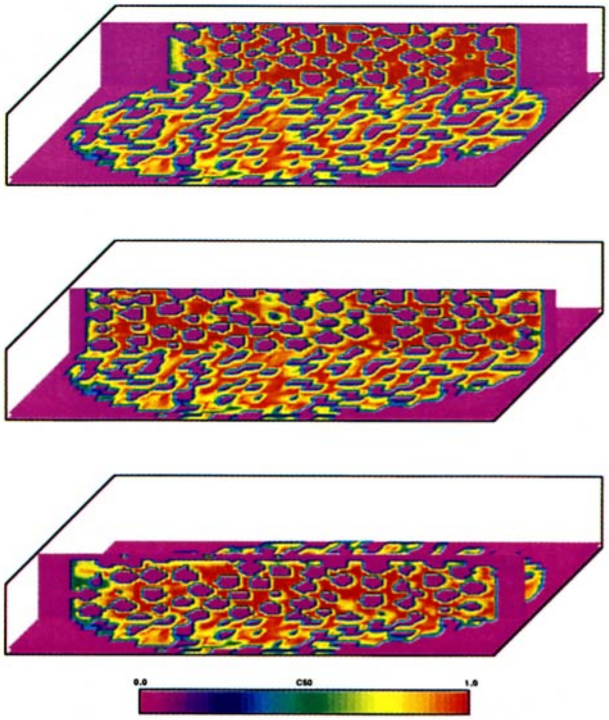

Figure 17. 3D plots of non-dimensionalized concentration distributions for t = 50 minute at the same cross sections as in Figure 16. Here, flow direction is from bottom to top and concentrations are non-dimensionalized by saturated concentration values. C50 refers to concentration values at t = 50 minute. The uncertainty in concentration values is about 5% at 95% confidence level.

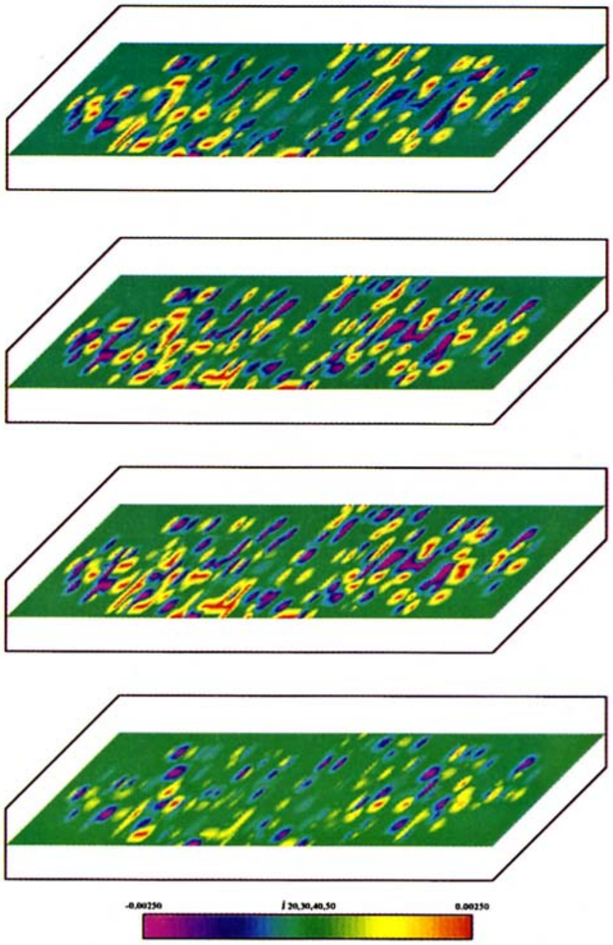

Figure 18. Distributions of axial microscopic (deviatoric) fluxes (mm/sec) as a function of time for the middle horizontal cross section in the porous medium. Here, flow direction is from bottom to top and non-dimensionalized values of concentration deviations are used for flux evaluations. j20,30,40,50 refer to flux values at 20, 30, 40, and 50 minute. The uncertainty in flux values is about 6% at 95% confidence level.

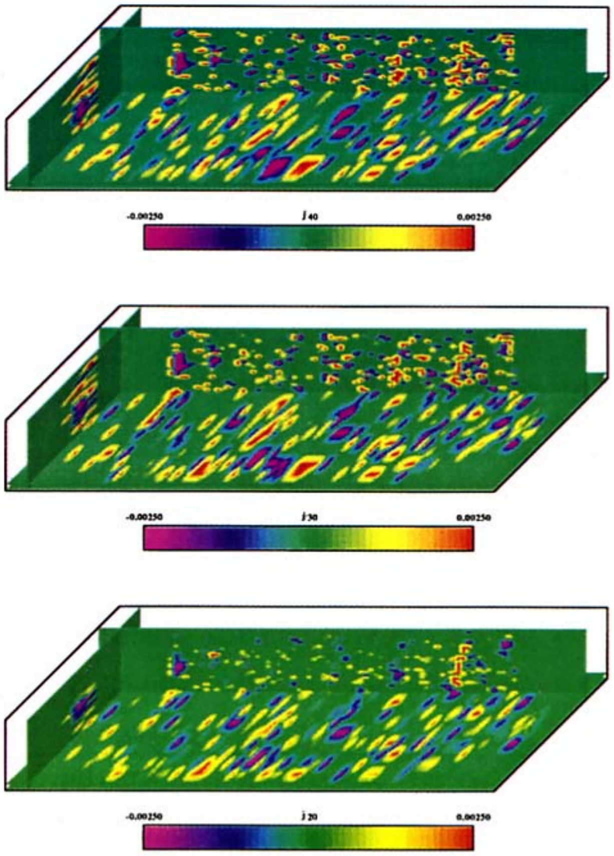

Figure 19. 3D plots of axial microscopic (deviatoric) fluxes (mm/sec) as a function of time. Here, flow direction is from bottom to top and non-dimensionalized values of concentration deviations are used for flux evaluations. j20, j30, and j40 refer to flux values at 20, 30, and 40 minute. The uncertainty in flux values is about 6% at 95% confidence level.

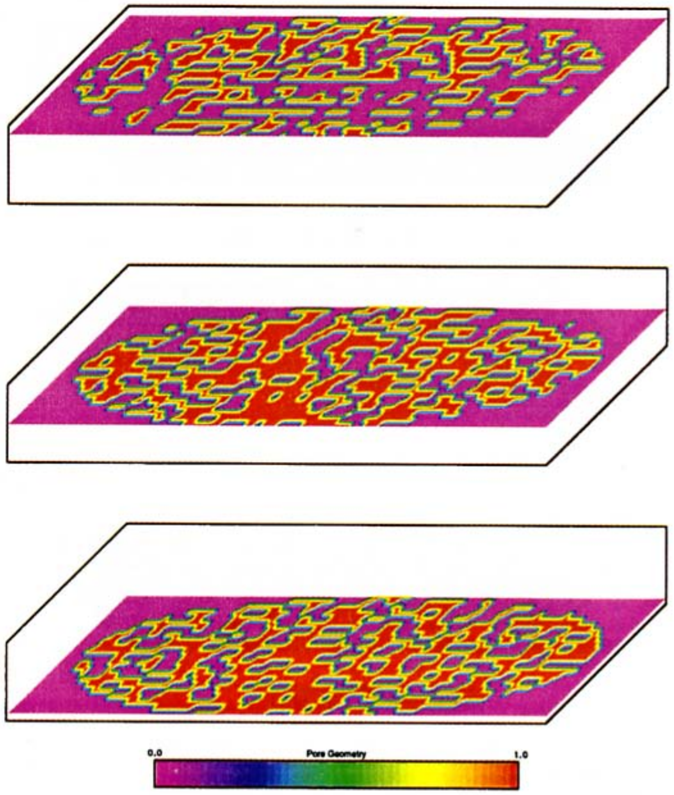

Figure 20. Distributions of pore geometry at 3 different horizontal cross sections within the porous medium. The cross sections are representative of the beginning, middle and end sections of the test section from the bottom to the top and are at the same locations as the previous plots. The uncertainty in porosity values is about 5% at 95% confidence level.

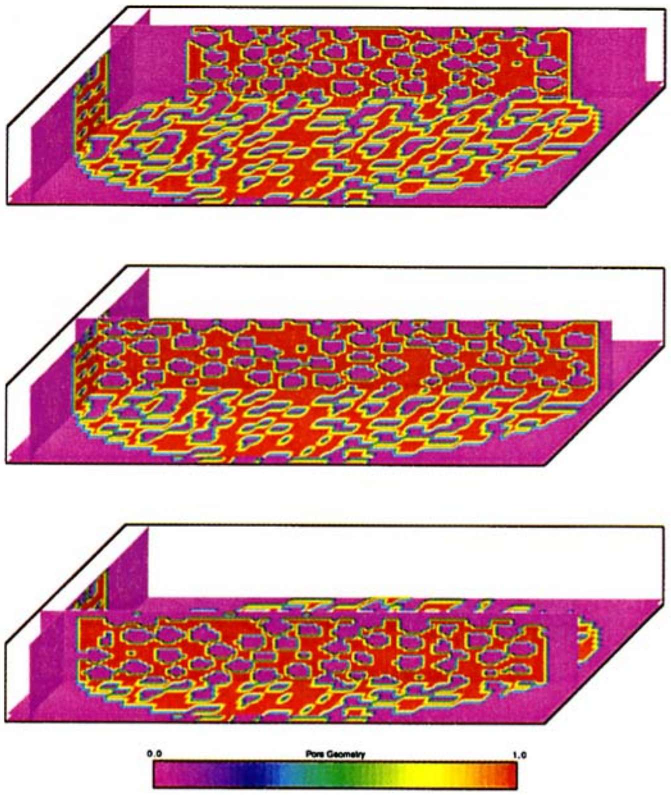

Figure 21. 3D plots of pore geometry at a horizontal and three different vertical cross sections within the test section. The cross sections are at the same locations as the previous plots. The uncertainty in porosity values is about 5% at 95% confidence level.

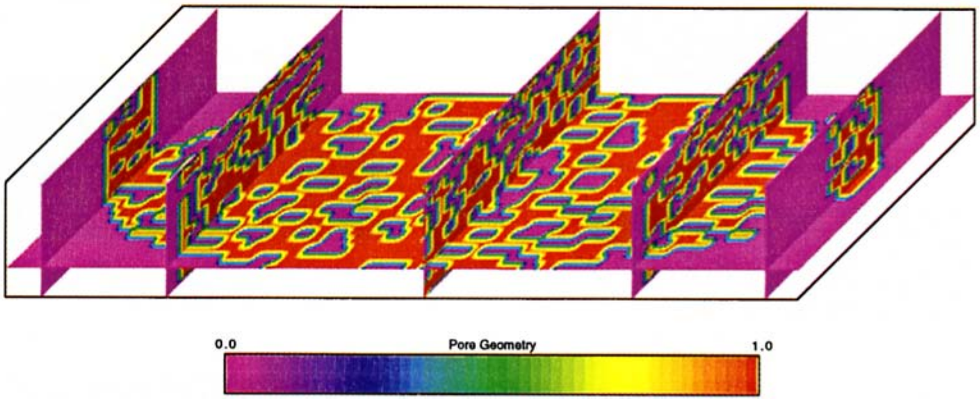

Figure 22. 3D plots of pore geometry at a horizontal and a vertical cross section within the test section. The uncertainty in porosity values is about 5% at 95% confidence level.

pected flow and solute move mostly through the high porous regions. Figure 21 also shows the pore geometry for both vertical and horizontal cross-sections of the porous column. These plots correspond to the previous Figs. 17 and 19. As one can observe from these figures, the high concentration, velocity, and microscopic flux regions in Figs. 17 and 19, correspond to the porous regions in Fig. 21. Figure 22 shows another view of the central regions of the column. As it is seen, the central regions of the column (near the longitudinal axis) have large areas of low porosity. This again explains the reason for the low flow and chemical transport at the central areas of the porous column.

The present experimental technique provides a novel and unique tool in measurement and analysis of flow and chemical transport within a porous medium. It provides a new approach in obtaining 3-D microscopic experimental data. These results are important in understanding of the physics of transport in porous media, and furthermore, in formulating sound physical models for the complicated problem of chemical transport in porous regions.

Conclusions

Microscale chemical flow and transport processes have been studied via a unique nonintrusive fluorescence imaging technique. A clear, experimental porous column was packed with clear, uniformly sized spherical beads and a refractive index-matched fluid. Under flowing conditions, the fluid was laced with latex microspheres or an organic dye to facilitate measurements of the pore-scale fluid velocity and solute concentration. The system was automated to obtain detailed images of the velocity, concentration, and pore geometry fields on a series of planes and as a function of time through a three-dimensional test section of the column. A complete flow experiment was carried out in which a steady flow field and the complete evolution of an injected dye front was imaged within the test section. Measurements of the microscopic geometry, velocity and concentration fields were used to estimate microscopic solute-fluxes, correlations of velocity and concentration, and appropriate ranges of the representative elementary volume (REV) for the medium.

The data provide detailed 3-D information on chemical flow and transport through the porous medium at high resolution and high accuracy. Observations of these 3-D plots and analysis of velocity and concentration correlation results show that the flow and chemical transport are more correlated near the concentration front. It is also observed that the concentration front moves through the porous medium in the form of small channels rather than a smooth front.

Determining an appropriate REV for the medium involves the identification of a range of bulk integration volumes over which averages of the velocity, concentration, or pore volume fraction are insignificant with respect to small variations in volume size. The measurements show that, for the slow-flow regime studied, the range of acceptable REV volumes, as determined from averaged concentrations, velocities, or porosities, differs; yet, a common range of acceptable REVs can be identified. For our system ($\mathrm{Re} \approx 10^{-3}$ and $\mathrm{Pe} \approx 75$), an estimate of an overall REV has been made which is about two orders of magnitude larger than the medium's particle volume.

It is important to recognize that the "fluctuation" in the averages, seen as a function of increasing integration volume radius, is produced by several factors. For the porosity, the medium geometry and structure is the sole source of small r_0 variability in Figs. 3 and 4. For the intrinsic velocity and concentration averages (Figs. 5–8), small r_0 fluctuation arises only from variations of velocity or concentration in the pores themselves (as indirectly influenced by the geometry, flow, and diffusion processes). For the concentration results, molecular diffusion appears to dampen variability across the pore spaces such that the averaging fluctuation is quite small; this, of course, may vary for solutes with different diffusivities. It is possible that different velocity distributions will affect the range of velocity REVs, although this effect is not expected to be significant if flows are maintained to be slow and laminar.

Acknowledgments

This work was conducted under the auspices of the U.S. Department of Energy by Lawrence Livermore National Laboratory under contracts W-7405-ENG-48 and 95-LW-026. It was supported by the Subsurface Science Program of the Office of Health and Environmental Research of the US DOE and the LLNL LDRD program.

References

Baveye, P., and Sposito, G., 1984, "The Operational Significance of the Continuum Hypothesis in the Theory of Water Movement Through Soils and Aquifiers," *Water Resources Research,* Vol. 20, pp. 521–530.

Bear, J., 1972, *Dynamics of Fluids in Porous Media,* Elsevier, New York, NY.

Bories, S. A., Charrier-Mojtabi, M. C., Houi, D., and Raynaud, P. G., 1991, "Non Invasive Measurement Techniques in Porous Media," *Convective Heat and Mass Transfer in Porous Media,* S. Kakac et al., (eds.), Kluwer Academic Publishers, Netherlands.

Darcy, H. P. G., 1856, *Les fontanes publiques de la villa de Dijon,* Victor Dalmont, Paris.

Derbyshire, J. A., Gibbs, S. J., Carpenter, T. A., and Hall, L. D., 1994, "Rapid Three-Dimensional Velocimetry by Nuclear Magnetic Resonance Imaging," *AIChE Journal,* Vol. 40, pp. 1404–1407.

Dybbs, A., and Edwards, R. V., 1984, "A New Look at Porous Media Fluid Mechanics—Darcy to Turbulent," *Fundamentals of Transport Phenomena in Porous Media,* Martinus Nijhoff Publishers, Boston, pp. 201–256.

Fick, A., 1855, Über Diffusion, *Annalen der Physik und Chemie,* Vol. 94, pp. 59–86.

Givler, R. C., and Altobelli, S. A., 1994, "A Determination of the Effective Viscosity for the Brinkman-Forchheimer Flow Model," *Journal of Fluid Mechanics,* Vol. 258, pp. 355–370.

Graham, T., 1833, "On the Law of Diffusion of Gases," *Philosophical Magazine,* Vol. 2, (Series 3), pp. 175–351.

Gray, W. G., 1975, "A Derivation of the Equations for Multi-Phase Transport," *Chemical Engineering Science,* Vol. 30, pp. 229–233.

Gray, W. G., Leijnse, A., Kolar, R. L., and Blain, C. A., 1993, *Mathematical Tools of Changing Spatial Scales in the Analysis of Physical Systems,* CRC Press, Boca Raton, FL.

Han, N. W., Bhakta, J., and Carbonell, R. G., 1985, "Longitudinal and Lateral Dispersion in Packed Beds: Effect of Column Length and Particle Size Distribution," *AIChE Journal,* Vol. 31, pp. 277–288.

Harleman, D. R. E., and Rumer, R. R., 1963, "Longitudinal and Lateral Dispersion in an Isotopic Porous Medium," *Journal of Fluid Mechanics,* Vol. 16, pp. 385–394.

Hassanizadeh, S. M., and Gray, W. G., 1979, "General Conservation Equations for Multi-Phase Systems: Averaging Procedures," *Advances in Water Resources,* Vol. 2, pp. 131–144.

Hassinger, R. C., and Von Rosenberg, D. U., 1968, "A Mathematical and Experimental Examination of Transverse Dispersion Coefficients," *Society of Petroleum Engineering Journal,* Vol. 243, pp. 195–204.

Jolls, K. R., and Hanratty, T. J., 1966, "Transition to Turbulence for Flow Through a Dumped Bed of Spheres," *Chemical Engineering Science,* Vol. 21, pp. 1185–1190.

Jolls, K. R., and Hanratty, T. J., 1969, "Use of Electrochemical Techniques to Study Mass Transfer Rates and Local Skin Friction to a Sphere in a Dumped Bed," *AIChE Journal,* Vol. 15, pp. 199–205.

Klotz, D., Seiler, K. P., Moser, H., and Neumaier, F., 1980, "Dispersivity and Velocity Relationship from Laboratory and Field Experiments," *Journal of Hydrology,* Vol. 45, pp. 169–184.

Li, T., Seymour, J. D., Powell, R. L., McCarthy, M. J., MacCarthy, K. L., and Ödberg, L., 1994, "Visualization of Flow Patterns of Cellulose Fiber Suspensions by NMR Imaging," *AIChE Journal,* Vol. 40, pp. 1408–1411.

Maxwell, J. C., 1860, "On the Process of Diffusion of Two or More Kinds of Moving Particles Among One Another," *Philosophical Magazine,* Vol. 20 (Series 4), pp. 21–38.

Montemagno, C. D., and Gray, W. G., 1995, "Photoluminescent Volumetric Imaging: A Technique for the Exploration of Multiphase Flow and Transport in Porous Media," *Geophysical Research,* Vol. 22(4), pp. 425–428.

Murphy, D., 1967, "Experimental Study of Low Speed Momentum Transfer in Packed Beds," Ph.D. thesis, Case Western Reserve University.

Musser, W. N., 1971, "Low Dispersion Columns for Large Scale Chromatographic Separations," Ph.D. thesis, Case Western Reserve University.

Northrup, M. A., Kulp, T. J., Angel, S. M., and Pinder, G. F., 1993, "Direct Measurement of Interstitial Velocity Field Variations in a Porous Medium Using Fluorescent Particle Image Velocimetry," *Chemical Engineering Science,* Vol. 48, pp. 13–21.

Peurrung, L., Rashidi, M., and Kulp, T. J., 1995, "Measurement of Porous Medium Velocity Fields and Their Volumetric Averaging Characteristics Using Particle Tracking Velocimetry," *Chemical Engineering Science,* Vol. 50(14), pp. 2243–2253.

Rashidi, M., and Banerjee, S., 1988, "Turbulence Structure in Free Surface Channel Flows," *Physics of Fluids,* Vol. 31, pp. 2491–2503.

Rashidi, M., Peurrung, L., Tompson, A. F. B., and Kulp, T. J., 1996, "Experimental Analysis of Pore-Scale Flow and Transport in Porous Media," *Advances in Water Resources,* Vol. 19(3), pp. 163–180.

Rashidi, M., and E. Dickenson, 1996. "Small Scale Flow Processes in Aqueous Heterogeneous Porous Media" ASME Fluids Engineering Conference, San Diego, CA, July 7–11.

Rashidi, M., 1996. *Non-Invasive Techniques in Multiphase Flows,* J. Chaouki, F. Larachi, and M. P. Dudukovic, eds., Elsevier, New York, NY, in press.

Rhoades, R. G., 1963, "Flow of Air in Beds of Spheres: A Statistical and Theoretical Approach," Ph.D. thesis, Rensselaer Polytechnic Institute.

Saleh, S., Thovert, J. F., and Adler, P. M., 1993, "Flow Along Porous Media by Particle Image Velocimetry," *AIChE Journal,* Vol. 39, pp. 1765–1776.

Schwartz, C. E., and Smith, J. M., 1953, "Flow Distribution in Packed Beds," *Industrial and Engineering Chemistry,* Vol. 45, pp. 1209–1218.

Shattuck, M. D., Behringer, R., Geordiadis, J., and Johnson, G. A., 1991, ''Magnetic Resonance Imaging of Interstitial Velocity Distributions in Porous Media,'' *Proceedings of ASME/FED on Experimental Techniques in Multiphase Flows,* Vol. 125, pp. 39–45.

Shattuck, M. D., Behringer, R., Johnson, G. A., and Geordiadis, J., 1995, ''Onset and Stability of Convention in Porous Media: Visualization by Magnetic Resonance Imaging,'' *Physical Review Letters,* Vol. 75(10), pp. 1934–1937.

Slattery, J. C., 1967, ''Flow of Viscoelastic Fluids Through Porous Media,'' *AIChE Journal,* Vol. 13, pp. 1066–1071.

Slattery, J. C., 1972, *Momentum, Energy, and Mass Transfer in Continua,* McGraw-Hill, New York, NY.

Soll, W. E., Celia, M. A. and Wilson, J. L., 1993, ''Micromodel Studies of Three-Fluid Porous Media Systems: Pore-Scale Processes Relating to Capillary Pressure-Saturation Relationships,'' *Water Resources Research,* Vol. 29, pp. 2963–2974.

Soll, W. E., and Celia, M. A., 1993, ''A Modified Percolation Approach to Simulating 3-Fluid Capillary Pressure Saturation Relationships,'' *Advances in Water Resources,* Vol. 16 (2), pp. 107–126.

Stefan, J., 1871, ''Über das Gleichgewicht und Bewegung, insbesondere die Diffusion von Gasgemengen,'' *Akademic der Wissenschaften in Wien, Mathematisch-Naturwissenschaftliche, Klasse, Abt. II,* Vol. 63, pp. 63–124.

Stephenson, J. L., and Stewart, W. E., 1986, ''Optical Measurements of Porosity and Fluid Motion in Packed Beds,'' *Chemical Engineering Science,* Vol. 41, pp. 2161–2170.

Wan, J., and Wilson, J. L., 1994, ''Visualization of the Role of the Gas-Water Interface on the Fate and Transport of Collids in Porous Media,'' *Water Resources Research,* Vol. 30, pp. 11–23.

Wegner, T. H., Karabelas, A. J., and Hanratty, T. J., 1971, ''Visual Studies of Flow in a Regular Array of Spheres,'' *Chemical Engineering Science,* Vol. 26, pp. 59–63.

Whitaker, S., 1967, ''Diffusion and Dispersion in Porous Media,'' *AIChE Journal,* Vol. 13, pp. 420–429.

Whitaker, S., 1969, ''Advances in Theory of Fluid Motion in Porous Media,'' *Industrial and Engineering Chemistry,* Vol. 61, pp. 14–28.

M. S. Cramer
Professor,
Department of Engineering Science and Mechanics,
Virginia Polytechnic Institute and State University,
Blacksburg, VA 24061-0219

S. T. Whitlock
Graduate Student,
Department of Aeronautics and Astronautics,
Stanford University,
Stanford, CA 94305

G. M. Tarkenton*
Graduate Student,
Department of Physics,
University of Texas at Austin,
Austin, TX 78712

Transonic and Boundary Layer Similarity Laws in Dense Gases

We discuss the validity of similarity and scaling laws for transonic flow and compressible boundary layers when dense gas effects are important. The physical mechanisms for the failure of each class of scaling law are delineated. In the case of transonic flow, a new similitude based on a modified small disturbance equation is presented.

Introduction

Similarity laws have traditionally played a critical role in engineering design, primarily due to their ability to predict trends and equivalencies among apparently diverse flows. For the most part, these laws have been developed solely in the context of the perfect gas theory. Because of the increasing importance of applications involving fluids other than air or water as well as high pressure applications, it would seem essential to have a clear understanding of any limits on the validity of the most common similarity laws. In response to this need, the present paper will provide a very brief overview of dense gas effects on the scaling laws for transonic flow and compressible boundary layers.

The dense gas regime of any fluid corresponds to temperatures and pressures on the general order of those of the thermodynamic critical point. Under these conditions, the ideal gas equation of state no longer gives an accurate prediction of the pressure and more complex equations, such as that due to van der Waals, are required. In all of the following we will restrict attention to single-phase vapors. We will also point out explicitly that the results obtained in the present paper are all based on the well known Navier-Stokes or Euler equations.

In spite of the additional complexity of the fluid response in the dense gas regime, the use of dense gases is not only necessary, but in some applications, advantageous. In both supercritical and subcritical Rankine cycles, dense gas effects can play a critical role in the performance of turbomachinery and heat transfer equipment. A second application involves the heavy gas wind tunnels described by Anderson (1991a,b) and Anders (1993). In these tunnels pressurized test gases having large molecular weights are employed to obtain a better matching of the test and flight Reynolds number. Thus, similarity laws play a central role in this application. Other wind tunnel applications include hypersonic tunnels having high pressure chambers; see, e.g., Enkenhus and Parazzoli (1970) and Simeonides (1987, 1990).

The following discussion provides a brief outline of the application of well known similarity and scaling laws to dense gases. In particular, we focus on transonic similarity laws and the scaling laws for compressible boundary layers. In the next section we survey key characteristics and complications involved in the study of dense gases. In the two sections following this overview we discuss how these physical effects may modify the standard rules of thumb employed in transonic flow and boundary layer theory.

Dense Gases

One of the most important differences between dense gases and ideal gases is the downward curvature and nearly horizontal character of the isotherms in the neighborhood of the critical point and the saturated vapor line. In the region where $\partial p/\partial V|_T \to 0$, the specific heat at constant pressure

$$c_p = c_v - T\left(\left.\frac{\partial p}{\partial T}\right|_V\right)^2 \Big/ \left(\left.\frac{\partial p}{\partial V}\right|_T\right) \tag{1}$$

can become quite large; this effect will be seen to be important in our discussion of boundary layers. Here c_v, p, T, and ρ are the specific heat at constant volume, pressure, temperature, and density, respectively. The quantity $V \equiv \rho^{-1}$ is the specific volume. For all but the lightest fluids, the region of downward curvature of the isotherms is associated with a decrease in the thermodynamic sound speed

$$a = \left(\left.\frac{\partial p}{\partial \rho}\right|_s\right)^{1/2} = \left(\gamma \left.\frac{\partial p}{\partial \rho}\right|_T\right)^{1/2}, \tag{2}$$

where s and γ are the fluid entropy and ratio of specific heats. This decrease in the sound speed with density is in marked contrast with the results of the perfect gas theory where the sound speed increases with isentropic or isothermal increases in the density or pressure. We will find that this decrease will play a critical role in the discussion of transonic similarity.

A second consideration which must be made in the dense gas regime is that the shear viscosity μ and thermal conductivity k are no longer independent of the pressure and density. The general variation of the shear viscosity and thermal conductivity with temperature and pressure can be found in any standard text on viscous flows; see e.g., White (1974). The complexity

---

* Current address: Institute for Advanced Physics, 8406 Red Willow Drive, Austin, TX 78736-3004.

Contributed by the Fluids Engineering Division for publication in the JOURNAL OF FLUIDS ENGINEERING. Manuscript received by the Fluids Engineering Division June 5, 1995; revised manuscript received March 25, 1996. Associate Technical Editor: M. M. Sindir.

of the behavior of μ can be anticipated by recalling that the viscosity of liquids tends to decrease with increasing temperature whereas that of gases tends to increase. The dense gas regime is a transition region between these two qualitatively different behaviors.

A key factor when considering thermal effects in boundary layers is the Prandtl number

$$\mathrm{Pr} \equiv \frac{\mu c_p}{k}. \tag{3}$$

Because μ and k tend to have roughly the same variation with T and p, the behavior of Pr tends to be controlled by the variation of c_p. This tendency is particularly evident in the supercritical regime where c_p becomes large. The strong variations of Pr observed in the dense gas regime also contrast with the perfect gas theory where the assumption of constant Prandtl number is usually satisfied to a reasonable degree of accuracy.

Transonic Similarity

We begin by considering the two-dimensional transonic small disturbance equation for an arbitrary gas:

$$\left(M_\infty^2 - 1 + 2\Gamma_\infty \frac{\phi_x}{U_\infty}\right)\phi_{xx} = \phi_{yy}. \tag{4}$$

Here ϕ is a disturbance potential, M_∞ and U_∞ are the freestream Mach number and flow velocity, and x and y are the streamwise and transverse spatial coordinates. The subscript ∞ will always denote conditions in the freestream. Following Thompson (1971), we refer to the thermodynamic quantity

$$\Gamma \equiv 1 + \frac{\rho}{a}\frac{\partial a}{\partial \rho}\bigg|_s \tag{5}$$

as the fundamental derivative of gasdynamics. Alternate forms of (5) have been given by a number of authors including Thompson (1971), Lambrakis and Thompson (1972), Wagner and Schmidt (1978), and Anderson (1991a,b). The fundamental derivative is known to be a measure of the intrinsic gasdynamic nonlinearity of the fluid, even in non-transonic applications; see, e.g., Hayes and Probstein (1958) and Thompson (1971). This fact is also clearly evident by the appearance of Γ as the coefficient of the ϕ_x term in (4).

Because of the importance of nonlinear effects in transonic flow, it will be useful to first give a short account of the numerical values taken on by Γ. In the perfect gas limit,

$$\Gamma \rightarrow \frac{\gamma + 1}{2}. \tag{6}$$

When we recall that $\gamma > 1$ for all fluids of practical interest, (6) may be used to show that $\Gamma > 1$ for all perfect cases. That is, there is a lower bound of unity on the nonlinearity in perfect gases. However, in the dense gas regime, the decrease in sound speed mentioned in the previous section may give rise to values of Γ which not only are less than one but may be less than zero. The minimum value of Γ on the critical isotherm tends to occur at densities roughly equal to one-half to two-thirds the critical density. Considerably lower values can be observed as the saturated vapor line is approached. The minimum value of Γ tends to decrease with molecular complexity. The pertinent parameter measuring the complexity is typically taken to be the ideal-gas specific heat $c_{v\infty}(T)$, evaluated at the critical temperature. A sequence of fluids representing increasingly large $c_{v\infty}(T_c)$ will tend to correspond to decreasing values of the minimum value of Γ. For further discussions of the variation and values of (5) we refer the reader to the fundamental studies of Bethe (1942), Zel'dovich (1946), Thompson and Lambrakis (1973), and Cramer (1989).

If we consider a single wing or turbine blade described by the equation $y = \epsilon L F(x/L)$, where L is the chord and $\epsilon > 0$ is a nondimensional measure of the thickness or angle of attack, the similarity law corresponding to (4) is easily derived. Here we define scaled variables as follows:

$$\xi \equiv \frac{x}{L}, \quad \eta \equiv \frac{y}{L}(|\Gamma_\infty|\epsilon)^{1/3}, \quad \varphi \equiv \frac{\phi}{U_\infty L}\left(\frac{\Gamma_\infty}{\epsilon^2}\right)^{1/3}. \tag{7}$$

When (7) are substituted in (4), we find that the boundary value problem for φ which satisfies the kinematic boundary condition at the wing and the condition of vanishing disturbances at infinity reads

$$(-K + 2\varphi_\xi)\varphi_{\xi\xi} = \varphi_{\eta\eta}$$

$$\varphi_\eta = \operatorname{sgn}(\Gamma_\infty)\, F'(\xi) \quad \text{on} \quad \eta \approx 0$$

$$\varphi_\xi, \varphi_\eta \rightarrow 0 \quad \text{as} \quad \xi, \eta \rightarrow \infty, \tag{8}$$

where $F'(\xi) \equiv dF/d\xi$, sgn (Γ_∞) denotes the sign of Γ_∞, and

$$K \equiv \frac{1 - M_\infty^2}{(\epsilon\Gamma_\infty M_\infty^2)^{2/3}} \approx \frac{1 - M_\infty^2}{(\epsilon\Gamma_\infty)^{2/3}} \tag{9}$$

is the usual transonic similarity parameter. According to the authors' literature review, it appears that W. M. Hayes was the first to recognize (9) as the appropriate generalization of the ideal gas transonic similarity parameter; see, e.g., Hayes (1954, 1958), Hayes and Probstein (1958).

Inspection of (9) reveals that two parameters are required to attain transonic similarity. The first is (9) and the second is the sign of Γ_∞ appearing in the wing boundary condition. Because most discussions of transonic similarity involve perfect gases, $\Gamma_\infty > 0$ and only (9) is considered. In order to save journal space we will also restrict our attention to $\Gamma_\infty > 0$ fluids. A more complete discussion can be found in the articles by Cramer and Tarkenton (1992) and Tarkenton and Cramer (1993).

The similarity discussed so far can be regarded as classical; the primary difference between the similarity expressed by (8) and the conventional perfect gas theory is the extension to include arbitrary fluids in addition to low pressure gases. From the point of view of both wind tunnel testing and turbine design the range of validity of (4) and (8) is of critical importance, particularly when a variety of fluids is to be considered. The breakdown in the classical similarity laws has been described by Cramer, Tarkenton, and Tarkenton (1992) who estimate a transonic similarity parameter (9) evaluated at the critical Mach number M_c for a standard airfoil section and a range of fluids of interest in energy recovery systems. By critical Mach number we mean the freestream Mach number at which the flow first becomes sonic on the wing or turbine blade. According to the classical transonic similarity laws, the critical value of (9) should be an invariant for all similar airfoil sections.

The variation of the critical similarity parameter with freestream density is plotted in Fig. 1 for steam, chlorobenzene, and perfluorotetrahydrofuran (FC-75); the choice of fluids is motivated by their widespread use as working fluids in power systems, see, e.g., Curran (1981). This plot is taken directly from the work of Cramer, Tarkenton, and Tarkenton (1992). Inspection of Figure 1 reveals that the variation in $K_c \equiv (1 - M_c^2)/(\epsilon\Gamma_\infty M_c^2)^{2/3}$, of the lighter fluids, i.e., steam and chlorobenzene, are relatively weak, whereas that for the heavier FC-75 is clearly non-negligible. We therefore conclude with Cramer, Tarkenton, and Tarkenton (1992) that transonic similarity and, by implication, the transonic small disturbance Eq. (4), is not valid in the dense gas regime for FC-75. We note that the low pressure (perfect gas) limit of K_c is essentially the same for each fluid. As expected, transonic similarity remains valid for all fluids in the perfect gas limit.

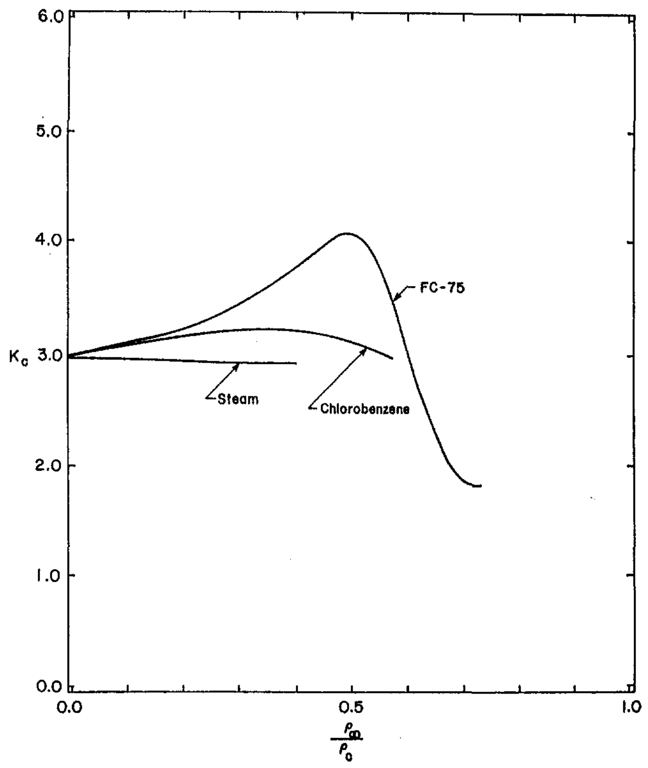

Fig. 1 Variation of the critical similarity parameter K_c for steam, chlorobenzene, and FC-75. The airfoil section is a circular arc airfoil at 0° angle of attack. The half-thickness is 0.06 of the chord.

As a second example, we consider SF_6 at a freestream temperature of 70°F and the same circular arc airfoil corresponding to that of Fig. 1. Values of M_c and K_c are recorded in Table 1 for various freestream pressures. The variation of K_c is very weak which is in complete agreement with the Euler calculations of Anderson (1991a,b) who concluded that the transonic similarity based on Γ_∞ is adequate for SF_6 for this range of pressures and temperatures.

The reason for the breakdown of transonic similarity can be seen by considering the higher order terms normally neglected in the transonic small disturbance theory. If Γ_∞ is sufficiently small, then the nonlinear term in (4) or (8) may be as small as terms correctly neglected in the $\Gamma_\infty = 0\ (1)$ theory. As a result, some of these higher-order terms play a non-negligible role even in the transonic small-disturbance theory. Inspection of Fig. 1 indicates that this is likely to occur for a wide range of fluids at moderate densities.

Extended transonic equations have been derived by Cramer (1991), Cramer and Tarkenton (1992), Kluwick (1993) and Tarkenton and Cramer (1993). In the first two studies derivations of the equations valid in the vicinity of a zero of Γ_∞ were presented. There it was shown that a term which is quadratic in ϕ_x/U_∞ must be included in the coefficient of the ϕ_{xx} term seen in (4); the similarity properties are discussed in detail by Cramer and Tarkenton (1992). The equation derived by Kluwick (1993) and Tarkenton and Cramer (1993) does not require the existence of a zero in Γ and may be applied to fluids having $\Gamma > 0$ for all pressures and temperatures. The two main restrictions in these latter studies are that the thermodynamic state of the freestream flow is in the neighborhood of the local minimum in Γ and that the local minimum in $|\Gamma|$ be small. If the scalings (7) are employed, the extension of (8) given by Kluwick (1993) and Tarkenton and Cramer (1993) is found to be

$$\begin{gathered}\left(-K + 2\varphi_\xi - K_2\varphi_\xi^2 + \tfrac{1}{3}K_3\varphi_\xi^3\right)\varphi_{\xi\xi} = \varphi_{\eta\eta} \\ \varphi_\eta = \operatorname{sgn}(\Gamma_\infty)\, F'(\xi) \quad \text{on} \quad y \approx 0 \\ \varphi_\xi, \varphi_\eta \to 0 \quad \text{as} \quad \xi, \quad \eta \to \infty, \end{gathered} \tag{10}$$

where the two new similarity parameters K_2 and K_3 are found to be

$$K_2 = \frac{\Lambda_\infty \epsilon^{2/3}}{\Gamma_\infty^{4/3}} = 0(1), \quad K_3 = \frac{\Xi_\infty \epsilon^{4/3}}{\Gamma_\infty^{5/3}} = 0(1), \tag{11}$$

and where Λ_∞ and Ξ_∞ are nondimensional versions of the first and second derivatives of Γ with respect to ρ; exact definitions of the latter may be found in the article by Cramer and Tarkenton (1993). As discussed there, the condition that the thermodynamic state be near a local minimum in Γ is enforced by requiring that Λ_∞ be small.

Thus when Γ_∞ is small, the additional nonlinearities required even in the lowest order small disturbance equation lead to additional similarity parameters (11) and naturally render the classical ($\Gamma_\infty = 0\ (1)$) similarity invalid. Finally, we note that a similitude nevertheless exists, even for small Γ_∞ flows. Because of the presence of four (rather than two) similarity parameters, this similarity tends to be relatively complicated.

Boundary Layers

We now consider compressibility scaling laws for boundary layers in dense gases. Here we restrict our attention to the simple case of an adiabatic flat plate in a steady, two-dimensional and laminar flow. In spite of the simplicity of the cases chosen, we believe that the results presented here can suggest at least some of the trends and phenomena to be expected in more complex configurations.

In the full incompressible limit, the flow necessarily reduces to the well known Blasius flow. Because of the self-similarity inherent in the Blasius solution, such a solution is invariant with respect to choice of fluid and the thermodynamic state of the freestream. For future reference we quote the well-known results for the skin friction, $c_f \equiv 2\tau_w/(\rho_\infty U_\infty^2)$, where ρ_∞ and U_∞ are the density and flow velocity of the freestream, and τ_w and T_w is the wall shear stress and the wall temperature. For the Blasius boundary layer, it is well known that

$$c_{fB} = \frac{0.664}{\mathrm{Re}_x^{1/2}}. \tag{12}$$

Here the Reynolds number $\mathrm{Re}_x \equiv U_\infty x/\nu_\infty$, where ν_∞ is the kinematic viscosity of the freestream.

At supersonic speeds, the skin friction is affected by the frictional heating even in the perfect gas limit. The physical reasons for this effect are that the temperature variations caused by viscous dissipation give rise to density and viscosity variations across the boundary layer. If these variations are strong enough, the violation of the assumption of constant properties which is intrinsic to the Blasius theory is enough to cause changes in the global flow quantities such as c_f. In particular, deviations from the Blasius values are expected whenever the Chapman-Rubesin parameter

$$l \equiv \frac{\mu\rho}{\mu_\infty\rho_\infty}, \tag{13}$$

where μ and μ_∞ are the local and freestream shear viscosities, deviates from unity. A standard scaling between the Blasius and $M_\infty > 0$ skin friction is

$$c_f = l_w^{1/2} c_{fB}, \tag{14}$$

Table 1 Critical Mach number and similarity parameter for SF_6, $T_\infty \approx$ 70°F and the airfoil section is identical to that of Fig. 1

p_∞	M_c	K_c
1.0 atm	0.804	3.01
5.0 atm	0.806	3.04
10.0 atm	0.810	3.06

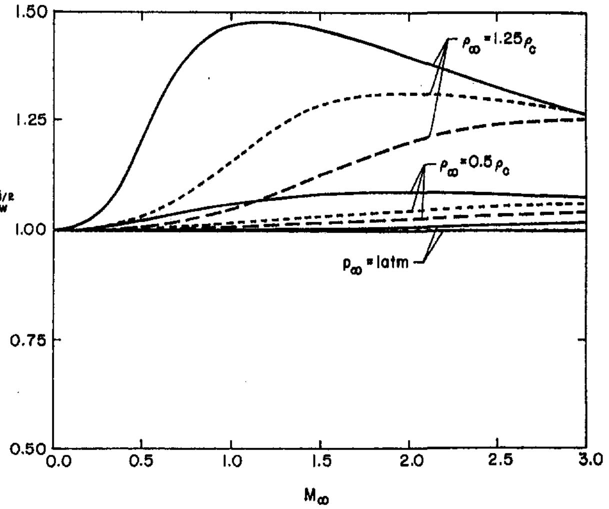

Fig. 2 Variation of the scaled skin friction for various fluids (—— N_2, - - - SF_6, and — — toluene). The freestream temperature is 1.01 T_c of the particular fluid in question.

where $l_w = \mu_w \rho_w / (\mu_\infty \rho_\infty)$ is the value of (13) at the plate. A more detailed discussion of (14) is found in White (1974). Here we simply point out that (15) does not necessarily depend on the low pressure gas assumption but is likely to break down if $l_w \not\approx 1$.

In order to evaluate the validity of (14) for compressible flows of dense gases, S. T. Whitlock (1992) has developed a boundary layer code capable of treating dense gases. The plate is flat with no imposed pressure gradient. As a result, the flow is self-similar and the classical Levy-Lees similarity variables were employed. A detailed discussion of the transforms and the resultant boundary layer equations can be found in Whitlock (1992). In order to account for high-pressure effects, the Martin-Hou (1955) equation of state and the dense gas viscosity and thermal conductivity models of Chung et al. (1984, 1988) were used. Because the flows were self-similar, standard finite-difference schemes can be employed. In the present study the well known second-order Davis-coupled version of the Crank-Nicolson scheme was used. In the interest of conserving space, we refer the reader to Whitlock (1992) for a full account of the numerical approach and accuracy.

Examples of our results are presented in Fig. 2 where the quantity

$$\frac{c_f}{c_{fB} l_w^{1/2}} \tag{15}$$

is plotted as a function of M_∞ for various fluids and thermodynamic states. Here c_f and l_w were computed from the finite difference scheme of Whitlock (1992).

The fluids chosen for our comparison are N_2, SF_6, and toluene. Molecular nitrogen is a natural benchmark fluid for comparison and SF_6 was chosen because of its use in the heavy gas wind tunnel program described by Anders (1993). Toluene is included because of its widespread use in Rankine cycle turbomachinery, see, e.g., Curran (1981). In each case, the freestream temperature was taken to be 1.01 T_c, where T_c is the temperature at the thermodynamic critical point of the particular fluid in question.

For each fluid, the freestream densities were chosen such that $p_\infty = 1$ atm, $\rho_\infty = 0.5\rho_c$, and $\rho_\infty = 1.25\rho_c$, where p_∞ is the freestream pressure, and ρ_c is the density of the fluid at its thermodynamic critical point. The one atmosphere case is expected to approximate perfect gas conditions. The cases having $\rho_\infty = 0.5\rho_c$, $T_\infty = 1.01T_c$ correspond to thermodynamic states located in the dense gas regime somewhat to the right of the saturated vapor line in the $p - V$ diagram. The freestream pressures for this dense gas case are $0.92p_c \approx 30.7$ atm, $0.92p_c \approx 34.2$ atm, and $0.93p_c \approx 37.8$ atm for N_2, SF_6, and toluene, respectively. The cases having $\rho_\infty = 1.25\rho_c$, $T_\infty = 1.01T_c$ are at supercritical pressures just to the left of the critical point in the $p - V$ diagram. For this reduced density, freestream pressures for N_2, SF_6, and toluene are $1.004\ p_c \approx 33.6$ atm, $1.003\ p_c \approx 37.2$ atm, and $1.003p_c \approx 40.6$ atm, respectively.

The variation of the skin friction with freestream Mach number is plotted in Fig. 2. In the one atmosphere case the variation of $c_f/(c_{fB} l_w^{1/2})$ is very weak for each fluid. The largest deviation from unity is about 2% which is for N_2 at $M_\infty = 3$. Nitrogen also has the largest variations in the dense gas case ($\rho_\infty = 0.5\rho_c$). The maximum deviations from one are about 9% for N_2 at $M_\infty \approx 2$, 6 percent for SF_6 at $M_\infty = 3$, and 4.5% for toluene at $M_\infty = 3$. The largest variations shown for each fluid are observed in the cases having $\rho_\infty \approx 1.25\rho_c$. The error in (14) is nearly 50 percent for N_2 at Mach numbers approximately equal to one.

From these simple examples we can immediately conclude that the scaling law (14) breaks down as the density increases. The physical reason for the breakdown is the strong variations of l across the boundary layer. As an example, we consider the case where $\rho_\infty = 0.5\rho_c$ and $M_\infty = 2$ in N_2. An examination of the numerical values for the variation in the viscosity revealed that it was nearly constant through the boundary layer with a local minimum of $\mu \approx 0.85\mu_\infty$ and a wall value of $\mu_w \approx \mu_\infty$. The density on the other hand decreases monotonically to a $\rho_w \approx 0.5\rho_\infty$. These and other flow details have been described by Whitlock (1992).

The deviation from the standard scaling is also seen to be weaker for the heavier fluids SF_6 and toluene. The reason for this is that the specific heats of the latter fluids tend to be larger than that for N_2. As discussed by Anderson (1991a) and Whitlock (1992), the frictional heating tends to decrease as the specific heats increase. As a result, the temperature variation across the boundary layer is weakened. Because the density is related to the temperature through the well known fact that the pressure is approximately constant across the boundary layer, the density variation is also significantly weaker when the specific heats are large. Because the shear viscosity depends on both ρ and T, the variation of (13) will be weaker in the heavier, more complex fluids.

Although the scaling law for c_f is always expected to break down in the dense gas regime, the numerical errors might be tolerable at moderate pressures. For example, we estimate the error at $T_\infty = 1.01T_c \approx 120$°F and $p_\infty = 10$ atm for SF_6 at a Mach number of 3 to be about 1.6 percent, which is considerably less than that encountered at the higher pressures.

Conclusions

The goal of this paper was to discuss classical similarity and scaling laws in the context of dense gases. The main conclusion regarding transonic similarity is that it is easily extended into the dense gas regime provided the nonlinearity parameter (5) is not small. As pointed out earlier, Γ can become small for fluids having moderately large specific heats. When such fluids are employed in their respective dense gas regimes, Γ can become small resulting in a breakdown in the classical similarity law. In contrast, relatively light fluids such as steam and air tend to have $\Gamma = O(1)$ even in the dense gas regime and are expected to satisfy the classical transonic similarity flows over most of the single-phase domain.

The compressibility scalings for boundary layers are seen to be inaccurate in most cases where dense gas effects are noticable. The classical scalings appear to be closely associated with the constant property assumptions; the Chapman-Rubesin parameter $l \equiv \mu\rho/\mu_w\rho_w$ and the Prandtl number are likely to be the most important properties. The trend for boundary layers appears to be the opposite of that for inviscid transonic flow in that the lighter, less complex fluids tend to be less likely to satisfy the scaling laws as the pressure is increased. The physical explanation is that frictional heating is stronger for the lighter, simpler fluids resulting in larger temperature and property variations.

We note that extensions of the transonic similarity are, in fact, possible. However, the authors are not aware of any simple extensions of (14) which are valid over most of the dense gas regime and further study is clearly needed here. We note that some progress has been made in the area of near-critical internal flows (see, e.g., Hall, 1971 or Hsu and Graham, 1976) and similar approaches may turn out to be useful for the laminar external flows of interest here.

Acknowledgments

This research was supported by the National Science Foundation under grant no. CTS-8913198.

References

Anders, J. B., 1993, "Heavy Gas Wind Tunnel Research at Langley Research Center" ASME Paper 93-FE-5.

Anderson, W. K., 1991a, "Numerical Study of the Aerodynamic Effects of Using Sulfur Hexafluoride as a Test Gas in Wind Tunnels," NASA Technical Paper 3086.

Anderson, W. K., 1991b, "Numerical Study on Using Sulfur Hexafluoride as a Wind Tunnel Test Gas," *AIAA Journal,* Vol. 29, pp. 2179–2180.

Bethe, H. A., 1942, "The Theory of Shock Waves for an Arbitrary Equation of State," Office of Scientific Research and Development Report No. 545.

Chung, T. H., Lee, L. L., and Starling, K. E., 1984, "Applications of Kinetic Gas Theories and Multiparameter Correlation for Prediction of Dilute Gas Viscosity and Thermal Conductivity," *Industrial Engineering Chemistry Fundamentals,* Vol. 23, pp. 8–23.

Chung, T. H., Ajlan, M., Lee, L. L., and Starling, K. E., 1988, "Generalized Multiparameter Correlation for Nonpolar and Polar Fluid Transport Properties," Industrial Engineering *Chemistry Research,* Vol. 27, pp. 671–679.

Cramer, M. S., 1989, "Negative Nonlinearity in Selected Fluorocarbons," *Physics of Fluids A,* Vol. 1, pp. 1894–1897.

Cramer, M. S., and Tarkenton, G. M., 1992, "Transonic Flows of Bethe-Zel'dovich-Thompson Fluids," *Journal of Fluid Mechanics,* Vol. 240, pp. 197–228.

Cramer, M. S., Tarkenton, L. M., and Tarkenton, G. M., 1992, "Critical Mach Number Estimates for Dense Gases," *Physics of Fluids,* Vol. 4, pp. 1840–1847.

Curran, H. M., 1981, "Use of Organic Working Fluids in Rankine Engines," *Journal of Energy,* Vol. 5, pp. 218–223.

Enkenhus, K. R., and Parazzoli, C., 1970, "Dense Gas Phenomena in a Free-Piston Hypersonic Wind Tunnel," *AIAA Journal,* Vol. 8, pp. 60–65.

Hall, W. B., 1971, "Heat Transfer Near the Critical Point," *Advances in Heat Transfer,* edited by T. F. Irvine and J. P. Hartnett, Vol. 7, pp. 1–86.

Hayes, W. D., 1954, "Pseudotransonic Similitude and First-Order Wave Structure," *Journal of The Aeronautical Sciences,* 21, No. 11, pp. 721–730.

Hayes, W. D., 1958, "Gasdynamic Discontinuities," *Fundamentals of Gasdynamics,* edited by H. Emmons, Princeton University Press.

Hayes, W. D., and Probstein, R. F., 1958, *Hypersonic Flow Theory,* Academic Press.

Hsu, Y.-Y., and Graham, R. W., 1976, *Transport Processes in Boiling & Two-Phase Systems,* Hemisphere Publishing.

Kluwick, A., 1993, "Transonic Nozzle Flow in Dense Gases," *Journal of Fluid Mechanics,* Vol. 247, pp. 661–688.

Lambrakis, K., and Thompson, P. A., 1972, "Existence of Real Fluids with a Negative Fundamental Derivative Γ," *Physics of Fluids,* Vol. 5, pp. 933–935.

Martin, J. J., and Hou, Y. C., 1955, "Development of an Equation of State for Gases," *AIChE Journal,* Vol. 1, pp. 142–151.

Simeonides, G., 1987, "The Aerodynamic Design of Hypersonic Contoured Axisymmetric Nozzles Including Real Gas Effects," Von Karman Institute for Fluid Dynamics Technical Memorandum 43.

Simeonides, G., 1990, The VKI Hypersonic Wind Tunnels and Associated Measurement Techniques, Von Karman Institute for Fluid Dynamics Technical Memorandum 46.

Tarkenton, G. M., and Cramer, M. S., 1993, "Transonic Flows of Dense Gases," ASME Paper 93-FE-9.

Thompson, P. A., 1971, "A Fundamental Derivative in Gasdynamics," *Physics of Fluids,* Vol. 14, pp. 1843–1849.

Thompson, P. A., and Lambrakis, K., 1973, "Negative Shock Waves," *Journal of Fluid Mechanics,* Vol. 60, pp. 187–208.

Wagner, B., and Schmidt, W., 1978, "Theoretical Investigations of Real Gas Effects in Cryogenic Wind Tunnels," *AIAA Journal,* Vol. 16, pp. 580–586.

White, F. M., 1974, Viscous Fluid Flow, McGraw-Hill.

Whitlock, S. T., 1992, "Compressible Flows of Dense Gases in Boundary Layers," M. S. thesis, Virginia Polytechnic Institute and State University, Blacksburg, Virginia.

Zel'dovich, Ya., B. 1946, "On the Possibility of Rarefaction Shock Waves," *Zhurnal eksperimentalnoi i teoreticheskoi fiziki,* Vol. 16, No. 4, pp. 363–364.

Kunio Hijikata
Professor.

Yuji Suzuki
Research Associate.

Kenji Iwana
Graduate Student.

Department of Mechano-Aerospace
Engineering,
Tokyo Institute of Technology,
2-12-1 Oh-okayama, Meguro-ku,
Tokyo 152, Japan

Flow Visualization by Velocity-Pressure Cross-Correlation

For a better understanding of turbulent structure, a new flow visualization method of the time averaged structure of the turbulence has been developed by using wall pressure fluctuations to detect the velocity fluctuations of the flow. Velocity fluctuations were visualized by the measured velocity-wall pressure cross-correlation with the whole flow field for various time-delays between two measured values. Turbulence structures of a backward-facing step flow were investigated for three different flow regions—the recirculating flow just behind the step, the reattachment flow, and the boundary layer flow far down stream from the step. Sequential contour maps of cross-correlation values were calculated to display movement and deformation of turbulent structures both qualitatively and quantitatively.

1 Introduction

Researchers studying turbulent flow have been interested in the practical applications to enhance heat and mass transfer. In order to control these transport phenomena resulting from turbulent motion, it is necessary to know the detailed structure of turbulence. Experimental studies regarding turbulent structure can be divided into two groups. One group has tried to analyze the turbulent flow by quantitative measurements of the flow characteristics, such as velocity, pressure and so on (Didden and Ho, 1985 and Schewe, 1983). However, this approach is not suitable for recognizing the general nature of turbulent flow, because of the limitation on the number of measuring points. On the other hand, there is flow visualization (Yule, 1978 and Hussain et al., 1981), in which the general structure of the flow can be measured qualitatively, but not quantitatively. In recent years, several new combined techniques have been proposed (Adrian, 1986 and Talomon et al., 1986) which use visualization and carry out quantitative measurements simultaneously. This paper develops one of these combined techniques to investigate turbulent flow from a new viewpoint.

The large eddy turbulence structures are found mainly by velocity visualization using hydrogen bubbles or other tracer techniques. The pressure field can also give us important information about large eddy motion (Dinkelacker et al., 1977). Most of the visualized data, however, show only an instant in turbulent motion, while showing the mean characteristics of the turbulence requires visual data accumulation by a conditional sampling method. From this standpoint, this paper develops a new flow visualization method for the time-averaged turbulence structure by using a wall pressure fluctuation not only as a signal for the conditional sampling but also as a velocity fluctuation detector for the flow.

By accumulating the cross-correlation data, the time-mean structure of the velocity fluctuation can be obtained and the time delay of the cross-correlation gives us the phase information between the velocity and the pressure fluctuations. Because the fundamental pressure equation is a Poisson equation, which has no time derivative term, the pressure fluctuation contains instantaneous information of the velocity fluctuation in the whole flow field. Namely, the velocity fluctuation structure can be detected by using a pressure fluctuation as a reference and can be visualized by measuring the velocity-wall pressure cross-correlation. By using the velocity-pressure cross-correlation, many studies of the structure of coherent motions of a turbulent boundary layer have been reported (Kobashi and Ichijo, 1984; Johanson et al., 1987; Kim and Hussain, 1993, and so on).

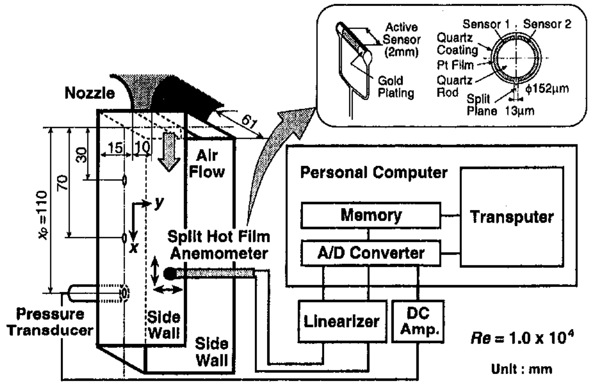

Fig. 1 Experimental apparatus

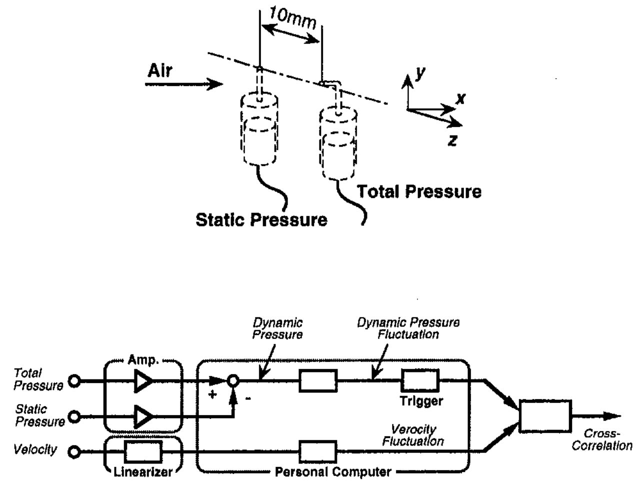

Fig. 2 Measurement of shear stress

A relation between the flow field estimated from the pressure and velocity cross-correlation and visualized patterns of the wall pressure fluctuations were investigated for an impinged flow (Hijikata and Mimatu, 1985). It was verified that the movement of high cross-correlation areas corresponds to the movement of the pressure fluctuation lumps. The high cross-correlation re-

---

Contributed by the Fluids Engineering Division for publication in the JOURNAL OF FLUIDS ENGINEERING. Manuscript received by the Fluids Engineering Division May 19, 1994; revised manuscript received February 28, 1996. Associate Technical Editor: M. Gharib.

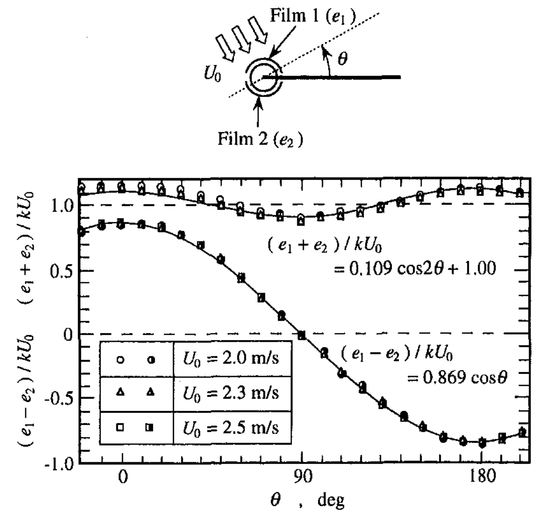

Fig. 3 Calibration of split film probe

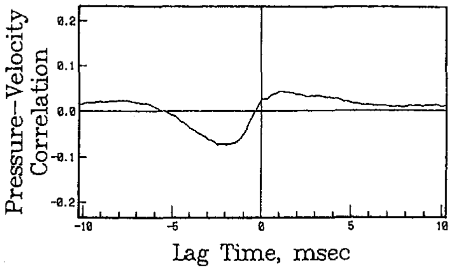

Fig. 4 Typical velocity-pressure cross-correlation [ρ_{pu}, x_p = 110 (mm), x = 106 (mm), y = 10 (mm)]

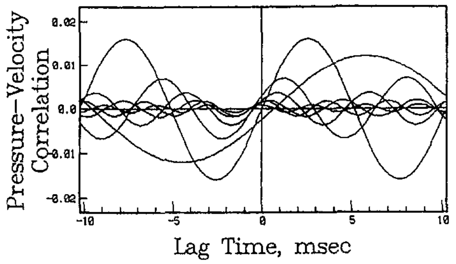

Fig. 5 Each frequency component of cross-correlation [ρ_{pu}, x_p = 110 (mm), x = 106 (mm), y = 10 (mm)]

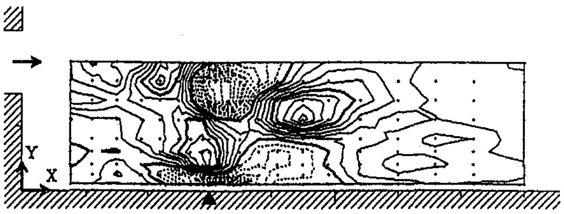

Fig. 6 Typical contour of velocity-pressure cross-correlation

gion has the same size as that of the pressure-fluctuation lumps in the pressure visualization, and the traveling velocities are the same.

The pressure field in the backward step flow was investigated, since three different flow regimes exist in that flow: a recirculation region after the nozzle exit, a reattachment region, and a boundary layer region in the down stream. The sequential contour maps of cross-correlation were calculated to display the deformation and the movement of turbulent structures both qualitatively and quantitatively. In the recirculation region, pressure patterns are mainly affected by the main flow characteristics, but in the reattachment region, the oncoming flow to the reattachment wall is more important.

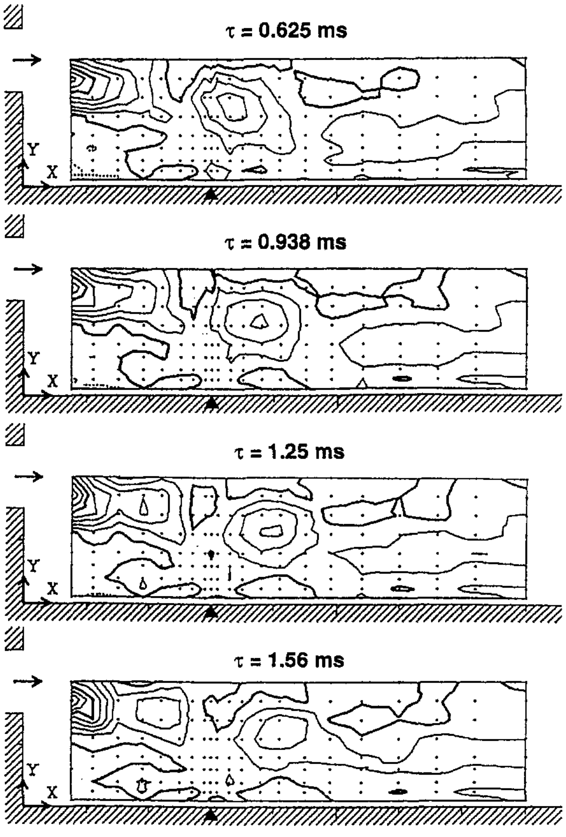

Contour Interval = 0.01

Fig. 7 Change of cross-correlation contour with time [ρ_{pu}, x_p = 30 (mm)] ($p \geq 90$ percent of maximum amplitude pressure fluctuation)

Nomenclature

D_0 = nozzle width, 61 mm
h = nozzle height, 10 mm
H = step height, 15 mm
P, p = time mean and fluctuation component of wall pressure
Re = Reynolds number U_0h/ν
ρ_{pu} = cross-correlation between pressure and velocity u
ρ_{pv} = cross-correlation between pressure and velocity v
$\rho_{p\omega}$ = cross-correlation between pressure and vorticity ω
U, u = velocity and fluctuation of velocity in x direction
U_0 = mean velocity at nozzle exit
V, v = velocity and fluctuation of velocity in y direction
x = direction parallel to the bulk flow
x_p = pressure-measuring point in x direction
y = direction vertical to the wall
τ = delay time
ω = vorticity

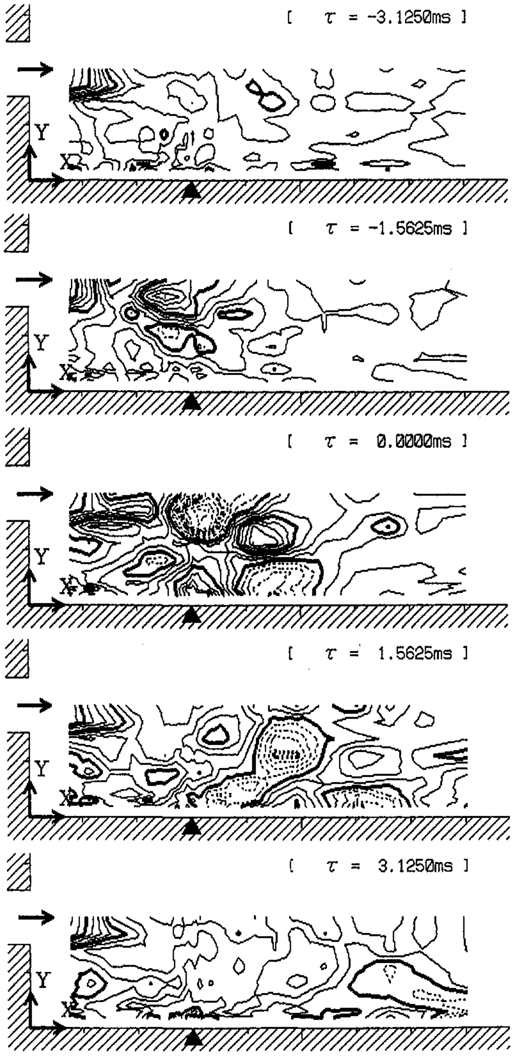

Fig. 8(a) Contour of velocity-pressure cross-correlation [ρ_{pu}, x_p = 30 (mm)] (contour interval = 0.025, solid line = POSITIVE, dotted line = NEGATIVE)

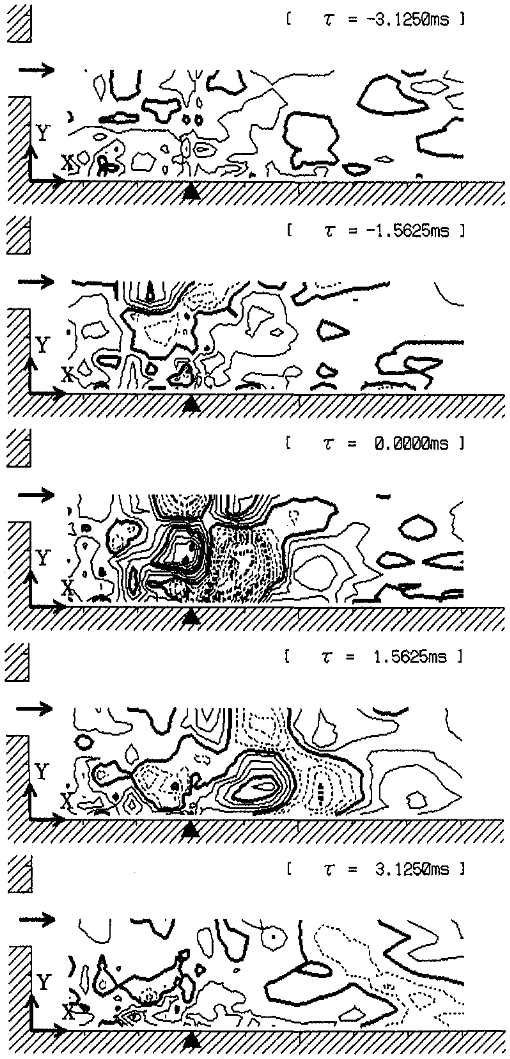

Fig. 8(b) Contour of velocity-pressure cross-correlation [ρ_{pv}, x_p = 30 (mm)] (contour interval = 0.025, solid line = POSITIVE, dotted line = NEGATIVE)

2 Experimental Apparatus

The schematic of the experimental apparatus for the measurement of the velocity-pressure cross-correlation and the data processing are shown in Fig. 1. At the exit of a 61 mm × 10 mm rectangular nozzle, a backward facing step of 15 mm was installed. The Reynolds number Re using the nozzle height as the characteristic length, was fixed at 10^4. The reattachment point was approximately 70 mm from the step. The pressure was measured by a semiconductor pressure transducer through a small hole (0.6 mm I.D.) on the channel wall. To measure the shear stress, a static and a total pressure probes were mounted on the wall as shown in Fig. 2. The distance between two probes is 10 mm. A square root of the difference of two signals is considered to proportional of the wall shear stress.

The velocity fluctuation in the step flow was measured by a split hot film anemometer able to traverse the whole velocity field. The obtained two velocity components (u, v) were analyzed by a Fast Fourier Transform (FFT). The cross-correlation was nondimensionalized by the auto-correlation of each signal. The delay time τ between two signals of the velocity and the pressure was varied between -10 ms to 10 ms, and 1000 sampled signals were averaged.

3 Data Acquisition and Processing

The large amount of experimental data and complex calculations required effective data acquisition and processing. Therefore, the experiment used a bus master type transputer and a high speed A/D converter boards mounted on a PC. The two signals from the split film probe were amplified and linearized by hot-wire amplifiers, and then transferred to the AD converter. The wall pressure measured by the semi-conductor transducer were also acquired. 1024 data of each signals of 12 bits, were transferred to PC memory by DMA (Direct Memory Access). Since the bus-master type transputer can control the PC memory as its own one, high speed data processing was realizable without special software. The transputer works by the parallel C, which is compatible to the normal C language.

The first stage of the data processing was to obtain the two velocity components (u, v) from the two signals (e_1, e_2) of the split film probe. In Fig. 3, calibration curves of the probe obtained by rotating the probe at a uniform velocity are shown. A vertical axis shows a sum and a difference of the two signals ($e_1 + e_2$, $e_1 - e_2$) divided by the uniform velocity U_0 and by the amplification constant of the probe k. A horizontal axis shows an angle of the split plane measured from the plane perpendicular to the uniform velocity. Under three different uniform velocity conditions, the following two relations agree well with the data.

$$\frac{e_1 - e_2}{kU_0} = 0.869 \cos \theta$$

$$\frac{e_1 + e_2}{kU_0} = 0.109 \cos 2\theta + 1.0 \qquad (1)$$

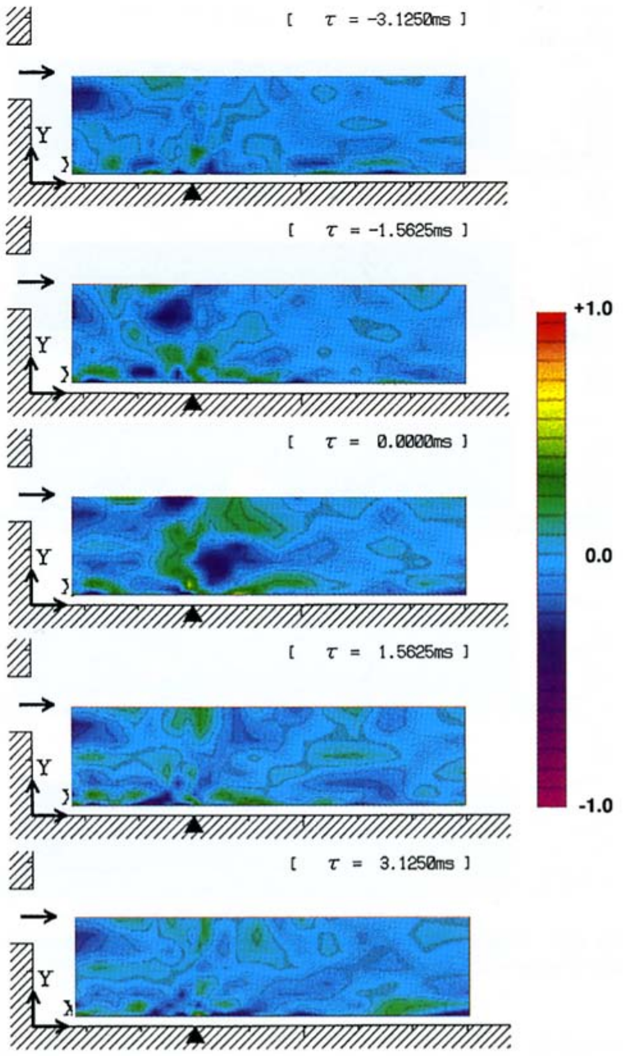

Fig. 8(c) Color contour of pseudo vorticity-pressure cross-correlation [$\rho_{p\omega}/(\rho_{p\omega})_{\max}$, x_p = 30 (mm)] (($\rho_{p\omega})_{\max}$ = 1.18, $(\rho_{p\omega})_{\min}$ = −0.960)

From these relations, the velocity perpendicular to the split plane of $U = U_0 \cos\theta$ and the absolute velocity U_0 were calculated. From these values, the other velocity component V was calculated by following equation.

$$V = \sqrt{U_0^2 - U^2} \tag{2}$$

After the FFT of the fluctuation components of u, v, and p, cross-power spectrums were obtained using the following correlation:

$$S_{xy}(f_k) = X^*(f_k) \cdot Y(f_k) \tag{3}$$

where * implies complex conjugate and

$$X(f_k) = \frac{1}{N} \sum_{n=0}^{N-1} x(n) \exp\left(\frac{-i2\pi nk}{N}\right)$$

$$Y(f_k) = \frac{1}{N} \sum_{n=0}^{N-1} y(n) \exp\left(\frac{-i2\pi nk}{N}\right). \tag{4}$$

The cross-corrleation of R_{xy} is calculated from S_{xy} as follows:

$$R_{xy}(\tau_m) = \frac{1}{N} \sum_{k=0}^{N-1} S_{xy} \exp\left(\frac{i2\pi mk}{N}\right) \tag{5}$$

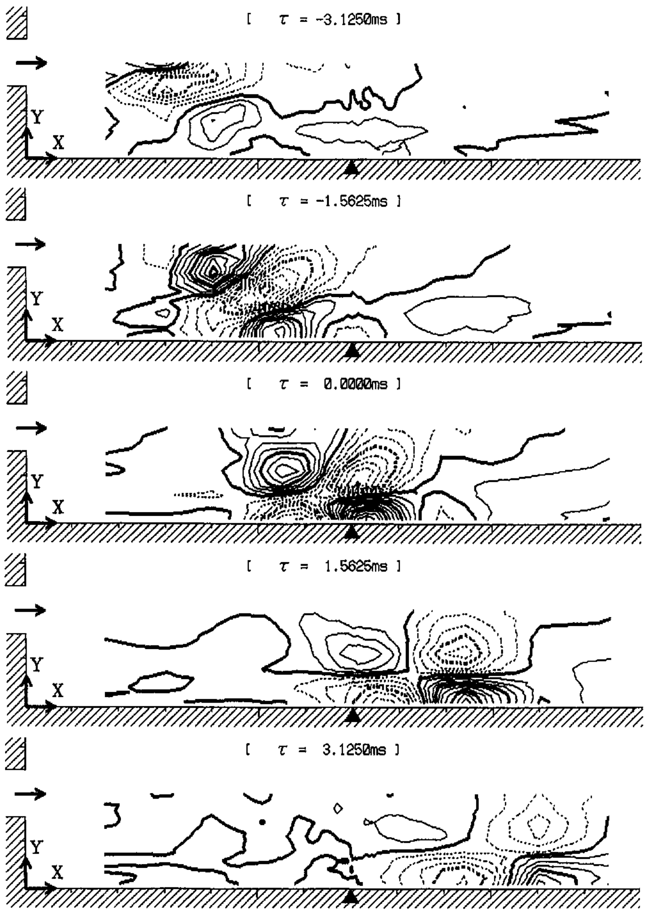

Fig. 9(a) Contour of velocity-pressure cross-correlation [ρ_{pu}, x_p = 70 (mm)] (contour interval = 0.025, solid line = POSITIVE, dotted line = NEGATIVE)

The cross-correlation function ρ_{xy} is a normalized of the cross-correlation.

$$\rho_{xy}(\tau_m) = \frac{R_{xy}(\tau_m)}{\sqrt{R_{xx}(0) \cdot R_{yy}(0)}} \tag{6}$$

where $R_{xx}(0)$ and $R_{yy}(0)$ are the auto-correlation at $\tau = 0$, which are equal to the root mean square of $x(n)$ and $y(n)$, respectively.

By filtering the cross-power spectrum we can separate the motion of each frequency components of the turbulent motion.

4 Conditional Sampling

The wall pressure was measured at three different points, one each located in the recirculation, the reattachment, and the boundary layer regions. For each pressure measuring point, the velocity was measured in the whole flow field. For one velocity measuring point, the cross-power spectrums of p-u and p-v were calculated, but these power spectrums were different in every measurement, because the instantaneous flow motion is different. Therefore, it is necessary to distinguish whether the data include special fluctuation motion. For example, if a positive peak pressure fluctuation occurs in the measured data, then there is reason to believe that some special fluctuation motions exist in the flow. Because only the amplitude and the sign of the pressure fluctuation can be measured, the conditional sampling condition can only depend on these properties. The simplest sampling condition is to accept all the measured data for processing.

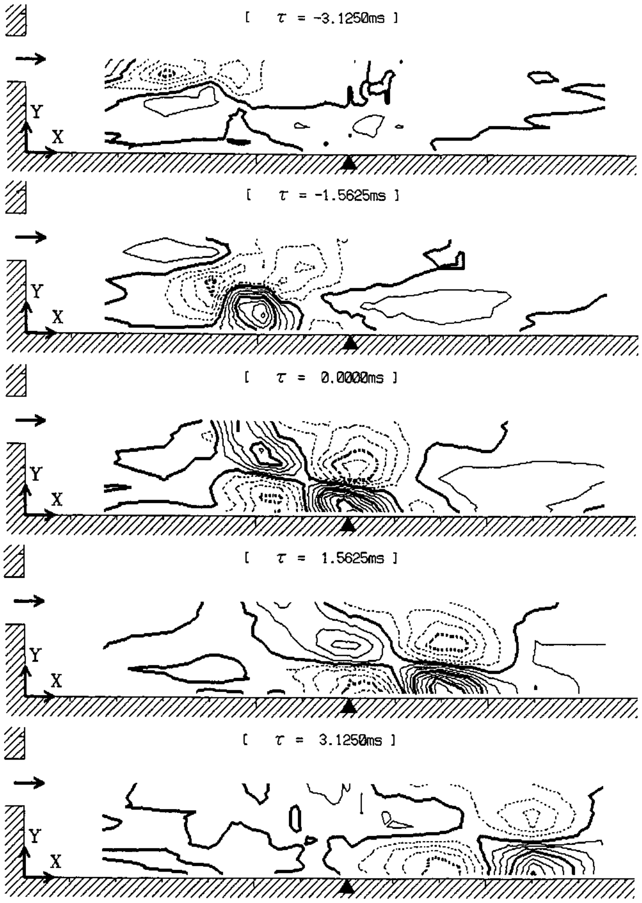

Fig. 9(*b*) Contour of velocity-pressure cross-correlation [ρ_{pv}, x_p = 70 (mm)] (contour interval = 0.025, solid line = POSITIVE, dotted line = NEGATIVE)

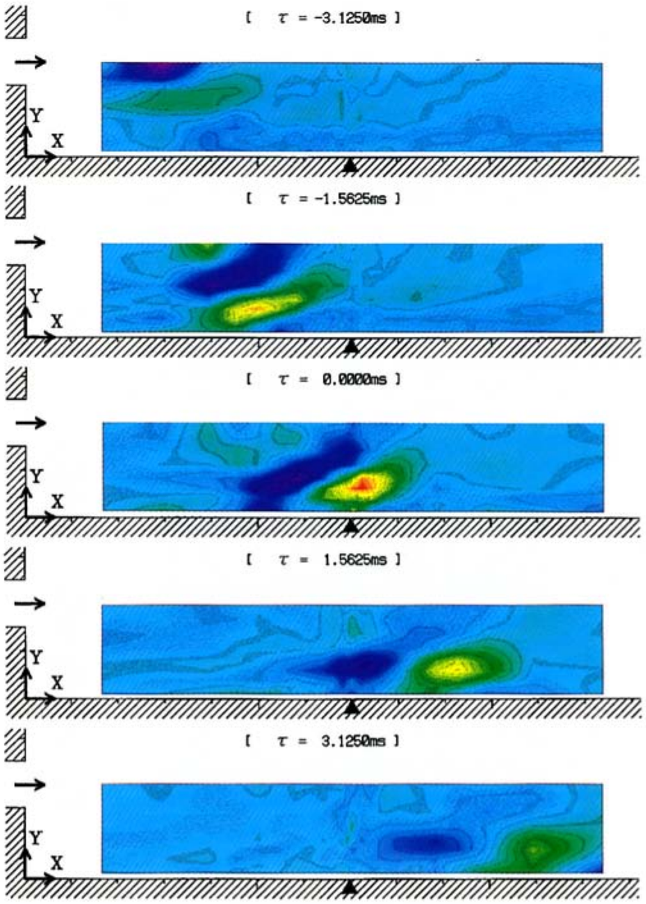

Fig. 9(*c*) Color contour of pseudo vorticity-pressure cross-correlation [$\rho_{p\omega}/(\rho_{p\omega})_{\max}$, x_p = 70 (mm)] (($\rho_{p\omega})_{\max}$ = 0.783, $(\rho_{p\omega})_{\min}$ = −0.654)

Since the measured data contain other unnecessary information of fluctuation motion, an averaging more than the 1000 times is necessary in the conditional sampling. A typical pressure-velocity cross-correlation is shown in Fig. 4. In the figure, the positive correlation appears in the positive time lag region, and negative one in the negative time lag. The cross-correlation pattern is different at different measuring point. The peak of the cross-correlation becomes larger when the distance between the velocity and the pressure measuring points becomes shorter, and the time lag between the peaks becomes smaller.

The cross-correlation as shown in Fig. 4 consists of many frequency components, which is shown in Fig. 5. The every frequency's peak has different amplitude and it appears at different time-lag, which implies that the fluctuating motion of different size eddies move differently.

Figure 6 shows a typical contour of the cross-correlation function ρ_{pu}, where the wall pressure was measured in the recirculating region. Just above the pressure measuring point, a positive cross-correlation region exists. On the contrary, a negative correlation region exists between the positive correlation region and the wall. This figure shows the impingement of the lump of the velocity fluctuation.

5 Results and Discussion

5.1 Effect of Conditional Sampling. In order to show the effect of the conditional sampling, the contour of the cross-correlation function ρ_{pu} is visualized under different sampling condition. The pressure fluctuation was used as a conditional sampling condition, and a threshold magnitude and sign for the sampling were changed. The results showed that the sign of the threshold condition has no effect on the visualized result. However, by changing the threshold magnitude, the visualized pattern changes. When the pressure in recirculation region immediately downstream was measured under the new condition, all the lumps of the velocity fluctuation moved downstream under the simple averaging condition. However, when the cross-correlation was averaged under the condition of an existence of high amplitude pressure fluctuation, the lump of the velocity fluctuation moved upstream in the recirculating region as shown in Fig. 7. Since the pressure fluctuation at the wall is mainly caused by the velocity fluctuation at the free shear layer of the recirculating flow, the averaging can detect this shear layer structure, and the lump of the velocity fluctuation moves downstream by the simple averaging. On the contrary, the pressure fluctuation generated near the wall can only be detected by the conditional sampling. In the figure, the contour of the cross-correlation moves upstream near the wall, but it moves downstream at the free stream shear layer.

5.2 Visualization of Velocity Fluctuation. In order to show the size and the motion of the eddy intuitively, contours of the pressure-velocity cross-correlation (ρ_{pu}, ρ_{pv}) are shown for the different delay time τ in Figs. 8(*a*), (*b*), 9(*a*), (*b*), and 10(*a*), (*b*) for the three regions. In each region, the pressure has a different behavior. In the recirculating zone, the pressure is nearly constant, but it increases due to the impingement at the reattachment region. The measurement of the cross-correlation was carried out with this in mind. The horizontal and vertical axes in all figures indicate the velocity measuring point in the flow space. The solid lines represent the positive correlation,

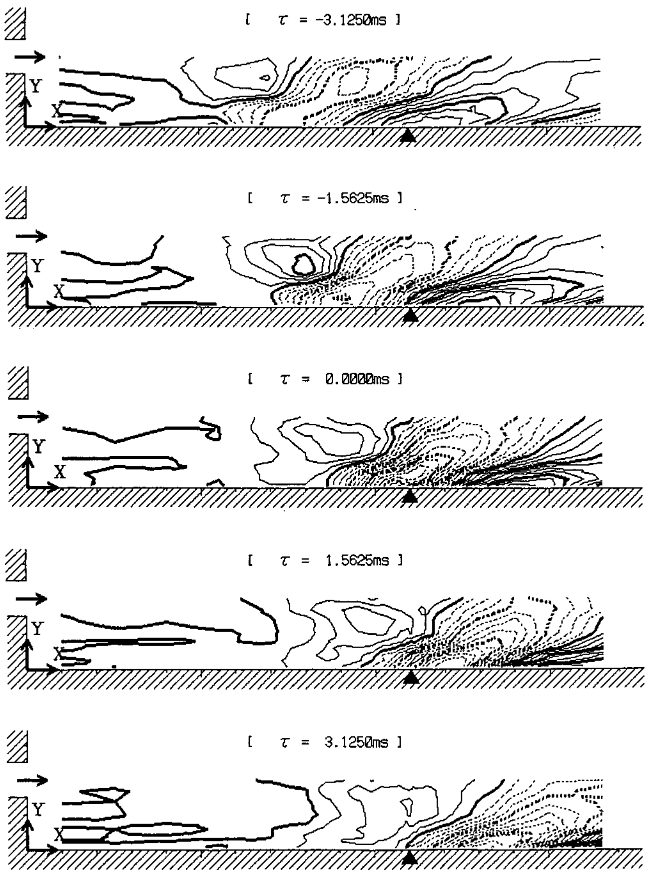

Fig. 10(*a*) Contour of velocity-pressure cross-correlation [$\rho_{pu}, x_p = 110$ (mm)] (contour interval = 0.025, solid line = POSITIVE, dotted line = NEGATIVE)

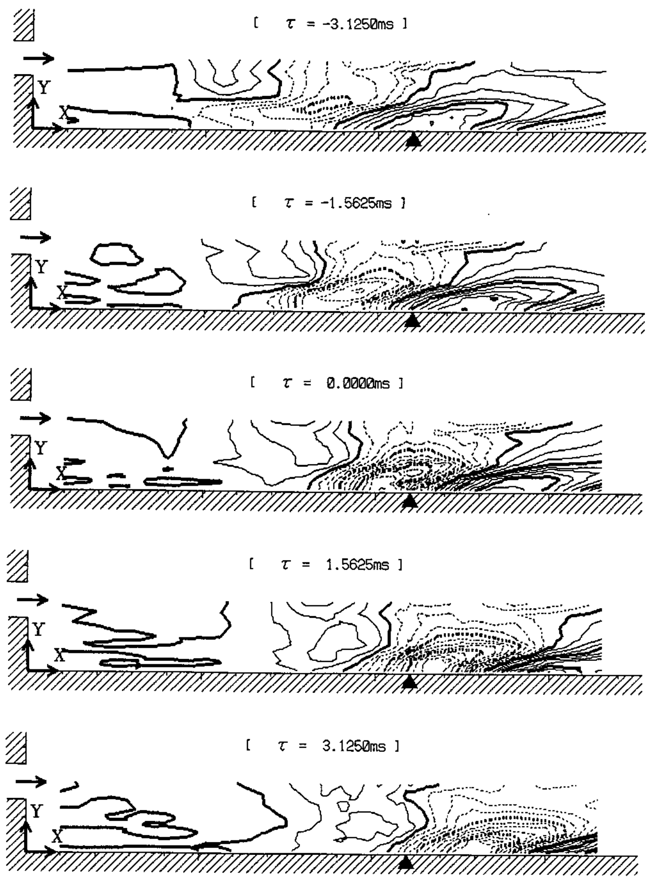

Fig. 10(*b*) Contour of velocity-pressure cross-correlation [$\rho_{pv}, x_p = 110$ (mm)] (contour interval = 0.025, solid line = POSITIVE, dotted line = NEGATIVE)

which means the wall pressure increase as the velocity increases, and the dotted lines indicate a negative value, which means the pressure increases as the velocity decreases. The fluid flows from the left-hand side to the right. The pressure measurement point on the channel wall is indicated by the solid triangle.

The contours of ρ_{pu} and ρ_{pv} in the recirculation region are shown in Figs. 8(*a*), (*b*), where τ is the time-delay between the pressure fluctuation and the velocity fluctuation. A positive value of τ means the velocity fluctuation occurs after the pressure fluctuation. In the figure, the absolute maximum correlation for a time-lag of $\tau = 0$, located just above the pressure measuring point, is negative. the result implies that the pressure increase at the wall in the recirculating zone is caused by the acceleration of the main flow, whose characteristics are quite reasonable and coincide with the well-known fact that the pressure in the separated bubble is nearly constant. From this figure, the pressure fluctuation appears to be generated by the periodic velocity change in the main flow. The near wall phenomena have few effects on the wall pressure fluctuation as shown in Fig. 7.

In the reattachment region shown in Figs. 9(*a*), (*b*), the pressure change is caused by the acceleration of the fluid flow, which implies that the impingement of the flow on the wall is dominant. However, the velocity fluctuation lump influencing the wall pressure is not entrained along the stream line. In the main flow, the negative correlation predominates, which generates the positive correlation in the recirculating zone and leads to the velocity lump impingement on the wall. This mechanism is different from the stagnation flow caused by a jet impingement (Hijikata and Mimatu, 1987).

In the boundary layer flow farther downstream as shown in Figs. 10(*a*), (*b*), the pressure increase is caused by the velocity reduction (negative values of correlation) and the eddy size is slightly larger than in Figs. 8 or 9. Its shape is not round and is inclined in the upward flow direction. In this region, the trace of the center of the highest cross-correlation is nearly parallel to the wall.

5.3 Pseudo-Vorticity Contour. By using the sequential data of the velocity-pressure cross-correlation, we can easily trace the large eddy motion which affects the wall pressure fluctuation. However, the structure shown in these figures is not directly corresponding to the eddy motion, because the eddy structure should be shown by the vorticity, but the direct measurement of the vorticity is difficult. Instead, the following variable is derived:

$$\rho_{p\omega} = \frac{\partial \rho_{pv}}{\partial x} - \frac{\partial \rho_{pu}}{\partial y} . \tag{7}$$

The cross-correlation between the vorticity in the flow and pressure on the wall is not exactly equal to Eq. (7). However, in a mean sense, it is closely related to Eq. (7). It will be referred to the pseudo vorticity-pressure cross-correlation, hereafter. From the two cross-correlation data of ρ_{pu} and ρ_{pv}, the pseudo vorticity-pressure cross-correlation is calculated using Eq. (7) and shown in Figs. 8(*c*), 9(*c*), and 10(*c*). In the recirculation region, the movement of the strong fluctuation structures is not observed, but at the nozzle exit, a negative region of correlation by the shear exists in Fig. 8(*c*). In Fig. 9(*c*), where the pressure measuring point is in the reattachment region, a pair of vortices having different rotation clearly exists

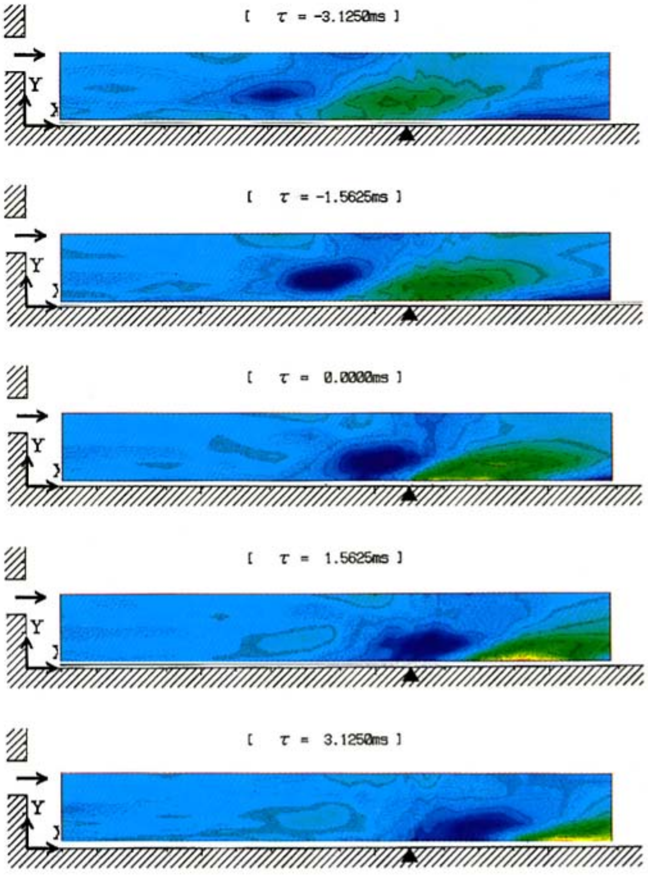

Fig. 10(*c*) Color contour of pseudo vorticity-pressure cross-correlation $[\rho_{p\omega}/(\rho_{p\omega})_{\max}, x_p = 110\ (\mathrm{mm})]\ ((\rho_{p\omega})_{\max} = 1.28, (\rho_{p\omega})_{\min} = -0.661)$

and their motion and deformation of vorticity can be traced. The pair of vortices is originally located vertically in the main flow, but then changes to a horizontal position relative to the wall after passing the reattachment point. In the boundary-layer flow, as shown in Fig. 10(*c*), the positive contours of the cross-correlation make angles of about 20 degrees from the wall.

5.4 Frequency Analysis of Cross-Correlation. The cross-correlation can be separated into frequency components, which summed, approximate the structure. In the frequency domain, the data was divided into low and high frequency components as the first step, and then summed to reconstruct the cross-correlation in the velocity fields. In the case of the cross-correlation between pressure and vorticity, low frequency component is considered to describe the large eddy motion, and high frequency, the small. these two contours of cross-correlation of $(\rho_{p\omega})_{\mathrm{low}}$ and $(\rho_{p\omega})_{\mathrm{high}}$ are shown in Figs. 11(*b*) and (*c*). In these figures, islands of contours in $(\rho_{p\omega})_{\mathrm{low}}$ are much larger than that in $(\rho_{p\omega})_{\mathrm{high}}$, which correspond to large and small eddies. the data suggest that large eddies are able to move through the reattachment point, which small eddies are reduced by reattachment on the wall. Therefore, in Figs. 11(*a*), (*b*) and (*c*), the flow structure is mainly composed of large eddies in the region downstream from the reattachment point.

5.5 Shear Stress-Velocity Cross-Correlation. Both positive and negative correlation regions were observed for the pressure-velocity cross-correlation. However, for the cross-correlation between the velocity fluctuation and the shear stress fluctuation obtained from the wall dynamic pressure fluctuation, only one positive high correlation region was detected near the wall in Fig. 12, which was measured downstream from the reattachment point by using I-type hot wire anemometer. This is because the shear stress fluctuation is caused by the velocity fluctuation in the flow direction. Hence, the velocity fluctuation has the same sign as the shear stress fluctuation. In this experiment, the total pressure fluctuation is much larger than the static one. Thus the cross-correlation between the fluctuation of the velocity and the wall shear stress, influenced the dynamic pressure, can provided more obvious information of a large scale structure of a turbulent shear flow near the wall than the velocity-static pressure cross-correlation shown in Fig. 10. However, sweep and ejection events cannot be observed at the present time.

6 Uncertainty Estimates

Considering the measurement error, errors due to the sensitivity of the pressure transducer were the most dominant; other errors were negligible. The accuracy of the pressure fluctuations, which were calculated from the signals translated by 12 bits A/D converter, was no more than 8 bits. This calculation of cross-correlation was accurate to three significant figures. Therefore, the bias limit of the measurement was 0.005 relative to the value of the nondimensional cross-correlation.

For each measured point, 1000 sampled signals were averaged to obtain the cross-correlation. The precision index of all

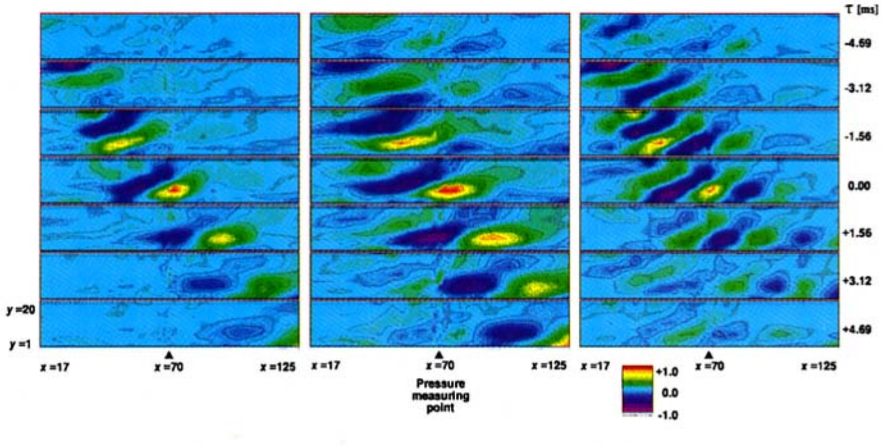

(*a*) (*b*) (*c*)

Fig. 11 Contour of pseudo vorticity-pressure cross-correlation $[\rho_{p\omega}/(\rho_{p\omega})_{\max}, x_p = 70\ (\mathrm{mm})]$. **(*a*) All frequencies** $((\rho_{p\omega})_{\max} = 0.783, (\rho_{p\omega})_{\min} = -0.654)$; **(*b*) low frequencies** $[48.8 \sim 293.0\ \mathrm{Hz}]\ ((\rho_{p\omega})_{\max} = 0.211, (\rho_{p\omega})_{\min} = -0.195)$; **(*c*) high frequencies** $[341.8 \sim 585.9\ \mathrm{Hz}]\ ((\rho_{p\omega})_{\max} = 0.178, (\rho_{p\omega})_{\min} = -0.190)$.

measured points (about 200 pints) was considered 1.5 times the maximum absolute cross-correlation.

Accordingly, in the case of Fig. 8(a), the uncertainty at 95 percent confidence for the velocity-pressure cross-correlation (ρ_{pu}) distribution was 9.4 percent. The uncertainties of other distributions (Figs. 6–12) were similarly about 10 percent.

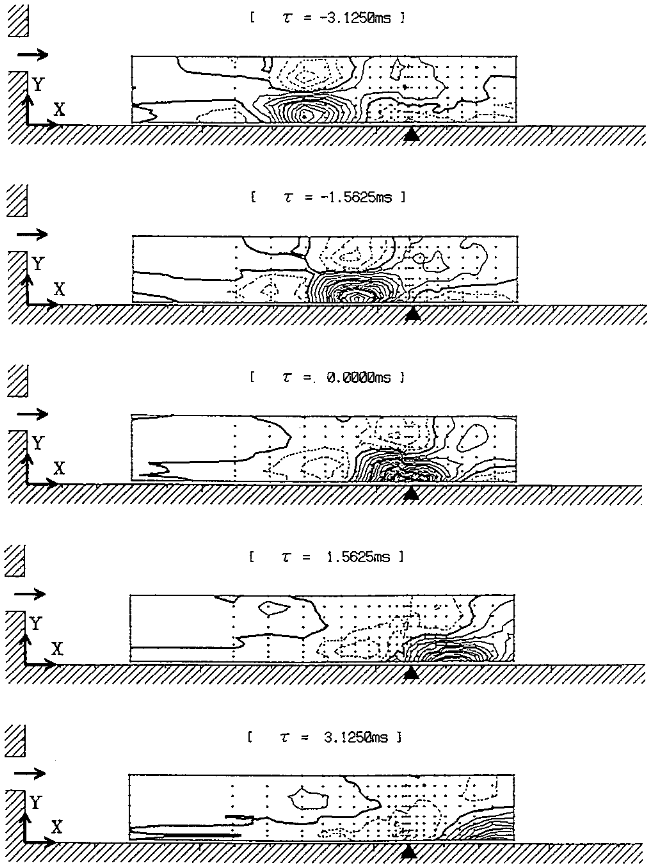

Fig. 12 Contour of Shear Stress-Velocity Cross-Correlation [x_p = 110 (mm)] (contour interval = 0.02, solid line = POSITIVE, dotted line = NEGATIVE)

7 Conclusions

The visualization of the flow characteristics by using contours of the velocity-pressure cross-correlation were carried out, and the following conclusions were obtained:

(1) From the contours of the velocity-pressure cross-correlation, the size of the high-correlation region was determined which corresponds to the mean size of eddies.

(2) A use of a split hot film anemometer provides the ability to measure two velocity components and to obtain pseudo-vorticity cross-correlation to the pressure fluctuation and eddy motions.

(3) From the frequency analysis of the cross-correlation, the large and the small eddies are clearly separated in the reattachment region and their motion was visualized.

References

Adrian, R. J., 1986, "Multi-Point Optical Measurements of Simultaneous Vectors in Unsteady Flow—A Review," *International Journal of Heat and Fluid Flow*, Vol. 7, No. 2, pp. 127–145.

Didden, N., and Ho, C. M., 1985, "Unsteady Separation in a Boundary Layer Produced by an Impinging Jet," *Journal of Fluid Mechanics*, Vol. 160, pp. 235–256.

Dinkelacker, A., Hessel, M., Meier, G. E. A., and Schewe, G., 1977, "Investigation of Pressure Fluctuations Beneath a Turbulent Boundary Layer by Means of an Optical Method," *Physics of Fluids*, Vol. 20, Part II, pp. 216–224.

Hijikata, K., and Mimatu, J., 1985, "Holographic Visualization of Pressure Distribution on the plate by Jet Impingement," *Proceedings of the International Symposium on Fluid Control and Measurement*, Tokyo, pp. 685–690.

Hijikata, K., and Mimatu, J., 1987, "Turbulent Structure Near the Stagnation Point of an Axisymmetric Impinging Jet," *Proceedings of the 6th Symposium on Turbulent Shear Flow*, Toulouse, pp. 221–226.

Hussain, A. K. M. F., and Clark, A. R., 1981, "On the Coherent Structure of the Axisymmetric Mixing Layer: A Flow-Visualization Study," *Journal of Fluid Mechanics*, Vol. 104, pp. 263–294.

Johansson, A. V., Her, J.-Y., and Haritonidis, J. H., 1987, "On the Generation of High-Amplitude Wall-Pressure Peaks in Turbulent Boundary Layers and Spots," *Journal of Fluid Mechanics*, Vol. 175, pp. 119–142.

Kim, J., and Hussain, J., 1993, "Propagation Velocity of Perturbations in Turbulent Channel Flow," *Physics of Fluids A*, Vol. 5, pp. 695–706.

Kobashi, Y, and Ichijo, M., 1986, "Wall Pressure and its Relation to Turbulent Structure of a Boundary Layer," *Experiments in Fluids*, Vol. 4, pp. 49–55.

Schewe, G., 1983, "On the Structure and Resolution of Wall-Pressure Fluctuations Associated with Turbulent Boundary-Layer Flow," *Journal of Fluid Mechanics*, Vol. 134, pp. 311–328.

Talomon, A. M., Kunen, J. M. G., and Ooms, G., 1986, "Simultaneous Flow Visualization and Reynolds-Stress Measurement in a Turbulent Boundary Layer," *Journal of Fluid Mechanics*, Vol. 163, pp. 459–478.

Yule, A. J., 1978, "Large-Scale Structure in the Mixing Layer of a Round Jet," *Journal of Fluid Mechanics*, Vol. 89, Part 3, pp. 413–432.

R. D. Joslin
Leader, LFC Project Team,
Fluid Mechanics and Acoustics Division,
NASA Langley Research Center,
Hampton, VA 23681-0001

G. Erlebacher
Senior Research Fellow,
Institute for Computer Applications in
Science and Engineering

M. Y. Hussaini
Eminent Scholar Chair in
High Performance Computing,
Florida State University,
Tallahassee, FL 32306-4052

Active Control of Instabilities in Laminar Boundary Layers—Overview and Concept Validation

This paper (the first in a series) focuses on using active-control methods to maintain laminar flow in a region of the flow in which the natural instabilities, if left unattended, lead to turbulent flow. The authors review previous studies that examine wave cancellation (currently the most prominent method) and solve the unsteady, nonlinear Navier-Stokes equations to evaluate this method of controlling instabilities. It is definitively shown that instabilities are controlled by the linear summation of waves (i.e., wave cancellation). Although a mathematically complete method for controlling arbitrary instabilities has been developed, the review, duplication, and physical explanation of previous studies are important steps for providing an independent verification of those studies, for establishing a framework for the work which will involve automated transition control, and for detailing the phenomena by-which the automated studies can be used to expand knowledge of flow control.

Introduction

Most studies to date have been restricted to maintaining laminar flow through the use of a technique termed ''wave cancellation.'' The wave-cancellation method assumes that a wave-like disturbance can be linearly cancelled by introducing another wave with similar amplitude but is out of phase. The key is to determine the parameters of the downstream wave which counter (cancel) the evolution of the upstream generated wave. Milling (1981) and Liepmann and Nosenchuck (1982a, b) tested the feasibility of this concept in water tunnels with flat plates and a zero pressure gradient. Using two vibrating wires (one in an upstream and one in a downstream location) to generate traveling waves 180 deg out of phase, Milling (1981) showed that a wave with a 0.6-percent amplitude could be reduced (cancelled) to a disturbance with a 0.1-percent amplitude and a profile that no longer resembled a wave shape. By using hot strips to generate and control traveling waves, Liepmann and Nosenchuck (1982a, b) obtained wall-shear results that indicate a partial wave cancellation, which led to a 30-percent delay in transition. Liepmann and Nosenchuck (1982b) also noted that the transition to turbulence could be accelerated if the two disturbance generators were in phase; this technique may be useful to force the flow into a turbulent state, for example, to prevent an undesirable flow separation. Finally, Liepmann and Nosenchuck (1982b) showed that a comparable stabilization by steady heating would require a 2000-percent increase in energy over the unstable wave-cancellation technique. In an experimental wind-tunnel facility, Thomas (1983) used electromagnetic generators to study and control traveling waves in a boundary layer on a zero-pressure-gradient flat-plate model. With an optimal choice of phase and amplitude for the second wave, Thomas (1983) showed that a two-dimensional (2D) disturbance with an approximate amplitude of 1 percent was reduced to 0.2 percent through partial wave cancellation, and a transition delay was realized. However, similar to previous experiments, complete relaminarization was not accomplished. Thomas postulated that an interaction between background disturbances and the primary wave led to increased levels of three dimensionality, which prevented complete relaminarization. Thomas also determined that wave interactions degrade the effectiveness of the cancellation technique and suggested that the control be as close as possible to the primary wave generator to decrease the effect of wave interactions. Based on the study of Liepmann and Nosenchuck (1982a, b), Ladd and Hendricks (1988) employed adaptive heating to control 2D instabilities in a laminar boundary layer on an axisymmetric body (ellipsoid) in a water tunnel. Similar to the above experiments, some degree of wave cancellation was obtained for the 2D instabilities; however, as Ladd and Hendricks noted, the naturally occurring waves on an ellipsoid are highly three dimensional (3D), which makes cancellation much more difficult to achieve. Finally, unlike the previous experiments that used artificially produced Tollmien-Schlichting (TS) waves, Pupator and Saric (1989) and Ladd (1990) examined the cancellation of random disturbances on a flat plate in a wind tunnel and on an axisymmetric body in a water tunnel, respectively. With periodic suction and blowing used as the actuator, both studies showed a reduction in the random disturbance amplitudes.

Various theoretical and computational studies have been aimed at understanding the physics of this wave-cancellation process. The linear asymptotic theory analysis by Maestrello and Ting (1984) indicated that small amounts of local periodic heating can excite disturbances which actively control the TS waves that travel on a flat plate in water. One of the first Navier-Stokes simulations of active control was conducted by Biringen (1984), who used a temporally-growing instability formulation in a laminar channel flow. Using suction and blowing as the control, Biringen (1984) observed approximately a 50-percent reduction in the amplitudes of the 2D instabilities and a decrease in the growth of the 3D instabilities; the Reynolds stress that resulted from the control was nearly zero due to the destruction of the streamwise and wall-normal disturbance velocities. Metcalfe et al. (1985) used solutions of the Navier-Stokes equations in the temporally-growing instability formulation to study the effect of a moving wall on unstable waves traveling in a laminar flow on a flat plate. By using an energy analysis, they showed that the wall motion causes the Reynolds-stress term to become

---

Contributed by the Fluids Engineering Division for publication in the JOURNAL OF FLUIDS ENGINEERING. Manuscript received by the Fluids Engineering Division October 17, 1994; revised manuscript received June 4, 1996. Associate Technical Editor: W. S. Saric.

negative, which implies a feed of energy from the perturbed flow back into the mean flow. In effect, this energy analysis showed how a perturbation to an unstable flow can be stabilizing. However, Metcalfe et al. (1985) pointed out that downstream of the suction and blowing the unstable residual wave began to grow at about the same rate as prior to the control. Bower et al. (1987) and Pal et al. (1991) used the 2D Orr-Sommerfeld equation to study and control instability-wave growth by superposition. They show within the limits of linear stability theory and the parallel-flow assumption that waves (even multi-frequency waves) can be cancelled. Laurien and Kleiser (1989) used solutions of the Navier-Stokes equations in the temporally-growing instability formulation to study the effects of unsteady suction and blowing on unstable 2D and 3D waves traveling in a parallel laminar flow on a flat plate; Kral and Fasel (1989) used solutions of the Navier-Stokes equations in the spatially-growing instability formulation to study the effect of unsteady heating on unstable 2D and 3D waves traveling in a nonparallel laminar flow on a flat plate. The 3D modes are secondary instabilities arising from a threshold amplitude of the 2D wave. Both studies showed that transition can be delayed (or accelerated) by superposing disturbances out of phase (in phase) with the primary TS wave and that control is only effective if it is applied at an early stage of transition, where the 2D wave is dominant. Finally, Danabasoglu et al. (1991) used solutions of the Navier-Stokes equations in the spatially-growing instability formulation to study the effect of unsteady suction and blowing on unstable 2D and 3D waves traveling in a laminar channel flow. Consistent with the previous Navier-Stokes studies, transition was delayed by superposition of out-of-phase control disturbances on the disturbances that were generated upstream. Additionally, a 2D TS wave with an amplitude as large as 3 percent of the channel centerline velocity was suppressed by approximately 85 percent with wave cancellation.

All of the previous active-control studies were undertaken with the a priori assumption that wave cancellation was accomplished by the linear superposition (or forcing) of waves with 180 deg phase shifts. None of these previous studies were able to achieve complete (or exact) instability removal (wave cancellation) from the flow, except for the linear studies reported Bower et al. (1987) and Pal et al. (1991) which could obtain cancellation because the nonlinear governing equations were reduced to a linear system. The present paper definitively documents the fundamental reason for the reductions in amplitudes of the instabilities in previous experiments and computations by the addition of a control wave, demonstrates why complete wave cancellation was not possible in the previous studies, explains why the wave regains its exponential growth characteristic a small distance downstream of the control wave, and describes why wave cancellation is not possible in the true 3D nonlinear transition case.

Numerical Experiments

These tasks are accomplished by numerical example using a coupled high-order finite-difference/spectral methods direct numerical simulation (DNS) code which solves the full nonlinear, unsteady Navier-Stokes equations. Described by Joslin et al. (1992, 1993), the spatial discretization entails a Chebyshev collocation grid in the wall-normal direction, fourth-order finite differences for the pressure equation, sixth-order compact differences for the momentum equations in the streamwise direction, and a Fourier sine and cosine series in the spanwise direction on a staggered grid. For time marching, a time-splitting procedure is used with implicit Crank-Nicolson differencing for normal diffusion terms and an explicit three-stage Runge-Kutta method. The influence-matrix technique is employed to solve the resulting pressure equation (Helmholtz-Neumann problem). At the inflow boundary, the mean base flow is forced and, at the outflow, the buffer-domain technique is used.

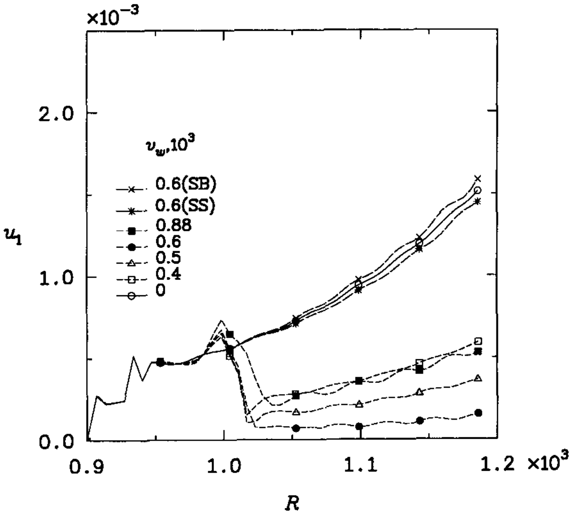

Fig. 1 Active control of Tollmien-Schlichting waves in flat-plate boundary layer. (SB = Steady Blowing, SS = Steady Suction).

For the present Navier-Stokes computations, the grid has 661 streamwise and 61 wall-normal points. The far-field boundary is located $75\delta_0^*$ from the wall, and the streamwise distance is $308\delta_0^*$ from the inflow (where δ_0^* is the displacement thickness at the inflow of the computational domain). For the time marching, a time-step size of 320 steps per wave period is chosen for the three-stage Runge-Kutta method. Periodic suction and blowing through the wall is used to initiate and control disturbances, where v_f is the wall-normal velocity amplitude of the initial disturbance and v_w is the control amplitude. A sufficiently refined grid and small enough time step are used to displace the numerical techniques from the flow physics.

A small-amplitude disturbance (v_f = 0.0001) with a frequency ω = 0.0774 and an inflow Reynolds number R = 900 is used for this investigation. A number of simulations were conducted to control the growth of TS waves within the boundary layer. Results from these simulations are shown in Fig. 1, where the amplitudes of the streamwise component (u_1) of the TS waves are shown with downstream distance (R). For the range of amplitudes shown, all unsteady control waves lead to significant decreases in amplitudes and growth rates as a result of and downstream of the control, which is spatially located just upstream of R = 1000. As expected from many previous linear studies and duplicated in Fig. 1, steady blowing is destabilizing, and steady suction is stabilizing. The steady control cases are included to qualitatively illustrate Liepmann and Nosenchuck's (1982b) hypothesis that steady control requires orders of magnitude more energy than is required for unsteady control to achieve similar control features. The results of Fig. 1 demonstrate that the small amplitudes required for nearly optimal unsteady wave cancellation barely influence the stability of the TS wave with steady suction or blowing.

The wave cancellation by the superposition principle has been assumed to be the reason for the decreased amplitudes and growth rates for the controlled waves. Metcalfe et al. (1985) showed that the moving wall causes a negative Reynolds stress, which implies an energy feed from the unstable flow into the mean flow and which leads to a more stable flow. An examination of the Reynolds stress in light of the above argument may lead to a similar conclusion for the present results; however, this cause-effect relationship is unlikely with the small-disturbance amplitudes generated by suction and blowing through a solid wall. Three simulations were conducted to ensure that linear superposition of individual instabilities was, in fact, responsible for the results shown in Fig. 1 and in the previous experiments and computations. Figure 2 shows the instantaneous streamwise

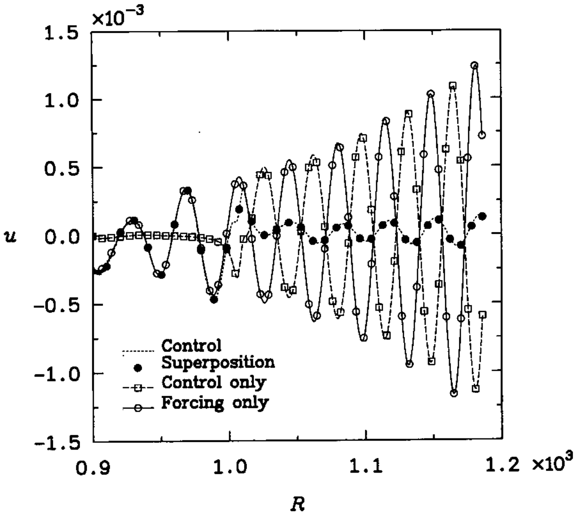

Fig. 2 Verification of superposition principle

velocity (u) with downstream distance (R) obtained in each of three ways: (1) force a disturbance with suction and blowing and with no control (Forcing only); (2) activate suction and blowing at the control location only with no upstream forcing (Control only); and (3) apply suction and blowing at an upstream location to generate a disturbance in the flow and activate suction and blowing control at a downstream location, which invokes wave-cancellation (Control). By discretely summing the control-only and forcing-only numerical results, the superposition results are obtained. Shown in Fig. 2, this linear superposed solution is identical to the wave-cancellation simulation. This comparison not only definitively validates the supposition that linear superposition is the reason for the previous experimental and computational results, but it explains the reason for the failure of the simulations to reach an exact cancellation of disturbances. If the waves had a spatial/temporal phase shift of exactly 180 deg and the amplitudes were exactly the same quantitative value for each streamwise location, then superposition would lead to a complete wave cancellation. Figure 2 shows that the control wave differs in both amplitude and phase from the initiated instability, where the control has a smaller amplitude than the disturbance. This difference leads to a superposed wave that has a reduced amplitude but retains some semblance of the wave shape and phase of the initial disturbance. Figure 2 also explains the phase shift of 180 deg between the control cases ($v_w = 0.0004$ and $v_w = 0.00088$) which are shown in Fig. 1. For $v_w = 0.0004$, the control amplitude is smaller than the initial disturbance and leads to the qualitatively superposed wave of Fig. 2. As the control amplitude (e.g., $v_w = 0.00088$) exceeds the disturbance amplitude, the resulting superposed wave falls in line with the control phase, which leads to a downstream evolving instability which has a phase shift of approximately 180 deg from the original upstream disturbance.

The process of introducing a control wave which exactly matches the phase and amplitude of the initial spatially-growing disturbance requires many significant digits of accuracy. This explains why exact wave cancellation was not possible in previous experiments, where such accuracy is not possible. Previous computations could obtain exact cancellation through optimizing the control phase and amplitude to match the initial instability, assuming the initial disturbance had an evolution which could be described by a linear system. This leads us to the final task of explaining why the instability regains its exponential growth characteristics in a short distance downstream.

The above results demonstrate that this process of wave cancellation is very sensitive to amplitude and phase of the control wave. If exact cancellation is not achieved, then the disturbance amplitude is significantly reduced and the semblance of the wave is primarily retained. Within the boundary layer, a redistribution of energy very quickly occurs whereby the dominant mode regains its momentum and begins to exponentially grow as prior to the introduction of the control wave. This process is not limited to the wave-cancellation technique, but occurs with the initiation process of a wave (e.g., vibrating ribbon, etc.).

Finally, the wave-cancellation technique will not work for the real transition problem because the underlying assumption of the technique resides in the ability to linearly superpose instabilities to delay transition for this problem and in general control the flow. The present results document the parameter sensitivities for a small-amplitude disturbance (i.e., the governing equations can be described by a linear system); however, when multiple instabilities are present and have the opportunity to nonlinearly interact, then the required control waves can self-interact and interact with the initial modes. This potential interaction would prohibit any hope for the superposition technique for real-world applications.

Conclusions and Future Directions

The present paper uses direct numerical simulation cases to definitively document that wave cancellation is the fundamental reason for the reductions in amplitudes of the instabilities in previous experiments and computations. It is shown that wave cancellation is very sensitive to the control parameters and usually leads to a downstream evolving wave which has a greatly reduced amplitude but resembles the wave instability. Because the downstream instability retains the wave characteristics, it regains its exponential growth a small distance downstream of the control wave input. Finally, previous studies obtained transition delays only when a 2D control was imposed when 3D instabilities had sufficiently small amplitudes because otherwise the superposition assumption becomes invalid. Hence, wave cancellation is not possible in the true 3D nonlinear transition case.

Much of the transition process involves small-amplitude disturbances and can therefore be described by linear systems. Hence, in a subsequent paper, the wave-cancellation process is automated under the linear superposition process such that a controller is evaluated; it receives information from sensors as input and provides a signal to control the actuator response as output. Clearly, this automation could only be successful for small-amplitude non-interacting modes. Available now in Joslin et al. (1995a) the results using this spectral controller indicate that a measure of wave cancellation is observed without using feedback. Feedback would lead to more optimal solutions by tuning the actuation amplitude.

The next paper for the flat-plate problem involves an actuator, a sensor downstream of the actuator, and the coupling of optimal control theory with the Navier-Stokes equations to form a closed-loop system for the control of arbitrary instabilities. For this formal theory, there is no a priori assumption of linear wave superposition; therefore, the potential exists for the control of nonlinear instabilities. Available now in Joslin et al. 1995b, the results of coupling the DNS and optimal control theory indicate that the mathematical system prescribes actuator control equivalent to the wave-cancellation concept. The future direction of this research should involve testing the coupled active flow control system for other practical aerodynamic problems (e.g., separation control).

Acknowledgments

This research was supported by NASA under contract NAS1-19480 while the authors (except first) were in residence at the Institute for Computer Applications in Science and Engineering, NASA Langley Research Center, Hampton, VA.

References

Biringen, S., 1984, ''Active Control of Transition by Periodic Suction-Blowing,'' *Physics of Fluids*, Vol. 27, No. 6, pp. 1345–1347.

Bower, W. W., Kegelman, J. T., Pal, A., and Meyer, G. H., 1987, ''A Numerical Study of Two-Dimensional Instability-Wave Control Based on the Orr-Sommerfeld Equation,'' *Physics of Fluids*, Vol. 30, No. 4, pp. 998–1004.

Danabasoglu, G., Biringen, S., and Streett, C. L., 1991, ''Spatial Simulation of Instability Control by Periodic Suction and Blowing,'' *Physics of Fluids*, Vol. 3, No. 9, pp. 2138–2147.

Joslin, R. D., Streett, C. L., and Chang, C.-L., 1992, ''Validation of Three-Dimensional Incompressible Spatial Direct Numerical Simulation Code—A Comparison with Linear Stability and Parabolic Stability Equations Theories for Boundary-Layer Transition on a Flat Plate,'' NASA Technical Paper 3205.

Joslin, R. D., Streett, C. L., and Chang, C.-L., 1993, ''Spatial Direct Numerical Simulation of Boundary-Layer Transition Mechanisms: Validation of PSE Theory,'' *Theoretical & Computational Fluid Dynamics*, Vol. 4, No. 6, pp. 271–288.

Joslin, R. D., Nicolaides, R. A., Erlebacher, G., Hussaini, M. Y., and Gunzburger, M. D., 1995a, ''Active Control of Boundary-Layer Instabilities: Use of Sensors and Spectral Controller,'' *AIAA Journal*, Vol. 33, No. 8, pp. 1521–1523.

Joslin, R. D., Gunzburger, M. D., Nicolaides, R. A., Erlebacher, G., and Hussaini, M. Y., 1995b, ''A Self-Contained, Automated Methodology for Optimal Flow Control—Application to Transition Delay,'' NASA Contractor Report 198215.

Kral, L. D., and Fasel, H. F., 1989, ''Numerical Investigation of the Control of the Secondary Instability Process in Boundary Layers,'' AIAA Paper 89-0984.

Ladd, D. M., and Hendricks, E. W., 1988, ''Active Control of 2-D Instability Waves on an Axisymmetric Body,'' *Experiments in Fluids*, Vol. 6, pp. 69–70.

Ladd, D. M., 1990, ''Control of Natural Laminar Instability Waves on an Axisymmetric Body,'' *AIAA Journal*, Vol. 28, No. 2, pp. 367–369.

Laurien, E., and Kleiser, L., 1989, ''Numerical Simulation of Boundary-Layer Transition and Transition Control,'' *Journal of Fluid Mechanics*, Vol. 199, pp. 403–440.

Liepmann, H. W., and Nosenchuck, D. M., 1982a, ''Control of Laminar-Instability Waves Using a New Technique,'' *Journal of Fluid Mechanics*, Vol. 118, pp. 187–200.

Liepmann, H. W., and Nosenchuck, D. M., 1982b, ''Active Control of Laminar-Turbulent Transition,'' *Journal of Fluid Mechanics*, Vol. 118, pp. 201–204.

Maestrello, L., and Ting, L., 1984, ''Analysis of Active Control by Surface Heating,'' AIAA Paper 84-0173.

Metcalfe, R. W., Rutland, C., Duncan, J. H., and Riley, J. J., 1985, ''Numerical Simulations of Active Stabilization of Laminar Boundary Layers,'' AIAA Paper 85-0567.

Milling, R. W., 1981, ''Tollmien-Schlichting Wave Cancellation,'' *Physics of Fluids*, Vol. 24, No. 5, pp. 979–981.

Pal, A., Bower, W. W., and Meyer, G. H., 1991, ''Numerical Simulations of Multifrequency Instability-Wave Growth and Suppression in the Blasius Boundary Layer,'' *Physics of Fluids A*, Vol. 3, No. 2, pp. 328–340.

Pupator, P., and Saric, W., 1989, ''Control of Random Disturbances in a Boundary Layer,'' AIAA Paper 89-1007.

Thomas, A. S. W., 1983, ''The Control of Boundary-Layer Transition Using a Wave-Superposition Principle,'' *Journal of Fluid Mechanics*, Vol. 137, pp. 233–250.

Chen-I Hung
Associate Professor.

Jung-Shun Tsai
Graduate Student.

Cha'o-Kuang Chen
Professor.

Department of Mechanical Engineering,
National Cheng Kung University,
Tainan, Taiwan

Nonlinear Stability of the Thin Micropolar Liquid Film Flowing Down on a Vertical Plate

A perturbation method is used to investigate analytically the nonlinear stability behavior of a thin micropolar liquid film flowing down a vertical plate. In this analysis, the conservation of mass, momentum, and angular momentum are considered and a corresponding nonlinear generalized kinematic equation for the film thickness is thereby derived. Results show that both the supercritical stability and the subcritical instability can be found in the micropolar film flow system. This analysis shows that the effect of the micropolar parameter R ($=\kappa/\mu$) *is to stabilize the film flow, that is, the stability of the flowing film increases with the increasing magnitude of the micropolar parameter R. Also, the present analysis shows that the micropolar coefficients,* Δ ($=h_0^2/j$) *and* Λ ($=\gamma/\mu j$)*, have very little effects on the stability of the micropolar film.*

Introduction

The instability problems of fluid film flowing down a vertical or inclined plate are common in many industrial applications, e.g., the finishing of coating, laser cutting process, and casting technology. It is known that macroscopic instabilities are disastrous to fluid flow. It would be highly desirable to know the flow configurations and their time dependence, in order to develop suitable conditions under which the homogeneous film growth could be obtained.

The problem of linear stability of isothermal film flow without taking into account surface tension was first studied numerically by Yih (1954). The pioneering work on the nonlinear stability of film flow using perturbation methods was provided by Benney (1966). Later on, Lin (1974), and Krishna and Lin (1977) presented the nonlinear stability analysis of an isothermal film flow with respect to the two- or three-dimensional disturbance of finite amplitude and finite bandwidth. Hwang and Weng (1987) showed that supercritical stability and subcritical instability are both possible for a liquid film flow system with and without interfacial phase change. Tsai et al. (1996) extended the nonlinear analysis to the stability of condensate film flow under the effect of magnetic field. An extensive review on the stability of falling liquid film can be referred to Chang (1994).

In recent years, the stability problem of interest has been extended to the flow of fluids in the presence of microstructures. A subclass of these fluids was named micropolar fluids by Eringen (1964) who first proposed the theory of micropolar fluids. Micropolar fluids exhibit certain microscopic effects arising from the local structure and microrotations of the fluid elements. In application, the micropolar fluids may be used to model some manmade fluids, such as the polymeric fluids, animal blood, fluids with additives, and liquid crystals, etc. The extension of the theory of micropolar fluids to cover the thermal effect was developed by Eringen (1967). Liu (1970, 1971) studied the flow stability of micropolar fluids and found that the initiation of instability was delayed due to the presence of microstructures in the fluid. Datta and Sastry (1976) studied the instability of a horizontal micropolar fluid layer which was heated from below. They found that the plot of Rayleigh number versus wave number has two branches separating the zones of stability. Ahmadi (1976) studied the same problem by employing a linear theory as well as an energy method. It was observed that the micropolar fluid layer heated from below is more stable as compared with the classical Newtonian fluid, and also found that, no subcritical instability region exists. Payne and Straughan (1989) investigated the Benard problem for a thermomicropolar fluid by the nonlinear energy stability method. They predicted the subcritical instability may possibly occur, but did not infer the existence of subcritical instabilities from their work. Later, Franchi and Straughan (1992) established a nonlinear energy stability analysis for the convection of the thermo-micropolar fluid with temperature dependent viscosity. They showed that the critical Rayleigh number depend strongly on the changes of the interaction coefficient κ, and indicated that the micropolar coefficient γ has very little influence on the convection threshold.

According to our reviews, the nonlinear stability of a thin micropolar liquid film flowing down a vertical plate has not been investigated in previous studies. These kinds of stability problems are important in many industrial applications. In this paper, the finite-amplitude stability of a micropolar liquid film that flows down a vertical wall will be studied. The method of multiple scales is applied to solve the nonlinear generalized kinematic equations, order by order, and that leads to a secular equation of Ginzburg-Landau type. By the nonlinear analysis, the interactions between the equilibrium finite amplitude and the micropolar parameters could be realized theoretically. Moreover, the sensitivity of micropolar parameters will be investigated in the present study.

Analysis

Consider a thin layer of an incompressible viscous micropolar fluid film flowing down a vertical wall, as shown in Fig. 1. The governing equations and associated boundary conditions are extended to the formulation of the generalized kinematic equation in the presence of microstructures. All physical properties are assumed to be constant. The physical system is formulated from the conservation of mass, momentum, and angular momentum. Based on the above assumptions, the governing equations and the corresponding boundary conditions are given as

Continuity equation:

$$\frac{\partial u^*}{\partial x^*} + \frac{\partial v^*}{\partial y^*} = 0, \qquad (1)$$

Contributed by the Fluids Engineering Division for publication in the JOURNAL OF FLUIDS ENGINEERING. Manuscript received by the Fluids Engineering Division May 23, 1995; revised manuscript received February 14, 1996. Associate Technical Editor: G. Karniadakis.

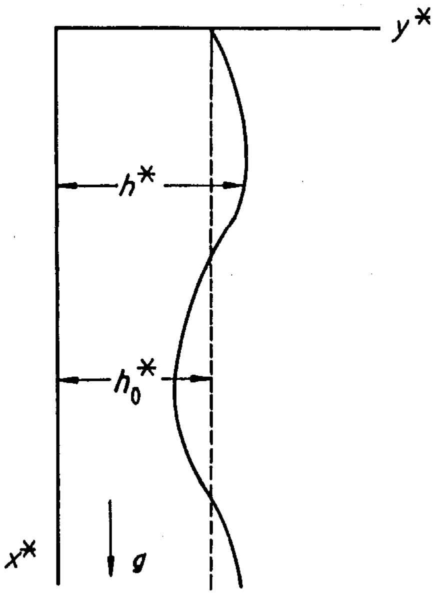

Fig. 1 Physical model and coordinate system

X-momentum equation:

$$\rho\left(\frac{\partial u^*}{\partial t^*} + u^* \frac{\partial u^*}{\partial x^*} + v^* \frac{\partial u^*}{\partial y^*}\right)$$

$$= -\frac{\partial P^*}{\partial x^*} + (\mu + \kappa)\left(\frac{\partial^2 u^*}{\partial x^{*2}} + \frac{\partial^2 u^*}{\partial y^{*2}}\right) + \kappa \frac{\partial N^*}{\partial y^*} + \rho g \quad (2)$$

Y-momentum equation:

$$\rho\left(\frac{\partial v^*}{\partial t^*} + u^* \frac{\partial v^*}{\partial x^*} + v^* \frac{\partial v^*}{\partial y^*}\right)$$

$$= -\frac{\partial P^*}{\partial y^*} + (\mu + \kappa)\left(\frac{\partial^2 v^*}{\partial x^{*2}} + \frac{\partial^2 v^*}{\partial y^{*2}}\right) - \kappa \frac{\partial N^*}{\partial x^*}, \quad (3)$$

Angular-momentum equation:

$$\rho j\left(\frac{\partial N^*}{\partial t^*} + u^* \frac{\partial N^*}{\partial x^*} + v^* \frac{\partial N^*}{\partial y^*}\right)$$

$$= -\kappa\left(\frac{\partial u^*}{\partial y^*} - \frac{\partial v^*}{\partial x^*}\right) - 2\kappa N^* + \gamma\left(\frac{\partial^2 N^*}{\partial x^{*2}} + \frac{\partial^2 N^*}{\partial y^{*2}}\right). \quad (4)$$

In the above equations, u^* and v^* are the velocity components in x^* and y^* directions, respectively, P^* the pressure, N^* the angular microrotation, ρ the density, μ the dynamic viscosity, κ the vortex viscosity, j the micro-inertia density, and γ the spin-gradient viscosity. The last term on the right-hand side of Eq. (2) is the body force due to gravity.

The fluid motion may be assumed to be affected by (i) viscous action, which is measured by μ, (ii) the effect of couple stresses, measured by γ, and (iii) the direct coupling of the microstructure to the velocity, measured by κ. Stokes (1985) showed that each of the constants μ, γ, and κ can have any value greater than, or equal to, zero, so that the ratios γ/μ and κ/μ, which are measures, respectively, of the relative strengths of the couple stress to the viscous effect and the microstructure coupling to the viscous effect, can have any value greater than, or equal to, zero. Kolpashchikov et al. (1983) determined the viscosity coefficients of micropolar fluid on the basis of viscometric and thermal measurements. The order of magnitude of the micro-inertia density, j, is comparable to l^2, where l is a material length depending on the size of microstructure. For most suspensions, the order of magnitude of l is about 10^{-3} to 10^{-5} cm (Eringen, 1980). The appropriate boundary conditions are:

At the plate ($y^* = 0$):

$$u^* = 0, \quad (5)$$

$$v^* = 0, \quad (6)$$

$$N^* = -\frac{1}{2}\left(\frac{\partial u^*}{\partial y^*} - \frac{\partial v^*}{\partial x^*}\right). \quad (7)$$

At free surface ($y^* = h^*$):

$$P^* + 2\mu \frac{\partial u^*}{\partial x^*}\left[1 + \left(\frac{\partial h^*}{\partial x^*}\right)^2\right]\left[1 - \left(\frac{\partial h^*}{\partial x^*}\right)^2\right]^{-1}$$

$$+ S \frac{\partial^2 h^*}{\partial x^{*2}}\left[1 + \left(\frac{\partial h^*}{\partial x^*}\right)^2\right]^{-3/2} = P_a^*, \quad (8)$$

$$\frac{\partial u^*}{\partial y^*} + \frac{\partial v^*}{\partial x^*} + 4 \frac{\partial h^*}{\partial x^*} \frac{\partial u^*}{\partial x^*}\left[\left(\frac{\partial h^*}{\partial x^*}\right)^2 - 1\right]^{-1} = 0, \quad (9)$$

$$N^* = 0, \quad (10)$$

$$\frac{\partial h^*}{\partial t^*} + u^* \frac{\partial h^*}{\partial x^*} - v^* = 0. \quad (11)$$

The boundary conditions at the interface, Eqs. (8) and (9), are the balance of normal and tangential stresses. In Eq. (8), P_a^* is the ambient pressure, and S is the surface tension. The discussion of boundary conditions for the angular velocity N at solid wall and at the free surface, shown in Eqs. (7) and (10), can be found in Datta and Sastry (1976) and Ahmadi (1976). Equation (11) is the free surface kinematic equation.

Nomenclature

$d = d_r + id_i$, complex wave celerity
g = gravitational acceleration
h = film thickness
h_o = local base flow film thickness
j = micro-inertia density
N = angular micro-rotation momentum
P = liquid pressure
P_a = ambient pressure
$R = =\kappa/\mu$, micropolar parameter
$\mathrm{Re} = =u_o h_o/\nu$, Reynolds number
t = time
$u_o = =gh_0^2/2\nu$, reference velocity
u, v = velocities along x- and y-directions, respectively
$W = =(S^3/2^4\rho^3\nu^4 g)^{1/3}$, dimensionless surface tension
x, y = coordinates along and transverse to the plate
α = wave number
$\Delta = =h_o^2/j$, micropolar parameter
$\Lambda = =\gamma/\mu j$, micropolar parameter
η = dimensionless disturbance film thickness
γ = spin-gradient viscosity
κ = vortex viscosity
ν = fluid kinematic viscosity
μ = fluid dynamic viscosity
ρ = liquid density
λ = disturbance wavelength

Superscripts

$*$ = dimensional quantities

Proceeding with the analysis, we define the following dimensionless quantities as:

$$x = \frac{\alpha x^*}{h_0^*}, \quad y = \frac{y^*}{h_0^*}, \quad t = \frac{\alpha u_0^* t^*}{h_0^*},$$

$$h = \frac{h^*}{h_0^*}, \quad u = \frac{u^*}{u_o^*}, \quad v = \frac{v^*}{\alpha u_o^*},$$

$$u_0^* = \frac{g h_0^{*2}}{2\nu}, \quad N = \frac{N^* h_o^*}{u_o^*}, \quad P = \frac{P^* - P_a^*}{\rho u_0^{*2}}, \quad \mathrm{Re} = \frac{h_0^* u_0^*}{\nu},$$

$$\alpha = \frac{2\pi h_0^*}{\lambda}, \quad W = \left(\frac{S^3}{2^4 \rho^3 \nu^4 g}\right)^{1/3}. \tag{12}$$

After applying the expressions in Eq. (12) into Eqs. (1)–(11), we have

$$u_x + v_y = 0, \tag{13}$$

$$(1 + R)u_{yy} + RN_y = -2 + \alpha\,\mathrm{Re}(p_x + u_t + uu_x + vu_y) - \alpha^2(1 + R)u_{xx}, \tag{14}$$

$$P_y = \alpha\,\mathrm{Re}^{-1}(1 + R)v_{yy} - \alpha R N_x - \alpha^2(uv_x + vv_y + v_t) + \alpha^3\,\mathrm{Re}^{-1}(1 + R)v_{xx}, \tag{15}$$

$$\Lambda N_{yy} - 2R\Delta N - R\Delta u_y = \alpha\,\mathrm{Re}(N_t + uN_x + vN_y) - \alpha^2(R\Delta v_x + \Lambda N_{xx}), \tag{16}$$

where

$$R = \frac{\kappa}{\mu}, \quad \Delta = \frac{h_o^{*2}}{j}, \quad \Lambda = \frac{\gamma}{\mu j}.$$

are the dimensionless material properties. Also, in the above equations, Re is the Reynolds number and α is the wave number. The subscripts (hereinafter) are represented for partial derivatives. If $R = 0$, the vortex viscosity effect of the particles in the micropolar fluid will be neglected, and the system reduce to the case of classical Newtonian fluid. For most micropolar fluids, the micropolar parameter R and Reynolds number Re are $O(\alpha^0)$. The dimensionless form of the corresponding boundary conditions now become:

at the solid wall ($y = 0$):

$$u = v = 0, \quad N = -\tfrac{1}{2}(u_y - \alpha^2 v_x)_{y=0}. \tag{17}$$

at the interface ($y = h$):

$$P + 2\alpha\,\mathrm{Re}^{-1} u_x(1 + \alpha^2 h_x^2)(1 - \alpha^2 h_x^2)^{-1} = 0, \tag{18}$$

$$u_y = \alpha^2 v_x + 4\alpha^2 u_x h_x(1 - \alpha^2 h_x^2)^{-1}, \tag{19}$$

$$N = 0, \tag{20}$$

$$h_t + uh_x - v = 0. \tag{21}$$

Since the long-wavelength (i.e., small wave number α) modes are the most unstable ones for film flow, we choose α as the perturbation parameter, then expand u, v, P, and N in the following form:

$$u = u_0 + \alpha u_1 + O(\alpha^2),$$

$$v = v_0 + \alpha v_1 + O(\alpha^2),$$

$$P = P_0 + \alpha P_1 + O(\alpha^2),$$

$$N = N_0 + \alpha N_1 + O(\alpha^2).$$

Now inserting the above expressions into Eqs. (13)–(21). The resulting equations are then solved order by order. In practice, the parameter W is usually of large value, so that $\alpha^2 W$ is taken to be of order one. The zeroth- and first-order solutions (given in the Appendix) are inserted into the dimensionless free surface kinematic equation, Eq. (21), and yields the following nonlinear generalized kinematic equation

$$h_t + A(h)h_x + B(h)h_{xx} + C(h)h_{xxxx} + D(h)h_x^2 + E(h)h_x h_{xxx} = 0 \tag{22}$$

where

$$A(h) = \left(\frac{4}{R + 2}\right)h^2,$$

$$B(h) = \frac{64\alpha\,\mathrm{Re}}{15(R + 2)^3}h^6 + \left[-\frac{32\alpha\,\mathrm{Re}}{m^2(R + 2)^3} + \frac{16\alpha\,\mathrm{Re}\Lambda}{R\Delta(R + 2)^3} + \frac{8\alpha\,\mathrm{Re}}{\Delta(R + 2)^3}\right] \times \left[\frac{h^4}{3} - \frac{h^3}{m}\coth(mh) + \frac{h^2}{m^2}\right],$$

$$C(h) = \frac{4\alpha^3 W\,\mathrm{Re}^{-2/3}}{3(R + 2)}h^3,$$

$$D(h) = \frac{128\alpha\,\mathrm{Re}}{5(R + 2)^3}h^5 + \left[-\frac{32\alpha\,\mathrm{Re}}{m^2(R + 2)^3} + \frac{16\alpha\,\mathrm{Re}\Lambda}{R\Delta(R + 2)^3} + \frac{8\alpha\,\mathrm{Re}}{\Delta(R + 2)^3}\right] \times \left[\frac{4h^3}{3} - \frac{3h^2}{m}\coth(mh) + h^3\,\mathrm{csch}^2(mh) + \frac{2h}{m^2}\right],$$

$$E(h) = \frac{4\alpha^3 W\,\mathrm{Re}^{-3/2}}{(R + 2)}h^2, \tag{23}$$

and

$$m = \left[\frac{R\Delta(R + 2)}{\Lambda(R + 1)}\right]^{1/2}.$$

When $R = 0$, Eq. (22) can be reduced to the equation, for the case without interfacial phase change, that was derived by Hwang and Weng (1987).

Stability Analysis

In this analysis, only the case of nonlinear stability is considered. The side-band stability analysis given in this section is restricted to the investigation of the threshhold amplitude for subcritical instability and supercritical stability. So, the dimensionless film thickness for the perturbed state is expressed as:

$$h = 1 + \eta, \quad \eta = O(\alpha), \tag{24}$$

where η is the perturbation of the stationary film thickness.

Then Eq. (24) is inserted into Eq. (22) and if terms up to the order of η^3 are kept, it yields the evolution of η as follows:

$$\eta_t + A\eta_x + B\eta_{xx} + C\eta_{xxxx} + D\eta_x^2 + E\eta_x\eta_{xxx} = -\left[\left(A'\eta + \frac{A''}{2}\eta^2\right)\eta_x + \left(B'\eta + \frac{B''}{2}\eta^2\right)\eta_{xx}\right.$$

$$+\left(C'\eta + \frac{C''}{2}\eta^2\right)\eta_{xxxx} + (D + D'\eta)\eta_x^2$$

$$\left. + (E + E'\eta)\eta_x\eta_{xx}\right] + O(\eta^4), \quad (25)$$

where the value of A, B, C, D, E and their derivatives are evaluated at $h = 1$.

I Linear Stability Analysis. To study the linear stability problem, the nonlinear terms of Eq. (25) are neglected and the linearized equation is obtained:

$$\frac{\partial \eta}{\partial t} + A\frac{\partial \eta}{\partial x} + B\frac{\partial^2 \eta}{\partial x^2} + C\frac{\partial^4 \eta}{\partial x^4} = 0. \quad (26)$$

Applying the normal mode analysis by assuming:

$$\eta = a\exp[i(x - dt)] + c.c. \quad (27)$$

In the above expression, a is the perturbation amplitude, $c.c.$ is the complex conjugate counterpart. The complex wave celerity d is given by:

$$d = d_r + id_i = A + i(B - C). \quad (28)$$

The flow is linearly unstable for $d_i > 0$, and on the other hand, flow is linear stable for $d_i < 0$. $d_i = 0$ gives the linear neutral-stability curve.

II Nonlinear Stability Analysis. Now we proceed to study the nonlinear stability problem. Following Krishna and Lin (1977), the method of multiple scales is used according to:

$$\frac{\partial}{\partial t} = \frac{\partial}{\partial t} + \epsilon\frac{\partial}{\partial t_1} + \epsilon^2\frac{\partial}{\partial t_2}, \quad (29)$$

$$\frac{\partial}{\partial x} = \frac{\partial}{\partial x} + \epsilon\frac{\partial}{\partial x_1}, \quad (30)$$

$$\eta(\alpha, x, x_1, t, t_1, t_2) = \epsilon\eta_1 + \epsilon^2\eta_2 + \epsilon^3\eta_3, \quad (31)$$

where ϵ is a small parameter such that

$$t_1 = \epsilon t, \quad t_2 = \epsilon^2 t, \quad x_1 = \epsilon x. \quad (32)$$

Then, Eq. (25) becomes

$$(L_0 + \epsilon L_1 + \epsilon^2 L_2)(\epsilon\eta_1 + \epsilon^2\eta_2 + \epsilon^3\eta_3)$$

$$= -\epsilon^2 N_2 - \epsilon^3 N_3, \quad (33)$$

where

$$L_0 = \frac{\partial}{\partial t} + A\frac{\partial}{\partial x} + B\frac{\partial^2}{\partial x^2} + C\frac{\partial^4}{\partial x^4}, \quad (34)$$

$$L_1 = \frac{\partial}{\partial t_1} + A\frac{\partial}{\partial x_1} + 2B\frac{\partial}{\partial x}\frac{\partial}{\partial x_1} + 4C\frac{\partial^3}{\partial x^3}\frac{\partial}{\partial x_1}, \quad (35)$$

$$L_2 = \frac{\partial}{\partial t_2} + B\frac{\partial^2}{\partial x_1^2} + 6C\frac{\partial^2}{\partial x^2}\frac{\partial^2}{\partial x_1^2}, \quad (36)$$

$$N_2 = A'\eta_1\eta_{1x} + B'\eta_1\eta_{1xx} + C'\eta_1\eta_{1xxxx}$$

$$+ D\eta_{1x}^2 + E\eta_{1x}\eta_{1xxx}, \quad (37)$$

$$N_3 = A'(\eta_1\eta_{2x} + \eta_{1x}\eta_2 + \eta_1\eta_{1x_1})$$

$$+ B'(\eta_1\eta_{2xx} + 2\eta_1\eta_{1xx_1} + \eta_{1xx}\eta_2)$$

$$+ C'(\eta_1\eta_{2xxxx} + 4\eta_1\eta_{1xxxx_1} + \eta_{1xxxx}\eta_2)$$

$$+ D(2\eta_{1x}\eta_{2x} + 2\eta_{1x}\eta_{1x_1}) + E(\eta_{1x}\eta_{2xxx} + 3\eta_{1x}\eta_{1xxx_1}$$

$$+ \eta_{1xxx}\eta_{2x} + \eta_{1xxx}\eta_{1x_1}) + \tfrac{1}{2}A''\eta_1^2\eta_{1x} + \tfrac{1}{2}B\eta_1^2\eta_{1xx}$$

$$+ \tfrac{1}{2}C''\eta_1^2\eta_{1xxxx} + D'\eta_1\eta_{1x}^2 + E'\eta_1\eta_{1x}\eta_{1xxx}. \quad (38)$$

Equation (33) is then solved order by order. The equation for $O(\epsilon)$ is $L_0\eta_1 = 0$. The solution is of the following form:

$$\eta_1 = a(x_1, t_1, t_2)\exp[i(x - d_r t)] + c.c. \quad (39)$$

Then the solution of η_2 and the secular condition for the equation of $O(\epsilon^3)$ are given, respectively, as:

$$\eta_2 = ea^2\exp[2i(x - d_r t)] + c.c., \quad (40)$$

$$\frac{\partial a}{\partial t_2} + D_1\frac{\partial^2 a}{\partial x_1^2} - \epsilon^{-2}d_i a + (E_1 + iF_1)a^2\bar{a} = 0, \quad (41)$$

where

$$e = e_r + ie_i$$

$$= (16C - 4B)^{-1}(-B' + C' - D + E - iA'),$$

$$D_1 = B - 6C,$$

$$E_1 = (-5B' + 17C' + 4D - 10E)e_r - A'e_i$$

$$+ (-\tfrac{3}{2}B'' + \tfrac{3}{2}C'' + D' - E'),$$

$$F_1 = (-5B' + 17C' + 4D - 10E)e_i + A'e_r + \tfrac{1}{2}A''. \quad (42)$$

In the above expressions, the overbar denotes the complex conjugate. Equation (41) would be used to investigate the nonlinear behavior of fluid film flow. Strictly speaking, this expansion is only valid for wavenumbers close to neutral and not near-critical when α approaches zero. The effects of the near-zero wavenumber modes on wave dynamics can be important, but we are unable to capture it with the resolution of Eq. (42). For a filtered wave, there is no spatial modulation, the solution of this equation may be written as

$$a = a_o\exp(-ibt_2). \quad (43)$$

Substituting the above expression into Eq. (41) and neglecting the second term, one can obtain the following equations

$$\frac{\partial a_o}{\partial t_2} = (\epsilon^{-2}d_i - E_1 a_o^2)a_o, \quad (44)$$

$$\frac{\partial[b(t_2)t_2]}{\partial t_2} = F_1 a_o^2. \quad (45)$$

Equation (44) is the so-called Ginzburg-Landau equation. Of course, if E_1 were zero, the Ginzburg-Landau equation can be reduced to the equation that is obtained from linear theory. The second term of the right-hand side of Eq. (44) is due to the nonlinearity. Equation (45) is the modification of the wave speed of the infinitesimal disturbance due to the nonlinear effect. In the linearly unstable region ($d_i > 0$), the condition for the existence of a supercritically stable wave is $E_1 > 0$, and, finally, the amplitude (ϵa_0) is obtained as

$$\epsilon a_o = \left(\frac{d_i}{E_1}\right)^{1/2}, \quad (46)$$

and the nonlinear wave speed is given as

$$Nc_r = \epsilon^2 b = d_r + d_i\left(\frac{F_1}{E_1}\right)^{1/2}. \quad (47)$$

On the other hand, in the linearly stable region ($d_i < 0$), if $E_1 < 0$, the film flow presents the behavior of subcritical instability, and ϵa_o is the threshold amplitude.

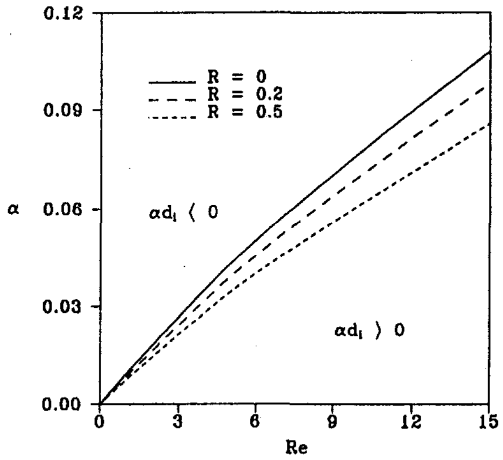

Fig. 2 **Neutral stability curve for micropolar film flow with different values of micropolar parameter *R***

Results and Discussions

The linear stability analysis yields the neutral stability curve which is determined by $\alpha d_i = 0$. The α-Re plane is separated into two regions. One is the linearly stable region where small disturbances are decaying with time and the other one is the linearly unstable region where small perturbations will grow as time increases. In order to study the effect of micropolar parameter on the stability of film flow, the dimensionless surface tension is fixed to be a constant value in all numerical calculations, i.e., $W = 6173.5$. The results obtained for the case of classical Newtonian flow (by setting $R = 0$) agree with those found by Hwang and Weng (1987) in a previous study.

I Linear Stability Results. Figure 2 shows that the neutral stability curves for micropolar film flow with different values of micropolar parameter R. It is indicated in Fig. 2, when R is increased further, the linearly stable region ($\alpha d_i < 0$) will be expanded.

Figure 3 displays the comparison of the temporal film growth rate of micropolar fluid ($R = 0.2, 0.5$) with that of Newtonian flow ($R = 0$). It is shown that the increase of value of R will reduce the temporal growth rate. Furthermore, it can be found that both the wave number of neutral mode and maximum growth rate become larger when the value of R is decreased. In other words, the larger the value of micropolar parameter R, the more stable liquid film will be. Tables 1 and 2 present the dependence of the critical wave numbers on the various micropolar parameters, Δ and Λ. Table 1 shows the variation of the critical wave numbers with micropolar parameters Δ for $R = 0.5$ and $\Lambda = 1000$, whereas, Table 2 presents the variation of the critical wave numbers with micropolar parameter Λ for $R = 0.5$ and $\Delta = 1$. Results show that the micropolar parameter, Δ and Λ, have very little effects on the stability of film flow.

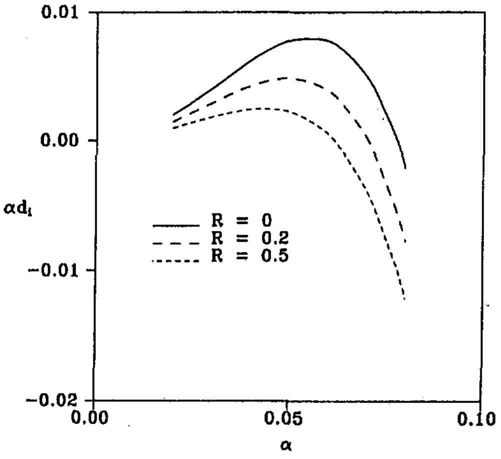

Fig. 3 **Temporal growth rate of micropolar flow (R = 0.2 and 0.5) with those of Newtonian flow (R = 0)**

Table 1 ***The results about the critical wave numbers with different micropolar parameters Δ (R = 0.5, Λ = 1000)***

	Re = 5	Re = 10	Re = 15
Δ = 0.01	0.034315	0.061141	0.085719
Δ = 0.1	0.034333	0.061174	0.085740
Δ = 1	0.034335	0.061178	0.085770

II Nonlinear Stability Results. The nonlinear stability analysis is used to study whether the finite amplitude disturbance in the linearly stable region will cause instability (subcritical instability) and to study whether the subsequent nonlinear evolution of disturbance in the linearly unstable region will redevelop to a new equilibrium state with a finite amplitude (supercritical stability) or grow to be unstable. By inspecting the nonlinear amplitude, Eq. (44), one can find that the negative value of E_1 will make the system become unstable. This kind of instability in the linearly stable region is called subcritical instability; i.e., the disturbance amplitude is larger than the threshold amplitude, then the amplitude will increase although the prediction from using the linear theory is stable. On the other hand, such instability in the subcritical unstable region will cause the system to reach an explosive state.

The hatched area in Figs. 4(a)–4(c) near the neutral stability curve, reveals that both subcritical instability ($d_i < 0$, $E_1 < 0$) and the explosive solution ($d_i > 0$, $E_1 < 0$) are possible for all values of R in the present study. The shaded region (unstable region) will be shrunk when R is increased. It is observed that supercritical stability ($d_i > 0$, $E_1 > 0$, the blank region in the linearly unstable region) is also possible. When R increases, the region of supercritical stability will be enlarged and the state is more stable.

From the nonlinear stability analysis, it is shown that the system will be unstable if the initial finite amplitude disturbance is greater than the subcritical unstable threshold amplitude. Figure 5 displays the threshold amplitude in the subcritical unstable region with different values of micropolar parameter R for the case of Re = 10. It is found that the threshold amplitude will become larger for the increasing micropolar parameter R, therefore, the film flow will be more stable.

In the linearly unstable region, the linear amplification rate is positive, while the nonlinear amplification rate is negative. Therefore, the linearly infinitesimal disturbance in the unstable region will not grow to an infinity, but rather, reach to an equilibrium amplitude that is obtained from Eq. (44). Figure 6 displays the supercritical stable amplitude of different values of micropolar parameter R for the case of Re = 10. It is found that the increase of R will lower the threshold amplitude, and the flow will be more stable.

Table 2 **The results about the critical wave numbers with different micropolar parameters Λ (R = 0.5, Δ = 1)**

	Re = 5	Re = 10	Re = 15
Λ = 100	0.034341	0.061189	0.085785
Λ = 1000	0.034335	0.061178	0.085770
Λ = 10000	0.034332	0.061173	0.085763

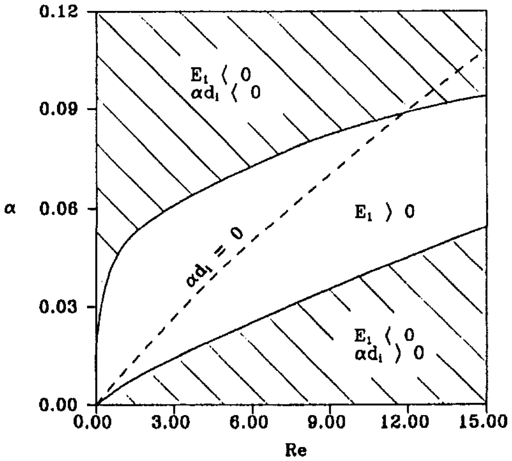

Fig. 4(*a*) Neutral stability curve of Newtonian film flow; $R = 0$

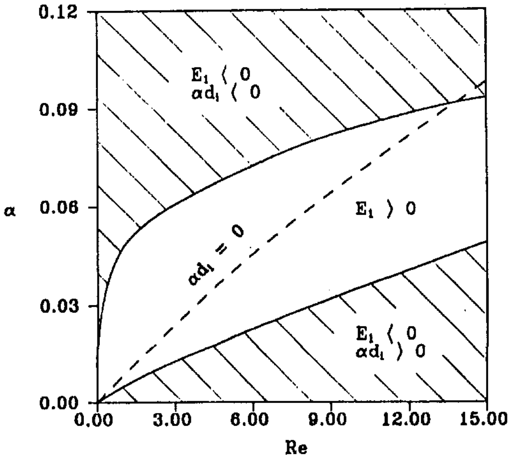

Fig. 4(*b*) Neutral stability curve of micropolar film flow; $R = 0.2$, $\Delta = 1$, $\Lambda = 1000$

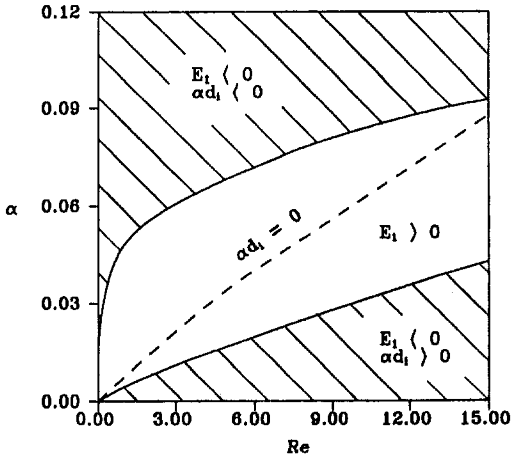

Fig. 4(*c*) Neutral stability curve of micropolar film flow; $R = 0.5$, $\Delta = 1$, $\Lambda = 1000$

The wave speed predicted by the linear theory, given in Eq. (28), will not change for all wave numbers; but the nonlinear wave speed, given by Eq. (47), can be influenced by the wave numbers and micropolar parameter R. The variations of the nonlinear wave speed with respect to wave number and different values of R are shown in Fig. 7. It is found that the nonlinear wave speed decreases with the increasing value of R.

Similarly, as mentioned in the linear stability analysis, the micropolar parameters Δ $(=h_o^2/j)$ and Λ $(=\gamma/\mu j)$ have very little influences on the results and characteristics of the threshold amplitude of subcritical instability or supercritical stability.

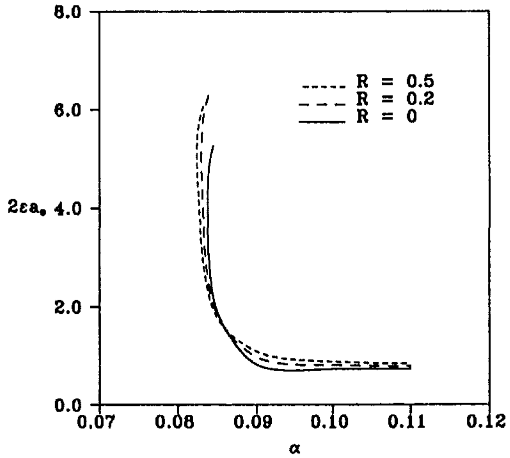

Fig. 5 Threshold amplitude in the subcritical unstable region with different micropolar parameter R for Re = 10

From the above discussion, the effect of micropolar parameter R will strongly affect the stability characteristics of film flow. The increase of the value of R will increase the stability of

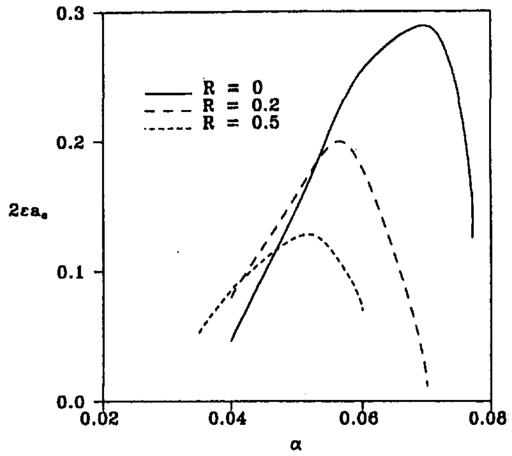

Fig. 6 Threshold amplitude in the supercritical stable region with different micropolar parameter R for Re = 10

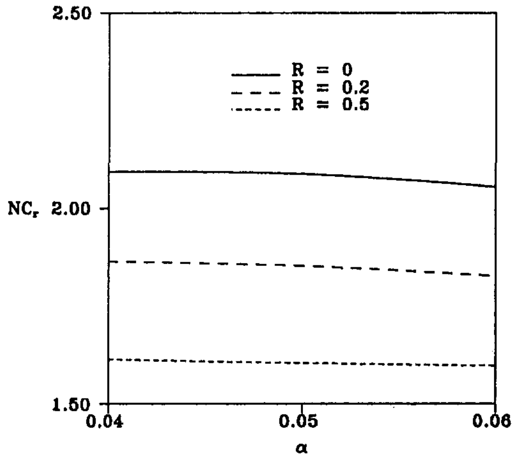

Fig. 7 Variation of nonlinear wave speed with several values of R; Re = 10

micropolar film flow. Because the effect of the microstructure in micropolar fluid will increase the effective viscosity, it can, therefore, reduce the convective motion of flow. But, the parameters Δ and Λ have no important effects on the stability of the micropolar film flow.

Conclusion

Nonlinear stability of a thin micropolar liquid film flowing down a vertical plate is investigated by a perturbation method. Solving the complex problem with the method of multiple scales, a nonlinear generalized kinematic equation, including the effects of angular microrotation and micropolar inertia is obtained. The theory of micropolar fluids can be used to model the couple stresses and body couples. The interactions between the stability of hydrodynamic micropolar film flow and the micropolar parameters are studied in detail.

First, the linear stability analysis is studied to obtain the neutral stability curve. The increase of micropolar parameter R will reduce the growth rate of amplitudes and, therefore, will expand the linearly stable region which result in a more stable film flow system. It should be noted that the linear stability analysis can only give the qualitative statements about the dynamic behavior of film flow, but it can not give any information for the cases of finite amplitude. Only by the nonlinear stability analysis, the stability of the flow with finite amplitude can be obtained.

From the results of the present nonlinear stability analysis, it is indicated that there exists a supercritical stability in the linearly unstable region where an infinitesimal disturbance will redevelop into a new equilibrium finite amplitude. Also, there exists a subcritical instability in the linearly stable region. The increase of the micropolar parameter R will increase the critical amplitude in the subcritically unstable region, and will reduce the amplitude of the supercritically stable waves and the nonlinear wave speed, therefore, the film flow is more stable. So, the application of vortex viscosity will strongly affect the stability characteristics of the micropolar film flow.

In consequence, the increase of the value of R, will strongly increase the stability, and the micropolar film fluid system will be more stable. Furthermore, the stability of the micropolar film flow is found to be strongly dependent on the interaction coefficient κ. But, the micro-inertia j, and the spin-gradient viscosity γ have little influence on the stability of the micropolar film flow.

In conclusion, we quote Eringen (1967), discussing his theory of micropolar fluids, who wrote "It should find important applications dealing with a variety of fluids. . . . Rich theoretical and experimental studies are awaiting further workers." The stability analysis of micropolar film flow will be an interesting subject in both theoretical and engineering application aspects.

References

Ahmadi, G., 1976, "Stability of a Micropolar Fluid Layer Heated from Below," *International Journal of Engineering Science*, Vol. 14, pp. 81–89.

Benney, D. J., 1966, "Long Waves on Liquid Films," *Journal of Mathematics and Physics*, Vol. 45, pp. 150–155.

Chang, H. C., 1994, "Wave Evolution on a Falling Film," *Annual Review of Fluid Mechanics*, Vol. 26, pp. 103–136.

Datta, A. B., and Sastry, V. U. K., 1976, "Thermal Instability of a Horizontal Layer of Micropolar Fluid Heated from Below," *International Journal of Engineering Science*, Vol. 14, pp. 631–637.

Eringen, A. C., 1964, "Simple Microfluids," *International Journal of Engineering Science*, Vol. 2, pp. 205–217.

Eringen, A. C., 1967, "Theory of Micropolar Fluids," *Journal of Mathematics & Mechanics*, Vol. 16, pp. 1–18.

Eringen, A. C., 1980, "Theory of Anisotropic Micropolar Fluids," *International Journal of Engineering Science*, Vol. 18, pp. 5–17.

Franchi, F., and Straughan, B., 1992, "Nonlinear Stability for Thermal Convection in a Micropolar Fluid with Temperature Dependent Viscosity," *International Journal of Engineering Science*, Vol. 30, pp. 1349–1360.

Hwang, C. C., and Weng, C. I., 1987, "Finite-Amplitude Stability Analysis of Liquid Films Down a Vertical Wall with and without Interfacial Phase Change," *International Journal of Multiphase Flow*, Vol. 13, pp. 803–814.

Kolpashchikov, V. L., Migun, N. P., and Prokhorenko, P. P., 1983, "Experimental Determination of Material Micropolar Fluid Constants," *International Journal of Engineering Science*, Vol. 21, pp. 405–411.

Krishna, M. V. G., and Lin, S. P., 1977, "Nonlinear Stability of a Viscous Film with Respect to Three-Dimensional Side-Band Disturbances," *The Physics of Fluids*, Vol. 20, pp. 1039–1044.

Lin, S. P., 1974, "Finite Amplitude Side-Band Stability of a Viscous Film," *Journal of Fluid Mechanics*, Vol. 63, pp. 417–429.

Liu, C. Y., 1970, "On Turbulent Flow of Micropolar Fluids," *International Journal of Engineering Science*, Vol. 8, pp. 457–466.

Liu, C. Y., 1971, "Initiation of Instability in Micropolar Fluids," *The Physics of Fluids*, Vol. 14, pp. 1808–1809.

Payne, L. E., and Straughan, B., 1989, "Critical Rayleigh Numbers for Oscillatory and Nonlinear Convection in an Isotropic Thermomicropolar Fluid," *International Journal of Engineering Science*, Vol. 27, pp. 827–836.

Stokes, V. K., 1984, *Theories of Fluids with Microstructures—An Introduction*, Chapter 6, Springer-Verlag, Berlin.

Tsai, J. S., Hung, C. I., and Chen, C. K., 1996, "Nonlinear Hydromagnetic Stability Analysis of Condensation Film Flow Down a Vertical Plate," *Acta Mechanica*, to appear.

Yih, C. S., 1954, "Stability of Parallel Laminar Flow with a Free Surface," *Proceedings of the 2nd U.S. National Congress of Applied Mechanics*, pp. 623–628.

APPENDIX

Zeroth-order solution:

$$u_o = \frac{2}{R+2}(-y^2 + 2hy),$$

$$v_o = -\frac{2}{R+2}y^2 h_x,$$

$$P_o = -\frac{4}{R+2}\alpha^2 W \,\mathrm{Re}^{-5/3} h_{xx},$$

$$N_o = \frac{2}{R+2}(y-h).$$

First-order solution:

$$u_1 = r_1 \cosh my + r_2 \sinh my + r_3 y^4 + r_4 y^3 + r_5 y^2 + r_6 y + r_7,$$

$$v_1 = r_1' \cosh my + r_2' \sinh my + r_3' y^4 + r_4' y^3 + r_5' y^2 + r_6' y + r_7'$$

$$p_1 = \frac{2}{R+2}(2\,\mathrm{Re}^{-1}(R+1) + R)(y-h)h_x,$$

$$N_1 = -\frac{R+1}{R}(mr_1 \sinh my + mr_2 \cosh my + 4r_3 y^3 + 3r_4 y^2 + 2r_5 y + r_6) + \frac{\mathrm{Re}}{R}\left[-2\alpha^2 W \,\mathrm{Re}^{-5/3} h_{xx}(y-h) + \frac{2}{R+2} h_{0t}(y^2 - h^2) + \frac{8hh_x}{3(R+2)^2}(y^3 - h^3)\right]$$

where

$$r_1 = \frac{8\,\mathrm{Re} h_{0t}}{m^5 \Lambda (R+2)(R+1)} \coth mh - \frac{4\,\mathrm{Re} h_{0t}}{m^3 (R+2)(R+1)} \times \coth mh - \frac{2Rh_{0t}}{m^3 \Lambda (R+2)(R+1)} \coth mh - \frac{\operatorname{csch} mh}{m} \frac{32\,\mathrm{Re} h^2 h_x}{m^4 \Lambda (R+2)^2 (R+1)} + \frac{\operatorname{csch} mh}{m} \times \frac{16\,\mathrm{Re} h^2 h_x}{m^2 (R+2)^2 (R+1)} + \frac{\operatorname{csch} mh}{m} \frac{8Rh^2 h_x}{m^2 \Lambda (R+2)^2 (R+1)}$$

$$
-\frac{\operatorname{csch} mh}{m}\frac{8\,\mathrm{Re}h_{0t}}{m^4\Lambda(R+2)(R+1)}+\frac{\operatorname{csch} mh}{m}
$$

$$
\times\frac{4\,\mathrm{Re}h_{0t}}{m^2\Lambda(R+2)(R+1)}+\frac{\operatorname{csch} mh}{m}\frac{2Rh_{0t}}{m^2\Lambda(R+2)(R+1)},
$$

$$
r_2=-\frac{8\,\mathrm{Re}h_{ot}}{m^5\Lambda(R+2)(R+1)}
$$

$$
+\frac{4\,\mathrm{Re}h_{ot}}{m^3(R+2)(R+1)}+\frac{2Rh_{ot}}{m^3\Lambda(R+2)(R+1)},
$$

$$
r_3=\frac{4\,\mathrm{Re}hh_x}{3m^2\Lambda(R+2)(R+1)},
$$

$$
r_4=\frac{4\,\mathrm{Re}h_{ot}}{3m^2\Lambda(R+2)(R+1)},
$$

$$
r_5=\frac{16\,\mathrm{Re}hh_x}{m^4\Lambda(R+2)^2(R+1)}-\frac{8\,\mathrm{Re}hh_x}{m^2(R+2)^2(R+1)}
$$

$$
-\frac{4Rhh_x}{m^2\Lambda(R+2)^2(R+1)}-\frac{2\alpha^2W\,\mathrm{Re}^{-3/2}h_{xxx}}{m^2\Lambda(R+1)},
$$

$$
r_6=-\frac{16\,\mathrm{Re}h^4h_x}{3m^2\Lambda(R+2)^2(R+1)}+\frac{8\,\mathrm{Re}h_{ot}}{m^4\Lambda(R+2)(R+1)}
$$

$$
-\frac{4\,\mathrm{Re}h^2h_{ot}}{m^2\Lambda(R+2)(R+1)}-\frac{4\,\mathrm{Re}h_{ot}}{m^2(R+2)(R+1)}
$$

$$
-\frac{2Rh_{ot}}{m^2\Lambda(R+2)(R+1)}+\frac{4\alpha^2W\,\mathrm{Re}^{-5/3}}{m^2\Lambda(R+1)}hh_{xxx},
$$

$$
r_7=-r_1,
$$

and

$$
h_{ot}=-\frac{4}{R+2}h^2h_x,
$$

$$
r_1'=\Bigg[-\frac{32\,\mathrm{Re}}{m^5\Lambda(R+2)^2(R+1)}+\frac{16\,\mathrm{Re}}{m^3(R+2)^2(R+1)}
$$

$$
+\frac{8R}{m^3\Lambda(R+2)^2(R+1)}\Bigg]\cdot(h^2h_{xx}\coth mh
$$

$$
+2hh_x^2\coth mh-mh^2h_x^2\operatorname{csch} mh),
$$

$$
r_2'=\Bigg[\frac{32\,\mathrm{Re}}{m^5\Lambda(R+2)^2(R+1)}-\frac{16\,\mathrm{Re}}{m^3(R+2)^2(R+1)}
$$

$$
-\frac{8R}{m^3\Lambda(R+2)^2(R+1)}\Bigg]\cdot(h^2h_{xx}+2hh_x^2),
$$

$$
r_3'=\frac{4\,\mathrm{Re}}{3m^2\Lambda(R+2)(R+1)}(hh_{xx}+h_x^2),
$$

$$
r_4'=-\frac{16\,\mathrm{Re}}{3m^2\Lambda(R+2)^2(R+1)}(h^2h_{xx}+2hh_x^2),
$$

$$
r_5'=\Bigg[\frac{16\,\mathrm{Re}}{m^4\Lambda(R+2)^2(R+1)}-\frac{8\,\mathrm{Re}}{m^2(R+2)^2(R+1)}
$$

$$
-\frac{4R}{m^2\Lambda(R+2)^2(R+1)}\Bigg]\cdot(hh_{xx}+h_x^2)-\frac{2\alpha^2W\,\mathrm{Re}^{-2/3}h_{xxxx}}{m^2\Lambda(R+1)},
$$

$$
r_6'=\frac{4\alpha^2W\,\mathrm{Re}^{-2/3}}{m^2\Lambda(R+1)}(hh_{xxxx}+h_xh_{xxx})+\frac{16\,\mathrm{Re}}{m^2\Lambda(R+2)^2(R+1)}
$$

$$
\times(h^4h_{xx}+4h^3h_x^2)-\frac{16\,\mathrm{Re}}{3m^2\Lambda(R+2)^2(R+1)}
$$

$$
\times(h^4h_{xx}+4h^3h_x^2)(h^2h_{xx}+2hh_x^2)
$$

$$
\times\Bigg[-\frac{32\,\mathrm{Re}}{m^4(R+2)^2(R+1)}+\frac{16\,\mathrm{Re}}{m^2(R+2)^2(R+1)}
$$

$$
+\frac{8R}{m^2\Lambda(R+2)^2(R+1)}\Bigg],
$$

$$
r_7'=-r_1'.
$$

Turbulent Flow in Longitudinally Finned Tubes

D. P. Edwards
Research Assistant.

A. Hirsa
Assistant Professor.

M. K. Jensen
Professor.

Department of Mechanical Engineering,
Aeronautical Engineering and Mechanics,
Rensselaer Polytechnic Institute,
Troy, NY 12180-3590

An experimental investigation of fully developed, steady, turbulent flow in longitudinally finned tubes has been performed. A two-channel, four-beam, laser-Doppler velocimeter was used to measure velocity profiles and turbulent statistics of air flow seeded with titanium dioxide particles. Mean velocities in axial, radial, and circumferential directions were measured over the tube cross sections and pressure drop in the tubes was measured at six stations along the test section length in order to calculate the fully developed friction factor. Four experimental tube geometries were studied: one smooth tube; two 8-finned tubes (fin height-to-radius ratios of 0.333 and 0.167), and one 16-finned tube (fin height-to-radius ratio of 0.167); Detailed measurements were taken at air flow rates corresponding to Reynolds numbers of approximately 5000, 25,000, and 50,000. Friction factor data were compared to literature results and showed good agreement for both smooth and finned tubes. The wall shear stress distribution varied significantly with Reynolds number, particularly for Reynolds numbers of 25,000 and below. Maximum wall shear stress was found at the fin tip and minimum at the fin root. Four secondary flow cells were detected per fin (one in each interfin spacing and one in each core region for each fin); secondary flows were found to be small in comparison to the mean axial flow and relative magnitudes were unaffected by axial flow rate at Reynolds numbers above 25,000. The fluctuating velocities had a structure similar to that of the smooth tube in the core region while the turbulence in the interfin region was greatly reduced. The principal, primary shear stress distribution differed considerably from that of the smooth tube, particularly in the interfin region, and the orientation was found to be approximately in the same direction as the gradient of the mean axial velocity, supporting the use of an eddy viscosity formulation in turbulence modeling.

Introduction

Enhancement techniques that improve the overall heat transfer characteristics of turbulent flow in tubes are important to heat exchanger designers. Due to their ease of manufacture and increased heat transfer rates, tubes with longitudinal, internal fins have been studied extensively. However, while empirical data have been obtained for the overall performance (friction factor and Nusselt number) of these tubes, a complete analysis of the flow structure within the tube has yet to be performed. A detailed investigation of the flow may provide useful information for the design of more efficient finned tubes.

Early investigations by Hilding and Coogan (1964), Lipets et al. (1964), Vasil'chenko and Barbaritskaya (1969), Bergles et al. (1971), and Watkinson et al. (1973, 1975) suggest that significant savings can be made from employing finned tubes. Carnavos (1979) obtained heat transfer and pressure drop data from more than 20 internally finned tubes with between 6 and 41 fins using air, water, and glycol. Comparison of these data and predictions that employ the hydraulic diameter in smooth tube correlations were found to overpredict both the Nusselt number and the friction factor by up to 36 percent.

The only detailed measurements of the turbulent flow structures were done by Trupp et al. (1981) for a tube with six fins of height (h/R) of 0.667 at Reynolds numbers of 50,000 and 71,000. It was found that each fin has four secondary flow cells associated with it, two in the interfin space and two in the core region of the flow; the secondary flow velocity was at most 4.5 percent of the mean axial velocity. The fin geometry used in this experiment is not typical of those used in heat exchanger applications, with larger numbers of much shorter fins being more typical. In addition to the atypical fin geometry, the narrow range of flow conditions failed to determine the effects of Reynolds number on the flow structure.

More detailed measurements of the flow over a wide range of fin geometry (considering both fin size and number) and flow conditions are required and an investigation was performed in which flow measurements were taken in adiabatic, fully developed, turbulent flow in a longitudinally finned, circular tube using a two-component laser-Doppler velocimeter (LDV). Three finned tubes were tested at three Reynolds numbers between 5000 and 50,000. Pressure drop, as well as mean axial velocity profiles (including near-wall measurements to predict wall shear stress), and secondary flows were measured. Turbulent stresses were also measured.

Experimental Apparatus

The experimental air flow loop is shown schematically in Fig. 1 and is described in detail by Edwards (1994). Flow was provided by a centrifugal fan and measured with an orifice flow meter. A settling plenum, containing one 25 mm thick section of honeycomb with 3.2 mm hexagonal cells followed by two #24 wire mesh screens 150 and 300 mm downstream and a smooth reducing nozzle was placed upstream of the test section to control the inlet conditions. Measurements at the nozzle exit revealed a turbulent intensity of 3.5 percent at a Reynolds number (based on exit diameter) of 50,000. The velocity and turbulent intensity at the nozzle exit were measured to be uniform across the diameter to within ±2 percent.

The test sections were attached to the flow loop at both ends by an o-ring sealed clamping mechanism that allowed for rotational adjustments of the tube and vertical and horizontal adjustments were possible at the downstream end to facilitate alignment of the test section with the LDV traverse. Titanium dioxide

---

Contributed by the Fluids Engineering Division for publication in the JOURNAL OF FLUIDS ENGINEERING. Manuscript received by the Fluids Engineering Division March 27, 1995; revised manuscript received August 23, 1995. Associate Technical Editor: P. R. Bandyopadhyay.

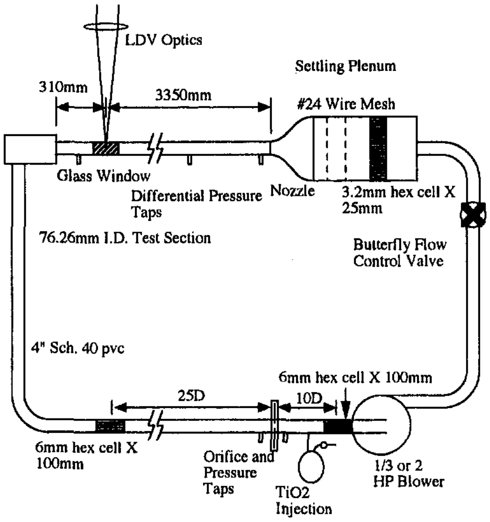

Fig. 1 Schematic of the adiabatic experimental flow loop

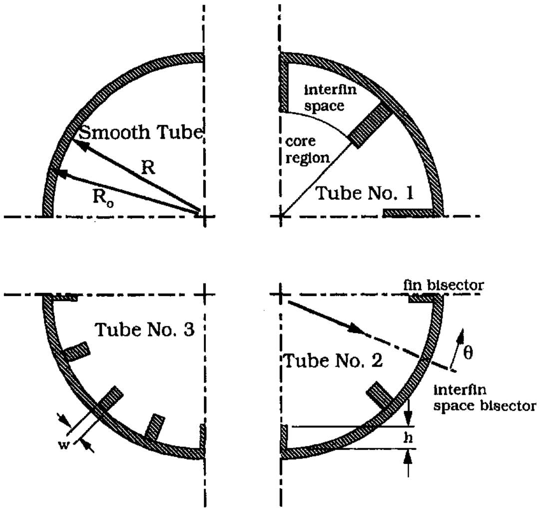

Fig. 2 Cross section of the finned tube test sections viewed axially

particles, having excellent optical properties and size (believed to be sub-micron sized) were selected as the seeding particle for this experiment.

The cross sections of the finned tube test sections used in this investigation are shown in Fig. 2. Parameters of importance are the inside radius (R), the number of fins (n), and the fin height (h) and width (w). A cylindrical coordinate system is used in this analysis in which the radial (r), circumferential (θ), and axial (z) coordinates fix a point in the flow. The circumferential coordinate is measured from a bisector of the interfin space toward the fin. The axial direction is positive in the direction of the mean flow.

Parameters for the three tubes tested are listed in Table 1. The test sections were made of smooth, clear acrylic tubing with an inside diameter of 76.26 mm, an outside diameter of 82.72 mm, and a length of 3.66 m. A thin-wall, precision-bored glass tube was placed approximately six diameters upstream of the exit to provide an access window for the LDV measurements. The velocity measurement location was 70–90 hydraulic diameters from the test section entrance, depending on the fin geometry. This length was required to assure that the mean, turbulent and secondary flows were fully developed. Pressure taps were located at six equally-spaced axial locations along the test section. Fully developed pressure drops were obtained with a precision methanol manometer between the third and sixth stations, some 30–50 hydraulic diameters from the entrance.

A two-channel, four-beam, LDV (TSI Model 9100-7), employing a two-watt argon laser's blue (488.0 nm) and green (514.5 nm) emissions and frequency shifting, was used to measure horizontal and vertical velocities, respectively. A three-dimensional traverse positioned the axis of the four beams on a horizontal plane, perpendicular to the test section axis. The system could be used to simultaneously measure axial and cir-

Nomenclature

A_{fn} = nominal flow area, πR^2 (ignoring area blocked by fins)
A_{fa} = actual flow cross sectional area (considering blockage due to fins)
dp/dz = pressure gradient
D_h = hydraulic diameter, $4{*}A_{fa}/P_w$
f = friction factor, $2(dp/dz)D_h/(\rho\bar{v}^2)$
h = fin height
l = mixing length
P_w = wetted perimeter
r = distance in radial direction, measured from tube axis
R = inside radius of test section
R_o = outside radius of tube
Re = Reynolds number, $\bar{v}D_h/\nu$
t_{Bi} = residence time of particle i in the LDV measuring volume
u_i = instantaneous velocity in i direction (r, z, θ)
u_i = time-averaged velocity component
u_i' = fluctuating velocity component
$u_{z\,\max}$ = maximum time-averaged axial velocity (measured at tube axis)
u^+ = time-averaged axial velocity in wall coordinates, $y\sqrt{\tau_w/\rho}/\nu$
$\overline{u_z'^2}$, $\overline{u_r'^2}$, $\overline{u_\theta'^2}$ = Reynolds normal stresses
$\sqrt{\overline{u_z'^2}}$, $\sqrt{\overline{u_r'^2}}$, $\sqrt{\overline{u_\theta'^2}}$ = fluctuating velocity components
$\overline{u_r'u_z'}$, $\overline{u_\theta'u_z'}$ = Reynolds primary shear stresses
$\overline{u_r'u_\theta'}$ = Reynolds secondary shear stress
$\overline{u_\alpha'u_\theta'}$ = principal, primary shear stress
$\bar{v}$ = mean axial velocity (averaged over the actual cross-sectional flow area)
w = fin width
y = distance from the wall
y^+ = distance from wall in wall coordinates, $y(\tau_w/\rho)^{0.5}/\nu$
z = distance in axial direction
α = angle (from $+\theta$ direction) of principal, primary shear plane
β = angle (from $+\theta$ direction) of gradient of mean axial velocity
γ = angle (from $+\theta$ direction) of eddy viscosity model principal, primary shear plane
θ = distance in circumferential direction, measured in degrees from the interfin space bisector toward the fin bisector
ν = kinematic viscosity
ν_t = turbulent viscosity
ρ = density
σ = standard deviation
τ_w = local wall shear stress
$\tau_{w\,\mathrm{av}}$ = average wall shear stress

cumferential velocity components or axial and radial velocity components of the flow depending upon the location of the measurement volume.

Measurements of air flow in a smooth tube at Reynolds numbers of 5000, 25,000, 50,000, and 100,000 were used to establish the experimental technique. Measurements of both mean velocity profiles and Reynolds stress profiles showed good agreement with the data of Laufer (1954). On the basis of these results, the following measurement uncertainties were estimated: mean axial velocity ± 2 percent; mean axial velocity near-wall ±7 percent; normal Reynolds stresses ± 8 percent; Reynolds shear stresses ± 15 percent; Secondary flows ± 15 percent. The integral average of the axial velocity across the tube cross section matched the orifice plate measurement to within ±5 percent.

Measurements within a finned tube were taken along a horizontal or vertical radial line using the traverse. Different radii could be examined by rotating the test section. Data taken on a horizontal radius measured axial and circumferential velocities while data taken on a vertical radius measured the axial and radial velocity components. The location of the measuring volume within the finned tube was calculated using the virtual location of the traverse (accurate to within 0.01 mm) along with three-dimensional corrections due to refraction in the curved glass using methods similar to Broadway and Karattan (1981) and Garavsky et al. (1989). The effects of curvature were most significant near the wall on vertical radii. Corrections included both the location of the beam crossings and the half angle between the beam pairs. All measurements were taken relative to the tube centerline. The centerline and angle of rotation were carefully measured by calculating vertical and horizontal displacements of known locations on the tube (particularly fin tips and outside wall diameter).

This method resulted in some gaps in the data where fins partially or completely blocked the incident laser beams. In particular, the circumferential measurements on radii that intersected fins were unobtainable. Radial measurements had less regular gaps due to fin blockage. For each geometry and flow condition, between 30 and 45 data points were taken in the core region and between 40 and 75 data points were taken in the interfin space, along different radii.

Results and Discussion

Friction Factor. Fully developed friction factor for the smooth tube and three finned tubes are shown in Fig. 3. The smooth tube data agree very well with literature data. The smooth tube data are well approximated by Blasius-type formulas. If the finned tubes' hydraulic diameters are used in the smooth tube correlations, the calculated friction factors are 5–25 percent lower than the measured values. This supports the findings of previous researchers who concluded that using the hydraulic diameter of finned tubes in smooth tube correlations is not sufficiently accurate. The finned tube data agree with Carnavos' correlations within ±10 percent for all three finned tubes. While Carnavos' correlation predicts friction factor well, the current data suggest that a Reynolds number exponent of −0.25 would be more appropriate for these three test sections for the Reynolds number range tested. The smooth tube and the finned tubes exhibit similar Reynolds number dependence, suggesting that the Reynolds exponent is not a function of geometry.

Table 1 Geometric parameters for the smooth tube and finned tube test sections

	Tube			
	No. 1	No. 2	No. 3	Smooth
number of fins, n	8	8	8	0
inside radius, R (mm)	38.13	38.13	38.13	38.13
fin height, h (mm)	12.70	6.35	6.35	—
fin width, w (mm)	4.76	4.76	3.17	—
nondim. fin height, h/R	0.333	0.167	0.167	—
fin aspect ratio, w/h	0.375	0.75	0.50	—
hydraulic diameter, D_h (mm)	36.84	50.66	38.30	76.26

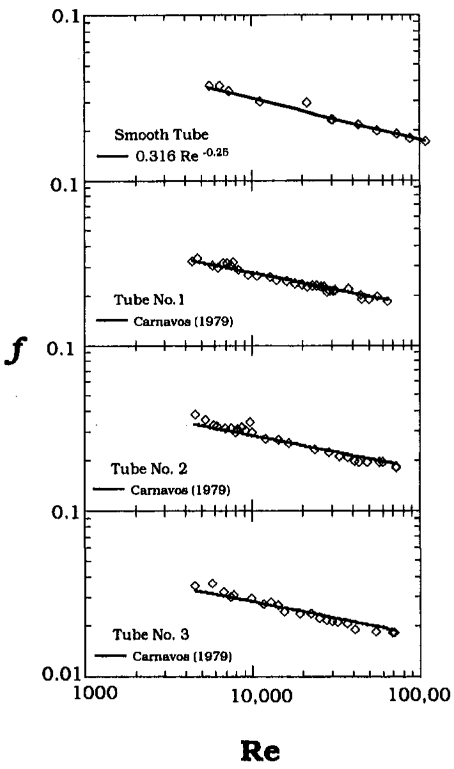

Fig. 3 Friction factor data for the smooth tube and the three finned tubes

Mean Axial Velocity. Velocity profiles for Tube No. 1 at a Reynolds number of 26,550 are shown in Fig. 4. The mean axial velocity profiles in this figure are typical of all three test sections at all flow rates. The core region has a very flat profile, typical of most turbulent duct flows. The nondimensionalized velocity in the interfin space is reduced 5–15 percent compared to that of the plain tube and shows a velocity "plateau" where the profile becomes quite flat. A local velocity maximum, as seen in the higher fin (h/R = 0.667) test sections of Trupp et al. (1981), was not found.

The effects of Reynolds number can be seen in Fig. 5. The nondimensionalized velocity is plotted against radius along the interfin space bisector for the smooth tube and the three test sections over a range of Reynolds numbers. The general velocity profile remains unchanged across the tube except that the profile becomes slightly flatter with increasing Reynolds number.

Near-Wall Velocity. The flow in the near-wall region is best examined by using turbulent wall coordinates, u^+ and y^+. An analysis of this type requires some knowledge of the wall shear stress distribution and its effects on the flow. Very near the wall, the flow can be considered one-dimensional because gradients perpendicular to the wall are much larger than velocity gradients along the wall. The u^+ versus y^+ profiles are plotted (Figs. 6(a) and 6(b)) along lines perpendicular to the tube and fin walls. Very near the wall $u^+ = y^+$ and is valid to y^+ of less than about 5. For the lower Reynolds number conditions, this viscous sublayer is thick enough to allow for direct measurement in this region, which can be used for calculation of the wall shear stress. When the viscous sublayer was too thin to allow direct measurement, an assumed velocity profile was needed.

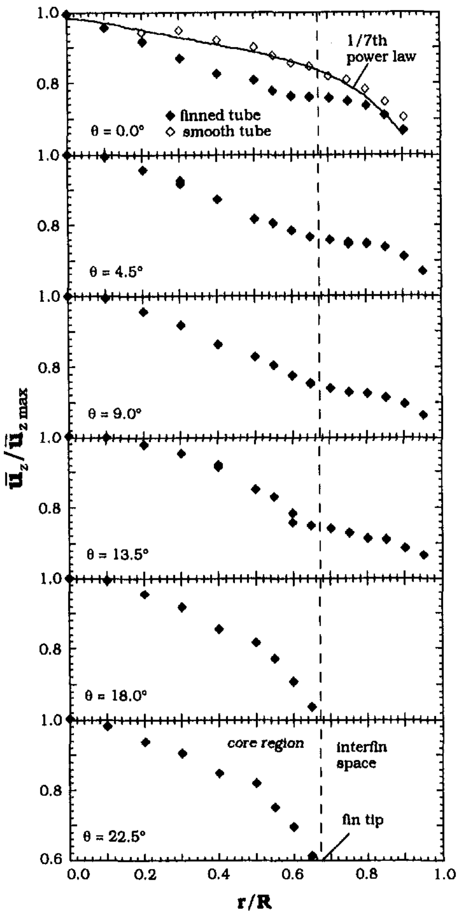

Fig. 4 Mean axial velocity profiles for Tube No. 1 at Re = 26,550 and a smooth tube at Re = 25,400. Note that the scale for each data set is 0.6 to 1.0.

For smooth tubes, the velocity profile is well described by the logarithmic law-of-the-wall for y^+ greater than about 30.

$$u^+ = 2.44 \ln y^+ + 5.0 \tag{1}$$

Between the viscous sublayer and this log-law region, a velocity profile can be calculated using Van Driest's mixing length formula:

$$l = 0.41y\left(1 - \frac{1}{e^{y^+}/26}\right) \tag{2a}$$

where

$$\nu_t = l^2\left|\frac{du}{dy}\right| \tag{2b}$$

Data for the smooth tube (shown in Fig. 6(*a*)) agree well with the predicted velocity profile. For smooth tubes, Van Driest's velocity profile is accurate for Reynolds numbers above about 4000. For the finned tubes, the viscous sublayer should be the same as for smooth tubes. Outside of the viscous sublayer, however, two-dimensional effects of the flow are expected to affect velocity profiles significantly. Near-wall velocity profiles for the finned tube are compared to Van Driest's velocity profile in Figs. 6(*a*) and 6(*b*). Velocity profiles at the tube wall, fin side, and fin tip are shown for Tube No. 1 at a Reynolds number of 4950 and for Tube No. 3 at 25,350. The near-wall velocity profile in finned tubes is approximated (±10 percent) by Van Driest's profile for $y^+ < 30$. For $10 < y^+ < 30$, Van Driest's model slightly underpredicts the velocity at all wall locations.

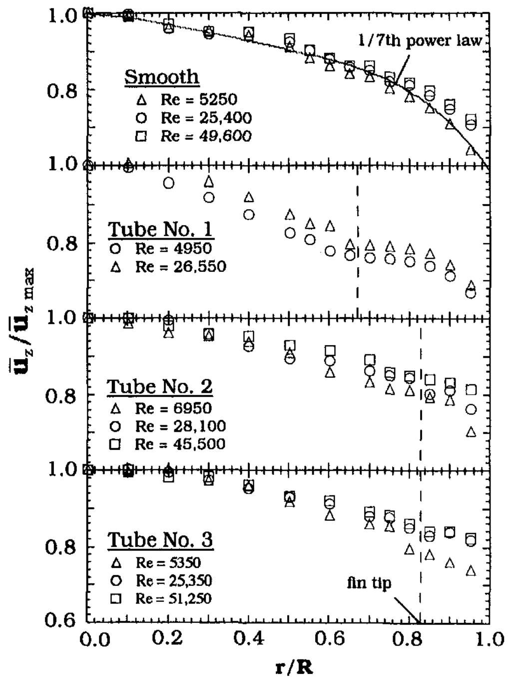

Fig. 5 Effect of Reynolds number on the mean axial velocity profiles at $\theta = 0$ for the smooth tube and the three finned tubes. Note that the scale for each data set is 0.6 to 1.0.

At $y^+ > 30$, the data do not show a consistent trend. The data scatter is considerably larger than the measurement uncertainty of ±2 percent. For flow conditions in which the viscous sublayer ($y^+ < 10$) was too thin to permit direct measurements, velocity was measured in the near-wall region ($y^+ < 30$) and the wall shear stress was calculated by fitting the data to Van Driest's velocity profile. The universality of the near-wall region was assumed to hold for the higher Reynolds numbers.

Wall Shear Stress. The measured velocity and wall distance are used to calculate the wall shear stress by fitting u^+ and y^+ to the Van Driest velocity profile. The measured wall

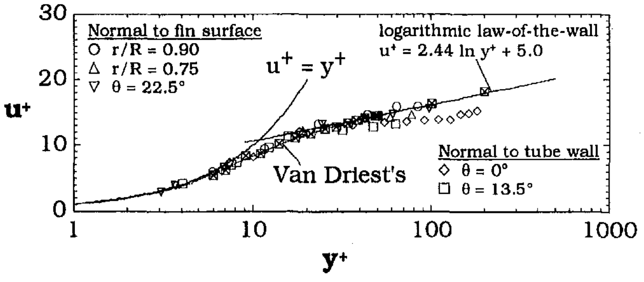

***Fig. 6(a)* Near wall velocity profile for Tube No. 1 at Re = 4,950 and the smooth tube at 25,400**

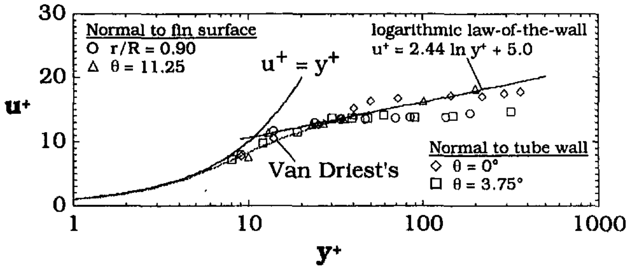

Fig. 6(*b*) Near wall velocity profile for Tube No. 3 at Re = 25,350

shear stress distribution for the three test sections is shown in Figs. 7(*a–c*) as a function of distance along the tube-fin perimeter. For each tube, the maximum wall shear stress occurs at the corner formed by the fin tip and fin wall. The minimum wall shear stress occurs at the corner of the tube and the fin. A local maximum is found on the tube wall. The measured shear stress, integrated over the tube perimeter yields a friction factor within 5 percent of the value calculated from the overall pressure drop. Reynolds number was found to have a large effect on the wall shear stress distribution between 5000 and 25,000, but considerably less of an effect between 25,000 and 50,000. At Reynolds numbers of 5000, the maximum and minimum shear stresses are, respectively, as much as 60 percent higher and 40 percent lower than the average. As Reynolds number increases, the variation in the wall shear stress is reduced to only ±25 percent of the mean at a Reynolds number of 25,000 and slightly less than 20 percent at 50,000.

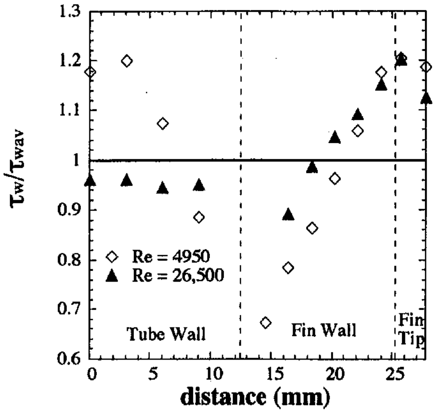

Fig. 7(*a*) Measured wall shear stress distribution for Tube No. 1. Abscissa is the linear distance along the finned tube perimeter measured from $\theta = 0.0$.

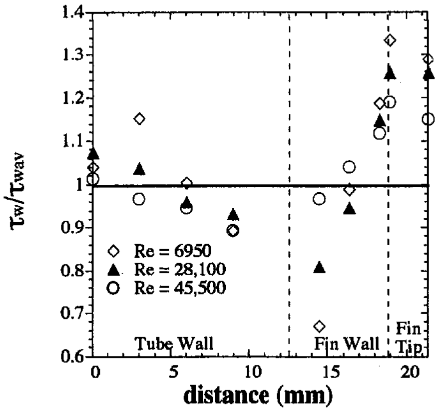

Fig. 7(*b*) Measured wall shear stress distribution for Tube No. 2. Abscissa is the linear distance along the finned tube perimeter measured from $\theta = 0.0$.

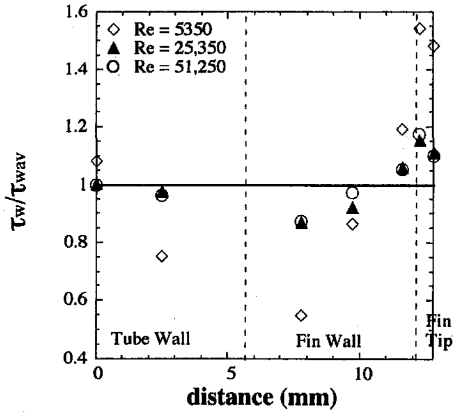

Fig. 7(*c*) Measured wall shear stress distribution for Tube No. 3. Abscissa is the linear distance along the finned tube perimeter measured from $\theta = 0.0$.

From Fig. 7, it is apparent that wall shear stress similarity does not exist for the finned tubes at Reynolds numbers less than about 50,000. Because similarity in the wall shear stress does not exist, similarity in the velocity profiles is not expected.

Secondary Flow. Secondary velocity profiles are shown in Figs. 8(*a*) and 8(*b*) for Tube No. 1 at Reynolds numbers of 4950 and 26,500. Typical secondary flow structure is shown schematically in Fig. 8(*c*). Figure 8(*a*) shows the radial velocity component of the flow, and Fig. 8(*b*) shows the circumferential velocity component of the secondary flows. The radial and tangential components (positive from the tube axis toward the tube wall and from the interfin space bisector toward the fin, respectively) are plotted along various radii. Two pairs of secondary flow cells were observed for each fin. The first pair is located entirely within the interfin space; flow is toward the tube wall on the interfin space bisector and toward the tube axis along the fin wall. The second pair is contained in the core region; flow is toward the tube axis along the interfin space bisector and toward the fin along the fin bisector.

Secondary flows increase with the axial flow Reynolds number. For Tube No. 1, the maximum secondary velocity increased from 3.2 percent of the mean axial flow to 5.2 percent at Reynolds numbers of 4950 and 26,500, respectively. Secondary flow velocities decrease as the numbers of fins increase and the fin height decreases. At a nominal Reynolds number of 25,000, the maximum secondary velocity was reduced from 5.2 to 3.1 percent of the mean axial velocity between Tube No. 1 and 2 (fin height is half of that in Tube No. 1). Similarly, at a Reynolds number of 25,000, the maximum secondary flow velocity was reduced from 3.1 to 1.9 percent between Tube No. 2 and 3 (Tube No. 2 has half as many fins as Tube No. 3).

Turbulent Kinetic Energy Distribution. The three components of the fluctuating velocity were combined to form the turbulent kinetic energy. and was used to show the effects of tube geometry and Reynolds number on the turbulent flow structure. In Fig. 9, the turbulent kinetic energy of the smooth tube and the finned tubes at a Reynolds number of about 5000 are shown. The core region for each of the finned tubes is very similar to that of the smooth tube. In the interfin region, a considerable reduction in turbulence is observed for each tube. Tube No. 3 shows higher levels of turbulence than tubes No. 1 and 2, probably due to the larger number of fins resulting in a larger wall region of turbulence generation. The point at which the turbulence reaches a maximum depends upon the fin height. For Tube No. 1 (fin tip at $r/R = 0.667$), the maximum occurs at a nondimensional radius (r/R) between 0.55 and 0.65. For Tubes No. 2 and 3 (fin tip at $r/R = 0.817$), the maxima occur between 0.65 and 0.8. For the smooth tube, however, the turbulence reaches a maximum near the tube wall.

Principal, Primary Shear Stress Distribution. Primary Reynolds shear stresses ($\overline{u'_r u'_z}$ and $\overline{u'_\theta u'_z}$) were measured in both the smooth and finned tubes. These primary shear stresses can be combined into a principal, primary shear stress, representing the magnitude of the primary shear stress. The principal shear stress acts in a plane (the principal shear plane) oriented at an angle α from the $+\theta$ direction. The principal, primary shear stress and orientation of the principal plane are defined as

$$\overline{u'_\alpha u'_z} = \sqrt{\overline{u'_r u'_z}^2 + \overline{u'_\theta u'_z}^2} \qquad (3)$$

$$\tan \alpha = \frac{\overline{u'_r u'_z}}{\overline{u'_\theta u'_z}} \qquad (4)$$

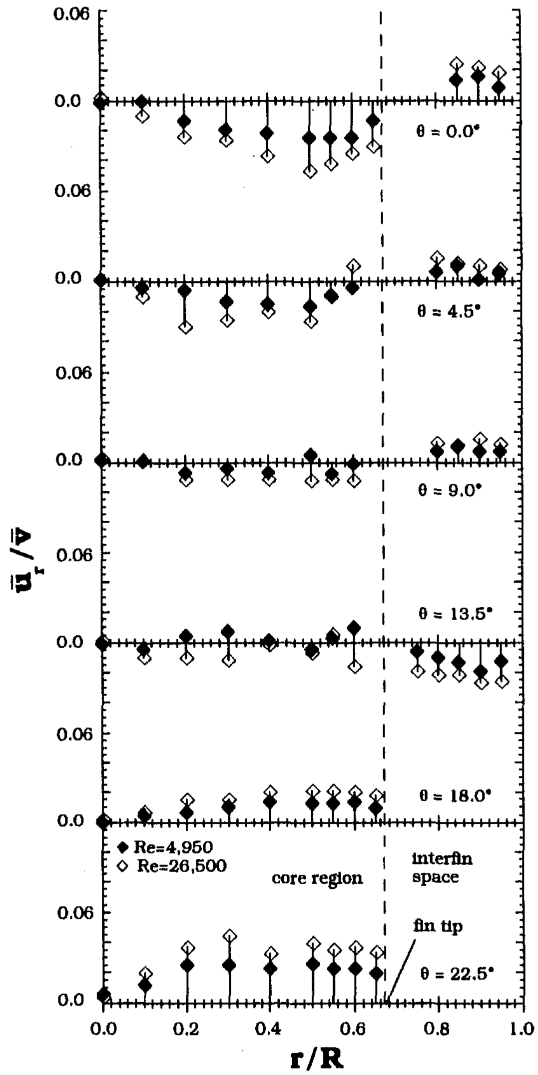

Fig. 8(*a*) Radial component of the secondary flow for Tube No. 1 at Reynolds numbers of 4950 and 26,500. Note that the scale for each data set is −0.06 to 0.06 (except $\theta = 22.5$). Lines are for clarity only.

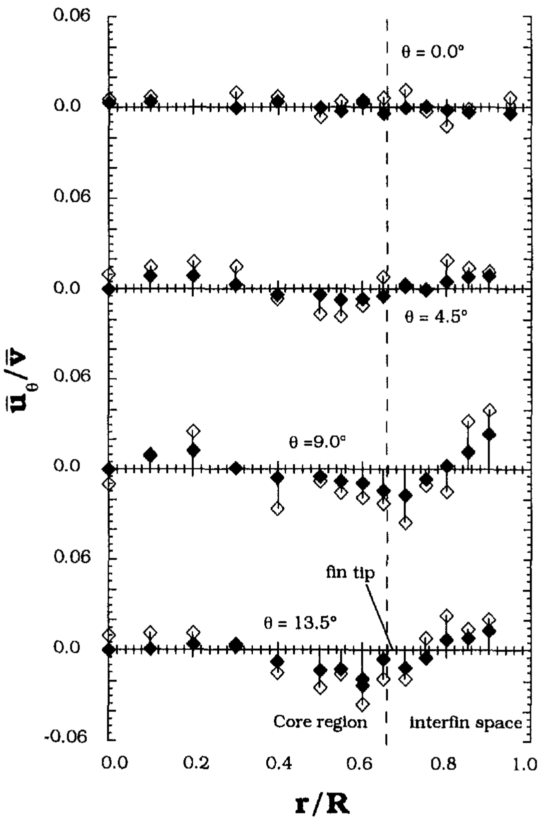

Fig. 8(*b*) Circumferential component of the secondary flow for Tube No. 1 at Reynolds numbers of 4950 and 26,500. Note that the scale for each data set is −0.06 to 0.06. Lines are for clarity only.

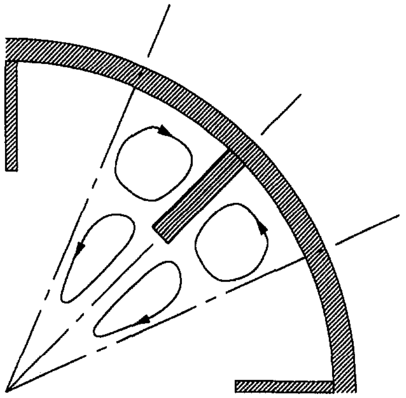

Fig. 8(*c*) Schematic of secondary flow cells in a typical finned tube. Each fin has four secondary flow cells.

For the smooth tube, the principal shear stress is equal to $\overline{u_r'u_z'}$ and α is equal to 90 degrees.

The distribution of the principal, primary shear stress is shown in Fig. 10. In the core region of the flow, the shear stress is larger for the finned tube than for the smooth tube but both increase in an approximately linear fashion. The shear stress in the finned tube rises more rapidly as the fin is approached. In the interfin region, however, the finned tube has much lower shear stress than the smooth tube. As with the turbulence level, the reduction in the principal shear stress can be accounted for by the reduction of the large turbulent length scales. As in smooth tubes, the larger eddies are primarily responsible for the shear stress terms. The absence of the larger eddies in the interfin region results in significantly reduced shear stresses.

Principal, Shear Plane Orientation. The principal plane was found to be oriented in approximately the same direction as the normal to isovels of the mean axial flow. The orientation of the normal to the mean axial velocity can be calculated from the gradient of the mean axial velocity. From Fig. 11, the gradient, oriented in the direction, n, is defined as

$$\text{grad } \bar{u}_z = \frac{1}{r}\frac{\partial \bar{u}_z}{\partial \theta}\,\mathbf{e}_r + \frac{\partial \bar{u}_z}{\partial r}\,\mathbf{e}_\theta \tag{5}$$

The angle β, measured from the $+\theta$ axis is

$$\tan\beta = \frac{\dfrac{\partial \bar{u}_z}{\partial r}}{\dfrac{1}{r}\dfrac{\partial \bar{u}_z}{\partial \theta}} \tag{6}$$

For each tube, at each Reynolds number, α and β were calculated from the Reynolds stress data and from mean axial velocity data at 25 to 35 locations. The results are shown in Fig. 12. While there is considerable scatter in the data, the data roughly demonstrate that α and β are equal, ±10 degrees. Scatter in the data can be attributed to calculations of both angles. Errors of approximately ±15 percent in the Reynolds shear stresses are accompanied by similar errors in the calculation of the gradients of the mean axial velocity. From these errors, an estimate for the calculation of the two angles is approximately ±10 degrees.

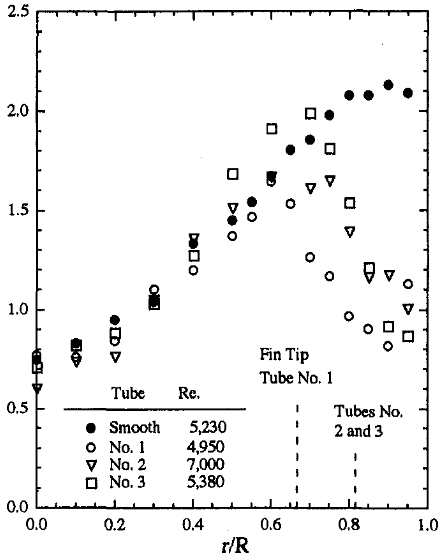

Fig. 9 Comparison of turbulent kinetic energy distribution along $\theta = 0$ for smooth and finned tubes (Re ~ 5,000)

While these errors prevent a conclusive statement that α and β are equal across the flow field, it suggests some important considerations for turbulence modeling. Eddy viscosity formulations are commonly used for modeling the primary shear stresses in both circular and noncircular ducts. This model is

$$\overline{u_r'u_z'} = -\nu_t \frac{\partial \bar{u}_z}{\partial r} \qquad (7a)$$

$$\overline{u_\theta'u_z'} = -\nu_t \frac{1}{r}\frac{\partial \bar{u}_z}{\partial \theta} \qquad (7b)$$

A corresponding principal shear stress for the model is

$$\overline{u_\gamma'u_z'} = -\nu_t \sqrt{\left(\frac{\partial \bar{u}_z}{\partial r}\right)^2 + \left(\frac{1}{r}\frac{\partial \bar{u}_z}{\partial \theta}\right)^2} \qquad (8)$$

This principal shear stress acts in a plane γ (oriented from the $+\theta$ direction)

$$\tan\gamma = \frac{\dfrac{\partial \bar{u}_z}{\partial r}}{\dfrac{1}{r}\dfrac{\partial \bar{u}_z}{\partial \theta}} \qquad (9)$$

Thus, by definition, γ equals β. From the experimental data it has been shown that α and β are equal (within experimental uncertainty). Thus, the use of an eddy viscosity model for the primary shear stresses will predict a principal, primary shear stress oriented in the same plane as experimentally determined. This type of analysis can be used to validate the use of an eddy viscosity model based on the orientation of the principal shear planes but does not include the magnitude of the shear stresses. Additionally, while the use of an eddy viscosity model for the primary shear stresses may be adequate, an isotropic turbulence model is needed to properly account for the secondary flows which arise due to turbulent secondary shear and normal stresses.

Conclusions

An experimental investigation was performed in which overall performance and velocity profile measurements in three finned tubes and a smooth tube were made. The following results and conclusions can be drawn from this study:

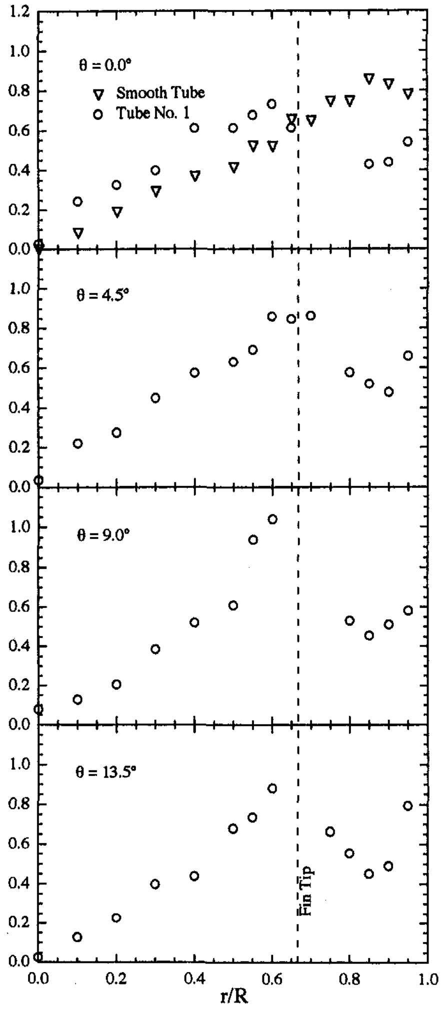

Fig. 10 Distribution of principal, primary shear stress for Tube No. 1 (Re = 4,950) and the smooth tube (Re = 5,230)

1. Measured friction factors were within ±10 percent of the correlation of Carnavos (1979). The data show that the dependence of friction factor on Reynolds number for the finned tubes was similar to that of smooth tubes.
2. Axial velocity profiles showed reduced velocities in the interfin space compared to smooth tube measurements. A velocity "plateau" in the interfin space was observed.
3. Two pairs of secondary flow cells were measured for each fin. The secondary flow velocity was at most 5.2 percent of the mean axial velocity and increased with larger Reynolds number, fewer fins, and taller fins.
4. A continuous law-of-the-wall appropriate for smooth tubes also fit the finned tube data for $y^+ < 30$, but a

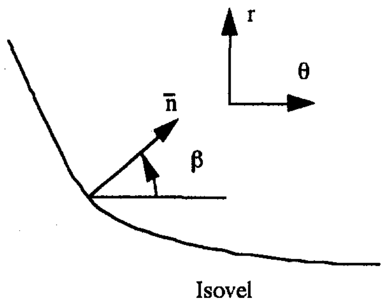

Fig. 11 Schematic showing normal to isovel and its orientation

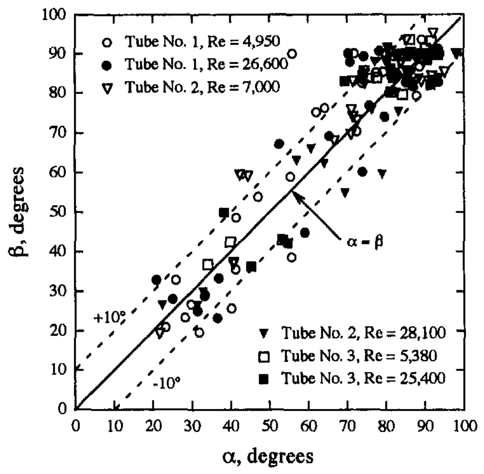

Fig. 12 Orientation of the principal, primary shear stress and the mean axial velocity gradient

universal profile was not observed outside this near-wall region.

5. The maximum wall shear stress occurs at the fin tip and the minimum occurs at the fin root. Wall shear stress distributions were found to be strongly dependent on Reynolds number.
6. In the core region of the finned tubes, the turbulent structure is very similar to that of a smooth tube. For the interfin region, a large reduction in the turbulence was observed. This has been attributed to the reduction in the largest turbulent length scale in this region.
7. The primary shear stresses, when combined into a principal, primary shear stress, showed trends similar to the turbulent kinetic energy. The structure in the core region was similar to that of a smooth tube while the interfin region showed a marked reduction in the principal shear stress.
8. It was found that mean axial velocity gradients and principal shear stresses appear to act in the same plane. While experimental uncertainty prevents this from being proven conclusively, the results support the modeling of primary shear stresses with an eddy viscosity model.

Acknowledgments

This work was funded by the Rensselaer Polytechnic Institute High Temperature Technology Program, administered by the New York State Energy Research and Development Authority.

References

Bergles, A. E., Brown, G. S., and Snider, W. D., 1971, "Heat Transfer Performance of Internally Finned Tubes," 11th National Heat Transfer Conference, Tulsa, OK, ASME Paper 71-HT-31.

Broadway, J. D., and Karahan, 1981, "Correction of Laser Doppler Anemometer Readings for Refraction at Cylindrical Interfaces," *DISA Information*, No. 26, pp. 4–6.

Carnavos, T. C., 1979, "Cooling Air in Turbulent Flow with Internally Finned Tubes," *Heat Transfer Engineering*, Vol. 1, pp. 41–46.

Carnavos, T. C., 1979, "Heat Transfer Performance of Internally Finned Tubes in Turbulent Flow," *Advances in Enhanced Heat Transfer*, J. M. Chenoweth, J. Kaellis, J. W. Michel, and S. Shenkman, eds., ASME New York, pp. 61–67.

Edwards, D. P., 1994, "An Investigation of Turbulent Flow and Heat Transfer in Longitudinally Finned Tubes," PhD thesis, Rensselaer Polytechnic Institute, Troy, NY.

Garavsky, J., Hrbek, J., Chara, Z., and Severa, M., 1989, "Refraction Corrections for LDA Measurements in Circular Tubes within Rectangular Optical Boxes," *Dantec Information*, No. 08.

Hilding, W. E., and Coogan, C. H., 1964, "Heat Transfer and Pressure Loss Measurements in Internally Finned Tubes," Symposium on Air-Cooled Heat Exchangers, ASME, New York, pp. 57–85.

Kays, W. M., and London, A. L., 1984, *Compact Heat Exchangers*, McGraw-Hill, New York.

Laufer, J., 1954, "The Structure of Turbulence in Fully Developed Pipe Flow," NACA-TR 1174, pp. 417–434.

Lipets, A. U., Zholudov, Y. S., Antonov, A. Y., and Gromov, G. V., 1964, "The Temperature Regime and Hydraulic Resistance of Tubes with Internal Longitudinal Fins," *Heat Transfer-Soviet Research*, Vol. 1, pp. 86–94.

Trupp, A. C., Lau, A. C. Y., Said, M. N. A., and Soliman, H. M., 1981, "Turbulent Flow Characteristics in an Internally Finned Tube," *Advances in Heat Transfer-1981*, ASME, HTD-18, pp. 11–19.

Vasil'chenko, Y. A., and Barbaritskaya, M. S., 1969, "Resistance with Nonisothermal Fluid Flow in Tubes with Longitudinal Fins," *Thermal Engineering*, Vol. 16, pp. 17–23.

Watkinson, A. P., Miletti, D. L., and Tarassoff, P., 1973, "Turbulent Heat Transfer and Pressure Drop in Internally Finned Tubes," *AIChE Symposium Series No. 131*, Vol. 69, pp. 94–103.

Watkinson, A. P., Miletti, D. L., and Kubanek, G. R., 1975, "Heat Transfer and Pressure Drop of Internally Finned Tubes in Turbulent Air Flow," *ASHRAE Transactions*, No. 2347, Vol. 81, pp. 330–337.

A Comparison of Some Recent Eddy-Viscosity Turbulence Models

F. R. Menter
Head of Software Development,
ASC GmbH, 83607 Holzkirchen, Germany;
Formerly, NASA Ames Research Center

The performance of recently developed eddy-viscosity turbulence models, including the author's SST model, is evaluated against a number of attached and separated adverse pressure gradient flows. The results are compared in detail against experimental data, as well as against the standard k-ε model. Grid convergence was established for all computations. The study involves four different, state-of-the-art finite difference (finite volume) codes.

Introduction

With the maturing of numerical methods and the ever-widening scope of computational fluid dynamics (CFD), the need for accurate as well as robust turbulence models becomes increasingly more urgent. There is certainly no shortage of turbulence models among which to choose. However, making the decision which turbulence model is best for the intended type of applications is a difficult task. Over the last four years, the present author has developed a test base for the evaluation of turbulence models (Menter, 1992, 1993, 1994a, b; Menter and Rumsey, 1994). The test cases have been selected to cover a wide area of increasingly difficult flowfields that are relevant with respect to aerodynamic applications. The test base is used to periodically evaluate the performance of newly developed turbulence models and to compare the results with those of existing models. All models are tested with the same numerical methods, on identical grids and with the same boundary conditions. Grid convergence was established by using at least two, in most cases three, successively refined grids and to ensure that the results were within plotting accuracy with one another.

One of the most interesting developments in the last years with respect to eddy-viscosity models is the re-emergence of one-equation models, starting with the Baldwin-Barth (BB) model (Baldwin and Barth, 1990). (Note, however, that one-equation models have been used in Russia for a considerable period of time. Gulyaev et al., 1993; Nee and Kovasznay, 1969) The BB model has gained widespread interest and is now implemented into a large number of codes. However, recent investigations (Spalart, 1994; Menter, 1994c) into the mathematical properties of this model have shown that the underlying equations are ill-conditioned near viscous-inviscid interfaces (shear layer edge) and that the solutions of this model depend strongly on the grid density in that area. In the present paper the one-equation model developed by Spalart and Allmaras (SA) (Spalart, 1994) which avoids the problems of the BB model is tested.

Another new development is the application of the renormalization group (RNG) theory to the derivation of eddy-viscosity turbulence models (Yakhot and Orszag, 1986; Yakhot and Smith, 1992; Yakhot et al., 1992). While the early versions of the model were not fit for use in flows of practical interest, because of their inability to predict the logarithmic region of a turbulent boundary layer, the version of the model given in Yakhot et al. (1992) remedies this shortcoming and has gained widespread interest. This model is called the RNG model in this paper, although it is not entirely derived from RNG theory. An expansion technique was employed in order to arrive at a variable coefficient in front of the production of dissipation ($c_{\epsilon 1}$) term. In the course of the analysis a free parameter is introduced that was used for calibration of the logarithmic layer.

One of the problems in conducting this study was that no low Reynolds number terms were available for the RNG model. Thus, the equations cannot be integrated to the surface. In previous computations, the RNG model was always solved in combination with wall-function boundary conditions. This was not considered desirable, because it would necessitate that the different models are solved on different grids, which would cloud the comparison. The RNG model was therefore transformed (exactly) to a k-ω formulation, following the approach given by Menter (1994b). This allows the use of the standard k-ω sub-layer treatment in the near wall region ($y^+ < \sim 60$) combined with the high Reynolds number RNG formulation for the rest of the flow. In order to demonstrate that the present near wall treatment does not affect the high Reynolds number performance of the RNG model, two of the test cases were repeated with wall functions.

The standard k-ϵ model, included as a point of reference, was solved in the same way, so that the differences between the results of the two-equation models are truly due to differences in the high Reynolds number formulation of the models and not due to differences in the grids and/or boundary conditions.

The comparisons also include the author's k-ω based shear-stress transport (SST) eddy-viscosity model (Menter, 1993, 1994b). This model was specifically developed for improved prediction of adverse pressure gradient flows. It is based on the assumption that in an adverse pressure gradient flow, the principal turbulent shear stress obeys the same transport equation as the turbulent kinetic energy. Computations with this model have been reported by Menter (1993, 1994b) and Menter and Rumsey (1994).

In a study like this, it is very important to ensure that the models are implemented properly. All in all, four different Reynolds averaged Navier-Stokes methods INS2D, INS3D, CFL3D and a research code developed by Huang and Coakley (1992) have been used for various cases in this comparison. In addition, an equilibrium boundary layer code, as well as three different (self-similar) free shear layer codes were employed. Furthermore, grid refinement studies were performed for all test cases.

One-Equation Turbulence Model

Spalart-Allmaras (SA) Model. The SA model solves one transport equation for the high Reynolds number eddy viscosity, $\tilde{\nu}_t$:

Contributed by the Fluids Engineering Division for publication in the JOURNAL OF FLUIDS ENGINEERING. Manuscript received by the Fluids Engineering Division March 28, 1995; revised manuscript received April 1, 1996. Associate Technical Editor: D. P. Telionis.

$$\frac{D\tilde{\nu}_t}{Dt} = c_{b1}\tilde{\nu}_t\tilde{S} - c_{w1}f_w\left(\frac{\tilde{\nu}_t}{d}\right)^2 + \frac{c_{b2}}{\sigma}\frac{\partial\tilde{\nu}_t}{\partial x_j}\frac{\partial\tilde{\nu}_t}{\partial x_j} + \frac{1}{\sigma}\frac{\partial}{\partial x_j}\left((\tilde{\nu}_t + \nu)\frac{\partial\tilde{\nu}_t}{\partial x_j}\right) \quad (1)$$

where d is the distance to the nearest surface. The eddy viscosity is given by:

$$\nu_t = \tilde{\nu}_t f_{v1}; \quad f_{v1} = \frac{\chi^3}{\chi^3 + c_{v1}^3}; \quad \chi = \frac{\tilde{\nu}_t}{\nu} \quad (2)$$

With S being the absolute value of the vorticity, the production term reads:

$$\tilde{S} = S + \frac{\tilde{\nu}_t}{\kappa^2 d^2} f_{v2}; \quad f_{v2} = 1 - \frac{\chi}{1 + \chi f_{v1}} \quad (3)$$

The blending function f_w is defined as:

$$f_w = g\left[\frac{1 + c_{w3}^6}{g^6 + c_{w3}^6}\right]^{1/6};$$

$$g = r + c_{w2}(r^6 - r); \quad r = \frac{\tilde{\nu}_t}{\tilde{S}\kappa^2 d^2} \quad (4)$$

The coefficients are:

$$c_{b1} = 0.1355, \quad \sigma = \tfrac{2}{3}, \quad c_{b2} = 0.622, \quad \kappa = 0.41, \quad c_{w2} = 0.3$$

$$c_{w3} = 2, \quad c_{v1} = 7.1, \quad c_{w1} = \frac{c_{b1}}{\kappa^2} + \frac{1 + c_{b2}}{\sigma} \quad (5)$$

The wall boundary condition is $\tilde{\nu}_t = 0$. In the freestream (inflow) small values are specified for $\tilde{\nu}_t$ (compared to the molecular viscosity).

Two-Equation Turbulence Models

General Form. The two-equation models are based on a blending of the Wilcox k-ω model (Wilcox, 1993) in the sublayer with the corresponding k-ϵ model for the rest of the flowfield. In order to arrive at a set of equations that can be blended, the k-ϵ model is transformed to a k-ω formulation, introducing additional cross diffusion terms. The original k-ω model is then multiplied by a blending function F_1 and the transformed k-ϵ model by $(1 - F_1)$ and the corresponding equations of each model are added together. The blending function is designed to be equal to one near the surface and zero away from the surface. This procedure allows all two-equation models to be solved with the same sublayer model and on the same grids, so that differences in the solutions are truly due to differences in the high Reynolds number form of the equations.

The general form of the equations is:

$$\rho\frac{Dk}{DT} = \tau_{ij}\frac{\partial u_i}{\partial x_j} - \beta^*\rho k\omega + \frac{\partial}{\partial x_j}\left(\sigma^*\mu_t\frac{\partial k}{\partial x_j}\right) \quad (6)$$

$$\rho\frac{D\omega}{Dt} = \gamma\frac{\tau_{ij}}{\nu_t}\frac{\partial u_i}{\partial x_j} - \beta\rho\omega^2 + \frac{\partial}{\partial x_j}\left(\sigma\mu_t\frac{\partial\omega}{\partial x_j}\right) + (1 - F_1)\rho\frac{2\sigma_2}{\omega}\frac{\partial k}{\partial x_j}\frac{\partial\omega}{\partial x_j} \quad (7)$$

The last term in Eq. (7) is a result of the transformation of the k-ϵ model to a k-ω formulation. In the case that the diffusion coefficients of the k- and the ϵ-equations in the k-ϵ model are not equal, an additional diffusion term appears in the ω-equation. For the standard k-ϵ model this term is small and free shear layer computations by Menter (1993) have shown that it does not have a significant impact on the results. It is therefore neglected. For the RNG k-ϵ model, the diffusion coefficients are equal and the transformation is exact. The function F_1 is a blending function that goes from one near the surface to zero away from the surface. The function F_1 is also used to blend the constants of the standard Wilcox k-ω model with those of the transformed k-ϵ model

$$\phi = F_1\phi_1 + (1 - F_1)\phi_2 \quad (8)$$

where ϕ stands for any constant of the two-layer model (e.g., γ), ϕ_1 for the corresponding constant of the Wilcox k-ω model (e.g., γ_1) and ϕ_2 for the corresponding k-ϵ model constant (e.g., γ_2). The transformed k-ϵ model constants are:

$$\gamma_2 = c_{\epsilon 1} - 1; \quad \beta_2 = (c_{\epsilon 2} - 1)c_\mu;$$

$$\beta_2^* = c_\mu; \quad \sigma_2^* = \frac{1}{\sigma_k}; \quad \sigma_2 = \frac{1}{\sigma_\epsilon} \quad (9)$$

For the standard k-ϵ model they are obtained from $c_\mu = 0.09$, $c_{\epsilon 1} = 1.44$, $c_{\epsilon 2} = 1.92$, $\sigma_k = 1$ and $\sigma_\epsilon = 1.17$ (note that a value of 1.17 is used for σ_ϵ instead of $\sigma_\epsilon = 1.3$ in order to satisfy the logarithmic portion of the profile for $\kappa = 0.41$.) The turbulent stress tensor is defined as:

$$\tau_{ij} = \mu_t\left(\frac{\partial u_i}{\partial x_j} + \frac{\partial u_j}{\partial x_i} - \frac{2}{3}\frac{\partial u_k}{\partial x_k}\delta ij\right) - \frac{2}{3}\rho k\delta_{ij} \quad (10)$$

The eddy viscosity is computed from:

$$\nu_t = \frac{\mu_t}{\tau} = \frac{k}{\omega}. \quad (11)$$

The Two-Layer k-ϵ Model. In the k-ϵ 2L model the coefficients ϕ_2 are computed from the transformation of the coefficients of the standard k-ϵ model (see Eq. (9)):

$$\beta_2^* = 0.09; \quad \sigma_2^* = 1.0; \quad \kappa = 0.41$$

$$\gamma_2 = 0.44; \quad \sigma_2 = 0.857; \quad \beta_2 = \left(\gamma_2 + \frac{\sigma_2\kappa^2}{\sqrt{\beta_2^*}}\right)\beta_2^* \quad (12)$$

The coefficients of the k-ω model have to be changed slightly in order to recover the correct c_f-distribution for a flat plate boundary layer.

$$\beta_1^* = 0.09; \quad \sigma_1^* = 0.5; \quad \kappa = 0.41;$$

$$\gamma_1 = \frac{5}{9}; \quad \sigma_1 = 0.4; \quad \beta_1 = \left(\gamma_1 + \frac{\sigma_1\kappa^2}{\sqrt{\beta_1^*}}\right)\beta_1^* \quad (13)$$

The eddy-viscosity is again computed from Eq. (11). The missing element is the blending function F_1. For the k-ϵ 2L model the blending function is built on two arguments, Γ_1, Γ_2, which ensures that the switch between the models takes place just outside the viscous sublayer.

The two arguments are:

$$\Gamma_1 = \frac{500\nu}{y^2\omega}; \quad \Gamma_2 = \frac{4\rho\sigma_2 k}{y^2 CD_{k\text{-}\omega}}$$

$$CD_{k\text{-}\omega} = \max\left(\rho\frac{2\sigma_2}{\omega}\frac{\partial k}{\partial x_j}\frac{\partial\omega}{\partial x_j}; \ 10^{-20}\right) \quad (14)$$

$CD_{k\text{-}\omega}$ being the positive part of the cross-diffusion term already computed in Eq. (7) and y being the distance to the closest surface. The blending function is computed from Γ_1 and Γ_2 as follows:

$$\Gamma = \min(\Gamma_1, \Gamma_2); \quad F_1 = \tanh(\Gamma^4) \quad (15)$$

In the sublayer ω varies like $1/y^2$ (Wilcox, 1993) so that Γ_1 is constant and F_1 is equal to one. In the logarithmic layer Γ_1 is proportional to $61.5/y^+$ so that the function F_1 changes from one to zero in the range of $50 < y^+ < 110$. The argument Γ_2 comes into play only near the boundary-layer edge (where Γ_1 can become large as ω becomes small) and ensures that F_1 does not jump back to one near the boundary-layer edge.

The Two-Layer RNG k-ϵ Model. The RNG model is solved in exactly the same way as the two-layer k-ϵ model, except that the coefficients in the high Reynolds number portion of the equations are the exact transformation of the coefficients of the RNG k-ϵ model. The coefficients of the RNG model are: $c_{\epsilon 1} = 1.42 - f_\eta$, $c_{\epsilon 2} = 1.68$, $c_\mu = 0.085$, $\sigma_k = \sigma_\epsilon = 0.7179$. The coefficient $c_{\epsilon 1}$ in the RNG model is a function of $\eta = Sk/\epsilon = S/\omega/c_\mu$

$$f_\eta = \frac{\eta\left(1 - \dfrac{\eta}{4.38}\right)}{1 + 0.015\eta^3} \tag{16}$$

The transformed coefficients are:

$$\beta_2^* = 0.085; \quad \sigma_2^* = 1.39;$$

$$\gamma_2 = 0.42 - f_\eta; \quad \sigma_2 = 1.39; \quad \beta_2 = 0.0578 \tag{17}$$

The blending function F_1 is the same as for the k-ϵ 2L model and so are the coefficients for the near wall model (Eqs. (13, 15)).

The Shear Stress Transport (SST) Model. The SST model is an attempt to combine the best elements of existing eddy viscosity models. Like the k-ϵ 2L model it is based on a blending of the k-ω model near walls with the standard k-ϵ model away from the surface. However, unlike the previous two models, where the Wilcox model is only used in the sublayer, the SST model takes advantage of the Wilcox model's superior performance also in the logarithmic layer. The blending to the k-ϵ model takes place in the wake portion of the boundary layer. In addition, the definition of the eddy viscosity is altered in order to account for the transport of the principal turbulent shear stress in adverse pressure gradient boundary layers. It is this last change that has greatly improved the models performance for strong adverse pressure gradient flows. The coefficients for this model are:

$$\beta_1^* = 0.09; \quad \sigma_1^* = 0.85; \quad \kappa = 0.41;$$

$$\gamma_1 = \frac{5}{9}; \quad \sigma_1 = 0.5; \quad \beta_1 = \left(\gamma_1 + \frac{\sigma_1 \kappa^2}{\sqrt{\beta_1^*}}\right)\beta_1^* \tag{18}$$

$$\beta_2^* = 0.09; \quad \sigma_2^* = 1.0; \quad \kappa = 0.41$$

$$\gamma_2 = 0.44; \quad \sigma_2 = 0.857; \quad \beta_2 = \left(\gamma_2 + \frac{\sigma_2 \kappa^2}{\sqrt{\beta_2^*}}\right)\beta_2^* \tag{19}$$

The blending function is defined as:

$$\Gamma = \min(\max(\Gamma_1, \Gamma_3), \Gamma_2);$$

$$F_1 = \tanh(\Gamma^4); \quad \Gamma_3 = \frac{\sqrt{k}}{\beta_1^* \omega y} \tag{20}$$

It can easily be shown that Γ_3 is equal to 2.5 in the log-layer (turbulent length scale divided by the distance to the surface). F_1 is therefore equal to one throughout the log-layer and goes to zero in the wake region of the boundary layer (due to the y-dependency in the denominator of the arguments).

Table 1

Flow	k-ϵ/SST	RNG	SA	Experiment
Far wake	0.256	0.308	0.339	0.365
Mix. layer	0.100	0.100	0.109	0.115
Plane jet	0.102	0.142	0.143	0.100–0.110
Round jet	0.122	0.175	0.256	0.086–0.095

Standard two-equation models fail to give accurate results for strong adverse pressure gradient flows. This shortcoming was attributed by Menter (1993) to the definition of the eddy-viscosity, Eq. (11). For boundary-layer flows, Eq. (11) is equivalent to the following relation between the principal turbulent shear stress $-\overline{u'v'}$ and the turbulent kinetic energy k:

$$-\overline{u'v'} = \sqrt{\frac{\text{Production}_k}{\text{Dissipation}_k}}\, a_1 k \tag{21}$$

with a_1 being Bradshaw's constant. Equation (21) is not substantiated by experimental data. Instead, the experimental evidence suggest the relation:

$$-\overline{u'v'} = a_1 k \tag{22}$$

Equation (22) can be enforced in a boundary layer flow by redefining the eddy-viscosity as follows:

$$\nu_t = \frac{a_1 k}{\Omega}; \quad \Omega = \left|\frac{\partial u}{\partial y}\right| \tag{23}$$

In order to avoid the singular behavior for $\Omega = 0$, the SST model uses the following definition of the eddy-viscosity:

$$\nu_t = \min\left(\frac{k}{\omega}; \frac{a_1 k}{\Omega F_2}\right) \tag{24}$$

The function F_2 is a blending function that is equal to one inside boundary layers and goes to zero for free shear layers (where Eq. (22) is not valid):

$$\Gamma = \max(2 \cdot \Gamma_3; \Gamma_1); \quad F_2 = \tanh(\Gamma^2) \tag{25}$$

Equation (24) ensures that Eq. (22) is satisfied for adverse pressure gradient flows. $-\overline{u'v'}$ therefore satisfies the same transport equation as the turbulent kinetic energy, giving the model it's name. In general flows, Ω is replaced by the absolute value of the vorticity.

Results and Discussion

Free Shear Layer Computations. Computations have been performed on the basis of the self-similar equations as given by Wilcox (1993) for a far wake, a mixing layer, a plane and a round jet (note that the factor S_k for the round jet in Wilcox (1993) should be $2U$ instead of U). A comparison of the computed and the experimental spreading rates is given in Table 1. The SST model and the standard k-ϵ model are identical for free shear layers. The experimental spreading rates are cited from Wilcox (1993). The performance of the k-ϵ model is well known; it underpredicts the spreading rate of the far wake and somewhat overpredicts the spreading rates of the round jet. Note, however, that the far wake analysis is only valid in the asymptotic limit of small wake deficits. For the more important near wake, the k-ϵ is known to give accurate results (Kline et al., 1981). The RNG and the SA models predict the far wake and the mixing layer with good overall accuracy, but significantly overpredict the plane and even more so the round jet.

Boundary-Layer Computations. Flat-plate zero-pressure gradient boundary-layer computations have been performed with every code and turbulence model to assure that the model implementation is correct. Due to their calibration, all models give good results for this flow. The results are not shown here.

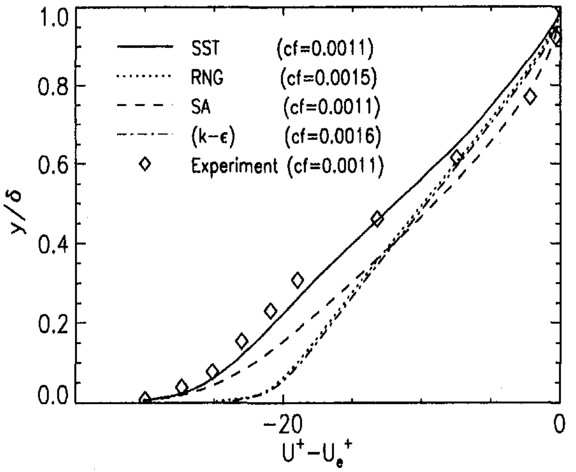

Fig. 1 Defect layer velocity profiles for self-similar adverse pressure gradient flow ($\beta_t = 8.7$)

Self-Similar Boundary-Layer Flow. Self-similar boundary-layer solutions serve as a good first indication of how well a model will perform in more complex adverse pressure gradient flows. The equations for self-similar boundary-layer flows are given by Wilcox (1993). The resulting ordinary differential equations are solved with a 1D code. Figure 1 shows results for the self similar adverse pressure gradient flow of Clauser (Kline et al., 1981).

The k-ϵ model and the RNG model both overpredict the wall-shear stress significantly (40–50 percent) whereas the SA and the SST model give very accurate results for c_f. The SA model predicts a somewhat fuller velocity profile than the SST model. It is interesting to note that the RNG model and the k-ϵ model predict very similar velocity profiles. Note that the self-similar equations do not involve the transformation of the RNG model to a k-ω formulation and that the equations are solved with wall-function boundary conditions. However, a second computation was performed with the RNG model in its k-ω formulation and the results were the same.

Adverse Pressure Gradient Flow With Separation. The next flow is an adverse pressure gradient flow, developing in the axial direction of a circular cylinder (axisymmetric) (Driver, 1991). The pressure gradient is imposed on the cylinder by diverging wind-tunnel walls. Computations were run with the INS2D code on a 90 × 90 and a 120 × 120 grid without changes in the plotted solution. Figures 2 and 3 show the wall pressure, c_p, and wall skin friction, c_f, distributions, respectively. The suffix 2-L in the labels of the plots refers to the fact that the models are solved in a two-layer approach, with the k-ω model used in the sublayer. Figure 4 shows the corresponding velocity profiles.

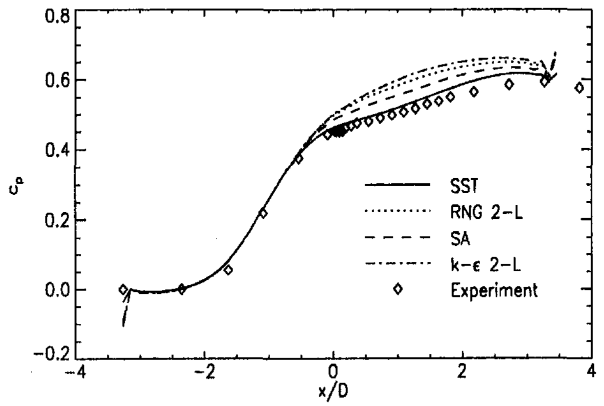

Fig. 2 C_p-distribution for Driver's case CS0

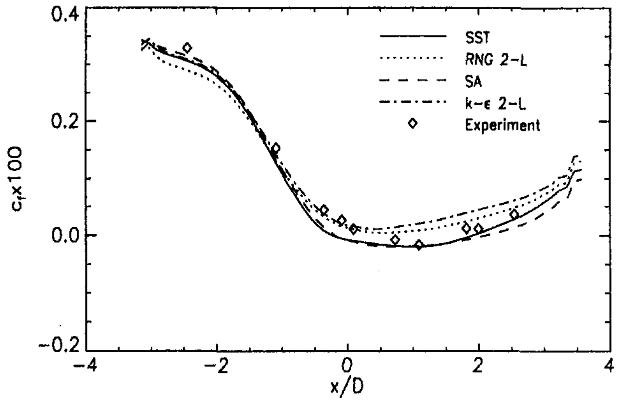

Fig. 3 C_f-distribution for Driver's case CS0

As for the self-similar case, the RNG and the standard k-ϵ model do not predict enough retardation. Note that the RNG model gives improved results compared to the standard k-ϵ model, due to the fact that in nonequilibrium flows the η-dependency of the coefficient $c_{\epsilon 1}$ somewhat reduces the eddy-viscosity. However, the effect is not sufficient to cause separation and to reproduce the experimental data. Again, the SA model predicts significantly better results than the k-ϵ and the RNG model, but gives slightly fuller velocity profiles than the experiments. The SST model is in very good agreement with the data as already reported in Menter (1994b).

Figure 5 shows the turbulent shear-stresses profiles corresponding to the velocity profiles shown in Fig. 4. For separated flows, it is of great importance to predict the shear-stresses ahead of separation correctly. Note that the amount of separation that is predicted by the different models does correlate with their ability to predict the shear-stress at the first profile shown in Fig. 5.

Backward Facing Step Flow. The backward facing step flow is one of the most widely used cases to evaluate the performance of turbulence models. In the present study, the flow as reported Driver and Seegmiller (1985) is computed. The grid consists of 120 × 120 grid points and grid independence has been confirmed on a 240 × 240 grid. The computations have been performed with the INS2D code. Figure 6 shows the computed wall shear stress distributions for the different models compared to the experiment. Good results have been reported

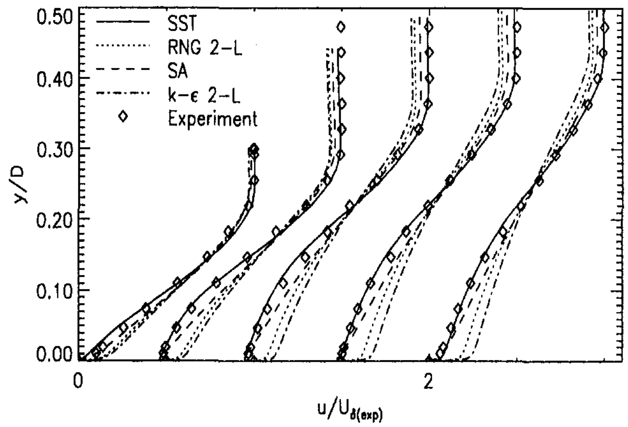

Fig. 4 Velocity profiles for Driver's case CS0 at $x/D = -0.091, 0.363, 1.088, 1.633, 2.177$

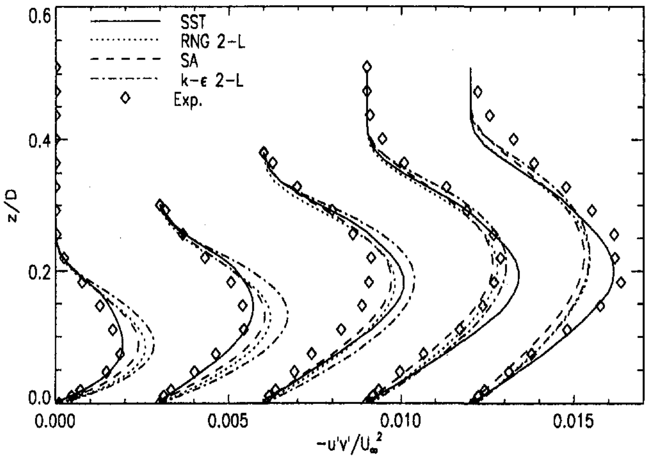

Fig. 5 Turbulent shear-stress profiles for Driver's case CS0 at x/D = −0.091, 0.363, 1.088, 1.633, 2.177

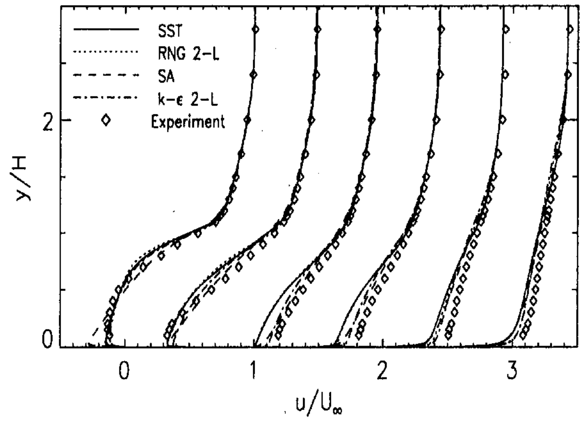

Fig. 7 Velocity profiles for back-step flow at x/h = 2, 4, 6.5, 8, 14, 32

for the RNG model for a back-step flow by Yakhot and Smith (1992) and these findings are confirmed by Fig. 6. Note however, that the specific c_f-distribution is to some extent a result of the sublayer modeling involving the k-ω model. The k-ϵ model predicts a somewhat too low reattachment length and the SA model seems to have too much backflow in the recirculation region and a slow recovery of the wall shear stress. The SST model gives very similar results to the RNG model, but a lower c_f in the recovery region. Figure 7 shows the velocity profiles for this flow. As expected from the c_f-distribution, the SA model predicts too much back-flow in the recirculation region. All models fail to predict the correct recovery, and so does any other model the author has tested. The velocity profiles do not accelerate enough near the surface, not only for the back-step flow, but for all flows recovering from a separation. Note also that the SST and the RNG model do produce almost identical velocity profiles, despite the fact that the solutions for the adverse pressure gradient flows shown earlier were very different from one another. This demonstrates that the back-step flow alone, although it is an important test case, does not allow one to judge the quality of a turbulence model. Turbulence model testing has to involve a significant number of flows.

NACA 4412 Airfoil at α = 13.87 Deg Angle of Attack. This experiment has been reported by Coles and Wadcock (1979). It is an incompressible airfoil flow at maximum lift condition and a chord Reynolds number of 1.52×10^6. Transition occurred within about 2 percent of chord for all models. Numerical tests have shown that the transition location has little influence on the predictions, as long as it is far enough upstream to prevent laminar separation. Unlike earlier comparisons, the solid wind tunnel walls are included in the present computations, via the Chimera capability of the INS2D code. The wind tunnel (background) grid consists of 101×101 points and the airfoil grid has 321×51 points. Grid independence was confirmed by independently changing the background grid to 140×140 and the airfoil grid to 431×81 points. Figure 8 shows the velocity profiles for this flow. In order to demonstrate that the two-layer treatment based on the k-ω formulation does not negatively affect the predictions with the RNG model, the model was coded in its original k-ϵ formulation and solved with wall function boundary conditions. To ensure that the first grid point off the surface was at a $y^+ = 30-40$, 16 points were eliminated from the airfoil grid near the surface in the body normal direction. The results of that computation are included in Fig. 8. As in the computation of Driver's adverse pressure gradient flow, it is apparent that the RNG model does not predict separation. The two different computations with the RNG model (with and without wall functions) give very similar results. Differences between the two solutions are most likely due to the inability of the wall function grid to resolve the boundary layer in the leading edge region of the airfoil. Both computations do not predict the retardation of the flow due to the pressure gradient. The SA model gives significantly better results than the RNG and the k-ϵ model, but again does not give quite enough separation. The results for the SST model show the best agreement with the experiment.

Transonic Bump Flow. The following results are for the transonic bump flow experiment as reported by Bachalo and Johnson (1979). The computations have been performed with the CFL3D code of the NASA Langley Research center. G. P.

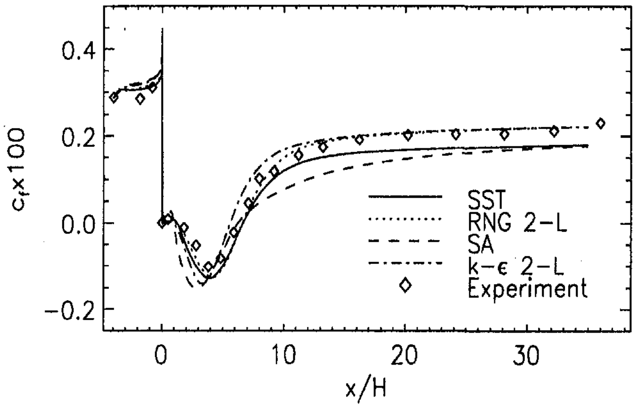

Fig. 6 Wall-shear stress distribution for back-step flow

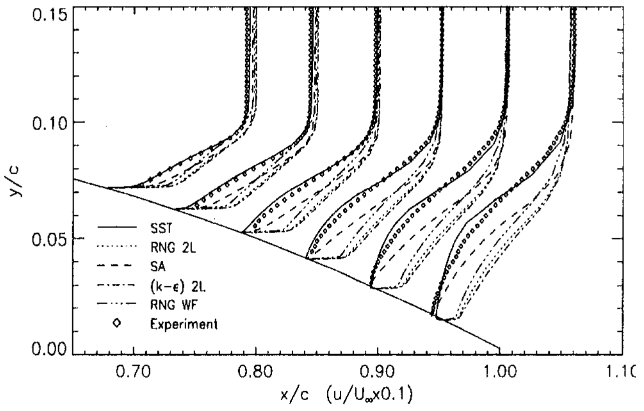

Fig. 8 Velocity profiles for NACA 4412 airfoil

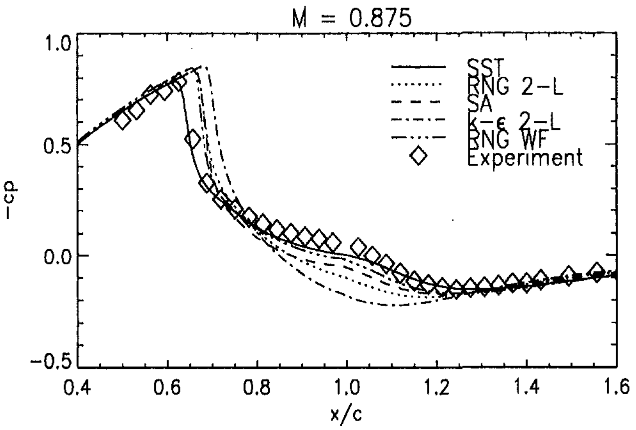

Fig. 9 Wall pressure distribution for transonic bump flow (M = 0.875)

Huang of the Eloret Institute was kind enough to recompute the flow with his code using the RNG model in a k-ϵ formulation with wall function boundary conditions. Figure 9 shows the wall pressure distribution for a Mach number of M = 0.875. Both codes predict the same shock location for the RNG model. In the separated region downstream of the shock, differences between integration to the surface and wall function boundary conditions have to be expected. The k-ϵ model predicts a shock location significantly too far downstream. The SA and the RNG models are in better agreement with the data but predict shock locations still downstream of the experimental shock position. Again the SST model gives the best agreement with the experiments. The RNG model performs better in this flow compared to incompressible flows due to the increase in η as a result of the shock wave.

Conclusions

Four turbulence models have been tested against a variety of test cases. All computations have been performed with identical grids and boundary conditions using state-of-the-art computer codes. Grid refinement tests were performed for all flows. It was found that the RNG k-ϵ model does not significantly improve on the predictions of adverse pressure gradient flows, compared to the standard k-ϵ model. The SST model gave the best agreement for the adverse pressure gradient cases, due to its calibration for these flows. The SA model gives significantly better results than the k-ϵ model but tends to somewhat underpredict separation. All models failed to predict the flow recovery for the backstep flow.

Acknowledgment

This work was funded by the NASA Ames Research Center. The author wants to thank George Huang for performing the transonic computations with the RNG model with wall function.

References

Bachalo, W. D., and Johnson, D. A., 1979, "An Investigation of Transonic Turbulent Boundary Layer Separation Generated on an Axisymmetric Flow Model," AIAA Paper 79-1479, Williamsburg, VA.

Baldwin, B. S., and Barth, T. J., 1990, "A One-Equation Turbulence Model for High Reynolds Number Wall Bounded Flows," NASA TM-102847.

Coles, D., and Wadcock, A. J., 1979, "Flying-Hot-Wire Study of Flow Past a NACA 4412 Airfoil at Maximum Lift," *AIAA Journal,* Vol. 17, No. 4.

Driver, D. M., and Seegmiller, H. L., 1985, "Features of a Reattaching Turbulent Shear Layer in Divergent Channel Flows," *AIAA Journal,* Vol. 23, No. 2, pp. 163–171.

Driver, D. M., 1991, "Reynolds Shear Stress Measurements in a Separated Boundary Layer," AIAA Paper 91-1787.

Gulyaev, A. N., Kozlov, V. Y., and Secundov, A. N., 1993, Universal Turbulence Model "ν_t–92". Ecolen Report, Moscow.

Huang, G. P., and Coakley, T. J., 1992, "An Implicit Navier-Stokes Code for Turbulent Flow Modeling," AIAA paper 92-0547.

Kline, S. J., Cantwell, B. J., Lilley, G. M., eds.: 1980–1981, AFOSR-HTTM Stanford Conference on Complex Turbulent Flows. Comparison of Computation and Experiment, Stanford University, Stanford, CA.

Menter, F. R., 1992, "Performance of Popular Turbulence Models for Attached and Separated Adverse Pressure Gradient Flows," *AIAA Journal,* Vol. 30, No. 8, pp. 2066–2072.

Menter, F. R., 1993, "Zonal Two Equation k-ω Turbulence Models for Aerodynamic Flows," AIAA Paper 93-2906, Orlando, Fl., 1993.

Menter, F. R., 1994a, "A Critical Evaluation of Promising Eddy-Viscosity Turbulence Models," *Proceedings Intern. Symp. on Turbulence, Heat and Mass Transfer,* Portugal, pp. 13.4.1–13.4.6.

Menter, F. R., and Rumsey, C. L., 1994, "Assessment of Two-Equation Models for Transonic Flows," AIAA Paper 94-2343, Colorado Springs, CO.

Menter, F. R., 1994b, "Two-Equation Eddy-Viscosity Turbulence Models for Engineering Applications," *AIAA Journal,* Vol. 32, No. 8, pp. 1598–1605.

Menter, F. R., 1994c, "Eddy Viscosity Transport Models and their Relation to the k-ϵ Model," NASA TM-108854, Nov.

Nee, V. W., and Kovasznay, L. S. G., 1969, "Simple Phenomenological Theory of Turbulent Shear Flows," *The Physics of Fluids,* Vol. 12, No. 3, pp. 473–484.

Spalart, P. R., and Allmaras, S. R., 1994, "A One-Equation Turbulence Model for Aerodynamic Flows," La Recherche Aerospatiale, No. 1, pp. 5–21.

Wilcox, D. C., 1993, *Turbulence Modeling for CFD,* DCW Industries, Inc., La Canada, CA.

Yakhot, V., and Orszag, S. A., 1986, "Renormalization Group Analysis of Turbulence. I. Basic Theory," *Journal of Scientific Computing,* Vol. 1, No. 3.

Yakhot, V., and Smith, L. M., 1992, "The Renormalization Group, the ϵ-Expansion and Derivation of Turbulence Models," *Journal of Scientific Computing,* Vol. 7, No. 1.

Yakhot, V., Orszag, S. A., Tangham, S., Gatski, T. B., and Speciale, C. G., 1992, "Development of Turbulence Models for Shear Flows by a Double Expansion Technique," *Physics of Fluids A4* (7), July, pp. 1510–1520.

T. J. Rohloff
Graduate Student Researcher.

I. Catton
Professor.

Department of Mechanical,
Aerospace and Nuclear Engineering,
University of California,
Los Angeles, CA 90024-1597

Low Pressure Differential Discharge Characteristics of Saturated Liquids Passing Through Orifices

An experimental investigation has been performed to determine the effect of variation in the length-to-diameter ratios on the discharge characteristics of saturated liquids passing through square edge orifices subjected to low pressure differentials. Experiments were performed to confirm reported results for sharp edge orifices and for round edge orifices with appreciable ratios of inlet corner radius to orifice diameter.

Introduction

A sizable quantity of information is available in the literature about flow of a saturated liquid through an orifice. Most of these studies, however, involve relatively large differences in pressure across the orifice (e.g., Fox and Stark, 1989; Numachi et al., 1960). Certain applications, such as designing multi-stage-flash desalination systems, require accurate knowledge of the flow rate of saturated liquids through an orifice that will result from relatively low differential pressures. Unfortunately, most of the information available in the literature is either for large ΔP or is presented qualitatively. Consequently, there is no comprehensive technique available for calculating the flow characteristics associated with small differential pressures for saturated liquid passing through an orifice of arbitrary geometry.

When a saturated liquid passes through an orifice, the pressure drops faster than the evaporation process can take place, leading to a metastable state as defined by Carey (1992), and exits the orifice with a certain amount of superheating. The rate of evaporation is dictated by the kinetics of the phase change process, and based on the observations described in the literature (e.g., Danforth, 1941; Uchida and Nairai, 1966), the resulting evaporation of the liquid passing through the orifice is too slow to maintain complete local thermodynamic equilibrium. The resulting degree of liquid superheat at the orifice exit is reported to be primarily a function of the orifice geometry. Saturated liquid flow characteristics of three commonly encountered geometries (depicted in Fig. 1 for sharp, square, and round edge inlets) are discussed below in comparison to the flow of a subcooled liquid. In both cases (saturated and subcooled), the flows are characterized by a discharge coefficient defined as,

$$C_d = \frac{\dot{m}''}{\sqrt{2\rho\Delta P}}$$

where $\dot{m}''$ is the average mass flux through the orifice and ΔP is the pressure difference across the orifice plate.

Sharp Edge Orifice. The flow of a saturated liquid through a sharp edge orifice is reported to be unaffected by the state of the liquid. If the fluid enters the sharp edge inlet as either a saturated or superheated liquid, it will behave as if it were subcooled. This behavior is widely reported in the literature as evidenced by this partial list of relevant papers: Benjamin and Miller (1941), Uchida and Nariai (1966), Numachi et al. (1960), Behbahani et al. (1989), and Monroe (1956). No limits were reported for complete metastability (i.e., no effects due to vaporization) of a liquid passing through a sharp edge orifice issuing into either liquid or gaseous downstream regions.

Square Edge Orifices. A certain degree of metastability is also observed for flow through square edge orifices, but in this case, the characteristics of the flow are reported to be affected by vapor formation within the length of the orifice. The flow characteristics have been found to be a function of L/d and the state (gas or liquid) of the downstream region. If $L/d \lesssim 1$ then, a cold liquid entering a square edge orifice will separate from the orifice wall at the inlet corner and will never reattach (Lichtarowicz et al., 1965). This same behavior is observed for a saturated liquid passing through an orifice for $L/d \lesssim 3$ (Uchida et al., 1966 and Bailey, 1951). However, unlike with a subcooled liquid, it is reported that the discharge coefficient for saturated liquid remains constant when L/d is increased from 0 to 3 as is depicted in Fig. 2 for the flow of subcooled liquid. This implies that the discharge coefficient should approach that of a sharp edge orifice. Uchida et al. (1966), Bailey (1951), Behbahani et al. (1989), and Romig et al. (1966) all report that short square edge orifices with saturated liquid behave the same as if the inlet were sharp. These studies mostly involved relatively large pressure differentials except for Bailey (1951) who gives low pressure differential results for a limited range of L/d.

For $3 \lesssim L/d \lesssim 12$, the difference between cold and saturated flow patterns become more pronounced. Lichtarowicz et al. (1965) demonstrates that a cold liquid will reattach to the orifice wall downstream of the vena contracta for $L/d \gtrsim 1$ independent of the downstream conditions. Bailey (1951) observed, however, that a liquid near the saturation point flowing through a square edge orifice may or may not reattach. If the two phase jet issues into a liquid region, then the flow will sometimes reattach, but if it issues into a vapor region the flow is likely to remain unattached. Assuming the flow never reattaches, then the discharge coefficient is observed to be similar to that of the sharp edge orifice. This behavior is demonstrated by Uchida et al. (1966) for $L/d < 10$ and by Behbahani et al. (1989) and Bailey (1951) for $L/d = 10.2$ and 9.9, respectively.

If $L/d \gtrsim 12$ for a square edge orifice, Uchida et al. (1966) observes that vaporization reduces the flow rate dramatically, and that the fluid is likely to exit as a two phase froth. As L/d increases beyond 12 then vaporization causes the total flow rate to decline and the total pressure drop to increase, and the discharge coefficient declines rapidly with increasing L/d for saturated liquid flow.

Contributed by the Fluids Engineering Division for publication in the JOURNAL OF FLUIDS ENGINEERING. Manuscript received by the Fluids Engineering Division May 22, 1995; revised manuscript received November 15, 1995. Associate Technical Editor: Jong H. Kim.

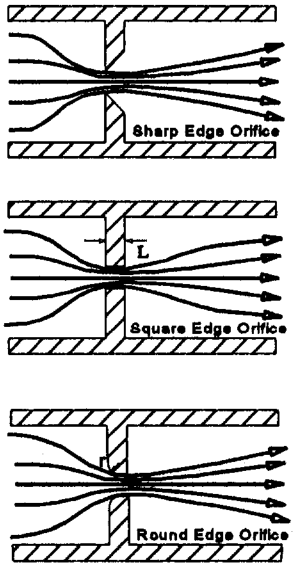

Fig. 1 Orifice Geometry

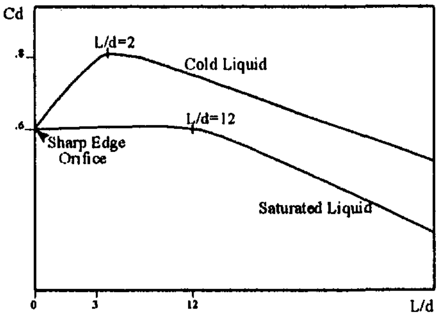

Fig. 2 Discharge coefficient versus aspect ratio for square orifices (derived from the results of Uchida et al., 1966 and Lichtarowicz et al., 1965)

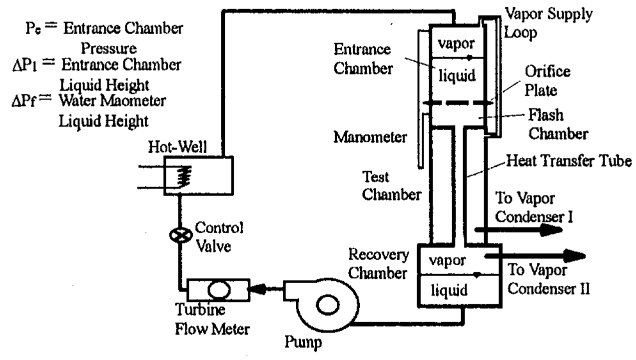

Fig. 3 Experimental apparatus

Round Edge Orifice. Rounding the inlet edge has the effect of delaying the separation of the incoming fluid from the orifice wall. This result has two subsequent effects. First, the flow contracts to a lesser extent (or not at all) as it passes through the orifice ($C_c = A_j/A_0$ approaches unity). And second, a saturated liquid remains in a metastable state for a greater distance into the orifice. Hence, the effects of vaporization are reduced. Danforth (1941) studied the flow of saturated liquid through orifices with rounded inlets ($r/d = 1.5$). The discharge coefficients measured for the flow of cold liquid were close to unity for the orifices used in Danforth's work ($C_d \approx C_c \approx 1$), i.e., the cold liquid flow did not separate from the orifice wall due to a large degree of rounding of the inlet edge. The small difference from unity was probably caused by loses due to friction through the finite length of the orifice ($L/d \approx 2$). Saturated liquid was found to have the same flow characteristics as the subcooled liquid ($C_d \approx 1$) provided that the overall pressure drop was not too great.

The work presented below is an experimental investigation of the flow characteristics associated with relatively low pressure differentials for saturated water passing through an orifice. Experiments were performed to determine the effect of a variation of L/d for saturated water passing through a square edge orifice, and to confirm the expected results for sharp edge orifices and round edge orifices with appreciable values of r/d. Note, a more comprehensive presentation of saturated liquid orifice flows can be found in Rohloff (1995).

Experimental Apparatus and Procedure

The apparatus used in this study, depicted in Fig. 3, was designed to operate over a saturation temperature range of 50°C to 105°C, with flow rates ranging from 3.2×10^{-5} m^3/s to 1.9×10^{-4} m^3/s. During operation, the height of the saturated water in the entrance chamber is manually controlled by adjusting the control valve and is measured using the liquid level tube, ΔP_1, mounted on the side of the entrance chamber. It is important to note here that the water near the top of the chamber is saturated at pressure P_e, and that as the pressure increases due to hydrostatic head between the liquid-vapor interface and the orifice plate, the constant temperature liquid becomes subcooled. The effect of this subcooling on the performance of the orifice plate is measured by simply varying the liquid head. The difference in pressure between the flashing chamber and the entrance chamber, ΔP_f, is measured using a water manometer connected between the two. The total pressure drop across the orifice plate is then the sum of ΔP_1 and ΔP_f.

Measurements taken for each data point include system temperatures, the pressure in the entrance chamber, the brine flow rate, the liquid head ΔP_1, and the flash chamber/entrance chamber pressure differential. The system pressure was recorded for the purpose of ensuring that the system was indeed at the saturation state. The orifice geometries used for both saturated water and cold water measurements are:

Sharp Edge—d = 3.87 mm
Square Edge—d = 5.64 mm, L = 12.19, 9.65, 7.11, 4.57, 2.03 mm

Nomenclature

A_0 = area of the orifice cross section (m^2)
A_j = area of the fluid jet cross section (m^2)
C_c = contraction coefficient
C_d = discharge coefficient
d = orifice diameter (m)
dP_f = pressure differential between upstream and downstream vapor spaces (Pa)
dP_1 = liquid head above the orifice (Pa)
g = coefficient of gravity (m/s^2)
L = length of the orifice bore (m)
$\dot{m}$ = mass flow rate (kg/s)
$\dot{m}''$ = mass flux (kg/m$^2\cdot$s)
P = fluid pressure (Pa)
r = radius of curvature of the inlet edge of the orifice (m)
Re$_d$ = Reynolds number ($\rho U_o d/\mu$)
T = temperature (K)
μ = dynamic viscosity (N$\cdot$s/m^2)
ρ = fluid density (kg/m^3)

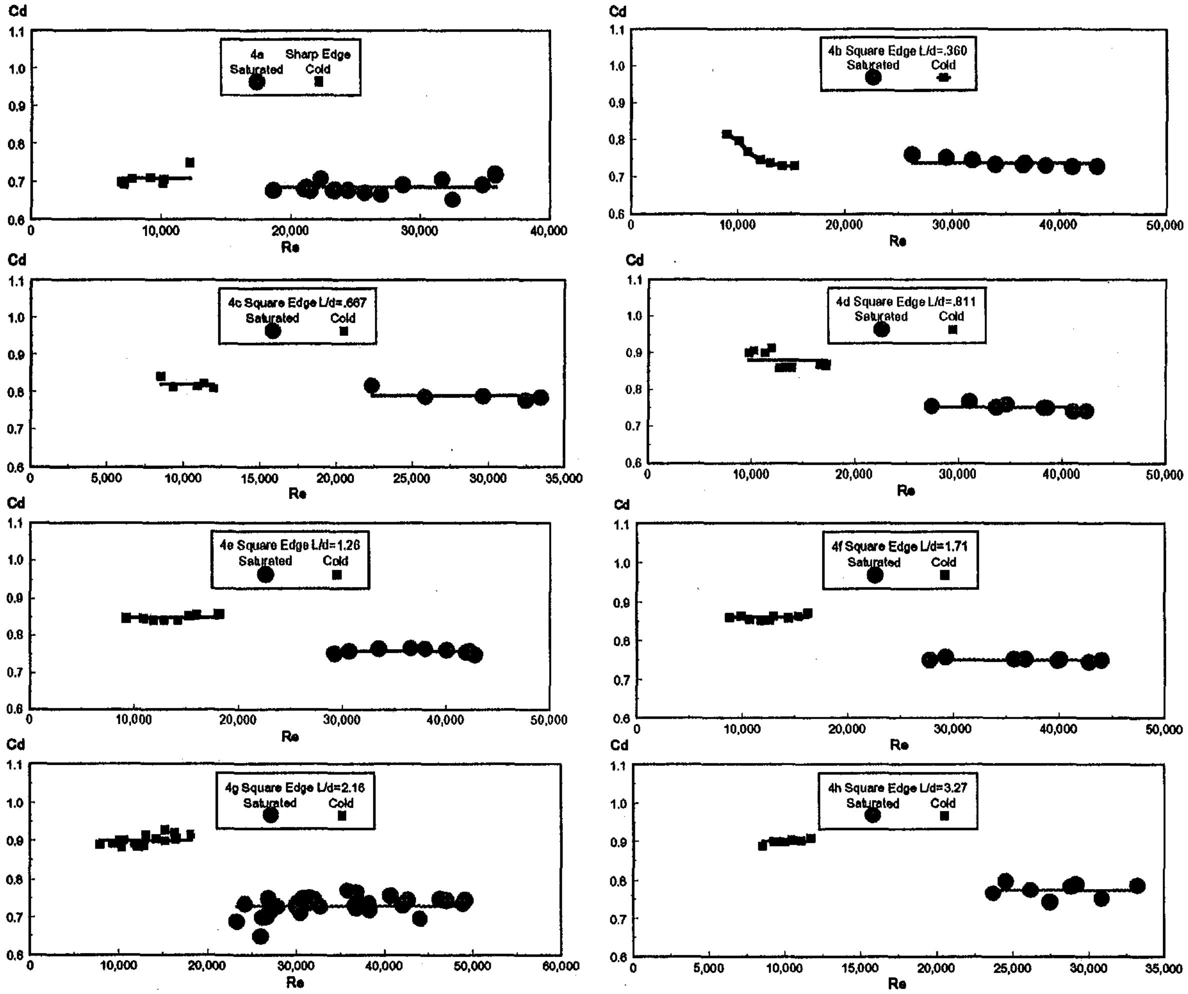

Fig. 4 Sharp edge and square edge orifice results ($P = \pm 7$ percent and $B = -14$ percent as defined in the Appendix)

Square Edge—$d = 3.81$ mm, $L = 12.45, 2.54$ mm
Round Edge—$d = 5.11$ mm, $r = 4.2$ mm,
$L = 12.70, 6.35$ mm

Results and Discussion

The data obtained for each orifice geometry consisted of pressure differentials, flow rates and fluid temperatures. These were used to calculate the discharge coefficient for both cold and saturated water as a function of the Reynolds number. An analysis of the errors inherent in the experimental measurements is given in the Appendix. The discharge coefficient given as a function of the Reynolds number is graphed for each orifice configuration in Figs. 4 and 5.

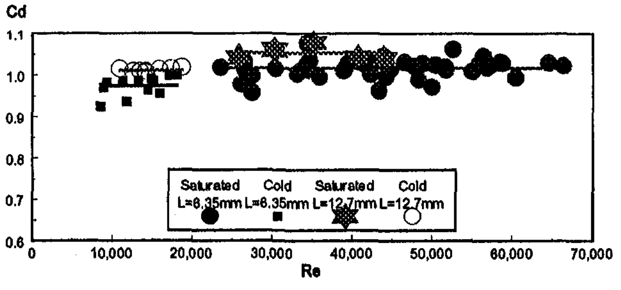

Fig. 5 Round edge orifice results ($P = \pm 7$ percent and $B = -14$ percent as defined in the appendix)

Sharp Edge and Square Edge Results. The results for the sharp edge orifice, given in Fig. 4(*a*), show that the discharge coefficient for this geometry is independent of Reynolds number over the observed range for both cold and saturated water. The discharge coefficient was also found to be fairly independent of the state of the liquid ($C_{d,\text{cold}} \approx C_{d,\text{saturated}}$). The differences between the average values of $C_{d,\text{cold}}$ and $C_{d,\text{saturated}}$ were less than 3 percent, which is approximately equal to the standard deviation of the sharp edge orifice results reported in the Appendix.

The results for square edge orifices are given in Figs. 4(*b*) through 4(*h*). For saturated water, the discharge coefficient was found to be relatively independent of both Re_d and L/d, and was found to have an average value of $C_{d,\text{square}} = 0.75$. However, a significant difference, greater than the maximum standard deviation ($\sigma_{\text{max}} = 4$ percent), was observed between the flow characteristics of the two states. Under certain circumstances with cold water, the discharge coefficient was found to be a function of Re_d. The decreasing trend of C_d with increasing Re_d in Fig. 4(*b*) might have been expected from the results of Lichtarowicz et al. (1965) in which it is shown that for $L/d \lesssim 1$, C_d increases with Re_d until it reaches a maximum before dropping quickly down to a constant value independent of Re_d.

The average value of $C_{d,\text{cold}}$ ($C_{d,\text{cold}} \approx 0.88$) was observed to be considerably larger than the saturated water value for length to diameter ratios greater than $L/d \approx 1$. As L/d was decreased below $L/d \approx 1$, the value of the discharge coefficient decreased until $C_{d,\text{cold}} \approx C_{d,\text{saturated}}$. A graph of C_d as a function of L/d is given in Fig. 6 for both cold and saturated water.

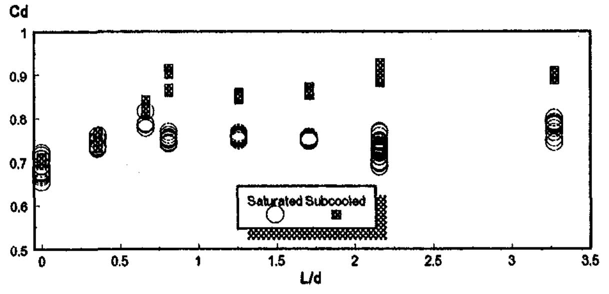

Fig. 6 Square edge orifice discharge coefficients

Uchida et al. (1966) reports that saturated liquid passing through short square edge orifices ($L/d < 12$) behaves approximately the same as if the orifices were sharp edged. This behavior was not observed in the data presented here as is evidenced in Fig. 6. Instead, the saturated liquid flows were observed to behave in a somewhat metastable manner up to a value of L/d in the range of 0.7 to 0.8. In each case for $L/d < 0.7$, $C_{d,\text{cold}}$ was slightly greater than $C_{d,\text{sat}}$, and it is postulated that vapor generation at the inlet edge may be playing a role.

At first inspection, it may seem that it is possible that the metastable behavior in short orifices is caused by the small degree of subcooling which results from the liquid head above the orifice. In other words, the increased pressure due to hydrostatic head of the constant temperature liquid would cause the water entering the orifice to be slightly subcooled, and vapor formation would subsequently start at a point further along the length of the orifice then if the liquid were saturated as it entered. However, this theory can be discounted by considering that a very wide range of liquid heads was used in obtaining the data, and no trend was found to suggest that the subsequent liquid subcooling was at all important.

In summary, the flow of saturated water through square edge orifices exhibits the same behavior as cold water up to a critical value of $L/d \approx 0.7$. Beyond this critical value, the discharge coefficient becomes fairly constant with L/d for values of $L/d < 3$. This level region is similar to the behavior described in the literature, but it occurs at a value of the discharge coefficient greater than that observed for sharp edge orifices. Following the discussions presented in the literature, C_d should remain relatively constant up to $L/d \approx 12$. Beyond this point, the discharge coefficient should decrease. A more detailed graph of C_d vs. L/d for saturated water up to values of $L/d > 12$ would be very informative and would continue the development a comprehensive approach to calculating discharge coefficients.

Round Edge Orifice Results. The results obtained for the round edge orifices ($r/d = .82$) are given in Fig. 5. Once again, the discharge coefficient was found to be independent of Reynolds number for both cold and saturated water, and was found to be slightly dependent on the state of the liquid ($C_{d,\text{cold}} < C_{d,\text{saturated}}$ by less than 5 percent, while the standard deviations ranged from 0.5 to only 4 percent). The cold water discharge coefficients were found to be lower than those for saturated water by a couple percent on average. This implies that the saturated liquid passes more freely through the orifice than cold water (i.e., $C_{d,\text{sat}}$ is closer to unity). From this it can be deduced that vaporization is not taking place within the round edge orifice. If it were, the vapor inside the orifice would reduce the available liquid flow area, and the flow would be more restricted ($C_{d,\text{cold}}$ would be greater than $C_{d,\text{sat}}$). Since this is not the case, it can be concluded that the saturated liquid passing through the round edge orifice is completely metastable within the passage. This conclusion agrees well with the results of Danforth (1941) for round edge orifices with $r/d = 1.5$.

Observations. A metastable behavior was observed for cold water tests with $L/d = 0.811$ (Fig. 4(*d*)). Two distinct levels of the liquid head were found to be stable for some of the flow rates. The greater liquid head was not recorded, but it was very close to the two phase results given in Fig. 4(*d*). It was possible to knock the system out of the steady state corresponding to the greater liquid head by using the vacuum pump to decrease the pressure downstream of the orifice plate. Once the system was in the lower liquid head state, it would not revert back to the greater one.

Partial reattachment of liquid jets may be important for intermediate values of L/d. Fox et al. (1989) observed that completely detached jets passing through square edge orifice are unstable for certain intermediate values of L/d and will tend to partially reattach along the edge of the orifice. If the length of the orifice is reduced below some critical value, the jet will remain detached along the entire bore independent of the state of the system. In between these two flow regimes, there should exist values of L/d for which either stable flow pattern might be observed. In other words, for a certain range of values of L/d both detached and partially attached flow patterns should be possible depending on the state of the system. This theory is supported by the above observations. The jump from the greater liquid head state to the lesser liquid head state described in the observations can be explained as a shift from partially attached flow to completely detached flow. The flow regimes for square edge orifices with $L/d < 3$ can therefore be divided into the three sections described above.

Recommendations for Calculating $C_{d,\text{sat}}$. Evidence suggests that discharge coefficients for saturated water can be estimated with the cold liquid correlations for sharp edge orifices, round edge orifices with $r/d > 0.5$, and square edge orifices with $L/d < 0.7$. The performance of square edge orifices with $0.7 < L/d < 12$ can be approximated with C_d evaluated at $L/d = 0.7$. This procedure for calculating saturated liquid discharge coefficients is summarized by the following:

Saturated Liquid Discharge Coefficient.

Sharp Edge Orifice: $C_{d,\text{sat}} = C_{d,\text{cold}} \approx 0.6$
Square Edge Orifice:
$C_{d,\text{sat}}(L/d) = C_{d,\text{cold}}(L/d)$ for $L/d \lesssim 0.7$
$C_{d,\text{sat}}(L/d) = C_{d,\text{cold}}(@L/d = 0.7)$ for $L/d \gtrsim 0.7$
Round Edge Orifice: $C_{d,\text{sat}} = C_{d,\text{cold}}$ for $r/d \gtrsim 0.5$.

An example application of these recommendations is demonstrated using the cold liquid procedures outlined in McGreehan et al. (1988). The results of these calculations are graphed in Fig. 7. Note that saturation curves were only drawn for $r/d = 0.0$ and $r/d \geq 0.5$. The cold water curves for $0.0 < r/d < 0.5$ were included to demonstrate the behavior of cold liquid in this region. It is theorized that the associated saturation curves in

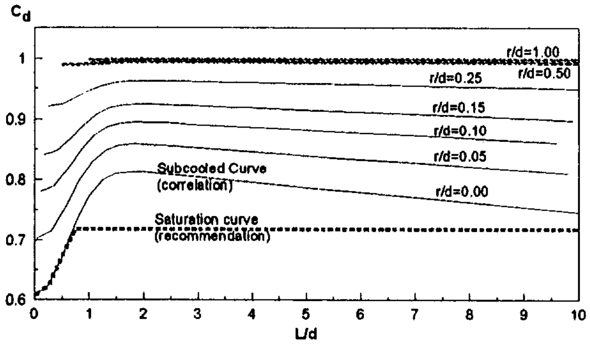

Fig. 7 Cold liquid discharge coefficients evaluated using the procedure outlined in McGreehan et al. (1988) compared to recommended saturated liquid procedure

this region will follow the subcooled curves up to greater values of L/d as r/d is increased from 0.0 to 0.5. Beyond this value of r/d the curves are nearly identical for the region of interest $(L/d < 12)$.

References

Bailey, B. F., 1951, "Metastable Flow of Saturated Water," *Trans. ASME*, Paper No. 51--SA-55, pp. 1109–1116.

Behbahani, A. I., Weisman, J., and Shen, P. K., 1989, "Apparent Contradictions in Observations of the Discharge of Two-Phase Mixtures Through Restrictions," *Chem. Eng. Comm.*, Vol. 77, pp. 171–181.

Benjamin, M. W., and Miller, J. G., 1941, "The Flow of Saturated Water Through Throttling Orifices," *Trans. ASME*, pp. 419–429.

Blevins, R. D., 1992, *Applied Fluid Dynamics Handbook*, Krieger Publishing, Malabar, Florida.

Carey, V. P., 1992, *Liquid-Vapor Phase-Change Phenomena*, Hemisphere Publishing, Washington.

Danforth, J. L., 1941, Flow of Hot Water Through a Rounded Orifice Master of Science Thesis from the Massachusetts Institute of Technology.

Fox, T. A., and Stark, J., 1989, "Characteristics of Miniature Short-Tube Orifice Flows," *Part C: Journal of Mechanical Engineering Science*, Proc. Instn. Mech. Engrs. Vol. 203, pp. 351–358.

Idelchik, I. E., 1986, *Handbook of Hydraulic Resistance 2nd ed.*, Hemisphere Publishing Corporation, Washington.

Lichtarowicz, A., Duggins, R. K., and Markland, E., 1965, "Discharge Coefficients for Incompressible Non-Cavitating Flow Through Long Orifices," ASME *Journal of Mechanical Engineering Science*, Vol. 7, No. 2, pp. 210–219.

McGreehan, W. F., and Schotsch, M. J., 1988, "Flow Characteristics of Long Orifices with Rotation and Corner Radiusing," ASME *Journal of Turbomachinery*, Vol. 110, pp. 213–217, April 1988.

Miller, R. W., 1983, *Flow Measurement Engineering Handbook*, McGraw-Hill, New York.

Monroe, E. S. Jr., 1956, "Flow of Saturated Boiler Water Through Knife-Edge Orifices in Series," *Trans. ASME*, Paper No. 54--A-118, pp. 373–377.

Numachi, F., Yamabe, M., and Oba, R., 1960, "Cavitation Effect on the Discharge Coefficient of the Sharp-Edge Orifice Plate," ASME *Journal of Basic Engineering*, Vol. 82, pp. 1–11, March.

Rohloff, T. J., 1995, Discharge of Saturated Liquid Through Orifices Subjected to Low Pressure Differentials, Master of Science Thesis from UCLA.

Romig, R. P., Rothfus, R. R., and Kermode, R. I., 1966, "Partial Vaporization in Orifices and Valves," *Industrial and Engineering Chemistry Process Design and Development*, Vol. 5, No. 3, July, pp. 342–350.

Uchida, H., and Nariai, H., 1966, "Discharge of Saturated Water Through Pipes and Orifices," *Proc. of the Third International Heat Transfer Conference*, Vol. 5, pp. 1–12.

APPENDIX

The discharge coefficient is presented in this study as a function of Reynolds number. Both of these parameters are found to be functions of the experimentally measured values such that

$$\mathrm{Re}_d \sim \frac{\dot{m}\rho}{d\mu},$$

$$C_d \sim \frac{\dot{m}}{d^2(\Delta P_f + \Delta P_1)^{1/2}}.$$

The maximum fractional error of each of these quantities is then given by

$$\frac{\delta \mathrm{Re}_d}{\mathrm{Re}_d} = \frac{\delta\rho}{\rho} + \frac{\delta\mu}{\mu} + \frac{\delta\dot{m}}{\dot{m}} + \frac{\delta d}{d},$$

$$\frac{\delta C_d}{C_d} = \frac{\delta\dot{m}}{\dot{m}} + 2\frac{\delta d}{d} + \frac{1}{2}\frac{\delta(\Delta P_f + \Delta P_1)}{(\Delta P_f + \Delta P_1)}.$$

The maximum fractional error is calculated here instead of the more commonly used quadratic value so that an upper bound on the expected error can be obtained.

Several problems were encountered with the turbine flow meter during the experimental measurements. The accuracy of the flow measurements are therefore not expected to be better than $\pm 6 \times 10^{-6}$ m^3/s. The differential pressure between the entrance chamber and the flashing chamber exhibited relatively large fluctuations during operation. These fluctuations were characteristic of the experimental set-up and could not be corrected without major alterations. The accuracy of these measurements are estimated to be in the range of ±1 cm. The total error in the pressure differential is then estimated to be approximately ±1.5 cm. The accuracy of the diameter measurement is estimated at about ±0.1 percent, and the properties are considered known to an accuracy of $\delta\rho = 0.5$ kg/m^3 and $\delta\mu = 2.5 \times 10^{-6}$ N·s/m^2.

These estimates of the experimental error are applied with the experimental measurements in the overall fractional error relations given above. The results of these calculations are summarized by

	$\delta\ \mathrm{Re}_d/\mathrm{Re}_d$	$\delta C_d/C_d$
Average	0.056	0.074
Maximum	0.123	0.152

The estimated precision for the discharge coefficient is found to be as large as 15 percent for some of the measurements. The average value of the expected precision of C_d is taken to be $P = 7$ percent.

Standard Deviation. The standard deviation was calculated for each set of data as a measure of the precision of the experimental results. The standard deviation is defined as

$$\sigma = \sqrt{\frac{(C_d - \bar{C}_d)^2}{N - 1}}$$

where $\bar{C}_d$ is the average value of C_d for the data set, and N is the number of data points in the set. The results of these calculations, presented below, show that the standard deviation ranged from 0.5 to 4.5 percent. This is well within the average expected precision of approximately 7 percent.

Saturated Water

Inlet Geom.	L (mm)	d (mm)	r (mm)	$\bar{C}_d$	σ	$\bar{C}_d/\sigma$
sharp	0.0	3.87	0.0	.685	.018	.027
square	12.19	5.64	0.0	.729	.024	.033
	9.65	5.64	0.0	.750	.004	.005
	7.11	5.64	0.0	.758	.006	.008
	4.57	5.64	0.0	.752	.009	.012
	2.03	5.64	0.0	.729	.011	.015
	12.45	3.81	0.0	.774	.019	.025
	2.54	3.81	0.0	.790	.015	.019
round	12.7	5.11	4.2	1.052	.016	.015
	6.35	5.11	4.2	1.017	.016	.016

Cold Water

Inlet Geom.	L (mm)	d (mm)	r (mm)	$\bar{C}_d$	σ	$\bar{C}_d/\sigma$
sharp	0.0	3.87	0.0	.708	.019	.027
square	12.19	5.64	0.0	.900	.014	.016
	9.65	5.64	0.0	.860	.006	.007
	7.11	5.64	0.0	.850	.007	.008
	4.57	5.64	0.0	.880	.023	.026
	2.03	5.64	0.0	.761	.034	.045
	12.45	3.81	0.0	.888	.039	.043
	2.54	3.81	0.0	.820	.013	.016
round	12.7	5.11	4.2	1.012	.004	.004
	6.35	5.11	4.2	.974	.023	.023

Fixed Error. Despite concentrated efforts to prevent systematic measurement errors, the experimental results were consistently higher than expected. A very large database exists in the literature describing the discharge characteristics of cold incompressible liquids through sharp edge orifices. Given these conditions, it is generally accepted that $C_d \approx 0.6$. However, Fig. 4(*a*) shows that the experimental results obtained here were consistently 14 percent higher than the expected value. It is therefore assumed that fixed errors for all of the data presented here are at least equal to this value, i.e., $B = 14$ percent.

The total uncertainty is calculated from the experimental precision and fixed errors by $U = (P^2 + B^2)^{1/2} = 16$ percent. This is a large value for the total uncertainty in the discharge coefficient, but it is important to note that both magnitude and direction of the fixed errors are known so that values greater than the experimental values need not be considered.

Hui Li
Assistant Professor,
Department of Mechanical Engineering,
Faculty of Engineering,
Kagoshima University,
1-21-40, korimoto, Kagoshima City,
Japan
Assoc. Mem. ASME

Yuji Tomita
Professor,
Department of Mechanical Engineering,
Kyushu Institute of Technology,
1-1, Sensuicho, Tobata, Kitakyushu City,
Japan

An Experimental Study of Swirling Flow Pneumatic Conveying System in a Horizontal Pipeline

In order to reduce power consumption, pipe wear and particle degradation in pneumatic conveying system, a swirling flow pneumatic conveying (SFPC) system is proposed in this paper, and an experimental study focuses on the SFPC system in a horizontal pipeline in terms of the overall pressure drop, solid flow patterns, power consumption and the additional pressure drop. Polystyrene, polyethylene, and polyvinyl pellets with mean diameters of 1.7, 3.1, and 4.3 mm, respectively, were transported as test particles in a horizontal pipeline of 13 m length and 80 mm inside diameter. The initial swirl number was varied from 0.58 to 1.12, the mean air velocity from 9 m/s to 24 m/s, and the solid mass flow rate from 0.43 kg/s to 1.17 kg/s. It is found that in the lower gas velocity range, the pressure drop, the power consumption and additional pressure drop for SFPC were lower than those for axial flow pneumatic conveying. The critical and minimum air velocities were decreased by SFPC, the maximum reduction rates being 13 and 17 percent, respectively. The fluctuation of wall static pressure for SFPC was also decreased.

Introduction

Pneumatic conveying, which uses air to transport particles through a pipeline, has been successfully used for many years in the chemical and industrial processes, such as catalytic cracking in the petroleum industry and the production of synthetic fuels from coal in energy conversion systems. The application also extends to drying and transport of grains and other solid materials. Until recently, the solids were nearly always transported in form of a suspension. However, the major disadvantage of pneumatic conveying has been high cost of power consumption, pipe wear and particle degradation. To solve these problems, low velocity and dense-phase pneumatic conveying have been used recently. Unfortunately, this conveying mode can cause blockage and unstable flow, and high costs.

To reduce power consumption, blockage, particle degradation and pipe wear, a new method in which a swirling flow is used in a pneumatic conveying system, called swirling flow pneumatic conveying (SFPC) system, is proposed in this paper. An experimental study focuses on a SFPC system in a horizontal pipeline in terms of the overall pressure drop, solid flow patterns, power consumption, and the additional pressure drop.

Background of the Research

It is well-known that wear of the pipe wall and attrition of the product in pneumatic conveying increase with the second to sixth power of air velocity, and a lower air velocity produces a reduction of investment costs. Because conventional pneumatic conveying, which is called axial flow pneumatic conveying (AFPC) here, has only an axial velocity component of air, the suspended force acting on particles is too small in a horizontal pipeline. Therefore air velocity cannot be lowered below a certain value since a minimum velocity must be maintained for a safe operation of pneumatic conveying system. To avoid deposition of particles in the pipeline, a higher air velocity is required, but this increases the power consumption, attrition and wear, and the efficiency is low.

One of the main factors influencing pneumatic conveying is the carrying medium. The factor that governs the various flow phases in gas-solids mixture is the kinetic energy distribution of air along the pipeline. For pneumatic conveying, a large kinetic energy of air is required to accelerate particles to terminal velocity in an acceleration region, and less kinetic energy of air is require to replenish the lost kinetic energy of particles as a results of impact and friction in a remaining region. On the other hand, for long conveying distance, i.e., for relatively high pressure drop, because of air expansion the air velocity increases downstream and the air kinetic energy of AFPC along conveying pipe increases. Therefore, deposits are apt to form in the acceleration region as the air velocity is lower. Thus the optimum distribution of air kinetic energy along the pipeline is a large kinetic energy in the acceleration region, and less kinetic energy in the remaining region.

Swirling flow has been widely applied in various fields of industry, since it has a large energy. From the mean kinetic energy distribution of air along the axial direction in a long pipe (Li and Tomita, 1994), it is found that swirling flow has a large mean kinetic energy at the inlet, and the kinetic energy decreases along the axial direction. This shows the possibility of applying swirling flow to pneumatic conveying.

When applying a swirling flow to pneumatic conveying, it is of decisive importance to select a swirler having small pressure drop. In the present study a swirling flow is generated at the conveying pipeline inlet by a vaned swirler with various vane angles. To express the swirl intensity, the swirl number S is used as an important similarity parameter of swirling flow, and is defined as follows.

$$S = \frac{2\pi\rho_a \int_0^R uwr^2 dr}{2\pi\rho_a R \int_0^R u^2 r dr} \tag{1}$$

where u and w are the axial and tangential velocities, respec-

---

Contributed by the Fluids Engineering Division for publication in the JOURNAL OF FLUIDS ENGINEERING. Manuscript received by the Fluids Engineering Division July 18, 1995; revised manuscript received March 14. Associate Technical Editor: M. W. Reeks.

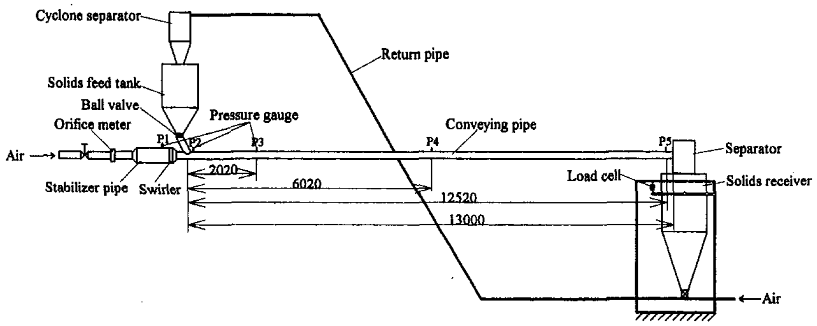

Fig. 1 Experimental equipment

Table 1 Properties and dimensions for conveyed particles

Particle	Shape	Average diameter (mm)	Density (kg/m^3)	Floating velocity (m/s)
Polystyrene	Spherical	1.65	976	5.90
Polyethylene	Cylindrical	3.13	946	7.20
Polyvinyl	Discal	4.26	1419	8.24

Table 2 Locations of wall pressure measurement from the inlet of conveying pipe

Wall pressures	P_1	P_2	P_3	P_4	P_5
Locations (mm)	stabilizer pipe	20	2020	6020	12520

tively, R is the pipe radius, and ρ_a is the air density. The swirl number expresses a ratio of the angular momentum flux to the product of the pipe radius and axial momentum flux.

Experimental Apparatus and Procedure

The experimental facility for the present study is of the positive pressure type and is shown schematically in Fig. 1. Air from a blower flows through the calibrated nozzle and the vaned swirler in the stabilizer pipe, and picks up the solid materials fed by gravity from the feed tank at the inlet of conveying pipeline. Then, the solids-air mixture enters the conveying pipeline and at the pipeline exit the solids are separated from the solids-air mixture by the separator. The conveying pipeline consisted of a horizontal smooth acrylic tube of 80 mm inside diameter and about 13 m length.

Three types of solids were conveyed: polystyrene, polyethylene and polyvinyl pellets, and their properties and dimensions are given in Table 1.

The air flow rate was measured by the orifice meter. The pressure distribution along the pipeline was measured at 4 locations with semiconductor pressure transducers (Table 2), and the solids mass flow rate was measured by a load cell. Three vaned swirlers of different initial swirl number S_0 which were measured at the inlet of conveying pipeline by Li and Tomita (1994) are used.

The mean air velocity U_a is from 9 m/s to 24 m/s and the solid mass flow rate G_s from 0.43 kg/s to 1.17 kg/s. The initial swirl number S_0 was varied from 0.58 to 1.12.

For the estimated average uncertainty of the present experiment, the total pressure drop is ±11.59 percent, the mean air velocity is ±8.1 percent, and the solids mass flow rate is ±6.04 percent.

Results and Discussion

Total Pressure Drop. To compare with an AFPC system, the pressure drop due to the vaned swirler must be included in the total pressure drop of the SFPC system. Here the total pressure drop Δp_t between the stabilizer pipe and the exit of conveying pipe are considered. For steady state flow, Δp_t can be calculated as follows:

$$\Delta p_t = \Delta p_s - \frac{1}{2}\rho_a\left[1 - \left(\frac{D}{D_0}\right)^4\right]U_a^2 \qquad (2)$$

where Δp_s is the wall static pressure of stabilizer pipe before the vaned swirler, D and D_0 are the diameters of pipeline and stabilizer pipe, respectively.

Figure 2 shows graphs of the pressure drop versus the air velocity with the solids mass flow rate as a parameter for polyethylene pellets. According to the initial swirl number S_0, three SFPC are defined, which are called swirl1 flow ($S_0 = 0.58$), swirl2 flow ($S_0 = 0.94$) and swirl3 flow ($S_0 = 1.12$), respectively. The air velocity at the minimum total pressure drop is defined as the minimum velocity or saltation velocity, and the air velocity when a strongly fluctuating pressure drop of plug-flow type occurs is called the critical velocity. The two velocities are of particular importance in the design of solid-gas conveying systems.

Comparing between SFPC and AFPC in Fig. 2, at a high air velocity, the pressure drop of SFPC is higher than that of AFPC.

Nomenclature

D = conveying pipe diameter
D_0 = stabilizer pipe diameter
E = power consumption coefficient
G_s = mass flow rate of solids
g = gravity acceleration
L = length of conveying pipe
m_t = solids/air mass flow rate ratio
p_w = wall static pressure
Q_a = volumetric flow rate of air
R = conveying pipe radius
r = radial coordinate
S = swirl number
S_0 = initial swirl number
U_a = mean air velocity
U_{cr} = critical velocity
$U_{\min}$ = minimum velocity
u, w = components of air velocity
Δp_a = pressure drop by air only
Δp_s = wall static pressure of stabilizer pipe
Δp_t = total pressure drop
Δp_z = additional pressure drop due to solids
λ_z = additional pressure drop coefficient due to solids
ρ_a = air density

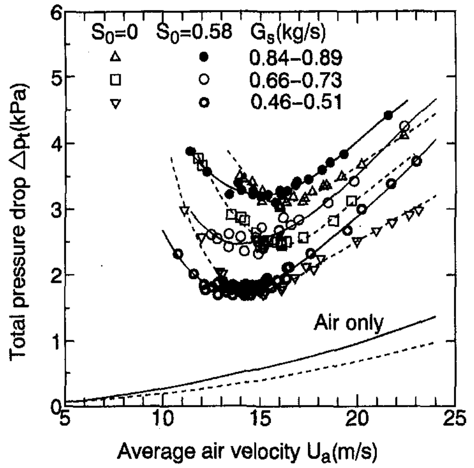

Fig. 2(a) Comparison of SFPC ($S_0 = 0.58$) and AFPC ($S_0 = 0$) total pressure drop for conveyed polyethylene pellets (Uncertainty in $\Delta p_t = \pm 11.59$ percent, in $U_a = \pm 8.1$ percent, in $G_s = \pm 6.04$ percent)

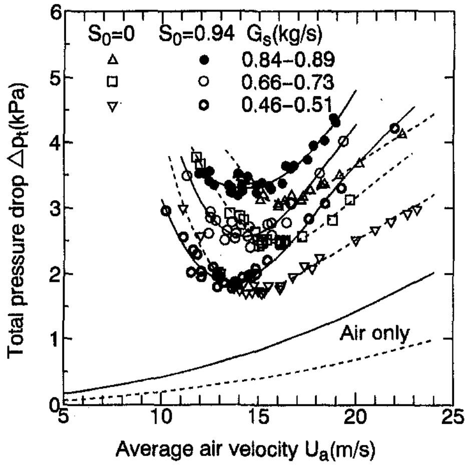

Fig. 2(b) Comparison of SFPC ($S_0 = 0.94$) and AFPC ($S_0 = 0$) total pressure drop for conveyed polyethylene pellets (Uncertainty in $\Delta p_t = \pm 11.59$ percent, in $U_a = \pm 8.1$ percent, in $G_s = \pm 6.04$ percent)

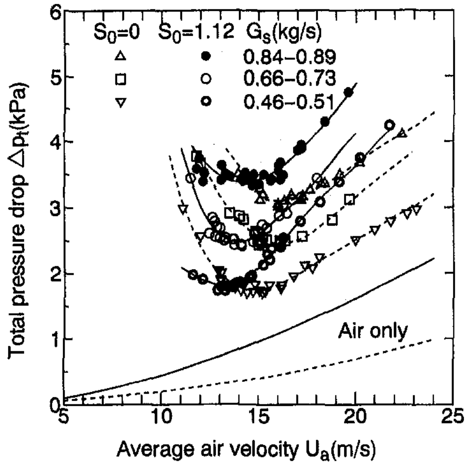

Fig. 2(c) Comparison of SFPC ($S_0 = 1.12$) and AFPC ($S_0 = 0$) total pressure drop for conveyed polyethylene pellets (Uncertainty in $\Delta p_t = \pm 11.59$ percent, in $U_a = \pm 8.1$ percent, in $G_s = \pm 6.04$ percent)

However, below and near the minimum velocity of SFPC, the pressure drop becomes lower than that of AFPC. For small G_s, using a weak swirling flow can reduce the pressure drop, and a strong swirling flow can reduce the pressure drop for large G_s flow.

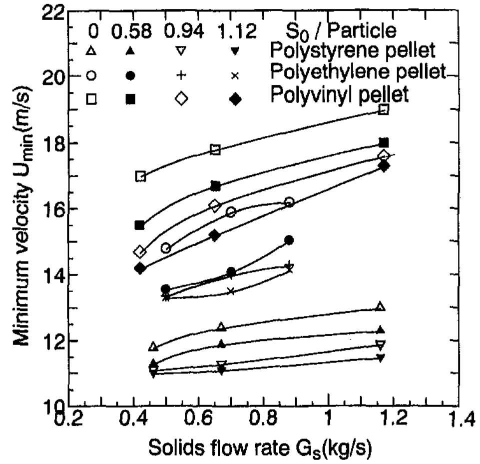

Fig. 3 Minimum velocity of swirling flow pneumatic conveying (Uncertainty in $U_{min} = \pm 8.1$ percent, in $G_s = \pm 6.04$ percent)

The relation which shows the minimum velocity versus the solids flow rate with the initial swirl number and the solids as parameters is illustrated in Fig. 3. Using SFPC, the minimum velocity can be reduced 7.5–17 percent, and with increasing initial swirl number, the minimum velocity decreases. For conveying particles having large floating velocity, the reduction rate is apparently large.

Figure 4 shows the critical velocity versus the initial swirl number with the solids flow as a parameter. As the initial swirl intensity increases, the critical velocity decreases, and the maximum reduction rate for swirling flow is 13 percent over the swirl number range considered here. For conveying particles having a large floating velocity, the swirling flow is the most effective.

Flow Pattern. In order to analyze the flow mechanism of SFPC, the flow patterns of polyethylene particles in the neighborhood of the feeder are visualized on the basis of the photographs.

Axial Flow Pneumatic Conveying. The flow patterns of solids are illustrated in Fig. 5 where the mass flow rate is kept constant at $G_s = 0.81$ kg/s and the air velocities are $U_a = 17.81$ and 15.08 m/s, respectively. At high air velocity (Fig. 5(*a*)), a part of the solids is carried in the form of strands sliding along the bottom of the pipeline as a moving bed while the remainder is conveyed above the sliding strands as a suspended flow. For

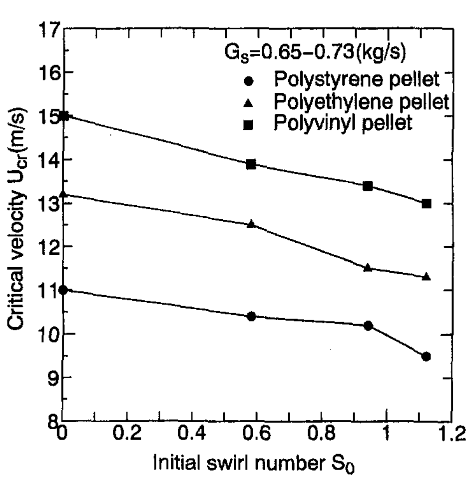

Fig. 4 Critical velocity of swirling flow pneumatic conveying (Uncertainty in $U_{cr} = \pm 8.1$ percent, in $S = \pm 9.47$ percent)

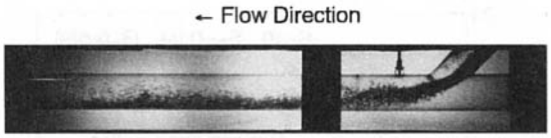

Fig. 5(*a*) $U_a = 17.81$ m/s, $G_s = 0.81$ kg/s

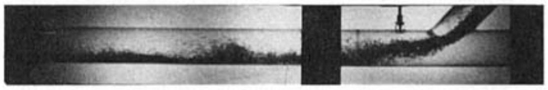

Fig. 5(*b*) $U_a = 15.08$ m/s, $G_s = 0.81$ kg/s

Fig. 5 Flow patterns of polyethylene pellets for AFPC

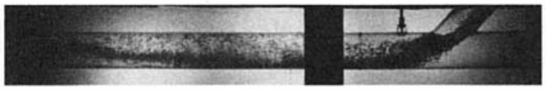

Fig. 6(*a*) $U_a = 18.59$ m/s, $G_s = 0.853$ kg/s

Fig. 6(*b*) $U_a = 15.09$ m/s, $G_s = 0.865$ kg/s

Fig. 6 Flow patterns of polyethylene pellets for SFPC ($S_0 = 0.58$)

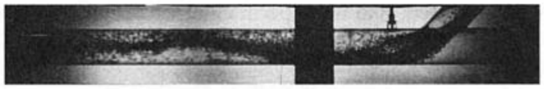

Fig. 7(*a*) $U_a = 17.83$ m/s, $G_s = 0.86$ kg/s

Fig. 7(*b*) $U_a = 14.42$ m/s, $G_s = 0.89$ kg/s

Fig. 7 Flow patterns of polyethylene pellets for SFPC ($S_0 = 0.94$)

Fig. 8(*a*) $U_a = 17.20$ m/s, $G_s = 0.85$ kg/s

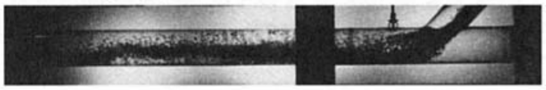

Fig. 8(*b*) $U_a = 14.14$ m/s, $G_s = 0.888$ kg/s

Fig. 8 Flow patterns of polyethylene pellets for SFPC ($S_0 = 1.12$)

decreasing air velocity (Fig. 5(*b*)), the solids settle out and form a fixed bed, over which the particles strand slide along. The first fixed layer of sediment appears in the neighborhood of the feeder. This sediment fills up a portion of the pipe cross-sectional area, and therefore results in large pressure drop and fluctuations. Further reduction of the air velocity results in quite unstable flow and threatens blockage.

Swirling Flow Pneumatic Conveying. Figures 6–8 show the solids flow patterns of SFPC for three different initial swirl intensities. On decreasing air velocity at a constant mass flow rate, different flow patterns can be observed. For high air velocity, a swirling particle flow pattern is observed in the acceleration region, and a strong swirl flow shows the strong swirling particle flow pattern. As reduction of velocity, the swirling particle flow becomes weak. For swirll flow ($S_0 = 0.58$) the particle flow pattern is similar to AFPC. Since particles are suspended by the effect of air circumferential velocity component even for low velocity, the air velocity when deposition of particles appears is lower than that of AFPC. Thus, at lower velocity, the total pressure drop and energy consumption for SFPC are reduced. Since high velocity particles are fully suspended easily for AFPC, the total pressure drop for high velocities is lower than that of swirling particle flow in SFPC. The results are similar to other kinds of particles.

Wall Pressure. For studying the stability of a pneumatic conveying system at lower velocity, the fluctuation of wall static pressures along the conveying pipeline were measured. The frequency response of the pressure transducer is 8.3 Hz. Figure 9 illustrates the variation of pressure versus time for AFPC and SFPC. It is found that SFPC has a small fluctuation of pressure, and should yield stable conveying.

Power Consumption. To express the power consumption of a pneumatic conveying system, the power consumption coefficient E, which is calculated from the total pressure drop in the system, solids flow rate and the air flow rate, is used according to the following equation:

$$E = \frac{\Delta p_t Q_a}{g G_s L} \tag{3}$$

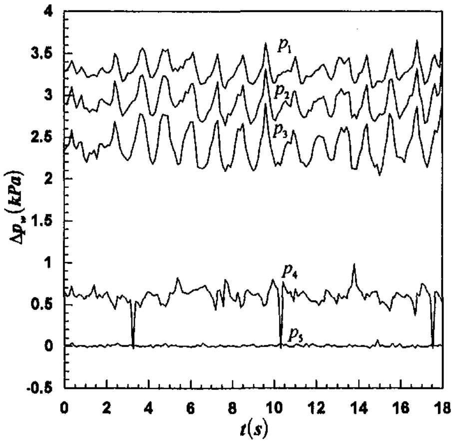

Fig. 9(*a*) Axial flow pneumatic conveying: $U_a = 13.88$ m/s, $G_s = 0.86$ kg/s

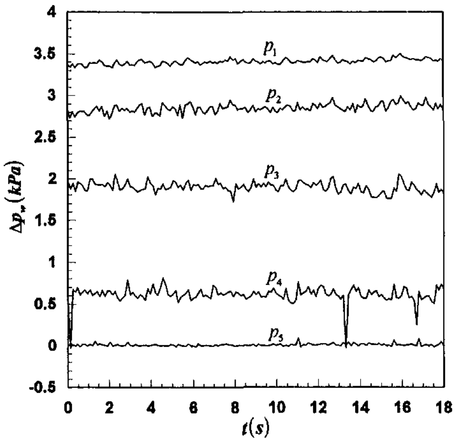

Fig. 9(*b*) Swirling flow pneumatic conveying ($S_0 = 1.12$): $U_a = 13.59$ m/s, $G_s = 0.88$ kg/s

Fig. 9 Fluctuation of wall static pressure for conveyed polyethylene pellets (Uncertainty in $p_w = \pm 8.56$ percent)

where Q_a is the volumetric flow rate of air, and g is the gravity acceleration.

Figure 10 illustrates E for polyethylene pellets versus air velocity with the initial swirl number as a parameter. At high velocity E of SFPC is large, but below the velocity for the minimum E of AFPC, the E of SFPC becomes smaller. The reduction rate of power consumption by SFPC is 14–20 percent. Among three initial swirl intensities, E of swirll flow (S_0 = 0.58) shows the maximum reduction rate. For increasing G_s, E decreases at high velocity, but there are no differences at lower velocity for SFPC.

Additional Pressure Drop. The total pressure drop Δp_t of pneumatic conveying can be resolved into the following components:

$$\Delta p_t = \Delta p_a + \Delta p_z \tag{4}$$

where Δp_a is the total pressure drop of clean air including the pressure drop of the vaned swirler for SFPC, and Δp_z is the additional pressure drop due to the presence of the particles.

As proposed by Barth (1958), the additional pressure drop coefficient λ_z is calculated by

$$\Delta p_z = \Delta p_t - \Delta p_a = m_t \lambda_z \frac{L}{D} \frac{\rho_a U_a^2}{2} \tag{5}$$

where m_t is the mass flow rate ratio ($m_t = G_s/G_a$). The additional pressure drop coefficient λ_z for polyethylene particles is shown as a function of Froude number $F_r = U_a/\sqrt{gD}$ in Fig. 11. It can be clearly seen that λ_z decreases with an increase in Froude number F_r, however, for high F_r, λ_z of SFPC increases, because particles take on a swirling motion, particle-wall collision frequency increases, and trajectory of particles becomes long. It is also found that λ_z for SFPC is not only dependent on F_r, but also dependent on G_s. For high F_r, λ_z of AFPC is lower than that of SFPC. But, because the velocity for which sediment appears is lower or the sediment is less, in range of lower F_r, λ_z for SFPC becomes lower than that of AFPC.

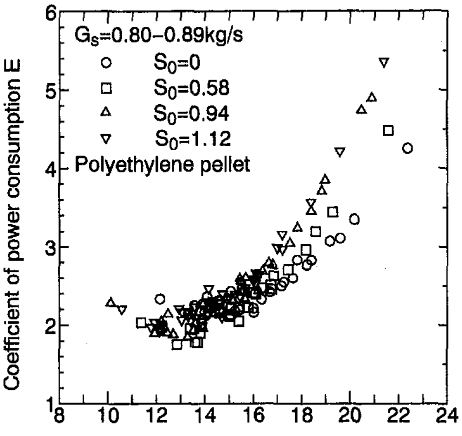

Fig. 10 Comparison of SFPC and AFPC power consumption coefficient for conveyed polyethylene pellets (Uncertainty in E = ±12.31 percent, in U_a = ±8.1 percent)

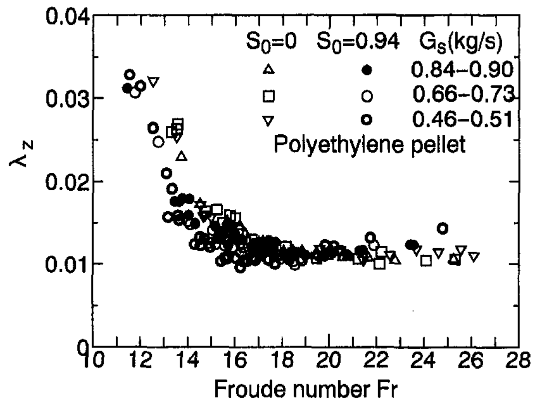

Fig. 11 Comparison of SFPC and AFPC additional pressure drop coefficient for conveyed polyethylene pellets (S_0 = 0.94) (Uncertainty in λ_z = ±11.81 percent, in F_r = ±8.8 percent)

Conclusions

In the present study a swirling flow pneumatic conveying system is proposed, and an experimental investigation focuses on the overall pressure drop, solid flow patterns, power consumption and the additional pressure drop. The following statements summarize the more important conclusion.

(1) In the lower air velocity range, the total pressure drop, the power consumption and additional pressure drop for the swirling flow pneumatic conveying are lower than those for axial flow pneumatic conveying.

(2) The critical and minimum air velocities are decreased by the swirling flow pneumatic conveying, the maximum reduction rates being 13 percent and 17 percent, respectively.

(3) The fluctuation of pressure for the swirling flow pneumatic conveying is decreased.

(4) Lower air velocity are used, thus possibly reducing wear of the conveying pipe wall and particle degradation.

Acknowledgment

This work was performed as part of the research which was supported by a scientific research fund granted by Japanese Ministry of Education (No. 03650152).

References

Barth, W., 1958, "Stromungsvorgange beim Transport von Festteilchen und Flussigkeitsteilchen in Gasen," *Chemie-Ing Techn*, Vol. 30, pp. 171–180.

Li, H., and Tomita, Y., 1994, "Characteristics of Swirling Flow in a Circular Pipe," ASME JOURNAL OF FLUIDS ENGINEERING, Vol. 116, pp. 370–373.

J. Wu
CSIRO, Division of Building, Construction
and Engineering,
Highett, Vic. 3190, Australia

J. Sheridan
Department of Mechanical Engineering,
Monash University,
Clayton, Vic. 3168, Australia

M. C. Welsh
CSIRO, Division of Building, Construction
and Engineering,
Highett, Vic. 3190, Australia

Velocity Perturbations Induced by the Longitudinal Vortices in a Cylinder Wake

This paper presents data showing the three-dimensional vortical structures in the near wake region of circular cylinders. The in-plane velocity field was measured using a digital Particle Image Velocimetry (PIV) technique. The vortical structures are found to include inclined counter-rotating longitudinal vortices in the braids joining consecutive Kármán vortices. A simple vortex-pair model is proposed to estimate velocity perturbation induced by the longitudinal vortices in the near wake region. The perturbation resulting from the longitudinal vortices is shown to induce spanwise velocity modulation and a velocity spike of a nominally two-dimensional vortex street.

Introduction

It has been recognised in recent years that the wake of a bluff body develops three-dimensional vortical structures. Williamson (1988), Williamson et al. (1995), Wei and Smith (1986), Welsh et al. (1992), Bays-Muchmore and Ahmed (1993), and Wu et al. (1994a, 1994b, 1996) have all shown that the three-dimensional vortical structures include inclined pairs of counter-rotating longitudinal vortices, having streamwise and transverse vorticity components. They form rib-like structures in the braids joining successive Kármán vortices. Similar three-dimensional vortical structures were shown to exist in plane mixing layers by Bernal and Roshko (1986), among others.

The development of three-dimensional instabilities and the formation of small-scale longitudinal vortices are related to local turbulence production and fine-scale velocity fluctuations (Hussain, 1986, Ferre et al., 1990) in turbulent wake flows. An understanding of the fluid dynamics involved is of great interest to fluid mechanics in general and in particular to engineering technologies and computational fluid dynamics.

Wu et al. (1994b) showed, using a digital PIV technique, that the vorticity of longitudinal vortices is twice that of the Kármán vortices upon which the former are superimposed. This is consistent with the theory of Meiburg and Lasheras (1988) that the longitudinal vortices are being stretched by the spanwise vortices (i.e., Kármán vortices). This strong vorticity field induced by the longitudinal vortices could be significant in the development of the Kármán vortex street. The present work sought to explore this further by quantifying the velocity perturbation induced in the wake by the longitudinal vortices.

In this paper, the same digital PIV technique (Wu et al. 1994b) was used to obtain instantaneous in-plane velocity distributions in the wake of a circular cylinder. Quantitative information of the strength of the longitudinal vortices and their influence on the velocity distributions were obtained. The data obtained make it possible to analyse the velocity perturbation resulting from the longitudinal vortices, and to develop a simple model that can predict the amplitude of the spanwise velocity modulation and the magnitude of apparent velocity spikes.

It will be shown that the spanwise velocity modulation can be as large as two thirds of the freestream velocity, due to the perturbation of the longitudinal vortices. Spanwise velocity profiles of wakes are rarely reported, partly because of the difficulty of capturing three-dimensional features using conventional single-point probes and partly because of the lack of understanding of flow three-dimensionalities. There has, however, been some success in using single sensors to measure the time-mean spanwise velocity profile in mixing layer investigations. Huang and Ho (1990) studied the small-scale transition process of a mixing layer using an X-wire probe. They measured the spanwise distribution of the time-mean streamwise velocity profile. The profiles contained clear wavy patterns, which they pointed out were due to the formation of streamwise vortices (longitudinal vortices). The amplitude of the wavy pattern varies from $0.1\bar{U}$ to $0.2\bar{U}$ ($\bar{U}$ is the average velocity of the mixing layer), depending on streamwise distance.

Experimental Arrangement and Facilities

Water Tunnel and Test Models. A return-circuit water tunnel schematically shown in Fig. 1 was used for the experiments. Water was pumped into a settling chamber containing filters and a honeycomb and then passed through a 4:1 contraction before entering the working section. The water leaving the working section flowed via a 440 mm long duct into an outlet reservoir tank. The working section is 770 mm long with a cross-section of 244 by 244 mm. The walls are transparent, being made of acrylic.

Circular cylinders used in these experiments were made of 244 mm long polished plexiglass with diameters of 3.3, 6.4 and 9.4 mm. End-plates were used to reduce the possible interference of the boundary layer forming along the test section walls. The freestream velocity was uniform to within 1 percent outside the boundary layers and the longitudinal turbulence level was typically 0.1 percent when band-pass filtered between 0.08 and 20 Hz. No clear spectral spikes were evident in the longitudinal velocity signal.

PIV Technique. Flow was seeded with hollow microsphere beads with a mean diameter $< 30\ \mu m$. An 8W argon-ion continuous laser beam was transmitted through a 50 μm diameter multi-mode optical fibre and spread into a light sheet using a cylindrical lens. The light scattered from the particles in the laser sheet was recorded using a "Videk" digital CCD camera with a spatial resolution of 1280 × 1024 pixels; the light intensity signal was digitised into 256 levels (8-bit) on a personal computer. Single-frame, multiply-exposed particle images were sampled and processed using software based on the Young's fringe method to give the in-plane velocity distribution. The words in-plane will be used in the paper to refer to the two-

---

Contributed by the Fluids Engineering Division for publication in the JOURNAL OF FLUIDS ENGINEERING. Manuscript received by the Fluids Engineering Division April 5, 1995; revised manuscript received April 15, 1996. Associate Technical Editor: M. Gharib.

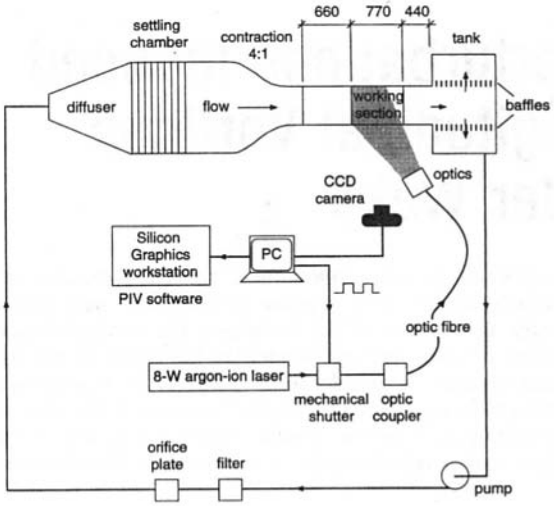

Fig. 1 Experimental setup

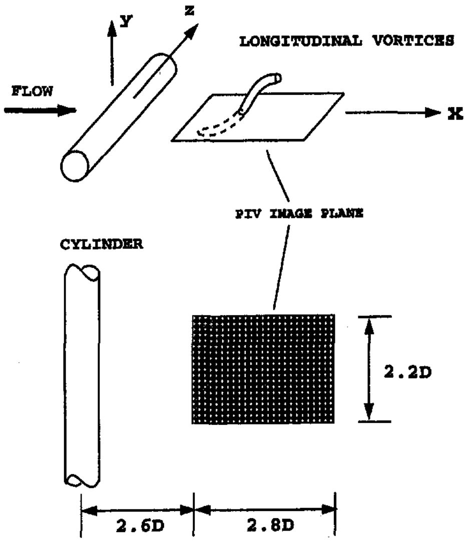

Fig. 2 The PIV image plane was in the centerline plane of the cylinder and 2*D* behind the back of the cylinder. The image size was 2.8 × 2.2*D*.

dimensional plane where the PIV measurement was conducted to give two velocity components in that plane. The principle of the PIV technique was outlined in the early work of Barker and Fourney (1977). Excellent reviews are available on PIV techniques, and readers are referred to Adrian (1991) and Buchhave (1992). In the present application, the Young's fringe pattern was found by performing FFT calculations on a Silicon Graphics workstation and an algorithm was used to calculate the spacing and orientation of the fringe patterns to determine the velocity vectors.

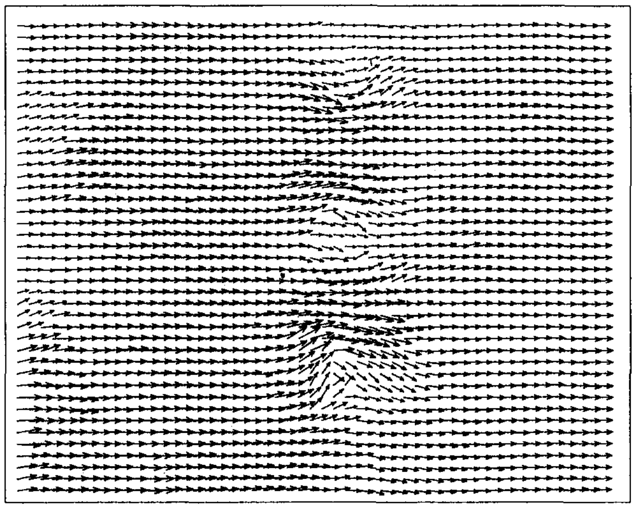

Fig. 3(*a*)

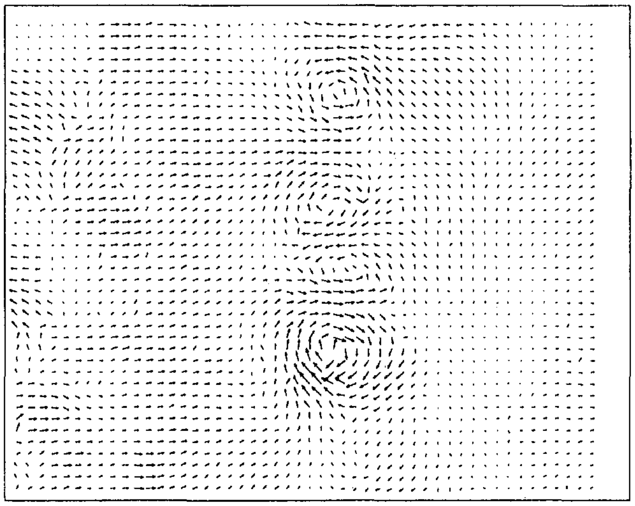

Fig. 3(*b*)

Fig. 3 Velocity vector field with frame of reference (*a*) fixed to the cylinder, (*b*) moving with the vortices at 60 percent U_0. The velocity grid resolution was 0.5 mm, $D = 9.4$ mm, Re = 550.

The uncertainty of the velocity measurement is 4 percent at a confidence level of 95 percent. The uncertainty of circulation is equal to that of the velocity measurements.

Results

Overview. The experiments were conducted at Reynolds numbers ranging from 140 to 550. Because of the limited space, data will be presented only for Re = 550, which is well above

Nomenclature

d = vortex core diameter (mm)
D = diameter of cylinder (mm)
Re = Reynolds number based on D and U_0 (non.)
U_0 = freestream velocity (m/s)
u, w = streamwise and spanwise flow velocity (m/s)
u_{max} = maximum of spanwise profile of u (m/s)
u'_{max} = the amplitude of velocity spike (m/s)
$\bar{u}$ = spanwise average of u (m/s)
x, y = streamwise and transverse coordinate, zero at cylinder center (mm)
z = spanwise coordinate (mm)
δu_{max} = the amplitude of spanwise modulation of u (m/s)
δw_{max} = the amplitude of variation of w (m/s)
Γ = circulation of a longitudinal vortex (m^2/s)
ω_y = y-direction vorticity component, normal to the measurement plane (1/s)

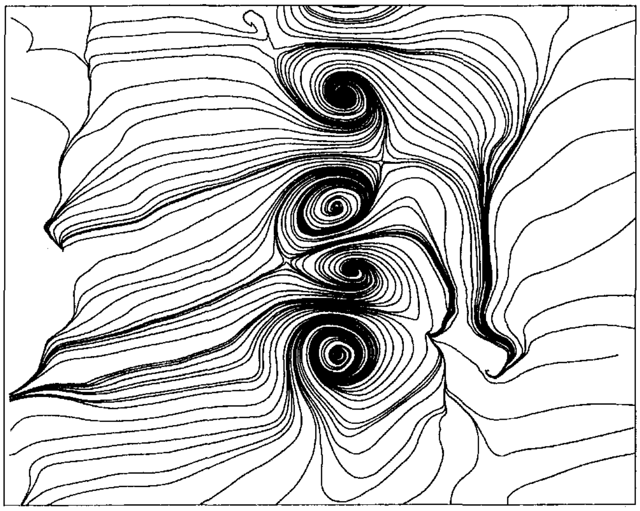

Fig. 4(*a*)

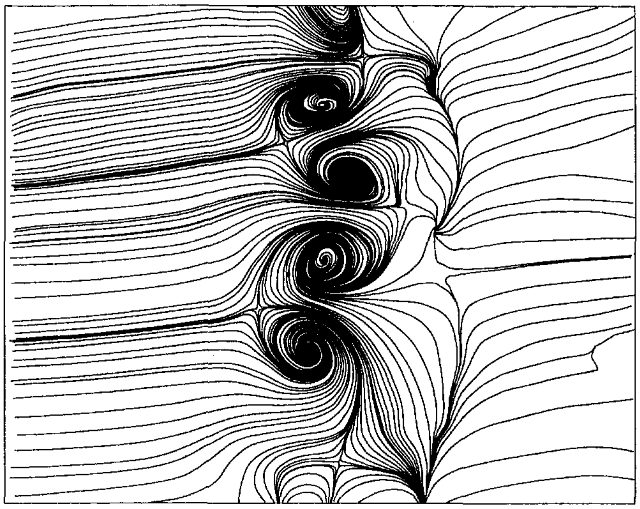

Fig. 4(*b*)

Fig. 4 Typical streamline patterns at two arbitrary instants, sampled randomly in time at Re = 550 (the streamlines here are not drawn at constant intervals)

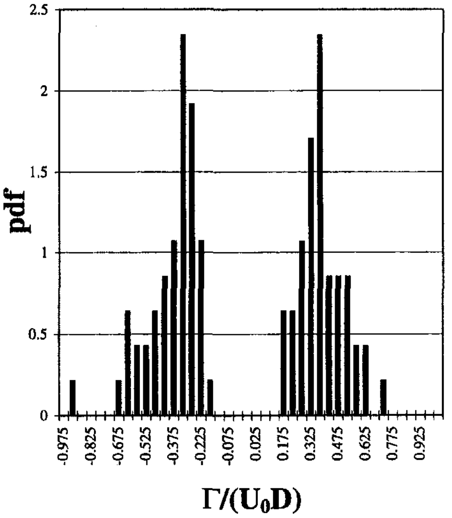

Fig. 5 Probability density function distribution of circulation of longitudinal vortices at Re = 550, the data are normalized by U_0 and D, the number of samples is 50

the transitional range for the onset of the three-dimensional vortices (occurs at Re ≈ 175, Williamson (1988) and Wu et al. (1994a)).

Instantaneous in-plane velocity distributions were measured in a transverse plane located $2D$ behind the back of the cylinder and in a plane passing through the cylinder centre-line, as shown in Fig. 2. The measurement plane was chosen to cut across the inclined longitudinal vortices joining consecutive Karman vortices in the wake. The measurement plane covered an area of $2.8D$ in the streamwise and $2.2D$ in the spanwise directions. A typical velocity vector field, showing flows in the transverse plane, is presented in Figs 3(*a*) and (*b*) at Re = 550. The frame of reference in Fig. 3(*a*) is fixed to the cylinder while in Fig. 3(*b*) it moves with the vortices. Pairs of vortices can be seen to be spinning in opposite directions along the cylinder span.

Two typical instantaneous streamline patterns, as calculated from the velocity data, are shown in Fig. 4, in a frame of reference moving with the vortices. The counter-rotating longitudinal vortices, being intersected by the measurement plane, are evident as the mushroom-type structures. As an interesting comparison, readers are referred to the hydrogen-bubble flow patterns presented by Wei and Smith (1986) and Wu et al. (1994a).

Spanwise Velocity Modulation. Clearly, the action of longitudinal vortices will distort the velocity field of a vortex street resulting in spanwise velocity modulation. The extent of this distortion can be quantified from the PIV measurements.

To do this, the circulation of a longitudinal vortex has been estimated by integrating vorticity over the area in which the vorticity ω_y is greater than 10 percent of ω_{ymax}, where ω_y is the vorticity perpendicular to the measurement plane and ω_{ymax} is the maximum vorticity perpendicular to the measurement plane. It should be pointed out that the circulation obtained in the current measurement plane represents the circulation of the inclined longitudinal vortices, as the circulation along a closed line surrounding a vortex is independent of the way the line is drawn. A typical probability density function distribution (or histogram) of measured circulation of longitudinal vortices, is plotted in Fig. 5 for Re = 550. This has been calculated from 50 frames of randomly sampled particle images. Clearly the strength of the positive and the negative vorticity in the two

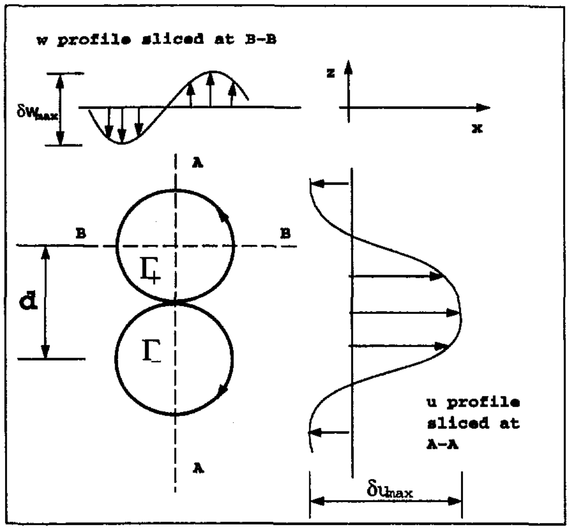

Fig. 6 A simple velocity perturbation model, flow induced by a pair of ideal Rankine-vortex

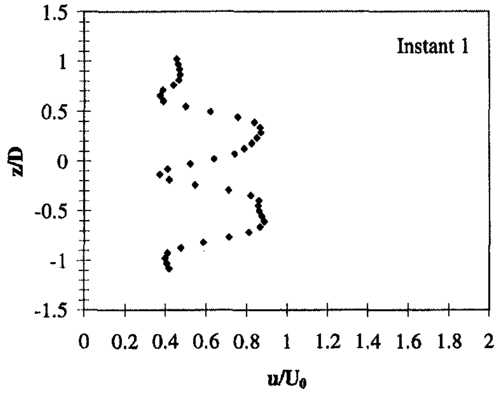

Fig. 7(*a*)

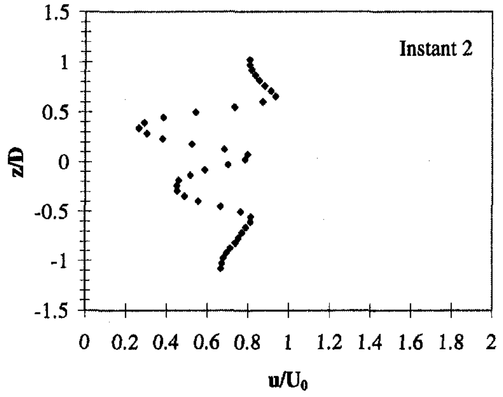

Fig. 7(*b*)

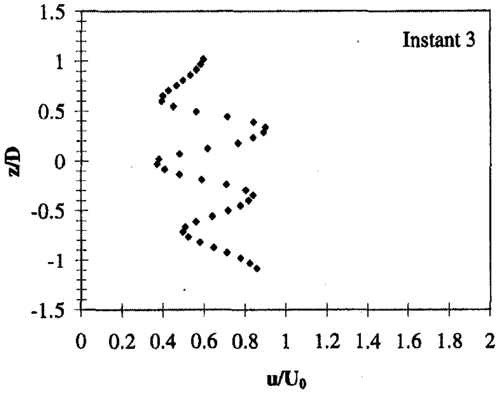

Fig. 7(*c*)

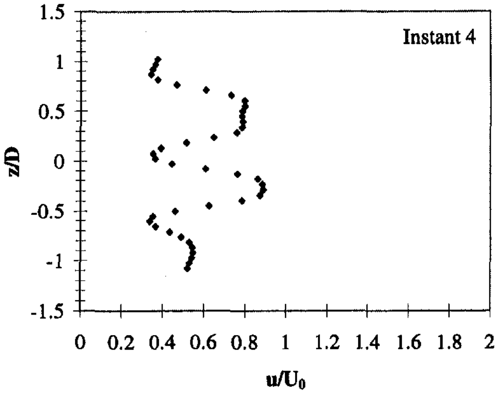

Fig. 7(*d*)

Fig. 7 Velocity spanwise modulation at 4 arbitrary instants, streamwise velocity component *u* variation along cylinder span, the instantaneous data were sampled randomly at Re = 550

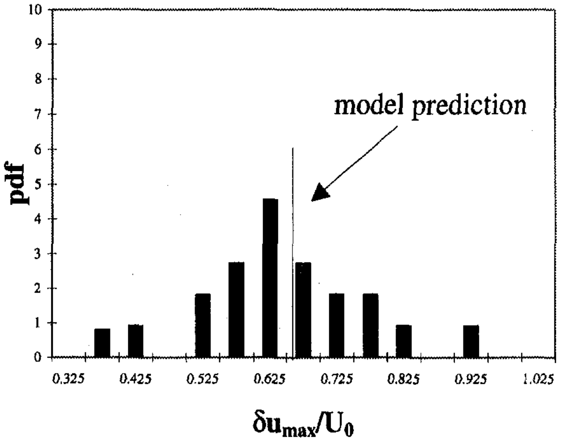

Fig. 8 Probability density function of the velocity modulation amplitude at Re = 550

parts of a vortex pair is statistically balanced, as is expected. The mean circulation can be expressed as:

$$\Gamma \approx 0.39 U_0 D \tag{1}$$

where U_0 is the freestream velocity and D is the cylinder diameter. Measurements performed for a range of Reynolds numbers reveal that this correlation is valid when the Reynolds number is well above a transitional range, i.e., Re $> 250 \sim 300$.

Now that the circulation of the longitudinal vortices is known, the induced spanwise velocity modulation can be estimated by considering an ideal vortex pair in the x-z plane, as schematically shown in Fig. 6, where the z-axis corresponds to the cylinder axis (spanwise direction). The parameter δu_{max} shown in the figure is used to characterise the level of velocity spanwise modulation. Based on the above ideal vortex pair model, it is elementary to show:

$$\delta u_{max} \approx \frac{2.67\Gamma}{\pi d} \tag{2}$$

where d is the average vortex core diameter. Substituting the correlation for Γ in (1), we get:

$$\delta u_{max} \approx 0.33 \frac{U_0 D}{d} \tag{3}$$

The vortex core diameter is found to be $d \approx 0.5\ D$, which is approximately half of the spanwise wavelength of the vortices (the spanwise wavelength of the vortices has been found to be approximately equal to one cylinder diameter by Williamson

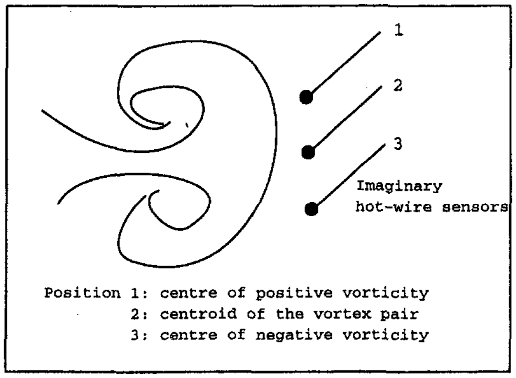

Fig. 9 Places of an imaginary hot-wire probe, No. 1: aligned to the center of the positive vorticity, No. 2: aligned to the centroid of the vortex pair, No. 3: aligned to the centre of the negative vorticity

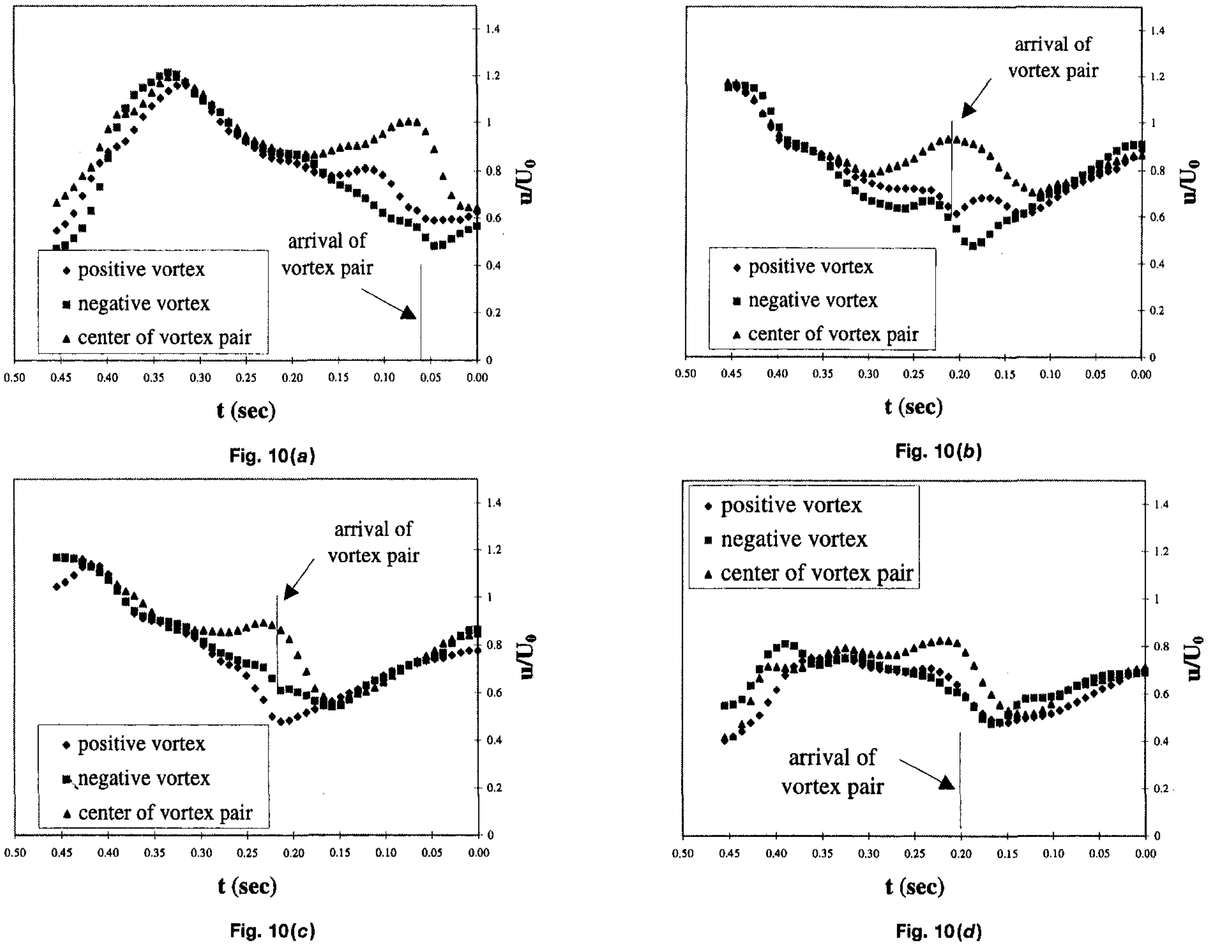

Fig. 10(*a*)

Fig. 10(*b*)

Fig. 10(*c*)

Fig. 10(*d*)

Fig. 10 Temporal velocity fluctuation obtained by invoking Taylor's hypothesis. The three curves correspond to the probe being at the centre of the positive vortex (vorticity), at the center of the negative vortex (vorticity) and at the centroid of a vortex pair, respectively, the convective velocity used for transform is 0.8U_0. The data were sampled at 4 arbitrary instants.

(1988), Bays-Muchmore and Ahmed (1993), and Wu et al. (1994a)). The amplitude of the spanwise velocity modulation can therefore be estimated as below, where $d = 0.5D$ is used:

$$\delta u_{max} \approx 0.66U_0 \tag{4}$$

Typical spanwise modulations of the streamwise velocity component, u, sliced through the centres of pairs of longitudinal vortices, are plotted in Fig. 7 at four instants. It should be noted that the spanwise variation of u/U_0 is dependent on the streamwise location where the measurement is made. As the u/U_0 velocity profiles in Fig. 7 are all taken slicing through the centres of the longitudinal vortices they represent the maximum influence produced. On the other hand, the influence of the spanwise vortices is to produce a background velocity variation in the streamwise direction, this becomes clear when a streamwise slice of the measurement plane is plotted as shown later in Fig. 10. The probability density function distribution of the modulation amplitude δu_{max} has been calculated and the result is shown in Fig. 8. The prediction based on the forementioned model is also indicated in the figure and there is reasonable agreement between the model and the data.

In passing, it should be noted that it is also possible to provide information on the induced spanwise velocity component w. In a similar fashion, a parameter δw_{max} is defined in Fig. 6 to characterize the induced spanwise velocity component. In this case, the meaningful velocity profile is taken from a slice (e.g., B-B in Fig. 6) through the centre of the one of the two vortices. The result based on the present PIV measurement is:

$$\delta w_{max} \approx 0.41U_0 \tag{5}$$

Velocity Spike. Imagine if an Eulerian probe (e.g., a hot-wire probe or a LDA) were placed in a bluff body wake to measure the velocity variation with time. Velocity fluctuations caused by the longitudinal vortices would be sensed by the probe if it were placed at the right position at the right time. With instantaneous velocity data measured using the PIV technique, it is possible to "animate" such an event. Taylor's frozen flow hypothesis is assumed to be valid for a very short period of time, during which the flow structures containing the vortices are to be convected downstream unchanged and at the convective velocity of the vortex street. This transformation is expressed as:

$$f(x) = f(U_c t) \tag{6}$$

where x and t are spatial and temporal coordinates, $f(x)$ is the spatial distribution of a certain fluid quantity, U_c is the convection velocity, and $f(U_c t)$ is the temporal distribution derived from $f(x)$.

Typical velocity time evolution signals as seen by the imaginary stationary probes placed at the centre of a positive vortex (i.e., with positive vorticity), the center of a negative vortex and the centroid of the vortex pair as shown in Fig. 9 are plotted in Figs 10(a), (b), (c), and (d) where time increases from right to left corresponding to flow from left to right. The arrival of a vortex pair in time is indicated by the vertical dotted lines, calculated from the spatial position of the centroid of the vortex pairs. A velocity spike clearly emerges at the time of arrival of vortex pairs and the fluctuation is maximum when the "probe" is located at the centroid of a vortex pair. It is seen that the

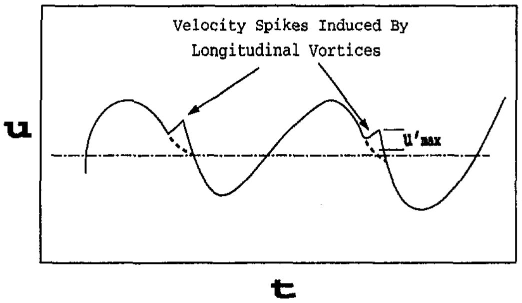

Fig. 11 Conceptual diagram on the effect of generation of velocity spikes due to the action of the longitudinal vortices in a cylinder wake

amplitude of the velocity spike is very sensitive to where the 'probe' is placed. The amplitude reduces substantially when the probe is shifted away from the centroid of a vortex pair.

In summary, in addition to the pure periodic velocity oscillation expected to be detected by a hot-wire (or LDA) probe placed in the wake of a bluff body, spikes, as illustrated in Fig. 11, should exist in the time velocity fluctuation signal of a three-dimensional vortex street behind a bluff body. It is useful to estimate the amplitude of the velocity spikes, u'_{max}, as defined in Fig. 11. An estimation of u'_{max} can be made from the spanwise variation of the streamwise velocity component (shown in Fig. 7):

$$u'_{max} = u_{max} - \bar{u} \approx \delta u_{max}/2 \tag{7}$$

where u_{max} and $\bar{u}$ represent the maximum and the spanwise average of u component, respectively. Using the previous results, it is concluded that $u'_{max} \approx 0.33U_0$. The prediction is in reasonable agreement with the measurements (see, for example, the data in Fig. 10).

Concluding Remarks

A digital Particle Image Velocimetry (PIV) technique has been used to measure the velocity field in the wake of circular cylinders. The instantaneous in-plane velocity distributions obtained in a plane parallel to the cylinder axis reveal the perturbations to the flow induced by the inclined longitudinal vortices. Pairs of these vortices along the cylinder span have been shown to produce the mushroom-type structures in the streamline patterns. Spanwise instantaneous velocity modulations generated by the longitudinal vortices are presented. A simple vortex-pair model is suggested to predict the modulation amplitude and is found to agree well with the measurements. The mechanisms of velocity spikes are illustrated by using Taylor's hypothesis, together with data and correlation for their characterisation.

The velocity spikes caused by the longitudinal vortices contribute to an increase in high frequency components in the flow's kinetic energy spectrum. The amplitude of these spikes can be estimated when the strengths of the longitudinal vortices are known. The present paper provides a way to predict the amplitude of the spikes. It is recognised that in a real situation, the longitudinal vortices are not located in a fixed spanwise position (Wu et al., 1994a), instead they are being generated randomly across the cylinder span. The velocity fluctuations associated with the velocity spikes may look irregular for a stationary probe.

Acknowledgment

J. Wu and J. Sheridan acknowledge the support from an Australian Research Council grant. The authors wish to thank R. F. La Fontaine and L. Welch for many helpful discussions and technical assistance during the experiments.

References

Adrian, R. J., 1991, "Particle Imaging Techniques for Experimental Fluid Mechanics," *Annual Review of Fluid Mechanics,* Vol. 23, pp. 261–304.

Barker, D. B., and Fourney, M. E., 1977, "Measuring Fluid Velocities with Speckle Patterns," *Optics Letters,* Vol. 1, No. 4, pp. 135–137.

Bays-Muchmore, B., and Ahmed, A., 1993, "On Streamwise Vortices in Turbulent Wakes of Cylinders," *Physics of Fluids A,* Vol. 5, No. 2, pp. 387–392.

Bernal, L. P., and Roshko, A., 1986, "Streamwise Vortex Structure in Plane Mixing Layers," *Journal of Fluid Mechanics,* Vol. 170, pp. 499–525.

Buchhave, P., 1992, "Particle Image Velocimetry—Status and Trends," *Experimental Thermal and Fluid Science,* Vol. 5, pp. 586–604.

Ferre, J. A., Mumford, J. C., Savill, A. M., and Ciralt, F., 1990, "Three-dimensional Large-eddy Motions and Fine-scale Activity in a Plane Wake," *Journal of Fluid Mechanics,* Vol. 210, pp. 371–414.

Huang, Lein-Saing, and Ho, Chih-Ming, 1990, "Small-scale Transition in a Plane Mixing Layer," *Journal of Fluid Mechanics,* Vol. 210, pp. 475–500.

Hussain, A. K. M. Fazle, 1986, "Coherent Structures and Turbulenc," *Journal of Fluid Mechanics,* Vol. 173, pp. 303–356.

Meiburg, E., and Lasheras, J. C., 1988, "Experimental and Numerical Investigation of the Three-dimensional Transition in Plane Wakes," *Journal of Fluid Mechanics,* Vol. 190, pp. 1–37.

Wei, T., and Smith, C. R., 1986, "Secondary Vortices in the Wake of Circular Cylinders," *Journal of Fluid Mechanics,* Vol. 169, pp. 513–533.

Welsh, M. C., Soria, J., Sheridan, J., Wu, J., Hourigan, K., and Hamilton, N., 1992, "Three-dimensional Flows in the Wake of a Circular Cylinder," *Album of Visualization, The Visualization Society of Japan,* Vol. 9, pp. 17–18.

Williamson, C. H. K., 1988, "The Existence of Two Stages in the Transition to Three-dimensionality of a Cylinder Wake," *Physics of Fluids,* Vol. 31, No. 11, pp. 3165–3168.

Williamson, C. H. K., Wu, J., and Sheridan, J., 1995, "Scaling of streamwise vortices in wakes", *Physics of Fluids,* Vol. 7, No. 10, pp. 2307–2309.

Wu, J., Sheridan, J., Soria, J., and Welsh, M. C., 1994a, "An Experimental Investigation of Streamwise Vortices in the Wake of A Bluff Body," *Journal of Fluids & Structures,* Vol. 8, pp. 621–635.

Wu, J., Sheridan, J., Welsh, M. C., Hourigan, K., and Thompson, M., 1994b, "Longitudinal Vortex Structures In a Cylinder Wake," *Physics of Fluids,* Vol. 6, No. 9, pp. 2883–2885.

Wu, J., Sheridan, J., Welsh, M. C., and Hourigan, K., 1996, "Three-dimensional Vortex Structures in a Cylinder Wake", *Journal of Fluid Mechanics,* Vol. 312, pp. 201–222.

Stokes Layers in Horizontal-Wave Outer Flows

J. E. Choi
Graduate Research Assistant,
Presently, Research Scientist,
Hyundai Corporation.

M. K. Sreedhar
Postdoctoral Associate.

F. Stern
Professor and Research Engineer.

Department of Mechanical Engineering/
Iowa Institute of Hydraulic Research
The University of Iowa,
Iowa City, Iowa 52242-1585

Results are reported of a computational study investigating the responses of flat plate boundary layers and wakes to horizontal wave outer flows. Solutions are obtained for temporal, spatial, and traveling waves using Navier Stokes, boundary layer, and perturbation expansion equations. A wide range of parameters are considered for all the three waves. The results are presented in terms of Stokes-layer overshoots, phase leads (lags), and streaming. The response to the temporal wave showed all the previously reported features. The magnitude and nature of the response are small and simple such that it is essentially a small disturbance on the steady solution. Results are explainable in terms of one parameter ξ (the frequency of oscillation). For the spatial wave, the magnitude and the nature of the response are significantly increased and complex such that it cannot be considered simply a small disturbance on the without-wave solution. The results are explainable in terms of the two parameters λ^{-1} and x/λ (where λ is the wavelength). A clear asymmetry is observed in the wake response for the spatial wave. An examination of components of the perturbation expansion equations indicates that the asymmetry is a first-order effect due to nonlinear interaction between the steady and first-harmonic velocity components. For the traveling wave, the responses are more complex and an additional parameter, c (the wave speed), is required to explain the results. In general, for small wave speeds the results are similar to a spatial wave, whereas for higher wave speeds the response approaches the temporal wave response. The boundary layer and perturbation expansion solutions compares well with the Navier Stokes solution in their range of validity.

Introduction

In a variety of applications, boundary layers and wakes are subject to oscillating outer flows. Of interest here are outer flows of uniform streams with superposed temporal, spatial, or traveling waves. Example applications are surface-piercing bodies and turbomachinery. A basic geometry is a flat plate aligned with the uniform stream.

The most extensive information is for laminar and turbulent boundary layers with temporal horizontal-wave outer flows (Telionis, 1981). Boundary-layer (BL) and perturbation-expansion (PE) equations computations and data show that the flow is characterized by small-amplitude Stokes-layer overshoots, phase leads, and streaming. Except for high-frequency and/or strong-separation conditions, limited interactions occur between the mean and turbulent motions, i.e., the turbulence exhibits a quasi-steady response. Some of the recent numerical investigations on temporally oscillating turbulent boundary layer flows are a direct numerical simulation by Spalart and Baldwin (1989) and a Reynolds-averaged Navier Stokes (RANS) calculation by Hanjalic et al. (1993). These new studies also confirm the quasi-steady response of temporally oscillating transitional-turbulent boundary layers with a marked transition phase followed by a laminarization phase in each cycle.

Relatively limited information is available for spatial waves and has yet to be put in the context of Stokes layers. Stern (1986), Stern et al. (1989, 1993), and Choi and Stern (1993) investigated the boundary-layer and wake of a surface-piercing flat plate with a Stokes-wave outer flow which included detailed towing-tank experimental measurements. The plate and wave lengths are equal and the wave phase is fixed such that crests are coincident with the leading and trailing edges. Computation of BL, Navier-Stokes (NS), and RANS equations and data show significant wave-induced effects such as three-dimensional boundary-layer and wake responses with large overshoots and phase shifts, wave-induced separation, asymmetric wake responses with increased overshoots for regions of favorable pressure gradient and anisotropic/nonequilibrium nature of turbulence.

As in the case of spatial waves, very limited information is available for traveling horizontal-wave outer flows except for the work of Patel (1975, 1977). Approximate PE computations and data for laminar and turbulent boundary layers show increased overshoots and phase lags in comparison to the temporal wave. The above studies also indicate a dominant effect of the wave speeds on the response for both laminar and turbulent boundary layers. However, the measurements were obtained only for a single wave speed and low and medium reduced frequencies which somewhat limits the scope of the conclusions made. Only very limited turbulence measurements were made and they were found to be independent of the reduced frequencies considered.

Also of interest is related work for traveling vertical- or combined-wave outer flows; however, in distinction from the previous cases, unsteady lift effects predominate. Classic inviscid analytic solutions predict the unsteady lift amplitude reduction and phase shifts (Horlock, 1968). Data for foils with combined waves have confirmed the theory for low frequencies (Poling and Telionis, 1986). Recent experiments (Lurie, 1993) and computations (Paterson and Stern, 1993) concern the complex nature of the boundary-layer and wake response, especially near the trailing edge and in the near wake.

There appears a need to investigate, compile, and present the effects of different outer wave flows on boundary layers and wakes using computational and experimental techniques so as to present a unified picture. The present work attempts to do the computational part for laminar flows which is clearly an initial step taking into account the need to consider turbulent boundary layers and wakes. Thus, the primary objective of the present work is to determine the similarities and differences between the laminar boundary layer and wake responses due to

---

Contributed by the Fluids Engineering Division for publication in the JOURNAL OF FLUIDS ENGINEERING. Manuscript received by the Fluids Engineering Division February 17, 1994; revised manuscript received April 23, 1996. Associate Technical Editor: S. P. Vanka.

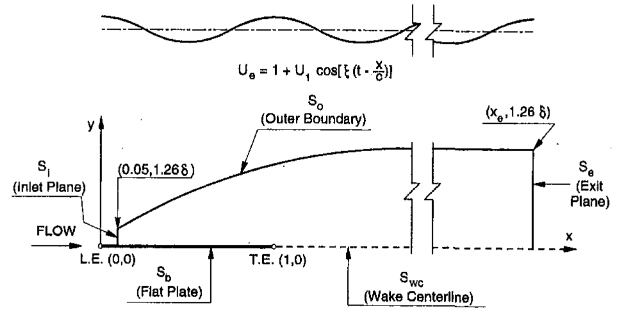

Fig. 1 Domain for boundary-layer wake computations with temporal-, spatial-, and traveling-wave external flows. For boundary-layer calculations the plate extends to the exit plane.

temporal, spatial, and traveling horizontal-wave outer flows. Another objective is to identify the physical mechanism responsible for the previously mentioned asymmetric wake response. To these ends, a model problem of a flat plate boundary layer and wake was selected and NS, BL, and PE solutions are obtained for a large range of outer flow conditions.

Model Problem

Consider the model problem of a flat plate laminar boundary layer and wake in an outer flow of a uniform stream with superposed temporal, spatial, or traveling waves (Fig. 1). The continuity and NS equations for unsteady two-dimensional incompressible flow are written in Cartesian coordinates with x positive downstream, y normal to the plate, and $(0, 0)$ at the plate leading edge:

$$\frac{\partial u}{\partial x} + \frac{\partial v}{\partial y} = 0 \tag{1}$$

$$\frac{\partial u}{\partial t} + u\frac{\partial u}{\partial x} + v\frac{\partial u}{\partial y} = -\frac{\partial p}{\partial x} + \frac{1}{\mathrm{Re}}\left(\frac{\partial^2 u}{\partial x^2} + \frac{\partial^2 u}{\partial y^2}\right) \tag{2}$$

$$\frac{\partial v}{\partial t} + u\frac{\partial v}{\partial x} + v\frac{\partial v}{\partial y} = -\frac{\partial p}{\partial y} + \frac{1}{\mathrm{Re}}\left(\frac{\partial^2 v}{\partial x^2} + \frac{\partial^2 v}{\partial y^2}\right) \tag{3}$$

where (u, v) are the velocity components in the (x, y) directions, p is the pressure, and $\mathrm{Re} = U_oL/\nu$ is the Reynolds number. All variables are nondimensionalized using U_o, L, and ρ.

The boundary and initial conditions are:

$$\left(u, v, \frac{\partial p}{\partial y}\right) = 0 \quad .05 \le x \le 1, \quad y = 0$$

$$\left(\frac{\partial u}{\partial y}, v, \frac{\partial p}{\partial y}\right) = 0 \quad 1 < x < x_{\text{exit}}, \quad y = 0$$

$$\left(u, \frac{\partial v}{\partial y}, p\right) = \left(U_e, -\frac{\partial u}{\partial x}, p_e\right) \quad .05 < x < x_{\text{exit}}, \quad y = \delta(x)$$

$$\left(\frac{\partial^2 u}{\partial x^2}, \frac{\partial p}{\partial x}\right) = 0 \quad x = x_{\text{exit}}$$

$$(u, v) = (u_B, v_B) \quad x = .05, \quad t = 0 \tag{4}$$

where (u_B, v_B) is the Blasius solution. The symmetry boundary condition on the wake centerline imposes a strong restraint on the wake development and is suited only for laminar flows as is the case in the present work. Also, the impostion of the Blasius profiles at the inlet is justified for the Reynolds numbers used in this study.

$$U_e = 1 + U_1 \cos\left[\xi(t - x/c)\right] \tag{5a}$$

such that

$$V_e = -\frac{U_1\xi}{c}\, y \sin\left[\xi(t - x/c)\right] \tag{5b}$$

$$-\partial p_e/\partial x = \xi U_1\left(1 - \frac{1}{c}\right)\cos\left[\xi(t - x/c) + \pi/2\right] + .5kU_1^2 \sin\left[2\xi(t - x/c)\right] \tag{5c}$$

$$-\partial p_e/\partial y = -\xi U_1\left(1 - \frac{1}{c}\right) \times \frac{\xi y}{c}\cos\left[\xi(t - x/c)\right] + \left(\frac{\xi U_1}{c}\right)^2 y \tag{5d}$$

$$p_e = U_1(c - 1)\cos\left[\xi(t - x/c)\right] - .25U_1^2 \cos\left[2\xi(t - x/c)\right] \tag{5e}$$

$$\omega_e = \left(\frac{\xi}{c}\right)^2 U_1 y \cos\left[\xi(t - x/c)\right] \tag{5f}$$

U_1 is the unsteady velocity amplitude, $\xi = \omega L/U_o$ is the frequency parameter (ω is the frequency), and $c = \lambda/T = \xi/k$ is the wave speed [λ is the wave length, T is the wave period ($= 2\pi/\xi$) and k is the wave number ($= 2\pi/\lambda$)]. Equation (5) corresponds to the traveling wave. For the specified U_e in (5a), relations (5b)–(5d) are obtained from (1)–(3), respectively, (5e) by integration of (5c), and (5f) by definition $\omega_e = -\partial V_e/\partial x$ using (5b).

The temporal wave is recovered for $c \to \infty$, i.e., $k = 0$:

$$U_e = 1 + U_1 \cos \xi t \tag{6a}$$

Nomenclature

c = wave velocity
k = wave number
L = reference length
$O(\ )$ = order of magnitude
p = pressure
Re = Reynolds number ($= U_oL/\nu$)
t = time
T = wave period
u, v = boundary layer or wake velocity
U, V = external-flow velocity
U_o = uniform-stream velocity
U_1 = (1) unsteady velocity amplitude
= (2) perturbation parameter
x, y = Cartesian coordinates
α = phase-shift angle
δ = boundary-layer or wake thickness
δ_ω = Stokes-layer thickness
γ = phase angle
λ = wave length
ν = kinematic viscosity
ξ = frequency
ω = dimensional frequency

Subscripts

cl = wake centerline
e = edge value
m = maximum value
o = steady solution
s = streaming
1 = first harmonic

such that

$$-\partial p_e/\partial x = \xi U_1 \cos(\xi t + \pi/2) \tag{6b}$$

$$p_e = -\xi U_1 x \cos(\xi t + \pi/2) \tag{6c}$$

which implies a phase lead retarded by u_t. For the temporal wave (5*b*), (5*d*), and (5*f*) are identically zero.

The spatial wave is recovered for $c \to 0$, i.e., $\xi = 0$:

$$U_e = 1 + U_1 \cos(\alpha - kx) \tag{7a}$$

such that

$$V_e = -kU_1 y \sin(\alpha - kx) \tag{7b}$$

$$-\partial p_e/\partial x = -kU_1 \cos[\alpha - kx + \pi/2] + .5kU_1^2 \sin[2(\alpha - kx)] \tag{7c}$$

$$-\partial p_e/\partial y = k^2 U_1 y \cos(\alpha - kx) + k^2 U_1^2 y \tag{7d}$$

$$p_e = -U_1 \cos(\alpha - kx) - .25U_1^2 \cos[2(\alpha - kx)] \tag{7e}$$

$$\omega_e = k^2 U_1 y \cos(\alpha - kx) \tag{7f}$$

which implies a phase lag enhanced by uu_x. Here α is the phase-shift angle.

The solutions are restricted to large Re and small U_1 and $\xi U_1(1 - 1/c)$ such that viscous-inviscid interaction is negligible and, additionally, for $(\xi^{-1}, \lambda^{-1}, \xi/\text{Re}, \lambda/\text{Re}^{1/2}) \ll 1$, the BL and PE approximations are valid. The formulation can be extended to finite-thickness geometries (e.g., foils) such that $U_o = U_o(x, y)$; however, incorporation of viscous-inviscid interaction is required and the applicability of the BL and PE solutions is more restricted.

The results are analyzed by decomposing $u(x, y, t[\alpha])$ into steady (i.e., with-out wave) $u_o(x, y)$, streaming $u_s(x, y)$, and first-harmonic response amplitude $u_1(x, y)$ and phase $\gamma(x, y)$ components

$$u(x, y, t[\alpha]) = u_o(x, y) + u_s(x, y) + u_1(x, y) \cos[\xi t[\alpha] - kx + \gamma(x, y)] \tag{8}$$

where

$$u_s(x, y) = \frac{1}{T[2\pi]} \int_0^{T[2\pi]} u(x, y, t[\alpha])dt[d\alpha] - u_o(x, y) \tag{9}$$

$$u_1(x, y) = \left\{ \frac{2}{T[2\pi]} \int_0^{T[2\pi]} [u(x, y, t[\alpha]) - u_s(x, y) - u_o(x, y)]^2 dt[d\alpha] \right\}^{1/2} \tag{10}$$

$$\sin \gamma(x, y) = \frac{-2}{T[2\pi] u_1(x, y)} \int_0^{T[2\pi]} [u(x, y, t[\alpha]) - u_s(x, y) - u_o(x, y)] \sin(\xi t[\alpha] - kx)dt[d\alpha] \tag{11a}$$

$$\cos \gamma(x, y) = \frac{2}{T[2\pi] u_1(x, y)} \int_0^{T[2\pi]} [u(x, y, t[\alpha]) - u_s(x, y) - u_o(x, y)] \cos(\xi t[\alpha] - kx)dt[d\alpha] \tag{11b}$$

and $[\alpha]$, $[d\alpha]$, and $[2\pi]$ replace t or ξt, dt, and T, respectively, for the spatial wave. Figures are presented for u_1/U_1 and γ vs. η ($= y/\sqrt{\text{Re}_x}$, where $\text{Re}_x = U_o x/\nu$). Also presented are the maximum overshoot values u_{1m}/U_1, it's position η_{1m} and wall or wake-centerline phase angles γ_o vs. $\xi = \omega x/U_o$ for the temporal and traveling waves and vs. x/λ for the spatial waves.

Computational Methods

The NS solutions are obtained using the methods of Choi and Stern (1993) and Paterson and Stern (1993) for steady and unsteady flows, respectively. Both methods are based on Chen and Patel (1989, 1990), which have been extensively validated for a wide range of applications. The NS and continuity equations are written in the physical domain using Cartesian coordinates (x, y, z) and partially transformed (i.e., coordinates only) into nonorthogonal curvilinear coordinates (ξ, η, ζ) such that the computational domain forms a simple rectangular parallelepiped with equal grid spacing. The transformed equations are reduced to algebraic form using finite-analytic method spatial and second-order backward finite-difference temporal discretization. SIMPLER and PISO velocity-pressure coupling algorithms are used for steady and unsteady flow, respectively. The resulting implicit equations are solved using line-ADI with under-relaxation. The boundary and initial conditions are given in (4). The details of the edge values for different wave conditions are given in (5)–(7).

The BL and PE equations are derived following Telionis (1981). The derivation is complicated and, as already noted, requires $(\xi^{-1}, \lambda^{-1}, \xi/\text{Re}, \lambda/\text{Re}^{1/2}) \ll 1$. In consideration of the relative simplicity of the resulting equations, a straightforward finite difference method is used with first-order backward differences for the t- and x-derivatives, a central difference for the y-derivatives, and a lag-iterative algorithm for the nonlinear terms. The PE equations are solved successively and further analyzed through presentation of average values over the boundary-layer and wake thickness of the terms in the first-order equation

$$i(\xi - ku_o)u_1 + u_o \frac{\partial u_1}{\partial x} + u_1 \frac{\partial u_0}{\partial x} + v_o \frac{\partial u_1}{\partial y} + v_1 \frac{\partial u_o}{\partial y} = i(\xi - k)U_1 + \frac{1}{\text{Re}} \frac{\partial^2 u_1}{\partial y^2} \tag{12}$$

[where (u_i, v_i) are real for the zeroth-order ($i = 0$) and complex for first-order ($i = 1$)]. The averaged value is obtained as

$$\bar{\phi}_l(x) = \frac{1}{\delta} \int_0^{\delta} |\phi| dy \tag{13}$$

where $|\phi_1|$ ($1 = 1, 9$) is the magnitude of the ith term in (12) with the index increasing from left to right. The application of boundary conditions and initial conditions are straight forward and details are given in Choi (1993).

Computational Conditions and Uncertainty Analysis

Computations were performed to cover a wide range of parameters for temporal, spatial and traveling wave outer flows. The different computational conditions are summarized in Table 1. The range of values were specified both for validation through comparisons with previous studies and for investigation of the influences of the wave and pressure-gradient amplitudes and wave frequency, length and speed. For the temporal wave, for the boundary-layer region, NS, BL, and PE solutions were obtained for a large range of frequencies ($.01 \le \xi \le 5$). For the wake region, only BL and PE solutions were obtained for relatively low frequencies ($.19 \le \xi \le .94$). For the spatial wave, for both the boundary-layer and wake regions, NS, BL, and PE solutions were obtained for a range of wavelengths ($.2 \le \lambda^{-1} \le 10$). For the traveling wave, for the boundary-layer region, solutions were obtained for large ranges of frequency and wave speeds ($.1 \le \xi \le 5$ and $.3 \le c \le 10$) with NS solutions limited to low frequencies. For the wake region, only BL and PE solutions for relatively low frequencies ($.19 \le \xi \le .94$) and for wave speeds ($.3 \le c \le .10$) were obtained. For fixed wavelengths ($\lambda^{-1} = .2$ and 1) solutions were obtained with all the three methods for a wide range of frequencies

Table 1 Calculation conditions. BL and PE solutions obtained for all the above values. NS solutions obtained only for the underlined values

Temporal wave

Region	Wave/pressure gradient amplitude	Frequency (ξ)
Boundary layer	(1) $U_1 = -0.4$ and (2) $\xi U_1 = -0.13$	.01, .05, .1, .2, .3, .4, .522, .559, .6, .7, .8, .9, 1.0 1.1, 1.2, 1.3, 1.4, 1.47, 1.6, 1.7, 1.8, 1.9, 2.0, 2.2, 2.49 2.65, 2.8, 3, 3.2, 3.4, 3.6, 3.8, 4, 4.2, 4.4, 4.6, 4.8, 5.0
Wake	(3) $U_1 = -0.4$ and (4) $\xi U_1 = -0.13$	.188, .565, .942

Spatial wave

Region	Wave/pressure gradient amplitude	Wavelength^{-1} (λ^{-1})
Boundary layer and wake	(1) $U_1 = -0.4$ and (2) $kU_1 = -0.13$	.2, 1., 5., 10.

Traveling wave

Region	Wave/pressure gradient amplitude	Frequency (ξ)/wave speed (c)
Boundary layer	(1) $U_1 = -0.4$	ξ = .314, .628, .943, 1.257, 1.57 c = .3, .4, .5, .64, .77, 1., 2., 5., 10.
Boundary layer	(2) $U_1 = -0.4$	ξ = .1, .2, .522, .599, 1., 1.47, 2.49, 2.65, 5. c = .3, .5, .77, 1., 10.
Wake	(3) $U_1 = -0.4$	ξ = .188, .565, .942 c = .64, .77, 1., 10.
Boundary layer and wake	(4) $\lambda^{-1} = 0.2$ $\xi U_1(1 - 1/c) = -0.013$	(c,ξ) = (.2, .251), (.3, .377), (.4, .503), (.77, .968), (2., 2.513), (5., 6.28)
Boundary layer and wake	(5) $\lambda^{-1} = 1.0$ $\xi U_1(1 - 1/c) = -0.013$	(c,ξ) = (.2, 1.257), (.3, 1.885), (.4, 2.513), (.77, 4.838), (2, 12.566), (5, 31.416)

for both boundary layer and wake. For the above parameters, solutions were obtained keeping either the unsteady velocity amplitude constant or the amplitude of the pressure gradient constant. In summary, a large range of conditions were evaluated for all three waves and methods; however, the ranges for the wake region and NS solutions are relatively restricted being more computationally intensive. Due to limitations of the range of validity of the different approximations, especially for the BL and PE equations, each of the three techniques are often used to complement each other in presenting a unified picture. However, every attempt is made to compare the results obtained using the three techniques wherever the validity of the approximations permits. Although limited by approximations, the BL and PE approaches are also essential to the present study mainly because of the following reasons. First, they are inexpensive which enables us to obtain solutions for a wide range of parameters within their range of validity. Second, certain aspects of the flow are better understood by these methods, such as the PE method which allows us to understand the interactions between various components in the equations.

The solutions are for Re = 10^5, except the temporal and traveling wave NS solutions are for Re = 10^4. Numerical tests for large and small ξ indicated identical results for both Re. In general, the response was linear in U_1, which is consistent with previous results and supported the case of fixed pressure gradient for comparison of the quantitative differences between the three waves. The steady NS and BL and zero-order PE solutions correspond to the Blasius solution and wake, which was obtained to within a few percent, except for trailing-edge effects. Due to space limitations, the results and figures are provided only for a few selected cases which convey and support the major conclusions. The complete results are provided in Choi (1993).

The recent discussion in the CFD community on the numerical uncertainty analysis has led to the formulation of a set of guidelines and standards for reporting numerical inaccuracies. This is a necessary first step, but controversies and practical difficulties still exist in implementation. The derivation of the finite analytic method used in this paper precludes term-by-term error analysis. However, detailed comparisons have shown that the finite-analytic method is of comparable accuracy to second-order finite-difference methods. A numerical study using generalized Richardson extrapolation for a laminar flat-plate and fully developed annular flow seem to support this conclusion. Also note that, a few of the cases reported in this paper were repeated recently using a third-order finite difference scheme and similar results were obtained.

The grids were generated algebraically. A range of grids and computational domains were used depending on the method, region of interest (i.e., boundary layer or wake) and λ^{-1}. The solution domain for the wake calculation is indicated in Fig. 1. For the boundary layer calculations the plate extends all the way to the exit plane. The grid numbers, exit plane and time steps were determined based on grid independence and time-accurate studies for selected conditions (Choi, 1993). The shortest wave considered ($\lambda^{-1} = 10$) was described by at least 20 points in the axial direction. 100 time steps per period were used. The details are summarized in Table 2. The leading edge was not included in the domain while trailing edge resolution is given in Table 2. The convergence criterion was based on the residual

$$R(it) = \sum_i \sum_j (|\phi(it-1)| - |\phi(it)|)/\sum_i \sum_j |\phi(itl)| \quad (14)$$

where $\phi = p$ or $\mathbf{V}$, be at least 10^{-4}. For unsteady flow, 2–3 initial periods were usually sufficient to obtain periodic solutions. The NS solutions on the average required on the order of 1 CRAY YMP hour while the BL and PE solutions required only a few minutes. The memory requirements were less than 8 megawords for all the three methods.

Results and Discussion

As can be seen from the previous section and Table 1, a wide range of wave parameters were covered in the present computational study to understand the complex nature of boundary layer and wake responses to temporal, spatial and traveling outer waves. The response to the temporal wave is discussed first followed by spatial and traveling waves. The results are analyzed in terms of Stokes-layer overshoots, phase shifts, and streaming. Also discussed is the prediction of the separation

Table 2 Grid information

Boundary layer and perturbation expansion equations

Parameters	Steady BL $1/\lambda = 0.2, 1$	Steady BL $1/\lambda = 5, 10$	Steady BL and wake $1/\lambda = 0.2, 1$	Steady BL and wake $1/\lambda = 5, 10$	Unsteady BL all ξ	Unsteady BL and wake all ξ
Inlet bound.(x/L)	0.05	0.05	0.05	0.05	0.06	0.06
Outlet bound.(x/L)	1.50	1.50	10.00	5.00	1.50	5.00
$\Delta x/L$(T.E.)	0.001	0.005	0.01	0.005	0.02	0.02
Top bound.(y/δ)	1.26	1.26	1.26	1.26	1.26	1.26
$\Delta y/\delta$ (even grid)	0.0124	0.0124	0.0124	0.0124	0.06	0.0155
Grid no. (X-dir)	146	291	996	991	76	248
Grid no. (Y-dir)	101	101	101	101	51	81

Navier stokes equation

Parameters	Steady BL and wake $1/\lambda = 0.2, 1$	Steady BL and wake $1/\lambda = 5, 10$	Unsteady BL and wake all ξ
Inlet bound.(x/L)	0.05	0.05	0.05
Outlet bound.(x/L)	10.00	5.00	5.00
$\Delta x/L$(T.E.)	0.016	0.01	0.009
Top bound.(y/δ)	1.26	1.26	1.26
$\Delta y/\delta$ (min)	0.015	0.01	0.00004
Grid no. (X-dir)	171	495	150
Grid no. (Y-dir)	23	23	75

starting point, which is defined as the initial axial position for which reverse flow occurs.

Temporal Wave

Boundary-Layer Response. The response of the boundary layer to a temporal wave displayed all the well known features of the flow: velocity overshoots, phase leads, and streaming. While the velocity overshoots and phase leads showed good comparison with the data, streaming was almost zero and no data was available. The magnitude and nature of the response were small and simple such that the response can be considered as essentially a small disturbance on the steady solution. Shown in Fig. 2 are u_{1m}/U_1, η_{1m}, and γ_o vs. ξ $(= \omega x/U_o)$, including comparisons with the data (Hill and Stenning, 1960) and previous calculations (Telionis, 1981). The position of the overshoot monotonically decreases from low to high ξ. At the wall and in the inner part of the boundary layer, the phase angle increases linearly for small ξ and then merges with the high ξ value of 45 degrees. It was found that the single parameter ξ is sufficient to describe the results. The results are identical for the same values of ξ whether $\xi = \omega L/U_o$ and varying ω, or $\xi = \omega x/U_o$ and varying $x < L$. To see the effect of ξ on separation, separation starting points were obtained for the different ξ values. It was found that separation is delayed for increasing ξ. Most of the above features of the flow were discussed previously by Telionis (1981), including, additionally, that increasing constant steady adverse pressure gradient increases the velocity overshoot amplitudes.

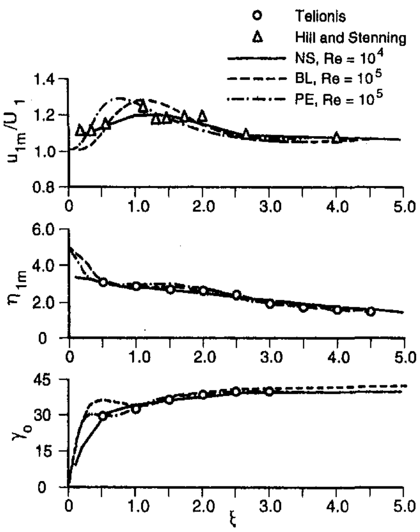

Fig. 2 Maximum first-harmonic overshoot values and wall phase angle values: boundary layer, temporal wave

The differences between the three solutions for u_1, γ, and the separation starting points are relatively small. The NS solution showed larger and smaller maximum velocity overshoots for small and medium ξ, respectively (i.e., a less pronounced peak spread over a larger region). The differences between the solutions for u_s (not shown here) were significant with the PE solution displaying complex profiles with large ξ dependency. Note that the differences between the NS and BL and PE solutions for small ξ are expected; since, the order-of-magnitude estimates used in deriving the latter two equations require $\delta_\omega/\delta = O(1)$, which is violated (i.e., for small ξ, $\delta_\omega/\delta > 1$).

Wake Response. Some typical results of the response of the wake to a temporal outer wave are displayed in Fig. 3 which shows u_1/U_1 and γ versus η profiles for three values of

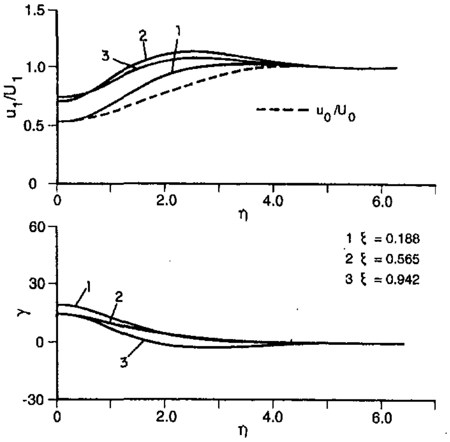

Fig. 3 First-harmonic amplitude and phase at $x = 1.5$: wake, temporal wave (BL equation solutions shown)

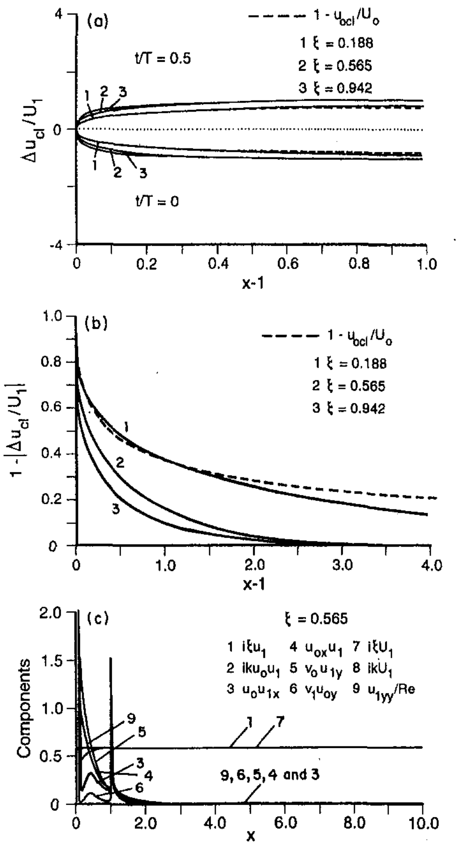

Fig. 4 Wake response: temporal wave, (*a*) wake centerline velocity, (*b*) velocity defect, (*c*) averaged values of perturbation-expansion equation components for ξ = .565. (BL equation solutions shown in *a* and *b*.)

frequency parameter $\xi = (.188, .565, .942)$ at $x = 1.5$, including comparison with the steady solution. The BL and PE solutions are similar (except for the streaming profiles, not shown here, which are negligible) and display trends as described earlier for the boundary-layer, but with reduced response. Here again, the nature of the response is essentially a small disturbance on the steady solution. The profiles of u_{1m}/U_1, u_{sm}, η_{1m}, η_{sm} and γ_o vs. ξ (not shown here) all displayed similar trends in Fig. 2 over the plate, but with some trailing edge effects. In the far wake, the velocity overshoots, streaming and phase leads monotonically decrease such that ultimately a plug flow is achieved.

Figures 4(*a*) and (*b*) show the wake-centerline velocity $\Delta u_{c1}/U_1$ and the defect $1 - |\Delta u_{cl}/U_1|$ (where $\Delta u_{cl} = u_{cl} - u_{ocl} - u_{scl}$). Consistent with u_1/U_1, the response is similar to the steady solution, but with faster recovery for increasing ξ. For the larger ξ values, recovery is achieved at $x - 1 = 2.75$. The wake response is symmetric. Shown in Fig. 4(*c*) is the boundary layer and wake averaged values of the first-order PE Eq. (12) for $\xi = .565$. In the far wake, the terms 1 and 7 are the dominating terms and are in balance (i.e., $u_1 = U_1$).

Spatial Wave

Boundary-Layer Response. As was the case for the temporal wave, the spatial wave is also seen to be characterized by velocity overshoots, phase lags (in this case), and streaming; however, there are significant differences between the two outer flows. The magnitude and the nature of the response are significantly increased and complex such that it cannot be considered simply a small disturbance on the without-wave solution. The dependency of the response on λ^{-1} was found to be very strong, i.e., *the characteristics of the response vary significantly for the* specified values of λ^{-1}. For small and large λ^{-1} (.2 and 10), the response is relatively small, whereas for medium $\lambda^{-1} = 1$ (and 5) the response is extreme. Some typical curves are shown in Fig. 5 which displays u_1/U_1 and γ vs. η profiles for the wavelength parameters $\lambda^{-1} = 0.2$ and 1 at $x = 1$. In both cases, the overshoots are considerably larger than the temporal wave. Large phase lags are observed, as are streaming velocities (not shown here). In the outer part of the boundary layer, the phase is nearly 0. For $\lambda^{-1} = .2$ and 1, the NS solution phase-angle response is similar to that for the BL and PE solutions. However, for higher values of λ^{-1} (not shown here) there are significant deviations.

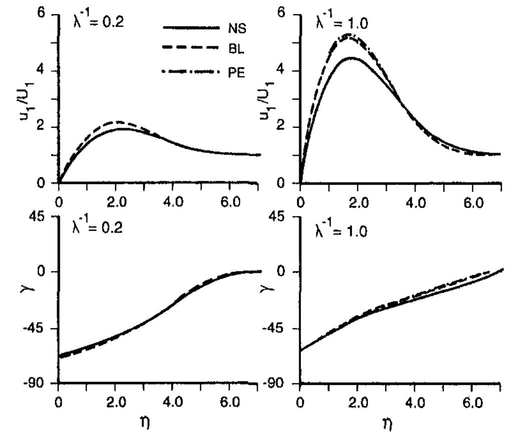

Fig. 5 First-harmonic amplitude and phase at x = 1.0: boundary layer, spatial wave

Shown in Fig. 6 are u_{1m}/U_1, η_{1m}, and γ_o versus x/λ for two values of λ^{-1} (0.2 and 1). Also shown in Fig. 6 is $u_{1m}/(U_1\sqrt{\mathrm{Re}_x})$ versus x/λ for the same two values. The maximum overshoot values are seen to require $1/\sqrt{\mathrm{Re}_x}$ scaling, because the values monotonically increase with x/λ unless normalized by $a\delta$ (where a is a constant) whereas $u_{1m}/(U_1\sqrt{\mathrm{Re}_x})$ displays a maximum overshoot near $x/\lambda = 1$ and then monotonically decreases toward its asymptotic value. For $\lambda^{-1} = 5$ and 10 (not shown here) the trends are similar both with and without scaling, i.e., both u_{1m}/U_1 and $u_{1m}/(U_1\sqrt{\mathrm{Re}_x})$ display maximum overshoots near $x/\lambda = 1$ and then monotonically decrease towards their asymptotic values, which decrease with increasing λ^{-1}. Recall that $1/\sqrt{\mathrm{Re}_x}$ scaling is required for $v_o(x, y)$.

In addition to the differences between the solutions already described, the NS solutions are found to display smaller overshoots. These differences between the NS solutions and BL and

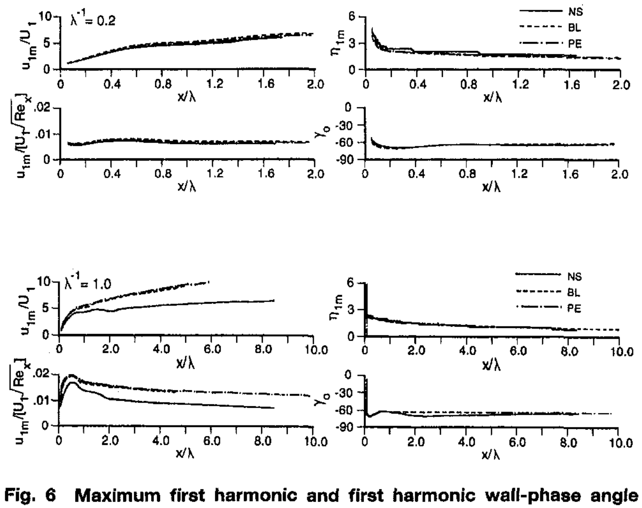

Fig. 6 Maximum first harmonic and first harmonic wall-phase angle values: boundary layer, spatial wave

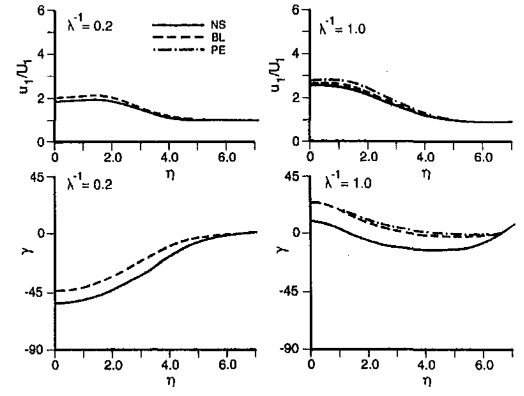

Fig. 7 First-harmonic amplitude and phase at $x = 1.5$: wake, spatial wave

PE solutions are seen to increase for increasing λ^{-1}. This is clearly evident from Figs. 5 and 6. Note that deviations between the NS solution and BL and PE solutions for large λ^{-1} are expected; since, the order-of-magnitude estimates used in deriving the latter are no longer valid. Unlike the temporal wave, a single parameter is not sufficient to characterize the results, i.e., both x/λ and λ^{-1} are required as is $1/\sqrt{\mathrm{Re}_x}$ scaling. The separation starting point was computed for each value of λ^{-1} and the results indicated that separation is delayed for increasing λ^{-1}.

Wake Response. Shown in Fig. 7 are the u_1/U_1, and γ vs. η profiles for the wave-length parameter $\lambda^{-1} = 0.2$ and 1 at $x = 1.5$. As was the case for the boundary-layer, the magnitude and nature of the response is such that it cannot be considered simply a small disturbance on the without-wave solution. The response of the wake is characterized by the reduced velocity overshoots, phase lags (or leads) and streaming in comparison with the boundary-layer response. Here also, the dependency on λ^{-1} was found to be strong. The maximum overshoot is for $\lambda^{-1} = 1$ and, here again, in all cases, the overshoots are considerably larger than for the temporal wave. For small and medium λ^{-1}, the three solutions are similar, whereas for the larger λ^{-1} values, the NS solutions indicate smaller overshoots and larger phase lags. The NS and BL solutions indicate relatively simple streaming velocity profile shapes with small magnitude in comparison to the PE solution. Profiles of u_{1m}/U_1, η_{1m}, η_{sm}, and γ_o (not shown here) all showed damped oscillations with increasing x/λ. In general, the three solutions displayed similar trends with the largest quantitative differences in the near wake.

Figures 8(a) and 8(b) show $\Delta u_{cl}/U_1$ and the envelope of the maximum and minimum $\Delta u_{cl}/U_1$ values and their difference (dashed line) for $\lambda^{-1} = 1$. The asymmetric nature of the wake response, henceforth wake bias, is clearly evident. Similar wake bias was observed for all λ^{-1} and all three solutions. The bias is symmetric with respect to the phase-shift angle. The bias amplitudes are defined from the maximum and minimum of the $\Delta u_{cl}/U_1$ difference curves. The extent of the bias varies from $(x - 1)/\lambda = 4$ to 35 for increasing λ^{-1}. Recovery is achieved at about $(x - 1)/\lambda = 5$ to 25 for increasing λ^{-1}. To see which terms are instrumental in producing the wake bias, we computed the boundary layer and wake averaged values of the first-order PE Eq. (12) which is shown in Fig. 8(c). It is clear that the terms 2 and 8 are the dominant terms, followed by terms 3 and 6 in the near wake. The terms 2 and 8 of the spatial wave in Fig. 8(c) are similar to the terms 1 and 7 (in Fig. 4(c)), which are the only nonnegligible terms for the temporal wave. Recall, no wake bias was noticeable for the temporal wave while a clear bias is seen for the spatial wave. Therefore, the wake bias for the spatial wave, is attributed to the influences of the additional nonnegligible terms 3 and 6. These two terms arise from the convective acceleration and an examination of these two terms reveals that the bias is a first-order effect due to nonlinear interaction between the steady and first-harmonic velocity components.

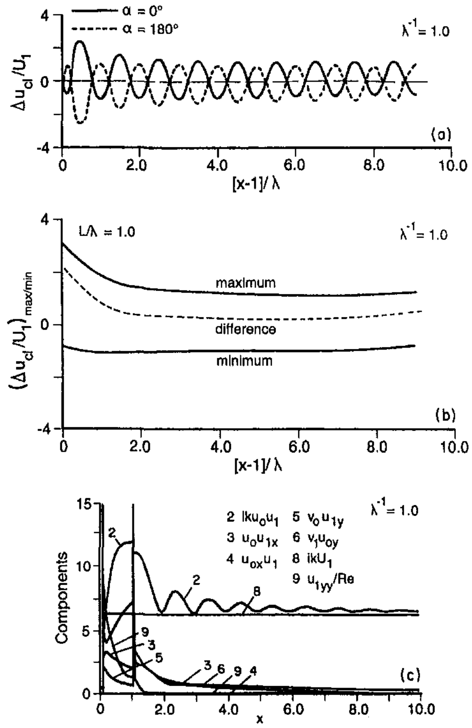

Fig. 8 Wake response: spatial wave, (a) wake centerline velocity, (b) envelope of maximum and minimum and their difference, (c) averaged values of perturbation-expansion equation components. (BL equation solutions shown in a and b.)

Traveling Wave

Boundary-Layer Response. As a first step, an attempt is made to compare boundary-layer response to a traveling wave with the data. The data were reportedly obtained for a wave speed $c = 0.77$. However, as pointed out by Graham (1993), the experiments were performed in an open test section wind tunnel with the wave generators fixed at the contraction exit walls such that $c = 0.5$ is, in fact, a more likely value. To clear the issue we obtained solutions for both $c = 0.5$ and 0.77 at the experimental values of ξ. At $c = 0.5$ large overshoots were observed, while at $c = 0.77$ there were no overshoots. The data (Patel, 1975) show large over shoots. Phase was nearly identical for both solutions even though the phase at $c = 0.77$ showed marginally better comparison with data. The solution at $c = 0.5$ and data are shown in Fig. 9. Note that Patel's (1975) approximate PE solutions for low and high ξ showed fairly good agreement with the data whereas the present solutions show better agreement only when the speed is adjusted to a lower value. This discrepancy between the present solutions and the

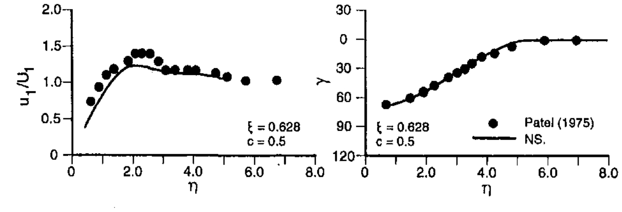

Fig. 9 First-harmonic amplitude and phase at $x = 1.0$: boundary layer, traveling wave

data and previous solutions indicates the need for additional investigations; both computational and experimental.

Figure 10(*a*) shows u_1/U_1 and γ versus η for fixed c and variable ξ. The $c = .3$ trends are similar and consistent with those for the spatial wave for the range of ξ (i.e., λ^{-1}) investigated, which, unfortunately is restricted to long and medium wave lengths. It was not possible to obtain BL and PE solutions for small wavelengths due to the required large $\xi U_1(1 - (1/c))$ and associated large response amplitudes. The $c = 10$ trends are similar and consistent with those for the temporal wave, in this case, for the complete ξ range of interest. For large ξ and $c = 1$ (not shown here), u_1/U_1 displays a nearly linear variation across the boundary layer and γ displays large leads. For small ξ, the profile is somewhat fuller, although there is no overshoot, and γ is nearly zero. The streaming velocity (not shown here) is minimum. The intermediate c values indicate a smooth transition between the spatial and temporal waves. In Fig. 10(*b*) is shown u_1/U_1 and γ versus η for fixed ξ and variable c. The small ξ response indicates negligible influence of c (i.e., λ^{-1}) for the long-wave range investigated compared to large ξ response.

Profiles of maximum overshoot values and their positions and wall phase angle values (not shown here) also displayed similarity to the spatial and temporal waves for low and high values of c, respectively. So also did profiles of u_1/U_1 and γ versus η for fixed $\xi U_1(1 - (1/c))$ and λ^{-1} values and various c values. The boundary layer separation is found to be delayed for increasing ξ and λ^{-1}.

In summary, an additional parameter c is required to explain the results compared to the spatial and temporal waves, and the small and large c results are similar to those for the spatial and temporal wave, respectively.

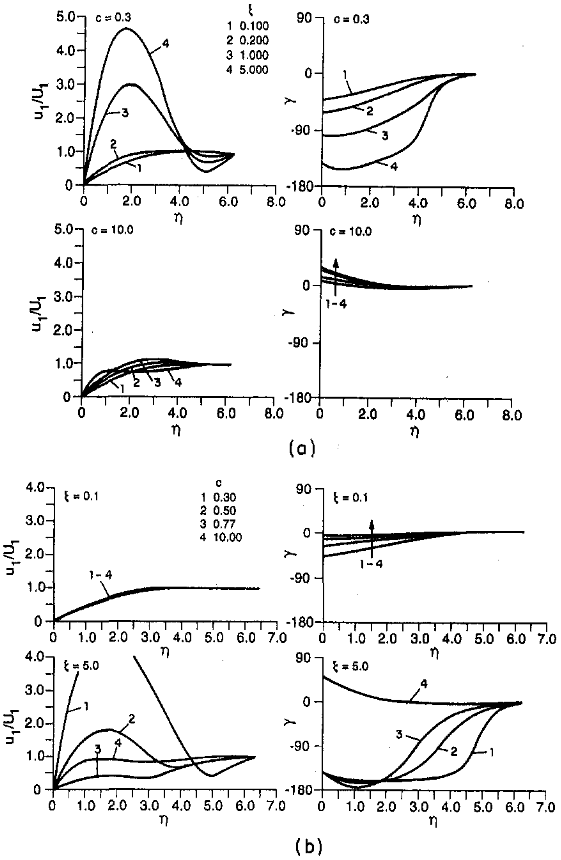

Fig. 10 First-harmonic amplitude and phase at $x = 1.0$: boundary layer, traveling wave, (*a*) fixed c and variable ξ, (*b*) fixed ξ and variable c (NS solutions shown)

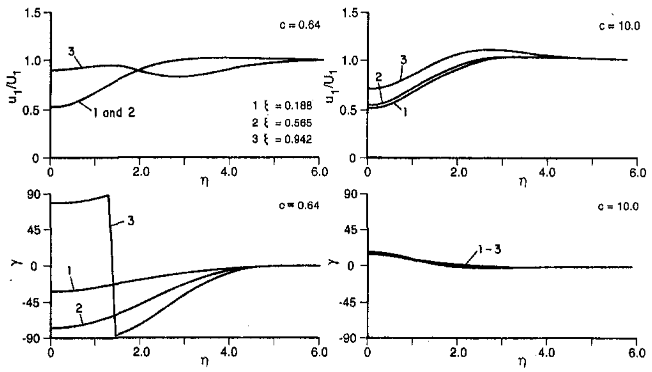

Fig. 11 First-harmonic amplitude and phase at $x = 1.5$: wake, traveling wave (BL equation solutions shown)

Wake Response. The wake response also showed the limiting responses for small and large wave speeds, with the temporal wave response recovered for the large wave speeds and the spatial wave response for smaller wave speeds. Note that for the specified ξ range, $c = .64$ appears to be a mixed condition, i.e., in the transition range between the spatial and temporal waves. The results for $c = 10$ on the other hand exhibits the temporal-wave characteristics. Shown in Fig. 11 are some typical curves which displays u_1/U_1 and γ versus η for two values of c (.64 and 10) at $x = 1.5$.

For traveling waves with fixed λ^{-1} (not shown here) and $.2 < c < 5$, the results indicate the following. For $\lambda^{-1} = .2$ and low and high c results are similar and consistent with those for the spatial and temporal waves, respectively, for the same parameter values. The situation is almost similar for waves with $\lambda^{-1} = 1$ except that the response magnitudes and nonlinearities for the low c values are extreme, i.e., even larger and more complex than those for the spatial wave.

Wake centerline velocity responses (not shown here) are more asymmetric and complex compared to the spatial wave. This complexity of the nature of the wake bias is also evident in the boundary layer and wake averaged values (also not shown here) of the PE Eq. (12).

Summary and Conclusions

Results are presented for the model problem of a flat-plate boundary layer with temporal-, spatial- and traveling-wave external flows. For the temporal wave, close agreement with previous experimental and computational studies is observed. The magnitude and nature of the response are small and simple such that it is essentially a small disturbance on the steady solution. The results are explainable in terms of the single parameter ξ. Boundary-layer separation is delayed for increasing ξ. The wake response is smaller in comparison to the boundary-layer response and no wake bias is observed and plug flow is attained with faster recovery for increasing ξ.

For the spatial wave, analogous Stokes-layer behavior is observed, but with significantly increased magnitudes and complex nature of the response such that it cannot be considered a small disturbance on the without-wave solution. Main features are explainable in terms of the two parameters λ^{-1} and x/λ. The boundary-layer response maximum overshoot values require $1/\sqrt{\mathrm{Re}_x}$ scaling. The boundary-layer separation is delayed for increasing λ^{-1}. For the wake response, a clear bias is observed. This is attributed to nonlinear interaction between the steady and first-harmonic velocity components. In the far wake, damped oscillatory plug flow is recovered with faster recovery for increasing λ^{-1}.

For the traveling wave, an additional parameter, the wave speed c is required to explain the results. Poor agreement with the previous experimental and computational study is observed for the boundary-layer response magnitude unless the wave speed is adjusted to a lower value. The limiting behavior for small and large wave speeds approached the spatial and temporal waves, respectively. A smooth transition between the two for intermediate values is also observed. The boundary-layer separation is delayed for increasing ξ and λ^{-1}. The wake response also showed similar limiting behaviors for small and large c values, except for the extreme response for small c and medium λ^{-1}. The wake centerline velocity responses were more complex compared to the temporal and spatial wave.

All three flows are of practical importance with regard to a large variety of applications. The temporal wave problem has wide-spread applications and most of the study up to this date has been in this area. The spatial wave is closely related to ship hydrodynamics problems involving surface-piercing bodies and associated wavy free-surface effects. Undoubtedly, other similar applications exist. The traveling wave problem represents a more general version of temporal and spatial wave problems and has relevance to a host of engineering and technological applications such as in helicopter aerodynamics, ship-hydrodynamics, propeller-hull interaction, hydroaccoustics, rotor-stator interaction in turbines etc. Previous studies indicate unsteady lift effects and complex boundary layer and wake responses for foils in the presence of travelling wave unsteadiness. The present model problem provides basic information on oscillatory external-flow pressure gradient effects on boundary layer and wake without complexities facilitating the identification of the essential features of the three flows. These studies are critical to enhance our understanding of some features which are more fundamental in nature such as the role of such outer waves on the generation and sustenance of the underlying small scale turbulence and their possible interactions. While some work has been done on temporal waves, the results of the present study indicates that further efforts are required to determine the nature of the interaction between the mean and turbulent motions; since, it appears that the conclusions found for temporal waves are not necessarily applicable to spatial and traveling waves, at least for laminar flows. This is especially true for travelling waves where there is enough evidence that the wave speed has a major effect on the boundary layer and wake responses and very little is known regarding the effect of responses on turbulent quantities.

Acknowledgments

This research was sponsored by the Office of Naval Research under grant N00014-92-K-1092 under the administration of Dr. E. P. Rood. The calculations were performed on the CRAY supercomputers of the Naval Oceanographic Office and National Aerodynamic Simulation Program.

References

Chen, H. C., and Patel, V. C., 1989, "The Flow around Wing-Body Junctions," *Proc. Symposium on Numerical and Physical Aerodynamic Flows,* Vol. 4.

Chen, H. C., and Patel, V. C., 1990, "Solutions of Reynolds-Averaged Navier-Stokes Equations for Three-Dimensional Incompressible Flows," *Journal of Computational Physics,* Vol. 88, No. 2.

Choi, J. E., 1993, "Role of Free-Surface Boundary Layer Conditions and Nonlinearities in Wave/Boundary-Layer and Wake Interaction," Ph.D. thesis, The University of Iowa.

Choi, J. E., and Stern, F., 1993, "Solid-Fluid Juncture Boundary Layer and Wake with Waves," *Proceedings Sixth International Conference on Numerical Ship Hydrodynamics,* Iowa City, Iowa.

Graham, M., 1993, private communication.

Hanjalic, K., Jakirlic, S., and Hadzic, I., 1993, "Computation of Oscillating Turbulent Flows at Transitional Re-numbers," *Turbulent Shear Flows,* Vol. 9, J. C. Andre et al., eds., Springer-Verlag, pp. 324–342.

Hill, P. G., and Stenning A. H., 1960, "Laminar Boundary Layers in Oscillating Flow," ASME *Journal of Basic Engineering,* pp. 593–608.

Horlock, J. 1968, "Fluctuating Lift Forces on a Airfoils moving through Transverse and Chordwise Gusts," ASME *Journal of Basic Engineering,* pp. 494–500.

Lurie, E. H. 1993, "Unsteady Response of a Two-Dimensional Hydrofoil Subject to High Reduced Frequency Gust Loading," M. S. thesis, Dept. of Ocean Engg., MIT, Cambridge, MA.

Paterson, E., and Stern, F., 1993, "Computation of Unsteady Viscous Flow with Application to the MIT Flapping-Foil Experiment," *Proceedings Sixth International Conference on Numerical Ship Hydrodynamics,* Iowa City, Iowa.

Patel, M. H., 1975, "On Laminar Boundary Layers in Oscillatory Flow," *Proceedings of the Royal Society of London,* Series A, Vol. 347, pp. 99–123.

Patel, M. H., 1977, "On Turbulent Boundary Layers in Oscillatory Flow," *Proceedings of the Royal Society of London,* Series A, Vol. 353, pp. 121–143.

Poling, D., and Telionis, D., 1986, "The Response of Airfoils to Periodic Disturbances-The Unsteady Kutta Condition," *AIAA Journal,* Vol. 24, No. 2, pp. 193–199.

Spalart, P. R., and Baldwin, B. S., 1989, "Direct Simulation of a Turbulent Oscillating Boundary Layer," *Turbulent Shear Flows,* 6, J. C. Andre et al., eds., Springer-Verlag, 417–440.

Stern, F., 1986, "Effects of Waves on the Boundary Layer of a Surface-Piercing Body," *Journal of Ship Research,* Vol. 30, pp. 256–274.

Stern, F., Hwang, W. S., and Jaw, S. Y., 1989, "Effects of Waves on the Boundary Layer of a Surface-Piercing Flat Plate: Experiment and Theory," *Journal of Ship Research,* Vol. 33, pp. 63–80.

Stern, F., Choi, J. E., and Hwang, W. S., 1993, "Effects of Waves on the Wake of a Surface-Piercing Flat Plate: Experiment and Theory," *Journal of Ship Research,* Vol. 37, pp. 102–118.

Stern, F., Kim, H. T., Zhang, D. H., Toda, Y., Kerwin, J., and Jessup, S., 1994, "Computation of Viscous Flow Around Propeller-Body Configurations: Series 60 CB = 0.6 Ship Model," *Journal of Ship Research,* Vol. 38, pp. 137–157.

Telionis, D. P., 1981, *Unsteady Viscous Flow,* Springer-Verlag, New York.

Z. J. Zhang[1]
Graduate Research Assistant.

F. Stern
Professor.

Department of Mechanical Engineering,
Iowa Institute of Hydraulic Research,
The University of Iowa,
Iowa City, Iowa 52242

Free-Surface Wave-Induced Separation

Free-surface wave-induced separation is studied for a surface-piercing NACA 0024 foil over a range of Froude numbers (0, .2, .37, .55) through computational fluid dynamics of the unsteady Reynolds-averaged Navier-Stokes and the continuity equations with the Baldwin-Lomax turbulence model, exact nonlinear kinematic and approximate dynamic free-surface boundary conditions, and a body/free-surface conforming grid. The flow conditions and uncertainty analysis are discussed. A topological rule for a surface-piercing body is derived and verified. Steady-flow results are presented and analyzed with regard to the wave and viscous flow and the nature of the separation.

Introduction

Free-surface wave-induced separation (i.e., separation solely due to free-surface wave-induced effects) involves the complexities of free-surface deformations, vorticity, and turbulence in addition to the already formidable subject of 3-D boundary-layer separation. Such effects are a unique and poorly understood problem of ship and platform hydrodynamics due to wavemaking and/or ambient waves and are important with regard to ship performance and signatures and platform stability.

The phenomenon was first identified by Chow (1967) using vertical (surface-piercing) and horizontal (submerged) foils, which were designed for insignificant separation at large depths. It was also studied by Stern et al. (1989, 1993) using a foil-plate model (surface-piercing flat plate with attached wave-generating upstream horizontal submerged foil). These studies showed the dependence of the streamwise and depthwise extent of the separation region on Froude number (Fr) and wave steepness and that the transverse extent is wedge shaped with significant free-surface vorticity and turbulence. Stern et al. (1986, 1989, 1993) additionally obtained computational fluid dynamics (CFD) solutions for a Stokes-wave/flat-plate flow, which simulates the experimental geometry. In comparison to the experimental data, the extent is grossly over/under predicted for the laminar/turbulent solutions. However, the computed separation region is qualitatively similar and indicates a saddle point of separation and a nodal point of attachment on the plate and the free-surface, respectively, and associated vortical flow. Beaver (1991) and Pogozelski et al. (1994) also performed experimental studies for surface-piercing foils, however, their focus was on bow flow and yaw effects, respectively. Also of relevance, are other studies on steady and unsteady 3-D separation and wave breaking.

The present project was initiated specifically to study free-surface wave-induced separation through CFD and towing-tank experiments for a surface-piercing NACA 0024 foil (Fig. 1). As with Chow's foil, the NACA 0024 foil has insignificant separation at large depths. The approach is a combined effort whereby the CFD and experiments provide cross guidance for development and validation. This paper solely concerns the CFD, as the experiments are in progress, although some preliminary data are included.

In the following, descriptions are provided of the computational method, conditions, and uncertainty analysis. A topological rule for a surface-piercing body is derived. Then, results are presented for both zero and nonzero Fr. The approach of Chapman and Yates (1991) for describing 3-D separation is used in conjunction with the TOPO module of the FAST flow visualization program (Globus et al., 1991) to facilitate the analysis.

Computational Method

The CFD method is the method of Tahara and Stern (1994a) for solving the Reynolds-averaged Navier-Stokes (RANS) and continuity equations with the Baldwin-Lomax turbulence model, exact nonlinear kinematic and approximate dynamic free-surface boundary conditions, and a body/free-surface conforming grid. The method was shown to be one of the best at the recent CFD Tokyo Workshop (1994). The workshop indicated that the status of CFD for ship hydrodynamics is such that the steady resistance and flow are nearly at the accuracy of the data, although certain detailed flow features of the wave pattern and viscous flow are inadequately resolved, indicating the need for improvements in both numerics (iterative and grid convergence and accuracy) and modeling (geometry, turbulence model, and free-surface boundary conditions). Such improvements are expected to follow in conjunction with extensions for applications to more complex flows and, in particular, unsteady flows. Herein, the method is further assessed through the present application of steady free-surface wave-induced separation. We recognize the shortcomings of the Baldwin-Lomax turbulence model for separated flows. However, its use is justified by the combination of lack of knowledge and complexity of the present problem and that there is no accepted alternative. Also, unsteady-flow effects are important and under investigation, but beyond the scope of the present paper.

The method is based on modifications and extensions of the precursory interactive approach of Tahara et al. (1992) and Tahara and Stern (1994b). The core viscous-flow solver is based on Chen and Patel (1989, 1990) which has been validated for a variety of benchmark cases and applications. Stern et al. (1996) provide a detailed description, including extensions for naval combatants with bulbous bows and transom sterns utilizing multi-block domain decomposition and propeller-hull interaction utilizing the method of Stern et al. (1994). The following provides a summary.

The unsteady RANS and continuity equations are transformed from Cartesian coordinates (X, Y, Z) in the physical domain to numerically-generated, boundary-fitted, nonorthogonal, curvilinear coordinates (ξ, η, ζ) in the computational domain. A partial transformation is used, i.e., coordinates but not velocity components (U, V, W). The equations are solved using a regular grid, finite-analytic spatial and first-order backward difference temporal discretization, PISO-type pressure (P) al-

---

[1] Currently project engineer at Neural Applications Corporation, 2600 Cross Park Rd, Oakdale Research Park, Coralville, Iowa 52241-3212.

Contributed by the Fluids Engineering Division for publication in the JOURNAL OF FLUIDS ENGINEERING. Manuscript received by the Fluids Engineering Division August 1, 1995; revised manuscript received May 14, 1996. Associate Technical Editor: D. P. Telionis.

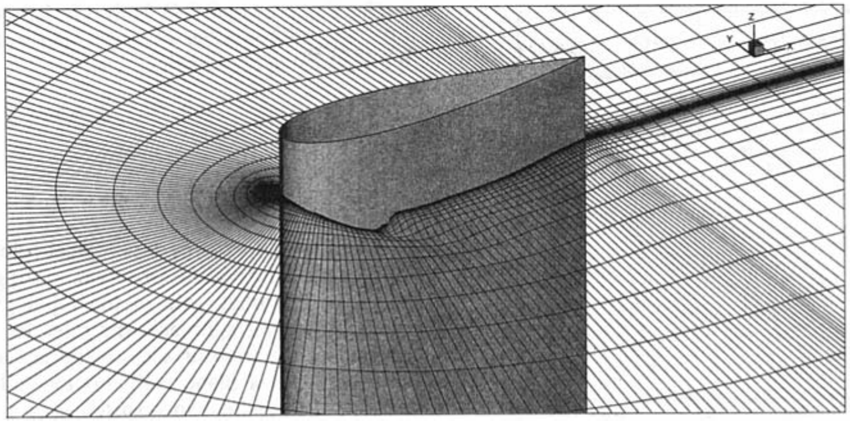

Fig. 1 Surface-piercing NACA 0024 foil: Fr = 0.37, free-surface conforming grid

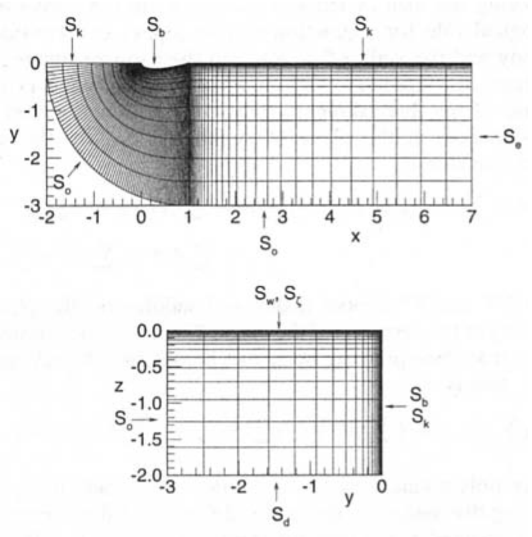

Fig. 2 Half-solution domain

gorithm, and the method of lines. For steady flow, time serves as a convergence parameter and the grid is updated at each time step to conform to both the body and free surface.

It was only possible to obtain steady solutions when a half solution domain was used, which apparently is equivalent to a splitter plate. Referring to Fig. 2, the specified boundaries are the body surface S_b, the exit plane S_e, the symmetry plane S_k, the outer boundary S_o, the deep boundary S_d, and the free-surface S_ζ (or simply ζ) which for zero Fr becomes the symmetry waterplane S_w. The boundary conditions for zero Fr are: on S_b, $(U, V, W) = \partial P/\partial n = 0$ (where n is normal to the body); on S_e, axial diffusion and pressure gradient are assumed negligible, i.e., $\partial^2 (U, V, W)/\partial X^2 = \partial P/\partial X = 0$; on S_k, $\partial(U, W, P)/\partial Y = V = 0$; on S_w and S_d, $\partial(U, V, P)/\partial Z = W = 0$; and on S_o, $U = U_\infty$, $W = \partial P/\partial n = 0$ (where n is normal to the surface), and V is determined from the continuity condition. For nonzero Fr, the boundary conditions are similar, except on S_ζ, where exact nonlinear kinematic and approximate dynamic free-surface conditions are applied on the exact free surface, which is determined as part of the solution; i.e., the dynamic conditions $\partial(U, V, W)/\partial Z = 0$ and $P = \zeta/\mathrm{Fr}^2$ are applied to velocity and pressure with ζ determined through the solution of the exact nonlinear kinematic condition using a Beam and Warming linear multi-step scheme with both explicit and implicit 4th-order artificial dissipation and local time stepping based on the local velocity magnitude. The boundary conditions for ζ are: on S_o, $\partial\zeta/\partial n = 0$; and on S_e, $\partial\zeta/\partial X = 0$.

The grids are obtained using both elliptic and algebraic methods. A base body-conforming C-grid is generated using a 2-D elliptic method, which includes the geometry above the waterplane S_w. Subsequent body/free-surface conforming grids are constructed utilizing the 2-D base grids at each ξ, $\zeta(x, y, t)$ solution, ζ-coordinate interpolation, and stacking to form the complete 3-D grid. In order to accurately compute the free-surface elevation, finer grids are generated on the free surface and used in the solution of the kinematic condition, such that the numbers of grid points are doubled in the ξ and η directions, and linear interpolation is used to transfer information between the free-surface and viscous grids.

Conditions and Uncertainty Analysis

The conditions simulate the experiments, i.e., Fr = (0.2, 0.37, 0.55) and the corresponding Re = $(0.822, 1.52, 2.26) \times 10^6$. Additionally, a zero Fr solution was obtained, which is equiva-

Nomenclature

C_{dp} = pressure drag coefficient
C_{dt} = drag coefficient
C_f = frictional drag coefficient
C_p = pressure coefficient
Fr = Froude number, $U_\infty/\sqrt{gL}$
L = characteristic length (foil chord length)
N = node
N_a = node of attachment
N_s = node of separation
P = pressure
q_x, q_y, q_z = vorticity-flux components in Cartesian coordinates
Re = Reynolds number, $U_\infty L/v$
S = saddle
S_a = saddle of attachment
S_s = saddle of separation
U_∞ = freestream velocity
U, V, W = velocity components in Cartesian coordinates
$x, y, z; (X, Y, Z)$ = Cartesian coordinates
U_τ = wall-shear velocity, $U_\tau = \sqrt{\tau_w/\rho}$
y^+ = near-wall spacing, $y^+ = \dfrac{yU_\tau}{v}$
ϵ = grid-convergence parameter
ξ, η, ζ = transformed coordinates
$\omega_x, \omega_y, \omega_z$ = vorticity components
τ_w = wall shear stress

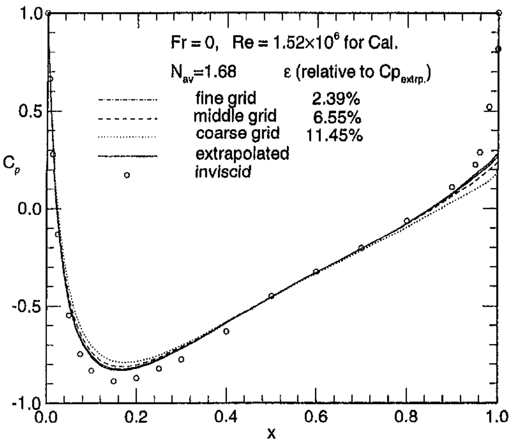

Fig. 3 Surface pressure: Fr = 0

lent to the deep solutions for nonzero Fr. The grids used are discussed next in conjunction with uncertainty analysis. The ASME guidelines for numerical uncertainty (Freitas, 1993) are observed through iterative and grid convergence tests and an order-of-accuracy study. Note that the derivation of the finite-analytic method precludes term-by-term error analysis and that equation error depends on both cell Re and aspect ratio. Iterative convergence was established for all cases by reduction of the residuals by at least three orders of magnitude to $10^{-6}/10^{-5}$ taking $10^3/10^4$ iterations for zero and nonzero Fr, respectively. Grid convergence tests were done for (Fr, Re) = $(0, 1.52 \times 10^6)$. Grid convergent solutions (i.e., solution differences $\epsilon \leq 2\%$) were obtained for: 111×30 grid points; with body boundary-layer and wake and leading- and trailing-edge clustering; aspect ratio = 100–450; and near-wall spacing $y^+ < 5$. On this basis, three grids were selected for Richardson's extrapolation for determination of the spatial order n and $3n$ benchmark solution under the assumption of equal dimensional spatial order (i.e., only three grids were used). Unfortunately, the result was problematic in that the entire solution did not display asymptotic limit behavior (i.e., monotonically decreasing ϵ), e.g., the surface pressure (Fig. 3) and (C_{dt}, C_{dp}) indicated $n = 1.68$ and (1.4, 1.1), respectively, whereas C_f indicated monotonically increasing ϵ. However, as already noted, for noninteger refinement and decreasing y^+, U_τ indicated monotonic convergence with $\epsilon \leq 2$ percent. Analysis for laminar flat-plate boundary layer and fully developed annular flow with $\mathrm{Re} = 10^3 - 10^4$ and uniform grids with aspect ratio $= 5 - 112$ indicates $n = 1.5 - 2.5$. The Fr = (0.2, 0.37, 0.55) solution grids were similar to that described above, but with $111 \times 30 \times 20$ points, near free-surface stretching, and $y^+ = (3, 5, 8)$, respectively. The calculations were performed on C90 supercomputers and required 2.55 sec CPU per time step and 8 MW (mega words), with an efficiency of 200 MFLOPS.

Topological Rule for a Surface-Piercing Body

Topological study has played an important role in the analysis of separated flows. The theories of topology provide the rules which apply to flows that are kinematically possible. Several rules for skin-friction lines have been established which apply to different flow-geometry configurations. Tobak and Peak (1982) summarized the following rules:

(a) For an isolated closed 3-D body:

$$\sum N - \sum S = 2 \tag{1}$$

where N and S and ΣN and ΣS denote single and total number of nodes and saddles, respectively.

(b) For a closed 3-D body (B) connected to a plane wall (P), the total number of nodes and saddles on the body and the wall ($P + B$) satisfies:

$$(\sum N - \sum S)_{P+B} = 0 \tag{2}$$

or

$$(\sum N + 2) - \sum S = 2. \tag{3}$$

There are no existing topological rules for a free surface or surface-piercing bodies. Observation suggests that a free surface plays an important role in the topological structure of such flows. As a first approach, the rules for skin-friction lines are applied to the free-surface streamlines and the free surface is considered as a plane wall topologically. These assumptions remove the apparent inconsistency of combining the free-surface and body-surface streamline vector fields. Since the body goes to infinity at the deep end, the topological rule can be deduced by introducing a plane of symmetry at the deep end [following the idea of Hunt et al. (1978) in the derivation of topological rule for a junction of two pipes] and considering the body and the wall, $(B + P)$, and their mirror image about the plane of symmetry, $(B' + P')$, as a closed 3-D body. Because of the three dimensionality of the flow, saddles and/or nodes exist at the plane of symmetry. So, for the whole system, the rule is:

$$\begin{aligned}[(\sum N - \sum S)_{P+B} + 2] + [(\sum N - \sum S)_{P+B} + 2]_{\text{image}}& \\ + \sum N^* - \sum S^* = 2& \end{aligned} \tag{4}$$

where N^* and S^* denote nodes and saddles on the plane of symmetry at the deep end of the body. Therefore, the topological rule for a surface-piercing body can be obtained by taking half of (4), that is:

$$(\sum N_{P+B} + \tfrac{1}{2} \sum N^*) - (\sum S_{P+B} + \tfrac{1}{2} \sum S^*) = -1 \tag{5}$$

Since only a half domain is calculated for steady flow, in the following discussion, nodes and saddles not at the center plane will be counted twice without further explanation. Also, note that some node-saddle-node (N-S-N) and/or saddle-node-saddle (S-N-S) combinations are so clustered that it is difficult to distinguish among them. In this case, they are considered as one node and/or saddle, respectively, from the point of view of a larger scale. This normally will not cause difficulties in the study of topological structure of the flow (Chapman and Yates, 1991).

Solutions and Discussions

Fr = 0. Figure 3 provides a comparison of the surface pressure with the inviscid solution. The C_p values are nearly the same as the inviscid theory, but with reduced pressure minimum and elimination of the erroneous trailing-edge stagnation point. Included are all three solutions used for Richardson's extrapolation and the extrapolated benchmark. The wall-shear stress is consistent with expectation, although a small region of separation over the last 3 percent L is present (refer to deep solutions for nonzero Fr). Fig. 4(a) presents the drag coefficients for the Fr = 0 solution. Since no data for NACA 0024 is available, comparison is made with NACA 0025 and 0012 data, (Hoerner, 1951). The frictional drag coefficient C_f decreases with Re; the pressure drag coefficient C_{dp} shows a small increase with Re; and the total drag coefficient shows a mild decrease with Re due to the combined effects of the C_f(Re) decrease and C_{dp}(Re) increase. The C_{dt} values are between those for the NACA 0025 and 0012 data; however, the rate of decrease with Re is larger than indicated by the data.

The flow has no significant separation: it attaches to the foil along a line of attachment at the leading edge and leaves the

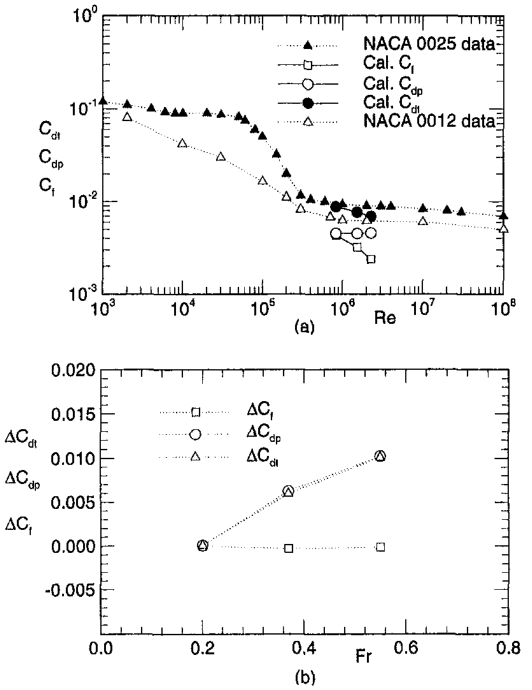

(a)

(b)

Fig. 4 Drag coefficients

surface along a line of separation at the trailing edge. However, for the purpose of topological description, only one point on the attachment/separation line is designated as the node of attachment/separation, respectively. Corresponding to the node of attachment and node of separation, there are two saddles on the free surface (at the leading and trailing edges) and two saddles at the deep end [refer to Fig. 9(*a*), the topological structure of Fr = 0.20]. The entire pattern satisfies (5).

Fr = 0.20, 0.37, and 0.55. For the nonzero Fr cases, in order to show the wave effects on the global parameters of the flow, Fig. 4(*b*) presents both the pressure and frictional drag difference coefficients, which are obtained by subtracting the deep solution. As Fr increases, the pressure drag coefficient increases due to the effects of the bow wave. The frictional drag coefficient, on the other hand, decreases as Fr increases from 0.2 to 0.37 and then increases a little as Fr increases further to 0.55, which is consistent with the size changes of the separation region.

Figure 5 shows the wave profiles along the body and comparison with preliminary experimental data. The CFD solutions show several important features of the profiles. At Fr = 0.2, the wave profile is similar to a typical ship wave profile and the wave length is slightly greater than the wave length given by Kelvin wave theory ($\lambda = 2\pi\ \mathrm{Fr}^2$). At Fr = 0.37 and 0.55 separation occurs for $x < \lambda$ and the wave profiles are different from those of ships. The wave profile is relatively flat in the separation region and the flat region is smaller for Fr = 0.55 than Fr = 0.37. Data are shown for both low and high Re, with the latter corresponding to the conditions of the CFD. For Fr = 0.2, the wave profile shows very close agreement with the data and the data shows no Re dependence. For Fr = 0.37 and 0.55, the CFD solutions are qualitatively similar with the data; however, the agreement is better with the low Re data. The minimum/maximum amplitudes in the separation region shown for the Fr = 0.37 and 0.55 data indicate the degree of unsteady effects. The bow-wave peak for Fr = 0.37 and 0.55 are 6.2 percent L and 14 percent L, respectively.

Figure 6 shows the free-surface perspective view with the wave elevation enlarged by 5. For Fr = 0.2, the perspective view of the free surface shows a pattern which is similar to ship flow. For Fr = 0.37, it shows a different wave system from that of the low Fr case. The bow wave becomes more significant; the wave steepness is larger; and the free-surface is relatively flat in the separation region, except for depressions near the vortex cores. For Fr = 0.55, the free-surface has an even more complicated wave system, with increases in bow-wave peak, wave steepness, and distortion of the free surface in the separation region.

The body-surface pressure and wall-shear stress contours are presented in Figs. 7 and 8, respectively. The separation region is shown by the negative wall-shear stress values. For Fr = 0.20, the wave effects are limited to a region very close to the free surface and the separation region is very small. The flow recovers to 2-D at about $z = -0.3$. For Fr = 0.37, the wave effects become strong, extend to about $z = -1$, and the separation region at free surface is about 78 percent L. For Fr = 0.55, the wave effects become even stronger and extend to about $z = -1.2$. The separation region is about 54 percent L, which is smaller than Fr = 0.37 since the point of separation is pushed down stream. For all the three Fr, the deep solution pressure shows agreement with the Fr = 0 solution. They also all indicate no significant separation at the deep end.

Figures 9(*a–c*) are sketches of the topological structure of the flow and are based on examination of the flow as per, e.g., Figs. 10, 11, and 12. Figure 10 shows an example of the body skin-friction lines and the free-surface streamlines. Figure 11 shows the cross section vectors in three planes. Figure 12 presents the vortex cores and focal points obtained by the FAST analysis.

For Fr = 0.2 (Fig. 9(*a*)), although the separation region is relatively small, it shows a different topological structure from Fr = 0. The flow still attaches to the foil along the node line, but the line of attachment in Fr = 0 bifurcates into a node of attachment (N1) at $z = -.03$ on the body surface and a saddle of attachment (S1) at the juncture of the free surface and body

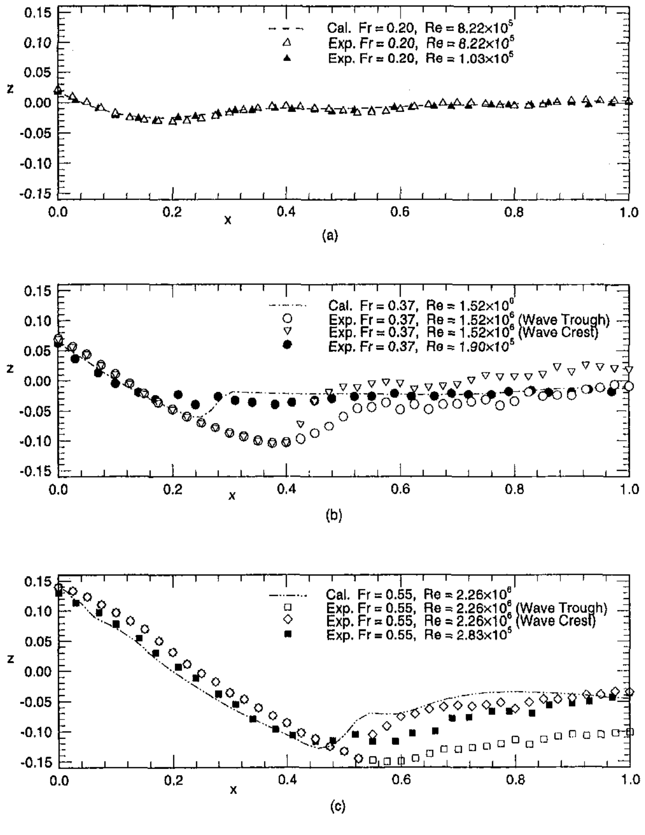

(a)

(b)

(c)

Fig. 5 Wave profiles: (*a*) Fr = 0.20, (*b*) Fr = 0.37, and (*c*) Fr = 0.55

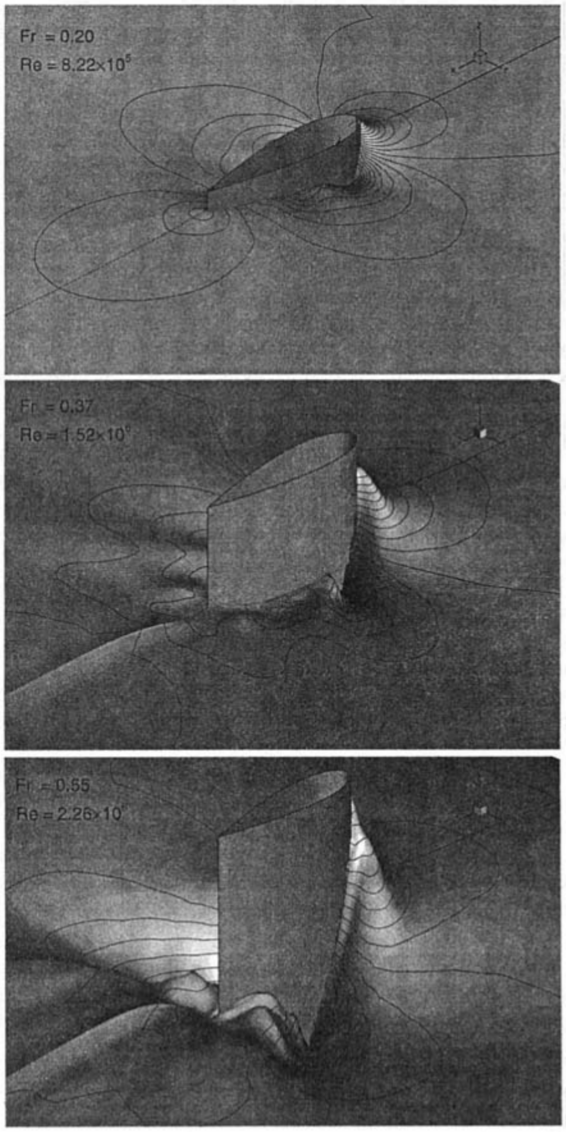

Fig. 6 Free-surface perspective view

surface. The flow that reaches the body above the nodal point will have a positive vertical velocity component; it goes upward to the free surface and forms the bow wave and the saddle (S1). The flow that reaches the body below this node (N1) will have a negative vertical velocity component, which decreases with depth and tends to zero at the deep end.

The flow is attached to the foil for more than 95 percent of the foil surface. It separates at the saddle of separation (S2) at $x = 0.94$ on the free surface, and the separation region extends downward to $z = -0.04$. On the free surface, the separated flow forms a tiny recirculation region, which extends to $x = 1.02$, where another saddle point (S3) is located. On the body surface, associated with the saddle of separation (S2), there is a saddle-node-saddle combination, where flow from the saddle points are attracted toward the node (N2) and leaves the surface at this nodal point to form the recirculating flow. There is another node (N4) at $x = 0.96$, $z = -0.2$, due to the bifurcation of the line of separation in Fr = 0 into a $N_s - S_s - N_s - S_s$ combination near the trailing edge. In general, the whole separation region is very small in scale and has no significant effect on the whole flow field. There are five nodes and three saddles on the body surface, two nodes and four saddles on the free surface, and two saddles at the deep end; the entire pattern satisfies (5).

For Fr = 0.37 (Fig. 9(*b*)), the topological structure of the flow is significantly different from that of the low Fr case. The flow still attaches to the foil in a similar pattern as in Fr = 0.20 case, but since the wave effect is stronger, the saddle point (S1) at the foil/free-surface juncture goes off the body to about $x = -0.02$ on the free-surface. Correspondingly, the node of attachment (N1) goes downward to $z = -0.12$. A bow vortex (also called a necklace vortex) is formed in this node-saddle region and it goes downstream along the body before the flow separates.

The flow is attached to the foil until it reaches the saddle point (S2) at $x = 0.22$. The separatrix of this saddle point forms the boundary of the separation region on the free surface. Below the free surface, the flow separates along the line of separation (separatrix), which emanates from the saddle of separation (S2). This line of separation goes downstream toward the trailing edge as well as toward the deep end; before reaching the trailing edge, it turns to form a node of separation (N2) at $x = 0.98$, $z = -0.22$. The extension of the separation lines on the free surface and foil surface toward the off body 3-D flow forms a separation surface which envelops the recirculation region. Near the trailing edge, flow from the non-separated region is attracted into the separation region by the node of separation (N2). The whole recirculation region extends to $x = 1.3$ in the wake, where there is a node of attachment (N5) to the free surface. Near this node of attachment, flow from the upstream and below the free surface is entrained toward the free surface and it rolls up to form two vortices; one goes downstream into the far wake and the other goes upstream to join the recirculating flow. The flow driven by this upstream going vortex rolls up again before it reaches the separation surface and forms another

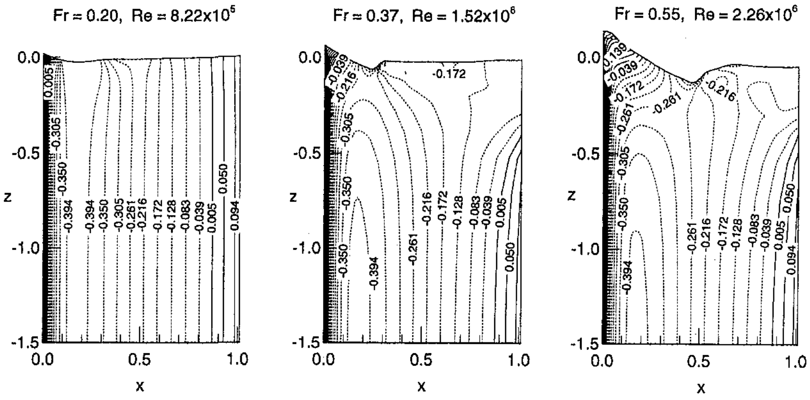

Fig. 7 Body-surface pressure contours

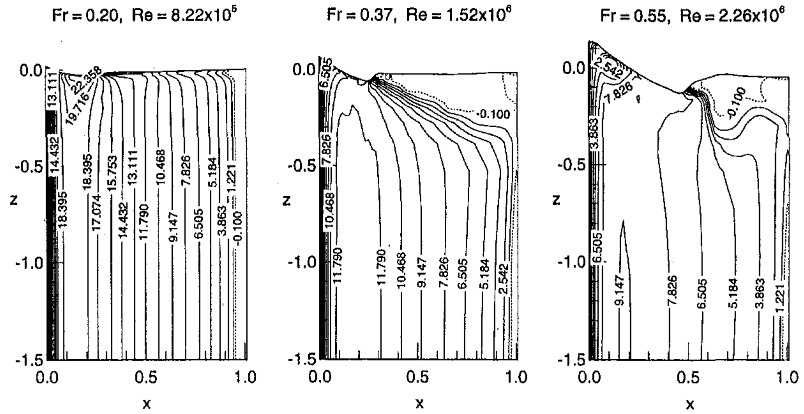

Fig. 8 Wall-shear stress contours

vortex, which is considered the major (in scale) vortex of this flow. This major vortex drives flow upward to the free surface.

In the separation region, at $x = 0.82$, $z = -0.21$ on the body surface, there is another saddle (S3), and another node (N3) associated with this saddle. A part of the flow entrained toward the foil from the wake by the upstream going vortex leaves the body surface at this saddle-node region and forms a secondary separation, which results in a minor (in scale) vortex off the body surface. The saddle point from which the secondary separation originates also affects the formation of the major vortex. It divides the major vortex into two parts; the upper part goes upward to the free surface and the lower part goes back into the recirculation region in the wake. On the free surface, the flow is mainly entrained toward the free surface in the separation region, but, part of it will be entrained back to the recirculation region; the rest will go to the wake.

In general, at Fr = 0.37, separation is very significant both in scale and influence on the whole flow field. On the free surface the separation region is about 78 percent L, and it extends to $z = -0.25$ to the deep end. There are five saddles and three nodes on the free surface, five nodes and three saddles on the body surface, and two saddles at the deep end of the foil; the entire pattern satisfies (5).

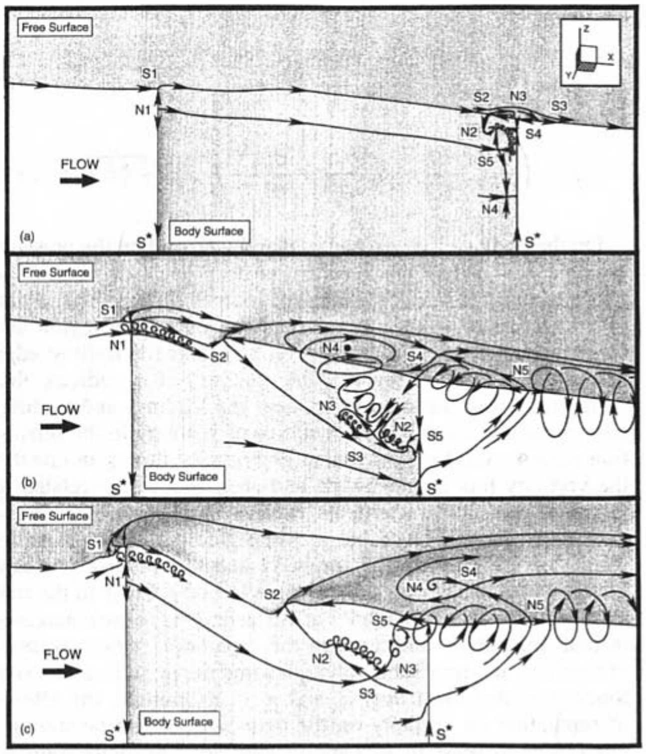

Fig. 9 Topological structures: (a) Fr = 0.20, (b) Fr = 0.37, and (c) Fr = 0.55

For Fr = 0.55, Fig. 9(c), the topological structure has some common features as well as differences as compared with the Fr = 0.37 case. The flow still attaches to the foil with a combination of $N_a - S_a$ and a bow vortex; this is very similar as in Fr = 0.37. The effect of high Fr forces the saddle of attachment (S1) further upstream to about $x = -0.10$ and the node of attachment (N1) further downward to $z = -0.16$. On the free surface, the separation point (S2) moves further downstream to $x = 0.54$ and the separation region is smaller than Fr = 0.37. On the body surface, the flow separates along the separatrix (line of separation) of this saddle of separation. This line of separation turns as it goes downstream and deep and it forms a node of separation (N2) at $x = 0.67$ and $z = -0.16$. This node of separation attracts flow from the surrounding region along the body surface and the flow leaves the surface at this point into the recirculation region. Below and downstream of this point there is a saddle of separation (S3) at $x = 0.76$, $z = -0.24$. Flow leaves the foil surface along the separatrix of this saddle point. Very similar as in the Fr = 0.37 case, there is a node point (N5) at $x = 1.3$ on the free surface. This node of attachment on the free surface attracts flow toward the free surface. Before flow reaches the free surface it rolls up to form two vortices; one goes to the wake and the other goes upstream into the recirculation region. The upstream going vortex attracts flow from the saddle of separation (S2) and the free surface and then the flow reattaches to the foil at a node of attachment (N3) at $x = 0.93$, $z = -0.15$. The flow attached to this nodal point will go to the node of separation (N2), the saddle of separation (S3), and the free surface.

Since the separation point is pushed down stream by the high Fr effect, the upward flow entrainment to the free surface is not as strong as the Fr = 0.37 case in the afterbody region and no corresponding vortex is observed in the flow field. However, on the free surface, the topological pattern is very close to Fr = 0.37 case. There are three nodes and five saddles on the free surface, five nodes and three saddles on the body surface, and two saddles at the deep end; the entire pattern satisfies (5).

Also presented and discussed are the vorticity and vorticity flux on the body and free surface for Fr = 0.37 (Figs. 13 and 14), which provides additional insight on wave and separation effects on vorticity. Vorticity flux is defined in analogy to heat flux: $q_i = -n_j\,(\partial \omega_i/\partial x_j)$, where positive and negative values correspond to vorticity sinks and sources, respectively. The three components of vorticity flux in Cartesian coordinates are: on the body surface,

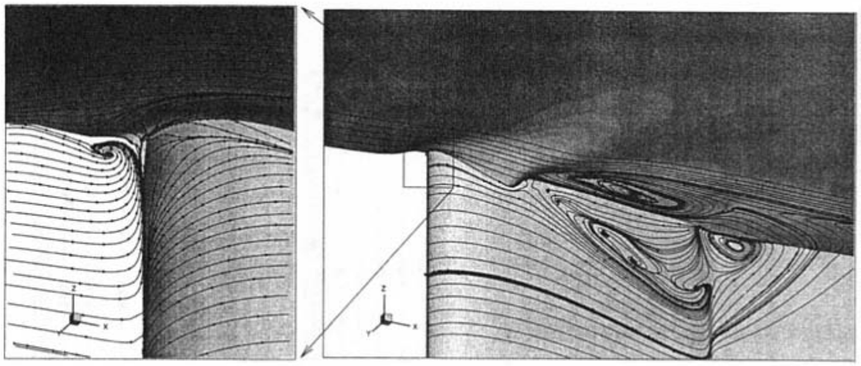

Fig. 10 Body-surface skin-friction lines and free-surface streamlines

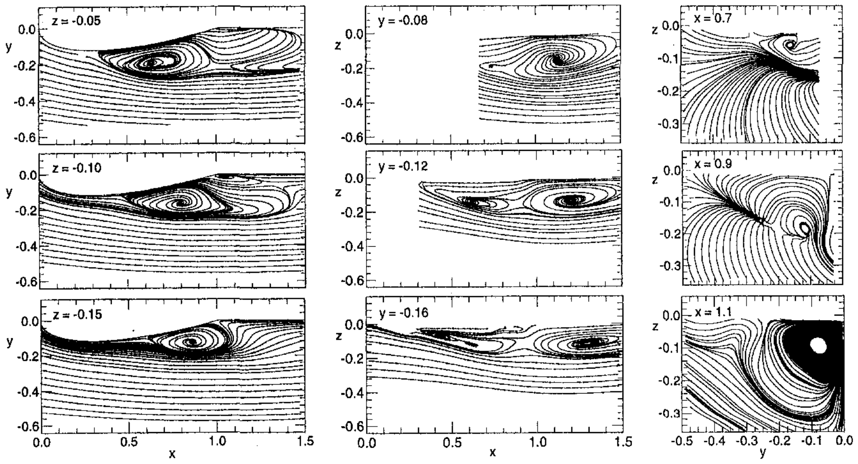

(a)

(b)

(c)

Fig. 11 Cross section vectors: (*a*) *X*-*Y* section, (*b*) *X*-*Z* section, and (*c*) *Y*-*Z* section

$$q_x = -\frac{\mathrm{Re}P_z}{\sqrt{\eta_x^2 + 1}} \tag{6}$$

$$q_y = -\frac{\mathrm{Re}P_z\eta_x}{\sqrt{\eta_x^2 + 1}} \tag{7}$$

$$q_z = -\frac{\mathrm{Re}}{\sqrt{\eta_x^2 + 1}}(\eta_x P_y - P_x) \tag{8}$$

and on the free surface,

$$q_x = \left(-\zeta_x\frac{\partial\omega_x}{\partial x} - \zeta_y\frac{\partial\omega_x}{\partial_y} + \frac{\partial\omega_x}{\partial z}\right)\Big/\sqrt{\zeta_x^2 + \zeta_y^2 + 1} \tag{9}$$

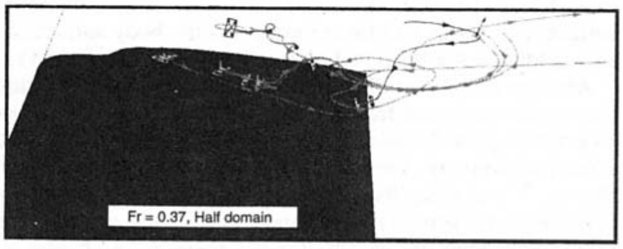

Fig. 12 Result from FAST analysis: vortex cores and focal points

$$q_y = \left(-\zeta_x\frac{\partial\omega_y}{\partial_x} - \zeta_y\frac{\partial\omega_y}{\partial_y} + \frac{\partial\omega_y}{\partial_z}\right)\Big/\sqrt{\zeta_x^2 + \zeta_y^2 + 1} \tag{10}$$

$$q_z = \left(-\zeta_x\frac{\partial\omega_z}{\partial_x} - \zeta_y\frac{\partial\omega_z}{\partial_y} + \frac{\partial\omega_z}{\partial_z}\right)\Big/\sqrt{\zeta_x^2 + \zeta_y^2 + 1}. \tag{11}$$

On the body surface, q_x and q_y mainly depend on the pressure gradient p_z, so they are zero at the deep end, where $p_z = 0$. Close to the free surface, there are sources of ω_x in the region of $x < 0.5$, $z > -0.3$ and a part of the separation region and sinks near the saddle of separation and near the trailing edge below the separation region. The contours of q_y indicate that there are two major sinks of ω_y near the leading- and trailing-edge areas and a small area of source of vorticity in the separation region. Another component of vorticity flux q_z dominates the vorticity flux in magnitude and area. Since q_z is related to the axial pressure gradient, its value is significant even at the deep end, where a favorable pressure gradient causes a strong source of vorticity on the forebody and the adverse pressure gradient causes a strong sink on the afterbody. Close to the free surface, the source of vorticity in the leading-edge area increases in both magnitude and area; in the separation region, sources of vorticity are dominant, although some minor sinks also exist. Since q_z is dominant over q_x and q_y in magnitude, the effects of separation on vorticity on the body surface can be summarized as an increase in area and magnitude of vorticity sources.

On the free surface, the vorticity-flux contours show a source of ω_x on the forebody and mainly sinks in the separation region.

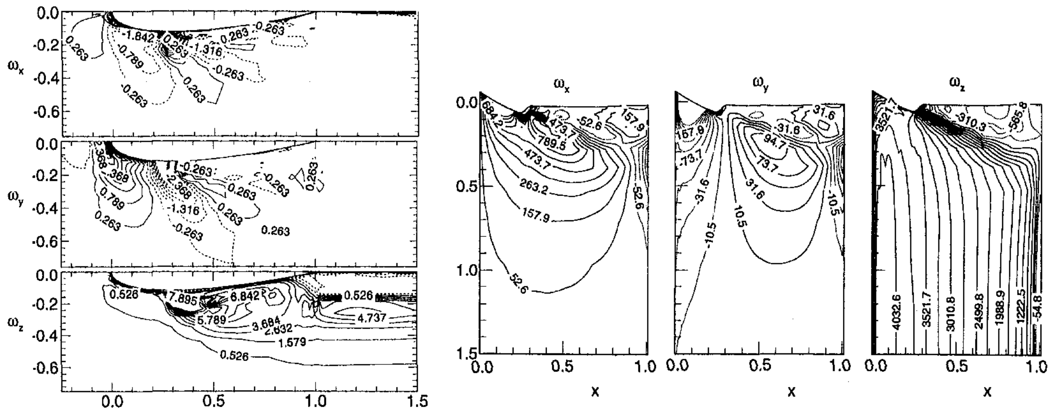

(a)

(b)

Fig. 13 Vorticity contours on (*a*) free-surface and (*b*) body surface, Fr = 0.37

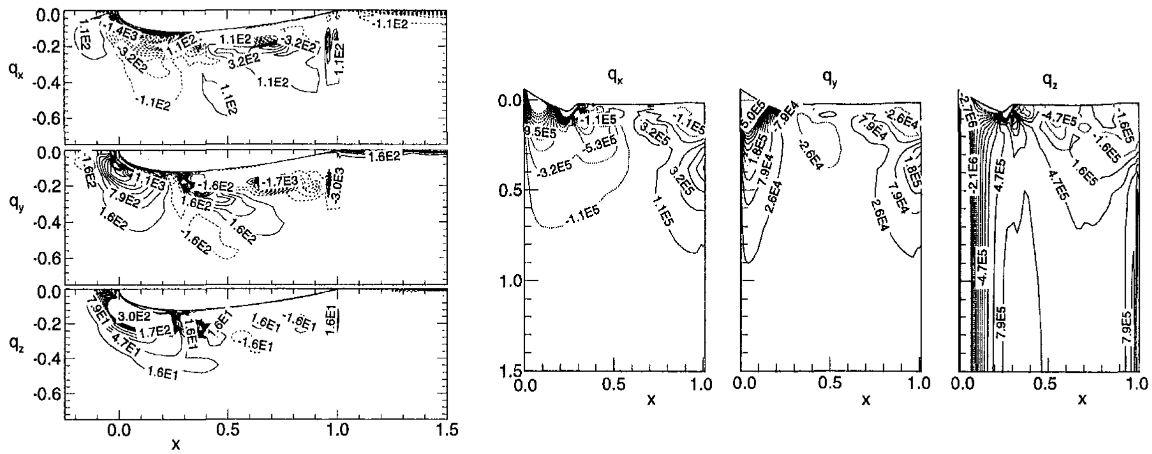

(a)

(b)

Fig. 14 Vorticity-flux contours on (*a*) free-surface and (*b*) body surface, Fr = 0.37

The contours of q_y show sinks of ω_y on the free surface and a very small region of sources in the separation region. The q_z contours indicate sinks of vorticity over most parts of the free surface. In general, the free surface is a sink of vorticity; the vorticity generated at the body surface fluxes into the free surface. However, the magnitude of the vorticity generation on the body surface is much larger than that of the vorticity flux into the free surface, so the rest of vorticity goes into the wake. It should be noted that the approximations made in the free-surface boundary conditions (i.e., $U_z = 0$ and $V_z = 0$) introduces uncertainty in the vorticity components ω_x and ω_y at the free surface and therefore to the vorticity fluxes. More detailed investigation is needed to determine the nature and magnitude of this uncertainty.

Concluding Remarks

Free-surface wave-induced separation is studied for a surface-piercing NACA 0024 foil over a range of Fr through CFD of the unsteady RANS and continuity equations with the Baldwin-Lomax turbulence model, exact nonlinear kinematic and approximate dynamic free-surface boundary conditions and a body/free-surface conforming grid. Uncertainty analysis is discussed through iterative and grid convergence tests and an order-of-accuracy study. The topological rule for a surface-piercing body is derived and verified. Zero and nonzero Fr flow results are presented and analyzed with regard to the wave and viscous flow and nature of the separation.

The study indicates that a surface-piercing NACA 0024 foil facilitates isolation of free-surface wave-induced separation with a scale sufficient for detailed CFD and experimental analysis. The drag coefficients, free-surface waves, and the separation patterns are all Fr dependent. The bow-wave peak increases with Fr and the separation region increases as Fr increases from small (0.20) to medium (0.37) and then decreases as Fr increases further to high (0.55). Associated with the wave pattern, the pressure drag coefficient increases with Fr and the frictional drag coefficient increases and then decreases with Fr as per the separation region. The separation region is relatively flat at medium Fr (0.37) and becomes highly distorted at high Fr (0.55). The separation pattern and vortex system are complicated and Fr dependent. For medium Fr (0.37), the flow has two major vortices in the separation region, one goes up to the free surface and the other goes downstream into the wake. There is also a secondary separation and associated vortices but the scale is much smaller. The free surface is mainly a sink of vorticity. A part of the vorticity generated at the body surface fluxes up into the free surface and the rest goes to the wake. This study also shows that the flow is naturally unsteady for higher Fr and the steady-state solution can be obtained only when a half domain is used with a symmetry boundary condition on the center plane.

The study is useful both in providing insight on this complicated problem and for guidance of the experiments. However, there are several uncertainty issues which need to be addressed in future work. The numerical uncertainties are relatively small in comparison to the modeling uncertainties such that future work should focus on the latter. First, more study is needed to evaluate the performance of a hierarchy of turbulence models for prediction of free-surface wave-induced separated flows. Second, more study is needed in the determination of the inaccuracy of the approximations used for the free-surface boundary conditions and further developments for more accurate treatments. Third, in order to understand the unsteady-flow effects, further CFD study is needed to obtain time-accurate unsteady solutions. Meanwhile, experimental data is required to validate the CFD. Finally, more mathematical study is required for validation of the topological rule.

Acknowledgments

This research was sponsored by the Office of Naval Research under grant N00014-92-K-1092 under the administration of E. P. Rood. The computations were performed on the NAS and POPS C90 super computers. The first author would like to thank Dr. Yusuke Tahara, now of the University of Osaka Prefecture, Japan, for his valuable guidance at the early stage of this study. The paper is dedicated to L. Landweber to whom so many of us are indebted for his deep physical and analytical understanding of ship hydrodynamics and generous mentoring.

References

Beaver, W. E., 1991, "PACT Surface Piercing Foil Experiments - Experiment Description and Force Data," DTRC Report, DTRC/SHD-1358-01, Apr.

CFD Workshop Tokyo, *Proceedings Vol. 1 and 2,* Ship Research Institute Ministry of Transport Ship & Ocean Foundation, 22–24 Mar. 1994.

Chapman, G. T., and Yates, L. A., 1991, "Topology of Flow Separation on Three-dimensional Bodies," *Applied Mechanics Review,* Vol. 44, No. 7, July, pp. 329–345.

Chen, H. C., and Patel, V. C., 1989, "The Flow Around Wing-body Junctions," *4th Symp. Num. Phys. Aspects Aerodyn. Flows,* Long Beach, CA.

Chen, H. C., and Patel, V. C., 1990, "Solutions of Reynolds-Averaged Navier-Stokes Equations for Three-Dimensional Incompressible Flows," *Journal of Computational Physics,* Vol. 88, No. 2, pp. 305–335.

Choi, J.-E., and Stern, F., 1993, "Solid-Fluid Juncture Boundary Layer and Wake With Waves," *Proc. 6th International Conference on Numerical Ship Hydrodynamics,* Iowa City, IA, Aug., pp. 215–238.

Chow, S. K., 1967, "Free-Surface Effects on Boundary-Layer Separation on Vertical Struts," Ph.D. thesis, The University of Iowa, Iowa City, IA.

Freitas, C. J., 1993, "Editorial Policy Statement on the Control of Numerical Accuracy," ASME JOURNAL OF FLUIDS ENGINEERING, Vol. 115, pp. 339–340.

Globus, A., Levit, C., and Lasinski, T., 1991, "A Tool for Visualizing the Topology of Three-Dimensional Vector Fields," NASA Report, RNR-91-017, Apr.

Hoerner, S. F., *Aerodynamic Drag,* The Otterbein Press, Dayton, Ohio, 1951.

Hunt, C. R., Abell, C. J., Peterka, J. A., and Woo, H., 1978, "Kinematical Studies of the Flows Around Free or Surface-Mounted Obstacles; Applying Topology to Flow Visualization," *Journal of Fluid Mechanics,* Vol. 68, pp. 179–200.

Pogozelski, E., Katz, J., and Huang, T., 1994, "Flow Structure Around a Surface-Piercing Blunt Body," *Proc. 20th ONR Symposium on Naval Hydro.,* Santa Barbara, CA, Aug.

Stern, F., 1986, "Effects of Waves on the Boundary Layer of a Surface-Piercing Body," *Journal of Ship Research,* Vol. 30, No. 4, Dec., pp. 256–274.

Stern, F., Hwang, W. S., and Jaw, S. Y., 1989, "Effects of Waves on the Boundary Layer of a Surface-Piercing Flat Plate: Experiment and Theory," *Journal of Ship Research,* Vol. 33, No. 1, Mar., pp. 63–80.

Stern, F., Choi, J. E., and Hwang, W. S., 1993, "Effects of Waves on the Wake of a Surface-Piercing Flat Plate: Experiment and Theory," *Journal of Ship Research,* Vol. 37, No. 2, June, pp. 102–118.

Stern, F., Kim, H. T., Zhang, D. H., Toda, Y., Kerwin, J., and Jessup, S., 1994, "Computation of Viscous Flow Around Propeller-Body Configurations: Series 60 $C_B = 0.6$ Ship Model," *Journal of Ship Research,* Vol. 38, No. 2, June, pp. 137–157.

Stern, F., Paterson, E. G., and Tahara, Y., 1996, "CFDSHIP-IOWA: Computational Fluid Dynamics Method for Surface-Ship Boundary Layers and Wakes and Wave Fields," IIHR Report (in preparation), IIHR, The University of Iowa, Iowa City, Iowa.

Tahara, Y., Stern, F., and Rosen, B., 1992, "An Interactive Approach for Calculating Ship Boundary Layers and Wakes for Nonzero Froude Number," *Journal of Computational Physics,* Vol. 98, No. 1, Jan., pp. 33–53.

Tahara, Y. and Stern, F., March 1994a, "A Large-Domain Approach for Calculating Ship Boundary Layers and Wakes for Nonzero Froude Numbers," *Proc. CFD Workshop Tokyo 1994,* Vol. 1, Tokyo, Japan, pp. 45–55 (to appear *Journal of Computational Physics*).

Tahara, Y., and Stern, F., 1994b, "Validation of an Interactive Approach for Calculating Ship Boundary Layers and Wakes for Nonzero Froude Number," *Journal of Computers and Fluids,* Vol. 23, No. 6, pp. 785–816.

Tobak, M. and Peak, D. J., 1982, "Topology of 3D Separated Flows," *Annual Review of Fluid Mechanics,* Vol. 14, pp. 61–85.

Chao-Yi Chen
Research Fellow.

P. J. Kim
Graduate Student.

D. T. Walker
Assistant Professor.

Department of Naval Architecture
& Marine Engineering,
University of Michigan,
Ann Arbor, MI 48109-2145

Angular Bias Errors in Three-Component Laser Velocimeter Measurements

For three-component laser velocimeter systems, the change in projected area of the coincident measurement volume for different flow directions will introduce an 'angular' bias in naturally sampled data. In this study, the effect of turbulence level and orientation of the measurement volumes on angular bias errors was examined. The operation of a typical three-component laser velocimeter was simulated using a Monte Carlo technique. Results for the specific configuration examined show that for turbulence levels less than 10 percent no significant bias errors in the mean velocities will occur and errors in the root-mean-square (r.m.s.) velocities will be less than 3 percent for all orientations. For turbulence levels less than 30 percent, component mean velocity bias errors less than 5 percent of the mean velocity vector magnitude can be attained with proper orientation of the measurement volume; however, the r.m.s. velocities may be in error as much as 10 percent. For turbulence levels above 50 percent, there is no orientation which will yield accurate estimates of all three mean velocities; component mean velocity errors as large as 15 percent of the mean velocity vector magnitude may be encountered.

1 Introduction

In simple free shear layers, such as wakes and jets, there is a single dominant mean velocity component in the "streamwise" direction. The other two mean velocity components, the "secondary-flow" velocities, are typically an order of magnitude smaller than the streamwise mean velocity. The angular bias which is the subject of this study can introduce errors in the streamwise and secondary-flow mean velocities which are up to 10–15 percent of the mean streamwise velocity. As a result, the secondary flow velocities (which determine the flow pattern in the cross-flow plane) can be in error by more than 100 percent. Understanding the effects of this type of bias, and how to avoid them, can be critical to obtaining useful and reliable information from laser velocimeter measurements.

McLaughlin and Tiederman (1973) identified and defined the general category of statistical bias. They argued that the measurement rate $\dot{N}$ for a laser velocimeter is given by $\dot{N} = N'''A_p|\vec{V}|$ where N''' is the number concentration of scattering particles, $|\vec{V}|$ is the magnitude of the instantaneous velocity vector and A_p is the area of the measurement volume projected on a plane normal to the velocity vector. From this equation, they deduced that for uniform particle concentration and constant A_p, $\dot{N}$ will be proportional to $|\vec{V}|$. For a turbulent flow where the velocity varies, more measurements will be acquired during periods of high velocity than when the velocity is low, and biased statistics will result. This is generally referred to as "velocity bias." Angular bias results from the change in the projected area of the measurement volume A_p for different velocity vector directions. This type of bias was alluded to in McLaughlin and Tiederman (1973) and Edwards et al. (1987) as well as Dimotakis (1976), but has received little attention.

Other types of bias errors have been identified in the past. Whiffen et al. (1979) discussed fringe bias (sometimes called angular bias), which is caused by the requirement that a particle cross sufficiently many fringes as it transits the measurement volume. This bias can be eliminated by frequency shifting. A geometric bias associated with the imposition of temporal coincidence requirements in three-component velocity measurements was identified by Brown (1989), and recommendations for the appropriate setting of the coincidence time window were made.

Since angular bias is a type of statistical bias, methods for eliminating statistical bias should be effective in combatting it; however, these methods are often impractical for three-component laser velocimeters. Edwards et al. (1987) outlined sampling schemes which result in data which is free of statistical bias. All the schemes required that the particle arrival rate be at least five times the temporal Taylor microscale. For three-component laser velocimeter systems, it is often impossible to meet this requirement. Several generic features of three-color three-component laser velocimeter systems contribute to this behavior. These include the smaller size of the coincident measurement volume, which requires a higher particle concentration. (Quite often, attenuation of the incident laser beams and the scattered light limits the maximum particle concentration.) Obtaining coincidence on three measurement channels and the use of the weaker violet line of the Argon ion laser for the third component also contribute to a lower measurement rate. As a result, statistical bias often cannot be eliminated by sampling appropriately and the bias must be either corrected for, or minimized.

Many schemes have been proposed to correct for statistical bias. In Edwards et al. (1987), it was concluded that the weighting scheme proposed by McLaughlin and Tiederman (1973) was unreliable for one- or two-component measurements because the actual magnitude of the velocity was unknown and A_p varies. When using a three-component laser velocimeter, the magnitude of the velocity vector is known and so the weighting scheme of McLaughlin and Tiederman can be used to correct for velocity bias. This does not, however, correct for the change in A_p with velocity vector direction. Dimotakis (1976) suggested that the effect of area change could be corrected for by empirically determining the projected area in all possible directions. This can be impractical.

For turbulent flows, statistical bias errors in individual-realization laser velocimeter measurements using natural sampling are inevitable. The portion of the bias related to the variation

---

Contributed by the Fluids Engineering Division for publication in the JOURNAL OF FLUIDS ENGINEERING. Manuscript received by the Fluids Engineering Division May 12, 1995; revised manuscript received January 26, 1996. Associate Technical Editor: R. E. Arndt.

in the velocity magnitude can be corrected by weighting with the velocity magnitude. The effect of the change in projected area, however, must also be considered. This effect can be minimized by choosing the appropriate orientation for the measurement volumes. In what follows, we present simulations of a typical laser velocimeter system in which the turbulence level and the measurement volume orientation relative to the mean velocity vector are varied systematically. The angular bias errors in the calculated velocity statistics are identified. The results show how angular bias will affect the results of measurements and are used as the basis for recommendations regarding measurement-volume orientations which minimize the effect of angular bias.

2 Simulation Methods

The performance of a typical three-component laser velocimeter configuration was simulated using a Monte Carlo method. The laser velocimeter system was assumed to consist of a two component sub-system and a single-component sub-system with their measurement volumes at the same point in space. The individual measurement volumes were 25:1:1 ellipsoids of revolution. The long axes of the ellipsoids crossed at an angle of 45 deg (see Fig. 1(*a*)). The coincident measurement is roughly 2.6:1.1:1 but is not ellipsoidal: its shape is discussed below. Independent particles passing through the space surrounding the measurement volumes were modeled. The particles were distributed randomly in space and their vector velocities conformed to Gaussian isotropic turbulence with a prescribed turbulence intensity.

The measurement volumes intersected at the center of a box in three-dimensional space. Each side of the box had a length equal to the major diameter of the ellipsoidal measurement volumes. The three coordinates describing the position of a particle in the box enclosing the ellipsoids were generated using uniform random number generators. The instantaneous velocity vector was the sum of a specified mean velocity vector in the streamwise direction (x-direction) and of a fluctuating velocity vector. Each component of the fluctuating velocity vector was generated separately using Gaussian random number generators with a specified standard deviation (turbulence intensity). A unique path for each particle was determined from its position and the vector velocity. If the particle path passed through the intersection volume of the two ellipsoids (the coincident measurement volume), the velocity was recorded. The statistics calculated from the recorded data are equivalent to those which result from laser velocimeter measurements, including the effects of an angular bias.

This procedure was repeated until sufficient realizations were generated for converged statistics. Ten thousand realizations were used for the lower-turbulence-level cases while forty thousand were needed for highest-turbulence-level case. These ensemble sizes were chosen based on estimates of the uncertainty in the calculated statistics. For 95 percent confidence, the incertainty in the estimated mean velocity is twice the r.m.s. value divided by square-root of the ensemble size; for the r.m.s. velocity, it is twice the r.m.s. velocity divided by the square-root of twice the ensemble size. (This assumes that the velocities obey Gaussian distributions; this is true for "true" velocity distributions, but the biased distributions are slightly non-Gaussian.) In the results presented below, the maximum uncertainty for the resulting mean velocities was 1 percent of the mean streamwise velocity at 95 percent confidence. The uncertainties for the estimated r.m.s. velocities was less than 2 at 95 percent confidence for all cases.

There are many advantages of using this simulation procedure. The velocity bias of McLaughlin and Tiederman (1973) is absent since the probability of obtaining a validation is inherently independent of the velocity magnitude. The fringe bias proposed by Whiffen et al. (1979) is not present since all the particles passing through the coincident measurement volume are validated. It also eliminates the geometric bias proposed by Brown (1989) since true spatial coincidence, rather than temporal coincidence, is imposed. The only type of bias that can occur in this type of simulation is the angular bias due to the change in A_p.

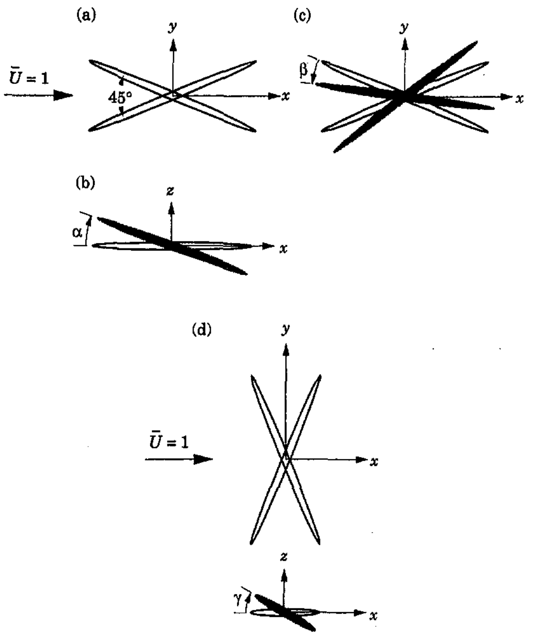

Fig. 1 Schematics of the coincident measurement volume for two measurement volumes intersecting at the center with an included angle 45 deg. (*a*) Top view of the arrangement. (*b*) Side view showing the case of pure pitch ($0 < \alpha < 180$ deg, $\beta = \gamma = 0$). (*c*) Top view showing the case of pure yaw ($\alpha = 0$, $0 < \beta < 180$ deg, $\gamma = 0$) (*d*) Combined top view and side view showing the case of pure roll ($\alpha = 0$, $\beta = 90$ deg, $0 < \gamma < 180$ deg).

3 Results

The approach to this problem is organized as follows: A velocity field with a mean x-direction velocity of unity is assumed; the mean velocities in the y- and z-directions are zero. The measurement volumes which comprise the three-component laser velocimeter can have any orientation. The reference configuration has the measurement volumes lying in the x-y plane and the bisector of their 45 deg included angle parallel to the x-axis (see Fig. 1(*a*)). Departures from this configuration can be specified using a pitch angle α shown in Fig. 1(*b*), a yaw angle β (Fig. 1(*c*)), and a roll angle γ. The cases of pure pitch ($0 < \alpha < 180$ deg, $\beta = 0$) and pure yaw ($0 < \beta < 180$ deg, $\alpha = 0$) will be examined in addition to the case of roll for $\beta = 90$ and $0 < \gamma < 180$ deg (see Fig. 1(*d*)). These three cases cover many of the possible measurement-volume orientations encountered in practice.

The turbulence level (intensity) is defined as $u'/\bar{U}$ where u' is the root-mean-square (r.m.s.) streamwise velocity and $\bar{U}$ is the mean streamwise velocity. The turbulence is isotropic so $u' = v' = w'$. For simple turbulent flows (shear layers, jets, wakes, etc.) the turbulence level can be as much as 30 percent; however, the turbulence level for more complex flows can be in excess of 100 percent. Four different turbulence levels (10, 30, 50, 100 percent) were used in the simulations.

The intersection of the two ellipsoids defines the shape of the coincident measurement volume. For $\alpha = \beta = \gamma = 0$, the projection of the coincident measurement volume in the x-direction is elliptical with a minor diameter equal to the diameter of one of the individual measurement volumes d_m, and a major diameter which is $d_m/\cos 22.5$ deg. This yields $A_p = \pi d_m^2/$

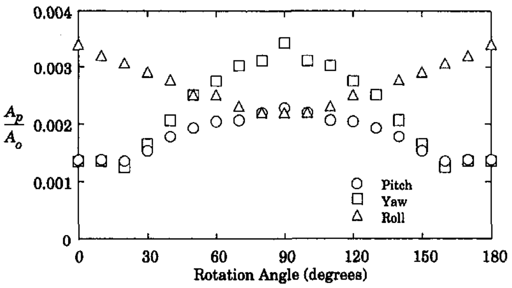

Fig. 2 Projected area of the coincident measurement volume A_p/A_o in the mean flow direction as a function of rotation angles for the cases of pure pitch ($0 < \alpha < 180$ deg, $\beta = \gamma = 0$), pure yaw ($\alpha = 0$, $0 < \beta < 180$ deg, $\gamma = 0$), and pure roll ($\alpha = 0$, $\beta = 90$ deg, $0 < \gamma < 180$ deg)

4 cos 22.5 deg. For $\beta = \gamma = 0$ and $\alpha = 90$ deg (or $\alpha = 0$, $\beta = 90$ deg and $\gamma = 90$ deg), the projection in the x-direction is diamond-shaped with a major diagonal equal $d_m/\sin 22.5$ deg, and a minor diagonal of $d_m/\cos 22.5$ deg ($A_p = d_m^2/\sin 22.5 \cdot \cos 22.5$ deg). For $\alpha = \gamma = 0$ and $\beta = 90$ deg, the projection in the x-direction is again elliptical with a minor diameter equal to the diameter of the measurement volume, but now with a major diameter which is $d_m/\sin 22.5$ deg ($A_p = \pi d_m^2/4 \sin 22.5$ deg). The last case is the largest attainable projected area. Figure 2 shows A_p as a function of orientation (α, β, γ). Due to the complicated shape of the coincident measuring volume, A_p was calculated using the simulation code. The turbulence level was set to zero so that the particles randomly positioned in the box around the measurement volume each had a purely x-direction velocity. For a given orientation of the measurement volume, then, the fraction of particles validated as having passed through the coincident measurement volume is equal to A_p (projected in the x-direction) divided by A_o, the area of the box projected in the x-direction. The nature of the three specific orientations is of note: From the figure, it can be seen that for pitch (α), the minimum A_p occurs at zero and 180 deg, while for yaw (β) there are low values near zero and 180 deg, but the minimum A_p occurs at 22.5 and 157.5 deg (corresponding to one of the ellipsoids aligned with the x-axis). The maximum A_p occurs at 90 deg for both cases. For roll at $\beta = 90$ deg, the maximum A_p occurs for $\gamma = 0$ and 180 deg and the minimum for 90 deg.

For the flow fields examined here, the two velocity components (U and V) behave as shown in Fig. 3. The circular contours are lines of constant probability density for U and V. The dashed lines represent specific flow angles ϕ (the angle between the instantaneous velocity vector and the mean velocity vector). The mean velocity $\bar{U}$ is indicated on the figure ($\bar{V}$ is zero). As shown, the figure represents a flow with a moderate turbulence level. As the turbulence level increases, the contours of the probability density function (p.d.f.) increase in diameter and the range of possible flow angles increases.

From the figure it is clear that if some flow angles ϕ are preferentially measured, some areas of the probability density function will be emphasized. This will result in bias in the calculated mean and r.m.s. velocities. If, for example, A_p is large for $\phi > 0$ and small for $\phi < 0$, measurements from the upper half of the p.d.f. will be more likely than ones from the lower half, resulting in a positive $\bar{V}$. A more subtle case is when A_p is at a minimum for $\phi = 0$, and increases for $|\phi| > 0$. This emphasizes large V velocities (positive and negative) and de-emphasizes large $\bar{U}$ velocities. As a result, $\bar{V}$ will be unaffected, but v' will increase and $\bar{U}$ will decrease. The effect of these bias errors will be more pronounced when the turbulence levels are high (large changes in ϕ). Since the turbulence is isotropic, figure 3 also represents the behavior in the U-W plane. (Note that this discussion of angular bias in terms of V could have been made for W.)

In the following sections, the effect on the mean and r.m.s. velocities caused by changing the orientation of the measurement volumes is examined for different turbulence levels. Representative probability density functions are then presented to illustrate the effect of the angular bias.

3.1 Velocity Statistics. Figure 4 shows the calculated mean and the r.m.s. velocities for varying pitch angle α. The mean velocities are normalized by the true value of $\bar{U}$, $\bar{U}_t = 1$. The r.m.s. velocities are normalized by their true values, the specified turbulence intensity. In each figure there are four sets of data representing the four different turbulence levels.

Figure 4(a) shows the normalized mean streamwise velocity $\bar{U}$. For all the turbulence levels, $\bar{U}$ is biased low for $\alpha = 0$. The bias increases with increasing turbulence level. For this orientation, the projected area in the mean flow direction is at a minimum. Any nonzero flow angle in the x-y or x-z plane has a larger projected area. Hence, the calculated mean velocity will be biased toward nonzero flow angles. As discussed in regard to Fig. 2, this will result in a decrease in the $\bar{U}$ velocity, as is shown in Fig. 4(a). The error introduced can be as much as 15% for the highest turbulence level. The r.m.s. streamwise velocity exhibits errors of only a few percent at low turbulence levels, and a maximum error of 7 for the 100 percent turbulence level case at $\alpha = 0$. For this case, where near-zero flow angles (large ± U fluctuations) are de-emphasized, there is a corresponding decrease in u'. As α is increased, the bias in $\bar{U}$ decreases to a minimum at $\alpha = 90$ deg. For the higher turbulence levels, there is still some bias in $\bar{U}$ (about 3 percent). For this orientation (with the measurement volumes lying in the y-z plane), A_p decreases with increasing flow angle in the x-z plane, but A_p increases with increasing flow angle in the x-y plane. There is a larger increase in A_p from the latter, than decrease in area from the former, and so the velocity is biased low by a small amount.

Figure 4(c) shows the mean vertical velocity $\bar{W}$ as a function of α and 4(f) shows the results for w'. The $\bar{W}$ velocity is correct (unbiased) for $\alpha = 0$. Since, for this orientation, the statistics will be biased toward both large positive and negative flow angles, bias will not affect the $\bar{W}$ velocity, but will cause an elevation of w', as seen in Fig. 4(f). A similar result is obtained for $\bar{W}$ at $\alpha = 90$ deg where no bias is in evidence. At about $\alpha = 30$ deg, there is a positive $\bar{W}$; the error is on the order of 5–7 percent. For this orientation, there is a large increase in A_p with flow angle (i.e., $dA_p/d\alpha > 0$ in figure 3 for $\alpha = 30$ degrees). This results in a greater likelihood of measuring a positive W velocity than a negative one and, hence, the observed bias. For $\alpha = 150$ deg, $dA_p/d\alpha < 0$ and $\bar{W}$ is biased negative. Again, the bias is most pronounced for large turbulence levels.

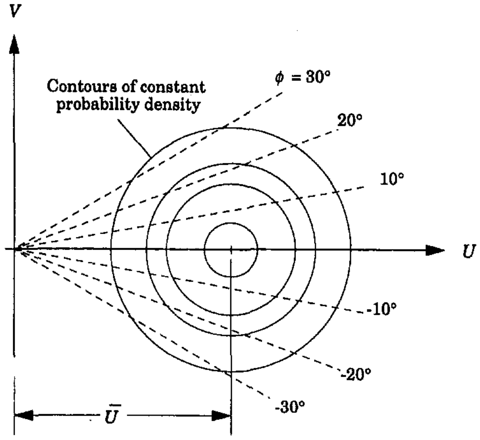

Fig. 3 Relationship between the probability density function for the velocity (shown as contour lines) and the instantaneous flow angle ϕ

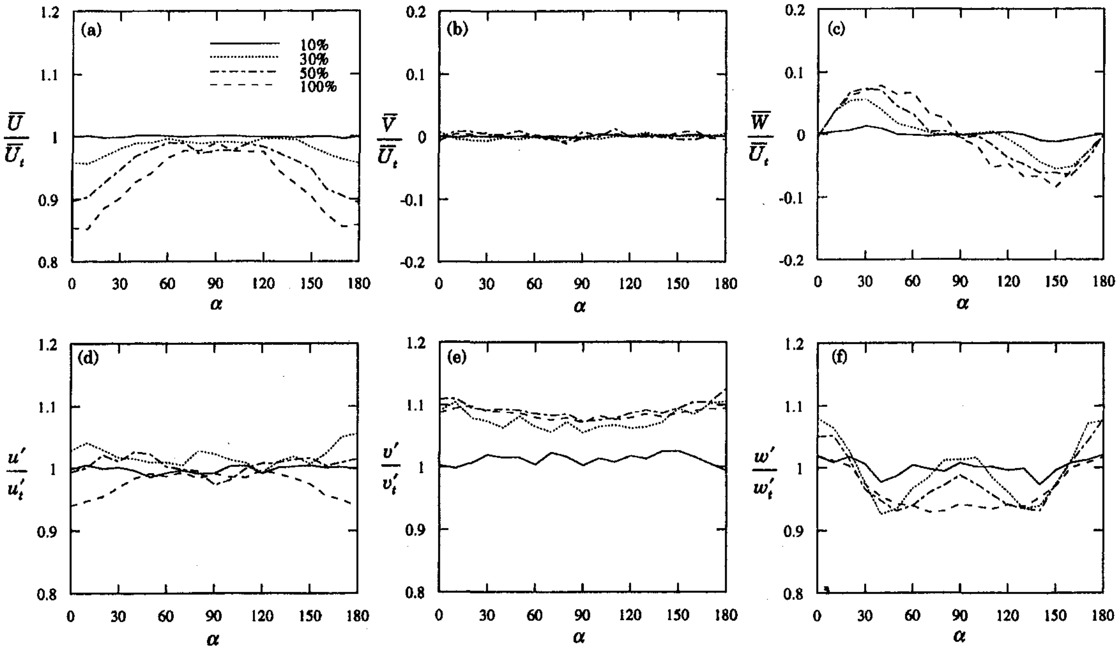

Fig. 4 The calculated mean and r.m.s. velocities for all three velocity components for varying pitch angle α and turbulence intensities from 10–100 percent. (*a*) Mean streamwise velocity $\bar{U}/\bar{U}_t$. (*b*) Mean transverse velocity $\bar{V}/\bar{U}_t$. (*c*) Mean crossflow velocity $\bar{W}/\bar{U}_t$. (*d*) R.m.s. streamwise velocity u'/u'_t. (*e*) R.m.s. transverse velocity v'/v'_t. (*f*) R.m.s. cross-flow velocity w'/w'_t. Mean velocities are ±1 percent and r.m.s. velocities are ±2 at 95 percent confidence.

For intermediate values of α, ($30 < \alpha < 60$; $120 < \alpha < 150$ deg) w' is biased low because the bias toward positive or negative W, respectively, effectively 'narrows' the distribution of W. Near $\alpha = 90$ deg, the projected area only decreases slightly for positive and negative flow angles in the x-z plane and the result is little bias for the lower turbulence levels. At $\alpha = 90$ deg, the case for 100 percent turbulence intensity is biased low due to the large range of flow angles encountered and the corresponding decrease in projected area.

Figure 4(*b*) shows the behavior of the mean transverse velocity $\bar{V}$ with pitch angle α. For all α, the change in projected area is symmetrical for positive and negative flow angles associated with the V velocity. As a result, the calculated value of $\bar{V}$ equals its true value (zero); and bias effects will be limited to the r.m.s. velocities. For all angles, Fig. 4(*e*) shows that v' is elevated by 7–10 percent. For all these orientations, the maximum area of the measurement volume is that projected in the x-z plane, normal to the V velocity. Hence, the projected area increases with increasing flow angle in the x-y (U-V) plane. This will bias the calculated statistics toward large magnitude V velocities and, hence, v' will be high as observed.

Figure 5 shows the normalized mean and r.m.s. velocities for the various turbulence levels versus yaw-angle β. In fig. 5(*a*), $\bar{U}$ is shown as a function of β. At $\beta = 0$ and 180 deg, the projected area of the measurement volume is near its minimum (see Fig. 3). Hence, it is more probable to acquire a velocity with larger ϕ. As β increases, the effect of the bias on $\bar{U}$ decreases and, for the two lowest-turbulence-level cases, it nearly vanishes for 45 deg $< \beta <$ 135 deg. For the higher turbulence level cases, the $\bar{U}$ velocity is biased up to 10 percent high at $\beta = 90$ deg. For this orientation, with the measurement volumes in the x-y plane, but with the bisector of the included angle between the measurement volumes aligned with the y-axis, the maximum projected area is for the x-direction. Large flow angles, therefore, are associated with a decrease in the projected area and so, the $\bar{U}$ velocity will be biased toward high values, and the bias will be greatest at high turbulence levels. The behavior of u' is shown in Fig. 5(*d*) and it essentially parallels the behavior for variation in pitch angle α, with at most a few percent bias in u', except for the highest-turbulence-level cases.

Figure 5(*b*) shows the mean transverse velocity $\bar{V}$. For intermediate angles, $\beta = 30$ and 150 deg, approximately, $\bar{V}$ is biased negative and positive respectively. The same argument used to explain the behavior of $\bar{W}$ in Fig. 4(*b*) applies here: The change in projected area with flow angle favors negative V velocities over positive ones near $\beta = 30$ deg and vice versa near $\beta =$ 150 deg. Since $dA_p/d\beta > dA_p/d\alpha$, the bias errors are larger, ranging from 8–15 percent. The behavior of v' for variation in yaw (shown in Fig. 5(*e*)) is similar to that for w' with pitch (α) variation and, so, the discussion of Fig. 4(*f*), again applies to Fig. 5(*e*). The magnitude of the bias errors for v' shown in Fig. 5(*e*) are larger than those in Fig. 4(*f*) for w' due to the larger changes in A_p. The maximum bias errors for v' are slightly in excess of 10 percent.

Figure 5(*c*) shows the mean vertical velocity $\bar{W}$. Due to the symmetry of the projected area with respect to change in flow angle associated with the W velocity, $\bar{W}$ is not biased. Figure 5(*f*) shows that the bias errors in w' are largest near $\beta = 0$ and 180 deg, where the maximum change in projected area with flow angle occurs for the U-W plane. This results in errors up to 8 percent for w'.

Results for roll displacement of the measurement volume for $0 < \gamma < \pi$ with $\beta = \pi/2$ (see Fig. 1(*d*)) are shown in Fig. 6. In Fig. 6(*a*), the results for $\bar{U}$ for different turbulence levels versus γ are shown. When $\gamma = 0$ for this orientation, the maximum A_p is in the direction of $\bar{U}$ and so any nonzero flow angle will result in a decrease in A_p. For $\gamma = 0$ and 180 deg, $\bar{U}$ is biased high, since the change in projected area biases the mean velocity toward small flow angles and, hence, large U velocities. As γ increases, the change in A_p with γ decreases, as does the bias. At $\gamma = 90$ deg, the projected area increases with increasing flow angle in the U-W plane, while it decreases with increasing flow angle in the U-V plane. The former increase is slightly more pronounced than the latter decrease, and the result is the slight negative bias observed in $\bar{U}$. These same effects introduce only a few percent error into u' over the full range of γ, as shown in Fig. 6(*d*). The projected area change is symmetric

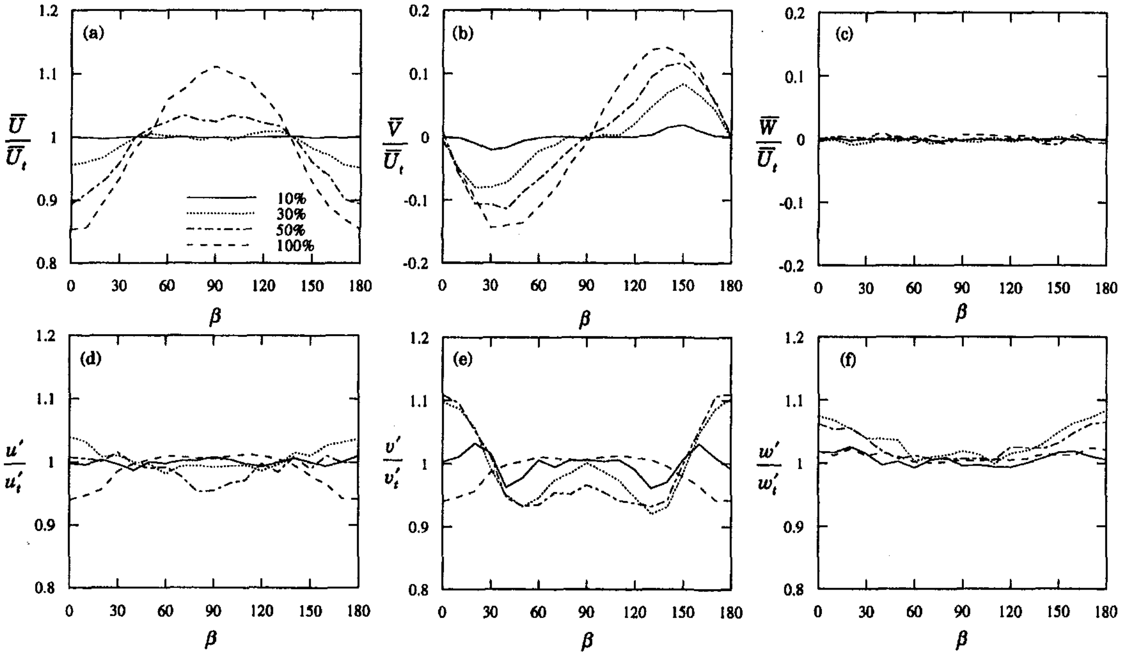

Fig. 5 The calculated mean and r.m.s. velocities for all three velocity components for varying yaw angle β and turbulence intensities from 10–100 percent. (*a*) Mean streamwise velocity $\bar{U}/\bar{U}_t$. (*b*) Mean transverse velocity $\bar{V}/\bar{U}_t$. (*c*) Mean crossflow velocity $\bar{W}/\bar{U}_t$. (*d*) R.m.s. streamwise velocity u'/u'_t. (*e*) R.m.s. transverse velocity v'/v'_t. (*f*) R.m.s. cross-flow velocity w'/w'_t. Mean velocities are ±1 percent and r.m.s. velocities are ±2 at 95 percent confidence.

about the x-y plane for all values of γ and so $\bar{V}$ is unaffected, as shown in Fig. 6(*b*). For the higher turbulence levels, v' is consistently biased low; this is due to the decrease in A_p for flow angles associated with large V velocities, which makes the measurement of small-magnitude V velocities more probable than large ones. The $\bar{W}$ velocities (shown in Fig. 6(*c*)) behave like $\bar{W}$ for yaw variation (shown in Fig. 5(*c*)) and the explanation is similar. The maximum bias errors range from 4–7 percent due to the relatively small change in projected area. The behavior of w' is shown in Fig. 6(*f*); the maximum bias of 5–7 percent observed at $\gamma = 90$ deg results from the increase in projected area associated with large flow angles in the U-W plane which emphasizes the larger magnitude W velocities and therefore increases w'.

3.2 Probability Density Functions. In this section, we demonstrate the connection between the observed behavior of the statistics, which results from angular bias, and the probabil-

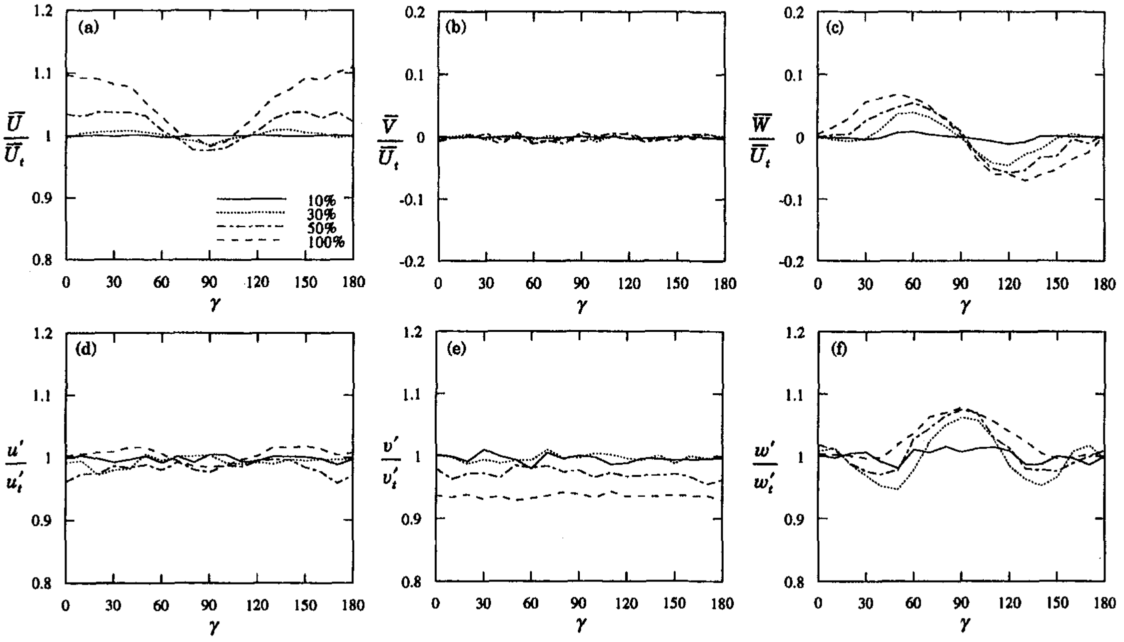

Fig. 6 The calculated mean and r.m.s. velocities for all three velocity components for varying roll angle γ and turbulence intensities from 10–100 percent. (*a*) Mean streamwise velocity $\bar{U}/\bar{U}_t$. (*b*) Mean transverse velocity $\bar{V}/\bar{U}_t$. (*c*) Mean crossflow velocity $\bar{W}/\bar{U}_t$. (*d*) R.m.s. streamwise velocity u'/u'_t. (*e*) R.m.s. transverse velocity v'/v'_t. (*f*) R.m.s. crossflow velocity w'/w'_t. Mean velocities are ±1 percent and r.m.s. velocities are ±2 at 95 percent confidence.

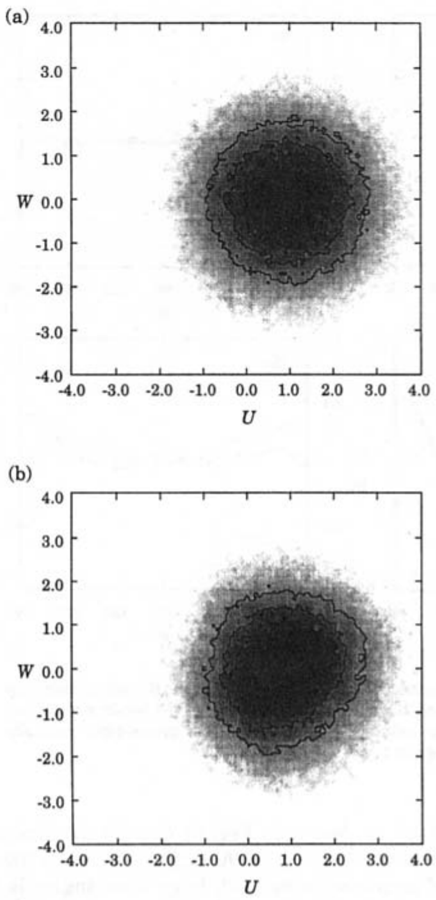

Fig. 7 Comparison of the joint probability density function (p.d.f.) between the true statistics and the biased statistics. (*a*) The true *U-W* joint p.d.f. (*b*) The biased *U-W* joint p.d.f. for turbulence level 100 percent for pitch angle α at 30 deg.

ity density functions of the velocities, discussed above in connection with Fig. 2. Figure 7 shows the joint p.d.f. for the U and V velocities for a case with a turbulence level 100 percent for $\alpha = 30$, $\beta = 0$, and $\gamma = 0$ deg. For this case, shown in Fig. 4, $\bar{U}$ is biased roughly 10% low and $\bar{W}$ is positive and about 7 percent of $\bar{U}$. The levels of both u' and w' are low by a few percent. Figure 7(*a*) shows the true joint p.d.f., while Fig. 7(*b*) shows the biased distribution. The p.d.f.s were estimated using 100,000 realizations, for both cases. In Fig. 7(*a*) the true p.d.f., the distribution is symmetrical about the mean velocity, and the contours form concentric circles about the mean, as is expected. In Fig. 7(*b*) it is clear that while the overall size of the distribution has not changed appreciably (indicating only small changes in the associated r.m.s. velocities), the shape of the contours has been subtly altered. Negative flow angles have been deemphasized in favor of positive flow angles, consistent with the behavior of the projected area. This results in the low values of $\bar{U}$ and positive values of $\bar{W}$ observed.

Figure 8 shows the one dimensional p.d.f.s for three velocity components for the same case as shown in Fig. 7 (turbulence level of 100 percent at $\alpha = 30$, $\beta = 0$, and $\gamma = 0$ deg). The biased results (symbols) are compared to the true data (lines) and, again, 100 000 realizations were used to generate the p.d.f.s. In Fig. 8(*a*), the true p.d.f. of the U velocity is compared to the biased distribution made up of laser velocimeter validations; p.d.f.s for V and W are shown in Figs. 8(*b*) and 8(*c*), respectively. Consistent with the previous discussion for this case, the distribution for U has clearly shifted to lower values, due to the bias against larger flow angles. The distribution for W has shifted toward positive velocities due to the larger projected area for positive flow angles in the U-W plane. Since the largest projected area for this orientation is in the y direction (the x-z plane) the data will be biased toward large positive and negative V velocities. The p.d.f. for V shows that the probability of obtaining a near-zero V velocity is conspicuously low. As a result, v' is biased high, but there is no bias in the mean velocity.

4 Conclusions and Recommendations

For three-component laser velocimeter systems, the change in projected area of the coincident region of the measurement volumes for different flow directions will introduce an ''angular'' bias in naturally sampled data. In this study, the effect of turbulence level and orientation of the measurement volumes on angular bias errors in three-component laser velocimetry was examined. The prototype laser velocimeter consisted of two individual measuring volumes which were 25:1:1 ellipsoids which cross so that their major axes are oriented at a 45 deg

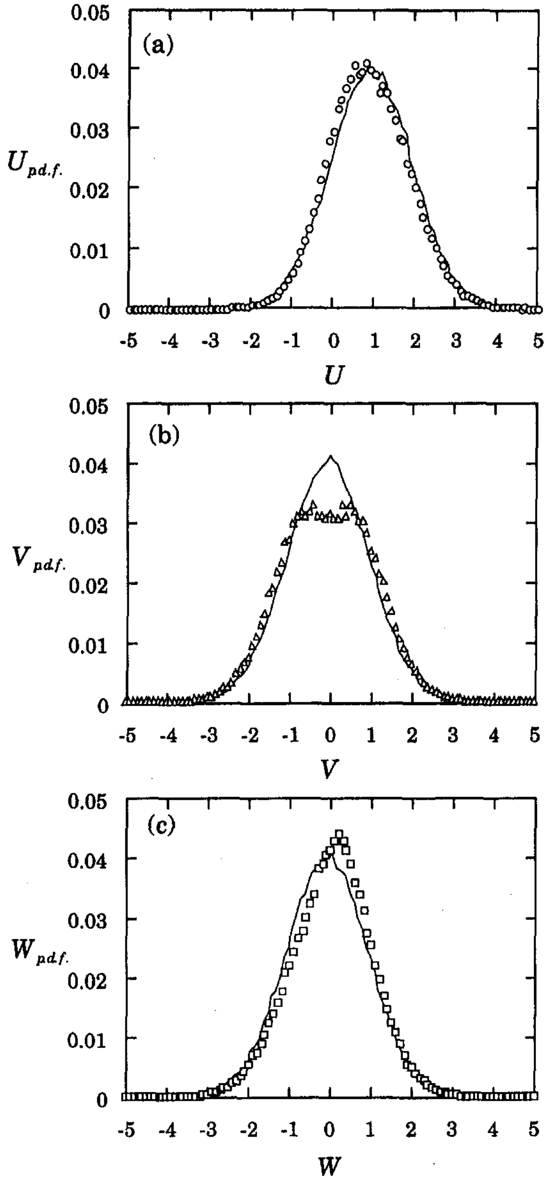

Fig. 8 Probability density function for the three velocity components. Solid lines represent the true p.d.f. and the symbols are the biased p.d.f. for turbulence level 100 percent for pitch angle α at 30 deg. (*a*) Streamwise component *U*. (*b*) Transverse component *V*. (*c*) Vertical component *W*.

included angle. Turbulence levels were varied from 10–100 percent and a broad range of orientations were examined. The operation of the laser velocimeter was simulated using a Monte Carlo technique.

The results of this study on the effects of angular bias on mean and r.m.s. velocity estimates can be summarized as follows:

- For turbulence levels less than 10 percent no significant bias error in the mean velocities will occur. Errors in the r.m.s. velocities will be less than 3% for all orientations.
- For turbulence levels around 30 percent, mean velocity bias errors less than 5 percent of the mean streamwise velocity $\bar{U}$ result for mean velocity vectors which range ±30 deg relative to long axis of the coincident measurement volume ($60 < \alpha < 120$ or $60 \text{ deg} < \beta < 120 \text{ deg}$). However, the r.m.s. velocities may be in error as much as 10% for these cases.
- For turbulence levels of 50–100 percent, there is no orientation which will yield good estimates of all three mean velocities; errors as large as 15 percent of $\bar{U}$ may be encountered. The minimum error results from an orientation where the plane of the measurement volumes is oriented normal to the mean flow direction. Errors of as much as 10% for the r.m.s. velocities can again be expected.

A few caveats are in order: These estimates are for isotropic turbulence, where there is no correlation between the various component velocity fluctuations. They also apply strictly only in the absence of velocity bias (which can presumably be removed through weighting with the magnitude of the instantaneous velocity vector) and other biases such as fringe bias. These results are also for a specific configuration where the measurement volumes cross at an included angle of 45 deg. For systems which have larger included angles, the changes in A_p will be smaller and so the effect of angular bias will be lessened. For systems which have smaller included angles, the changes in A_p are more pronounced and the potential for angular bias errors is increased.

Acknowledgment

This work was supported by the Fluid Dynamics Program of the Office of Naval Research under Grant Number N00014-92-J-1750, monitored by Dr. E. P. Rood. The efforts of one of the authors (PJK) were supported by an Office of Naval Research Graduate Fellowship. This support is gratefully acknowledged.

References

Brown, J. L., 1989, "Geometric bias and time coincidence in 3-dimensional laser Doppler velocimeter systems," *Experimental Fluids* Vol. 7, pp. 25–32.

Dimotakis, P. E., 1976, "Single scattering particle laser Doppler measurements of turbulence," *AGARD Conference No. 193.* NATO-AGARD. 10-1-10-14.

Edwards, R. V., Adrian, R., Boutier, A., Dybbs, A., Eaton, J., George, W., Meyers, J., Stevenson, W. and Yanta, W., 1987, "Report of the Special Panel on Statistical Bias Problems in Laser Velocimetry." ASME JOURNAL OF FLUIDS ENGINEERING Vol. 109, pp. 89–93.

McLaughlin, D. K. and Tiederman, W. G., 1973, "Biasing correction for individual realization laser anemometer measurements in turbulent flow." *Physics of Fluids,* Vol. 16, pp. 2082–2088.

Whiffen, M. C., Lau, J. C. and Smith, D. M., 1979, "Design of LV Experiments for Turbulence Measurements," *Laser Velocimetry and Particle Sizing,* Thompson, H. D. & Stevenson, W. H., eds. Hemisphere, pp. 197–207.

Chendong Huang[1]

Rhyn H. Kim
Professor.

Department of Mechanical Engineering
and Engineering Science,
The University of North Carolina at
Charlotte,
Charlotte, NC 28223

Three-Dimensional Analysis of Partially Open Butterfly Valve Flows

A numerical simulation of butterfly valve flows is a useful technique to investigate the physical phenomena of the flow field. A three-dimensional numerical analysis was carried out on incompressible fluid flows in a butterfly valve by using FLUENT, which solves difference equations. Characteristics of the butterfly valve flows at different valve disk angles with a uniform incoming velocity were investigated. Comparisons of FLUENT results with other results, i.e., experimental results, were made to determine the accuracy of the employed method. Results of the three-dimensional analysis may be useful in the valve design.

Introduction

Butterfly valves are one of the oldest types of valves known. They are mainly used for both on-off and throttling services involving large flows of gases and liquids at relatively low pressure. The advantages are lightweight and easier to bring the valve from fully open to fully closed very quickly.

The three main parts of butterfly valve are the body, the shaft, and the valve disk. There are some investigations reported about internal flow visualization and numerical simulation of butterfly valves. For example, Ito (1988) using an optical technique obtained peculiar behaviors of cavitating flows around a butterfly valve. The visualization of butterfly valve flows (Kitamura et al., 1983) was made by using bubble and tracer particles to study upstream and downstream flows in relation to flow structures.

Addy et al. (1985), Morrison and Dutton (1989, 1991) investigated compressible flow characteristics of butterfly valve flows. Lacor and Hirsch (1988) also investigated the butterfly valve flows with Euler code in the immediate vicinity of the valve disk. Eom (1988) treated with the butterfly valve as a controlling device for flows. But none of them investigated three-dimensional throttled flow patterns with different valve openings.

Two-dimensional numerical simulation of butterfly valve flows has been investigated for the flow patterns, velocity distributions, and evaluation of the discharge coefficients of the butterfly valves (Kim, Wu, 1992). The assumption used for a two-dimensional analysis was an incompressible flow within two infinitely long parallel plates with a finite width.

The two-dimensional analysis yielded a reasonable qualitative preliminary result. It showed that the computed pressure loss coefficients differ from those of the published valves as the valve opening increases, though the trend of changes of the pressure loss coefficients between the two results was agreeable (Blevins, 1984). One possible explanation is that even if the mathematical model is a two-dimensional flow between the two plates, the friction coefficient used in the pressure drop was that of a circular tube. A more significant reason could be that a two-dimensional flow model was inaccurate around the valve plane for the flows. Computed results for the wide open valve flow were only agreeable with the published results within a reasonable error limit. Therefore, in the present study, a three-dimensional mathematical model for the flows was used to investigate the butterfly valve flows with the same assumptions as used in Kim and Wu (1992).

The objective of this study is to provide a three-dimensional (3D) numerical flow visualization of incompressible flows around the butterfly valve which reveals velocity fields, pressure distributions, streamlines, particle paths, and flow separations. The numerical visualization is made by using preBFC (FLUENT, 1993) to set up geometry and grid, and FLUENT (FLUENT, 1993) to solve difference equations that are postulated from the conservation of the mass and momentum of a fluid in motion. Turbulence is modeled by the k-ϵ model (Launder, 1974). A 45 degree opening of the butterfly valve was presented because the valve opening is approximately a mid way between the wide open and closed valve conditions. Hydraulic characteristics in different valve disk angles are presented in the thesis (Huang, 1994). A comparison of FLUENT results and Blevins' (1984) results for pressure loss coefficients at different valve disk angles was made to show a reasonable agreement between the two cases.

Physical System and Computational Analysis

Fluid flows in a circular pipe, and the disk is a flat circular plate. The pipe diameter, D is 25.4 mm. α is the valve disk angle from 0 to 90 degree, measured from the horizontal position. W_{in} is the incoming velocity, which is 0.9144 m/s in Z direction. The thickness of valve disk is 0.0016 m. The upstream length L_1 and downstream length L_2 should be several times of the pipe diameter in order to get enough entry length and a fully developed flow downstream. We will take the upstream length L_1 two times the pipe diameter and L_2 eight times the pipe diameter. A trial and error method was used to reach the length L_1 and L_2. The fluid passing the valve is water. Its density ρ is 999 Kg/m^3. The dynamics viscosity μ is 1.12×10^{-3} N.S/m^2.

Assumptions for this physical model used with body fitted coordinates are:

- Three-Dimensional Flow
- The fluid is incompressible and steady.
- The incoming velocity W_{in} is uniform and only in the Z direction.
- Velocity is zero at the surface of the pipe and the valve disk.
- Turbulence is described by a two equation k-ϵ model.

FLUENT is a two part program consisting of a preprocessor, preBFC, and a main module. We use preBFC to define the geometry and a structured grid for our model. Then we transfer the grid information from preBFC to FLUENT via a grid file.

---

[1] Research Engineer, AMPS, Inc., 4667 Freedom Dr., Ann Arbor, MI 48108.

Contributed by the Fluids Engineering Division for publication in the JOURNAL OF FLUIDS ENGINEERING. Manuscript received by the Fluids Engineering Division May 20, 1994; revised manuscript received February 14, 1996. Associate Technical Editor: H. Hashimoto.

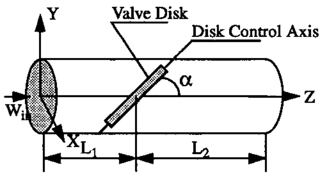

Fig. 1 Simplified model and coordinate system

Transport equations, momentum equation, continuity equation, Reynold stress assumption, and turbulent viscosity assumption are a set of control equations (Anderson et al., 1984) which were solved numerically. FLUENT was used to get the velocity components U_i ($i = 1, 2, 3$) and pressure.

FLUENT, which used the Semi-Implicit Method for Pressure-Linked Equations (SIMPLE) (Patankar, 1980) algorithm with an iterative line-by-line matrix solver and a multigrid acceleration, provided the velocity and pressure as solutions for the butterfly valve flows.

In the process of solutions, FLUENT requires a user to set up a domain, boundary conditions and fluid properties before it solves the difference equations. Here we consider a uniform inlet velocity (0.9144 m/s) in the Z direction. The inlet turbulent kinetic energy is 1.351×10^{-3} m^2/s^2, kinetic energy dissipation is 9.176×10^{-3} m^2/s^3. Other boundaries, such as pipe wall and valve surface, their velocity are zero. But the wall turbulent used the FLUENT default wall boundary conditions (FLUENT, 1993). All of these boundary conditions and properties are inputted to the FLUENT case files. With valve disk angles of 20, 30, 45, 60, 70 degrees, grid networks of $10 \times 16 \times 82$ nodes are used in the fluid domain. It is necessary to compute the variables in the half of the butterfly valve flows due to a symmetry about the Y-Z plane, as shown in Fig. 1.

For α equal to 0, 20, 30, 45 degrees, we use the iterative line-by-line matrix solver. This line-by-line approach is also referred to as the Line-Gauss-Seidel (LGS) method. The disk angles of 60 and 70 degrees have too skew grid lines near the boundary, and have large cell aspect ratios. Actually, they are in a nonisotropic conditions in terms of turbulence. The multigrid method accelerates the convergence of such problems by enforcing a global balance over larger regions of the grid, in effect "smoothing" the nonisotropy that exists on the local scale.

Because of the valve disk, the Cartesian or cylindrical coordinate system does not yield well fitting grid net work. We should use a body fitted coordinated system. In Fig. 2, a view of surface I from a direction perpendicular to the valve disk, is a circular disk, and the pipe boundary is of elliptic shape. Because the Y-O-Z plane is a symmetric plane for valve flows, the tilted disk as a half circle takes at least nine points, since preBFC requires nine points for a half circle.

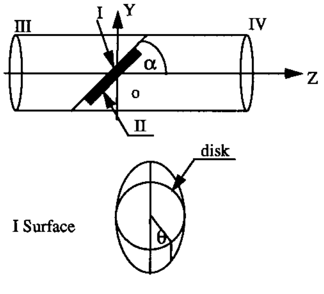

Fig. 2 A view of the tilted surface normal to the surface

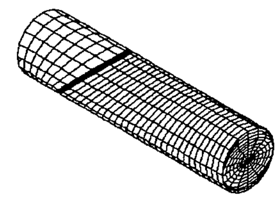

Fig. 3(*a*) Isometric view of the surface grid of 45 degree open

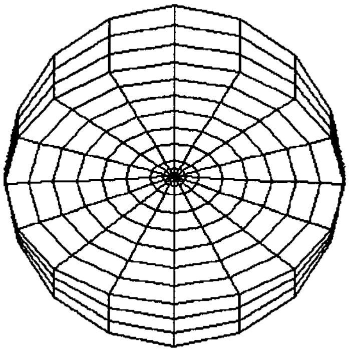

Fig. 3(*b*) A front view of the surface grid of 45 degree open

In order to set up the nine points in the circular disk and elliptic boundary, we make nine fan shape segments with a identical central angle, i.e., the angle θ of the point from the axis symmetry, changes from 0 to 180 degrees, each angular step being 22.5 degrees (Fig. 3(*b*)). Consider the thickness of the disk, t, then nine point coordinates are calculated by the formulas:

$$X = R \sin\theta \tag{1}$$

$$Y = -\left(R\cos\theta - \frac{t}{2}\cot\alpha\right)\sin\alpha \tag{2}$$

$$Z = -\left(R\cos\theta + \frac{t}{2}\tan\alpha\right)\cos\alpha \tag{3}$$

The disk angle α changes from 0, 20, 30, 45, 60, 70 degrees for different disk open conditions, and R is the disk radius. For the elliptical pipe boundary in the same surface.

For the elliptical pipe boundary in the same surface (surface-I), its coordinates are determined by

$$X = R \sin\theta \tag{4}$$

$$Y = -R\cos\theta \tag{5}$$

$$Z = Y\cot\alpha - \frac{t}{2}\csc\alpha \tag{6}$$

The surface-III has a fixed Z coordinate, and the X, Y coordinates are the same as the surface-I. We set up the surface-III for a elliptic and a circular boundaries according to two boundary surfaces of the surface I.

Grid coordinates for the surface-II of the disk boundary are:

$$X = R \sin\theta \tag{7}$$

$$Y = -\left(R\cos\theta + \frac{t}{2}\cot\alpha\right)\sin\alpha \tag{8}$$

$$Z = -\left(R\cos\theta - \frac{t}{2}\tan\alpha\right)\cos\alpha \tag{9}$$

Grid coordinates for the surface-II of circle pipe boundary are:

$$X = R \sin\theta \tag{10}$$

$$Y = -R\cos\theta \tag{11}$$

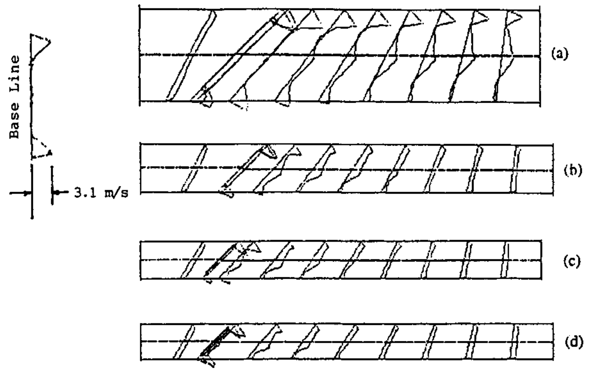

Fig. 4 ***W*** **velocity profiles on a *Y-Z* plane with the disk angle of 45 at the downstream distance of (*a*) 3D; (*b*) 6D; (*c*) 8D; (*d*) 9D**

$$Z = Y \cot \alpha + \frac{t}{2} \csc \alpha \tag{12}$$

The surface-IV has a fixed Z coordinate; the X, Y coordinates are the same as surface-II. We set up elliptical and circular boundaries of the surface-IV as the boundary of surface III.

After we set up internal body grid points and pipe surface grids, we interpolate the grid points in each surface, then interpolate the whole body grid points to form the grid net. The last step of grid generation is to smooth the grid.

The 45 degree surface grid isometry and the front view are shown in Fig. 3. In order to make calculation easy, we take straight lines as the I lines, and elliptical lines as J lines. Also, to satisfy the tilted angle of α, we need to have series of tilted surfaces as K surface.

Because of the tilted angle of the disk, the grid lines in the inside zone of the tube are the ellipses (view from the Z-direction) while the grid lines in the outside zone through which the fluid flows are the circles densely placed together in the grid network. And the projection of the disk surface on a vertical plane upstream and downstream have different centers because of the thickness of the disk.

The grid lines in a preBFC grid define the faces of the cells or control volumes. The corners of cells, defined by intersecting grid lines, are called nodes or grid points. Thus, the number of grid points in any given direction is one more than the number of cells in that direction.

For our butterfly valve flow, we set up cells as ($I \times J \times K = 9 \times 15 \times 81$), and we have nodes $10 \times 16 \times 82$, i.e., 13,120 nodes for α equal to 20, 30, 45, 60, 70 degrees.

Results and Discussion

The disk angle of 45 degree is approximately a mid way between the wide open and closed valve conditions. Thus we focus the results of this flow field upstream and downstream of the disk and farther downstream.

(1) How long should the pipe length be downstream of the disk to stabilize turbulent flows?

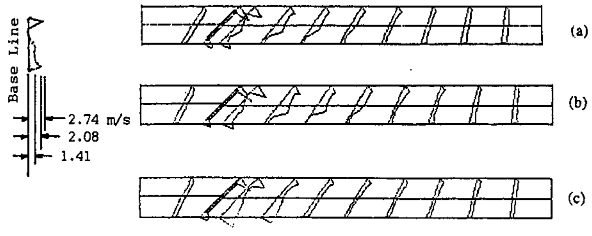

Fig. 5 ***W*** **velocity profiles on a *Y-Z* plane with the valve angle 45 at different nodes (*a*) 10 × 16 × 52; (*b*) 10 × 16 × 82; (*c*) 18 × 16 × 82**

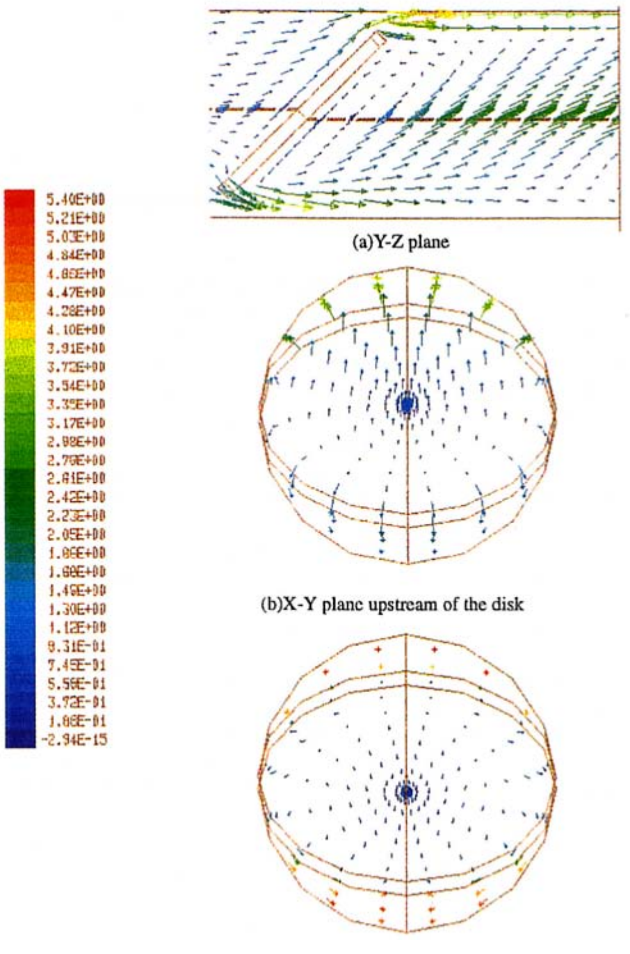

(a)Y-Z plane

(b)X-Y plane upstream of the disk

(c)X-Y plane downstream of the disk

Fig. 6 Velocity vectors on different planes at the disk angle of 45 degree

Blevins (1984) suggested in determining the pressure drop for butterfly valve experiments that the static pressure measurement point downstream from the pivot point (L_2) be a distance of $(5 \sim 10)D$ for turbulence stabilization. Because of the high Reynolds number (Re $> 20{,}000$), the minimum length of L_2 was tried in order to reduce the nodes and consequently calculation time. Figure 4(a), (b), (c), (d) show profiles of the W-velocity components of the butterfly valve flows with different L_2. The base line is the tilted line. The magnitude of the velocity is perpendicular to the base line. The L_2 being 3D case (Fig. 4(a)) shows the reverse flows at the exit while the cases with L_2 = 6D, 8D, and 9D do not revere the reverse flows. It seems that these three cases have reached stable turbulent conditions. But when the case of L_2 being 6D is compared with those of L_2 = 8D and L_2 = 9D, the $W_{\max}$ values are different. Comparing the flow of L_2 = 8D with the flow of L_2 = 9D, the $W_{\max}$ velocities are only within a 2 percent difference. Therefore, we choose the length L_2 being 8D as the best length. Then for all the flows with different disk angles except 0 degree, we choose L_1 = 2D and L_2 = 8D.

(2) How many cells are necessary to properly visualize the 45 degree flow?

Actually, the total number of computational cells depends on a number of factors: the accuracy required from the computation, the size of the memory of the available computer, and the cost of the CPU time required. The more cells in the computation, the greater the accuracy of the solutions is, and the longer the computer time takes to obtain solution. Since the trend of the convergency was observed from the computation process,

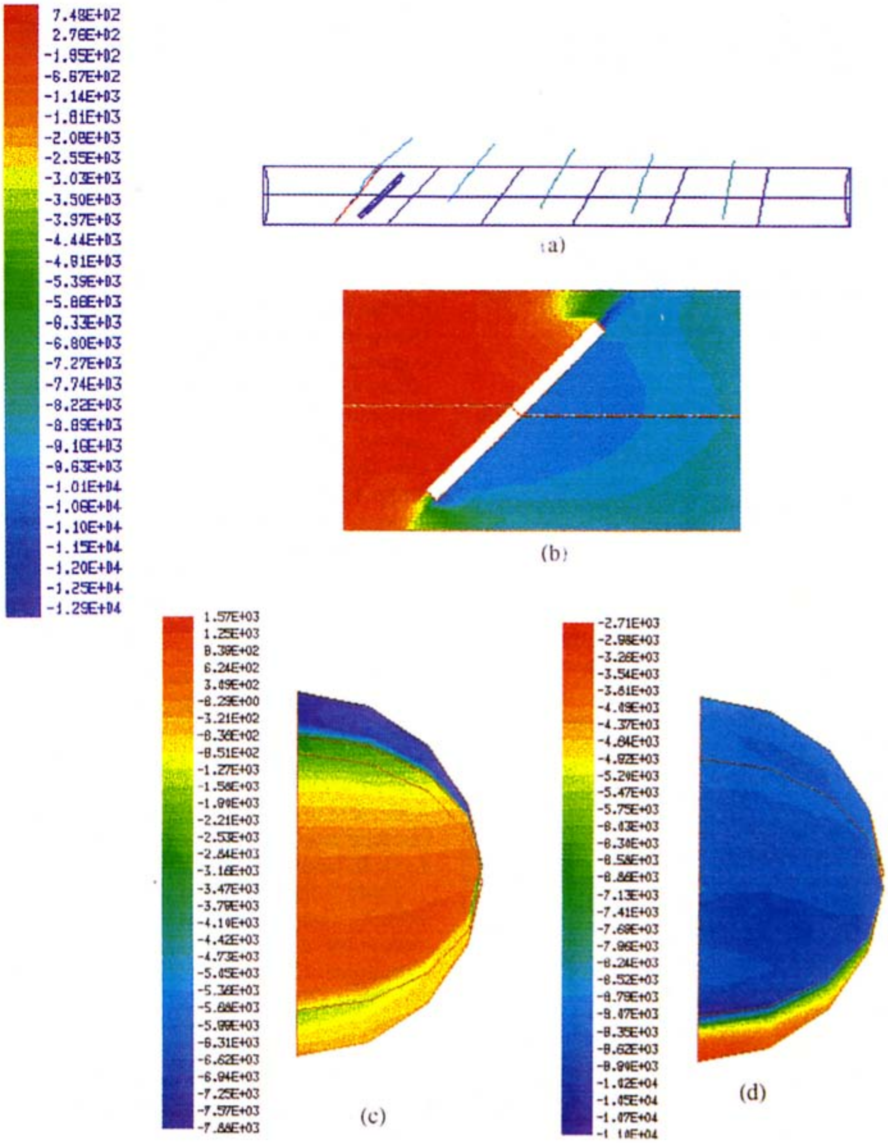

Fig. 7 L2-8D, 13120 cells and valve angle 45 degree with (*a*) pressure profiles on a *Y-Z* plane; (*b*) pressure contours on a *Y-Z* plane; (*c*) pressure contours on *X-Y* plane upstream of the valve disk; (*d*) pressure contours on *X-Y* plane downstream of the valve disk

we took the possible maximum number of cells in FLUENT available to the University computing facility. FLUENT in the UNCC computing system allows us to define the maximum number of computational cells to be 25,000.

Figure 5 shows the profiles of the W-velocity component with nodes of ($10 \times 16 \times 52$), ($10 \times 16 \times 82$), and ($18 \times 16 \times 82$). In these three grid systems, the total number of nodes are 8320, 13120 and 23616, respectively. The profiles show similar trends, but the value of $W_{\max}$ are different. $W_{\max}$ of the grid with ($10 \times 16 \times 82$) nodes is smaller than $W_{\max}$ of the grid with ($18 \times 16 \times 82$) nodes by 1 percent, but computation with the former node system saves CPU time by 200 percent. Certainly, the changes in the maximum pressure are not so close as those of $W_{\max}$. But the residuals are of the order of 10^{-4}, which are of the same order as velocity residuals. Based on this reasoning, the pressure should be as accurate as the velocity is. Considering an improvement of the accuracy and the CPU time, using the ($10 \times 16 \times 82$) node grid for computation is appropriate for all the angles.

The velocity vectors are shown in Fig. 6 in the Y-Z, X-Y planes, respectively for the angle of 45 degree.

Figure 6(a) shows the fluid passing the disk then forming a vortex and a secondary flow zone. When the incompressible fluid encounters a stagnation point (the left lower corner of the valve disk), the fluid is separated, one branch fluid going up, the other coming down around the valve disk. The fluid which goes up is accelerated around the valve and passes the upper corner of the valve disk. The fluid which comes down is accelerated around the lower corner. However, the lower corner of the valve disk is too abrupt in the change of the cross sectional area for the fluid. The momentum in the enhanced boundary layer around the valve disk is not sufficient to impel the boundary layer into the unfavorable pressure gradient. As a result, the boundary layers are separated and a vortex zone is formed then trailed off in the wake as free shear layers. But the fluid which goes up is accelerated around the valve disk surface, gradually, and the boundary layer doesn't separate.

Figure 6(b) is a projection of the velocity vectors on a x-y plane at $K = 14$. The grid line $K = 15$ represents the tilted surface of the disk. Figure 6(b) exhibits that: (1) The lower region of the disk becomes almost a stagnant area essentially because of the tilted disk and then the fluid separates. In the

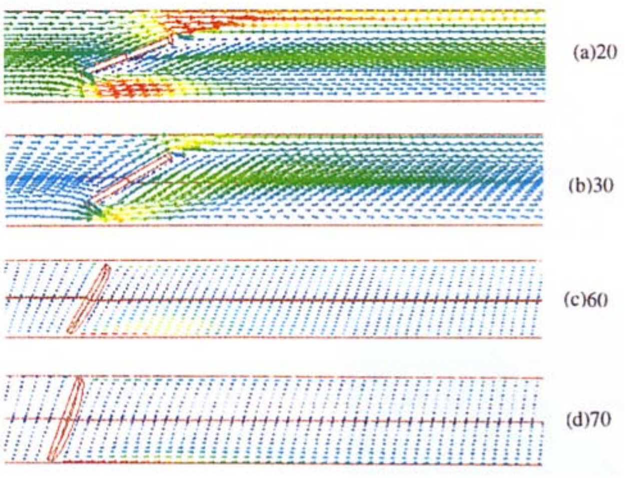

Fig. 8 Velocity vector on a *Y-Z* plane, with the valve disk angle (*a*) 20 degree; (*b*) 30 degree; (*c*) 60 degree; (*d*) 70 degree

Table 1 Maximum and minimum values of *W*-velocity components and pressure for different downstream lengths

L_2	3D	6D	8D	9D
$W_{\max}$ (m/s)	4.373	5.190	5.187	5.212
$W_{\min}$ (m/s)	−0.9024	−1.256	−1.257	−1.191
P_{emax} (Pa)	−8020.5	−10379	−9217.5	−8564.4
P_{inlet} (Pa)	6995.2	450.89	450.74	450.32
W_{emax} (m/s)	3.0017	2.2633	1.7982	1.5488

upper region, the fluid flow is accelerated while in the lower region, the velocity gradually increases. (2) The resultant velocity of the x-, y-components makes the fluid turn toward the middle of the tube in the lower region.

Figure 6(*c*) is a projection of the velocity vectors on a x-y plane at $K = 20$. The grid line $K = 19$ represents the tilted surface of the disk downstream. Figure 6(*c*) shows that within the center region of the disk, the fluid flows toward the lower region from the center, but the fluid flows outward in the upper region of the disk, indicating that the secondary flow occurs clockwise on the right hand side and counterclockwise on the left hand side of the disk. At the outside of the disk, the fluid flows toward the z-axis, yielding a complex field of the resultant velocity for a short distance until the fluid becomes fully developed.

Figure 7(*a*) shows the pressure profiles on Y-Z planes. The pressure profiles (green and red color) are shown against blue base lines. Upstream of the disk the pressure is positive, while downstream of disk, the pressure changes to negative. The pressure profiles are extended to the outside of the tube because of pressure perpendicular to the base lines.

Figure 7(*b*) reveals the pressure contours on the Y-Z plane. Figure 7(*b*) clearly shows, in the corner of the valve disk, the pressure decreases toward the Z direction. As previously discussed (Fig. 6), in this region, exists the negative pressure gradient, then the boundary layer would separate from this section to form a free shear layer in the wake. The lower left corner of the valve disk is the area with the pressure reduction.

Figure 7(*c*) shows the pressure contours on a X-Y plane upstream of the disk. The lower side of the valve disk becomes a stagnation area earlier than the upper side. Over this area fluid is accelerated as it goes up and the pressure decreases eventually. Beyond this area, the fluid is accelerated very quickly, so the pressure value changes from positive to negative.

Figure 7(*d*) shows the pressure contours on a X-Y plane downstream of the disk. As explained above (Fig. 7(*b*)), Fig. 7(*d*) shows a negative pressure gradient on the lower side of the valve disk. Inside the elliptical area, the smallest pressure is near the edge of the valve disk and the pressure reduces eventually from the top to bottom sides in the valve disk area. However, outside the valve disk, the fluid is accelerated, and in the region beyond the valve disk, the fluid is accelerated faster than the region above the valve disk.

Figure 8 shows pattern changes of the throttled flow as the disk is turned toward different positions, from 20 to 70 degrees. As the angle changes, we can see that (1) there exist different vortex zones; the larger the angle is, the bigger vortex zone is; (2) the faster velocity zone (the red color zone) becomes reducing to the smaller zone, but the magnitude of the velocity becomes larger; (3) the boundary layer separation point becomes closer to the valve disk, and causes the vortex. As the angle increases, the fluid flow passing the valve disk area becomes narrow. Then the fluids with the larger angle are more accelerated than the fluids with the smaller angle. Induced pressure drops increase. The negative pressure gradient zone also increases. Finally, the boundary layer separates to form the vortex.

The maximum and minimum values of the U, V, W velocity components and the pressure P are listed in Tables 1–3.

Table 1 shows the maximum values of the W-velocity component with different distances of L_2, downstream of the disk for the incoming uniform velocity of 0.9144 m/s, with the disk angle of 45 degrees. The $W_{\max}$ velocity component increases with the increasing L_2. But the exit $W_{\max}(W_{\text{emax}})$ decreases with the increasing L_2. And the node next to the exit maximum pressure (P_{emax}) decreases except the L_2 equal to 3D case, because the L_2 being equal to 3D case still has reverse flows. The node next to the inlet maximum pressure (P_{inmax}) keeps almost constant except the $L_2 = 3D$ case because in this case we used $L_1 = D$, and for others $L_1 = 2D$ was used.

Table 2 lists the maximum and minimum values of the W-velocity component and pressure as the number of nodes increase for the 45 degree open condition. We compared the maximum values of the W-velocity components at the exit, W_{emax} for the grid of the node numbers of 8320, 13120, and 23616, resulting in 57 percent and 80 present for the increasing number of nodes.

Table 3 shows the values of the maximum U, V, W velocity components, the exit and inlet pressures, the exit maximum W velocity, W_{emax}, the average of the exit velocity, $\bar{C}_{ex}$, the average of the pressure drop $\Delta\bar{P}$. $W_{\max}$, P_{exit} (the next node of the exit pressure), $\Delta\bar{P}$ values increase with the angle increment. The incoming velocity of the fluid is 0.9144 m/s for all of the opening of the disk angles. The pressure at the inlet (the next node of inlet) fluctuates because at this point, there is a turbulent condition.

The energy loss due to partial openings of the valves is generally a function of: (1) The geometry of the valve body, (2) The surface roughness of the valve, (3) The position of the valve disk, (4) Reynolds number, (5) The direction of the flow. The present study analyzed the different valve disk positions, and these are compared with the existing values.

There is significant uncertainty in the resistance of valves because of the wide variety of valve designs, the lack of the geometric similarity within the various sizes of even one design,

Table 2 Comparison of values with different number of nodes

$I \times J \times k$ cells	$10 \times 16 \times 52$	$10 \times 16 \times 82$	$18 \times 16 \times 82$
$W_{\max}$ (m/s)	5.187	5.199	5.222
$W_{\min}$ (m/s)	−1.257	−1.356	−2.275
P_{exit} (Pa)	−9217.5	−11324	−12716
P_{inlet} (Pa)	450.74	238.30	522.27
W_{emax} (m/s)	1.7982	2.2976	2.4483

Table 3 Maximum and minimum values of *U*-, *V*-, *W*-, velocity components and pressures for different valve disk angles

Angle	0	20	30	45	60	60
U_{max} (m/s)	0.2772	0.4046	1.099	0.7691	0.3290	0.3913
U_{min} (m/s)	−0.2354	−0.3081	−0.7117	−1.1040	−0.1284	−1.9640
V_{max} (m/s)	0.3363	0.4371	1.1390	1.8790	1.398	1.586
V_{min} (m/s)	−0.5165	−0.7417	−1.8810	−3.3120	−1.076	−1.448
W_{max} (m/s)	1.1720	1.7260	2.5350	5.1990	5.945	13.84
W_{min} (m/s)	−0.0925	−0.5003	−0.5678	−1.356	−0.6548	−1.506
P_{inlet} (Pa)	153.33	594.28	323.89	238.30	957.22	836.99
P_{exit} (Pa)	−504.63	−757.71	−6507.9	−11324	−64868	−432610
W_{emax} (m/s)	1.1722	1.1585	2.4517	2.2976	1.81	1.97
$\bar{C}_{ex}$ (m/s)	0.5855	0.9044	1.2325	1.155	0.9506	1.05
$\Delta\bar{P}$ (Pa)	657.96	926.0523	2529.2	9007	32320	295570

and the paucity of data which takes into account the downstream influence of the valve.

According to pressure loss coefficient analysis (Huang, 1994), we calculate the pressure loss coefficient k_l:

$$k_l = \left(\frac{C_1^2}{2} + \frac{P_1 - P_2}{\rho}\right)\frac{2}{C_2^2} - \left(1 + \frac{fL}{D}\right) \quad (13)$$

where P_1 and P_2 refer to the static pressure upstream and downstream of the valve disk. And C_1, C_2 are resultant velocities in upstream and downstream, respectively. L is the distance between P_1 and P_2. D is the tube hydraulic diameter. And f is the circular pipe friction factor in the turbulence flow.

Blevins (1984) compiled the pressure loss coefficients of butterfly valves with different disk configurations. Computed coefficients, k_l are to be compared with those of Blevins (1984).

Figure 9 presents variations of the pressure losses as the disk angle changes at $\mathrm{Re} = 2 \times 10^4$. Simulated solutions for pressure loss coefficients are compared with four different experimental values reported by Blevins (1984). In general, the resistance of a partially closed valve is a function of the disk angle. It also shows the tendency of the current 3D analysis for k_l is similar to those of experiments.

The case A of Fig. 9 is a thin disk, B is a blunt disk, C is a thin flap disk, and D is a streamlined disk. Our results are based on a thin and abrupt disk, but thickness is 0.0016 m. Compared the thickness with the pipe diameter 0.0254 m, it is very thin. So we can see it as a streamlined disk. That is the reason from Fig. 9, the 3D results are closer to the case D than any others.

Our 3-D computational results can be helpful for designing a butterfly valve disk. Designing a valve disk intends to satisfy various requirements, such as stable flow regulation, smooth shut-off performance, and low cavitation characteristics. Although our simplified circular disk may not be precise enough, the results give us insight and would lead to understand the 3-D flow fields, i.e., velocity and pressure distributions. Thus, the present study provides a basis for external forces which will give an approximation of stress distributions on the disk with changes of the disk angle. Cavitation characteristics are evaluated by a cavitation index, based on two phase pressure distributions of upstream, downstream of the disk. This type of problems is out of scope of the current study.

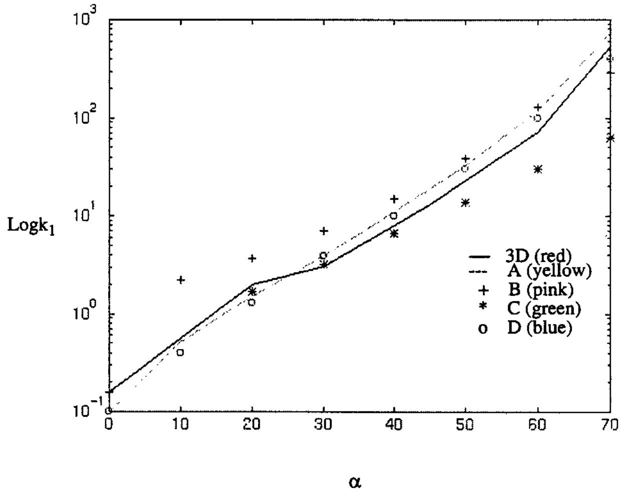

Fig. 9 Pressure loss coefficient A: thin flap disk (yellow), B: blunt disk (pink), C: thin flap disk (green), D: streamlined flat disk (blue), E: 3D numerical modeling (red)

Conclusion

FLUENT has been applied to investigate three dimensional fluid phenomena of butterfly valve flows. The computational studies have shown that the flow field through the butterfly valve is very complex and depends upon the valve disk angle.

We used a three-dimensional fluid model to consider the fluid flows. Velocity and pressure fields were obtained by applying FLUENT to the governing equations in the finite difference form which are the continuity equation, momentum equation, and the k-ϵ model for the turbulent flow.

In order to determine an optimum length downstream of the disk, L_2, several lengths with diameter multiples 3D, 6D, 8D, and 9D were used with a disk angle of 45 degrees.

Flow patterns downstream of the disk varied as the length, L_2 increased. At the distance of L_2 = 8D downstream, the flow seemed to have a fully developed flow pattern. Thus, the distance L_2 downstream of the disk was determined to be 8D. Subsequent computations were carried out with L_2 = 8D.

Also, in order to determine an optimum node number, several nodes 8320, 13120, 23616 were used with the disk angle of 45 degrees. Comparing the CPU time and the calculation accuracy, we selected the grid with 13120 nodes as our calculation basis. Subsequent computations were carried out with 13120 nodes.

In all of these calculations, we are using a thin flap valve disk model. Comparison was made between the 3D model and results considered by Blevins (1984), who compiled A: thin, B: blunt disk, C: thin flap, and D: streamlined flap. The 3D model gives a reasonable agreement with those of Blevins (1984). And the 45 degree open condition is agreeable with the experimental results.

In general, the computational investigation obtained with the three dimensional model agrees with the results of valve experiments. However, it is recognized that larger grid numbers will yield more accurate results but take more CPU time. The results of the current three dimensional study of butterfly valve flows give sufficient accurate results.

References

Addy, A. L., Morris, M. J., and Dutton, J. C., 1985, "An Investigation of Compressible Flow Characteristics of Butterfly Valves," ASME JOURNAL OF FLUIDS ENGINEERING, Vol. 107, Dec., pp. 512–517.

Anderson, D. A., Tannehill, J. C., and Pletcher, R. H., 1984, *Computational Fluid Mechanics and Heat Transfer,* Hemisphere and McGraw-Hill.

Blevins, Robert D., Chapter 6, 1984, *Applied Fluid Dynamics Handbook,* Van Nostrand Reinhold, New York, pp. 84–88.

Eom, K., 1988, "Performance of Butterfly Valves as a Flow Controller," ASME JOURNAL OF FLUIDS ENGINEERING, Vol. 110, Mar., pp. 16–19.

FLUENT, *User's Manual,* Ver. 4.11, 4.2, Fluent Inc., 1991, 1993.

Huang, Chendong, 1994, "Three Dimensional Analysis of Butterfly Valve Flows," MS thesis, Department of Mechanical Engineering and Engineering Science, University of North Carolina at Charlotte, April.

Ito, Yukio, 1988, "A Peculiar Behavior of Cavitating Flow Around a Butterfly Valve," *Trans. Jpn. Soc. Mech. Eng.,* Serial B, Vol. 54, No. 508, Dec., pp. 3317–3324.

Kim, R. H., and Wu, N. Y., 1992, "Numerical Simulation Butterfly Valve Fluid Flow," *Proceedings of the FLUENT User's Group Meeting,* pp. 296–313.

Kim, R. H., and Huang, C., 1993, "3-D Analysis Butterfly Valve Fluid Flow," *Proceedings of the FLUENT User's Group Meeting,* pp. 43–57.

Kitamura, M., Yamazaki, K., Okada, Y., and Hashimoto, K., 1993, "Visualizing Flows in Butterfly Valves," Kubota, Ltd., Flow Visualization III, *Proceedings of the 3rd Inter. Sym. on Flow Visualization,* Sept. 6–9, Univ. of Michigan, Ann Arbor, Michigan, Ed., W. J. Yang, Hemisphere Publishing Corp.

Lacor, C., and Hirsch, C., 1988, "Numerical Simulation of the Three-Dimensional Flow around a Butterfly Valves," ASME Fluids Eng. Div. Publ. FED, Vol. 69, *Flows in Non-Rotating Turbomachinery Components.*

Launder, B. E., and Spalding, D. B., 1974, *Comp. Methods Appl. Mech. Eng.,* Vol. 3, pp. 269.

Lyons, Jerry L., and Lyons, 1975, *Encyclopedia of Valves,* Van Nostrand Reinhold, New York.

McPherson, M. B., et al., 1957, "Butterfly Valve Flow Characteristics," *ASCE J. Hydraulics Div.* 83(1), paper 1167-1.

Morris, M. J., and Dutton, J. C., 1989, "Compressible Flow Characteristics of Butterfly Valves," ASME JOURNAL OF FLUIDS ENGINEERING, Vol. 111, pp. 400–407, Dec.

Morris, M. J., and Dutton, J. C., 1989, "Aerodynamics Torque Characteristics of Butterfly Valves in Compressible Flow," ASME JOURNAL OF FLUIDS ENGINEERING, Vol. 111, pp. 392–409, Dec.

Morris, M. J., and Dutton, J. C., 1991, "An Experimental Investigation of Butterfly Valve Performance Downstream of an Elbow," ASME JOURNAL OF FLUIDS ENGINEERING, Vol. 113, pp. 81–85, Mar.

Morris, M. J., and Dutton, J. C., 1991, "The Performance of Two Butterfly Valves Mounted in Series," ASME JOURNAL OF FLUIDS ENGINEERING, Vol. 113, pp. 419–423, Sept.

Patankar, S. V., 1980, *Numerical Heat Transfer and Fluid Flow,* Hemisphere Publishing, N.Y.

Schlicting, H., 1968, *Boundary Layer Theory,* 6th Ed., McGraw-Hill, New York.

Wu, Ningyan, 1992, "Numerical Simulation of Butterfly Valve Flows," Master's Thesis, Department of Mechanical Engineering and Engineering Science, University of North Carolina at Charlotte.

Viscosity Correction Factor for Rotameter

J. Wojtkowiak
Adjunct Professor.

Cz. O. Popiel
Professor.

Heat and Fluid Flow Group,
Institute of Environmental Engineering,
Poznan University of Technology,
60-965 Poznań, Piotrowo 3A, Poland

This paper describes how the developed formula for rotameter flow coefficient using the rotameter scale provided by a manufacturer and valid for a specific fluid and for design (or calibration) flow conditions allow us to determine the actual flow rate at measurement conditions and for different fluid having different viscosity or allow us to determine the viscosity correction factor. The developed theory has been verified experimentally using typical rotameter equipped with the plumb type float, for water of 15°C and having a flow rate range from 10 to 100 l/hr. A very good agreement between theoretical calculation and calibration results was obtain for water flow at 88°C. In this case the kinematic viscosity ratio was $\nu_{15}/\nu_{88} = 3.46$ *and the density correction factor was* $F_{dens} = 1.019$ *and the viscosity correction factor varied from* $F_{visc} = 1.095$ *at 100 l/hr to* $F_{visc} = 1.93$ *at 10 l/hr.*

Introduction

The rotameter is the most common variable-area flowmeter. Due to its many advantages it belongs to the most economical instrument for measuring flows in pipe of 50 mm in diameter and under. The rotameter consists of tapered metering tube and a float moving vertically exposing a variable annular area to the flow (Fig. 1). As the buoyancy and weight forces of the float are constant the differential pressure across the float resulting from the Bernoulli's equation also remains constant (neglecting a boundary layer thickness, contraction and, in gases, expansion effects). To accept a given flow rate the float height changes to expose the annular flow area between the float and tapered tube. Therefore the float height being function of the annular flow area for the tapered tube is an indication of the flow rate.

The rotameters are usually design and calibrated for a specific fluid and temperature, for example, for water at 15°C or for air at 1.01325 bar and 15°C. For fluid of different density and viscosity a correction factor should be applied. The density correction factors resulting from the basic theory of rotameter are commonly known and given, for example, in the handbook of Miller (1989). The viscosity correction factor practically is not available and the rotameter should be calibrated with the new fluid at actual temperature. To avoid the influence of viscosity the special float designs are recommended. A "viscosity limit" (or so call "viscosity immunity ceiling"), below which no viscosity correction is required, is sometime given for special float shapes (Fischer and Porter).

In this paper, a relatively simple and efficient procedure for predicting the viscosity correction factor is presented. The method is applied to predict the actual flow rate of water at 88°C (kinematic viscosity $\nu_{88} = 0.331 * 10^{-6}$ m^2/s) using a design rotameter scale valid for water at 15°C (kinematic viscosity $\nu_{15} = 1.146 * 10^{-6}$ m^2/s). A very good agreement between experimental calibration and calculation results is demonstrated.

Rotameter Scale Reading Reduction

Rotameter Basic Equation. Resulting from the Bernoulli's equation, from a sum of the forces acting on the float at static equilibrium at any float position and from the mass flow continuity for a constant-density fluid the basic equation for rotameter is (Miller, 1989)

$$Q = \alpha A[2V_{fl}g(\rho_{fl} - \rho)/(A_{fl}\rho)]^{0.5} \tag{1}$$

where the flow coefficient α is introduced to correct for factors not included in the analysis such as viscosity, flow contraction, boundary layer and flow wake behind the float. It is assumed that the flow coefficient is a function of Reynolds number $\alpha = \alpha(\mathrm{Re})$ typical for a given shape of float. The Reynolds number based on the gap width is

$$\mathrm{Re} = U(D - d_{fl})/\nu \tag{2}$$

or

$$\mathrm{Re} = 4Q/[\pi(D + d_{fl})\nu] \tag{3}$$

Flow Correction Factors. The theoretical relationship between the flow rate at actual (measurement) flow conditions $Q_{\mathrm{th}}(h)$ and the rotameter scale reading $Q_{\mathrm{des}}(h)$ is obtained writing Eq. (1) first for design conditions

$$Q_{\mathrm{des}}(h) = \alpha(\mathrm{Re}_{\mathrm{des}})A(h)[2V_{fl}g(\rho_{fl} - \rho_{\mathrm{des}})/(A_{fl}\rho_{\mathrm{des}})]^{0.5} \tag{4}$$

and next for the actual flow conditions

$$Q_{\mathrm{th}}(h) = \alpha(\mathrm{Re}_{\mathrm{th}})A(h)[2V_{fl}g(\rho_{fl} - \rho_{\mathrm{th}})/(A_{fl}\rho_{\mathrm{th}})]^{0.5} \tag{5}$$

Dividing the above two Equations by sides we obtain

$$Q_{\mathrm{th}}(h) = Q_{\mathrm{des}}(h)\alpha(\mathrm{Re}_{\mathrm{th}})/\alpha(\mathrm{Re}_{\mathrm{des}}) \times \{\rho_{\mathrm{des}}(\rho_{fl} - \rho_{\mathrm{th}})/[\rho_{\mathrm{th}}(\rho_{fl} - \rho_{\mathrm{des}})]\}^{0.5} \tag{6}$$

In the case temperature changes we ignore the effect of temperature expansion of float and tube material on the annular flow area. In Eq. (6) we can readily distinguish the density correction factor

$$F_{\mathrm{dens}} = \{\rho_{\mathrm{des}}(\rho_{fl} - \rho_{\mathrm{th}})/[\rho_{\mathrm{th}}(\rho_{fl} - \rho_{\mathrm{des}})]\}^{0.5}$$

and the viscosity correction factor

$$F_{\mathrm{visc}} = \alpha(\mathrm{Re}_{\mathrm{th}})/\alpha(\mathrm{Re}_{\mathrm{des}})$$

To determine the viscosity correction factor we have to know the function $\alpha = \alpha(\mathrm{Re})$.

Function $\alpha = \alpha(\mathrm{Re})$. To determine this function we will use the rotameter scale valid for design (or calibration) conditions provided by the manufacturer. For more precise laboratory measurements or for old rotameters having unknown scale it is recommended to perform a new calibration test (at least for the upper and lower range limits).

Contributed by the Fluids Engineering Division for publication in the JOURNAL OF FLUIDS ENGINEERING. Manuscript received by the Fluids Engineering Division May 12, 1995; revised manuscript received January 15, 1996. Associate Technical Editor: J.A.C. Humphrey.

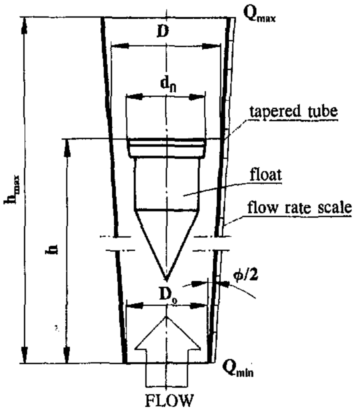

Fig. 1 Rotameter equipped with a plumb type float (only float is in a scale)

From Eq. (4) for a given rotameter we have

$$\alpha(\mathrm{Re}_{\mathrm{des}}) = Q_{\mathrm{des}}(h)/A(h)\{A_{fl}\rho_{\mathrm{des}}/[2V_{fl}g(\rho_{fl} - \rho_{\mathrm{des}})]\}^{0.5} \quad (7)$$

From this equation, we will eliminate all variables except Reynolds number. In first step, we will eliminate $Q_{\mathrm{des}}(h)$ using Eq. (3)

$$Q_{\mathrm{des}}(h) = \mathrm{Re}\pi[D(h) + d_{fl}]\nu_{\mathrm{des}}/4 \quad (8)$$

where: $D(h) = D_o + 2htg(\phi/2)$, and instead of $A(h)$ we will introduce an expression resulting from a rotameter geometry shown in Fig. 1.

$$A(h) = \pi\{[D_o + 2htg(\phi/2)]^2 - d_{fl}^2\}/4 \quad (9)$$

Now Eq. (7) is

$$\alpha(\mathrm{Re}, h) = \mathrm{Re}\nu_{\mathrm{des}}/\{[D_o + 2htg(\phi/2) - d_{fl}] \times [2V_{fl}g(\rho_{fl} - \rho_{\mathrm{des}})/(A_{fl}\rho_{\mathrm{des}})]^{0.5}\} \quad (10)$$

In the second step, we will find a function $h = h(\mathrm{Re})$ to eliminate the variable h. Knowing that the pressure drop across the float is almost constant we can assume a linear dependence between a flow rate and an annular flow area

$$Q_{\mathrm{des}}(h) = c_1A(h) + c_2 \quad (11)$$

and after using Eq. (9) we have

$$Q_{\mathrm{des}}(h) = c_1\pi\{[D_o + 2htg(\phi/2)]^2 - d_{fl}^2\}/4 + c_2 \quad (12)$$

Constants c_1 and c_2 will be determined from the lower and upper limits of the rotameter scale valid in the design (or calibration) conditions (e.g., for water at 15°C)

$$\text{at } h = 0 \quad \text{is} \quad Q_{\mathrm{des}}(h = 0) = Q_{\mathrm{min}}$$

$$\text{at } h = h_{\mathrm{max}} \quad \text{is} \quad Q_{\mathrm{des}}(h = h_{\mathrm{max}}) = Q_{\mathrm{max}}$$

Therefore we have

$$Q_{\mathrm{min}} = c_1\pi(D_o^2 - d_{fl}^2)/4 + c_2$$

$$Q_{\mathrm{max}} = c_1\pi\{(D_o + 2h_{\mathrm{max}}tg(\phi/2))]^2 - d_{fl}^2\}/4 + c_2$$

from which we receive

$$c_1 = (Q_{\mathrm{max}} - Q_{\mathrm{min}})/\{\pi h_{\mathrm{max}}tg(\phi/2)[D_o + h_{\mathrm{max}}tg(\phi/2)]\}$$

$$c_2 = Q_{\mathrm{min}} - (Q_{\mathrm{max}} - Q_{\mathrm{min}})(D_o^2 - d_{fl}^2)/\{4h_{\mathrm{max}}tg(\phi/2)[D_o + h_{\mathrm{max}}tg(\phi/2)]\}$$

Constants c_1 and c_2 are determined by the upper and lower flow rate limits of the scale valid for the design (or calibration) conditions and by the geometry of the tapered tube and float system. The accuracy of these constants depends on the precision of the design (or calibration) scale and as well as on the accuracy of the geometrical parameters of the rotameter.

After comparison of the right sides of Eqs. (8) and (12) and using expression $D(h) = D_o + 2htg(\phi/2)$ and after few transformations one can obtain

$$h = [\mathrm{Re}\nu_{\mathrm{des}} - 2c_1D_o + (\mathrm{Re}^2\nu_{\mathrm{des}}^2 + 4\,\mathrm{Re}c_1d_{fl}\nu_{\mathrm{des}} + 4c_1^2d_{fl}^2 - 16c_1c_2/\pi)^{0.5}]/[4c_1tg(\phi/2)] \quad (13)$$

Finally introducing Eq. (13) to Eq. (10) we obtain a general expression on the flow coefficient

$$\alpha(\mathrm{Re}) = 2c_1\,\mathrm{Re}\nu_{\mathrm{des}}/\{\{\mathrm{Re}\nu_{\mathrm{des}} - 2c_1d_{fl} + [\mathrm{Re}^2\nu_{\mathrm{des}}^2 + 4\,\mathrm{Re}c_1d_{fl}\nu_{\mathrm{des}} + 4c_1^2d_{fl}^2 - 16c_1c_2/\pi]^{0.5}\} \times [2V_{fl}g(\rho_{fl} - \rho_{\mathrm{des}})/(A_{fl}\rho_{\mathrm{des}})]^{0.5}\} \quad (14)$$

In Fig. 2 a plot of the flow coefficient versus Reynolds number obtained with the above formula and using data from Table 1 is shown (solid line). The relationship for $\alpha(\mathrm{Re})$ is generally valid for a given float, if we may assume a geometrical similarity for the whole range of the Reynolds numbers. The flow coefficient α at the lowest Reynolds number (Re = 95.8) was obtained for the minimum flow of water at 15°C when the float was at the bottom of the rotameter scale, where in our case the ratio of diameters was $D_o/d_{fl} = 1.0125$, and at the highest Reynolds number (Re = 936.3) for the maximum flow of water

Nomenclature

A = annular area between float and tapered metering tube = $A(h)$ (m^2)
A_{fl} = maximum float area = $A_{fl} = \pi d_{fl}^2/4$ (m^2)
c_1, c_2 = rotameter constants (m/s) and (m^3/s)
D = internal diameter of tapered metering tube = $D(h)$ (m)
D_o = internal diameter of tapered metering tube at minimum flow rate (related to minimum annular area) = $D(h = 0)$) (m)
d_{fl} = maximum float diameter (m)
g = gravity (m/s^2)
h = position (height) of float edge against scale giving flow rate reading (m)
h_{max} = maximum position (height) of float giving maximum flow rate reading (m)
Re = Reynolds number = $U(D - d_{fl})/\nu$
U = average velocity of fluid in an annular cross section between float and metering tube (m/s)
V_{fl} = float volume (m^3)
Q = flow rate (l/hr)
Q_{min} = minimum flow rate (l/hr)
Q_{max} = maximum flow rate (l/hr)
α = flow coefficient
ν = kinematic viscosity of fluid (m^2/s)
ρ = fluid density (kg/m^3)
ρ_{fl} = density of float material (kg/m^3)
ϕ = cone angle of tapered metering tube (rad)

Subscripts

des = design (or manufacturer calibration) conditions of rotameter scale e.g. water at temperature of 15°C
exp = result of experiment
th = theoretical calculation (at measurement conditions)

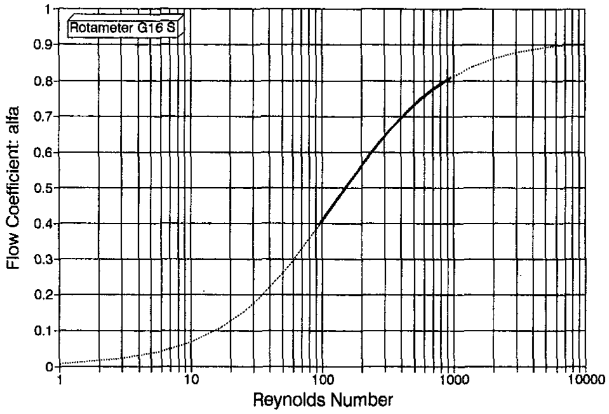

Fig. 2 Flow coefficient $\alpha = \alpha(\mathrm{Re})$ versus Reynolds number for rotameter equipped with a plumb type float (VEB Medingen, Dresden). Uncertainty in $\alpha = \pm 0.012$ and in Re = ±2 at $Q_{\min}$, and in $\alpha = \pm 0.010$ and in Re = ±2.8 at $Q_{\max}$. For all the uncertainty estimates, the assumed odds were 20:1.

at 15°C when the float was at the top of the rotameter scale, where $D_{\max}/d_{fl} = 1.06$. We see that the ratios of tube and float diameters are in a narrow range. Therefore our relationship represented by a solid line is generally valid for a given float because we may assume a geometrical similarity of the rotameter tube and float systems. Dashed parts of the $\alpha(\mathrm{Re})$ curve are its extrapolations obtained with the formula (14) assuming that at $\mathrm{Re} < 95.8$ and at $\mathrm{Re} > 936.3$ they are valid for fluids having higher or lower viscosity than water at 15°C, respectively.

Moreover we also assume that an effect of slightly different float upstream flow structures for a float in the lower and upper part of the rotameter tube can be neglected.

Procedure for Rotameter Scale Reduction. Using rotameter for a fluid of different viscosity then viscosity of fluid for which the rotameter scale (at design or calibration conditions) is valid, the flow rate indicated on the scale has to be reduced to the flow measurement conditions with Eq. (6). The flow coefficients α_{des} and α_{th} one has to determine from the formula (14) in which the Reynolds number $\mathrm{Re}_{\mathrm{des}}$ is calculated from Eq. (3) in which the expression $D(h) = D_o + 2htg(\phi/2)$ and the expression on h resulting from Eq. (12)

$$h = \{[4(Q_{\mathrm{des}} - c_2)/(c_1\pi) + d_{fl}^2]^{0.5} - D_o\}/[2tg(\phi/2)] \quad (15)$$

is used

$$\mathrm{Re}_{\mathrm{des}} = 4Q_{\mathrm{des}}(h)/\{\pi\nu_{\mathrm{des}}[(4[Q_{\mathrm{des}}(h) - c_2]/(c_1\pi) + d_{fl}^2)^{0.5} + d_{fl}]\} \quad (16)$$

Table 1 Technical data of the rotameter type: G16 S (VEB Medingen)

	Symbol	Value
Lower limit of rotameter scale (l/hr)	$Q_{\min}$	10
Upper limit of rotameter scale (l/hr)	$Q_{\max}$	100
Height of rotameter scale (mm)	$h_{\max}$	203.5 ± 0.05
Minimum diameter of tapered tube (at $h = 0$, mm)	D_0	16.2 ± 0.002
Maximum diameter of tapered tube (at $h_{\max}$, mm)	$D_{\max}$	16.96 ± 0.002
Taper of rotameter tube	$tg(\phi/2)$	$(1867 \pm 13) \times 10^{-6}$
Maximum float diameter (mm)	d_{fl}	16 ± 0.002
Minimum and maximum gap (mm)	$D - d_{fl}$	0.2 ÷ 0.96
Maximum float area (mm^2)	A_{fl}	201.06 ± 0.06
Density of float material (stainless steel, kg/m^3)	ρ_{fl}	7850
Float volume (mm^3)	V_{fl}	2846 ± 7

Uncertainties in directly measured and derived variables are at 20:1 odds.

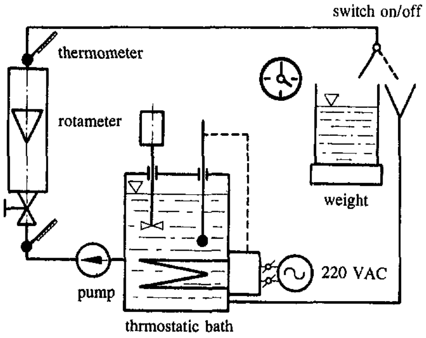

Fig. 3 Rotameter calibration set up for cold and hot water

The value of $\alpha_{\mathrm{th}} = \alpha(\mathrm{Re}_{\mathrm{th}})$ cannot be calculated so simply as the value of $\alpha_{\mathrm{des}} = \alpha(\mathrm{Re}_{\mathrm{des}})$ because the Reynolds number $\mathrm{Re}_{\mathrm{th}}$ is a function of unknown flow rate $Q_{\mathrm{th}}(h)$, whereas $\mathrm{Re}_{\mathrm{des}}$ was a function of the rotameter reading $Q_{\mathrm{des}}(h)$. This inconvenience we can overcome in the following way. As previously, the Reynolds number is calculated from Eq. (3) and after introduction the expression $D(h) = D_o + 2htg(\phi/2)$ we obtain the relationship between $\mathrm{Re}_{\mathrm{th}}$ and $Q_{\mathrm{th}}(h)$:

$$\mathrm{Re}_{\mathrm{th}} = 4Q_{\mathrm{th}}(h)/\{\pi\nu_{\mathrm{th}}[D_o + 2htg(\phi/2) + d_{fl}]\} \quad (17)$$

Accepting that for the flow rates $Q_{\mathrm{des}}(h)$ and $Q_{\mathrm{th}}(h)$ we have the same position of the float, the variable h in Eq. (17) can be replaced by Eq. (15). In the result we obtain

$$\mathrm{Re}_{\mathrm{th}} = 4Q_{\mathrm{th}}(h)/\{\pi\nu_{\mathrm{th}}[(4[Q_{\mathrm{des}}(h) - c_2]/(c_1\pi) + d_{fl}^2)^{0.5} + d_{fl}]\} \quad (18)$$

Introduction of Eq. (18) into (14) gives

$$\alpha_{\mathrm{th}} = \alpha[Q_{\mathrm{th}}(h)] \quad (19)$$

and introducing Eq. (19) into Eq. (6) gives the equation

$$Q_{\mathrm{th}}(h) = f[Q_{\mathrm{th}}(h)] \quad (20)$$

in which the only unknown value is the actual flow rate $Q_{\mathrm{th}}(h)$.

The solution of the above equation can be obtain with one of known numerical methods. We have used a relatively simple and effective iterative technique employing the spreadsheet QuattroPro.

Step 0: Calculate the density correction factor resulting from Eq. (6) $F_{\mathrm{dens}} = \{\rho_{\mathrm{des}}(\rho_{fl} - \rho_{\mathrm{th}})/[\rho_{\mathrm{th}}(\rho_{fl} - \rho_{\mathrm{des}})]\}^{0.5}$ and the flow coefficient $\alpha_{\mathrm{des}} = \alpha(\mathrm{Re}_{\mathrm{des}})$ from Eq. (14) and using Eq. (16).

Step 1: Assume the first value of $Q_{\mathrm{th}}(h)$ equal to the value of the flow rate indicated by the rotameter scale, i.e., $Q_{\mathrm{th}}(h) \approx Q_{\mathrm{des}}(h)$.

Step 2: Calculate $\mathrm{Re}_{\mathrm{th}}$ with Eq. (18) using the latest value of $Q_{\mathrm{th}}(h)$.

Step 3: Calculate $\alpha(\mathrm{Re}_{\mathrm{th}})$ with Eq. (14) using the latest value of $\mathrm{Re}_{\mathrm{th}}$.

Step 4: Calculate new value of $Q_{\mathrm{th}}(\mathrm{Re})$ with Eq. (6) using the latest value of $\alpha(\mathrm{Re}_{\mathrm{th}})$.

Step 5: If the new value of $Q_{\mathrm{th}}(\mathrm{Re})$ is different from the previous one, for example by 0.1 percent, the calculation is continued starting from the STEP 2 using the latest value of $Q_{\mathrm{th}}(h)$. We will stop the calculation when the difference of new and previous value of $Q_{\mathrm{th}}(h)$ is lower then 0.1 percent.

Table 2 Results of measurements and calculations for rotameter G16 S (VEB Medingen)

$T \approx 15°C$						$T_{exp} \approx 88°C$							
SCALE		MEASUREMENTS				MEASUREMENTS			CALCULATIONS				
Q_{des} (1/hr)	Re_{des}	T_{exp} (°C)	Q_{exp} (1/hr)	Q_{exp}/Q_{des}	δ_{des} %	T_{exp} (°C)	Q_{exp} (1/hr)	Q_{exp}/Q_{des}	Q_{th} (1/hr)	Re_{th}	δ_{th} (%)	α_{th}/α_{des}	Q_{th}/Q_{des}
6	57.6	15.2	7.87	1.311	32.7	86.9	13.62	2.271	15.55	506.6	−14.2	2.545	2.594
10	95.8	15.0	10.36	1.036	3.5	87.6	17.24	1.724	19.69	644.8	−14.2	1.931	1.968
15	143.6	14.8	15.16	1.010	1.0	—	—	—	—	813.1	—	—	—
20	191.2	14.6	20.85	1.042	4.1	87.9	29.53	1.477	29.15	979.8	−1.3	1.467	1.495
30	286.0	15.3	32.13	1.071	6.6	88.6	41.68	1.389	40.14	1323	3.7	1.313	1.338
40	380.3	15.3	41.93	1.048	4.6	88.0	52.35	1.309	50.36	1644	3.8	1.235	1.258
50	474.2	15.3	51.71	1.034	3.3	88.4	62.95	1.259	60.56	1981	3.8	1.189	1.211
60	567.5	15.2	60.68	1.011	1.1	87.7	72.25	1.204	70.73	2289	2.1	1.157	1.179
70	660.4	15.2	70.56	1.008	0.8	88.2	83.43	1.192	81.01	2628	2.9	1.135	1.157
80	752.9	15.1	80.84	1.010	1.0	88.7	94.29	1.179	90.71	2969	3.8	1.119	1.140
90	844.8	15.0	89.76	0.997	−0.3	88.7	104.1	1.156	101.5	3292	2.5	1.106	1.127
95	890.6	15.0	93.92	0.989	−1.1	89.0	108.7	1.144	106.5	3466	2.0	1.101	1.121
100	936.3	14.9	98.96	0.990	−1.0	88.4	114.1	1.141	111.7	3604	2.1	1.095	1.116

where $\delta_{des} = 100(Q_{exp} - Q_{des})/Q_{exp}$, and $\delta_{th} = 100(Q_{exp} - Q_{th})/Q_{exp}$.

This calculation procedure is fast convergent and only a few iterations are needed to obtain the final value of $Q_{th}(h)$. Now we can also determine the viscosity correction factor $F_{visc} = \alpha(Re_{th})/\alpha(Re_{des})$.

Experimental Verification

The correctness of the developed theory and the calculation procedure of the viscosity correction factor has been tested experimentally using a typical rotameter design equipped with a plumb type float for water of 15°C and having a flow rate range from 10 to 100 l/hr (Table 1). The experimental setup is shown in Fig. 3. It is in fact a simple calibration apparatus to which a thermostatic bath is included. The flow rate was measured with a weight technique using a precise laboratory weight having a resolution of 0.1 g and a digital stop watch.

In Table 2 the results of calibration (measurements of the actual flow rate versus readings of the scale) of the tested rotameter for water at approx. 15°C and at 88°C, and as well as the results of the calculated flow rates and the viscosity correction factor for water at 88°C along the rotameter scale are presented. Some of these data are compared on the diagram in Fig. 4. We can see that readings of the scale and measurements of water flow rate at 15°C with the weight technique are relatively close (empty squares). Recorded discrepancies are within the guaranteed maximum error of ±2.5 l/hr (i.e., the error resulting from the relative maximum error of ±2.5 percent referred to the upper limit of the rotameter scale equal 100 l/hr). For example the highest discrepancy of 2.13 l/hr was recorded at $Q_{des} = 30$ l/hr.

The measurements of the water flow rate at the temperature of 88°C are located much higher then readings of the flow meter scale. At the upper limit of the rotameter scale (100 l/hr) the actual flow rate is equal $Q_{exp}/Q_{des} = 1.14$ of the scale reading and this departure from the scale reading rises up to the value of 1.72 at the lower limit of the scale (10 l/hr). These large divergences cause that measurements of the flow rate of hot water with the rotameter without new calibration or without using precise correction factors are not recommended.

The effect of temperature is stronger at lower flow rates when the annular gap between the float and tapered tube is narrower. The mean reason of the significant effect of temperature on the differences between the reading of the rotameter scale and the actual flow rates is the strong change of the viscosity of water with temperature (Popiel and Wojtkowiak, 1995). A kinematic viscosity of water at 15°C is $\nu_{des} = \nu_{15} = 1.146 \times 10^{-6}$ m²/s and at 88°C is $\nu_{th} = \nu_{88} = 0.331 \times 10^{-6}$ m²/s. In our case the calculated viscosity flow correction factor is varied from $F_{visc} = \alpha_{th}/\alpha_{des} = 1.095$ at $Q_{des} = 100$ l/hr to $\alpha_{th}/\alpha_{des} = 1.93$ at $Q_{des} = 10$ l/hr.

Influence of density is stable along the scale and very weak as the changes of water density are rather low. A density of water at 15°C is $\rho_{des} = 999.1$ kg/m³ and at 88°C is $\rho_{th} = 966.7$ kg/m³, and the density correction factor is $F_{dens} = \{\rho_{des}(\rho_{fl} - \rho_{th})/[\rho_{th}(\rho_{fl} - \rho_{des})]\}^{0.5} = 1.019$.

A comparison of the calculation results based on the developed theory predicting water flow rates at temperature of 88°C (solid line in Fig. 4) shows a very good agreement with the results of direct measurements of flow rate obtained with the weight technique (filled squares). The sources of some discrepancies can be an inaccuracy of the gap width determination which is more critical at lower flow rates when the gap is very small, and as well as an effect of the inlet flow structure and a slight departure from the geometrical similarity of the rotameter tube and float system. Generally, the differences between measured and calculated flow rates of water at 88°C are below the guaranteed maximum error for this rotameter (±2.5 l/hr). However, the local relative errors at low flow rates reach the values of 14.2 percent.

Conclusions

It was found that viscosity of fluid has a very strong effect on the readings of the rotameter having a plumb type float. The

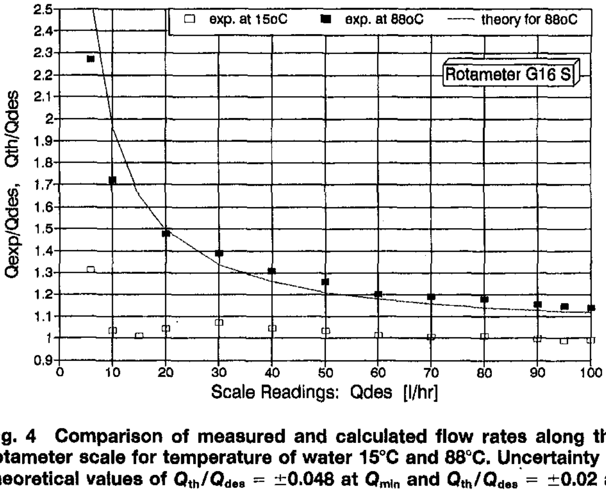

Fig. 4 Comparison of measured and calculated flow rates along the rotameter scale for temperature of water 15°C and 88°C. Uncertainty in theoretical values of $Q_{th}/Q_{des} = \pm 0.048$ at Q_{min} and $Q_{th}/Q_{des} = \pm 0.02$ at Q_{max}. Uncertainty in measured values of $Q_{exp}/Q_{des} = \pm 0.024$ at Q_{min} and $Q_{exp}/Q_{des} = \pm 0.01$ at Q_{max}. In scale readings $Q_{des} = \pm 0.2$ l/h. For all the uncertainty estimates, the assumed odds were 20:1.

calculation procedure for the viscosity flow correction factor for rotameter used in different conditions from design (or calibration) ones determined by manufacturer (i.e., usually for water at 15°C or for air at 15°C and 1.01325 bar) has been developed. The theory was tested experimentally with the typical rotameter for water at 15°C. A comparison of measured flow rates of water at 88°C and theoretically corrected readings of the rotameter scale showed a very good agreement. In this case the viscosity ratio was $\nu_{15}/\nu_{88} = 3.46$ and the viscosity correction factor varied from $F_{\text{visc}} = 1.095$ at the upper limit of the scale equal 100 l/h to 1.93 at the lower limit 10 l/hr.

The presented calculation procedure for viscosity correction is based on a geometrical similarity of the rotameter tube and float system, i.e., it is valid for low changes of the ratio of the rotameter tube and float diameters. Also the effect of inlet flow structure is neglected.

References

VEB Medingen: VEB MLW Prufgerate Werk Medingen, Dresden. Durchflussmesser Baureihe GSV (technical data of rotameter, type of tube: G16 S).

Fisher and Porter, *Instrumentation for Process/Power/Environmental*, General Catalog. Division B: Measurements and Transmission.

Miller, R. W., 1989, *Flow Measurement Engineering Handbook*, Second Edition, McGraw-Hill, pp. 6.23–6.27, 14.43–14.58.

Popiel, Cz.O., and Wojtkowiak, J., 1995, "Formulas for thermophysical properties of water for heat transfer calculations on PC (from 0°C to 150°C)." *Cieplownictwo Ogrzewnictwo Wentylacja*, No. 2 (299), Feb., pp. 55–58 (in Polish).

Particle-Surface Interactions in Heat Exchanger Fouling

D. Bouris
Research Assistant.

G. Bergeles
Professor.

Laboratory of Aerodynamics, Department of
Mechanical Engineering,
National Technical University of Athens,
5 Heroon Polytechniou Ave.,
15700 Zografou,
Athens, Greece

The problem of fouling is of vital importance to heat exchanger efficiency and should be considered during the design phase of the heat exchanger. The purpose of the present paper is to introduce a novel method to aid in the evaluation of the various parameters that affect the fouling phenomenon. The method considers the particle-surface interaction from the energy balance at the point of impaction and takes into consideration the material properties of the particle and surface as well as the effect of the surrounding flow field on the particle movement and impaction. The calculated deposition flux is used to form the deposit evolution in time considering the removal mechanisms resulting from fluid shear stress and the eroding impacts of the particles. The model is validated against experimental measurements of particle deposition from a two phase flow of hot gases around a circular cylinder. The experimentally measured flow field around a staggered tube bundle is also predicted and a fouling analysis is performed regarding the validity of fouling studies in scaled down model configurations. It is concluded that the actual dimensions of the heat exchanger configuration are of vital importance to its fouling behavior and scaling laws are difficult to apply.

I Introduction

Fouling is a major problem in many industrial applications such as turbomachinery (Tabakoff, 1984) and heat transfer (Taborek, 1972). The purpose of the present paper is to introduce a numerical method that will serve as an engineering tool to study the fouling phenomenon. More specifically, the method will be applied to heat exchanger fouling in lignite utility boilers; here the flue gases carry ash particles up to the superheater area and deposit them onto the tube surfaces thereby reducing heat transfer efficiency.

There have been many numerical models developed to predict the fouling phenomenon. The basic concept used to describe fouling is due to Kern and Seaton (1959) who define the growth of the deposit as the result of a deposition flux and a removal flux which will eventually reach equilibrium. They expressed this through an exponential equation. Through a series of papers, Cleaver and Yates (1973, 1976) formed a deposition model where deposition is expressed using the friction velocity and the particle concentration and the expression for the removal rate is from their turbulent burst theory using a critical wall shear stress. Though the approach is quite different, they develop an exponential equation similar in form to the one by Kern and Seaton. Papavergos and Hedley (1984) examined a number of deposition models but limited their comparisons to simple flow fields where the models took the flow into account through the particle relaxation time or the flow Reynolds number. Local surface conditions were most often ignored.

''Global'' models, such as those previously mentioned, have shown acceptable agreement with experimental measurements as far as deposit build up in time and overall exchanger efficiency is concerned. However, they don't provide information regarding the deposit distribution and the effect of flow field parameters, particle material, and heat exchanger configuration on the overall phenomenon. This would significantly help the design stage due to the importance of these parameters (Hein, 1977).

One of the most important mechanisms in particle deposition is the impaction mechanism. Rogers and Reed (1984) and Fichman and Pnueli (1985) both introduced an elastic-plastic impact model that provides a criterion for the adhesion or rebound of a particle impacting a solid surface based on the particle impact velocity and the material properties of both the particle and the surface. Although the models were much alike, the papers were directed toward different applications (surface coating and filtration, respectively). Wall et al. (1988) improved the original model by taking into account a dynamic yield limit to distinguish elastic from elastic-plastic impactions.

In heat exchanger fouling, the flow field is highly complex (Dowlati et al., 1992; Braun and Kudriavtsev, 1995) and should not be neglected. In the methodology to be presented here, the flow field (velocities and temperature) will be numerically predicted through a solution of the Navier Stokes and energy equations using a collocated control volume method based on the SIMPLE pressure correction algorithm, while the k-ϵ turbulence model will account for the effects of turbulence. A Lagrangian particle tracking method will be used (Burry and Bergeles, 1993) that takes into account the anisotropy of the turbulence. Knowledge of the flow field characteristics allows the direct evaluation of the effect of lift forces, thermophoretic forces, and turbulent fluctuations on the particle behavior. The impact-adhesion theory will be used in combination with the particle tracking method to form a novel deposition model, which will determine particle sticking or rebound after impaction. Material properties of the particles and tube surfaces are influenced by the local temperatures and will be considered due to the nature of the impact-adhesion model. After the deposition rate has been locally calculated, an exponential equation is used to calculate the evolution of the deposit in time, while the removal rate is calculated using the local fluid shear stress as well as an eroding shear stress which is calculated from the particle impactions. This leads to the calculation of the deposit distribution on the heat exchanger surfaces, making the method particularly well suited for heat exchanger design methodologies.

The full methodology will be used to predict the two-phase flow of combustion gases and particles around a circular cylinder in crossflow. The particle deposition rates to the surface of the cylinder will be compared with experimental measurements for various particle diameters. Finally, the fouling phenomenon on a staggered tube bundle arrangement will be studied. As will be shown, conflicting factors between the flow field and parti-

---

Contributed by the Fluids Engineering Division for publication in the JOURNAL OF FLUIDS ENGINEERING. Manuscript received by the Fluids Engineering Division September 24, 1995; revised manuscript received March 1, 1996. Associate Technical Editor: M. W. Reeks.

cles make it difficult to study the fouling phenomenon in scaled-down geometries since known similarity laws do not apply. This makes numerical studies essential for this type of engineering problem.

II The Impact-Adhesion Model

Theoretical Analysis. The novelty of the method presented here to calculate the deposition rate of particles impacting a surface rests in the fact that the calculation takes into account the local conditions before and during impact. These conditions are determined by the initial impact velocity, the material properties of the particle, and the surface and the influence of the flow field through the lift force and the thermophoretic force acting on the particle. The local temperature also affects the material properties of the particle and the surface.

The first part of the model is based on the original concept of Bitter (1963a) that the energy available to a particle just before it impacts onto a surface is the kinetic energy due to its velocity, while the most important energy loss mechanisms are plastic deformation (provided the impact velocity exceeds a certain limit defined by the material properties of the particle and surface) and elastic wave propagation during the first phase of the impact. The energy stored as elastic energy will be returned to the particle during the second phase which begins after the particle reaches the point where its velocity is zero. For a spherical particle with mass (m_p), radius ($R = d/2$), moving with a velocity (V) normal to a plane surface and impacting on to the surface, the following energy balance equation can be written (Wall et al., 1988):

$$Q_i - Q_L - Q_P = Q_E \qquad (1)$$

where the initial kinetic energy of the particle $Q_i = \frac{1}{2} m_p V^2$ is lost to plastic deformation and dissipated due to elastic wave propagation (a modification to Wall et al., 1988, based on Reed, 1985). The remaining stored elastic energy is then returned to the particle as kinetic energy. If this is larger than the energy due to attractive forces between particle and surface Q_E, Q'_A then the particle will rebound, otherwise it will stick to the surface. The attractive forces are mostly due to dispersion forces that are dependant on the electrical properties of the volume elements of the materials and the distance between them. They are present in all types of matter and are sometimes cited as the London dispersion forces (Fowkes, 1964).

For a particle of known size and velocity the full expressions for the terms in (1) are functions of material properties of the particle and the surface to which it impacts: E (Young's modulus), ν^P (Poisson's ratio), Y (Elastic yield limit of the softer of the two materials), ρ (particle density), and $\Delta\gamma = 2\sqrt{\gamma_p^d \gamma_s^d}$ (interfacial surface energy derived from the dispersive surface energies of the two materials, Fowkes, 1964). These expressions used by Rogers and Reed (1984) and then by Wall et al. (1988) were originally introduced by Bitter (1963a) based on the Hertz theory. However, they are rather complex and therefore only our modifications to the basic theory will be presented here. The impact-adhesion model without flow field effects has already been validated in Wall et al. (1988) for particles impacting surfaces of various materials. The only other addition presented to this part of the model is the energy loss due to elastic waves propagating away from the point of impaction that is important only in purely elastic impacts since it is the only energy loss mechanism present. Validation of this form of the model has been presented in Bouris-Burry and Bergeles (1994).

The novelty presented in this paper is the extension of the model to situations with a surrounding flow field. In this case, the shear stresses of the surrounding flow result in a force that acts on the particle in the direction of the velocity gradient and therefore becomes a lift force in the area near a wall. This lift force (Saffman, 1965) can be expected to play an important role in particle resuspension from the wall since shear stress is significant here. As stated by Cleaver and Yates (1973) the following expression can be used:

$$F_L = 0.83 \frac{\rho}{\nu} d^3 \left(\frac{\tau_w}{\rho}\right)^{(3/2)} \qquad (2)$$

If the lift force is assumed to be constant over the second phase of the impact when the particle begins to move away from the wall then the energy transferred to the particle will be:

$$Q_{\text{lift}} = F_L \delta, \quad \delta = \frac{r_t^2}{2R} \qquad (3)$$

where δ is defined by Bitter (1963a) and r_t is calculated from (Wall et al., 1988).

Nomenclature

A = area (m^2)
C_s, C_m, C_t, K_2 = constants
D_{cyl} = heat exchanger cylinder diameter (m)
E = Young's modulus (Pa)
F_L, Q_{lift} = lift force (N) and lift energy (J)
k = thermal conductivity (W/m/K)
m, $\dot{m}$ = mass (kg) and mass flux (kg/s)
Q'_A = attractive energy between particle and surface (J)
Q_E = stored elastic energy (J)
Q_i = initial kinetic energy of particle (J)
Q_L = energy dissipated due to elastic wave propagation (J)
Q_P = plastic deformation energy (J)
R = universal gas constant (8.315 kJ/kmol/K)
$R = d/2$ = particle radius and diameter (m)
r_t = radius of total contact area between particle and surface (m)
Stk = particle Stokes number
Stm, j''_p = nondimensional deposition rate and particle deposition flux (kg/m^2/s)
t = time (s)
T_0 = local temperature (K)
U_∞ = freestream velocity (m/s)
$u_\tau = (\tau_w/\rho)^{1/2}$ = friction velocity (m/s)
V = particle velocity (m/s)
Y = elastic yield limit (Pa)
δ = total approach between particle and surface (m)
$\Delta\gamma$, γ^d = interfacial surface energy and dispersive surface energy (J/m^2)
λ = molecular mean free path (m)
ν^P = Poisson's ratio
μ, ν = dynamic (kg/m/s) and kinematic (m^2/s) viscosity of fluid
ρ = density (kg/m^3)
$\rho_{p,\infty}$ = particle mass concentration at free stream (kg/m^3)
τ_{er}, τ_w = eroding particle shear stress and wall shear stress (kg/m/s^2)

Subscripts

p = particle
∞ = freestream
g = gas, fluid
d = deposit
r = rebound

It should be stated here that the range of (2) has been a matter of research lately. Hall (1988) measured the lift force acting on a particle near a wall and concluded that the Saffman expression is reasonably accurate only for particles with $\alpha^+ = Ru_\tau/\nu < 20$. In the present work, the lift force is considered negligible during the first phase of the impaction because the plastic deformation is almost always several orders of magnitude larger than the energy due to the lift force. On the other hand, during the second phase, the elastic energy remaining, the surface energy of adhesion and the energy due to the aerodynamic lift force are all influential to the rebound or adhesion of the particle. Furthermore, in the cases to be studied $\alpha^+ < 14$ which warrants the use of (2). Finally, the unsteadiness of the lift force has not been considered since its complexity is not in the scope of the model but it would provide an interesting topic for investigation.

After the energy balance, the normal rebound velocity can be calculated:

$$V_r = \left[\frac{2}{m_p}(Q_i - Q_P - Q_A' - Q_L + Q_{\text{lift}})\right]^{(1/2)} \qquad (4)$$

where Q_L is significant only for purely elastic deformations.

The impact adhesion model as presented above determines whether a particle of given impact velocity and material properties will stick or rebound from a surface whose material properties are also known. If rebound occurs then the normal rebound velocity is also calculated. At this stage it is assumed that the tangential velocity does not significantly influence rebound or adhesion of the particle but its influence will be considered as an eroding shear stress on the deposit in the next part of the model.

Prediction of Particle Deposition Onto a Cylinder in Crossflow. The impact adhesion model is now incorporated into the two-phase flow numerical procedure that has already been extensively tested (Burry and Bergeles, 1993; Balabani et al., 1994). The calculation of the flow field is accomplished through a collocated control volume procedure based on the SIMPLE pressure correction algorithm of Patankar and Spalding (1972) with the $k - \epsilon$ turbulence model and a stochastic Lagrangian particle tracking procedure (Burry and Bergeles, 1993) that takes the anisotropy of the turbulence into account through an algebraic Reynolds stress model. All of the equations are solved in orthogonal curvilinear coordinates.

The particle deposition model developed so far was validated against experimental measurements of particle deposition onto a circular cylinder in high temperature particle laden cross flow (Kim and Kim, 1992). In the experimental configuration the combustion gases flowing past the cylinder were laden with TiO_2 particles and the cylinder was covered with a platinum ribbon, which complies with the rigid body assumption since it was six times thicker than the maximum particle diameter. The Reynolds number of the flow past the cylinder was Re = 54 based on freestream velocity and cylinder diameter. The temperature of the flow and cylinder surface was 1603 K and 1171 K, respectively ($T_w/T_\infty = 0.731$) while the freestream turbulence before the cylinder was measured at 2.5 percent (r.m.s. velocity over mean flow velocity). Particle concentration at freestream was monitored not to overcome 10^{10} particles/m^3 to avoid effects of turbulence or Brownian coagulation. For the numerical predictions the concentration was kept at this limit for all particle sizes. The particles that had deposited onto the cylinder after a given time were counted and a particle deposition rate was calculated and nondimensionalized:

$$\text{St}_m = \frac{j_p''}{\rho_{p,\infty} U_\infty} \qquad (5)$$

For large particles the most important deposition mechanism is inertial impaction but small particle diameters are strongly influenced by large temperature gradients in the flow field. Molecular impactions on the hotter side of the particle deliver more momentum and result in a force acting in the opposite direction of the temperature gradient. This is significant only if the mean free path of the molecules is not negligible in relation to the dimension of the particle. The phenomenon is called thermophoresis and to account for this the thermophoretic force was added to the existing particle tracking method by introducing the new term into the equation used for particle tracking. The force due to thermophoresis is (Talbot et al., 1980):

$$F_T = -\frac{12\pi\mu\nu R C_S(k_g/k_p + C_t\lambda/R)}{(1 + 3C_m\lambda/R)(1 + 2k_g/k_p + 2C_t\lambda/R)}\,\frac{\nabla T}{T_o} \qquad (6)$$

where the mean free path is $\lambda = 0.43\nu/\sqrt{T}$ (λ/R is the Knudsen number), $C_s = 1.17$, $C_m = 1.14$ and $C_t = 2.18$ are empirically determined constants.

The flow field around the cylinder and the deposition onto its surface was numerically calculated with the impact adhesion model giving the distribution of particle mass flux depositing onto the cylinder. The fact that the Reynolds number of 54 is laminar raises the problem of stochastically modeling the particle trajectories since the turbulent fluctuations are needed for their statistical representation. Instead of arbitrarily imposing a turbulent fluctuation at each point based on the inlet turbulence intensity of 2.5 percent, it was considered preferable to model the transport of the inlet turbulence with the $k - \epsilon$ turbulence model. Parametric computations showed that the effect of the turbulence model on the mean velocities in the front of the cylinder (stagnation point to 90 deg) is negligible and will therefore not introduce significant deviations in the calculations since it is this region that mostly influences particle movement near the cylinder.

The material properties of the particle and surface are essential to the correct performance of the impact-adhesion model and are also influenced by the local temperature. Unfortunately, precise values are not always available. For the case presented here the values for the density, Young's modulus, and Poisson ratio were taken to be $\rho_{\text{TiO2}} = 4170$ kg/m^3, $\rho_{\text{Pt}} = 21450$ kg/m^3, $E_{\text{TiO2}} = 17$ GPa, $E_{\text{Pt}} = 67$ GPa, $\nu^P_{\text{TiO2}} = 0.47$, and $\nu^P_{\text{Pt}} = 0.45$, which were obtained from linear interpolation to their respective temperatures from the values at 20°C (*Mark's Handbook,* 1978) and the respective melting point temperatures. $\Delta\gamma = 0.166$ J/m^2 from Fowkes (1964), the elastic yield limit of Pt was also interpolated to the required temperature $Y = 38.7$ MPa and the thermal conductivities needed for the thermophoretic force were $k_{\text{TiO2}} = 3.78$ W/m/K and $k_{\text{gas}} = 0.091$ W/m/K at their respective temperatures.

The nondimensional deposition rates are shown in Fig. 1 and it is interesting to note that the values of the deposition rate are an order of magnitude larger for the 20 μm particles. This is mostly due to the fact that the smaller particles tend to follow the streamlines of the flow and do not impact onto the cylinder as easily as the larger ones. The thermophoretic force is more prominent in the smaller particle sizes and is responsible for their impaction onto the cylinder surface. This is evident from Fig. 2(*a*) where the mean impact angle is shown for the three particle sizes. The two smaller sizes impact at about 60 deg independent of the position on the cylinder whereas the 20 μm particles tend to reach a tangential impaction near the 90 deg point from stagnation. This proves that the impact angle for the 20 μm particles is determined by the angle of their approach to the cylinder while the smaller particles which follow the streamlines are pulled toward the cylinder surface by thermophoresis. It should also be noted that in the smaller particle sizes deposition is also found on the back of the cylinder which is due to particles entering the recirculation zone behind the cylinder as opposed to the larger particles, which simply fly out of the recirculation area due to their momentum.

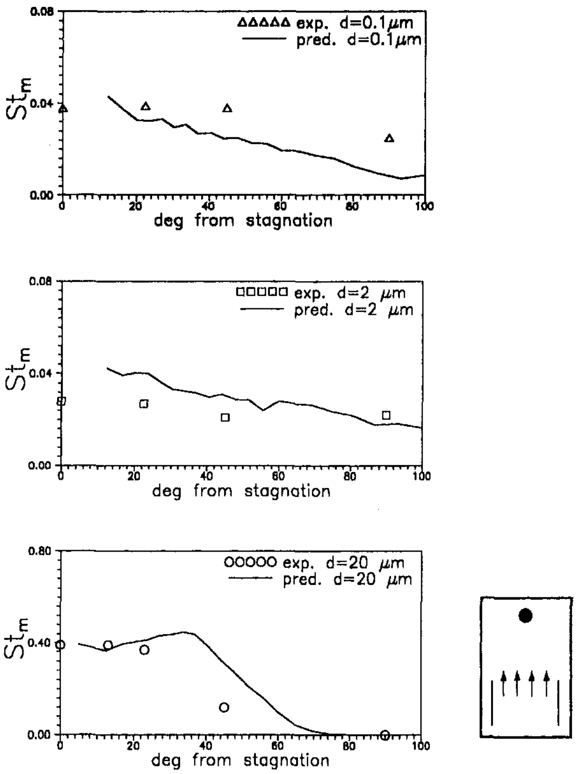

Fig. 1 Numerical prediction of the nondimensional deposition rate of various sizes of TiO_2 particles onto a *Pt* cylinder in crossflow (Re = 54) with a temperature difference between surface and fluid T_w/T_∞ = 0.731 (Kim and Kim, 1992)

In Fig. 2(*b*) another interesting fact can be seen, the smaller particles stick almost immediately upon impacting the surface while the larger particles have a tendency to bounce after their first contact with the cylinder surface. This can be explained by considering that the smaller particles are actually pulled toward the surface by thermophoresis while the larger particles impact onto the cylinder mostly due to their inertia and will therefore have a normal velocity large enough to result in one or two bounces before it is lost and can be overcome by the surface adhesion forces.

The discrepancies in Fig. 1 can be attributed to the uncertainties mentioned before regarding the flow field and the turbulence fluctuations that influence the particle trajectories. There is also a degree of uncertainty regarding the assumed linear variation of the material properties as a function of temperature. The variation of these properties is actually rather complex but it would be interesting to see the effect of the precise values with respect to temperature on the performance of the model. Finally, it should be noted that the reported experimental uncertainty was 5.3 percent for the measurement of the deposited particle size and number distribution and 4.5 percent for the same quantities at the inlet (Kim and Kim, 1992).

III Numerical Study of Heat Exchanger Fouling

In this section, the numerical model will be extended to account for the evolution of the deposit in time by using an exponential equation to relate the deposition rate that has been calculated to the parameters that will influence deposit removal (resuspension).

Evolution of the Deposit in Time. The expression that will be used to describe the evolution of the deposit in time is based on the Kern and Seaton (1959) concept of a deposit and a removal flux. If the removal flux is considered dependant on the local fluid shear stress and on the amount of mass already deposited, then integration will give the deposit mass as an exponential function of time:

$$m = \frac{\dot{m}_d}{K_2\tau_w}[1 - \exp(-K_2\tau_w t)] \qquad (7)$$

The above equation shows that for a given deposition rate and flow field conditions a maximum deposit (asymptotic deposit) is reached after a certain time and its mean value remains constant from then on. This is in accord with experimental and operational observations that confirm the existence of an asymptotic deposit. The term outside the brackets in (7) is the asymptotic deposit mass at which the mechanisms of deposition and removal will be in equilibrium.

The method used here is based on (7), where the deposition rate is calculated from the impact-adhesion model presented above, and the shear stress is calculated from the solution of the Navier-Stokes equations around the tubes. Experimental and industrial observations can help to determine the value of K_2, which is a parameter of the strength of the deposit. If the asymptotic deposit volume (and therefore mass) is known at a given position of the tube then the value of the constant can be determined and the deposit build up on the rest of the tube or on the other tubes of the bank can be predicted.

Due to the tangential velocity component of particles impacting a surface there will be a certain amount of "erosion" of the deposit and reentrainment back into the flow. This can be expressed as an eroding shear stress that acts along with the fluid shear stress, although it will have a different distribution on the surface. This shearing action can be expressed as:

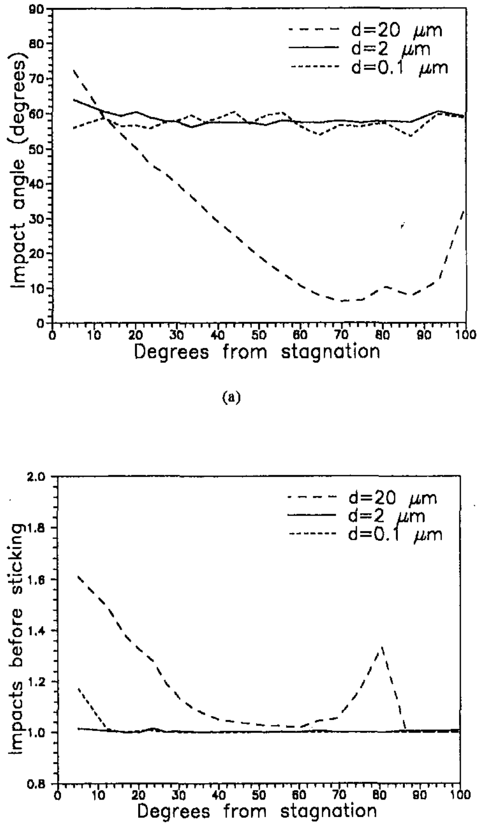

(a)

(b)

Fig. 2 (*a*) Mean impact angle and (*b*) Mean number of impacts before adhesion of various sizes of TiO_2 particles onto a *Pt* cylinder in crossflow (Re = 54) with a temperature difference between surface and fluid T_w/T_∞ = 0.731 (Kim and Kim, 1992)

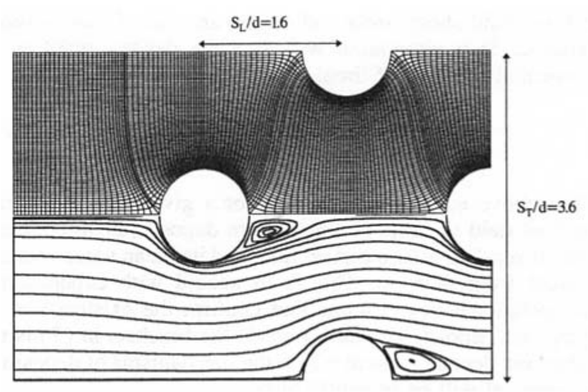

Fig. 3 Orthogonal curvilinear computational grid (129 × 71) and streamlines of the flow for Re = 13000 for a staggered tube bundle

$$\tau_{er} = \frac{\Sigma\,(\dot{m}_{\text{imp}} U_{\text{tang}})}{A} \tag{8}$$

where A is the area of the surface where the impacting mass flux is considered and the summation refers to all particles that impact onto that area. The above equation is of course an over simplification of the erosion process, however, it is not intended to play the part of an erosion model, only to represent the shearing action that the tangentially impacting particle mass flux will add to the fluid shear stress. The variation of the calculated erosion with impact angle is a rough approximation of the erosion of a soft and ductile material (Bitter, 1963b) (the high temperatures observed in utility boiler heat exchangers allow the deposit to be treated as such) which would normally have a maximum at about 10 deg impact angle instead of a perfectly tangential impact that is implied by (8). Considering the nature of the constant K_2 it can be taken to be the same for the shear stress due to the fluid and the eroding shear stress so (7) becomes:

$$m = \frac{\dot{m}_d}{K_2(\tau_w + \tau_{er})}\{1 - \exp[-K_2(\tau_w + \tau_{er})t]\} \tag{9}$$

At a given location of the surface and for a given deposition flux, the evolution of the deposit in time is dependent on the mass flux impacting at that location, the velocity of the impacting particles, and the shear stress of the fluid. The distribution of each of these properties on the surface is different. For the test cases that will be presented in the next section, the shear stress due to erosion and the fluid shear stress were of the same order of magnitude for a mass loading of 1 percent but for a mass loading of about 50 percent the shear stress due to erosion would be 1–2 orders of magnitude larger than the fluid shear stress (depending on the location on the surface of the tube where they are being compared).

Fouling in a Staggered Arrangement Heat Exchanger. The flow field in the staggered tube bundle arrangement of Fig. 3 was experimentally and numerically studied in Balabani et al. (1994). The numerical procedure is the same as the one used in Section 2.2 and the orthogonal curvilinear computational grid and the streamlines of the flow for a Reynolds number of 12858 (based on the tube diameter and the maximum velocity in the tube bank) are shown in Fig. 3. Comparison of the experimental measurements and the numerical calculations are presented in Fig. 4 for the mean axial velocities of the flow.

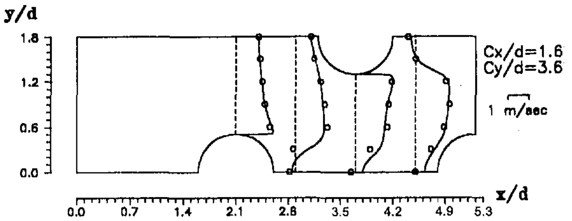

Fig. 4 Numerical predictions of the experimental measurements of the mean axial velocities (Balabani et al., 1994) in the staggered tube bundle of Fig. 3

Table 1 Particle size distribution for a typical lignite utility boiler

Particle diameter d_p (μm)	700	300	145	45
Percentage of total mass (%)	12.8	23.3	27.2	36.7

For the two-phase flow calculation the particles were taken to have the material properties of Al_2O_3 and a density of 2300 kg/m^3, which is closer to the actual density of the depositing ash particles in a lignite utility boiler superheater. The fluid and particle properties were taken at a temperature of 900°C and the material properties of the surface were those of steel at a temperature of 600°C.

The particle size distribution was taken from a typical lignite utility boiler size distribution and is presented in Table 1, while their inflow distribution was considered uniform. The total mass loading was 1 percent while the fluid velocity was taken to be 12 m/s, a typical value for utility boilers. The numerical procedure gave the distribution of the particle mass deposition flux on the tubes, the fluid shear stress on the tubes, and the eroding shear stress from the particle impactions. The K_2 constant was evaluated based on the industrial observation of the Public Power Corporation (PPC) of Greece that the maximum deposit height in a lignite utility boiler heat exchanger is about 1–2 tube diameters (Bouris-Burry and Bergeles, 1994). This was considered to be the maximum height for the stagnation point of the first tube and from this value the K_2 constant was calculated allowing the use of (9) for the calculation of the evolution of the deposit at all the other positions in the tube bundle.

Ideally, the deposition should be calculated for a short time period i.e., until the cylinder's shape begins to change, then the flow field should be solved again using the new tube shape and so on. This was neglected in the present calculation. Time dependence of the deposit is expected to lead to slower fouling rates than those predicted here due to the streamlining of the tube shape by the deposit and easier particle bypass of the tubes. With this in mind, the results indicate that the maximum (asymptotic) deposit is reached in about two weeks and the deposit formation can be seen in Fig. 5. It should be mentioned that at this stage of the computations the temperature variation (and therefore fluid density variation) of the fluid was neglected in order to limit the influential parameters to the particle Stokes numbers and the tube bundle arrangement for the analysis that will follow.

Table 2 allows a better understanding of the mechanisms involved in the adhesion process by presenting the values of the various energies involved in an impact. The values refer to 90 μm Al_2O_3 particles impacting a steel surface and the interfacial surface adhesion energy was taken to be 0.15 J/m^2, which is the value for the two substances slightly increased to account

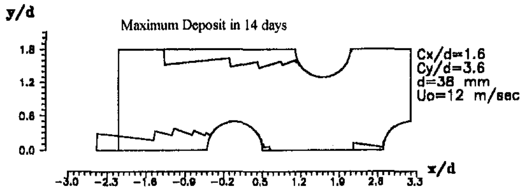

Fig. 5 Fouling in a full scale staggered tube bundle without temperature variation

Table 2 Characteristic values of energy time during particle impact to a surface

Impact velocity (m/s)	Initial kinetic energy (J)	Plastic deformation energy (J)	Surface adhesion energy (J)	Aerodynamic lift energy (J)	Rebound velocity (m/s)
15	$.987658\ 10^{-7}$	$.987182\ 10^{-7}$	$.256579\ 10^{-11}$	$.146483\ 10^{-11}$	0.32544
9.9	$.430224\ 10^{-7}$	$.429909\ 10^{-7}$	$.194538\ 10^{-11}$	$.96683\ 10^{-12}$	0.26337
5.1	$.114173\ 10^{-7}$	$.114012\ 10^{-7}$	$.125083\ 10^{-11}$	$.498125\ 10^{-12}$	0.18736
0.9	$.355557\ 10^{-9}$	$.352724\ 10^{-9}$	$.395626\ 10^{-12}$	$.880052\ 10^{-13}$	0.0758
0.015	$.987657\ 10^{-13}$	$.685559\ 10^{-13}$	$.354803\ 10^{-13}$	$.157696\ 10^{-14}$	0.0

for the sticky layer of condensed vapours that are always present in a utility boiler heat exchanger. For the aerodynamic lift force energy the value of the fluid shear stress was taken to be 2 kg/m s^2 while for the flow field that was studied typical values ranged from 0.3 at the front of the first cylinder to 12. at the 90 deg position and then to 0.1 at the 175–180 deg position. It is obvious that the aerodynamic lift force and the aerodynamic lift energy will follow the trend of the shear stress along the surface of the cylinders according to (2).

It is interesting to note that the plastic deformation energy is the main energy loss mechanism while the adhesion and aerodynamic lift energy are of the same order of magnitude. Allowing for the variation of the value of the fluid shear stress (which affects the aerodynamic lift force) along the tube surface it is obvious that the lift force is important to the adhesion process. The dependence of the aerodynamic lift energy on the impact velocity is due to δ in (3), which is the total approach between the particle and surface during impact. Another interesting observation is that the adhesion and aerodynamic lift energies become even more important at small impact velocities where plastic deformation is not as pronounced. The small velocities, at which the particles are shown to adhere to the surface, indicate that it is very difficult for a particle to adhere after a single impact. However, one or two bounces seem to be enough for the particle to lose a large amount of its initial energy and impact the surface with smaller velocities until it finally sticks. This was also observed for the TiO_2 particles impacting the Pt cylinder. Of course the mechanism is rather more complicated since the particle regains some of its energy from the surrounding flow field.

At this point, an attempt will be made to study the phenomenon in the same tube bundle arrangement but at a different scale. The utility boiler arrangement will be scaled down 3.8 times to give a tube diameter of 10 mm instead of the actual 38 mm and the Reynolds number will be kept constant by changing the inlet fluid velocity and keeping the fluid, particle, and surface properties the same. At first, the Stokes number of the particles will be kept constant, this being the parameter that actually defines the particle behavior with respect to the fluid flow. The Stokes number is defined:

$$\mathrm{St}k = \frac{\rho_p d_p^2 U_\infty}{D_{\mathrm{cyl}} 18 \mu_g} \tag{10}$$

and for the four original particle sizes of Table 1 the Stokes numbers corresponding to the case being examined were Stk(45 μm) = 1.73, Stk(145 μm) = 17.93, Stk(300 μm) = 76.77, and Stk(700 μm) = 418.01.

In order to keep the Stokes number constant, the particles are reduced in size to compensate for the reduction in size of the tube diameter and to keep the fluid properties the same. The new particle diameters are related to the old ones by:

$$d_{p2} = (3.8)^{(-1)} d_{pl} \tag{11}$$

thus resulting in diameters 11.85, 38.16, 78.95, and 184.23 μm.

However, this change in the diameter of the particles and therefore their mass means that by keeping the Reynolds number and the mass flow rate of the particles per unit area constant, the kinetic energy at impact of the particles corresponding to the same Stokes number is $(3.8)^{-3}$ times smaller and therefore their behavior during impaction will be different as shown in Fig. 6.

The change in the deposit build up can be explained by the reduction in the kinetic energy of the impacting particles, which changes the impact conditions. This is evident from the deposition further away from the stagnation point where particles directly impact onto the tube and instead of rebounding and being carried away as in the full scale configuration, they adhere. The dimensional spacing also plays an important role since the mass flow rate per unit area is the same but there is less area available for the particles to bypass the tubes.

The next test on the scaled down configuration was to adjust the particle size so that the impaction kinetic energy of the particles (a function of d_p^{-3}), as well as the Reynolds number of the flow, remains constant. Of course, the Stokes number is not maintained. The particle diameters now result as:

$$d_{p2} = (3.8)^{(-2/3)} d_{pl} \tag{12}$$

meaning diameters equal to 18.5, 59.5, 123.2, and 287.5 μm.

The result is shown in Fig. 7 where again there is a big difference in the fouling behavior of the tube bundle. Although the fouling rate is much slower than when the Stokes number was maintained constant, it is still faster than in the original case of the actual dimensions. However, the shape of the deposits are much closer to the original shapes of the full scale arrangement (Fig. 5). A possible explanation to this could lie in the difference in Stokes number, which is responsible for the change in deposition behavior behind the tubes. The deposit formation in this region depends more on Stokes number since it results from particles that have already impacted and are led to this area by the flow. The deposit in front of the tubes, which is a result of

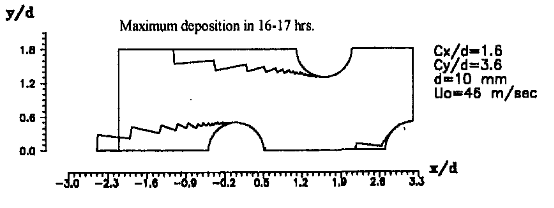

Fig. 6 Fouling in the staggered tube bundle of Fig. 5 scaled down 3.8 times but with the same Re number of the flow and the same particle Stokes numbers as for the actual dimensions

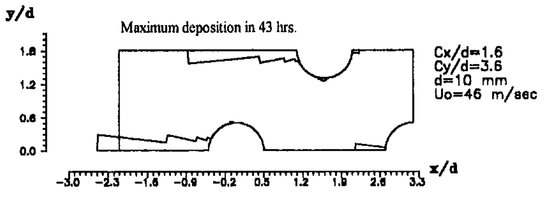

Fig. 7 Fouling in the staggered tube bundle of Fig. 5 scaled down 3.8 times but with the same Re number of the flow and the same kinetic energy of the particles as in the actual dimensions

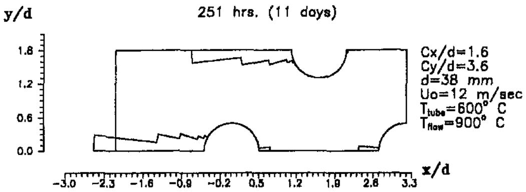

Fig. 8 Fouling in a full scale staggered tube bundle with temperature variation of the flow field. Fluid temperature: 900°C, Tube surface temperature: 600°C

more direct impaction, resembles closely the deposit in the full scale geometry. The shape of the deposit, as well as the time for maximum deposit, indicates that constant kinetic energy is more important than constant Stokes number as far as maximum deposition is concerned.

However, a definite similarity law could not be obtained. The conflicting mechanisms that are represented by the Reynolds number of the flow, the particle mass flow rate per unit area, the particle Stokes number, the kinetic energy of impaction of the particles, and the actual dimensions of the tube bundle could not be combined to give a reasonable method of scaling down the actual dimensions to study the fouling phenomenon.

Effect of the Tangential Impact Velocity. At this point, the initial condition that the tangential velocity during impaction is overlooked will be re-examined. The configuration of Fig. 5 is now solved accounting for the fluid density variation by solving the temperature equation for the flow. All other parameters regarding the flow and the particles are the same. The results are presented in Fig. 8 and it can be seen that the temperature difference leads to a faster fouling rate. There are two reasons directly related to this phenomenon. The first is the thermophoretic force that causes particles to be attracted to the colder tube surface, while the second is the larger density of the colder fluid in the vicinity of the tube, this will lead to increased drag on the particles (by about 30 percent) and cause them to impact onto the tube with smaller velocities thereby facilitating deposition.

Through a rather complex analysis of impact energies and material deformation, Bitter (1963b) reaches two expressions for the tangential rebound velocity. It actually turns out that this is dependant on the impact angle of the particle and that for an impact angle above a certain limit α_o, the tangential velocity becomes zero during impaction while below α_o the particle retains at least some of the tangential velocity all through the impact. The limiting impact angle α_o is most strongly influenced by the elastic yield limit Y and common values are between 12–25 degrees.

Depending on the impact angle the tangential rebound velocity V_{t2} is calculated and (8) becomes:

$$\tau_{er} = \frac{\Sigma\, [\dot{m}_{\text{imp}}(V_{t2} - V_{t1})]}{A} \tag{13}$$

The tangential erosion calculated with (13) gives a curve which has a maximum at the α_o impact angle as opposed to (8) which has a maximum at 0 degrees. This represents the tangential erosion of a ductile material as opposed to a brittle material which would have maximum erosion at a normal impaction (90 degrees). The deposit material inside a heat exchanger which can be found at temperatures around 900 K can be assumed to be ductile and therefore the above expressions can be used.

The resulting calculation is presented in Fig. 9 where the tangential rebound velocity is now calculated based on Bitter (1963b) assuming $\alpha_o = 20$ deg for Al_2O_3 (the value for Aluminum is 15 deg). The deposits are now spread out over the surface of the tube due to the smaller tangential rebound velocities, which make it more difficult for the particles to escape and causes them to stick further downstream and on the back of the cylinder. The overall result is an increase in the fouling rate by about 25 percent proving the importance of the tangential rebound velocity on the fouling process.

IV Conclusions

A numerical model has been developed to predict the deposition resulting from particles impacting a solid surface. The material properties of both particle and surface are taken into consideration as they affect the energy losses and the surface energies that will determine the sticking or rebound of the particle. The effect of the surrounding flow field is considered through a solution of the Navier Stokes equations and therefore the influence of local temperature on the material properties as well as the resulting thermophoretic force and the lift force are influential to the adhesion or rebound of the particle. The exact particle trajectory is also a result of the flow field calculation. The local shear stresses and the eroding particle impacts are considered as removal mechanisms and the evolution of the deposited mass in time is obtained. The model showed acceptable agreement with experimental measurements of particle mass flux deposited from high temperature particle laden gas flow around a circular cylinder. The effect of the thermophoretic force with regard to particle size was noted and the larger particles were found to deposit after one or two bounces. An analysis regarding the actual dimensions of a staggered arrangement heat exchanger tube bundle proved that the actual dimensions are extremely important to the fouling behaviour of the arrangement even though caution was taken to preserve various similarity laws for the flow and particles. Finally, the effect of the tangential velocity during impact and rebound was found to be an important factor in the fouling process.

The fouling phenomenon is undoubtedly very complex and can be found in many different situations. The numerical model presented in this paper is not intended to be a simulation of all the underlying mechanisms in fouling. Many of these, which could be of major importance in certain situations, have not been directly included in the model (e.g., chemical reactions, vapor condensation, vibration, flow field unsteadiness etc.). However, an attempt was made to include the most important mechanisms in utility boiler heat exchanger fouling without limiting the generality or expandability of the model. It is believed that the model can be a useful tool in heat exchanger design and as an operational guide for existing configurations. Investigation of the effect of different tube shapes and configurations on heat exchanger fouling and efficiency is the object of current research by the authors. Further study could be directed toward more exact values for the material properties, better flow field simulation through advanced turbulence modeling, and possibly a time resolved calculation to study the effect of unsteadiness and the deposit formation on the flow field.

Acknowledgments

The work presented in this paper was funded in part by the Commission of the European Communities under the JOULE II Program, contract number JOU2-CT92-0014. Collaborating partners were the National Technical University of Athens,

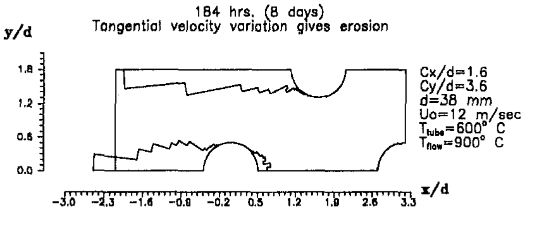

Fig. 9 As in Fig. 8 but with the tangential eroding shear stress of (13)

King's College London and the Public Power Corporation of Greece.

References

Balabani, S., Bergeles, G., Burry, D., and Yianneskis, M., 1994, "Velocity Characteristics of the Crossflow over Tube Bundles," *Proceedings, 7th International Symposium on Applications of Laser Anemometry to Fluid Mechanics,* Lisbon, 1994, Vol. II, pp. 39.3.1–39.3.8.

Bitter, J. G. A., 1963a, "A Study of Erosion Phenomena (Part I)," *Wear,* Vol. 6, pp. 5–21.

Bitter, J. G. A., 1963b, "A Study of Erosion Phenomena (Part II)," *Wear,* Vol. 6, pp. 169–190.

Bouris-Burry, D., and Bergeles, G., 1994, "A Model for the Deposition of Ash Particles Onto a Solid Surface," Eurotherm Seminar No. 40: Combined energy and water management in industry, Thessaloniki, Greece (in press).

Braun, M. J., and Kudriavstev, V. V., 1995, "Fluid Flow Structures in Staggered Banks of Cylinders Located in a Channel," ASME JOURNAL OF FLUIDS ENGINEERING, Vol. 117, pp. 36–44.

Burry, D., and Bergeles, G., 1993, "Dispersion of Particles in Anisotropic Turbulent Flows," *International Journal of Multiphase Flow,* Vol. 19, No. 4, pp. 651–664.

Cleaver, J., and Yates, B., 1973, "Mechanism of Detachment of Colloidal Particles From a Flat Substrate in a Turbulent Flow," *Journal of Colloid and Interface Science,* Vol. 44, No. 3, pp 464–474.

Cleaver, J., and Yates, B., 1976, "A Sub-Layer Model for the Deposition of Particles From a Turbulent Flow," *Chemical Engineering Science,* Vol. 30, pp. 983–992.

Dowlati, R., Chan, A. M. C., and Kawaji, M., 1992, "Hydrodynamics of Two-Phase Flow Across Horizontal In-Line and Staggered Rod Bundles," ASME JOURNAL OF FLUIDS ENGINEERING, Vol. 114, pp. 450–456.

Fichman, M., and Pnueli, D., 1985, "Sufficient Conditions for Small Particles to Hold Together Because of Adhesion Forces," ASME *Journal of Applied Mechanics,* Vol. 52, pp. 105–108.

Fowkes, F., 1964, "Attractive Forces at Interfaces," *Industrial and Engineering Chemistry,* Vol. 56, No. 12, pp. 40–52.

Hall, D., 1988, "Measurements of the Mean Force on a Particle Near a Boundary in Turbulent Flow," *Journal of Fluid Mechanics,* Vol. 187, pp. 451–466.

Hein, K., 1977, "Characteristics of Rheinisch Brown Coals with Respect to Their Combustion and Fouling Behaviour in Thermal Power Stations," ASME *Journal of Engineering for Power,* Oct. pp. 679–683.

Kern, D., and Seaton, R., 1959, "A Theoretical Analysis of Thermal Surface Fouling," *British Chemical Engineering,* Vol. 4, No. 5, pp. 258–262.

Kim, Y. J., and Kim, S. S., 1992, "Experimental Study of Particle Deposition Onto a Circular Cylinder in High Temperature Particle Laden Flows," *Experimental Thermal and Fluid Science,* Vol. 5, pp. 116–123.

Mark's Standard Handbook for Mechanical Engineers, 8th Ed., 1978, McGraw-Hill, NY.

Papavergos, P. G., and Hedley, A. B., 1984, "Review-Particle Deposition Behaviour from Turbulent Flows," *Chemical Engineering Research Des.,* Vol. 62, pp. 275–295.

Patankar, S. V., and Spalding, D. B., 1972, "A Calculation Procedure for Heat, Mass and Momentum Transfer in Three Dimensional Parabolic Flows," *International Journal of Heat and Mass Transfer,* Vol. 15, No. 10, pp. 1787.

Rogers, L. N., and Reed, J., 1984, "The Adhesion of Particles Undergoing an Elastic-Plastic Impact with a Surface," *Journal of Physics D: Applied Physics,* Vol. 17, pp. 677–689.

Saffman, P., 1965, "The Lift on a Small Sphere in a Slow Shear Flow," *Journal of Fluid Mechanics,* Vol. 22, pp. 385–400.

Tabakoff, W., 1984, "Review-Turbomachinery Performance Deterioration Exposed to Solid Particle Environment," ASME JOURNAL OF FLUIDS ENGINEERING, Vol. 106, pp. 125–134.

Taborek, J., Aoki, T., Ritter, R. B., Palen, J. W., and Knudsen, J. G., 1972, "Fouling: The Major Unresolved Problem in Heat Transfer," *Chemical Engineering Process,* Vol. 68, No. 2, pp. 59–67.

Talbot, L., Cheng, R. K., Schefer, R. W., and Willis, D. R., 1980, "Thermophoresis of Particles in a Heated Boundary Layer," *Journal of Fluid Mechanics,* Vol. 101, pp. 737–758.

Wall, S. M., John, W., and Goren, S. L., 1988, "Application of Impact Adhesion Theory to Particle Kinetic Energy Loss Measurements," *Particles on Surfaces 2,* Plenum Press, New York, K. L. Mittal, ed.

Possibility of Quantitative Prediction of Cavitation Erosion Without Model Test

Hiroharu Kato
Professor.

Akihisa Konno
Graduate Student.

Masatsugu Maeda
Research Associate.

Hajime Yamaguchi
Associate Professor.

Department of Naval Architecture
and Ocean Engineering,
University of Tokyo,
Hongo, Bunkyo, Tokyo 113, Japan

A scenario for quantitative prediction of cavitation erosion was proposed. The key value is the impact force/pressure spectrum on a solid surface caused by cavitation bubble collapse. As the first step of prediction, the authors constructed the scenario from an estimation of the cavity generation rate to the prediction of impact force spectrum, including the estimations of collapsing cavity number and impact pressure. The prediction was compared with measurements of impact force spectra on a partially cavitating hydrofoil. A good quantitative agreement was obtained between the prediction and the experiment. However, the present method predicted a larger effect of main flow velocity than that observed. The present scenario is promising as a method of predicting erosion without using a model test.

1 Introduction

In this paper, the authors propose a scenario for quantitative prediction of cavitation erosion. The prediction consists of the following six stages of estimation.

Stage 1: Cavity type and extent.
Stage 2: Cavity generation rate.
Stage 3: Number and size distribution of cavity bubbles.
Stage 4: Characteristics of collapsing bubble.
Stage 5: Impact force/pressure distribution on solid wall due to cavity bubble collapse.
Stage 6: Amount of erosion caused by successive impact forces.

The first stage, the estimation of cavity type and extent, has been studied extensively, and these properties can be predicted with confidence if viscous effects are taken into account. The last stage, solid surface deformation and removal, was also studied in detail recently by, for example, Franc et al. (1994). Therefore, our discussion focuses on stages 2–5.

The distribution of impact force, or pressure pulse height spectrum (Le et al., 1993) is a key value in erosion research. (Kato, 1992) First, we can measure and correlate it directly with erosion pit distribution. Second, we can estimate the impact force distribution using only fluid dynamic analysis, whereas metallugical considerations are necessary to estimate the amount of erosion from the impact force distribution. Therefore, the impact force distribution is the "bridge" between fluid dynamics and metallurgy.

The authors attempt to predict the impact force distribution on a partially cavitating hydrofoil and compare it with experiment. The overall scenario used to predict the amount of cavitation erosion was given by Kato (1992).

2 Estimation of Cavity Generation Rate

The rate of cavity condensation should be equal to the rate of cavity generation (evaporation). It is not clear how evaporation of liquid takes place at the liquid-vapor interface. However, it is thought that the liquid evaporates at the forepart of a sheet cavity and condenses at the rear part. If we can measure the vapor velocity inside the sheet cavity, we should find it equal to the condensation rate of the cavity.

Measurement of the vapor velocity inside a cavity is very difficult because the vapor density is very low. Therefore, the air flow rate of a ventilated cavity has often been measured instead, under the assumption that the flow rate necessary to maintain a certain length of cavity should be same for a vapor cavity and a ventilated cavity. (Brennen, 1969; Billet and Weir, 1975).

The measurement of a ventilated cavity was also made on a foil, named EN foil, the thickness of which was 8 percent chord. (Yoshihara et al., 1988; Kamono et al., 1993). The results are summarized in Fig. 1. The nondimensional flow rate C_Q increased sharply when the sheet cavity became unstable with periodic generation of cloud cavitation. This might be one of the reasons why cloud cavitation is so erosive. The data can be well fitted when C_Q is plotted against σ/α, where α is the angle of attack (Fig. 2). In Fig. 2, the reference length is the thickness of the foil. Changing the reference length to the foil chord, the authors derived the following empirical formula.

$$C_{Qc} = \frac{Q}{U_\infty Bc} = \frac{1.82 \times 10^{-6}}{1.14 \times 10^{-4} + (\sigma/(\alpha - \alpha_0))^5} \quad (1)$$

$$C_Q = \frac{Q}{U_\infty Bt} = C_{Qc}\frac{c}{t} = C_{Qc}\frac{1}{0.08}\,. \quad (2)$$

We assume that Eq. (1) is generally valid for a cavitating foil, and use it to estimate the cavity generation rate. This is an important assumption and will be examined later.

The appearance of ventilated cavitation is surprisingly similar to that of natural cavitation including shedding of cloud cavitation. This suggests that condensation is not significant at the rear part of a sheet cavity. Therefore, we can assume that the amount of cavity collapse in a cloud cavity is roughly equal to the amount of cavity generation.

3 Number and Size Distribution of Cavity Bubbles

The sheet cavity splits into many cavity bubbles at the rear end. The cavity bubbles collapse downstream and cause erosion. We must simulate this process adequately for quantitative erosion prediction. It is difficult to measure the number and size of the cavity bubbles during collapse, because the size changes rapidly.

If we can measure the distribution of air bubbles further downstream, we can estimate the distribution of cavity bubbles

---

Contributed by the Fluids Engineering Division for publication in the JOURNAL OF FLUIDS ENGINEERING. Manuscript received by the Fluids Engineering Division June 29, 1995; revised manuscript received February 20, 1996. Associate Technical Editor: Jong H. Kim.

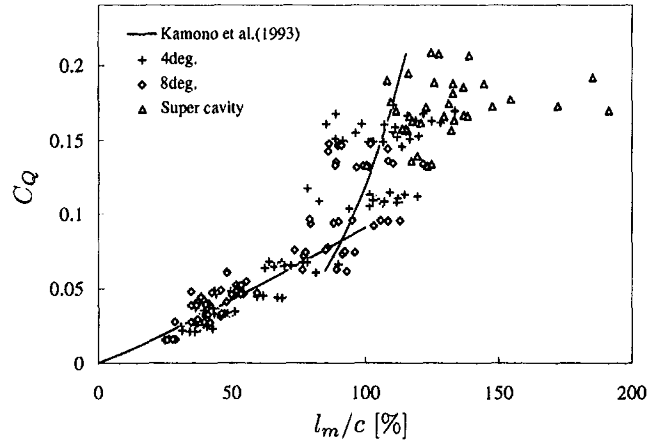

Fig. 1 Ventilation flow rate against cavity length on EN foil (α = 4, 8 deg, U_∞ = 4, 6, 8m/s)

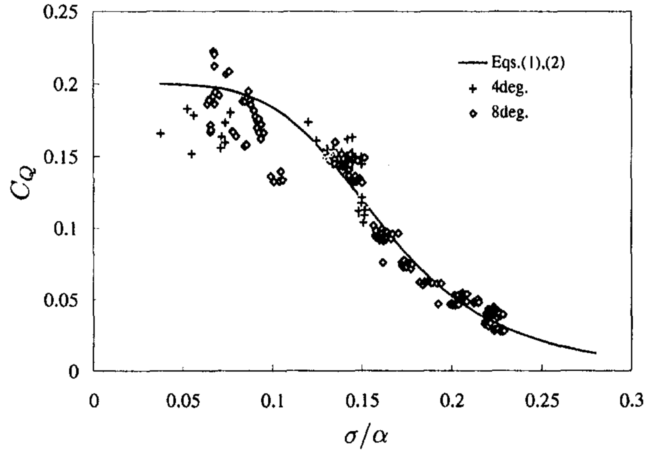

Fig. 2 Ventilation flow rate against σ/α (same data as Fig. 1)

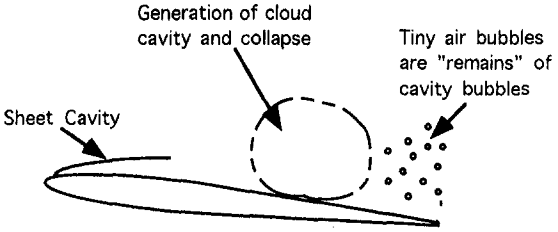

Fig. 3 Generation and collapse of cloud cavity

just before collapse, because the air bubbles downstream are "remains" of the cavity bubbles and their distributions should be similar. (Fig. 3) In fact, we can easily estimate the cavity bubble distribution from that of downstream air bubbles, if vapor and gas (air) pressures in the sheet cavity are known. Even if we cannot estimate the gas pressure in the sheet cavity, the distribution of gas bubbles should be proportional to that of cavitation bubbles, because each gas bubble corresponds to one cavitation bubble. Diffusion of gas into liquid can be neglected because of the short time scale involved.

There have been many measurements of small air bubbles in main flow. The number of air bubbles is few and easy to measure. (O'Hern et al., 1988; Report of ITTC, 1993). However, the measurement of air bubble distribution caused by cloud cavity collapse has rarely been attempted because of the difficulty involved. To our knowledge, our measurement, using off-axis holography, is the only one reported so far. The details are given by Yamaguchi et al. (1990) and Maeda et al. (1991).

Figure 4 shows the bubble number density distribution function downstream of a cavity cloud, and includes the bubble number density in main flow under a noncavitating condition. As seen in the figure, the number density of air bubbles is two orders of magnitude higher in cavity cloud than the density in main flow. The number density of bubbles increases rapidly with decrease in their size except for bubbles smaller than 20 μm in radius.

The following equations are obtained from experimental results:

$$\left.\begin{aligned} N &= 6.6\times10^{-7}R^{-4.36} \quad R \geq 2\times10^{-5}\ \mathrm{m} \\ N &= 6.6\times10^{-7}\times(2\times10^{-5})^{-4.36} \\ &= 2.0\times10^{+14} \quad R < 2\times10^{-5}\ \mathrm{m} \end{aligned}\right\} \tag{3}$$

As discussed before, the number density of cavitation bubbles should be given by an equation similar to Eq. (3) as follows:

$$\left.\begin{aligned} N &= KR^{-4.36} \quad R \geq R_o \\ N &= KR_o^{-4.36} = \text{const.} \quad R < R_o \end{aligned}\right\} \tag{4}$$

4 Characteristics of Collapsing Bubbles

There have been many theoretical studies on the collapse of a single bubble (Hickling and Plesset, 1964; Tomita and Shima,

Nomenclature

B = breadth of foil section [m]
c = chord [m]
C_p = pressure coefficient
C_Q = nondimensional flow rate defined by Eq. (2)
C_{Qc} = nondimensional flow rate defined by Eq. (1)
d = diameter [m]
F = impact force [N]
h = reference trajectory [m]
h_b = bubble layer thickness [m]
h_e = effective layer thickness [m]
I_{PF} = accumulative impact force on pickup
I_{PR} = accumulative collapsing rate on pickup
I_R = accumulative distribution of cavity bubbles
K = constant defined in Eq. (4)
l_m = mean length of cavity [m]
m = pressure ratio between p_o and p_∞ (or p_x)
N = bubble number density distribution function [m^{-4}]
p = pressure [Pa]
p_h = impact pressure due to collapsing bubble at h [Pa]
$p_{\max}$ = maximum impact pressure [Pa]
p_o = initial gas pressure in a bubble [Pa]
p_x = static pressure along foil section [Pa]
p_v = vapor pressure [Pa]
p_∞ = pressure at infinity [Pa]
Q = ventilated flow rate [m^3/s]
R = bubble radius [m]
$R_{\min}$ = minimum bubble radius [m]
R_o = bubble radius defined in Eq. (4) [m]
r = distance from center of bubble [m]
SD = standard deviation
t = thickness of foil section [m]
U_∞ = main flow velocity [m/s]
α = angle of attack [deg], air content [ppm]
α_0 = zero lift angle [deg]
α/α_s = air content ratio
ρ = density [kg/m^3]
σ = cavitation number = $(p_\infty - p_v)/1/2\rho U_\infty^2$
ϕ = probability of bubble collapse

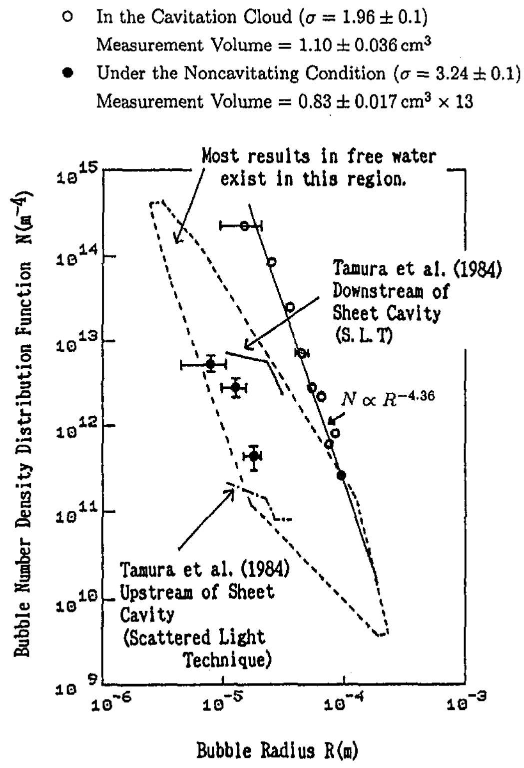

Fig. 4 Number density distribution of air bubbles downstream of cavity cloud. Distribution of air bubbles under a noncavitating condition is also shown for comparison (NACA0015, α = 8.4 deg, U_∞ = 7.8 m/s).

1977), of multiple bubbles (Blake, 1994; Takahira and Akamatsu, 1994), and of bubble clusters. (Morch, 1981; Chahine and Duraiswami, 1992). However, the mechanism of high impact pressure caused by a collapsing bubble is still not clear. The possible mechanisms are discussed by Kato (1992). In this paper, the authors assume that the shock wave caused by bubble collapse is the major mechanism and estimate the impact force distribution acting on a solid surface.

The authors also simplify the calculation by assuming a single spherical bubble in viscous compressible fluid. Tomita and Shima (1977) calculated the maximum pressure $p_{\max}$ generated when the bubble size becomes minimum at the final stage of collapse. The authors constructed a diagram of $p_{\max}$ and $R_{\min}$ (Fig. 5) using Tomita and Shima's calculation.

The governing parameter is m ($\equiv p_0/p_\infty$), where p_0 and p_∞ are the initial gas pressure inside the bubble and the pressure at infinity, respectively. It is interesting that both $p_{\max}$ and $R_{\min}/R$ are almost independent of the initial bubble size (R), if R is larger than 0.1 mm. The following are approximate equations expressing the analytical result.

$$\frac{p_{\max}}{p_\infty} = 0.345\ \mathrm{m}^{-1.8} \qquad m = p_0/p_\infty \tag{5}$$

$$\frac{R_{\min}}{R} = 1.502\ \mathrm{m}^{0.7}. \tag{6}$$

Tomita and Shima also showed that the shock wave propagates spherically and the pressure decreases as

$$p \propto 1/r$$

where r is distance from the center of the bubble. Therefore the impact pressure on solid wall, p_h, is

$$p_h = p_{\max}\frac{R_{\min}}{h}, \tag{7}$$

where h is the distance between the bubble center and the wall.

Of course, Eq. (7) is an approximation. For a detailed study we should take into account the effect of the wall on shock wave propagation. The analytical result shows that the impact pressure on a solid wall p_h is larger when a larger bubble collapses at the same distance h from the solid wall, because $R_{\min}$ increases with initial radius R in Eq. (7). It agrees with many experimental observations by other authors such as Pereira et al. (1995).

As shown in Fig. 5, the estimation of initial gas pressure inside the bubble is very important for the prediction of impact force distribution. The permanent gas in a cavity was studied in the 1960's. Gadd and Grant (1965) measured the gas pressure in a supercavity behind a disk. The following empirical equations were derived from their data.

$$\left.\begin{aligned} p_0 &= (0.017\alpha)p_v\ (\alpha\text{: ppm) for 3 in. disk} \\ &= (0.0039\alpha)p_v\ (\alpha\text{: ppm) for 5 in. disk} \end{aligned}\right\} \tag{8}$$

Brennen (1969) measured the pressure in a supercavity behind a sphere. He also constructed a theoretical model for gas convection from a cavity interface, which gave values almost twice those obtained in experiments. At present there is no reliable model of the gas convection.

5 Unsteady Sheet Cavitation With Periodic Generation of Cloud Cavitation

In this paper, the authors consider only sheet cavitation, which is the most common type of cavitation on fluid machinery blades.

With decreasing static pressure at constant angle of attack, a sheet cavity becomes longer and more unstable, followed by periodic generation of cloud cavitation, which generates the most severe erosion. Periodic generation of cloud cavitation increases the amount of cavity collapse as discussed in Section 2. Moreover, the cavity cloud contains a low-pressure vortex region in the center (Kubota et al., 1989), which prevents the cavity cloud from collapsing. This causes more violent collapse of cavity bubbles in the downstream region. This is why the generation of cloud cavities causes severe erosion.

As mentioned above, the estimation of cavity instability is essential for the prediction of erosion. Izumida et al. (1980) measured the unsteadiness of sheet cavity length on several foil sections. Sections with a bursting boundary layer, where the boundary layer on the suction side separates near the leading edge and does not reattach to the surface, generate stable cavitation. In contrast, sections with a nonbursting boundary layer,

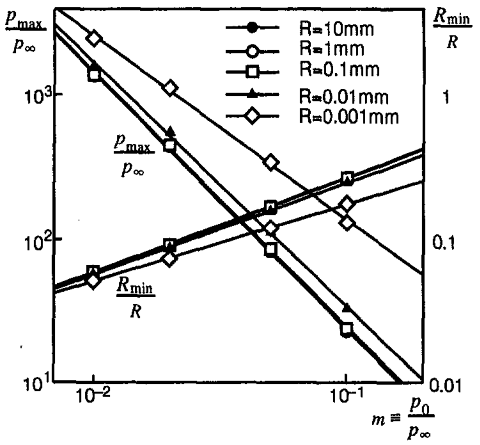

Fig. 5 Maximum impulse pressure $P_{\max}/P_\infty$ and minimum bubble radius $R_{\min}/R$ (P_∞ = 1.013 bar, T = 20 deg, γ = 1.4) (Calculated by Tomita and Shima (1977))

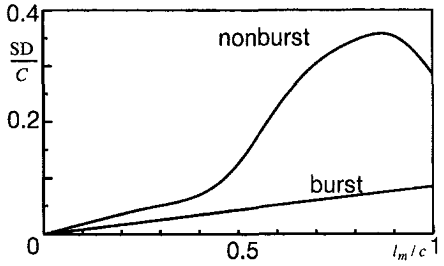

Fig. 6 Standard deviation of cavity end on a foil with bursting and nonbursting boundary layer

where the separated boundary layer reattaches to the surface soon after separation, create very unstable cavitation.

Recently Le et al. (1993) made a comprehensive study on a reverse plano-convex section (burst section) where the camber was negative. According to their result, the governing factor of unsteadiness is the cavity thickness. They did not test nonburst sections. With the present stage of knowledge, we cannot discuss the unsteadiness in detail, though it is one of the most important factors for the quantitative prediction of erosion.

The authors constructed a very simple diagram as shown in Fig. 6 where SD and l_m are standard deviation of unsteady cavity length and mean cavity length, respectively. This diagram is used for the estimation of cavitation in the following section.

6 Impact Force/Pressure Distribution on Solid Surface

As discussed in Section 4, if the ambient pressure of the collapsing bubble is determined, the impact pressure on a solid surface can be estimated using Eqs. (5)–(7). First we estimate the cavity collapsing region and the ambient pressure for collapse. The mean pressure distribution of a cavitating foil is given in Fig. 7. The distribution of cavity collapsing position should be Gaussian as illustrated in Fig. 7. It is assumed that the central cavity collapsing position is at the distance of SD from the mean trailing edge of the cavity (Position C in Fig. 7). It is logical to assume that the standard deviation of cavity collapsing position is equal to that of cavity length shown in Fig. 6. To simplify the problem, we also assume that the ambient pressure p_x, which is same as p_∞ in Eq. (5), is equal to the mean static pressure at the central position. The rate of increase of the ambient pressure that a bubble is subjected to in the closure region of a cavity is an important parameter which affects the impact pressure. However, this effect is not included in the present analysis.

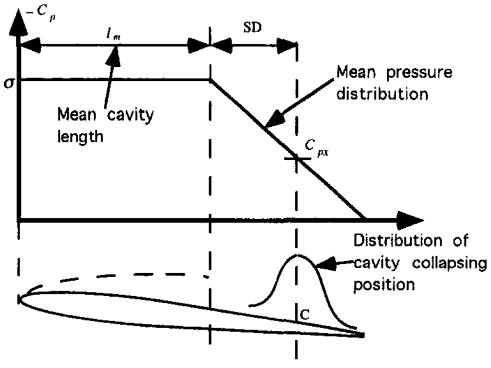

Fig. 7 Distribution of cavity collapsing position

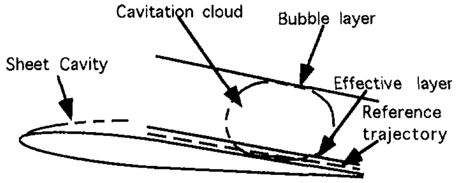

Fig. 8 Bubble layer, effective layer, and reference trajectory

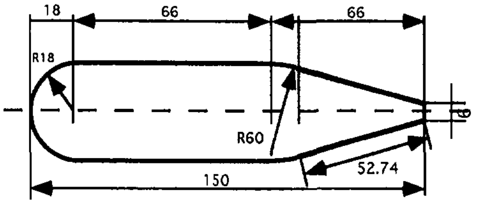

Fig. 9 Foil section for impact force measurement (KT section, c = 150 mm, s = 149 mm)

Second, we should estimate the bubble collapsing rate at a certain position on the solid surface. We might be able to estimate the collapsing rate from the estimated cavity generation rate (Eq. (1)) and the number density of bubbles (Eq. (4)), if we can measure the spatial distribution of bubbles. Such an analysis is, however, very time consuming, because we should calculate the impact pressure caused by each collapsing bubble.

Therefore, the authors introduce three reference length scales, "bubble layer thickness" (h_b), "effective layer thickness" (h_e), and "reference trajectory" (h). We assume that only the bubbles in the effective layer cause the impact pressure on the solid surface, and the trajectory of the bubbles can be represented by the reference trajectory (Fig. 8).

Now we can estimate the impact force/pressure spectrum using the above equations and compare the results with those of experiments.

7 Prediction of Impact Force/Pressure and Comparison With Experiment

The authors measured impact force spectra of collapsing cavity bubbles on a foil section, named KT section (c = 0.15 m). The shape of the section was specially designed for the impact force measurement and is shown in Fig. 9. The impact force pickup was of piezoelectric type as used by Maeda et al. (1994). Diameter of the detecting surface was only 1 mm, and the impact force was measured by a piezoceramic plate imbedded in the pickup.

The cloud cavitation collapsed at the rear part of the section, and the measurement was made mainly using the pickups at 70, 80, and 90 percent chords. The KT section is a nonbursting section, and generates severe cloud cavitation as seen in Fig. 10. The details were shown elsewhere. (Kato et al., 1994) The measurement results are shown in Figs. 11 and 12.

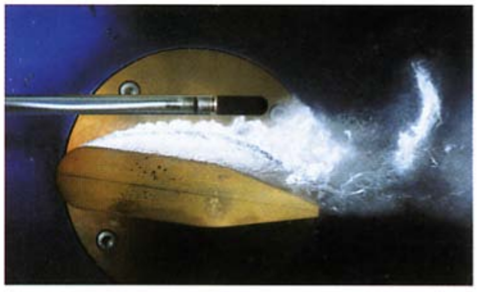

Fig. 10 Appearance of cloud cavitation (KT section, α = 8 deg, U_∞ = 12 m/s, σ = 1.25)

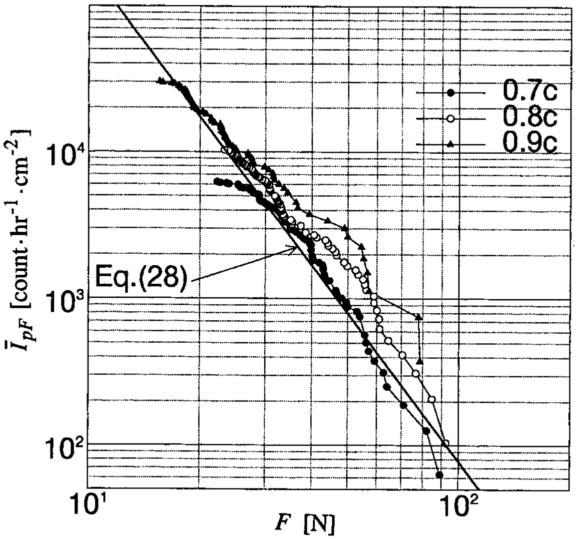

Fig. 11 Impact force spectra due to collapsing cavity bubbles on KT section (Solid lines are prediction using Eq. (28), α = 8 deg, U_∞ = 12 m/s, σ = 1.25, position of pickup: 80 percent c) (Uncertainty of data: ±10 percent for F and I_{PF})

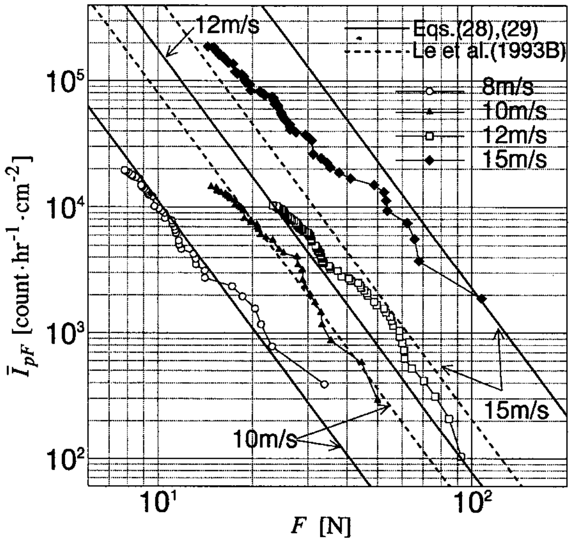

Fig. 12 Effect of main flow velocity on impact force spectra on KT section, (Solid lines are prediction using Eqs. (28) and (29), α = 8 deg, U_∞ = 8, 10, 12, 15m/s, position of pickup = 80 percent c). (Uncertainty of data: ±10 percent for F and I_{PF})

The authors calculated the impact force spectra using the prediction method described in Sections 2 through 6. The calculation was performed for the case of $\alpha = 8$ deg., $U_\infty = 12$ m/s, $\sigma = 1.25$ and 80 percent chord. The mean cavity length was about 60 percent chord and periodic generation of cavity cloud was observed. First, the authors estimated three length scales, h_b, h_e, and h as

$$h_b = 0.2c \ (c\text{: chord}), \quad h_e = 0.02c, \quad \text{and} \quad h = 0.01c. \tag{9}$$

The bubble layer thickness h_b was estimated from photographs of the cloud cavitation. The effective layer thickness h_e was assumed to be one-tenth of the bubble layer thickness. The reference trajectory should be along the center of the effective layer. Therefore $h = h_e/2$. If we increase the effective layer thickness, more bubbles cause erosion. However, the impact pressure of individual bubbles decreases because the distance h increases. Therefore those effects cancel each other to some extent.

Air content was measured as $\alpha/\alpha_s = 0.215$ which corresponded to 5.11 ppm.

According to Eq. (8), the gas pressure in the cavity was in the range of 0.056 ~ 0.24 kPa. We made the rather arbitrary assumption that

$$p_o = 0.10 \text{ kPa}. \tag{10}$$

The initial gas pressure (p_o) strongly affects on the impact pressure and its range on the solid surface (refer to Eqs. (5) and (6)), and should be examined in more detail in future.

Next, the region of cavity collapse and the static pressure were estimated as follows. As mentioned above, the mean length of sheet cavitation (l_m) was about 60 percent chord. The present section had a large leading edge radius (Fig. 9) and the boundary layer did not burst. The authors estimated the standard deviation of the unsteady cavity length SD as

$$\text{SD} = 0.2c \tag{11}$$

from Fig. 6. Then the center of the cavity collapsing region is

$$l_m + \text{SD} = 0.8c. \tag{12}$$

The static pressure (p_x) is

$$p_x = \frac{\rho}{2} U_\infty^2 (Cp_{0.8c} + \sigma). \tag{13}$$

Assuming a linear pressure distribution as shown in Fig. 7,

$$p_x = \frac{\rho}{2} U_\infty^2 \sigma \frac{c - 0.8c}{c - 0.6c} = \frac{\rho}{2} U_\infty^2 \frac{\sigma}{2} = 45 \text{ kPa}. \tag{14}$$

The static pressure p_x can be considered as p_∞ in Eqs. (5) and (6).

Cavity Generation Rate. Substituting $\sigma = 1.25$, $\alpha = 8$ deg and $\alpha_0 = 0$ deg into Eq. (1),

$$C_{Qc} = 0.00879. \tag{15}$$

Number and Size of Cavity Bubbles. The cavity generation rate should be equal to the total flow rate of cavity bubbles. Therefore, the following relation is valid.

$$C_{Qc} = \frac{Q}{U_\infty Bc} = \frac{1}{U_\infty Bc}\left(U_\infty B h_b \int_0^\infty \frac{4}{3}\pi R^3 N dR\right) \tag{16}$$

Substituting Eq. (4) into Eq. (16),

$$C_{Qc} = 12.68 \frac{h_b}{c} K R_o^{-0.36}.$$

$$\text{Then } K = 0.0789 \frac{c}{h_b} C_{Qc} R_o^{0.36}. \tag{17}$$

Assuming $R_o = 10^{-4}$ m, the distribution of cavity bubbles is given by Eq. (4) as

$$\left.\begin{array}{ll} N = KR^{-4.36} & R \geq 10^{-4} \text{ m} \\ N = KR_o^{-4.36} & R < 10^{-4} \text{ m} \end{array}\right\}, \tag{18}$$

where

$$K = 1.26 \times 10^{-4}.$$

Accumulative distribution of cavity bubbles I_R is obtained by integrating Eq. (18),

$$I_R = \int N dR = -3.75 \times 10^{-5} R^{-3.36} + \text{const}, \tag{19}$$

where

$$R > R_o = 10^{-4}\ \text{m}.$$

Collapsing Rate on a Pickup. As mentioned before, it is assumed that the spatial distribution of collapse is Gaussian. The normalized Gaussian distribution is

$$\frac{1}{\sqrt{2\pi}(\mathrm{SD})}\exp\left(-\frac{x^2}{2(\mathrm{SD})^2}\right) \tag{20}$$

where SD is the standard deviation. The probability of a bubble collapsing on a pickup of diameter d is

$$\phi \approx \frac{\frac{\pi}{4}d^2}{2\cdot\mathrm{SD}\cdot 1}\times 0.6826\times\frac{1}{\sqrt{2\pi}(\mathrm{SD})}, \tag{21}$$

where the center of the Gaussian distribution is situated on the pickup. This is the case in the present calculation (see Fig. 7).

Substituting $d = 10^{-3}$ m and SD $= 0.2c = 0.03$ m into Eq. (21),

$$\phi = 1.189\times 10^{-4}. \tag{22}$$

Then, the accumulative collapsing rate on the pickup (I_{pR}) is

$$I_{pR} = I_R\cdot U_\infty\cdot h_e\cdot\phi = 4.28\times 10^{-6} I_R\ (\text{bubble/sec})$$
$$= 1.962\ I_R\ (\text{bubble/cm}^2\text{hr}). \tag{23}$$

Combining Eqs. (19) and (23),

$$I_{pR} = -7.36\times 10^{-5}R^{-3.36} + \text{const.}\ (\text{bubble/cm}^2\text{hr}). \tag{24}$$

Impact Force. From Eqs. (10) and (14), $m = p_o/p_x = 2.22\times 10^{-3}$. Substituting m into Eqs. (5), (6), and (7),

$$p_h = 1.288\times 10^4 R\ (\text{MPa}), \tag{25}$$

where R is the radius of cavity bubbles in meters. If the pressure acts uniformly on the surface of a pickup 1 mm in diameter,

$$F = p_h\frac{\pi}{4}d^2 = 1.012\times 10^4 R\ (N). \tag{26}$$

Accumulative Impact Force on Pickup (I_{pF}). Substituting Eq. (26) into Eq. (24),

$$I_{pF} = -2.11\times 10^9 F^{-3.36} + \text{const.} \tag{27}$$

The accumulative distribution of impact force from the largest value ($\bar{I}_{pF}$) is

$$\bar{I}_{pF} = I_{pF}(\infty) - I_{pF}(F) = 2.11\times 10^9 F^{-3.36}, \tag{28}$$

where the unites are $\bar{I}_{pF}$:1/cm^{2}hr and F:Newton.

Equation (28) gives the distribution of impact force acting on the pickup at 80 percent c under the conditions of $\alpha = 8$ deg, $U_\infty = 12$ m/s, and $\sigma = 1.25$. The result of Eq. (28) is compared with the results of experiment as shown in Fig. 11. Quantitative agreement is obtained by assuming $h_e = 0.02c$ and $p_0 = 0.10$ kPa.

Effect of Main Flow Velocity. The effect of main flow velocity (U_∞) can be evaluated using the present method. The cavity generation rate Q should be proportional to U_∞, because C_{Qc} is independent of U_∞. Then the bubble number density distribution function (Fig. 4) is independent of U_∞, and the bubble collapsing rate should be proportional to U_∞.

The ambient pressure p_x is proportional to U_∞^2. The air content was kept almost constant in the present experiment, which resulted in a constant p_0 value. According to Brennen (1969), the gas flow rate from the cavity surface $M \propto U_\infty^{0.75}$, because $Q \propto U_\infty$, $p_o \propto U_\infty^{0.75-1} = U_\infty^{-0.25}$. Then, the assumption of constant p_0 also holds roughly according to the theoretical analysis.

Then, from Eqs. (5)–(7), the impact pressure on a solid surface p_h is

$$p_h = p_{\max}\frac{R_{\min}}{h} \propto \left(\frac{p_0}{p_x}\right)^{-1.8}\cdot p_x\cdot\left(\frac{p_0}{p_x}\right)^{0.7}\cdot R$$
$$= (U_\infty^{-2})^{-1.8}\cdot U_\infty^2\cdot(U_\infty^{-2})^{0.7}\cdot R \propto U_\infty^{4.2}. \tag{29}$$

Figure 12 shows the scaling of the flow velocity estimated using the present analysis in comparison with the results of measurement. The scaling proposed by Le et al. (1993B) is also shown, where it is assumed that both impact force and impact rate are proportional to main flow velocity. The experimental result seems to fluctuate between the results of the two analyses.

8 Conclusions

1. The authors presented a scenario for quantitative prediction of cavitation erosion. The authors also pointed out that the estimation of impact force/pressure spectrum is important for the prediction of erosion.
2. The rate of cavity generation was estimated from the measurement of air flow rate of a ventilated cavity. Number and size distributions of cavity bubbles were estimated from the measurement of air bubble distribution downstream of the cavity collapsing region. By combining them, the impact force/pressure spectrum on a solid surface was estimated, where the analytical result for a single bubble collapse was used.
3. The impact force spectrum was measured at the rear part of a cavitating foil using piezoelectric pickups. The estimation agreed well with the results of this measurement.
4. The present method seems promising for the quantitative prediction of cavitation erosion without using a model test. However, it involves several parameters which were assumed without experimental confirmation. These include the initial gas pressure inside a bubble, the spatial distribution of collapsing bubbles, the change of ambient pressure around collapsing bubbles, and the interaction of bubbles as well as that of a bubble and the solid wall.

Experimental, as well as theoretical verifications of the assumed values, are essential for the development of the proposed method.

Acknowledgments

The impact force pickups were supplied by Mr. M. Maeda, Mitsubishi Heavy Industries. The authors are very grateful for his kind supply of impact force pickups and advice. The authors also thank Ms. A. Tabeta for her assistance during preparation of the manuscript.

References

Billet, M. L., and Weir, D. S., 1975, "The Effect of Gas Diffusion on the Flow Coefficient for a Ventilated Cavity," ASME JOURNAL OF FLUIDS ENGINEERING, Vol. 97, pp. 501–506.

Blake, J. R., 1994, "Transient Inviscid Bubble Dynamics," *The Second International Symposium on Cavitation,* Tokyo, pp. 9–18.

Brennen, C., 1969, "The Dynamic Balances of Dissolved Air and Heat in Natural Cavity Flows," *Journal of Fluid Mechanics,* Vol. 37, Part 1, pp. 115–127.

Chahine, G. L., and Duraiswami, R., 1992, "Dynamical Interactions in a Multi-bubble Cloud," ASME JOURNAL OF FLUIDS ENGINEERING. Vol. 114, pp. 680–686.

Franc, J. P., Michel, J. M., Trong, N'Guyen. H., and Karimi, A., 1994, "From Pressure Pulses Measurements to Mass Loss Prediction: The Analysis of a Method," *The Second International Symposium on Cavitation,* Tokyo, pp. 231–236.

Gadd, G. E., and Grant, S., 1965, "Some Experiments on Cavities behind Disks," *Journal of Fluid Mechanics,* Vol. 23, Part 4, pp. 645–656.

Hickling, R., and Plesset, M. S., 1964, "Collapse and Rebound of a Spherical Bubble in Water," *The Physics of Fluids,* Vol. 7, No. 1, pp. 7–14.

Izumida, Y., Tamiya, S., Kato, H., and Yamaguchi, H., 1980, "The Relationship between Characteristics of Partial Cavitation and Flow Separation," *IAHR, Symposium 1980,* Tokyo, Vol. 1, pp. 169–181.

Kamono, H., Kato, H., Yamaguchi, H., and Miyanaga, M., 1993, "Simulation of Cavity Flow by Ventilated Cavitation on a Foil Section," *Cavitation and Multiphase Flow,* ASME, FED-Vol. 153, pp. 183–189.

Kato, H., 1992, "Recent Advances and Future Proposal on Cavitation Erosion Research," *International Symposium on Propulsors and Cavitation,* Hamburg, pp. 224–233.

Kato, H., and Yamaguchi, H., 1994, "Measurement of Impact Load and Erosion on a Foil Surface," *Workshop on Cavitation Erosion Research,* Tokyo.

Kubota, A., Kato, H., Yamaguchi, H., and Maeda, M., 1989, "Unsteady Structure Measurement of Cloud Cavitation on a Foil Section Using Conditional Sampling Technique," ASME JOURNAL OF FLUIDS ENGINEERING, June 1989, Vol. 111, pp. 204–210.

Le, Q., Franc, J. P., and Michel, J. M., 1993A, "Partial Cavities: Global Behavior and Mean Pressure Distribution," ASME JOURNAL OF FLUIDS ENGINEERING, Vol. 115, pp. 243–248.

Le, Q., Franc, J. P., and Michel, J. M., 1993B, "Partial Cavities: Pressure Pulse Distribution Around Cavity Closure," ASME JOURNAL OF FLUIDS ENGINEERING, Vol. 115, pp. 249–254.

Maeda, M., Yamaguchi, H., and Kato, H., 1991, "Laser Holography Measurement of Bubble Population in Cavitation Cloud on a Foil Section," *Cavitation '91, ASME,* FED-Vol. 116, pp. 67–75.

Maeda, M., Yamada, I., and Tagawa, M., 1994, "The Prediction of Cavitation Erosion on Pump Impeller by Measurement of Cavitation Bubble Collapse Impact Loads (Second Report)," *The Second International Symposium on Cavitation,* Tokyo, pp. 243–248.

Morch, K. A., 1981, "Cavity Cluster Dynamics and Cavitation Erosion," *Proceedings ASME Cavitation and Polyphase Flow Forum,* pp. 1–10.

O'Hern, T. J., et al., 1988, "Comparison of Holographic and Coulter Counter Measurements of Cavitation Nuclei in the Ocean," ASME JOURNAL OF FLUIDS ENGINEERING, Vol. 110, pp. 200–207.

Pereira, F., Avellan, F., and Dorey, J.-M., 1995, "Cavitation Erosion: Statistical Analysis of Transient Cavities," *International Symposium on Cavitation, CAV'95,* Deauville, France, pp. 257–264.

Report of ITTC Cavitation Committee, 5.3 Joint Bassin d'Essais des Carenes and Cavitation Committee Tests, 20th ITTC (1993), Vol. 1, pp. 206–214.

Takahira, H., and Akamatsu, T., 1994, "Dynamics of a Cluster of Bubbles in a Potential Flow," *The Second International Symposium on Cavitation,* Tokyo, pp. 263–268.

Tomita, Y., and Shima, A., 1977, "On the Behavior of a Spherical Bubble and the Impulse Pressure in a Viscous Compressible Liquid," *Bulletin of the JSME,* Vol. 20, No. 149, pp. 1453–1460.

Yamaguchi, H., Kato, H., Kamijo, A., and Maeda, M., 1990, "Development of a Laser Holography System for the Measurement of Cavitation Bubble Clusters," *Cavitation and Multiphase Flow Forum, ASME,* FED-Vol. 98, Toronto, Canada, pp. 115–119.

Yoshihara, K., Kato, H., Yamaguchi, H., and Miyanaga, M., 1988, "Experimental Study on the Internal Flow of a Sheet Cavity," ASME, FED-Vol. 64, pp. 94–98.

Y. Tsujimoto
Professor, Osaka University, Department of Mechanical Engineering, Toyonaka, Osaka 560, Japan
and
Visiting Researcher,
National Aerospace Laboratory,
Japan

S. Watanabe
Graduate Student,
Osaka University,
Engineering Science,
Toyonaka, Osaka,
Japan

K. Kamijo[1]
Director,
Rocket Propulsion Division,
National Aerospace Laboratory,
Kakuda Research Center,
Kakuda, Miyagi,
Japan

Y. Yoshida
Assistant Professor,
Osaka University,
Engineering Science,
Toyonaka, Osaka,
Japan

A Nonlinear Calculation of Rotating Cavitation in Inducers

In the previous linear analysis (Tsujimoto et al., 1993) it was found that there can be a backward rotating cavitation as well as a forward mode which rotates faster than impeller. Although some shaft vibration has been observed, which might be caused by the backward mode, experimental evidence has been obtained only for the forward mode. The purpose of the present study is to find out the factors which determine the amplitude of each mode of rotating cavitation by taking into account several nonlinearities. A time marching nonlinear 2-D flow analysis was carried out for this purpose. It was found that the increase of cavitation compliance at lower inlet pressure can be a factor which limits the amplitude. The mode selectivity is mainly dependent on the stability limit obtained by a linear analysis for which the phase delay of cavity has a most important effect.

Introduction

During the development stage of the liquid oxygen turbopump for the LE-7, the main engine of the H-II rocket, super-synchronous vibrations with frequencies 1.0 to 1.2 times as large as these of shaft rotational frequency was observed. This was caused by rotating cavitation and a method to suppress it has been experimentally found out (Kamijyo et al., 1993). By a linear analysis (Tsujimoto et al., 1993) it was found that the rotating cavitation is caused by positive mass flow gain factor, which is also the cause of the cavitation surge (Braisted and Brennen, 1980), and is completely different from rotating stall which is caused by positive slope of head characteristics. However, the linear analysis predicts another mode of rotating cavitation which rotates in the direction opposite to the inducer. Although a shaft vibration which might be caused by this mode has been also found in the LE-7 turbopump, we do not have the evidence of backward rotation.

The present study is intended to find out the possible factors which determine the amplitudes of each mode. A nonlinear calculation similar to that used by Greitzer and Moore (1986) is carried out. It is assumed that the flow is two dimensional and inviscid, and that the flow in the inducer is perfectly guided by the impeller blades; thus an actuator disk analysis was employed. The nonlinearities considered include; (1) nonlinearities of the upstream and downstream flows, (2) nonlinearities of the pressure performance of the impeller, and (3) nonlinearities of the cavitation characteristics. Effects of these nonlinearities are examined based on a simplification in which only the first circumferential harmonics of disturbances are retained.

Outline of Calculations

We consider a system as sketched in Fig. 1. The flow is sucked from a space with constant pressure $p_{-\infty}$ through an inlet duct with length l_1, and discharged to a space with pressure p_p through an outlet duct with length l_2. Then it is discharged to a space with pressure $p_{-\infty}$ through a throttle with infinitesimal length. We consider a sinusoidal disturbance with respect to y, with a wavelength s. All of the quantities are normalized with the wavelength s, rotational velocity U_T and the fluid density ρ, and the equations hereafter are written down with nondimensional quantities.

Flow in the Inlet Duct. The upstream flow can be assumed to be irrotational. Then the inlet velocities can be represented by

$$u_1 = U_1(t) + 2\pi e^{2\pi x}(a_1(t)\cos 2\pi y + b_1(t)\sin 2\pi y) \quad (1)$$

$$v_1 = 2\pi e^{2\pi x}(b_1(t)\cos 2\pi y - a_1(t)\sin 2\pi y)$$

To be strict to the boundary condition at the inlet ($x = -l_1$), we need to add another set of terms proportional to $e^{-2\pi x}$. However, we neglect these terms for brevity. We represent the pressure at the inducer inlet by

$$p_1 = P_1(t) + a_{p1}(t)\cos 2\pi y + b_{p1}(t)\sin 2\pi y$$

Then we can obtain the following relations from the unsteady Bernoulli's equation by using a Galerkin method (Moore and Greitzer, 1986).

---

[1] Currently Professor at Tohoku University, Institute of Fluid Science, Sendai, 980, Japan.

Contributed by the Fluids Engineering Division for publication in the JOURNAL OF FLUIDS ENGINEERING. Manuscript received by the Fluids Engineering Division November 2, 1994; revised manuscript received March 6, 1996. Associate Technical Editor: R. A. Arndt.

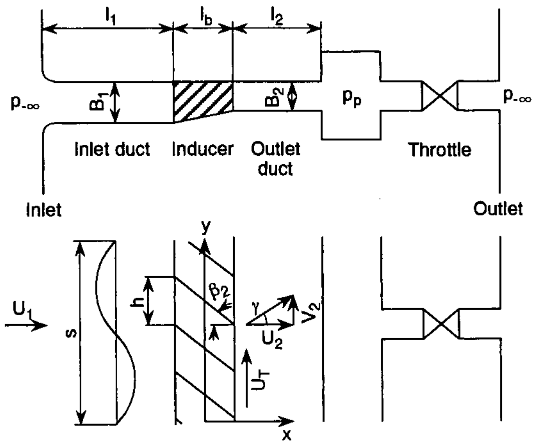

Fig. 1 Sketch of the inducer system

$$l_1 \frac{dU_1}{dt} = p_{-\infty} - P_1(t) - \tfrac{1}{2}U_1^2(t) - \tfrac{1}{2}(a_1^2 + b_1^2)$$

$$\frac{da_1}{dt} = 2\pi(-U_1 a_1 - a_{p1})$$

$$\frac{db_1}{dt} = 2\pi(-U_1 b_1 - b_{p1}) \qquad (2)$$

Flow in the Outlet Duct. The downstream flow is rotational with the vorticity shed from the inducer owing to the unsteadiness of the flow. Hence, the full term Euler's equation, with the continuity equation, was solved by a method similar to SMAC, combined with the Galerkin method by expressing the downstream flow field by

$$u_2(x, y, t) = U_2(x, t) + a_u(x, t) \cos 2\pi y + b_u(x, t) \sin 2\pi y$$

$$v_2(x, y, t) = V_2(x, t) + a_v(x, t) \cos 2\pi y + b_v(x, t) \sin 2\pi y$$

$$p_2(x, y, t) = P_2(x, t) + a_{p2}(x, t) \cos 2\pi y + b_{p2}(x, t) \sin 2\pi y \qquad (3)$$

In the calculation of downstream flow field, we may assume that the velocity distribution at the inlet and the pressure distribution at the outlet are given. At the inlet, or the outlet of the impeller, we apply Kutta's condition:

$$v_2(0, y, t) = 1 - u_2(0, y, t) \tan \beta_2 \qquad (4)$$

As will the described later, $u_2(0, y, t)$ at the new time step will be determined from the impeller pressure performance and $v_2(0, y, t)$ is determined from Eq. (4). At the outlet, the flow is discharged to a space with uniform pressure p_p and thus

$$p_2(l_2, y, t) = p_p = p_{-\infty} + \tfrac{1}{2}\zeta_t U_2^2$$

$$a_{p2}(l_2, t) = b_{p2}(l_2, t) = 0 \qquad (5)$$

where ζ_t is the loss coefficient of the outlet throttle.

The flow calculation in the outlet duct based on these boundary conditions gives the pressure distribution at the impeller outlet, which is used in the calculation of the entire system.

Pressure Increase Across Inducer. If we apply the unsteady Bernoulli's equation in a frame moving with the impeller, we obtain the following relations

$$P_2(t) - P_1(t) = \bar{\Psi} - l_b \frac{dU_2}{dt}$$

$$a_{p2} - a_{p1} = \Psi_c - l_b\left[\frac{da_u}{dt} + 2\pi b_u\right]$$

$$b_{p2} - b_{p1} = \Psi_s - l_b\left[\frac{db_u}{dt} - 2\pi a_u\right] \qquad (6)$$

where

$$\bar{\Psi} = \int_0^1 \Psi(y)dy, \quad \Psi_c = 2\int_0^1 \Psi(y) \cos 2\pi y dy,$$

$$\Psi_s = 2\int_0^1 \Psi(y) \sin 2\pi y dy$$

and $\Psi(y)$ is the static pressure increase determined from Euler's head minus incidence and through flow losses. l_b represents the inertia effect of the impeller flow channel and given by

$$l_b = \frac{(1 + B)l_i}{2b \cos \bar{\beta}}$$

where B is the ratio of flow channel heights, l_i is the nondimen-

Nomenclature

a, b = first-order Fourier coefficients of velocity and pressure fluctuations
B_1, B_2 = flow channel heights at inducer inlet and outlet
B = ratio of flow channel heights $(=B_1/B_2)$
h = blade spacing
K = cavitation compliance, $= -\partial(V_c/h^2)/\partial\sigma_1$
k_R^* = propagation velocity ratio of disturbance
k_I^* = damping rate of disturbance
l_1, l_2 = nondimensional inlet and outlet duct length
l_b = inertia effect of the impeller flow channel
l_i = nondimensional chord length
M = mass flow gain factor, $=\partial(V_c/h^2)/\partial\alpha_1$
P = nondimensional mean pressure
p = nondimensional pressure
s = wavelength of disturbance
S_t = nondimensional frequency, Eq. (11)
t = nondimensional time
U, V = nondimensional mean velocities in x and y directions
u, v = nondimensional total velocities in x and y directions
U_T = rotational velocity
V_c = cavity volume
W = nondimensional relative velocity
α_1 = incidence angle
α_k, α_m = phase delay of K, M
β_1, β_2 = inlet and outlet blade angle
γ = downstream mean flow angle
$\Delta t_k, \Delta t_m$ = time lag of K, M
ζ_T = throttle loss coefficient
ρ = fluid density
σ_1 = inlet cavitation number, $=(p_1 - p_c)/(\rho W^2/2)$
Ψ = coefficient of static pressure increase
ψ_{ts} = coefficient of total-to-static pressure increase
ω = dimensional angular frequency

Superscript

$-$ = annulus averaged quantity

Subscripts

1, 2 = upstream and downstream
c, s = sine and cosine components
p = plenum
$-\infty$ = upstream

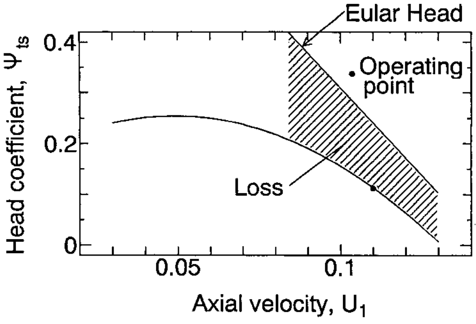

Fig. 2 Pressure performance of the inducer

sional chord length, and $\bar\beta = (\beta_1 + \beta_2)/2$ is the mean flow angle.

Continuity Across Inducer. We consider a distribution of cavity with volume V_c per blade with spacing h at the inducer inlet. Then the continuity relation across the inducer is

$$h\left(\frac{u_2}{B} - u_1\right) = \frac{\partial^*}{\partial t^*}(V_c) \tag{7}$$

where $\partial^*/\partial t^* = \partial/\partial t + \partial/\partial y$ is the time derivative in a frame moving with the inducer. Here, we assume $V_c = V_c(\sigma_1, \alpha_1)$ where σ_1 and α_1 are cavitation number and incidence angle at the inducer inlet. Then we can represent the change in cavity volume as

$$\delta V_c = (-K\delta\sigma_1 + M\delta\alpha_1)h^2 \tag{8}$$

where K and M are generalized cavitation compliance and mass flow gain factor. Here, we consider K and M to be functions of local instantaneous inlet pressure. We take into account the circumferential changes in K and M as well as in σ_1 and α_1

$$\begin{aligned} K &= \bar K + K_c \cos 2\pi y + K_s \sin 2\,\pi y \\ M &= \bar M + M_c \cos 2\,\pi y + M_s \sin 2\pi y \\ \sigma_1 &= \bar\sigma_1 + \sigma_{1c} \cos 2\pi y + \sigma_{1s} \sin 2\pi y \\ \alpha_1 &= \bar\alpha_1 + \alpha_{1c} \cos 2\pi y + \alpha_{1s} \sin 2\pi y \end{aligned} \tag{9}$$

Then we obtain the following relations from the continuity Eq. (8).

$$\begin{aligned} &\bar K \frac{d\bar\sigma_1}{dt} + \frac{1}{2} K_c\left(\frac{d\sigma_{1c}}{dt} + 2\pi\sigma_{1s}\right) + \frac{1}{2} K_s\left(\frac{d\sigma_{1s}}{dt} - 2\pi\sigma_{1c}\right) \\ &\quad = \bar M \frac{d\bar\alpha_1}{dt} + \frac{1}{2} M_c\left(\frac{d\alpha_{1c}}{dt} + 2\pi\alpha_{1s}\right) + \frac{1}{2} M_s\left(\frac{d\alpha_{1s}}{dt} - 2\pi\alpha_{1c}\right) \\ &\qquad + \left(\frac{s}{h}\right)\left(U_1 - \frac{U_2}{\mathrm{B}}\right) \\ &\bar K\left(\frac{d\sigma_{1c}}{dt} + 2\pi\sigma_{1s}\right) + K_c\frac{d\bar\sigma_1}{dt} \\ &\quad = \bar M\left(\frac{d\alpha_{1c}}{dt} + 2\pi\alpha_{1s}\right) + M_c\frac{d\bar\alpha_1}{dt} + \left(\frac{s}{h}\right)\left(a_1 - \frac{a_u}{B}\right) \\ &\bar K\left(\frac{d\sigma_{1s}}{dt} - 2\pi\sigma_{1c}\right) + K_s\frac{d\bar\sigma_1}{dt} \\ &\quad = \bar M\left(\frac{d\alpha_{1s}}{dt} - 2\pi\alpha_{1c}\right) + M_s\frac{d\bar\alpha_1}{dt} + \left(\frac{s}{h}\right)\left(b_1 - \frac{b_u}{B}\right) \end{aligned} \tag{10}$$

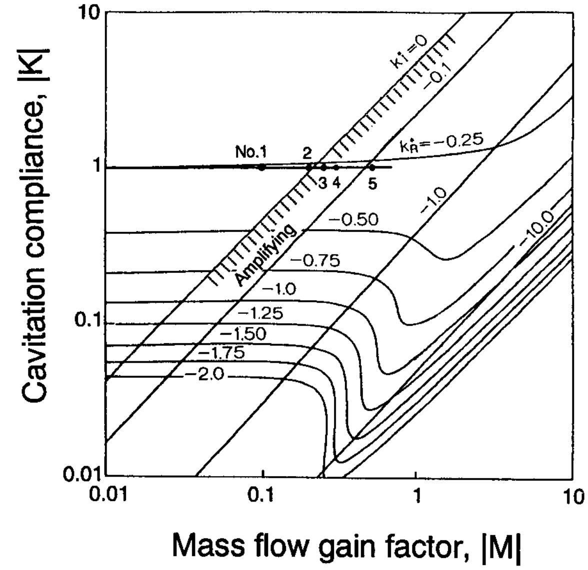

Fig. 3(*a*) Forward travelling mode

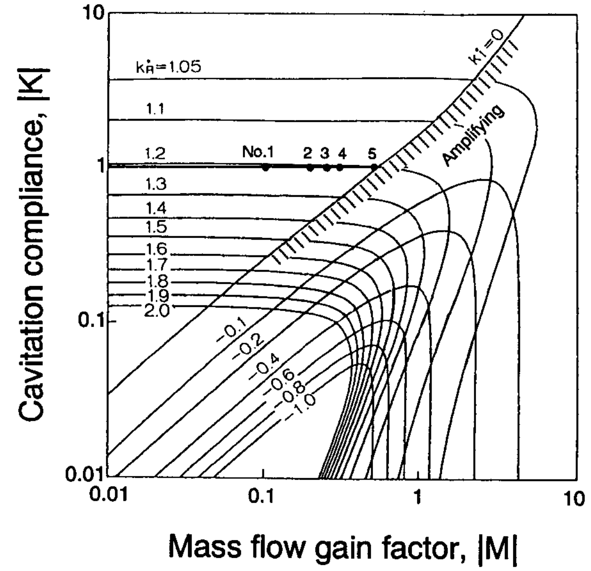

Fig. 3(*b*) Backward travelling mode

Fig. 3 Results of linear analysis without cavitation delay shown as a contour map of complex frequency k_i^*. The numbers in the figure correspond to the non-linear calculations in Table 1.

Time Marching Procedure

The following procedure was found to give the most stable numerical calculation.

(*a*) Determine the inlet cavitation numbers σ_1, σ_{1c}, and σ_{1s} and pressures P_1, a_{p1}, and b_{p1} at $t + \Delta t$ from Eq. (10) by using

Table 1 Nonlinear numerical results without cavitation delay

No.	$\|K\|$	$\|M\|$	Final propagation velocity ratio	Amplitude
1	1.0	0.1	1.19	Attenuate
2		0.2	−0.25	Attenuate
3		0.25	−0.251	Amplify
4		0.3	−0.254	Amplify
5		0.5	−0.261	Amplify

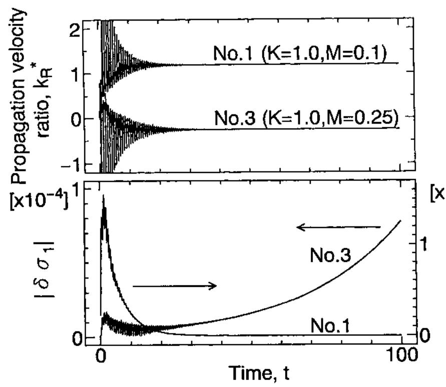

Fig. 4 Time history of the amplitude and propagation velocity ratio, for the case number 1 and 3 in Table 1

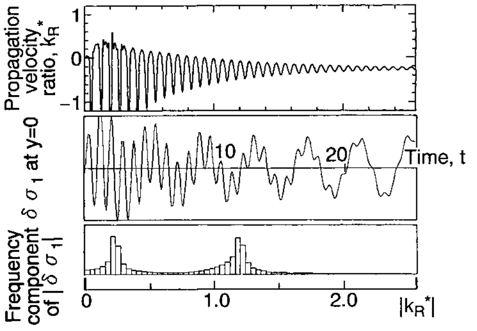

Fig. 5 Traveling velocity ratio, waveform, and its FFT analysis for the case number 3 in Table 1

the values at t for the terms other than $d\sigma_1/dt$, $d\sigma_{1c}/dt$ and $d\sigma_{1s}/dt$.

(b) Determine the upstream velocities U_1, a_1 and b_1 from Eq. (2), using the pressures determined above.

(c) Determine the impeller outlet axial velocities U_2, a_u and b_u from Eq. (6).

(d) Determine the outlet pressure $P_2(0, t)$, $a_{p2}(0, t)$ and $b_{p2}(0, t)$ by downstream flow calculation. Then return to procedure (a).

It was found that the procedure (a) is crucial in the present calculations. It is noted that the highest-order time derivatives comes from $d\sigma_1/dt$ in the continuity Eq. (7), in the linearized analyses of rotating cavitation and surge.

Results and Discussions

All of the following calculations are made for LE-7 LOX turbopump inducer for the cases with $l_1 = 5.0$, $l_2 = 1.0$, and for design points. The inlet total to outlet static pressure performance and the operating point are given in Fig. 2. The values of l_1 and l_2 are determined such that the cavitation surge margin determined from a linear analysis is beyond the rotating cavitation margin for all cases of present calculations. Our present model can correctly simulate also rotating stall and cavitation surge. Although not shown, it was confirmed that rotating stall can be simulated when the slope of pressure performance is positive. Cavitation surge occures when the inlet duct length is assumed to be short and the mass in the inlet duct is small. The frequency and the onset condition of rotating stall and cavitation surge were nearly the same as those obtained from linear analyses.

The Cases Without Cavitation Delay. Equation (8) states that the instantaneous cavity volume δV_c is determined from the inlet pressure $\delta\sigma_1$ and the incidence $\delta\alpha_1$ at that instant. In this subsection we will discuss about these cases with constant M and K. The results of linear analysis with $l_1 = l_2 = \infty$ is reproduced from Tsujimoto et al. (1992) and shown in Fig. 3(a), (b). $k_i^* = k_R^* + ik_I^*$ is the complex frequency and k_R^* is the propagation velocity ratio = propagation velocity/impeller velocity and k_I^* is the exponential damping rate. k_1^* with positive k_R^* shown in (a) represents the forward travelling mode and k_2^* in (b) the backward one. We note that the destabilizing region with $k_I^* < 0$ is larger for the backward mode and the amplifying rate $-k_I^*$ in the destabilizing region is also larger for the backward mode.

The results of the present nonlinear calculation are summarized in Table 1 for the conditions numbered in Fig. 3. The propagation velocity ratio is determined from the inlet axial velocity. The backward mode with $k_I^* = -0.25$ becomes amplifying between $M = 0.2$ (No. 2) and 0.25 (No. 3) which is in good agreement with the linear stability analysis. Although it is attenuating, we observe forward mode with $M = 0.1$ (No. 1). The time histories of the amplitude of inlet cavitation number fluctuation and the propagation velocity ratio are shown in Fig. 4 for the case number 1 and 3 in Table 1. The inlet cavitation number fluctuation and its FFT analysis for the case 3 is shown in Fig. 5. We observe frequency components at $|k_R^*| = 1.2$ and $|k_R^*| = 0.25$, which are close to the frequencies of the forward and backward modes shown in Fig. 3. The waveform clearly shows that the backward mode is amplifying while the forward mode is attenuating.

In the calculations in Table 1, which includes only the nonlinearities of the flow and of the inducer performance, the amplitude increased to the extent such that further time marching was not possible. We note here the fact that the *pressure cannot reduce significantly below the vapor pressure.* This effect might

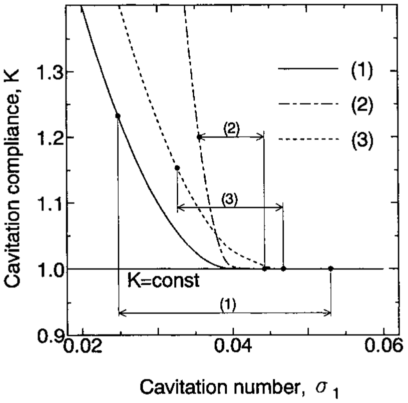

Fig. 6(a) Cavitation compliance as functions of inlet pressure

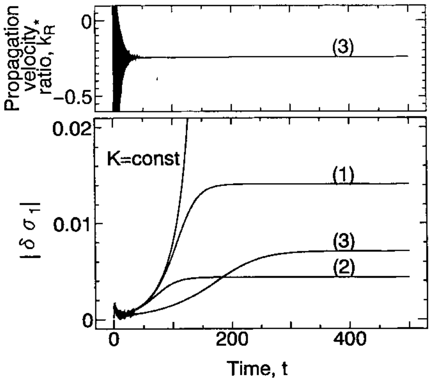

Fig. 6(b) Growth of amplitude, corresponding to cavitation compliance shown in (a)

Fig. 6 Effects of nonlinearity in cavitation characteristics

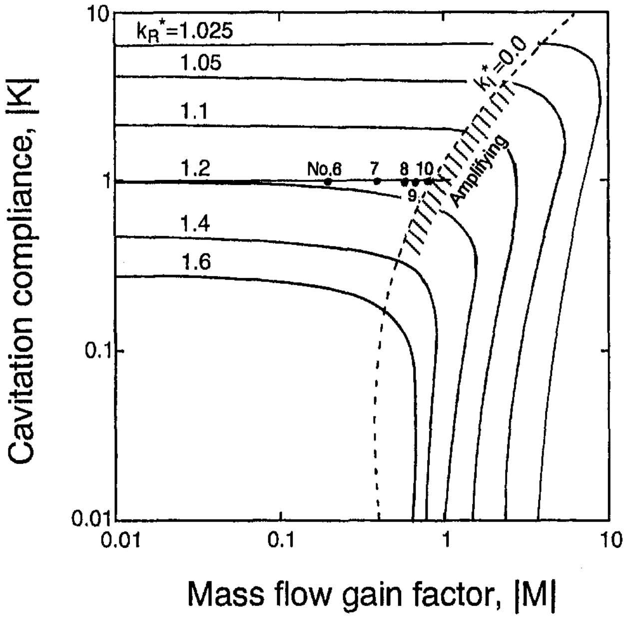

Fig. 7(*a*) Forward travelling mode

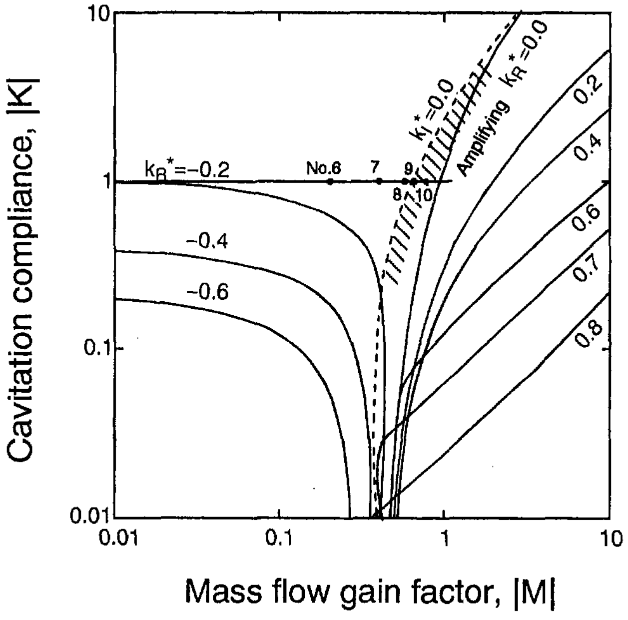

Fig. 7(*b*) Backward travelling mode

Fig. 7 Results of linear analysis with cavitation delay, $M = |M|e^{-i\alpha_m}$, $K = |K|e^{-i\alpha_k}$, with $\alpha_{k,m} = 2\pi(k_R^* - 1)\Delta t_{k,m}$, $\Delta t_k = 0.097$, $\Delta t_m = 0.194$. The numbers in the figure correspond to the nonlinear calculations in Table 2.

Table 2 Nonlinear numerical results with cavitation delay for forward and backward components

No.	$\|K\|$	$\|M\|$	Final propagation velocity ratio	Amplitude
6	1.0	0.2	1.21	Attenuate
7		0.4	1.19	Attenuate
8		0.6	−0.2	Attenuate
9		0.65	−0.2	Amplify
10		0.8	−0.2	Amplify

be expressed by increasing the cavitation compliance below certain inlet pressure. Figure 6(*b*) shows the results when the local cavitation compliance is determined from the local inlet pressure following the relation as shown in (*a*). It is clear that this effect can be a factor determining the amplitude. Figure 6(*a*) also shows the range which the inlet cavitation number exhibits after arriving at the steady oscillation for each case. It was found that the circumferential averages of the cavitation compliance for these three cases are very close to the linear stability value $K = 1.06$ for $M = 0.25$. However, the traveling direction was backward as expected from the linear analysis.

Effects of Cavitation Delay. The nondimensional frequency which a cavity on a blade experiences is

$$S_t = \omega h/U_T = 2\pi(h/s)|k_R^* - 1| \qquad (11)$$

where ω is the dimensional angular frequency and $s/h = N$ is the number of the blades. With $k_R^* = 1.2$ for forward mode and $k_R^* = -0.25$ for backward mode, we have $S_t = 0.42$ or 2.61, respectively. These values are significantly large and the quasi-steady assumption of the cavity response expressed by Eq. (8) might be invalid under such frequencies. In fact, recent theoretical analysis of unsteady blade surface cavitation (Otsuka, et al., 1994) predicts significant delay of cavity response both for inlet pressure and flow rate fluctuations. Experimental results by Brennen et al. (1982) and the bubbly flow model by Brennen (1978) also shows cavitation delay in the range of σ of the present interest. The cavitation delay can be taken into account by using $|M|e^{-i\alpha_m}$ and $|K|e^{-i\alpha_k}$ for M and K in the linear analysis. Otsuka et al.'s result suggests $\alpha_{k,m} = 2\pi(k_R^* - 1)\Delta t_{k,m}$, with $\Delta t_k = 0.097$ for inlet pressure fluctuation and $\Delta t_m = 0.194$ for incidence fluctuation. The results with the above phase lags are shown in Fig. 7. We find that the amplifying region is significantly reduced. However, the neutral stability curve is nearly the same for forward and backward travelling modes, with a slightly larger amplifying region for backward mode.

In the nonlinear calculations, the effects of the phase lag were taken into account by shifting the phase of the right-hand side of Eq. (8) in y-direction. Since we have two frequency components corresponding to the forward and backward mode, and the amount of the phase lag is dependent on the frequency, the total phase lag is determined by separating the fluctuations into those two components and giving phase lag to each components and summing up those components. The results are summarized in Table 2. We find that the results are similar to those in Table 1, except that the neutral stability point moved to $|M| = 0.60 - 0.65$, which is in agreement with the linear calculations.

In the above calculations, it was assumed that the phase lag of cavity is the same for backward and forward travelling components. However, it might be reasonable to consider that they are different. As an extreme case, we might assume no phase lag for forward component, and with the phase lag given by surge mode analysis for backward component. Then the linear stability map will be a combination of Fig. 3(*a*) and Fig. 7(*b*) and we have larger amplifying region for forward travelling mode. The results of the nonlinear calculations are given in Table 3. Although amplifying forward traveling mode appeared, it amplified to the extent that no further calculation was possible. In order to obtain finite amplitude forward travelling mode, it was further assumed that $|K|$ follows the curve (1) in Fig. 6(*a*). Figure 8 shows the result and we now have a steady forward travelling mode, and the travelling waveforms in inlet pressure $\delta\sigma_1$ and axial velocity δu_1 are shown in Fig. 9.

Table 3 Nonlinear numerical results with cavitation delay for backward component

$\|K\|$	$\|M\|$	Final propagation velocity ratio	Amplitude
1.0	0.2	1.21	Attenuate
	0.4	1.20	Attenuate
	0.5	1.19	Attenuate
	0.55	1.19	Amplify
	0.6	1.19	Amplify

The amplitude became finite with $0.55 < M < 0.7$ for this case, and with $0.25 < M < 0.5$ for the case with $|K|$ reduced by 0.5 from the curve (1) in Fig. 6(*a*).

Conclusion

The findings of the present study can be summarized as follows

1. Nonlinearities in the inducer pressure performance which includes the effects of the major flow loss or in the flow field are not the factors which determine the amplitude of rotating cavitation.
2. Increase of cavitation compliance at lower inlet pressure can be a factor to determine the amplitude.
3. Both forward and backward travelling rotating modes were observed in the nonlinear time marching calculations.
4. Phase lag of cavity response has a significant effect on rotating cavitation.
5. If we assume a larger phase lag for backward travelling mode and the increase of cavitation compliance at lower inlet pressure, we can simulate a stable forward travelling rotating cavitation which is observed in experiments.

The present calculations are based on various assumptions which should be experimentally verified. The present model can be used to study the interactions among cavitation surge, forward and backward rotating cavitation. These should be included in the next report. Flow visualizations show that rotating cavitation is by no means two-dimensional. 3-D flow effects and especially the effects of tip cavities should be taken into account. The present report is the first step into the study of these effects.

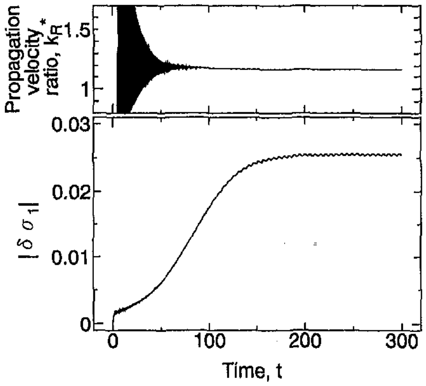

Fig. 8 **Finite amplitude forward travelling rotating cavitation, obtained by assuming phase lag for backward component and increase of cavitation compliance at smaller inlet pressure. $M = 0.60$, K = Fig. 6(*a*) curve (1).**

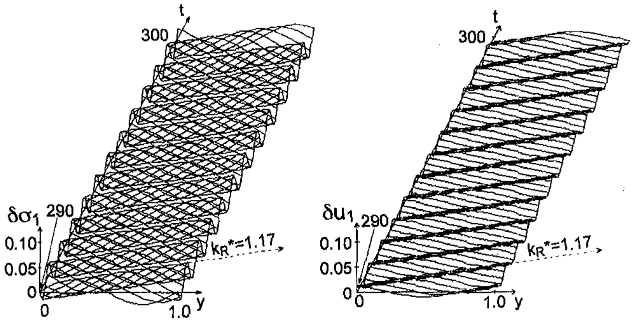

Fig. 9 **Forward propagation of the distribution of inlet cavitation number $\delta\sigma_1$ and axial velocity δu_1 with $k_R^* = 1.17$, corresponding to Fig. 8**

Acknowledgments

The authors are graceful to the stimulating discussions of Dr. T. Shimura at NAL and Dr. K. Yokota of Osaka University. Acknowledgments are also to Mr. M. Yasuda, who constructed the foundation of the present computer program as an undergraduate project. This study is partly supported by the Grant in Aid for Scientific Studies of the Ministry of Education.

References

Braisted, D. M., and Brennen, C. E., 1980, "Auto-oscillation of Cavitating Inducers," ASME *Symposium on Polyphase Flow and Transport Technology,* pp. 157–166.

Brennen, C. E., 1978, "Bubbly Flow Model for the Dynamic Characteristics of Cavitating Pumps," *Journal of Fluid Mechanics,* Vol. 89, Part 2, pp. 223–240.

Brennen, C. E., Meissner, C., Lo, E. Y., and Hoffman, G. S., 1982, "Scale Effects in the Dynamic Transfer Functions for Cavitating Inducers," ASME JOURNAL OF FLUIDS ENGINEERING, Vol. 104, pp. 428–433.

Kamijo, K., Yoshida, M., and Tsujimoto, Y., 1986, "Hydraulic and Mechanical Performance of LE-7 LOX Pump Inducer," *AIAA Journal of Propulsion and Power,* Vol. 9, No. 6, pp. 819–826.

Moore, F. K., and Greitzer, E. M., 1986, "A Theory of Post-stall Transients in Axial Compression Systems, Part I," ASME *Journal of Engineering for Gas Turbines and Power,* Vol. 108, pp. 68–76.

Otsuka, S., Tsujimoto, Y., Kamijo, K., and Furuya, O., 1994, "Frequency Dependence of Mass Flow Gain Factor and Cavitation Compliance of Cavitating Inducers," ASME *Symposium on Cavitation and Gas-Liquid Flows in Fluid Machinery and Devices,* FED-Vol. 190, pp. 119–126.

Tsujimoto, Y., Kamijo, K., and Yoshida, Y., 1992, "Theoretical Analysis of Rotating Cavitation in Rocket Pump Inducers," AIAA Paper 92-3209.

Tsujimoto, Y., Kamijo, K., and Yoshida, Y., 1993, "A Theoretical Analysis of Rotating Cavitation in Inducers," ASME JOURNAL OF FLUIDS ENGINEERING, Vol. 115, No. 1, pp. 135–141.

Fabrizio d'Auria
Graduate Student.

Luca d'Agostino
Associate Professor.

Dipartimento di Ingegneria Aerospaziale,
Università degli Studi di Pisa,
Via Diotisalvi 2,
56126 Pisa, Italy

Christopher E. Brennen
Professor,
California Institute of Technology,
Mechanical Engineering Dept. 104-44,
1201 E. California Blvd.
Pasadena, CA 91125

Dynamic Response of Ducted Bubbly Flows to Turbomachinery-Induced Perturbations

The present work investigates the dynamics of the three-dimensional, unsteady flow of a bubbly mixture in a cylindrical duct subject to a periodic pressure excitation at one end. One of the purposes is to investigate the bubbly or cavitating flow at inlet to or discharge from a pump whose blade motions would provide such excitation. The flow displays various regimes with radically different wave propagation characteristics. The dynamic effects due to the bubble response may radically alter the fluid behavior depending on the void fraction of the bubbly mixture, the mean bubble size, the pipe diameter, the angular speed of the turbomachine and the mean flow Mach number. This simple linearized analysis illustrates the importance of the complex interactions of the dynamics of the bubbles with the average flow, and provides information on the propagation and growth of the turbopump-induced disturbances in the feed lines operating with bubbly or cavitating liquids. Examples are presented to illustrate the influence of the relevant flow parameters. Finally, the limitations of the theory are outlined.

1 Introduction

Unsteady phenomena in liquid/gaseous mixtures in ducts are relevant to a number of technological applications (Brennen, 1994). Typical in this respect are modern cryogenic liquid propellant rockets in which the propellant storage pressure is close to the saturation value. This inevitably increases the possibility of cavitation in the propellant feed turbopumps, which often extends into the supply lines producing a bubbly two-phase mixture in the inlet line. This can lead to the onset of operational instabilities of the turbopump similar to the rotating stall and surge phenomena commonly observed in compressors (Brennen, 1994).

Extensive efforts have been made to include the effects of bubble dynamics, as well as liquid compressibility and relative motion, in the analysis of dispersed bubbly flow mixtures (van Wijngaarden, 1964, 1968, 1972; Stewart and Wendroff, 1984). Of particular relevance here are the studies of the dynamics of clusters of bubbles by Chahine (1982a, 1982b), Pylkkänen (1986), Omta (1987), d'Agostino and Brennen (1983, 1988, 1989), Kumar and Brennen (1990), Chahine et al. (1991), Mørch (1980, 1981, 1982), and Hansson et al. (1981). These investigations uniformly indicate that, even at relatively low void fractions, the complex interaction of a large number of bubbles with the pressure field drastically modifies the propagation of disturbances in the bubbly mixture and the spectrum of the internal oscillations of the flow (d'Agostino and Brennen, 1988, 1989).

The present paper is an extension of previous research efforts on the dynamics of bubbly and cavitating flows (d'Agostino and Brennen, 1983, 1988, 1989; d'Agostino et al., 1988; d'Auria et al., 1994) all of which were initiated by the paper by d'Agostino and Brennen (1983) in which the expression for the natural frequency of a cloud of bubbles was first derived. Here, a linear perturbation approach is applied to the more complex case of the three-dimensional unsteady flow of a bubbly mixture in a cylindrical duct subject to a periodic pressure excitation at one of the ends. Different wave propagation characteristics are observed which correspond to the various flow regimes previously defined (d'Agostino et al., 1988). The bubble dynamic effects strongly depend on the void fraction of the bubbly mixture, the mean bubble size, the pipe diameter, the angular speed of the turbomachine and the mean flow Mach number. Despite the inherent limitations of the linear approximation, this analysis illustrates some of the dynamic properties and fundamental phenomena of real bubbly liquids and contributes to the understanding of the flow instabilities occurring in several important engineering applications.

2 Basic Equations and Linearization

The basic equations employed are identical to those previously used by d'Agostino et al. (1983, 1988, 1989) and d'Auria et al. (1994). Relative motion between the liquid and the bubbles has a negligible effect on the results for this kind of flows (d'Agostino and Brennen, 1988) and will not be included here. Then, if $\mathbf{u}$ is the velocity of the mixture, with pressure p, unperturbed density ρ, speed of sound c, and bubble concentration β per unit liquid volume, the continuity equation for the mixture, neglecting the mass of the bubbles, becomes:

$$\nabla \cdot \mathbf{u} = \frac{1}{1+\beta\tau}\frac{D(\beta\tau)}{Dt} - \frac{1}{\rho c^2}\frac{Dp}{Dt} \tag{1}$$

where $D/Dt = \partial/\partial t + \mathbf{u}\cdot\nabla$ is the Lagrangian time derivative, and $\tau = 4\pi R^3/3$ is the volume of the bubbles, assumed spherical with radius R. The void fraction, $\alpha = \beta\tau/(1+\beta\tau)$, is assumed to be very small compared with unity. It is also assumed that no bubbles are created or destroyed so that β is a constant in the bubbly fluid. Neglecting body forces and viscous effects in the large-scale flow (viscous effects are included in the bubble dynamics), the momentum equation for the liquid becomes:

$$\frac{\rho}{1+\beta\tau}\frac{D_u\mathbf{u}}{Dt} = -\nabla p \tag{2}$$

The bubble radius is assumed given by the Rayleigh-Plesset

Contributed by the Fluids Engineering Division for publication in the JOURNAL OF FLUIDS ENGINEERING. Manuscript received by the Fluids Engineering Division August 31, 1995; revised manuscript received March 20, 1996. Associate Technical Editor: O. C. Jones.

equation (Plesset and Prosperetti, 1977; Knapp et al., 1970) modified as indicated by Keller et al. (see Prosperetti, 1984) to account for dissipation effects in the bubble dynamics (including liquid compressibility):

$$\left(1-\frac{1}{c}\frac{DR}{Dt}\right)R\frac{D^2R}{Dt^2}+\frac{3}{2}\left(\frac{DR}{Dt}\right)^2\left(1-\frac{1}{3c}\frac{DR}{Dt}\right)$$

$$=\left(1+\frac{1}{c}\frac{DR}{Dt}\right)\frac{p_R(t)-p(t+R/c)}{\rho}+\frac{R}{\rho c}\frac{dp_R(t)}{dt} \quad (3)$$

Here $p_R(t)$ is the liquid pressure at the bubble surface, related to the bubble internal pressure p_B (assumed uniform) by:

$$p_B(t)=p_R(t)+\frac{2S}{R}+4\mu\frac{1}{R}\frac{DR}{Dt}$$

where $p_B(t)$ is the sum of the liquid vapor pressure and the pressure of a fixed mass of noncondensable gas, and S is the surface tension of the liquid. Clearly, for the closure of the problem, the above equations must be supplemented by the mechanical and thermal equations of state and by the energy conservation equations for the two phases and the relevant boundary conditions.

The governing equations are now linearized by assuming decomposition into steady flow components (denoted by the subscript o) and small, time-harmonic complex fluctuations (indicated by the tilde) of frequency, ω. Thus, for instance:

$$p-p_o=\mathrm{Re}\{\tilde{p}\} \quad \text{where} \quad \tilde{p}=\hat{p}e^{-i\omega t},$$

and so on for the other flow variables. In the most general case ω is complex and the fluctuations consist of damped or amplified oscillations with amplification rate given by $\mathrm{Im}(\omega)$. For the sake of simplicity we first consider the case of zero mean flow ($\mathbf{u}_o=0$). Linearization of the momentum and energy equations for a bubble containing a perfect gas of uniform properties leads to a harmonic oscillator equation for each individual bubble (Prosperetti, 1984, 1977):

$$(-\omega^2-i\omega 2\lambda+\omega_B^2)\hat{R}=-\left(1+i\omega\frac{R_o}{c}\right)\frac{\hat{p}}{\rho R_o}$$

where $\omega_B=\omega_B(\omega)$ is the bubble natural frequency and the damping coefficient, $\lambda=\lambda(\omega)$, is given by the sum of three terms accounting for the viscous, acoustical, and thermal contributions to dissipation (Chapman and Plesset, 1972; d'Agostino and Brennen, 1988).

Elimination of $\hat{\mathbf{u}}$, $\hat{\beta}$, and $\hat{R}$ from the linearized equations yields the following Helmholtz equation for $\hat{p}$:

$$\nabla^2\hat{p}+k^2(\omega)\hat{p}=0 \quad (4)$$

with the free-space wave number k determined by the dispersion relation:

$$\frac{1}{c_M^2(\omega)}=\frac{k^2(\omega)}{\omega^2}$$

$$=\frac{1}{c_{Mo}^2}\left(\frac{\omega_{Bo}^2(1+i\omega R_o/c)}{\omega_B^2-\omega^2-i\omega 2\lambda}\right)+\frac{(1-\alpha)^2}{c^2} \quad (5)$$

Here $c_M(\omega)$ is the complex and dispersive (frequency dependent) speed of propagation of an harmonic disturbance of angular frequency ω in the free bubbly mixture, while:

$$\omega_{Bo}^2=\frac{3p_{Bo}}{\rho R_o^2}-\frac{2S}{\rho R_o^3} \quad \text{and} \quad c_{Mo}^2=\frac{\omega_{Bo}^2R_o^2}{3\alpha(1-\alpha)}$$

are, respectively, the natural frequency of oscillation of a single bubble at isothermal conditions in an unbounded liquid (Plesset and Prosperetti, 1977; Knapp et al. 1970) and the low-frequency sound speed in a free bubbly flow with incompressible liquid ($\omega \to 0$ and $c \to \infty$).

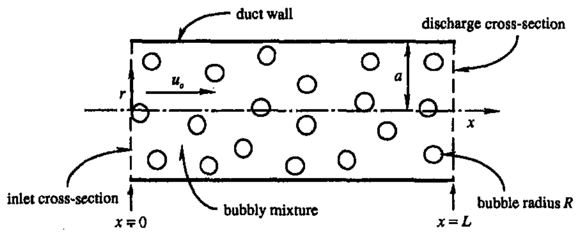

Fig. 1 Schematic of a bubbly flow in a cylindrical duct

3 Dynamics of a Bubbly Flow in a Cylindrical Duct

Now examine the three-dimensional, unsteady perturbation of a bubbly mixture in a cylindrical duct of length L and radius a, with rigid walls and arbitrary pressure excitation at the inlet cross section, $x=0$, as shown in Fig. 1. We shall see that the case of finite mean flow ($\mathbf{u}_o \neq 0$) can readily be obtained by an extension of the zero mean flow solution ($\mathbf{u}_o=0$) and we thereby begin with the latter. We examine the simple case of a finite length duct, $0 \le x \le L$. As an example, consider the case of a duct connected to a constant pressure reservoir, so that $\hat{p}|_{x=L}=0$. The other relevant boundary conditions are given by $\hat{u}_r|_{r=a}=0$ together with the regularity of the solution on the centerline and its periodicity in the azimuthal direction. By

Nomenclature

a = duct radius
c = speed of sound, Fourier coefficient
i = imaginary unit
J = Bessel function of the first kind
k = wave number
L = duct length
M = Mach number
N = number of blades
p = pressure
p_R = liquid pressure at bubble surface
R = bubble radius
r = radial coordinate
S = surface tension
t = time
$\mathbf{u}$ = fluid velocity vector
u = axial velocity
x = axial coordinate
$z_{m,n}$ = nth root of $J'_m(z)$
α = void fraction
β = bubble concentration per unit liquid volume
γ = specific heat ratio
λ = damping coefficient
μ = liquid viscosity
ϑ = angular coordinate
ρ = liquid density
τ = bubble volume
Ω = rotor angular speed
ω = frequency

Subscripts

B = bubble
L = Lagrangian
l = axial mode number
m = order of Bessel function J
n = order of $J'_m(z)$ roots
o = mean flow
s = Fourier index
x = axial

Superscripts

$\sim$ = perturbation quantity
$\wedge$ = complex amplitude of perturbation
$*$ = complex conjugate
$(\ )'$ = differentiation

standard methods (Lebedev, 1965), the separable solution (normalized, for convenience, at $x = 0$) for the finite length duct is found to be:

$$\tilde{p}_{m,n}(\omega) \approx J_m(z_{m,n}r/a)e^{\pm im\vartheta - i\omega t}\frac{\sin k_x(L-x)}{\sin k_xL} \qquad (6)$$

(or its complex conjugate), where $z_{m,n}$ is the nth non-negative root of $J'_m(z) = 0$, and the axial wave number is: $k_x(\omega) = \sqrt{k^2(\omega) - z^2_{m,n}/a^2}$ (principal branch). For a semi-infinite duct the radiation condition at $x = 0$ replaces the condition at $x = L$, and, with earlier notations, the corresponding solution is:

$$\tilde{p}_{m,n}(\omega) \approx J_m(z_{m,n}r/a)e^{i(\pm m\vartheta - \omega t + k_x x)} \qquad (7)$$

We consider, in particular, the solution for the idealized excitation generated by a turbomachine rotor with N blades and angular speed, Ω, located at the inlet cross-section ($x = 0$). The pressure excitation is assumed $2\pi/N$-periodic in the rotating angular coordinate $\vartheta' = \vartheta - \Omega t$ and can therefore be decomposed as:

$$p(r, \vartheta, 0, t) - p_o = \sum_{s=-\infty}^{\infty}\sum_{n=0}^{\infty} c_{sN,n}J_{\pm sN}(z_{\pm sN,n}r/a)e^{isN(\vartheta - \Omega t)}$$

where s is the harmonic index of the Fourier decomposition, $m = \pm sN \geq 0$ is the azimuthal mode number and $\omega = \pm sN\Omega \geq 0$ is the blade excitation frequency, with the upper and lower signs for $s \geq 0$ and $s < 0$, respectively. The coefficients:

$$c_{0,0} = \frac{N}{\pi a^2}\int_0^a rdr\int_{-\pi/N}^{\pi/N} p(r, \vartheta, t)d\vartheta$$

$$c_{sN,n} = \frac{N\int_0^a rJ_{\pm sN}(z_{\pm sN,n}r/a)dr\int_{-\pi/N}^{\pi/N} p(r, \vartheta, t)e^{-isN\vartheta}d\vartheta}{\pi a^2(1 - s^2N^2/z^2_{\pm sN,n})J^2_{\pm sN}(z_{\pm sN,n})} \qquad \text{for} \quad s, n \neq 0, 0$$

are readily obtained from the orthogonality properties of $e^{-isN\vartheta}$ and $J_{\pm sN}(z_{\pm sN,n}r/a)$ on the duct cross-section. Consistent with the linearization, the solution for the assigned pressure excitation $p(r, \vartheta, t)$ may be expressed by the series:

$$p(r, \vartheta, x, t) - p_o = \sum_{s=-\infty}^{\infty}\sum_{n=0}^{\infty} c_{sN,n}\begin{matrix}\tilde{p}_{sN,n}(sN\Omega)\\ \tilde{p}^*_{-sN,n}(-sN\Omega)\end{matrix}$$

with the upper conjugate solution valid for $s \geq 0$ and the lower valid for $s < 0$. The remaining flow variables are then readily obtained from the linearized governing equations.

The above treatment is easily extended to the case of non-zero mean flow velocity ($\mathbf{u}_o \neq 0$) by means of the Galilean transformation $x = x_L + u_o t$ between the absolute (Eulerian) frame and the Lagrangian frame (subscript L) moving with the bubbly mixture. In this frame the unperturbed fluid is at rest and the general solution for a finite length duct has the form:

$$\tilde{p}_{m,n}(\omega_L) \approx J_m(z_{m,n}r_L/a)e^{\pm im\vartheta_L - i\omega_L t}\frac{\sin k_x(L - x_L)}{\sin k_xL} \qquad (8)$$

where $\omega_L = \omega - u_o k_x$ is the Lagrangian frequency experienced by the bubbles in their trajectory and $k_x = k_x(\omega_L)$. Substituting the transformed coordinates $x_L = x - u_o t$, $r_L = r$ and $\vartheta_L = \vartheta$ we can confirm that the solution $\tilde{p}_{m,n}(\omega)$ for a stationary fluid given by equations (6) and (7) remains valid in the absolute frame provided that the excitation frequency is re-defined as $\omega = \omega_L + u_o k_x$. Therefore, for any assigned value of the Eulerian frequency, ω, the axial wave number k_x is the (generally complex) solution of the equation $k_x = k_x(\omega_L)$ with Lagrangian frequency $\omega_L = \omega - u_o k_x$.

The entire flow has therefore been determined in terms of the material properties of the two phases, the geometry of the duct, the nature of the excitation, and the quantities, R_o, p_o, $\mathbf{u}_o$, and α.

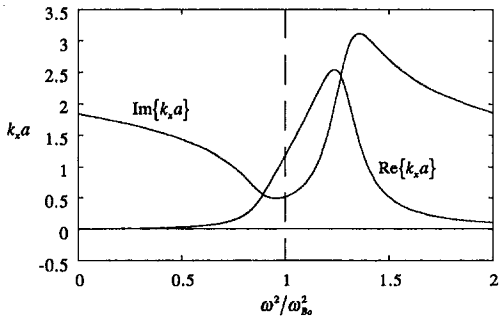

Fig. 2 Real part, Re(k_xa), and imaginary part, Im(k_xa), of the normalized damped axial wave number as a function of the square of the reduced frequency, ω/ω_{Bo}. The results shown are for the fundamental radial mode of the first azimuthal harmonic ($m = 1$, $n = 0$, $z_{m,n} = z_{1,0} = 1.8412$) and for $3\alpha(1 - \alpha)a^2/R_o^2 = 1$.

4 Results and Discussion

The results presented are intended to illustrate the most significant features and phenomena implicit in the above solution. We choose a duct of radius $a = 0.15$ m and length $L = 1$ m, containing air bubbles ($R_o = 0.001$ m, $\gamma = 1.4$, $\chi_G = 0.0002$ m^2/s) in water ($\rho = 1000$ kg/m^3, $\mu = 0.001$ Ns/m^2, $S = 0.0728$ N/m, $c = 1485$ m/s) at atmospheric pressure ($p_o = 10^5$ Pa). In addition, we must specify the void fraction, α. Note that the bubble interaction parameter, $3\alpha(1 - \alpha)L^2/R_o^2$, which could be much larger or smaller than unity, appears in all of these bubbly flow analyses. The dynamic response of the flow can be very different depending on $3\alpha(1 - \alpha)L^2/R_o^2$. The mean flow the Mach number $M_o = u_o/c_{Mo}$ also occurs as a parameter in the present solutions.

We first consider the general features of the propagation of disturbances of real frequency ω in the absence of mean flow. Note that the solution for a semi-infinite duct is oscillatory in ϑ, in t, and, in complex sense (damped or amplified), also in x, while its behavior in the radial direction is expressed by Bessel functions of integer order m, scaled by the factor $z_{m,n}/a$ in order to satisfy the kinematic boundary condition at the duct wall. In particular, the solution for $m = n = 0$ corresponds to plane axial waves. Wave propagation along the duct is regulated by the axial wave number, $k_x = k_x(\omega)$. In the undamped case k_x^2 is real (positive, zero, or negative) and the axial modes are either purely harmonic or exponential in space, with wavelength and amplification rate respectively determined by the real and imaginary parts of k_x. In the presence of dissipation k_x is neither real nor purely imaginary (see Fig. 2 for the sample case, $m = 1$ and $n = 0$) and the axial modes consist of harmonic oscillations with amplitude changing in the axial direction. Notice that k_x varies with ω and is generally different from the free-space wave number k because of the presence of the duct boundaries (except for the simple case of plane axial waves where $z_{m,n} = z_{0,0}$ vanishes). Thus, for any particular bubbly mixture, the axial modes will depend on the oscillation frequency and the duct geometry.

The behavior of k_x as a function of the frequency ω is most readily illustrated in the absence of damping (when the argument of the square root is real). Then the axial wave number is either real or purely imaginary depending on the sign of $k^2(\omega) - z^2_{m,n}/a^2$, with a first regular transition at the cut-off frequency:

$$\omega^2_{m,n} = \omega^2_{Bo}\Bigg/\left(1 + \frac{3\alpha(1 - \alpha)a^2/R_o^2}{z^2_{m,n}}\right) \qquad (9)$$

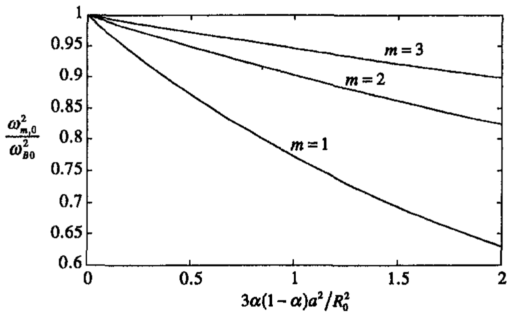

Fig. 3 Normalized cut-off frequency, $\omega^2_{m,0}/\omega^2_{Bo}$, as a function of the bubble interaction parameter, $3\alpha(1-\alpha)a^2/R_o^2$, for the fundamental radial mode ($n = 0$) of the lowest azimuthal harmonics ($m = 1, 2, 3$)

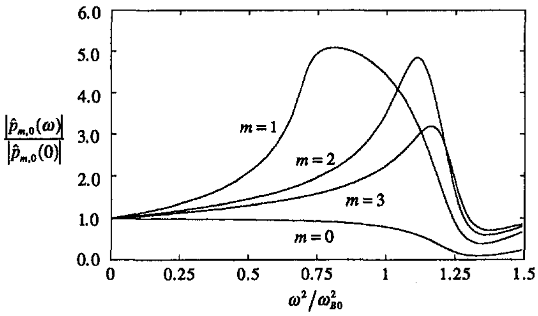

Fig. 4 Normalized amplitude of the pressure oscillations, $|\hat{p}_{m,0}(\omega)|/|\hat{p}_{m,0}(0)|$, as a function of the square of the reduced frequency, ω/ω_{Bo}, for the fundamental radial mode ($n = 0$) of the lowest azimuthal harmonics ($m = 0, 1, 2, 3$) in a semi-infinite duct with $3\alpha(1-\alpha)a^2/R_o^2 = 1$

and a second, *singular transition at the natural frequency*, ω_{Bo}, of an individual bubble in an infinite liquid (bubble resonance condition), where $k^2(\omega)$ has a simple pole. Notice that the cut-off frequencies are never greater than ω_{B0} and that they increase with the radial mode number, n, for any given azimuthal harmonic m. In addition, the cut-off frequencies decrease with the bubble interaction parameter $3\alpha(1-\alpha)a^2/R_o^2$ as shown in Fig. 3.

In the present problem the perturbations decay exponentially with attenuation rate $\text{Im}(k_x a)$ when their frequency ω is either lower than $\omega_{m,n}$ or greater than ω_{Bo}. On the other hand, they propagate harmonically with wave length $2\pi/\text{Re}(k_x)$ for frequencies in the range $\omega_{m,n} \le \omega \le \omega_{Bo}$. These three regimes are similar to the subsonic, supersonic and super-resonant regimes of flow identified by d'Agostino et al. (1988). As a result of the higher cut-off frequencies for the higher radial modes, appreciable wave-like propagation of m-lobed azimuthal excitation sources occurs when their frequency falls between the cut-off frequency $\omega_{m,0}$ of the fundamental radial mode ($n = 0$) and the bubble resonance frequency $\omega = \omega_{Bo}$.

When applied to the perturbation generated by a turbomachine with N blades and angular speed Ω, from earlier expressions of k^2, appreciable propagation of the sth harmonic disturbance will therefore occur when:

$$M_{|sN|} \ge \frac{z_{|sN|,0}}{|sN|} \tag{10}$$

where $z_{|sN|,0}/|sN|$ is the cut-off value of the blade tip Mach number $\text{M}_{|sN|} = \Omega a/c_M(|sN\Omega|)$. The values of $z_{|sN|,0}/|sN|$ are always slightly supersonic and approach unity as the azimuthal mode number sN tends to infinity. Values for $sN = 1, 2, 3, 4$, and 5 are, respectively, 1.36, 1.24, 1.18, 1.15, and 1.14.

In more familiar terms, we have determined that effective propagation of the disturbances generated by a turbomachine operating with bubbly flows is limited to the excitation from supersonic rotors not exceeding the bubble resonance condition $|sN\Omega| \le \omega_{Bo}$. This phenomenon is in line with well-established results for compressible nondispersive barotropic fluids (Tyler and Sofrin, 1962; Benzakein, 1972) and may have important implications for the onset and stability of rotating stall and cavitation in the suction lines of pumping systems operating with bubbly or cavitating flows. Note that, since the sonic speed in a bubbly mixture can be very small, it is not implausible to have a supersonic condition in a quite conventional pump.

The presence of a second region of exponential decay of the solution beyond the bubble natural frequency (termed super-resonant condition by d'Agostino et al., 1988) is the direct consequence of the dominance of the inertial forces, which prevent the bubbles from effectively responding to the excitation. Therefore super-resonant flows tend to behave in an essentially incompressible way, not dissimilar to subsonic flows.

From the relevant expression for $\tilde{p}$ note that free oscillations ($c_{m,n} = 0$) of bubbly flows in finite-length ducts can only occur when $\sin k_x L = 0$, a condition that, together with the dispersion relation, determines the natural frequencies $\omega_{m,n,l}$ and mode shapes $\tilde{p}_{m,n,l}$. In the absence of damping:

$$\omega^2_{m,n,l} = \omega^2_{Bo} \bigg/ \left(1 + \frac{3\alpha(1-\alpha)a^2/R_o^2}{z^2_{m,n} + l^2\pi^2 a^2/L^2}\right) \tag{11}$$

$$\tilde{p}_{m,n,l} \approx J_m(z_{m,n} r/a) e^{\pm im\vartheta - i\omega_{m,n,l}t} \sin \frac{l\pi x}{L} \tag{12}$$

where l is a positive integer. Notice that the natural frequencies $\omega_{m,n,l}$ always lie between the cut-off frequencies $\omega_{m,n}$ and ω_{Bo}. They also increase with the axial mode number l, and converge to ω_{Bo} as $l \to +\infty$. Just like the cut-off frequencies, the natural frequencies decrease with the increase in the parameter $3\alpha(1-\alpha)a^2/R_o^2$ and are substantially smaller than ω_{Bo} when it is of order unity or larger.

Now let us consider the effect of damping. The inclusion of damping (see Fig. 2) makes the axial wave number k_x (and therefore also the cut-off frequencies $\omega_{m,n}$) complex and eliminates the singularity at $\omega = \omega_{Bo}$, thereby blurring the transitions between the three propagation regimes. In addition, the higher frequencies are more severely damped than the lower frequencies so that the lower modes will predominate in any application. Except for these aspects, the general propagation features of the solution remain essentially unchanged for moderately damped flows like the present sample case of air bubbles in water. The rest of the results presented include damping (Fig. 4 onward).

The relative amplitudes of the pressure and bubble radius oscillations in a semi-infinite duct are shown in Figs. 4 and 5 as a function of frequency for the fundamental radial mode ($n = 0$) of the lowest azimuthal harmonics ($m = 0, 1, 2, 3$) with

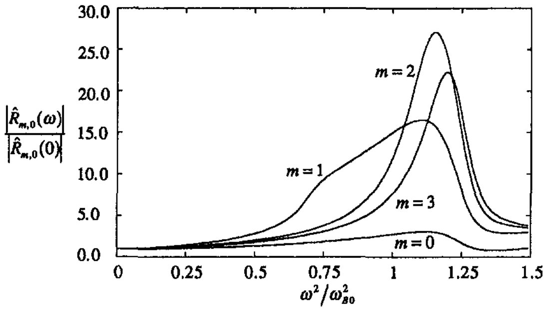

Fig. 5 Normalized amplitude of the bubble radius oscillations, $|\hat{R}_{m,0}(\omega)|/|\hat{R}_{m,0}(0)|$, as a function of the square of the reduced frequency, ω/ω_{Bo}, for the fundamental radial mode ($n = 0$) of the lowest azimuthal harmonics ($m = 0, 1, 2, 3$) in a semiinfinite duct with $3\alpha(1-\alpha)a^2/R_o^2 = 1$

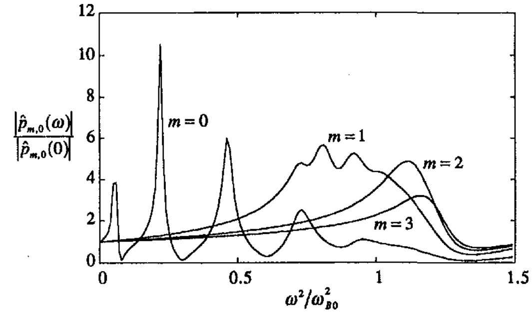

Fig. 6 Normalized amplitude of the pressure oscillations, $|\hat{p}_{m,0}(\omega)|/|\hat{p}_{m,0}(0)|$, as a function of the square of the reduced frequency, ω/ω_{Bo}, for the fundamental radial mode ($n = 0$) of the lowest azimuthal harmonics ($m = 0, 1, 2, 3$) in a finite-length duct with $3\alpha(1 - \alpha)a^2/R_o^2 = 1$

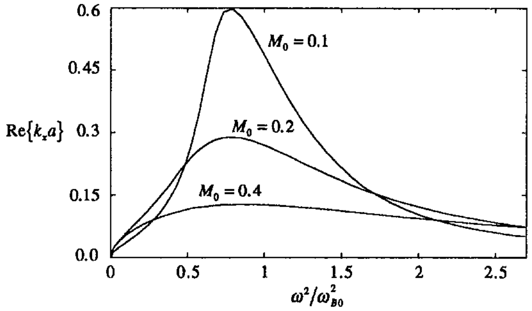

Fig. 8 Real part, $\mathrm{Re}(k_x a)$, of the normalized axial wavenumber for the fundamental radial mode of the first azimuthal harmonic ($m = 1$, $n = 0$, $\alpha_{m,n} = \alpha_{1,0} = 1.8412$) as a function of the square of the reduced frequency, ω/ω_{Bo}, in the absence of damping for $M_o = 0.1, 0.2, 0.4$ and for $3\alpha(1 - \alpha)a^2/R_o^2 = 1$

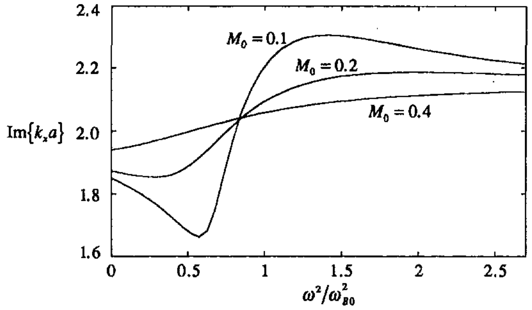

Fig. 9 Imaginary part, $\mathrm{Im}(k_x a)$, of the normalized axial wavenumber for the fundamental radial mode of the first azimuthal harmonic ($m = 1$, $n = 0$, $\alpha_{m,n} = \alpha_{1,0} = 1.8412$) as a function of the square of the reduced frequency, ω/ω_{Bo}, in the absence of damping with $M_o = 0.1, 0.2, 0.4$ and for $3\alpha(1 - \alpha)a^2/R_o^2 = 1$

$3\alpha(1 - \alpha)a^2/R_o^2 = 1$, (corresponding to a void fraction $\alpha \cong 1.5 \times 10^{-5}$ for the assumed values of the duct and bubble radii). The corresponding results for a finite-length duct are shown in Figs. 6 and 7. For all azimuthal harmonics the response of the bubble radius is maximum near the bubble resonance frequency, ω_{Bo}. Despite the rather large value of the bubble interaction parameter $3\alpha(1 - \alpha)a^2/R_o^2$, appreciable oscillations of the pressure and bubble radius are only observed for the zeroth and first azimuthal harmonics in the frequency range from $\omega_{m,0}$ ($\omega_{m,0} = 0$ for plane axial waves) to ω_{Bo}. The solution for the finite-length duct (Figs. 6 and 7) also shows clear evidence of resonant oscillations (amplitude peaks) of the zeroth and first azimuthal modes ($m = 0, 1$) at the corresponding natural frequencies, due to reflection of the flow disturbances by the downstream boundary condition. Additional computations have shown that the higher azimuthal harmonics start displaying appreciable resonant oscillations when the length of the duct is decreased. The same trend has been observed when increasing the duct radius for a given duct length. Thus the aspect ratio, L/a, plays a key role in the dynamics of a bubbly flow in a cylindrical duct.

Next we briefly discuss the extension of previous results to the case of nonzero mean flow velocity ($\mathbf{u}_o \neq 0$) by means of a few simple re-interpretations. In the first place, as shown in Section 3, the presence of a constant mean flow velocity $\mathbf{u}_o$ results in a complex value of the axial wave number even in non-dissipative flows (as illustrated in Figs. 8 and 9) but does not alter the formal expression for the pressure perturbation, given by Eqs. (6) and (7). This implies that the analysis for the zero mean flow case can be easily extended to the case of nonzero mean flow provided that the ($\cdot$) excitation frequency is redefined as $\omega = \omega_L + u_o k_x$. Moreover the fact that the axial wave number is now given by $k_x = k_x(\omega_L)$ and its imaginary part, $\mathrm{Im}(k_x)$, never vanishes (even in the absence of dissipation) implies a redefinition of the cut-off frequency: the condition for appreciable propagation of purely harmonic disturbances of real frequency ω through the bubbly mixture (which in the case of zero mean flow was given by $\mathrm{Im}(k_x) = 0$) is now replaced by the condition that $\mathrm{Im}(k_x)$ be a minimum. In other words, in the presence of mean flow, the cut-off frequency is given by the value of ω corresponding to the minimum of $\mathrm{Im}(k_x)$, as determined by the equation:

$$k_x = \sqrt{\frac{\omega_{Bo}^2}{c_{Mo}^2}\,\frac{(\omega - u_o k_x)^2}{\omega_{Bo}^2 - (\omega - u_o k_x)^2} - \frac{z_{m,n}^2}{a^2}} \qquad (13)$$

The dependence of the cut-off frequency on the Mach number, $\mathrm{M}_o = u_o/c_{Mo}$, for the fundamental radial mode and the lowest azimuthal harmonic is shown in Fig. 10. Notice the rapid decrease in the cut-off frequency for all azimuthal modes as the

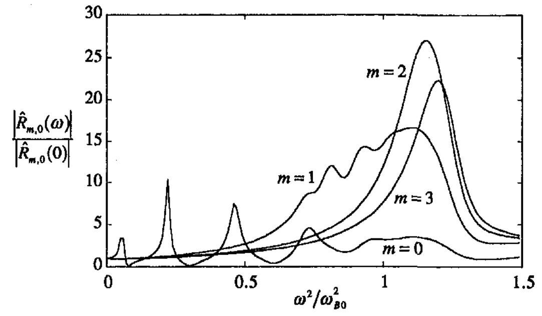

Fig. 7 Normalized amplitude of the bubble radius oscillations, $|\hat{R}_{m,0}(\omega)|/|\hat{R}_{m,0}(0)|$, as a function of the square of the reduced frequency, ω/ω_{Bo}, for the fundamental radial mode ($n = 0$) of the lowest azimuthal harmonics ($m = 0, 1, 2, 3$) in a finite-length duct with $3\alpha(1 - \alpha)a^2/R_o^2 = 1$

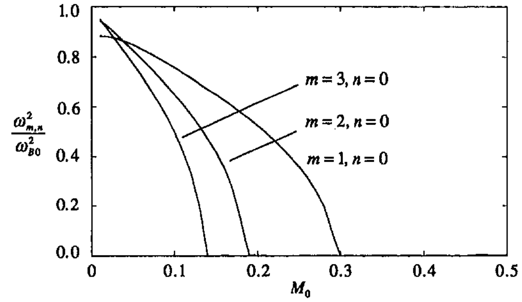

Fig. 10 Normalized cut-off frequency $\omega_{m,0}^2/\omega_{Bo}^2$ as a function of the flow Mach number $M_o = u_o/c_{Mo}$ for the fundamental radial mode ($n = 0$), the lower azimuthal harmonics ($m = 1, 2, 3$) and $3\alpha(1 - \alpha)a^2/R_o^2 = 1$

flow Mach number approaches unity. This feature is also characteristic of compressible flow solutions (Benzakein, 1972).

5 Limitations and Sensitivities

Restrictions to the validity of the present bubbly flow model result from the introduction of the continuum hypothesis, the use of the linear approximation, and the neglect of local interactions between the bubbles. The continuum approach requires the bubble radius, R_o, to be much smaller than any of the macroscopic length scales of the flow, here $a/z_{m,n}$, a/m and $1/|k_x|$ in the radial, azimuthal, and axial directions. This condition is increasingly restrictive for higher and higher harmonics, and therefore only a limited number of Fourier-Bessel components can be realistically included in the solution.

For the linear perturbation approach to hold, the excitation amplitude must not exceed some linear range, especially near resonance. This condition probably represents the most stringent restriction on the present analysis.

The error associated with the neglect of local bubble interactions can be neglected provided that $\alpha^{1/3} \ll |\omega_B^2/\omega^2 - 1|$ (d'Agostino and Brennen, 1988). Far from bubble resonance, this condition is generally satisfied in low void fraction flows.

6 Conclusions

This study reveals a number of important effects occurring in bubbly and cavitating flows in cylindrical ducts as a consequence of the strong coupling between the local dynamics of the bubbles and the global behavior of the flow. The propagation of disturbances along the duct is modified by the large reduction of the sonic speed, which becomes both complex (dissipative) and dispersive (frequency dependent). Additional modifications are introduced by the boundaries, which determine the excitation modes and their cut-off frequencies, and, in finite length ducts, the natural frequencies and mode shapes. The cut-off and natural frequencies never exceed the resonance frequency of individual bubbles, and are very much smaller when the parameter $3\alpha(1 - \alpha)a^2/R_o^2$ is of order unity or larger. Appreciable wave-like propagation of each excitation mode along the duct is limited to the frequency range between cut-off and the bubble resonance condition, and, except for plane waves, is characteristic of supersonic (but subresonant) flows, as defined by d'Agostino et al. (1988). In finite-length ducts, the same frequency range also contains the infinite set of natural frequencies of the resonant modes. The different propagation properties of subsonic, supersonic and super-resonant flows are due to the relative importance of pressure and inertial forces in the bubble dynamics at different excitation frequencies, as already outlined in previous papers (d'Agostino and Brennen, 1988).

In duct flows subject to excitation by a turbomachine, only the perturbations from supersonic rotors propagate effectively and are potentially capable of becoming self-sustaining when effectively reflected by the downstream boundary condition. Given the low sonic speed of bubbly mixtures, the cut-off conditions can readily be exceeded in high-speed turbopumps. This phenomenon is therefore potentially relevant to surge-like auto-oscillations and rotating cavitation instabilities in pumping systems operating with bubbly flows.

Because of the damping in the bubble dynamics the spectral response of the flow is therefore dominated by the lowest resonant frequencies which depend on the bubble interaction parameter, $3\alpha(1 - \alpha)a^2/R_o^2$. The increase of this parameter causes a substantial reduction in the bubble response peaks owing to the greater compliance of the flow, and a decrease in the corresponding frequencies results.

The length-to-radius ratio of the duct also plays an important role in the dynamics of this kind of flow. Higher modes display stronger oscillations as the aspect ratio L/a of the duct increases and the peak frequencies are strongly shifted towards lower values of ω/ω_{Bo}.

Finally, rather drastic modifications of the dynamic behavior of the bubbly mixture also occur when the mean flow velocity of the bubbly mixture becomes comparable to the low-frequency sonic speed. As in more conventional compressible flows, the most important effect of the mean flow arises from the rapid reduction of the cut-off frequencies of all fundamental modes as the Mach number approaches unity.

The present theory has been derived under fairly restrictive linearization assumptions and, therefore, is not expected to provide a quantitative description of unsteady bubbly flows in cylindrical ducts except in the acoustical limit. Bubble radius perturbations are often large in practical applications where the void fraction can be assumed to be small. Therefore the most serious limitation of the present theory is inherent in the linearization of the bubble dynamics.

Acknowledgments

This work has been supported by the Italian Department of Universities and Scientific & Technologic Research under the 1993 grant program for academic research and by the Office of Naval Research under grant number N-00014-91-K-1295. The authors wish to thank Professor T. Colonius for valuable discussions on the subject matter.

References

Brennen, C. E., 1994, "Hydrodynamics of Pumps," Concepts ETI Inc. and Oxford University Press.

Benzakein, M. J., 1972, "Research on Fan Noise Generation," *Journal of the Acoustical Society of America*, Vol. 51, No. 5, Part I, pp. 1427–1438.

Chahine, G. L., 1982a, "Pressure Field Generated by the Collective Collapse of Cavitation Bubbles," *IAHR Symposium on Operating Problems of Pump Stations and Power Plants*, Amsterdam, Netherlands, Vol. 1, Paper No. 2.

Chahine, G. L., 1982b, "Cloud Cavitation Theory," *14th Symposium on Naval Hydrodynamics*, Session I, p. 51.

Chahine, G. L., Duraiswami, R., and Lakshminarasimha, A. N., 1991, "Dynamical Interactions in a Bubble Cloud," ASME *Cavitation and Multiphase Flow Forum*, Portland, OR, pp. 49–54.

Chapman, R. B., and Plesset, M. S., 1972, "Nonlinear Effects in the Collapse of a Nearly Spherical Cavity in a Liquid," ASME *Journal of Basic Engineering*, pp. 172–183.

d'Agostino, L., and Brennen, C. E., 1983, "On the Acoustical Dynamics of Bubble Clouds," ASME *Cavitation and Multiphase Flow Forum*, Houston, TX.

d'Agostino, L., and Brennen, C. E., 1988, "Acoustical Absorption and Scattering Cross-Sections of Spherical Bubble Clouds," *J. Acoust. Soc. Am.*, No. 84 (6), pp. 2126–2134.

d'Agostino, L., and Brennen, C. E., 1989, "Linearized Dynamics of Spherical Bubble Clouds," *Journal of Fluid Mechanics*, Vol. 199, pp. 155–176.

d'Agostino, L., Brennen, C. E., and Acosta, A. J., 1988, "Linearized Dynamics of Two-Dimensional Bubbly and Cavitating Flows over Slender Surfaces," *Journal of Fluid Mechanics*, Vol. 192, pp. 485–509.

d'Auria, F., d'Agostino, L., and Brennen, C. E., 1994, "Linearized Dynamics of Bubbly and Cavitating Flows in Cylindrical Ducts," ASME *Cavitation and Multiphase Flow Forum*, Lake Tahoe, NV, pp. 59–66.

Hansson, I., Kedriniskii, V., and Mørch, K. A., 1981, "On the Dynamics of Cavity Clusters," *Journal of Applied Physics*, Vol. 15, pp. 1725–1734.

Knapp, R. T., Daily, J. W., and Hammit, F. G., 1970, *Cavitation*, McGraw Hill, New York.

Kumar, S., and Brennen, C. E., 1990, "Nonlinear Effects in Cavitation Cloud Dynamics," ASME *Cavitation and Multiphase Flow Forum*, Toronto, Ontario, Canada, pp. 107–113.

Lebedev, N. N., 1965, *Special Functions and Their Applications*, Prentice Hall.

Mørch, K. A., 1980, "On the Collapse of Cavity Cluster in Flow Cavitation," *Proceedings of the 1st International Conference on Cavitation and Inhomogeneities in Underwater Acoustics*, Springer Series in Electrophysics, Vol. 4, pp. 95–100.

Mørch, K. A., 1981, "Cavity Cluster Dynamics and Cavitation Erosion," ASME *Cavitation and Polyphase Flow Forum*, 1981, pp. 1–10.

Mørch, K. A., 1982, "Energy Considerations on the Collapse of Cavity Cluster," *Applied Scientific Research*, Vol. 38, p. 313.

Omta, R., 1987, "Oscillations of a Cloud of Bubbles of Small and Not So Small Amplitude," *Journal of the Acoustical Society of America*, Vol. 82 (3), pp. 1018–1033.

Plesset, M. S., and Prosperetti, A., 1977, "Bubble Dynamics and Cavitation," *Annual Review of Fluid Mechanics*, Vol. 9, pp. 145–185.

Pylkkänen, J. V., 1986, "Characteristics of Spherical Cloud Cavity," *Advancements in Aerodynamics, Fluid Mechanics and Hydraulics*, Arndt et al., eds., ASCE Conference, Minneapolis, MN, pp. 96–103.

Prosperetti, A., 1984, ''Bubble Phenomena in Sound Fields: Part One,'' *Ultrasonics,* Mar. pp. 69–78.

Prosperetti, A., 1977, ''Thermal Effects and Damping Mechanisms in the Forced Radial Oscillations of Gas Bubbles in Liquids,'' *Journal of the Acoustical Society of America,* Vol. 61, No. 1 (6), pp. 17–27.

Stewart, H. B., and Wendroff, B., 1984, ''Two-Phase Flows: Models and Methods,'' *Journal of Computational Physics,* Vol. 56, pp. 363–409.

Tyler, J. M., and Sofrin, T. G., 1962, ''Axial Flow Compressor Noise Studies,'' *SAE Transactions,* Vol. 70, pp. 309–332.

van Wijngaarden, L., 1964, ''On the Collective Collapse of a Large Number of Gas Bubbles in Water,'' *Proceedings of the 11th International Congress on Applied Mechanics,* Springer-Verlag, Berlin, pp. 854–861.

van Wijngaarden, L., 1968, ''On the Equations of Motion of Mixtures of Liquid and Gas Bubbles,'' *Journal of Fluid Mechanics,* Vol. 33, part 3, pp. 465–474.

van Wijngaarden, L., 1972, ''One-Dimensional Flow of Liquids Containing Small Gas Bubbles,'' *Annual Review of Fluid Mechanics,* Vol. 4, pp. 369–396.

Per Petersson
Research Associate,
Department of Water Resources
Engineering,
University of Lund,
Box 118, S-221 00 Lund, Sweden

Magnus Larson
Visiting Researcher,
Department of Civil Engineering,
University of Tokyo,
7-3-1 Hongo, Bunkyo-ku, Tokyo 113,
Japan

Lennart Jönsson
Associate Professor,
Department of Water Resources
Technology,
University of Lund,
Lund, Sweden

Measurements of the Velocity Field Downstream of an Impeller

The velocity field downstream of a model impeller operating in water was measured using a two-component laser doppler velocimeter. The investigation focussed on the spatial development of the mean velocity in the axial, radial, and circumferential direction, although simultaneous measurements were performed of the velocity unsteadiness from which turbulence characteristics were inferred. The measurements extended up to 12 impeller diameters downstream of the blades displaying the properties of the generated swirling jet both in the zone of flow establishment and the zone of established flow. The division between these zones was made based on similarity of the mean axial velocity profile. Integral properties of the flow such as volume and momentum flux were computed from the measured velocity profiles. The transverse spreading of the impeller jet and its development towards self-similarity were examined and compared with non-swirling jets and swirling jets generated by other means.

1 Introduction

In many environmental and technical/industrial applications there is a need to artificially induce flows in fluids and fluid mixtures. The purpose of flow generation could be to transport substances, keep solids in suspension, homogenize fluids with different properties, dissolve matter in liquids, enhance biological and chemical reactions, or modify the thermal conditions in a fluid. A submersible mixer is a flexible and efficient device for inducing such artificial flows. The mixer is a compact unit that consists of an impeller (a propeller operating at static conditions) and a motor. The rotating impeller generates a swirling jet with an initial size, velocity, and direction that depends on the characteristics and orientation of the impeller. The swirling jet penetrates through the fluid and grows in size as it entrains ambient fluid; simultaneously, a large-scale motion is induced in the fluid that largely depends upon the flow geometry. This large-scale flow pattern is in many applications of decisive importance for achieving the desired effects with the flow generation. Most mixer applications involve complex fluid dynamics regarding both the impeller flow and the large-scale motion that must be understood in detail to maximize the efficiency of the mixing operation.

Swirling jets appear in many other applications besides mixer-induced flows; propellers are often employed for the propulsion of airborne and marine vehicles, and the flow in the slipstream or wash has many similarities with the swirling jet generated by an impeller. In studies of propeller flows the focus is typically on the velocity field in the vicinity of the propeller and the development of the downstream flow field is of less concern. In contrast, both the generation and the downstream development of the swirling jet is of primary interest in mixer-induced flows, as well as any interaction with the flow boundaries and secondary flows induced by the jet. The limited number of investigations that exist of the velocity field downstream an impeller or propeller derive mainly from the fields of aerodynamics, naval architecture, and turbomachinery.

Biggers and Orloff (1975) measured velocities in the wake of a helicopter rotor at static conditions exposed to a free stream approximately oriented in the rotor plane. A two-component Laser Doppler Velocimeter (LDV) was employed to obtain time- and phase-averaged values on the velocity showing the effects of tip vortices, bound vortices, and blade wakes on the flow. Lepicovsky and Bell (1984) and Lepicovsky (1988) used an LDV to study the velocity field in the vicinity and between the blades of a static propeller. Axial, radial, and tangential time- and phase-averaged velocities and the corresponding turbulent fluctuations were determined. The most detailed measurements of the flow field in the vicinity of a propeller carried out to date were made by Hyun and Patel (1991a, b), who studied the flow around a marine propeller at the stern of an axisymmetric body in a wind tunnel. They made phase-averaged measurements using two- and three sensor hotwires for determining the mean and turbulent velocity field together with a five-hole yaw probe for obtaining the pressure. These measurements were also circumferentially averaged to yield overall aspects of the flow. Hamill and Johnston (1993) measured the mean axial velocity downstream a static propeller in water using a pitot tube.

A jet discharged into a large fluid body where boundary effects are negligible tends to develop towards a state of self-similarity (Townsend, 1976) with the mean and the turbulent velocity properties being independent on the details of the generating source for the jet. Thus, at some location downstream of an impeller or propeller it is expected that a generated free swirling jet displays self-similar properties. This location may be taken as the separation point between the zone of flow establishment (ZFE) and the zone of established flow (ZEF). In the present study, the division between ZFE and ZEF is based on similarity of the mean axial velocity profile (Albertson et al., 1950), which typically occurs closer to the source than similarity of the turbulence. Because the jet properties in the ZEF are independent of the detailed source characteristics, comparison between impeller jets and swirling jets generated by other techniques such as rotating pipes (Rose, 1962; Pratte and Keffer, 1972), specially designed nozzles (Chigier and Chervinsky, 1967, Farokhi et al., 1989), or twisted tapes (Duquenne et al., 1993) may be of interest.

In this study, the velocity field downstream an impeller operating in water was measured using a two-component LDV. The focus of the investigation was on the spatial development of the mean velocity in the axial, radial, and circumferential direction, although simultaneous measurements were performed of the velocity unsteadiness from which turbulence characteris-

---

Contributed by the Fluids Engineering Division for publication in the JOURNAL OF FLUIDS ENGINEERING. Manuscript received by the Fluids Engineering Division April 10, 1995; revised manuscript received December 4, 1995. Associate Technical Editor: Wing-Fai Ng.

tics were inferred. The measurements extended up to 12 impeller diameters from the impeller blades displaying the properties of the swirling jet both in the ZFE and ZEF. Integral properties of the flow such as volume and momentum flux were computed from the measured velocity profiles. The transverse spreading of the impeller jet and its development towards self-similarity were examined and compared with non-swirling jets and swirling jets generated by other means.

The objective of the experiments was to study a free impeller jet unaffected by any flow boundaries; however, since the measurements were performed in water the size of the experimental container employed was limited and this aim could not be completely realized. In order to minimize the effect of the container size, the experiments were performed in two different containers depending on the generated flow conditions. Although special efforts were made to minimize the boundary effects on the jet development, some low-frequency velocity fluctuations could not be eliminated which affected the measurements of the velocity unsteadiness. These fluctuations were related to the recirculation zone formed between the spreading jet and the side walls of the container.

2. Laboratory Experiments

2.1 Experimental Setup. A 1:10 model of the impeller from a Flygt 4501 mixer (Fahlgren and Tammelin, 1992) was used in the experiments. The three-blade model (Fig. 1(*a*)) impeller had an overall diameter of $D = 0.078$ m and a hub diameter of 0.015 m, and it was operated at a constant speed N (measured in rpm) throughout a specific experiment. The impeller was initially placed in a plexiglas tank with an inside bottom area of 0.98×0.98 m^2 and a water depth of 0.65 m. However, this setup only allowed velocity measurements to be performed relatively undisturbed by the circulation up to a distance of $5D$ from the impeller and for lower values on N. Thus, a different experimental setup (Fig. 1(*b*)) was employed in most of the measurements that involved a larger fluid body, which was obtained by closing of a section in a large glass-walled flume. The enclosed section was 2.5 m long with a rectangular cross section of 0.9×0.9 m^2, permitting relatively undisturbed measurements up to a distance of $12D$ downstream of the impeller. The water depth in the flume was 0.85 m during all experiments. The impeller was placed as centered as possible in the containers with respect to the focal length of the LDV system.

A two-component TSI LDV system was used for the velocity measurements. This system includes a 300-mW argon-ion laser (model L-300) which generates a mixed (multi-line) beam. The measurement volume is approximately 2.2 mm long in water with a diameter of 0.12 mm having 32 fringes. A backward-scattered mode is employed using the signal collection optics in the probe, and the signal is analyzed in the TSI 750 processor using burst autocorrelation technique and validation algorithms to ensure that measurements are made only on burst and not on noise. The raw data are transferred to a personal computer via direct memory access and stored for subsequent analysis. Most statistical flow parameters were calculated with TSI:s Flow Information Display (FIND) data analysis package.

A traversing system was developed to allow efficient and accurate measurements with the LDV at arbitrary cross sections downstream of the impeller. At each measurement section the

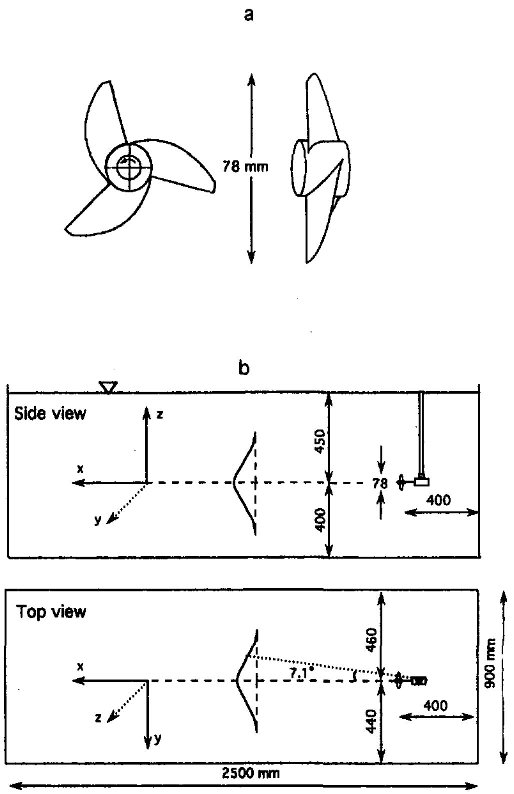

Fig. 1 (*a*) **Experimental impeller;** (*b*) **Experimental setup for measuring the velocity field downstream an impeller (note approximate jet size at 10*D* and spreading angle)**

Nomenclature

A = cross-sectional area of the experimental container
a = distance from virtual origin to impeller blades
D = impeller diameter
f_c = cutoff frequency for high-pass filtering
G_x = axial flux of linear momentum
G_{xo} = axial flux of linear momentum at the source
G_ϕ = axial flux of angular momentum
N = impeller speed
R = impeller radius
r = radial coordinate
r_m = radial distance to measurement position from jet center
r_o = radial distance to boundary between jet and return flow
$r_{0.5}$ = radial distance where $\bar{U} = \bar{U}_{\max}/2$
Q = volume flux
S = swirl number
U = axial velocity
$\bar{U}$ = mean axial velocity
U_p = peripheral velocity of impeller blades
$\bar{U}_{\max}$ = maximum of mean axial velocity
u = axial velocity unsteadiness
u_l = magnitude of low-frequency velocity fluctuation
$u_{\rm rms}$ = rms value of axial velocity unsteadiness
V = radial velocity
$\bar{V}$ = mean radial velocity
V_a = apparent radial velocity
v = radial velocity unsteadiness
$v_{\rm rms}$ = rms value of radial velocity unsteadiness
W = tangential velocity
$\bar{W}$ = mean tangential velocity
$\bar{W}_{\max}$ = maximum of mean tangential velocity
w = tangential velocity unsteadiness
$w_{\rm rms}$ = rms value of tangential velocity unsteadiness
x = horizontal coordinate
y = lateral coordinate
z = vertical coordinate
α = angle to measurement point
ρ = fluid density
Δs = deviation in measurement position from jet center

probe could automatically be moved in the y- and z-directions (see Fig. 1(b)), with a theoretical accuracy of $\frac{1}{80}$ mm (80 step per mm). The movement of the probe was initiated in the data acquisition routine in FIND via an external subroutine. By using an external laser beam to project the orientation of the impeller axis, the intersection of the LDV laser beams could be aligned with respect to the jet center. The jet center at a specific downstream location was locked as the "absolute-home-position" for the traversing system defining the starting point for the measurements at that section. The traverse was manually moved along a fixed rail between the different measurement sections in the x-direction.

2.2 Experimental Procedure. The experiments were carried out in water with a temperature of about 20°C. Before starting any measurements the impeller was operated for at least 20 minutes to allow for steady conditions to develop with respect to the induced circulation in the experimental container. The impeller was then engaged throughout the measurements, which typically lasted several hours. During an experimental case the impeller was running at a fixed speed and velocity measurements were performed with the LDV system at selected cross sections downstream of the impeller. All measurements were made in coincidence mode, and the coincidence window together with the shift frequency and direction were determined on the basis of the flow conditions in the jet (a function of the distance from the impeller and jet axis). Sampling was done in even time mode to compensate for statistical biasing. The water was seeded with metal-coated particles having a diameter of 9 μm.

Two velocity components can be measured simultaneously with the LDV system; thus, in order to obtain the velocity components in all three coordinate directions two sets of measurements were needed at each cross section. Lateral traversing (y-direction) through the jet produced the axial (U) and tangential (W) velocity component, whereas vertical traversing (z-direction) gave the radial velocity (V) together with U once more. The radial and tangential component could not be obtained simultaneously by lateral or vertical traversing. In order to measure coincidence dependent properties between V and W, including the Reynolds shear stress (*not discussed in this paper*), the LDV probe had to be oriented towards the jet (x-direction) and traversed horizontally (or vertically). This could only be achieved if the impeller was turned 90 deg toward the LDV probe, which severely restricted the size of the experimental container. A limited number of such measurements were nevertheless made for a few cross sections close to the impeller.

2.3 Measurements Uncertainty. The optimum sampling rate corresponds to a time interval between samples that is twice the integral time scale of the flow (Hyun and Patel, 1991a). The optimum sampling rate is a compromise between minimizing the amount of data to be collected and maximizing the convergence rate to obtain statistically stable estimates of the mean flow properties. In the present flow configuration there are several different characteristic time scales for the flow that affect the choice of sampling rate. These time scales involve turbulent fluctuations, periodic flow variations due to the impeller blades, and low-frequency fluctuations caused by recirculation in the container (to be discussed later). The latter fluctuations made long sampling times necessary before estimates of the flow properties converged to a satisfactory accuracy, especially at the most downstream locations. At these locations a low sampling rate had to be employed (20 Hz) to produce a manageable amount of data; however, since the main purpose of the study was to measure mean velocities this rate was adequate, although limited information was obtained on the fine structure of the turbulence. Higher sampling rates were employed closer to the impeller and for phase-averaged measurements (up to 1000 Hz).

Mean flow properties converged after about 5 min of measurements in the vicinity of the impeller, whereas 10 min was typically required at cross sections further downstream. At the edge of the jet and for the most downstream locations sampling periods of up to 15 min were employed to obtain convergence. The number of samples used to form averages ranged from 6000 to 18,000. The variation in measured mean velocities at the jet axis caused by random errors was estimated to ±0.5 percent of the mean axial velocity $\bar{U}$ for all components based on a 95 percent confidence level (Coleman and Steele, 1989), and the corresponding variation for the root-mean-square (rms) values was ±2 percent of respective rms value.

The influence of bias errors was more difficult to determine, and instead an attempt was made to directly determine the total error through repetitive measurements in single points as well as for complete cross sections. Bias errors arose primarily because of slight differences in probe alignment between repetitive measurements and effects of the periodicity generated by the blades, but velocity and fringe biasing as well as optical errors due to the experimental setup may have affected the measurements. Thus, the total error in the mean velocities was estimated to be about ±5 percent of $\bar{U}$, although for a limited number of measurements an error of ±10 percent was obtained. The total error in the rms values were in general less and ±5 percent of respective rms value represents a typical upper estimate. These estimates of the total error should be regarded as representative values, because the error could vary considerably from point to point and with respect to the studied component. In most cases the accuracy was better than the above-given values, although for example the radial component could show even larger errors at the jet center, as will be discussed later.

3 Results

The velocity components U, V, and W were measured at selected downstream locations for three different impeller speeds, namely $N = 600$, 1200, and 1800 rpm. For $N = 600$ rpm, measurements were performed mainly in the smaller tank, whereas for $N = 1200$ and 1800 rpm almost all measurements were obtained in the flume. Comparison between measurements in the tank and the flume at identical N produced the same results close to the impeller, whereas differences could be noted further away from the impeller, especially for W which was markedly affected by the side walls when the jet became large with respect to the cross-sectional area of the container. Measurements were performed at the following locations for respective N: $0.5D$, $1D$, $2D$, $3D$, $4D$, $5D$ (600 rpm); $0.064D$, $0.128D$, $0.256D$, $0.5D$, $1D$, $1.5D$, $2D$, $3D$, $4D$, $5D$, $6D$, $10D$, $12D$ (1200 rpm); and $0.128D$, $2D$, $4D$, $6D$, $8D$, $10D$, $12D$ (1800 rpm). For most of these locations a complete set of U, V, and W was obtained; however, at some locations the measurements were focussed primarily toward U.

The generated velocity field downstream the impeller may be decomposed into the following three parts (Hyun and Patel, 1991a): (1) a time-averaged velocity, (2) a velocity induced by the periodicity of the impeller blades, and (3) a turbulent fluctuation. The effect of the periodicity due to the rotating blades typically disappears a short distance downstream of the impeller and the flow may be regarded as axisymmetric and constant in the circumferential direction. Such a symmetry in the flow field implies that a measured time series yields all the information about the velocity at a point without resorting to phase-averaging. In the present study, little effect of the periodicity induced by the blades could be detected after $1D$, and after $2D$ no effect was observed from individual blades, although a slight oscillation with a period corresponding to N was still discernable at $1.5D$. The influence of the periodicity was investigated through spectral analysis of measured velocity time series obtained with a high sampling rate close to the impeller together with limited phase-averaged measurements. Hyun and

Patel (1991b) found in their laboratory measurements that the flow field could be considered rotationally symmetric after about $2D$.

Because the present measurements were performed in a limited water mass, boundary effects could not be entirely eliminated and the velocity field was partly affected by a large-scale circulation induced by the impeller jet. A recirculation zone formed outside the jet, both in the tank and the closed-off flume, and the flow in this zone caused low-frequency velocity fluctuations (compare Shih and Ho, 1994). These fluctuations were most pronounced for U, and the relative effect increased with distance downstream the impeller. Thus, as previously discussed, a long measurement time was required to obtain statistically stable estimates of the velocity properties, especially at the most downstream locations and at the edge of the jet. Tests in the flume that encompassed different measures for dampening the jet as it encountered the solid boundary downstream of the impeller did not eliminate these fluctuations; even if the downstream boundary was moved very far away from the impeller (not closing off the flume), the fluctuations were still noticeable. The only method to eliminate the fluctuations was to introduce a small base flow in the flume that washed away the recirculation zone (measurements not shown here).

The results of the velocity measurements are presented in the following sections focussing on the mean velocity in the three coordinate directions together with the corresponding velocity unsteadiness as expressed through the normal stresses. Measurements were made both in the ZFE and ZEF, where the division is made based on the similarity of the mean axial velocity profile (Albertson et al., 1950). The peripheral velocity of the impeller U_p ($= 2\pi NR$) is used to normalize the measured velocities in the figures, whereas the radial distance r is normalized with the impeller radius R and the axial distance measured from the impeller blades with D. The mean velocity components in the axial, radial, and tangential directions are denoted by $\bar{U}$, $\bar{V}$, and $\bar{W}$, respectively, and the corresponding velocity unsteadiness by u, v, and w. The velocity unsteadiness was in most locations dominated by the turbulent fluctuations in the jet, however, at some downstream locations the low-frequency fluctuations gave a significant contribution, primarily to u.

3.1 Mean Axial Velocity. Radial distributions (profiles) of $\bar{U}$ measured at different streamwise locations in the ZFE are shown in Fig. 2(a) for $N = 1200$ rpm. Only half of the impeller jet is displayed in the figure; in several cases the entire jet was traversed to confirm that the velocity profile was axisymmetric. At locations close to the impeller the profile has a marked trough in the jet center characteristic for strong swirl flows. The trough is caused by the centrifugal forces in the rotating jet and the blocking effect of the impeller hub. Immediately downstream the impeller, the maximum of the mean axial velocity $\bar{U}_{\max}$ occurs around $r/R = 0.5$, which approximately corresponds to the position where the impeller blades produce maximum thrust (Hyun and Patel, 1991a).

The measurements close to the impeller at cross-sections $0.064D$, $0.128D$, and $0.256D$ ($0.256D$ is not plotted in Fig. 2(a) for clarity) showed a contraction of the jet as far as $0.128D$, but no effect further downstream. A contraction of the jet is expected due to the initial strong inward movement of water into the impeller wash; however, for the impeller employed in the present study the contraction is confined to a short distance downstream of the impeller and at $0.256D$ the jet width is approximately D. Hyun and Patel (1991a) reported a contraction of the wash up to $0.6D$ downstream the propeller. At the edge of the jet close to the impeller $\bar{U}$ attains negative values indicating a reversed flow, which is typical immediately downstream the tip of propeller blades (Lepicovsky, 1988). Acceleration of the whole jet is observed to $0.5D$, and from $1D$ only the low-velocity core accelerates while a decrease in the maximum velocity occurs.

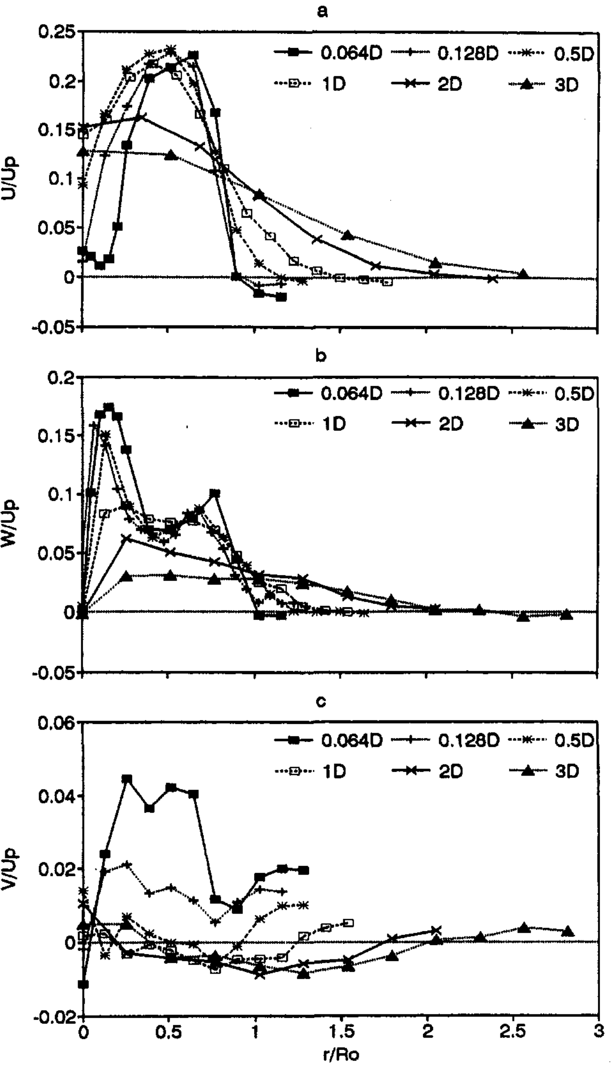

Fig. 2 Mean velocity profiles in the ZFE measured downstream an impeller ($N = 1200$ rpm): (a) axial, (b) tangential, and (c) radial component. (Representative total error: +/−5 percent of $\bar{U}$.)

For all impeller speeds investigated, $\bar{U}$-profiles could be well described by a Gaussian curve after approximately $3D$ (Fig. 2(a)). At this location $\bar{U}_{\max}$ has shifted to the jet centerline, and from about $3D$ a Gaussian velocity profile is maintained in the jet, as illustrated by Fig. 3(a) which displays profiles of $\bar{U}$ measured in the ZEF for $N = 1800$ rpm. Hamill and Johnston (1993) defined the end of the ZFE based on the location where a Gaussian velocity profile appeared, and measurements with different marine propellers indicated that this distance was about $2D$ for a propeller operating at static conditions.

3.2 Mean Tangential Velocity. At locations close to the impeller, two distinct peaks are noticeable in the mean tangential velocity profile ($0.064D$ to $1D$ in Fig. 2(b)). The first peak occurs around $0.15r/R$, which corresponds to the impeller hub radius, whereas the second peak is located at about $0.65r/R$. Thus, the inner peak is produced by the rotating hub and the outer peak is created by the impeller blades. The two peaks rapidly decrease, simultaneously as they merge, and approximately at $1.5D$ (profiles not shown in Fig. 2) there is only one peak in the tangential velocity that is located where $\bar{U}$ has its maximum. After the two peaks merge, the single maximum in the tangential velocity $\bar{W}_{\max}$ is first displaced towards the jet center, but after $\bar{U}$ has attained its maximum on the jet centerline $\bar{W}_{\max}$ continuously moves out from the center with distance

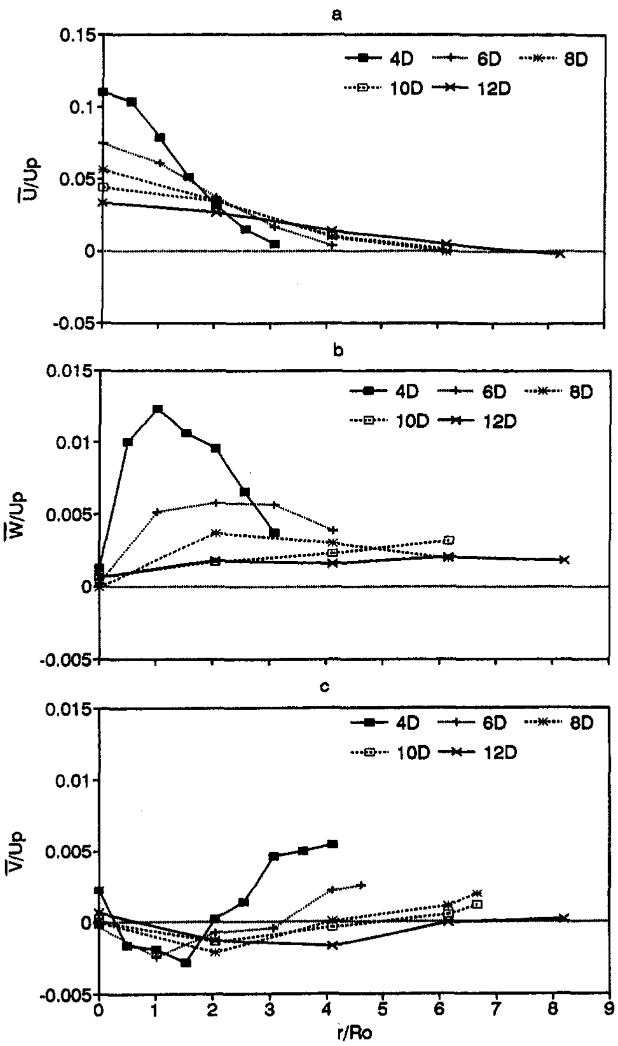

Fig. 3 Mean velocity profiles in the ZEF measured downstream an impeller (N = 1800 rpm): (a) axial, (b) tangential, and (c) radial component. (Representative total error: +/−5 percent of $\bar{U}$.)

downstream. Hyun and Patel (1991a) also measured a marked peak in $\bar{W}$ associated with a rotating hub that rapidly decreased in the downstream direction.

In the ZEF (Fig. 3(b)) the swirl decays at a high rate with corresponding less influence on the main flow development, as indicated by the location of $\bar{U}_{\max}$ at the jet centerline (Fig. 3(a)). Because of the disappearance of the off-axis peak in $\bar{U}$ the tangential profile no longer shows any indications of a pronounced local minimum during its decay toward zero velocity. At the most downstream locations and at the edge of the jet $\bar{W}$ attains a low, near-constant velocity just above zero that is most likely an effect of the limited water mass that was employed in the experiments. In a larger fluid mass $\bar{W}$ decays to zero at the jet edge more rapidly in the downstream direction (Farokhi et al., 1989).

For reasons of symmetry, the tangential velocity should be equal to zero in the jet center. The measurements presented in Figs. 2(b) and 3(b) show values close to zero in the jet center, indicating that the alignment of the probe was satisfactory for determining $\bar{W}$ during the experiments. The tangential velocity gradient is large close to the jet center, especially in the vicinity of the impeller, and even small deviations in the positioning of the probe may imply velocity values that are significantly different from the correct values. However, even small deviations could have marked implications for measurements of the radial velocity component close to the jet center, as will be discussed next.

3.3 Mean Radial Velocity. The measurements of $\bar{V}$ were taken by traversing the probe in the vertical direction. Similarly to $\bar{W}$, $\bar{V}$ should be equal to zero in the jet center; however, measuring these small radial velocities proved difficult in the vicinity of the impeller, and non-zero $\bar{V}$-values were often recorded close to the jet center. Farokhi et al. (1989) noted a peak in $\bar{V}$ close to the jet center in contradiction to physical arguments that they attributed to insufficient measurement resolution near the vortex (jet) center. Near the jet axis even small inaccuracies in measurement volume position imply that the measurements of $\bar{V}$ will be affected by the tangential velocity component (Duquenne et al., 1993).

For the two-component LDV used in the present measurements, if the traversing line of the measurement volume passes a small distance Δs beside the jet center, the apparent radial velocity V_a recorded is (see Fig. 4 for a definition sketch),

$$V_a = V \cos \alpha + W \sin \alpha \qquad (1)$$

where r_m is the radial distance from the jet center to the measurement point, and V and W are the true radial and tangential velocity components, respectively, at r_m, and $\sin \alpha = \Delta s / r_m$. When the measurement volume is at its closest position from the jet center, $r_m = \Delta s$, and $V_a = W$. Thus, instead of measuring zero velocity at the jet center the tangential component is recorded due to the deviation in position.

Another factor that makes reliable measurements of $\bar{V}$ close to the jet center difficult is the finite-size measurement volume of the LDV. The elliptic measurement volume has its major axis perpendicular to the jet axis when the traversing is performed for $\bar{V}$ implying that the obtained value represents an integrated value over a length of about 2.2 mm, which might affect the velocity measurement. Limited measurements were performed with the beams projecting in the axial direction, that is, towards the jet, recording W and V simultaneously using the smallest cross-section of the measurement volume; however, accurate results for $\bar{V}$ near the jet center was just as difficult to obtain as for vertical traversing. Instead, problems of measuring $\bar{V}$ accurately may also be related to small variations in the location of the jet axis, possibly connected with some type of jet instability phenomenon or small vibrations in the impeller mount.

Figures 2(c) and 3(c) show profiles of $\bar{V}$ in the ZFE and ZEF, respectively (negative velocity representing an outflow from the jet center). Immediately downstream the impeller in the ZFE $\bar{V}$ is mainly directed towards the jet center, which eventually eliminates the trough in the center of the jet. Further downstream in the ZEF, $\bar{V}$ is directed out from the jet center as the mean axial velocity profile becomes flatter. In most of the profiles the radial inflow (entrainment) into to the jet may be distinguished at the edge; however, at the most downstream locations this inflow is difficult to notice because of its low value and possible boundary effects.

3.4 Velocity Unsteadiness and Turbulence. Low-frequency velocity fluctuations u_l appeared in the flow attributed to the recirculation zone between the jet and the side walls.

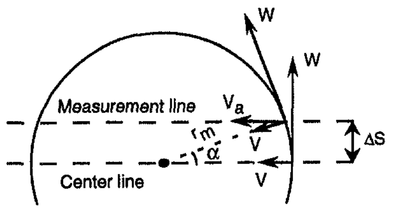

Fig. 4 Effect of deviation in measurement position on the radial velocity component

Because of long measurement periods the effect on the mean flow of u_l could be eliminated; however, measurements of the normal and Reynolds shear stresses were affected by u_l depending on the location of the measurement point. The relative effect of u_l on the measured stresses became more significant further downstream and at the edge of the jet. In the center of the jet and close to the impeller the influence of u_l was minor as determined from high-pass filtering of measured velocity time series. Immediately downstream the impeller the velocity unsteadiness is also influenced by the periodicity of the blades (Hyun and Patel, 1991b), but this effect was small after $1D$ in the present experiments, as discussed earlier. Only the normal stresses will be discussed in the following, since just two of the three Reynolds shear stresses (uv and uw) could be measured easily with the present experimental setup, implying that a complete picture of the shear stresses could not be obtained.

Figures 5(a–c) display the measured rms values, that is the turbulence intensities or (normal stresses)$^{0.5}$, for the three coordinate directions at selected downstream locations in the ZFE (N = 1200 rpm), and Figs. 6(a–c) show the corresponding values for the ZEF (N = 1800 rpm). In the ZFE marked off-axis peaks occur for all rms components ($u_{\rm rms}$, $v_{\rm rms}$, and $w_{\rm rms}$) that persist to about $2D$, after which the profiles change much more gradually with r. These off-axis peaks are located where the maximum radial gradient in $\bar{U}$ occurs and the magnitude of the peak is similar for $u_{\rm rms}$, $v_{\rm rms}$, and $w_{\rm rms}$. The latter two components also show a peak at the jet axis that is more distinct than for $u_{\rm rms}$. In the ZEF the rms values change at a low rate with r and the overall magnitude decays in the streamwise direction. The components $v_{\rm rms}$ and $w_{\rm rms}$ are approximately equal on the jet axis, as they should be due to symmetry (Pratte and Keffer, 1972).

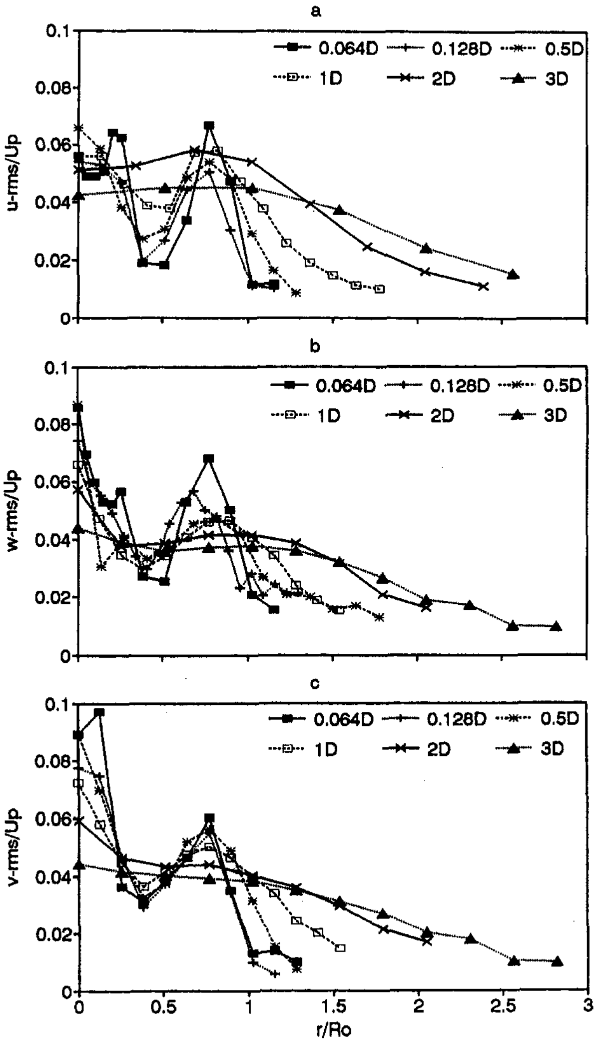

Fig. 5 **Rms profiles for the velocity unsteadiness in the ZFE measured downstream an impeller (N = 1200 rpm): (a) axial, (b) tangential, and (c) radial component. (Representative total error: +/−5 percent of $\bar{U}$.)**

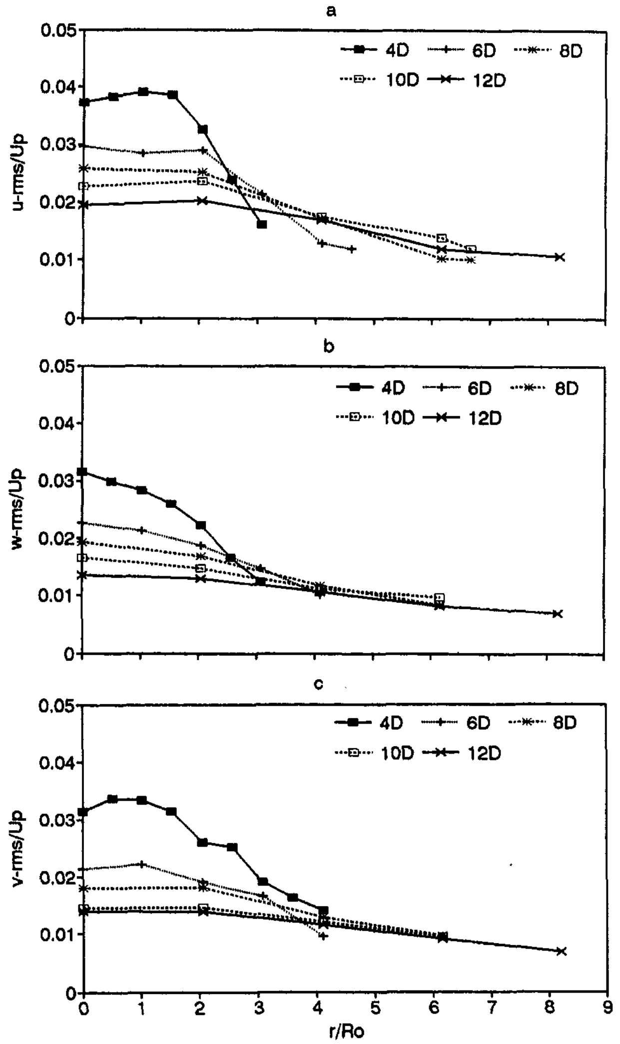

Fig. 6 **Rms profiles for the velocity unsteadiness in the ZEF measured downstream an impeller (N = 1800 rpm): (a) axial, (b) tangential, and (c) radial component. (Representative total error: +/−5 percent of $\bar{U}$.)**

If the rms values are scaled with the local velocity $\bar{U}_{\rm max}$, the relative velocity unsteadiness (for example, $u_{\rm rms}/\bar{U}_{\rm max}$) was found to increase with distance downstream, especially for the streamwise component. This is a typical development in a jet as the turbulence develops toward self-similarity, and for non-swirling jets such a state may not be obtained until after $40D$ (List, 1982). Pratte and Keffer (1972) showed an increase in the relative importance of $u_{\rm rms}$, $v_{\rm rms}$, and $w_{\rm rms}$ for swirling jets until about $12D$, after which self-similarity was observed. In the present experiments, the typical values of $u_{\rm rms}/\bar{U}_{\rm max}$, $v_{\rm rms}/\bar{U}_{\rm max}$, and $w_{\rm rms}/\bar{U}_{\rm max}$ are higher than corresponding measurements in non-swirling jets (List 1982) or swirling jets generated by other means (Pratte and Keffer, 1972).

The turbulent fluctuations are probably relatively larger in an impeller jet due to the violent flow generation; however, the low-frequency fluctuations also significantly affect the velocity unsteadiness. The influence from u_l is most pronounced for u, whereas v and w are not affected as much, that is, the fluctuations in the recirculation zone are primarily in the streamwise direction. To estimate how much u was affected by u_l, a selected number of measured time series of u were high-pass filtered using a cutoff frequency of $f_c = 0.2$ Hz. This cutoff frequency was determined by investigating how the rms-value dropped off with an increase in f_c; at approximately 0.2 Hz there was a distinct break point in this curve indicating a change in the characteristics of the velocity unsteadiness that was attributed to the low-frequency fluctuations. The filtered time series indicated an influence from u_l on u of about 10 percent close to the impeller, whereas the effect could be as much as 50 percent at the edge of the jet further downstream.

3.5 Flow Development and Self-Similarity. In order to investigate the approach towards self-similarity in the flow, $\bar{U}/\bar{U}_{\max}$ was plotted against $r/(x + a)$, where a is the distance from a virtual origin to the impeller blades (how a was determined is discussed in the next section). The present measurements indicated that $\bar{U}$ was approximately self-similar from a location where $\bar{U}_{\max}$ occurred on the jet centerline. A Gaussian profile fitted the data quite well from about 3–4D downstream of the impeller, as shown in Figs. 7(a) and (b). For swirling jets generated by other means similarity in $\bar{U}$ was noted from 4D downstream an orifice for weak swirl, whereas for strong swirl similarity was not observed until 10D (Chigier and Chervinsky, 1967). Rose (1962) and Pratte and Keffer (1972) observed similarity from about 6D for jets with moderate swirl. In general, swirling jets typically achieve self-similar properties more rapidly than corresponding nonswirling jets (Rose, 1962).

Other velocity quantities besides $\bar{U}$ were also investigated for self-similarity; however, no conclusive support could be found that $\bar{V}$, $\bar{W}$, or the normal stresses approached a state of self-similarity within a distance of 12D. There were indications that $\bar{W}$ became approximately self-similar after about 4D, but further downstream at about 8-10D the side walls seemed to markedly affect the flow development for this component and the $\bar{W}$-profile changed characteristics. The magnitude of the turbulence with respect to the mean flow increased in the downstream direction and self-similarity was not observed for any of the normal stresses. This is attributed to the limited distance downstream of the impeller for which measurements were made, but also to the influence of the side walls.

3.6 Radial Spread of the Jet. The radial spread of the jet with distance downstream is plotted in Fig. 8. The jet width that characterizes the spread was defined based on the radial distance $r_{0.5}$ where $\bar{U} = \bar{U}_{\max}/2$. The jet was observed to spread linearly at a half angle of 7.1 deg, and the angle is nearly the same for the three impeller speeds investigated. Close to the impeller a minor increase in the spread of the jet can be observed with an increase in the speed. The spread is similar to what Pratte and Keffer (1972) presented for a weakly swirling jet, which was almost twice that of a corresponding non-swirling jet in their experiment.

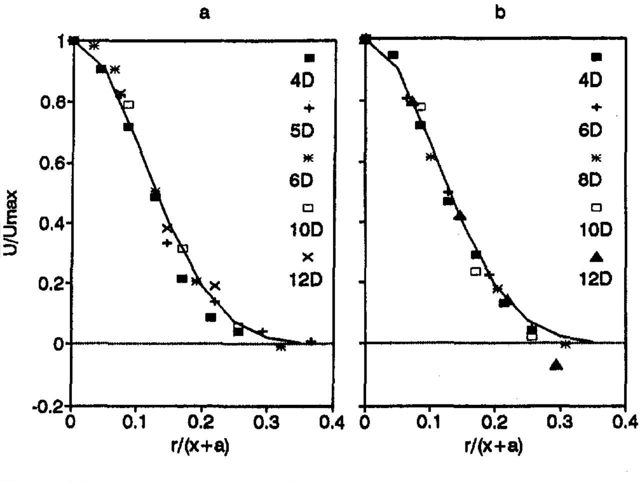

Fig. 7 Mean axial velocity profiles in ZEF measured downstream an impeller and a fitted Gaussian profile: (a) 1200 rpm, and (b) 1800 rpm. (Representative total error: +/−7 percent of $\bar{U}$.)

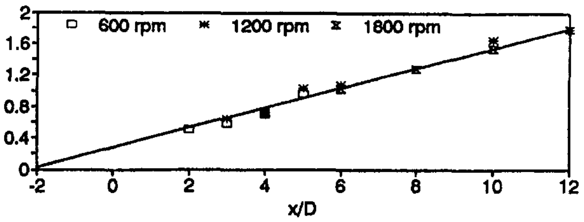

Fig. 8 Radial spread of an impeller jet. (Representative total error: +/−5 percent of $\bar{U}$.)

Chigier and Chervinsky (1967) investigated the dependence of the radial spread on the swirl numbers defined as, where G_ϕ is the axial flux of angular momentum given by,

$$S = \frac{G_\phi}{G_x R} \tag{2}$$

$$G_\phi = 2\pi\rho \int_0^\infty r^2 \bar{U}\bar{W} dr \tag{3}$$

and G_x the axial flux of linear momentum,

$$G_x = 2\pi\rho \int_0^\infty r\left(\bar{U}^2 - \frac{\bar{W}^2}{2}\right) dr \tag{4}$$

in which ρ is the fluid density. They found that the spreading angle increased with S up to about 10 deg after which the angle was approximately constant. However, it is apparent from previous studies that the spreading angle significantly depends upon the conditions at the discharge point (Chigier and Chervinsky, 1967). Formally, Eq. (4) is derived by eliminating the pressure term in the axial momentum equation using the radial momentum equation; thus, G_x also contains the streamwise pressure gradient (Hussein et al., 1994) and may more appropriately be called the jet axial thrust (Farokhi et al., 1989).

In the present study, S was calculated to 0.18, 0.23, and 0.26 for 600, 1200, and 1800 rpm, respectively, evaluated using Eqs. (2)–(4) at 2D and employing the impeller radius for R. The location 2D was employed to ensure that the flow is reasonably axisymmetric, which is an assumption used in the equations from which the swirl number is derived (Chigier and Chervinsky, 1967). Also, to facilitate comparison for the different impeller speeds, this was the closest location for which data existed for all speeds. The calculated swirl numbers correspond to weakly and moderately swirling jets generated by other means. No significant dependence for the spreading angle on S could be detected in the present measurements; however, as pointed out by Farokhi et al. (1989) S alone is not sufficient for uniquely characterizing a swirling jet in the near field, but other properties related to the velocity profile must be included.

A virtual origin was found for the impeller jet by extrapolating the line describing the radial spread back to the horizontal axis (Fig. 8). This produced a location for the virtual origin a = 2D upstream the impeller blades, which is similar to the 2.3D found by Chigier and Chervinsky (1967) and the 3D found by Pratte and Keffer (1972). The virtual origin may be considered as a point source of axial and angular momentum with zero mass flux that generates an equivalent jet in the ZEF as the impeller.

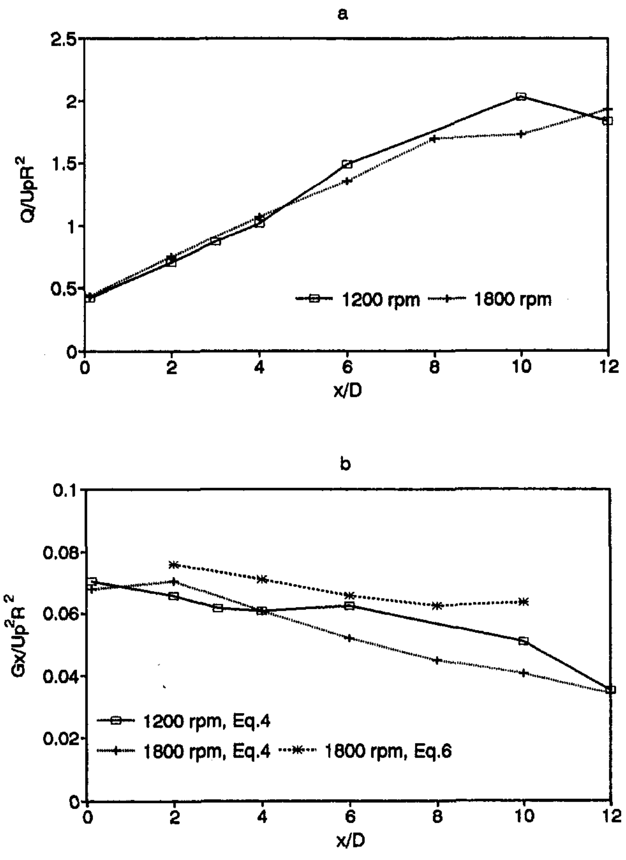

Fig. 9 Jet development downstream of an impeller: (*a*) volume flux (representative total error: +/−5 percent of $\bar{U}$), and (*b*) axial flux of linear momentum (representative total error: +/−10 percent of $\bar{U}$)

3.7 Volume and Momentum Flux. The volume flux Q was determined at downstream cross-sections by integrating the measured $\bar{U}$-profiles across the jet. Figure 9(*a*) displays the results for $N = 1200$ and 1800 rpm showing a linear growth with distance from the impeller, except at the most downstream locations where the side walls seem to affect the jet entrainment. The volume growth seems to be linear both in ZFE and ZEF with little difference in the slope of the curve. In the figure, Q was normalized with U_pR^2 to allow for comparison between different N; the figure indicates that this quantity scales Q well.

The axial flux of linear momentum as expressed by Eq. (4) is based on the assumption that the turbulent fluctuations (velocity unsteadiness) are of the same order and cancel out in the integration (Chigier and Chervinsky, 1967). Equation 4 was employed as a first approximation to evaluate the flux of linear momentum (i.e., jet thrust) downstream the impeller. The linear momentum G_x should be preserved in the jet if it is generated in a infinite fluid where boundary effects are absent. For the case of a jet discharged in a limited fluid volume a return flow will be generated that will consume some of the jet momentum, thus causing a momentum deficit downstream the jet depending on the strength of the return flow (Hussein et al., 1994).

Figure 9(*b*) illustrates the variation in the axial flux of linear momentum with distance from the impeller as determined by Eq. (4) for $N = 1200$ and 1800 (momentum flux normalized with $U_p^2R^2$). The figure displays a marked loss in G_x downstream the impeller which may partly be explained by a momentum loss due to the return flow. A simple analysis similar to Hussein et al. (1994) shows that the decay in G_x with x may be estimated as,

$$\frac{G_x}{G_{xo}} = 1 - \frac{\rho}{G_{xo}} \frac{Q^2}{A - \pi r_o^2} \tag{5}$$

where G_{xo} is the momentum flux at the source, Q the jet flow, A the cross-sectional area of the experimental container, and r_o the radial distance to the jet boundary where the return flow starts (assumed to have a constant velocity outside the jet). Estimations of the momentum decay for the present experimental cases indicated a typical loss of about 25 percent at 12D for 1800 rpm, which is less than measured according to Fig. 9(*b*) (r_o was set to the distance where $\bar{U} = \bar{U}_{\max}/100$).

However, analysis of the measurements showed that $u_{\rm rms}$ is consistently larger than $v_{\rm rms}$ and $w_{\rm rms}$. Thus, an estimate of G_x is needed that includes the normal stresses (Pratte and Keffer, 1972):

$$G_x = 2\pi\rho \int_0^\infty r\left(U^2 - \frac{W^2}{2} + \bar{u}^2 - \frac{\bar{w}^2 + \bar{v}^2}{2}\right) dr \tag{6}$$

Figure 9(*b*) also illustrates the momentum flux evaluated by using Eq. (6) for $N = 1800$ rpm (complete measurements were not obtained at all locations of the normal stresses to allow evaluation of Eq. (6) for $N = 1200$ rpm); the decrease in G_x that still occurs downstream the impeller using this equation is fully explainable in terms of the return flow.

Conclusions

A limited number of investigations have focussed on measuring the velocity field generated by an impeller (propeller), especially at locations several diameters D downstream of the impeller. The present study encompassed measurements of the mean axial, radial, and tangential velocity profiles up to 12D downstream a model impeller operating in water at three different speeds (600, 1200, and 1800 rpm). Simultaneous measurements of the velocity unsteadiness were made from which turbulence characteristics could be inferred. The properties of the swirling impeller jet were investigated both in the zone of flow establishment and the zone of established flow, where the division between the zones was made based on similarity of the mean axial velocity profile. Integral properties of the swirling jet were calculated from the measurements, such as volume and momentum flux, and the approach of the jet towards self-similarity was studied.

The maximum mean axial velocity immediately downstream the impeller occurred at a radial distance of about 0.25D, which approximately corresponds to the position where the impeller blades produce maximum thrust. Two peaks appeared in the mean tangential velocity profile close to the impeller, the first around $r = 0.075D$ produced by the impeller hub and the second around $r = 0.32D$ created by the blades. In this zone, the mean radial velocity displayed a strong inflow towards the jet center. After a distance of about 3–4D a Gaussian curve could well describe the mean axial velocity profile and self-similarity was obtained for this component. The mean tangential velocity profile decayed at a high rate downstream of this location with no marked peaks, and the mean radial velocity was directed outwards from the center along the inner portion of the jet and inwards along the outer portion.

Because the experiments were performed in a limited water mass, effects of large-scale circulation induced by the impeller jet could not be completely eliminated. A recirculation zone formed between the jet and the side walls caused low-frequency velocity fluctuations that affected the measurements of the velocity unsteadiness, especially the axial component. At locations close to the impeller the effect of these oscillations was small, implying that the unsteadiness represented the turbulence in the jet where the blade periodicity was negligible; however, at the most downstream locations and at the edge of the jet the influence on the velocity unsteadiness was significant. For all components, the rms value of the unsteadiness displayed an off-axis peak where the maximum in the radial gradient of the mean axial velocity occurred. These peaks persisted to about 2D after which unsteadiness profiles developed that changed gradually with the radial distance having their maximum in the jet center. The relative importance of the unsteadiness with respect to the mean flow (*that is, the rms velocities divided by the local maximum of the mean axial velocity*) increased with distance downstream, especially for the axial component.

The mean axial velocity profile became self-similar after 3–4D, whereas no conclusive support could be found that other quantities approached self-similarity within 12D. The radial spread of the jet in the zone of established flow, determined from the locations where the mean axial velocity was half of the velocity at the jet center, was linear with a spreading angle of 7.1 deg with little dependence on the swirl number. Linear extrapolation of the spreading angle made it possible to define a virtual origin for the jet 2D upstream of the impeller. The volume flux increased linearly with distance downstream the impeller until the side walls affected the entrainment at about 10D. Employing a simple model for the conservation of the axial flux of linear momentum (jet thrust) showed that the velocity unsteadiness should be included in the momentum integral and that the effect of the return flow must be taken into account when the jet occupies a significant portion of the ambient cross-section.

Acknowledgments

This research was supported by the Swedish Research Council for Engineering Sciences (TFR Dnr 93-80). The authors wish to thank Magnus Fahlgren at ITT Flygt AB for supplying the experimental impeller setup used in the investigation and for stimulating discussions during the preparation of this paper. Valuable assistance from Mr. Lennart Grahn during the laboratory experiments is also gratefully acknowledged.

References

Albertson, M. L., Dai, Y. B., Jensen, R. A., and Rouse, H., 1950, "Diffusion of Submerged Jets," *Transactions of the American Society of Civil Engineers,* Vol. 115, Paper No. 2409, pp. 639–697.

Biggers, J. C., and Orloff, K. L., 1975, "Laser Velocimeter Measurements of the Helicopter Rotor-Induced Flow Field," *Journal of the American Helicopter Society,* Vol. 20, Jan. pp. 2–10.

Chigier, N. A., and Chervinsky, A., 1967, "Experimental Investigations of Swirling Vortex Motion in Jets," ASME *Journal of Applied Mechanics,* Vol. 34, pp. 443–451.

Coleman, H. W., and Steele, W. G., 1989, *Experimentation and Uncertainty Analysis for Engineers,* Wiley, New York.

Duquenne, A. M., Guiraud, P., and Bertrand, J., 1993, "Swirl-Induced Improvement of Turbulent Mixing: Laser Study in a Jet-Stirred Tubular Reactor," *Chemical Engineering Science,* Vol. 48, No. 22, pp. 3805–3812.

Farokhi, S., Taghavi, R., and Rice, E. J., 1989, "Effect of Initial Swirl Distribution on the Evolution of a Turbulent Jet," *AIAA Journal,* Vol. 27, No. 6, pp. 700–706.

Fahlgren, M., and Tammelin, J., 1992, "The 3-D Velocity Field Near a Submerged Hydrofoil Impeller," *Scientific Impeller,* ITT Flygt AB, Vol. 1, No. 1, pp. 49–57.

Hamill, G. A., and Johnston, H. T., 1993, "The Decay of Maximum Velocity Within the Initial Stages of a Propeller Wash," *Journal of Hydraulic Research,* Vol. 31, No. 5, pp. 605–613.

Hussein, J. H., Capp, S. P., and George, W. K., 1994, "Velocity Measurements in a High-Reynolds-Number, Momentum-Conserving, Axisymmetric, Turbulent Jet," *Journal of Fluid Mechanics,* Vol. 258, pp. 31–75.

Hyun, B.-S., and Patel, V. C., 1991a, "Measurements in the Flow Around a Marine Propeller at the Stern of an Axisymmetric Body. Part 1: Circumferentially-Averaged Flow," *Experiments in Fluids,* Vol. 11, pp. 33–44.

Hyun, B.-S., and Patel, V. C., 1991b, "Measurements in the Flow Around a Marine Propeller at the Stern of an Axisymmetric Body. Part 2: Phase-Averaged Flow," *Experiments in Fluids,* Vol. 11, pp. 105–117.

Lepicovsky, J., 1988, "Laser Velocimeter Measurements in a Model Propeller Flowfield," ASME JOURNAL OF FLUIDS ENGINEERING, Vol. 110, pp. 350–354.

Lepicovsky, J., and Bell, W. A., 1984, "Aerodynamic Measurements About a Rotating Propeller with a Laser Velocimeter," *Journal of Aircraft,* Vol. 21, No. 4, pp. 264–271.

List, E. J., 1982, "Turbulent Jets and Plumes," *Annual Review of Fluid Mechanics,* Vol. 14, pp. 189–212.

Rose, W. G., 1962, "A Swirling Round Turbulent Jet," ASME *Journal of Applied Mechanics,* Vol. 29, pp. 615–625.

Pratte, B. D., and Keffer, J. F., 1972, "The Swirling Turbulent Jet," ASME *Journal of Basic Engineering,* Vol. 93, pp. 739–748.

Shih, C., and Ho, C.-M., 1994, "Three-Dimensional Recirculation Flow in a Backward Facing Step," ASME JOURNAL OF FLUIDS ENGINEERING, Vol. 116, pp. 228–232.

Townsend, A. A., 1976, *The Structure of Turbulent Shear Flow,* Cambridge University Press.

Journal of
Fluids
Engineering

Technical Briefs

Flow Resistance Correlation of Wire Nets in a Wide Range of Reynolds Numbers for Thermal Design of Electronic Equipment

Masaru Ishizuka[1]

1 Introduction

When considering the thermal design of electronic equipment, it is important to have high quality flow resistance data in order to obtain good ventilation in the final product. For example, a simple approach for the thermal design of electronic equipment using experimentally measured flow resistance coefficients was proposed by Ishizuka (1992). Although, the wire net used at an inlet vent or outlet vent in the casing is one typical component that causes flow resistance within a casing, the flow resistance data for electronic equipment ventilation is scarce. Although the flow resistance data for wire nets in the relatively higher Reynolds number range, for example, in the case of forced air and water convection have been reported by Collar (1939), Osaka et al. (1986), Schubauer et al. (1947), Taylor and Batchelor (1949), and Wieghardt (1953), only limited data in the lower Reynolds number range, namely, for natural air convection have been obtained by MacPhail (1939), Bernardi et al. (1976), and Ishizuka (1987). Ishizuka (1987) proposed a new correlation for the resistance coefficient of wire nets in the case of natural convection for practical use in the cooling of electronic equipment. However, most electronic equipment is cooled by natural air convection and forced air convection. Therefore, it is necessary to have a correlation which covers the data over a wide range of Reynolds numbers. In this brief, the flow resistance correlation of wire nets in a wide range of Reynolds numbers has been proposed for thermal design of electronic equipment casings.

2 Flow Resistance Coefficients of Wire Nets for Lower Reynolds Number Range

The evaluation method for the air flow resistance coefficient of wire nets in natural air convection was proposed by Ishizuka (1987) and the flow resistance coefficient values of several wire nets were obtained using the method. The two parameters, porosity coefficient β and Reynolds number Re based on a wire diameter d, and airflow average velocity in the duct u, were used to correlate the flow resistance coefficient of wire nets. The flow resistance coefficient K was defined as follows;

$$K = 2\Delta P/(\rho u^2) \tag{1}$$

where, ΔP is pressure loss and ρ is air density. The following empirical correlation for the flow resistance coefficient K of the wire nets can be obtained on the basis of the best fit to the measured data by Ishizuka (1987).

$$K = 28(\mathrm{Re}\beta^2/(1-\beta))^{-0.95} \tag{2}$$

where, the porosity coefficient β for a wire net is defined as follows

$$\beta = (s/(s+d))^2 \tag{3}$$

where, s is wire to wire interval. The Re in Eq. (2) lies in the range of $0.4 < \mathrm{Re} < 95.0$. In Eq. (2), the maximum uncertainty bands for K and Re were 4.1 and 16 percent, respectively.

3 Flow Resistance Coefficients of Wire Nets for Higher Reynolds Number Range

In the case of a relatively higher Reynolds number range, several researchers have reported results. Osaka et al. (1986) rearranged the correlations, obtained by Schubauer et al. (1947) and Wieghardt (1953), and compared their values with those obtained by themselves. Figure 1 shows the comparison. Here, the quantity C is the reduced factor and Re_1 is the Reynolds number which is based on the air velocity u_1 passing through wire nets is defined as follows.

$$K = C(1-\beta)/\beta^2 \tag{4}$$

where C can be a function of the Reynolds number or a constant. Collar (1939) explained the meaning of Eq. (4) by assuming that the resistance is proportional to the area of the wire net and to the square of the airflow speed through the wire spacing, which is inversely proportional to the porosity coefficient. Igarashi et al. (1992) also reported on the flow resistance of a vortex shedder in a circular pipe and indicated that the resistance coefficient K is given in the same way as Eq. (4) regardless of the Reynolds number and the constant C is proportional to the drag coefficient of the shedder in a uniform flow.

Using the parameters, C and Re_1, which are shown below, Osaka et al. (1986) presented three correlations to express the flow resistance coefficients in the higher Reynolds number.

$$\mathrm{Re}_1 = u_1\, d/\nu = \mathrm{Re}/\beta \tag{5}$$

$$C = 5.5\,\mathrm{Re}_1^{-1/3} \quad \text{by Schubauer et al. (1947)} \tag{6}$$

$$C = 6.5\,\mathrm{Re}_1^{-1/3} \quad \text{by Wieghardt (1953)} \tag{7}$$

$$C = 6.0\,\mathrm{Re}_1^{-1/3} \quad \text{by Osaka et al. (1986)} \tag{8}$$

---

[1] Senior Researcher, Energy & Mechanical Research Laboratories, Research and Development Center, Toshiba Corporation, 1, Komukai Toshiba-cho, Saiwai-ku, Kawasaki, 210, Japan. Mem. ASME

Contributed by the Fluids Engineering Division of THE AMERICAN SOCIETY OF MECHANICAL ENGINEERS. Manuscript received by the Fluids Engineering Division July 12, 1994; revised manuscript received February 14, 1996. Associate Technical Editor: H. Hashimoto.

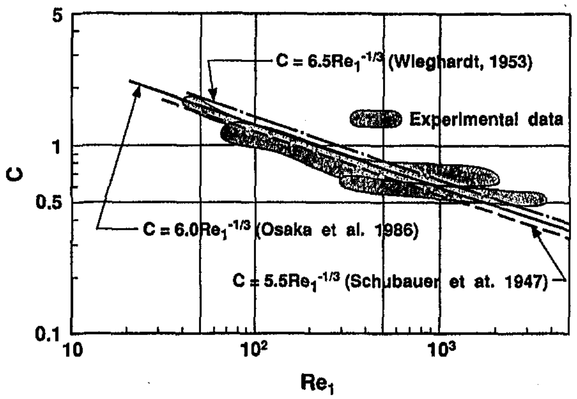

Fig. 1 Flow resistance coefficients of wire nets for higher Reynolds numbers

From the figure, Eq. (8) can be recommended as the correlation to express the flow resistance of the wire nets in the range of $\mathrm{Re}_l > 50$.

4 Correlating the Wide Range Reynolds Number Data

It is necessary to select the common parameter to correlate the flow resistance data of wire nets for both the lower and higher Reynolds number ranges. Therefore, a better approach is to consider the C value and Reynolds number, Re_l, as common parameters, since in case of $\mathrm{Re}_l > 50$ an improved expression as shown in Eq. (9) has been obtained to correlate the data reported by several researchers. Therefore, the data used to develop Eq. (2) needs to be rearranged by considering C value and Re_l. Figure 2 shows the results obtained by the correlation which included the data of Ishizuka (1987), Tailor et al. (1949), and Schubauer et al. (1947). The uncertainties of the data of other researchers were not reported in the literature. However, those could be estimated to be less than 3 percent by considering that the measurements were carried out in higher Reynolds number range. The data for $\mathrm{Re}_l < 50$ can be correlated as a straight line with a slope of -1.0 and the new correlation can be written as follows.

$$C = 70\ \mathrm{Re}_l^{-1} \text{ for } \mathrm{Re}_l < 50 \tag{9}$$

This result indicates that in order to correlate the lower Reynolds number data, a good choice would be to use the C value and Re_l. The figure shows that Eq. (9) intersects Eq. (8) at $\mathrm{Re}_l = 40$. These results led to the conclusion that the following two expressions would be needed to correlate the data over a wider Reynolds number range.

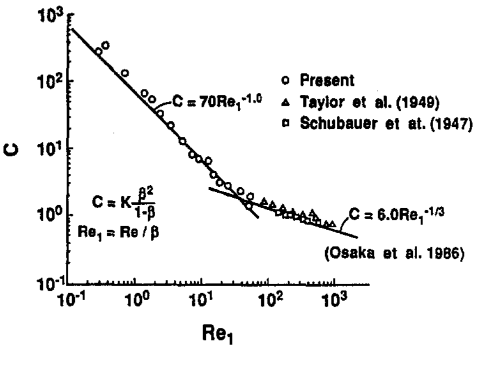

Fig. 2 The correlation of the data obtained in a wide range of Reynolds numbers

$$C = 70\ \mathrm{Re}_l^{-1} \quad \text{for} \quad \mathrm{Re}_l < 40$$
$$C = 6.0\ \mathrm{Re}_l^{-1/3} \quad \text{for} \quad \mathrm{Re}_l \geqq 40 \tag{10}$$

The uncertainty bands for C were estimated less than 18 percent for $\mathrm{Re}_l < 40$ and less than 5 percent for $\mathrm{Re}_l \geqq 40$.

5 Conclusions

The flow resistance correlation of wire nets in a wide range of Reynolds numbers has been proposed. The flow resistance coefficient correlation for wire nets obtained in the natural air convection was rearranged using the parameters of reduced resistance coefficient C and Reynolds number Re_l, defined in terms of the flow velocity through the wire net and the wire diameter. The results are plotted together with those obtained for the higher Reynolds number range by other researchers. Two expressions proposed for two Reynolds number range are presented below.

$$C = 70\ \mathrm{Re}_l^{-1} \quad \mathrm{Re}_l < 40$$
$$C = 6.0\ \mathrm{Re}_l^{-1/3} \quad \mathrm{Re}_l \geqq 40$$

These correlations are useful for the thermal design of electronic equipment casings.

References

Bernardi, R. T., Linehan, J. H., and Hamilton, L. H., 1976, "Low Reynolds Number Loss Coefficient for Fine-Mesh Screens," ASME JOURNAL OF FLUIDS ENGINEERING, Vol. 98, No. 4, pp. 762–764.

Collar, A. R., 1939, "The Effect of a Gauze on the Velocity Distribution in a Uniform Duct, British Aeronautical Research Council," Reports and Memoranda No. 1867.

Igarashi, T, Inagaki, S., and Nishida, K., 1992, "Flow Resistance of a Vortex Shedder in a Circular Pipe," *Trans. of JSME,* Vol. 58, No. 550, pp. 1655–1660 (in Japanese).

Ishizuka, M., 1987, "Air Flow Resistance of Wire Nettings in Natural Convection," ASME JOURNAL OF FLUIDS ENGINEERING, Vol. 109, pp. 389–393.

Ishizuka, M., 1992, "Thermal Design of a Laptop Computer by a Personal Computer," *Proc. of 1992 Intersociety Conference on Thermal Phenomena,* Feb., pp. 184–189.

MacPhail, D. C., 1939, "Experiments on Turning Vanes at an Expansion, British Aeronautical Research Council, Reports and Memoranda," No. 1879.

Osaka, H., Yamada, H., Hano, S., and Kageyama, T., 1986, "Fluid Flow through Plain Screens," *Trans. of Japan Society of Mechanical Engineers,* Vol. 52, No. 473, pp. 312–317 (in Japanese).

Schubauer, G. B., Spangenberg, W. G., and Klebanoff, P. S., 1947, "Aerodynamic Characteristics of Damping Screens," National Advisory Committee for Aeronautics, Technical Note 2001.

Taylor, G. I., and Batchelor, G. K., 1949, "The effect of Wire Gauze on Small Disturbances in a Uniform Stream," *Quarterly Journal of Mechanics and Applied Mathematics,* Vol. 2, pp. 1–45.

Wieghardt, K. E. G., 1953, "On the Resistance of Screens," *The Aeronautical Quarterly,* Vol. 4, pp. 186–192.

Turbulent-Spot Propagation in a Decelerating, Compressible Flow

J. P. Clark,[1] T. V. Jones,[2] and J. E. LaGraff[3]

Introduction

The most successful physical model for the transition process is that due to Emmons (1951). In this model, transition is

---

[1] Visiting Asst. Professor of Engineering, New Mexico Highlands University, Las Vegas, NM, 87701.

[2] D. L. Schultz Professor of Turbomachinery, Department of Engineering Science, University of Oxford, Parks Road, Oxford, England, OX1 3PJ.

[3] Professor of Aerospace Engineering, Department of Mechanical, Aerospace, and Manufacturing Engineering, Syracuse University, Syracuse, NY, 13244.

Contributed by the Fluids Engineering Division of THE AMERICAN SOCIETY OF MECHANICAL ENGINEERS. Manuscript received by the Fluids Engineering Division April 20, 1994; revised manuscript received February 20, 1996. Associate Technical Editor: Wing Ng.

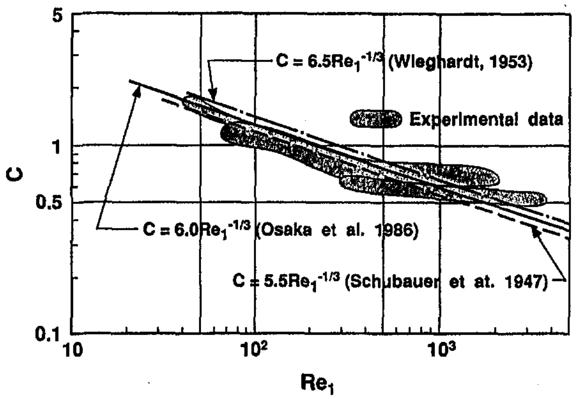

Fig. 1 Flow resistance coefficients of wire nets for higher Reynolds numbers

From the figure, Eq. (8) can be recommended as the correlation to express the flow resistance of the wire nets in the range of $Re_1 > 50$.

4 Correlating the Wide Range Reynolds Number Data

It is necessary to select the common parameter to correlate the flow resistance data of wire nets for both the lower and higher Reynolds number ranges. Therefore, a better approach is to consider the C value and Reynolds number, Re_1, as common parameters, since in case of $Re_1 > 50$ an improved expression as shown in Eq. (9) has been obtained to correlate the data reported by several researchers. Therefore, the data used to develop Eq. (2) needs to be rearranged by considering C value and Re_1. Figure 2 shows the results obtained by the correlation which included the data of Ishizuka (1987), Tailor et al. (1949), and Schubauer et al. (1947). The uncertainties of the data of other researchers were not reported in the literature. However, those could be estimated to be less than 3 percent by considering that the measurements were carried out in higher Reynolds number range. The data for $Re_1 < 50$ can be correlated as a straight line with a slope of -1.0 and the new correlation can be written as follows.

$$C = 70\,Re_1^{-1} \text{ for } Re_1 < 50 \tag{9}$$

This result indicates that in order to correlate the lower Reynolds number data, a good choice would be to use the C value and Re_1. The figure shows that Eq. (9) intersects Eq. (8) at $Re_1 = 40$. These results led to the conclusion that the following two expressions would be needed to correlate the data over a wider Reynolds number range.

$$\begin{aligned} C &= 70\,Re_1^{-1} \quad \text{for} \quad Re_1 < 40 \\ C &= 6.0\,Re_1^{-1/3} \quad \text{for} \quad Re_1 \geqq 40 \end{aligned} \tag{10}$$

The uncertainty bands for C were estimated less than 18 percent for $Re_1 < 40$ and less than 5 percent for $Re_1 \geqq 40$.

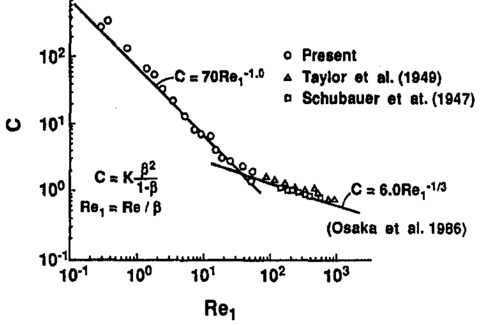

Fig. 2 The correlation of the data obtained in a wide range of Reynolds numbers

5 Conclusions

The flow resistance correlation of wire nets in a wide range of Reynolds numbers has been proposed. The flow resistance coefficient correlation for wire nets obtained in the natural air convection was rearranged using the parameters of reduced resistance coefficient C and Reynolds number Re_1, defined in terms of the flow velocity through the wire net and the wire diameter. The results are plotted together with those obtained for the higher Reynolds number range by other researchers. Two expressions proposed for two Reynolds number range are presented below.

$$\begin{aligned} C &= 70\,Re_1^{-1} \quad Re_1 < 40 \\ C &= 6.0\,Re_1^{-1/3} \quad Re_1 \geqq 40 \end{aligned}$$

These correlations are useful for the thermal design of electronic equipment casings.

References

Bernardi, R. T., Linehan, J. H., and Hamilton, L. H., 1976, "Low Reynolds Number Loss Coefficient for Fine-Mesh Screens," ASME JOURNAL OF FLUIDS ENGINEERING, Vol. 98, No. 4, pp. 762–764.

Collar, A. R., 1939, "The Effect of a Gauze on the Velocity Distribution in a Uniform Duct, British Aeronautical Research Council," Reports and Memoranda No. 1867.

Igarashi, T, Inagaki, S., and Nishida, K., 1992, "Flow Resistance of a Vortex Shedder in a Circular Pipe," *Trans. of JSME,* Vol. 58, No. 550, pp. 1655–1660 (in Japanese).

Ishizuka, M., 1987, "Air Flow Resistance of Wire Nettings in Natural Convection," ASME JOURNAL OF FLUIDS ENGINEERING, Vol. 109, pp. 389–393.

Ishizuka, M., 1992, "Thermal Design of a Laptop Computer by a Personal Computer," *Proc. of 1992 Intersociety Conference on Thermal Phenomena,* Feb., pp. 184–189.

MacPhail, D. C., 1939, "Experiments on Turning Vanes at an Expansion, British Aeronautical Research Council, Reports and Memoranda," No. 1879.

Osaka, H., Yamada, H., Hano, S., and Kageyama, T., 1986, "Fluid Flow through Plain Screens," *Trans. of Japan Society of Mechanical Engineers,* Vol. 52, No. 473, pp. 312–317 (in Japanese).

Schubauer, G. B., Spangenberg, W. G., and Klebanoff, P. S., 1947, "Aerodynamic Characteristics of Damping Screens," National Advisory Committee for Aeronautics, Technical Note 2001.

Taylor, G. I., and Batchelor, G. K., 1949, "The effect of Wire Gauze on Small Disturbances in a Uniform Stream," *Quarterly Journal of Mechanics and Applied Mathematics,* Vol. 2, pp. 1–45.

Wieghardt, K. E. G., 1953, "On the Resistance of Screens," *The Aeronautical Quarterly,* Vol. 4, pp. 186–192.

Turbulent-Spot Propagation in a Decelerating, Compressible Flow

J. P. Clark,[1] T. V. Jones,[2] and J. E. LaGraff[3]

Introduction

The most successful physical model for the transition process is that due to Emmons (1951). In this model, transition is

---

[1] Visiting Asst. Professor of Engineering, New Mexico Highlands University, Las Vegas, NM, 87701.

[2] D. L. Schultz Professor of Turbomachinery, Department of Engineering Science, University of Oxford, Parks Road, Oxford, England, OX1 3PJ.

[3] Professor of Aerospace Engineering, Department of Mechanical, Aerospace, and Manufacturing Engineering, Syracuse University, Syracuse, NY, 13244.

Contributed by the Fluids Engineering Division of THE AMERICAN SOCIETY OF MECHANICAL ENGINEERS. Manuscript received by the Fluids Engineering Division April 20, 1994; revised manuscript received February 20, 1996. Associate Technical Editor: Wing Ng.

considered to be the result of the random formation of ''spots'' of turbulence in the boundary layer over some finite region in the streamwise direction. These so-called turbulent spots grow as they convect downstream until the entire boundary layer is composed of them. At that point, the boundary layer is considered fully turbulent. The current state of knowledge regarding the transition process as it pertains to gas turbines is reviewed by Mayle (1991). In that paper, Mayle makes the case that transition may only be modeled with accuracy in turbomachinery flows through an acceptance of the ideas of Emmons (1951). Thus, an assessment of the effects of various flowfield parameters on transition must be an evaluation of the way in which they affect the formation and subsequent growth of turbulent spots.

In this experiment, an Isentropic Light-Piston Tunnel was employed to generate hot flows with Reynolds and Mach numbers consistent with those in modern gas turbines over the surface of a flat plate instrumented with thin-film gauges. The gas-to-wall temperature ratio was kept constant and equal to 1.4 throughout the tests, and the freestream turbulence intensity was 0.1 percent. Wide-bandwidth heat-flux instrumentation was used to assess the state of a boundary layer growing along the surface of the flat plate under the influence of various constant freestream pressure gradients. The instrumentation, together with a high-speed, multi-channel data-acquisition system, was used to track naturally-occurring turbulent spots as they proceeded downstream along the plate surface in the presence of an adverse pressure gradient. Further details regarding the facility and techniques used in the present study have been presented by Clark et al. (1992, 1993).

The key parameters, which must be measured to describe the propagation of turbulent spots, are the convection velocities of the leading and trailing edges as fractions of the local freestream velocity (C_{le} and C_{te}, respectively), the spreading angle (α), and a spot event-velocity normalized by the local freestream speed (C_s). In the present study, turbulent-spot trajectories were constructed by analyzing raw heat-flux traces via a digital intermittency detector of the type described by Hedley and Keffer (1974). From these trajectories, spot leading- and trailing-edge convection rates were determined. The lateral spreading angles of the spots were calculated through estimates of the rate-of-change of thin-film gauge coverage with streamwise distance. The characteristic spot-velocity was calculated by performing 2-point space-time correlations on the raw heat-flux traces. That is, the spot event-velocity was calculated in a manner consistent with treating the spot as a single eddy. Complete details of these analysis techniques have been presented in Clark et al. (1994).

Results and Discussion

In the paper by Clark et al. (1994), turbulent-spot trajectories were presented for both subsonic and supersonic constant velocity flows. It was found that, over the range of conditions tested ($0.24 \leq M_\infty \leq 1.86$), the spot leading- and trailing-edge fractional propagation rates were independent of the local Mach number of the flow. The same was true of the spot event-velocity when normalized by the local freestream speed. Quantitatively, the results of that study were in excellent agreement with the widely accepted values for spot convection rates in incompressible flows reported by Wygnanski et al. (1976).

Figure 1 is a set of turbulent-spot trajectories in the decelerating flow. Over the streamwise interval represented in the figure, the Mach number varies from 0.59 to 0.56 and the acceleration parameter, K, varies from 0 to -0.38×10^{-6}. Leading-edge, trailing-edge, and spot event-trajectories are plotted on the figure, and lines of constant fractional propagation rate are drawn for comparison. All three trajectories are well represented by lines of constant fractional propagation rate. However, it can be seen that all three spot celerities are reduced relative to accepted zero-pressure-gradient values of $C_{le} = 0.89$, $C_{te} = 0.5$, and $C_s = 0.65$ (Wgynanski et al., 1976). Each leading- and trailing-edge data point plotted on Fig. 1 was determined by a statistical analysis of the trajectories of approximately 50 individual spots, and the uncertainties on the measurements were within the boundaries of the symbols used on the plot. Again, the spots studied here occurred naturally in the boundary-layer transition process on the flat plate. The spots were not triggered in any way, and all measurements were made on the surface of the plate with thin-film gauges.

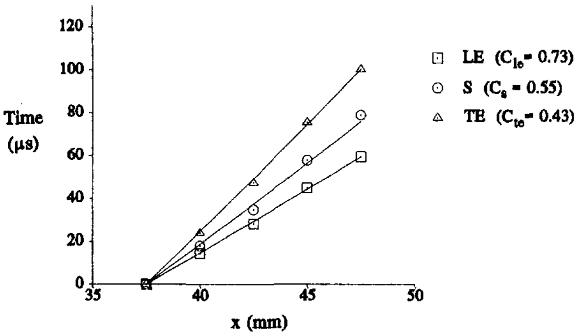

Fig. 1 Turbulent-spot leading-edge, trailing-edge, and event trajectories ($Re_u = 11 \times 10^6$ m^{-1})

The only results which may be compared with those in Fig. 1 are due to Gostelow et al. (1993). The authors of that study tracked artificially-generated turbulent spots in an approximately-constant adverse pressure gradient at incompressible conditions and noted that both the leading- and trailing-edges of the spots propagated at constant fractions of the local freestream velocity. They used streamwise velocity-perturbation intensities to mark the passage of the events at four measuring stations and observed a reduction in both the leading- and trailing-edge celerities of the spots with respect to established zero-pressure-gradient values. They provided enough information to enable the acceleration parameter to be determined at their first measuring station, and K was found to be $\approx -0.38 \times 10^{-6}$ at that location. Although no true surface measurements were obtained by Gostelow et al., they reported edge celerities at a distance from the wall of approximately $0.1\delta_L$ (δ_L was defined as the thickness of the undisturbed laminar boundary layer at the measurement station). At that location, the leading-edge was found to have a fractional propagation rate of 0.74, while that of the trailing edge was 0.43. The results of Gostelow et al. are in excellent agreement with data from the current study despite obvious differences between the experiment of Gostelow et al. and this one.

Turbulent-spot spreading angles were also estimated under the influence of the decelerating freestream. The spreading angles were determined over approximately the same intervals for which turbulent-spot trajectories were given above. The results are presented in Fig. 2 as trajectories of the spanwise limit of the spot trailing-edge in the streamwise-spanwise (i.e., x-z) plane. The trajectory of the lateral edge of the average turbulent spot in the x-z plane is depicted for flows with two different inlet unit-Reynolds-numbers (Re_u). The results are essentially coincident, and both have been plotted to extend the distance over which the spreading angle is measured. This is necessary due to the rapid coalescence of the turbulent spots into a fully turbulent boundary layer in this flow situation. Again, the Mach number varies from 0.59 to 0.55 over the streamwise interval represented in the figure. The spreading angle is increased significantly over the zero-pressure-gradient value of $\alpha \approx 8.2$ deg reported by Clark et al. (1994) for a constant velocity flow with $M_\infty = 0.55$.

The results plotted in Fig. 2 may also be compared to data from the study by Gostelow et al. (1993). They found the spreading angle of an artificially-triggered turbulent spot to be

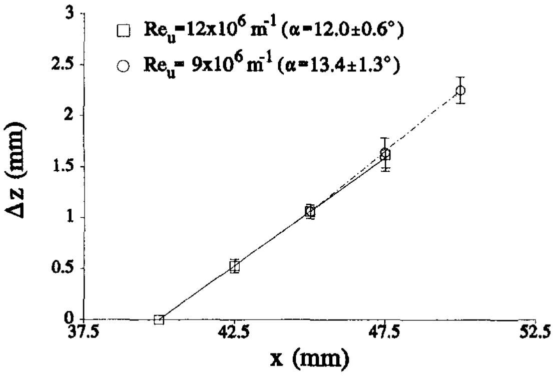

Fig. 2 Turbulent-spot trajectory in the *x-z* plane

increased dramatically over the accepted incompressible, zero-pressure-gradient value when the flow was decelerated. They studied a flow which could be characterized by the Falkner-Skan parameter $\beta = -0.052$, and used a number of different methods to define the lateral boundary of the spot. They concluded that the turbulent spot and its attendant wave packets spread at a semi-angle of nearly 30 deg with respect to the freestream. The turbulent region itself subtended an angle of approximately 20 deg with the local freestream velocity vector. It is unlikely that the wave packets which travel at the "wing-tips" of the turbulent spot affect the local heat-flux level enough to be included in the current analysis: thus the spreading angle determined by Gostelow et al. (1993) for the turbulent region alone should be compared to the present results. Keeping this in mind, there is qualitative agreement between the results of the current investigation and those of Gostelow and his coworkers. That is, adverse pressure gradients increase the spreading angles of turbulent spots significantly over those typically encountered in constant velocity flows.

The discrepancy between the magnitudes of the spreading angles measured by Gostelow et al. ($\alpha \approx 20$ deg) and the current authors ($\alpha \approx 13$ deg) is likely due to the difference in compressibility conditions between the two experiments. In Gostelow's experiment, the flowstream was incompressible: here, the Mach number is ≈ 0.6 over the measurement intervals indicated in Figs. 1 and 2. Clark et al. (1994) reported a significant decrease in spot spreading-angles with Mach number over the range $0.24 \leq M_\infty \leq 1.86$ in constant velocity flows. At Mach 0.55, α was measured at ≈ 8.2 deg, and this was a significant reduction (26%) relative to that measured at incompressible conditions (≈ 11 deg). Here, the measured spreading angle is reduced by 35 percent relative to that measured by Gostelow et al. in an adverse pressure gradient at incompressible speeds.

Acknowledgments

The work herein was supported by the U.S. AFOSR under grant numbers F49620-92-J-0079 and 89-0427 with Dr. Daniel Fant and Dr. James McMichael acting as technical monitors. Additional funding for J. P. Clark was provided by the British Overseas Research Student scholarship program and the Rudolph Light Senior Scholarship Fund at St. Catherine's College, Oxford.

References

Clark, J. P., Jones, T. V., and LaGraff, J. E., 1994, "On the Propagation of Naturally-Occurring Turbulent Spots," *Journal of Engineering Mathematics*, Vol. 28, pp. 1–19.

Clark, J. P., Magari, P. J., Jones, T. V., and LaGraff, J. E., 1993, "Experimental Studies of Turbulent-Spot Parameters Using Thin-Film Heat-Transfer Gauges," AIAA Paper No. 93-0544.

Clark, J. P., LaGraff, J. E., Magari, P. J., and Jones, T. V., 1992, "Measurement of Turbulent Spots and Intermittency Modelling at Gas-Turbine Conditions," NATO/AGARD CP-527, pp. 7.1–7.14.

Emmons, H. W., 1951, "The Laminar-Turbulent Transition in a Boundary Layer-Part 1," *Journal of the Aeronautical Sciences*, Vol. 18, pp. 490–498.

Gostelow, J. P., Hong, G., Melwani, N., and Walker, G. J., 1993, "Turbulent-Spot Development under a Moderate Adverse Pressure Gradient," ASME Paper No. 93-GT-377.

Hedley, T. B., and Keffer, J. F., 1974, "Turbulent/Non-Turbulent Decisions in an Intermittent Flow," *Journal of Fluid Mechanics*, Vol. 64, pp. 625–644.

Mayle, R. E., 1991, "The Role of Laminar-Turbulent Transition in Gas Turbine Engines," ASME *Journal of Turbomachinery*, Vol. 113, pp. 509–537.

Wygnanski, I., Sokolov, M., and Friedman, D., 1976, "On a Turbulent 'Spot' in a Laminar Boundary Layer," *Journal of Fluid Mechanics*, Vol. 78, pp. 785–819.

Sequential Production of mm-Sized Spherical Shells in Liquid-Liquid Gas Systems

Satoyuki Kawano,[1] Hiroyuki Hashimoto,[1] Akio Ihara,[1] and Keiji Shin[1]

A new device has been developed for sequential production of mm-sized solid spherical shells using liquid-liquid gas systems. This device comprises a cylindrical vessel, for containing two kinds of immiscible liquids, and a gas injection orifice, set at the center of the vessel's bottom. Solid spherical shells are successfully and sequentially produced by solidifying rising liquid spherical shells, formed sequentially at the horizontal interface between two immiscible liquids.

Introduction

Solid spherical shells have attracted considerable attention in various technological fields, mainly for their applicability. This includes their use as lightweight structural materials for spacecraft, as functional medicines, as high performance solid fuels, as buoyant catalytic agents, as energy storage systems, etc. (Lee et al., 1986). Generally, it is difficult to uniformly and sequentially produce mm-sized or larger spherical shells in a gravitational environment. To date, their production technique has been mainly limited to a method using annular nozzles. As for using annular nozzles, however, a very large apparatus (13.1 m in height), called a drop tower, is needed to solidify molten spherical shells (Kendall, 1986 and Lee et al., 1986). Demand has been rising for the development of a new and economical method for producing mm-sized solid spherical shells.

The present paper purposes a new simplified method for sequential production of mm-sized solid spherical shells, utilizing a device based on liquid-liquid gas systems. This device comprises a cylindrical vessel, for containing two immiscible liquids, and a gas injection orifice, equipped at the center of the vessel's bottom. Liquid spherical shells are formed sequentially, at the horizontal interface between two immiscible liquids, by effectively controlling the gas jet flow rate and by suitably selecting the properties of the liquids (Hashimoto and Kawano, 1989, 1990). Solid shells are produced by solidification of liq-

---

[1] Research Associate, Professor, Associate Professor, and Graduate Student, respectively, Institute of Fluid Science, Tohoku University, 2-1-1 Katahira, Aoba-ku, Sendai 980, Japan.

Contributed by the Fluids Engineering Division of THE AMERICAN SOCIETY OF MECHANICAL ENGINEERS. Manuscript received by the Fluids Engineering Division December 9, 1994; revised manuscript received January 29, 1996. Associate Technical Editor: M. W. Reeks.

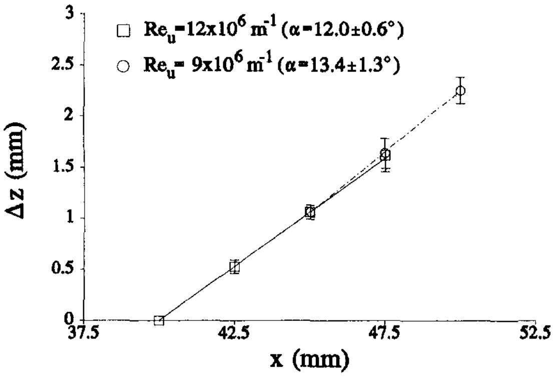

Fig. 2 Turbulent-spot trajectory in the *x-z* plane

increased dramatically over the accepted incompressible, zero-pressure-gradient value when the flow was decelerated. They studied a flow which could be characterized by the Falkner-Skan parameter $\beta = -0.052$, and used a number of different methods to define the lateral boundary of the spot. They concluded that the turbulent spot and its attendant wave packets spread at a semi-angle of nearly 30 deg with respect to the freestream. The turbulent region itself subtended an angle of approximately 20 deg with the local freestream velocity vector. It is unlikely that the wave packets which travel at the "wing-tips" of the turbulent spot affect the local heat-flux level enough to be included in the current analysis: thus the spreading angle determined by Gostelow et al. (1993) for the turbulent region alone should be compared to the present results. Keeping this in mind, there is qualitative agreement between the results of the current investigation and those of Gostelow and his co-workers. That is, adverse pressure gradients increase the spreading angles of turbulent spots significantly over those typically encountered in constant velocity flows.

The discrepancy between the magnitudes of the spreading angles measured by Gostelow et al. ($\alpha \approx 20$ deg) and the current authors ($\alpha \approx 13$ deg) is likely due to the difference in compressibility conditions between the two experiments. In Gostelow's experiment, the flowstream was incompressible: here, the Mach number is ≈ 0.6 over the measurement intervals indicated in Figs. 1 and 2. Clark et al. (1994) reported a significant decrease in spot spreading-angles with Mach number over the range $0.24 \leq M_\infty \leq 1.86$ in constant velocity flows. At Mach 0.55, α was measured at ≈ 8.2 deg, and this was a significant reduction (26%) relative to that measured at incompressible conditions (≈ 11 deg). Here, the measured spreading angle is reduced by 35 percent relative to that measured by Gostelow et al. in an adverse pressure gradient at incompressible speeds.

Acknowledgments

The work herein was supported by the U.S. AFOSR under grant numbers F49620-92-J-0079 and 89-0427 with Dr. Daniel Fant and Dr. James McMichael acting as technical monitors. Additional funding for J. P. Clark was provided by the British Overseas Research Student scholarship program and the Rudolph Light Senior Scholarship Fund at St. Catherine's College, Oxford.

References

Clark, J. P., Jones, T. V., and LaGraff, J. E., 1994, "On the Propagation of Naturally-Occurring Turbulent Spots," *Journal of Engineering Mathematics*, Vol. 28, pp. 1–19.

Clark, J. P., Magari, P. J., Jones, T. V., and LaGraff, J. E., 1993, "Experimental Studies of Turbulent-Spot Parameters Using Thin-Film Heat-Transfer Gauges," AIAA Paper No. 93-0544.

Clark, J. P., LaGraff, J. E., Magari, P. J., and Jones, T. V., 1992, "Measurement of Turbulent Spots and Intermittency Modelling at Gas-Turbine Conditions," NATO/AGARD CP-527, pp. 7.1–7.14.

Emmons, H. W., 1951, "The Laminar-Turbulent Transition in a Boundary Layer-Part 1," *Journal of the Aeronautical Sciences*, Vol. 18, pp. 490–498.

Gostelow, J. P., Hong, G., Melwani, N., and Walker, G. J., 1993, "Turbulent-Spot Development under a Moderate Adverse Pressure Gradient," ASME Paper No. 93-GT-377.

Hedley, T. B., and Keffer, J. F., 1974, "Turbulent/Non-Turbulent Decisions in an Intermittent Flow," *Journal of Fluid Mechanics*, Vol. 64, pp. 625–644.

Mayle, R. E., 1991, "The Role of Laminar-Turbulent Transition in Gas Turbine Engines," ASME *Journal of Turbomachinery*, Vol. 113, pp. 509–537.

Wygnanski, I., Sokolov, M., and Friedman, D., 1976, "On a Turbulent 'Spot' in a Laminar Boundary Layer," *Journal of Fluid Mechanics*, Vol. 78, pp. 785–819.

Sequential Production of mm-Sized Spherical Shells in Liquid-Liquid Gas Systems

Satoyuki Kawano,[1] Hiroyuki Hashimoto,[1] Akio Ihara,[1] and Keiji Shin[1]

A new device has been developed for sequential production of mm-sized solid spherical shells using liquid-liquid gas systems. This device comprises a cylindrical vessel, for containing two kinds of immiscible liquids, and a gas injection orifice, set at the center of the vessel's bottom. Solid spherical shells are successfully and sequentially produced by solidifying rising liquid spherical shells, formed sequentially at the horizontal interface between two immiscible liquids.

Introduction

Solid spherical shells have attracted considerable attention in various technological fields, mainly for their applicability. This includes their use as lightweight structural materials for spacecraft, as functional medicines, as high performance solid fuels, as buoyant catalytic agents, as energy storage systems, etc. (Lee et al., 1986). Generally, it is difficult to uniformly and sequentially produce mm-sized or larger spherical shells in a gravitational environment. To date, their production technique has been mainly limited to a method using annular nozzles. As for using annular nozzles, however, a very large apparatus (13.1 m in height), called a drop tower, is needed to solidify molten spherical shells (Kendall, 1986 and Lee et al., 1986). Demand has been rising for the development of a new and economical method for producing mm-sized solid spherical shells.

The present paper purposes a new simplified method for sequential production of mm-sized solid spherical shells, utilizing a device based on liquid-liquid gas systems. This device comprises a cylindrical vessel, for containing two immiscible liquids, and a gas injection orifice, equipped at the center of the vessel's bottom. Liquid spherical shells are formed sequentially, at the horizontal interface between two immiscible liquids, by effectively controlling the gas jet flow rate and by suitably selecting the properties of the liquids (Hashimoto and Kawano, 1989, 1990). Solid shells are produced by solidification of liq-

---

[1] Research Associate, Professor, Associate Professor, and Graduate Student, respectively, Institute of Fluid Science, Tohoku University, 2-1-1 Katahira, Aoba-ku, Sendai 980, Japan.

Contributed by the Fluids Engineering Division of The American Society of Mechanical Engineers. Manuscript received by the Fluids Engineering Division December 9, 1994; revised manuscript received January 29, 1996. Associate Technical Editor: M. W. Reeks.

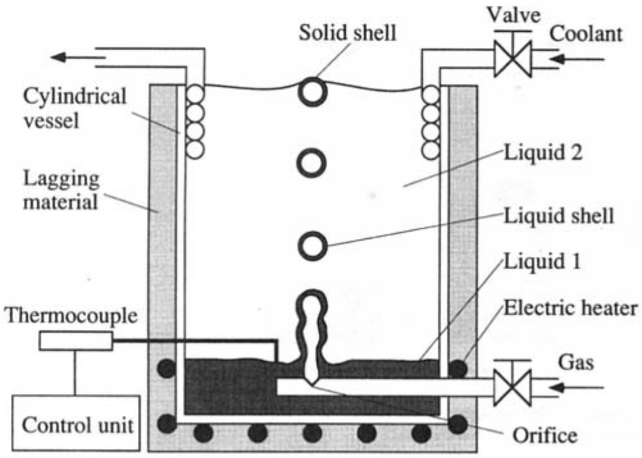

Fig. 1 Device for sequential production of solid spherical shells using liquid-liquid-gas systems

uid shells moving upward by buoyancy to the surface of the upper liquid, through a given temperature distribution. The first step for investigating the performance of the present device was carrying out experiments using a molten salt HTS (Heat Transfer Salt: $KNO_3 + NaNO_2 + NaNO_3$, 44 + 49 + 7 mol percent)-turbine oil-air system. It was possible to sequentially produce HTS solid spherical shells, diameter of 4.64 ~ 8.39 mm and a thickness of 0.06 ~ 0.14 mm. It was also possible to easily control the size of the shells by changing the gas flow rate through the orifice. Furthermore, solid shells, made of an alloy (Sn + Pb + Bi + In, 12 + 18 + 49 + 21 wt percent), and agar, were successfully produced using this system.

Sequential Production Device

Figure 1 shows a schematic of a device using liquid-liquid gas systems, designed for the sequential production of solid spherical shells based on previous basic data on buoyancy-driven motion (Kawano and Hashimoto, 1992) and heat/mass transfer characteristics (Hashimoto and Kawano, 1993) of liquid shells. The cylindrical vessel, made of stainless steel, is 180 mm in height, 3 mm in thickness and 180 mm in inner diameter. An electric heater is set around the lower part and outside the bottom of the cylindrical vessel. The coolant pipe, 8 mm in diameter and 5 mm in inner diameter, is set inside at the upper part of the cylindrical vessel's wall. Gas from a pump passes through a large surge tank, a float-type flowmeter, a conducting pipe with an inner diameter of 5 mm and then is injected into the lower liquid from an orifice. A thermocouple is set near the center of the liquid-liquid interface to maintain the interface at a uniform temperature, within ±2 K, by controlling the electric heater output.

Figure 2 shows, as a reference, photographs of the formation and the buoyancy-driven motion of a liquid shell in the similar device made by transparent acrylic vessel. The lower liquid (liquid 1) was a mixture of water and black ink, and the upper liquid (liquid 2) was kerosene. The inner diameter δ of the gas (air) injection orifice, the gas flow rate Q through the nozzle, and the fluid temperature were 0.5 mm, 0.217×10^{-6} m^3/s and 288 K, respectively. The density ρ and kinematic viscosity υ of the water-black ink mixture were $\rho = 999$ kg/m^3 and $\upsilon = 1.22 \times 10^{-6}$ m^2/s at 288 K, respectively. In kerosene, $\rho = 825$ kg/m^3 and $\upsilon = 2.08 \times 10^{-6}$ m^2/s at 288 K. Liquid 1 and liquid 2 had a height of 10 mm and 250 mm, respectively. From Fig. 2, the deformation of the liquid shell, just after formation at the liquid-liquid interface, is reduced gradually owing to the effect of interface tension during the upward motion. The liquid shell has a relatively good sphericity compared with the gas bubble, as reported by Mercier et al. (1974), although the effect of the gravity is important in the case of relatively large shell thickness. In Fig. 2, the equivalent diameter of the liquid shell is 5.66 mm and the equivalent shell thickness is 0.46 mm. The drop Reynolds number, based on the shell diameter, the terminal velocity, and the outer liquid kinematic viscosity, is 100 in order.

In liquid-liquid gas systems, the formation mechanism of liquid shells and the method of theoretical prediction of the diameter were already studied by the authors (Hashimoto and Kawano, 1989, 1990 and Kawano et al., 1993).

Experimental Results on HTS

Experimental Conditions. HTS was used as the material of solid spherical shells, i.e., as liquid 1 in the cylindrical vessel. The HTS used here had a relatively low melting temperature (415 K); its other physical properties were those well known. HTS is favorable for visual observation of solidification because it is transparent in the liquid phase and white in the solid phase. Turbine oil (ISO VG32), immiscible with HTS and stable at relatively high temperatures, was used as the upper liquid (liquid 2). In HTS, $\rho = 1976$ kg/m^3 and $\upsilon = 8.73 \times 10^{-6}$ m^2/s at 420 K. In turbine oil, $\rho = 787$ kg/m^3 and $\upsilon = 3.80 \times 10^{-6}$ m^2/s at 393 K. Liquid 1 and liquid 2 were set to be 15 mm and 135 mm in height, respectively. The outlet position of the orifice was set just below 7 mm from the liquid-liquid interface. Three different gas (air) injection orifices (inner diameter $\delta = 0.3$, 0.5 and 0.8 mm) were used. The volumetric flow rate Q through the orifice was changed within the range of $0.350 \times 10^{-6} \sim 2.58 \times 10^{-6}$ m^3/s at 294 K.

The required temperature T_s at the liquid-liquid interface was set at 423 K and the temperature T_c of the coolant was set at 294 K. The flow rate Q_L of the coolant was set at 6.81×10^{-6} m^3/s. We measured the temperature distribution along the center axis of the cylindrical vessel by a thermocouple without gas injection. Although complex and unsteady convection could be expected in the present system, we could maintain the inverse temperature gradient.

Geometrical Form of Solid Spherical Shells. Figure 3 shows a photograph of the solid spherical shells produced under conditions of $\delta = 0.3$ mm and $Q = 1.50 \times 10^{-6}$ m^3/s. In Fig. 3, the lower solid shell has been intentionally broken to allow observance of the solid spherical shell thickness. These solid shells are collected by a stainless wire net at the upper surface. It can be confirmed experimentally that the solid shells are of sufficiently spherical shape and with uniformly thin shell thickness.

The solid spherical shells were found to be spheres or oblate spheroids. Therefore, the equivalent diameter d_0 of a solid spherical shell is estimated by $d_0 = (d_r^2 \cdot d_z)^{1/3}$, where d_r and d_z are the horizontal and vertical diameters of a solid spherical shell, respectively ($d_r \geqq d_z$). The d_r and d_z were measured from more than 50 photographs by a film motion analyzer, which was a film projector with function of digitizing the coordinates. Figure 4 shows the size frequency distribution of solid spherical shells. It can be found that the size of solid shell has an approximately logarithmic probability distribution. This result corresponds to the fact that the size of the gas bubble produced from the single orifice and that of the liquid shell produced in liquid-liquid gas systems have similar logarithmic probability distributions (Hashimoto and Kawano, 1989).

Figure 5 shows the relationship between the logarithmic geometric mean diameter $\bar{d}_0$ and Q for various δ. The $\bar{d}_0$ increases along an increase in Q and δ, i.e. it can be said that $\bar{d}_0$ increases as the total inertia force of the bubble flow from the orifice increases. The $\bar{d}_0$ increases linearly with Q. In the present experiment, $\bar{d}_0$ could be varied widely, meaning that the production

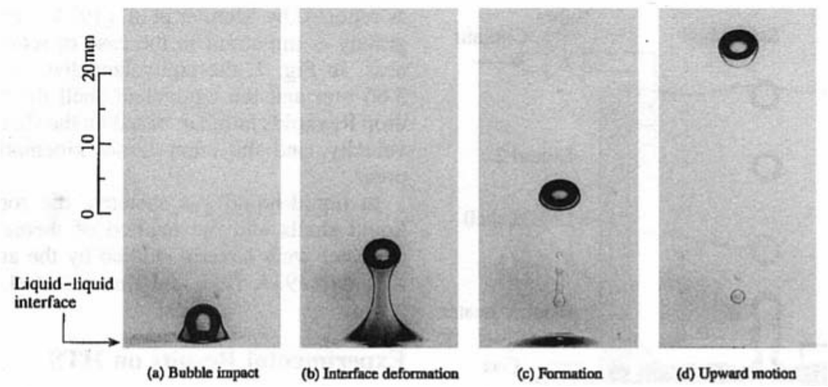

Fig. 2 Photographs of formation and buoyancy driven motion of liquid shell in liquid-liquid-gas systems (Liquid 1: a mixture of water and black ink; liquid 2: kerosene)

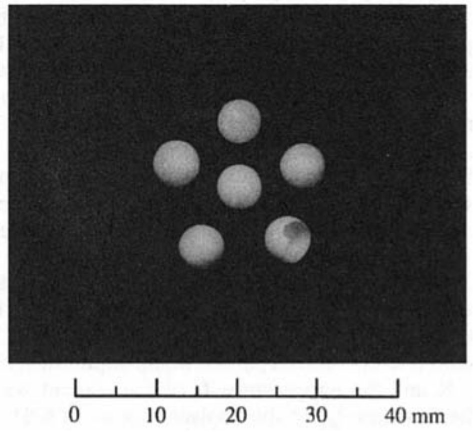

Fig. 3 Photograph of HTS (KNO_3 + $NaNO_2$ + $NaNO_3$, 44 + 49 + 7 mol percent) solid spherical shells

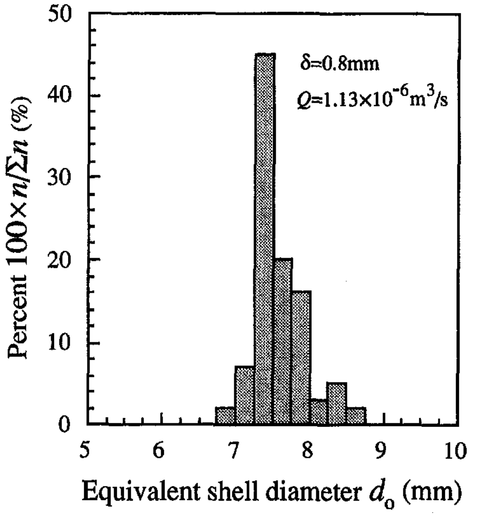

Fig. 4 Size frequency distribution of HTS solid spherical shells (Uncertainty in d_0 = ±0.438 mm at 20:1 odds)

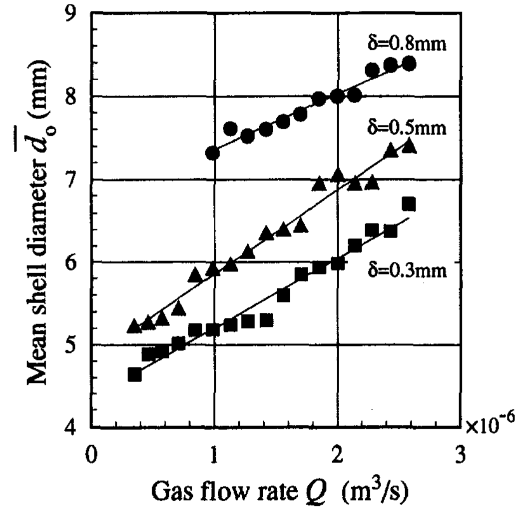

Fig. 5 Mean diameter of HTS solid spherical shells (Uncertainty in Q = $\pm 0.258 \times 10^{-6}$ m^3/s and in $\bar{d}_0$ = ±1.25 mm at 20:1 odds)

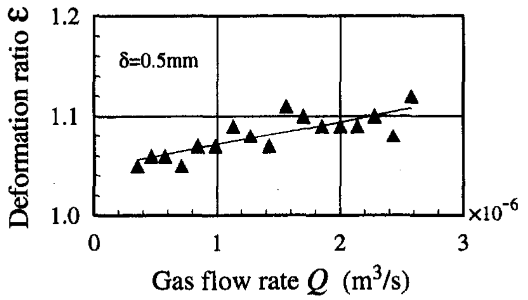

Fig. 6 Deformation ratio of HTS solid spherical shells (Uncertainty in Q = $\pm 0.258 \times 10^{-6}$ m^3/s and in ϵ = ±0.0813 at 20:1 odds)

device developed here has the advantage that $\bar{d}_0$ can be easily controlled.

The deformation ratio $\epsilon(= d_r/d_z)$ was calculated. Figure 6 shows the representative relationship between ϵ and Q at δ = 0.5 mm. The value of ϵ is in the range of $\epsilon = 1.05 \sim 1.12$ for various δ. The value of ϵ increases slightly and linearly along an increase in Q and that ϵ is not depend strongly on δ. The sphericity of the solid shell was better than that of the gas bubble because the liquid shell could not be deformed as the gas bubble, owing to the small interface mobility (Mercier et al., 1974). The sphericity of the HTS solid shell was also better than that of the black ink liquid shell, produced in black ink-kerosene-air system (Kawano and Hashimoto, 1992), and than that of the liquid shell shown in Fig. 2. One of the reasons for this may be the smaller drop Reynolds number of the HTS liquid shell due to the larger υ of turbine oil.

The shell thickness ξ was measured by a microscope. The mean value of ξ was determined from more than 50 solid spherical shells. The shell thickness was confirmed to be almost uni-

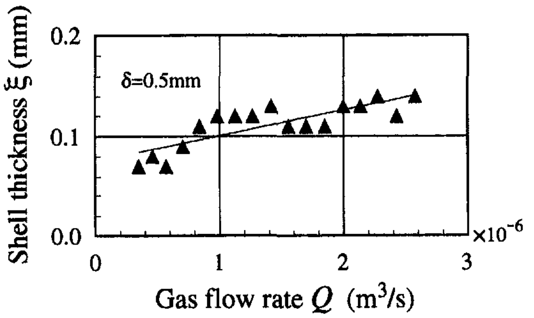

Fig. 7 Shell thickness of HTS solid spherical shells (Uncertainty in $Q = \pm 0.258 \times 10^{-6}$ m³/s and in $\xi = \pm 0.0390$ mm at 20:1 odds)

form at any point of shell. Figure 7 shows the representative relationship between ξ and Q at $\delta = 0.5$ mm. The value of ξ is in the range of $\xi = 0.06 \sim 0.14$ mm for various δ. It is found that the mean value of ξ slightly and linearly increases along an increase in Q and that ξ is not depend strongly on δ. The value of ξ was much smaller than the our previously reported value of ξ, which was 0.41 mm in the case of $\bar{d}_0 = 4.82$ mm in the black ink-kerosene-air system (Hashimoto and Kawano, 1989), and than that in the case shown in Fig. 2. Because of larger ρ of molten HTS, the value of ξ must be small for the upward motion of the liquid shell. Here, the value of ξ in the annular nozzle was in the range of $0.05\ \bar{d}_0 \sim 0.1\ \bar{d}_0$ (Kendall, 1986).

Production Frequency. Figure 8 shows the relationship between production frequency f and Q for various δ. It can be seen that the value of f increases along an increase in Q in the range of small Q, reaches a maximum and then decreases along an increase in Q in the range of large Q. The production pattern of the liquid shell should be stable in the range of small Q because the liquid shells are small and stable. However, the production pattern becomes unstable in the range of large Q, that is, it may increase the possibility of realization that the rising gas bubbles pass through the liquid-liquid interface without production of liquid shells. This causes the rapid decrease of f. This tendency is promoted by increasing the total inertia force of bubble flow from the orifice, however, an increase of f may be possible by a selection of some liquids with more suitable properties (Hashimoto and Kawano, 1990). In the present experiment, the maximum f was about 5, a much smaller value than $f = 24$ in the previous experiment of the black ink-kerosene-air system at $\delta = 0.4$ mm and $Q = 1.13 \times 10^{-6}$ m³/s (Hashimoto and Kawano, 1989). The reason for this is that the v of HTS and turbine oil are larger than those of black ink and kerosene. Therefore, the fluid motion during the production of liquid shell in the HTS-turbine oil-air system becomes slow. Furthermore, in the HTS-turbine oil-air system, the value of ξ is very small, so that badly deformed shells are easily broken during the upward motion. This result corresponds to the experimental fact that HTS solid shells are of nearly spherical shape.

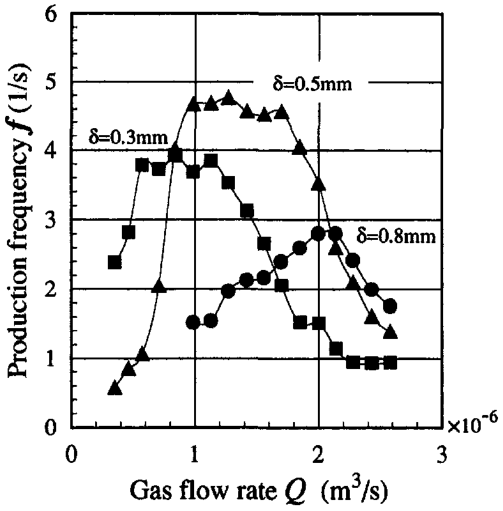

Fig. 8 Production frequency of HTS solid spherical shells (Uncertainty in $Q = \pm 0.258 \times 10^{-6}$ m³/s and in $f = \pm 0.797$ at 20:1 odds)

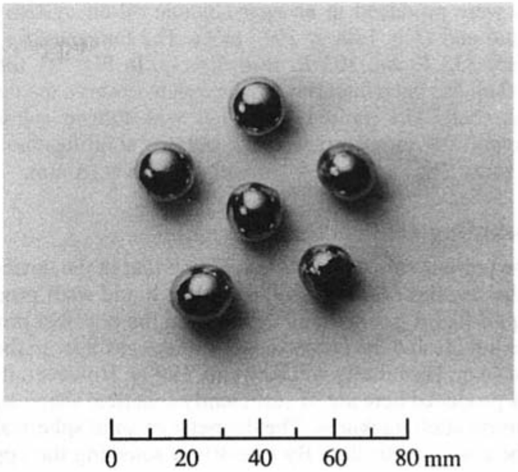

Fig. 9 Photograph of alloy (Sn + Pb + Bi + In, 12 + 18 + 49 + 21 wt percent) solid spherical shells

Experimental Results on Other Materials

An alloy (Sn + Pb + Bi + In, 12 + 18 + 49 + 21 wt percent), which was called solder, was tested considering the fact that metallic spherical shells were useful in lightweight structural materials and buoyant catalytic agents. Figure 9 shows solid spherical shells made of an alloy. They were produced in an alloy-glycerine-air system at $\delta = 1.0$ mm and $Q = 14.5 \times 10^{-6}$ m³/s. The temperatures T_s and T_c were 353 K and 328 K, respectively. In Fig. 9, the lower metallic shell has been intentionally broken to observe the thickness of the shell. Metallic shells have a high surface tension and can easily attain a spherical shape. The $\bar{d}_0$ was 15.5 mm and ξ was 0.10 mm.

Agar, a type of hemicellulose, was also used, considering its applications in functional foods and unique culture mediums in biology. Figure 10 shows solid spherical shells made of agar.

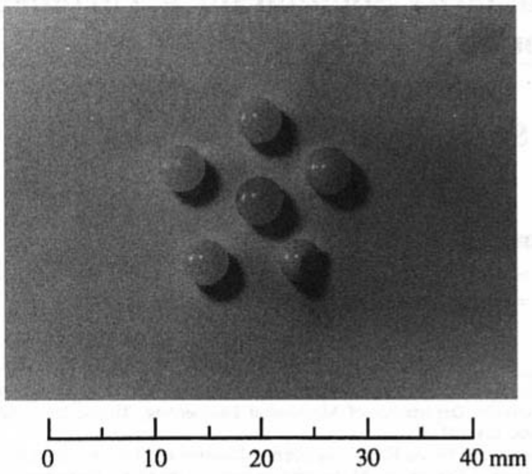

Fig. 10 Photograph of agar solid spherical shells

They were produced in an agar-silicone oil-air system at $\delta = 0.3$ mm and $Q = 1.88 \times 10^{-7}$ m^3/s. The temperatures T_s and T_c were 333 K and 303 K, respectively. In Fig. 10, the lower agar shell has been intentionally broken to observe the thickness of the shell. The molten agar shell was able to solidified at relatively low temperature range but the solidification took a long time. The $\overline{d}_0$ was 4.42 mm and ξ was 0.18 mm.

Concluding Discussions

The present value of f is smaller than that in the device using annular nozzles (Kendall, 1986). Also, liquid shell production in liquid-liquid gas systems depends on the physical properties of the liquids and the characteristics of the gas flow in the lower liquid (e.g., Hashimoto and Kawano, 1990). However, the solid shells produced here are of sufficiently spherical shape and have a uniform shell thickness. The diameter of solid spherical shells can be easily controlled. By effectively selecting the upper liquid, the flow characteristics of the liquid shells, such as the upward velocity or the oscillations of the liquid shell interfaces, may be easily controlled as well. As the present device solidifies the liquid shell by cooled liquid, selecting a suitable cooling system enables a simple and cost efficient spherical shell production. The main advantage of the mm-sized spherical shell production device proposed here is its simple structure.

References

Hashimoto, H. and Kawano, S., 1989, "Formation of Encapsulated Liquid Drops in Liquid-Liquid Gas Systems," *Proceedings of International Conference on Mechanics of Two-Phase Flows*, Taipei, pp. 341–346.

Hashimoto, H. and Kawano, S., 1990, "A Study on Encapsulated Liquid Drop Formation in Liquid-Liquid Gas Systems: Fundamental Mechanism of Encapsulated Drop Formation," *JSME International Journal*, Series II, Vol. 33, pp. 729–735.

Hashimoto, H. and Kawano, S., 1993, "Mass Transfer around a Moving Encapsulated Liquid Drop," *International Journal Multiphase Flow*, Vol. 19, pp. 213–228.

Kawano, S. and Hashimoto, H., 1992, "Drag Coefficient of a Spherical Encapsulated Liquid Drop," *JSME International Journal*, Series II, Vol. 35, pp. 151–157.

Kawano, S., Hashimoto, H. and Azima, T., 1993, "A Study on Compound Jet Instability and Formation of Encapsulated Liquid Drops in Liquid-Liquid-Gas Systems," *Proceedings of the International Symposium on Aerospace and Fluid Science*, Sendai, pp. 371–378.

Kendall, J. M., 1986, "Experiments on Annular Liquid Jet Instability and on the Formation of Liquid Shells," *Physics of Fluids*, Vol. 29, pp. 2086–2094.

Lee, M. C., Kendall, J. M. Jr., Bahrami, P. A., and Wang, T. G., 1986, "Sensational Spherical Shells," *Aerospace America*, Vol. 24, pp. 72–76.

Mercier, J. L., da Cunha, F. M., Teixeira, J. C., and Scofield, M. P., 1974, "Influence of Enveloping Water Layer on the Rise of Air Bubbles in Newtonian Fluids," ASME, *Journal of Applied Mechanics*, Vol. 96, pp. 29–34.

Similarity Solution for a Turbulent Round Jet

R. Seffal[1] and E. E. Michaelides[1]

Nomenclature

C_μ = turbulence model parameter
$C_{\epsilon 1}$ = turbulence model parameter
$C_{\epsilon 2}$ = turbulence model parameter
d = diameter of the jet orifice
F = dimensionless stream function
G = dimensionless turbulent kinetic energy
H = dimensionless turbulent dissipation function
k = turbulent kinetic energy
P = rate of turbulent kinetic energy production
r = radial direction coordinate
R = second order correlation function
u = mean axial velocity
u' = fluctuating axial velocity
u_0 = centerline axial velocity distribution
u_{00} = jet axial velocity at orifice exit
U = similarity variable
v = mean radial velocity
v' = fluctuating radial velocity
x = axial direction coordinate
ϵ = turbulent dissipation function
η = a similarity variable
ξ = a similarity variable
ν = kinematic viscosity of fluid
ν_t = eddy viscosity of fluid
σ_k = model parameter
σ_ϵ = model parameter
μ = viscosity of fluid
Ψ = dimensional stream function

I Introduction

Turbulent round jets are encountered in a variety of forms in engineering and natural systems. Examples include flows inside combustors, chemical mixing processes, and water purification systems. Experimental results on round jets by Abramovich (1963) and Wygnanski and Fiedler (1969), and Kumar et al. (1989) have shown that the round (axisymmetric) jet is self-similar. The experimental data of Abramovich (1963) and List (1982) showed that, when the shear stress and the longitudinal turbulence intensity across the jet axis are scaled by the mean axial velocity, self-similarity is observed at $x/d \geq 8$. The feature of self-similarity in other shear and boundary layer flows has been explained by Townsend (1976) as being the manifestation of the principle of "moving equilibrium." A recent study by George (1989) links the self-similarity feature to conditions of the jet source. More recent experimental work by Hussein et al. (1994), supports the self-similarity feature of the turbulent jet. The same authors attribute the apparent discrepancy between their experimental results and those of Wygnanski and Fiedler (1969) to the differences in the type of jet produced: they assert that Wygnanski and Fiedler used a partly confined jet with significant return flow, while their jet was completely free.

Among the similarity solutions, Wollmers and Rotta (1977) used the self-preserving property of a turbulent jet and developed a k-kl model to solve the turbulence closure problem. So (1986) obtained similarity solutions for a round jet by assuming a velocity profile in the form of a gaussian error function. This assumption is very restrictive because it does not allow the shape of the velocity profile to evolve from the governing equations, but compels them to accommodate the assumed velocity profile. Paullay et al. (1985) used the principle of "moving equilibrium," to derive a similarity solution for plane and radial jets. Their solution is not general enough to include the round axisymmetric jets, which are most commonly met in engineering practice, because the governing equations used are not applicable to round jets.

We followed essentially the method by Paullay et al. (1985) and derived a similarity solution for the turbulent, axisymmetric round jet, without using any assumptions about the shape of the velocity profile. In this short paper, we present the results of calculations based on our similarity solution and compare these results with experimental data and 2-D numerical compu-

---

[1] Graduate Research Assistant and Associate Dean for Research and Professor, respectively, Department of Mechanical Engineering, Tulane University, New Orleans, LA 70118.

Contributed by the Fluids Engineering Division of The American Society of Mechanical Engineers. Manuscript received by the Fluids Engineering Division September 29, 1995; revised manuscript received January 6, 1996. Associate Technical Editor: D. P. Telionis

They were produced in an agar-silicone oil-air system at $\delta = 0.3$ mm and $Q = 1.88 \times 10^{-7}$ m^3/s. The temperatures T_s and T_c were 333 K and 303 K, respectively. In Fig. 10, the lower agar shell has been intentionally broken to observe the thickness of the shell. The molten agar shell was able to solidified at relatively low temperature range but the solidification took a long time. The $\overline{d}_0$ was 4.42 mm and ξ was 0.18 mm.

Concluding Discussions

The present value of f is smaller than that in the device using annular nozzles (Kendall, 1986). Also, liquid shell production in liquid-liquid gas systems depends on the physical properties of the liquids and the characteristics of the gas flow in the lower liquid (e.g., Hashimoto and Kawano, 1990). However, the solid shells produced here are of sufficiently spherical shape and have a uniform shell thickness. The diameter of solid spherical shells can be easily controlled. By effectively selecting the upper liquid, the flow characteristics of the liquid shells, such as the upward velocity or the oscillations of the liquid shell interfaces, may be easily controlled as well. As the present device solidifies the liquid shell by cooled liquid, selecting a suitable cooling system enables a simple and cost efficient spherical shell production. The main advantage of the mm-sized spherical shell production device proposed here is its simple structure.

References

Hashimoto, H. and Kawano, S., 1989, "Formation of Encapsulated Liquid Drops in Liquid-Liquid Gas Systems," *Proceedings of International Conference on Mechanics of Two-Phase Flows,* Taipei, pp. 341–346.

Hashimoto, H. and Kawano, S., 1990, "A Study on Encapsulated Liquid Drop Formation in Liquid-Liquid Gas Systems: Fundamental Mechanism of Encapsulated Drop Formation," *JSME International Journal,* Series II, Vol. 33, pp. 729–735.

Hashimoto, H. and Kawano, S., 1993, "Mass Transfer around a Moving Encapsulated Liquid Drop," *International Journal Multiphase Flow,* Vol. 19, pp. 213–228.

Kawano, S. and Hashimoto, H., 1992, "Drag Coefficient of a Spherical Encapsulated Liquid Drop," *JSME International Journal,* Series II, Vol. 35, pp. 151–157.

Kawano, S., Hashimoto, H. and Azima, T., 1993, "A Study on Compound Jet Instability and Formation of Encapsulated Liquid Drops in Liquid-Liquid-Gas Systems," *Proceedings of the International Symposium on Aerospace and Fluid Science,* Sendai, pp. 371–378.

Kendall, J. M., 1986, "Experiments on Annular Liquid Jet Instability and on the Formation of Liquid Shells," *Physics of Fluids,* Vol. 29, pp. 2086–2094.

Lee, M. C., Kendall, J. M. Jr., Bahrami, P. A., and Wang, T. G., 1986, "Sensational Spherical Shells," *Aerospace America,* Vol. 24, pp. 72–76.

Mercier, J. L., da Cunha, F. M., Teixeira, J. C., and Scofield, M. P., 1974, "Influence of Enveloping Water Layer on the Rise of Air Bubbles in Newtonian Fluids," ASME, *Journal of Applied Mechanics,* Vol. 96, pp. 29–34.

Similarity Solution for a Turbulent Round Jet

R. Seffal[1] and E. E. Michaelides[1]

Nomenclature

C_μ = turbulence model parameter
$C_{\epsilon 1}$ = turbulence model parameter
$C_{\epsilon 2}$ = turbulence model parameter
d = diameter of the jet orifice
F = dimensionless stream function
G = dimensionless turbulent kinetic energy
H = dimensionless turbulent dissipation function
k = turbulent kinetic energy
P = rate of turbulent kinetic energy production
r = radial direction coordinate
R = second order correlation function
u = mean axial velocity
u' = fluctuating axial velocity
u_0 = centerline axial velocity distribution
u_{00} = jet axial velocity at orifice exit
U = similarity variable
v = mean radial velocity
v' = fluctuating radial velocity
x = axial direction coordinate
ϵ = turbulent dissipation function
η = a similarity variable
ξ = a similarity variable
ν = kinematic viscosity of fluid
ν_t = eddy viscosity of fluid
σ_k = model parameter
σ_ϵ = model parameter
μ = viscosity of fluid
Ψ = dimensional stream function

I Introduction

Turbulent round jets are encountered in a variety of forms in engineering and natural systems. Examples include flows inside combustors, chemical mixing processes, and water purification systems. Experimental results on round jets by Abramovich (1963) and Wygnanski and Fiedler (1969), and Kumar et al. (1989) have shown that the round (axisymmetric) jet is self-similar. The experimental data of Abramovich (1963) and List (1982) showed that, when the shear stress and the longitudinal turbulence intensity across the jet axis are scaled by the mean axial velocity, self-similarity is observed at $x/d \geq 8$. The feature of self-similarity in other shear and boundary layer flows has been explained by Townsend (1976) as being the manifestation of the principle of "moving equilibrium." A recent study by George (1989) links the self-similarity feature to conditions of the jet source. More recent experimental work by Hussein et al. (1994), supports the self-similarity feature of the turbulent jet. The same authors attribute the apparent discrepancy between their experimental results and those of Wygnanski and Fiedler (1969) to the differences in the type of jet produced: they assert that Wygnanski and Fiedler used a partly confined jet with significant return flow, while their jet was completely free.

Among the similarity solutions, Wollmers and Rotta (1977) used the self-preserving property of a turbulent jet and developed a k-kl model to solve the turbulence closure problem. So (1986) obtained similarity solutions for a round jet by assuming a velocity profile in the form of a gaussian error function. This assumption is very restrictive because it does not allow the shape of the velocity profile to evolve from the governing equations, but compels them to accommodate the assumed velocity profile. Paullay et al. (1985) used the principle of "moving equilibrium," to derive a similarity solution for plane and radial jets. Their solution is not general enough to include the round axisymmetric jets, which are most commonly met in engineering practice, because the governing equations used are not applicable to round jets.

We followed essentially the method by Paullay et al. (1985) and derived a similarity solution for the turbulent, axisymmetric round jet, without using any assumptions about the shape of the velocity profile. In this short paper, we present the results of calculations based on our similarity solution and compare these results with experimental data and 2-D numerical compu-

---

[1] Graduate Research Assistant and Associate Dean for Research and Professor, respectively, Department of Mechanical Engineering, Tulane University, New Orleans, LA 70118.

Contributed by the Fluids Engineering Division of THE AMERICAN SOCIETY OF MECHANICAL ENGINEERS. Manuscript received by the Fluids Engineering Division September 29, 1995; revised manuscript received January 6, 1996. Associate Technical Editor: D. P. Telionis

tations obtained with a commercial package. The agreement of the results and experiments shows that the similarity solution yields accurate results.

II The Governing Equations of a Turbulent Round Jet. The jet is assumed to be axisymmetric and vertical, ensuing into a stagnant fluid of the same density. The experimental data by List (1982) suggest that there is a virtual origin (pole) of the jet, which is taken to be the origin of the coordinate system. The flow field is divided into two regions: The first is the near-jet region ($x < 8d$) where ring vortices have been experimentally observed and the turbulence structure deviates substantially from a Gaussian distribution as shown by Townsend (1976). He asserted that the mean flow in this region is not self-similar. The second region is downstream of the near-jet region ($x > 8d$) where the mean flow is self-similar. In this region, the turbulence fluctuations of the velocity components are anisotropic, with Gaussian distributions.

The mass and momentum conservation equations for an incompressible axisymmetric jet are as follows:

$$\frac{\partial(ur)}{\partial x} + \frac{\partial(vr)}{\partial r} = 0 \qquad (1)$$

and

$$u\frac{\partial u}{\partial x} + v\frac{\partial u}{\partial r} = \frac{1}{r}\frac{\partial}{\partial r}\left(\nu_t r\frac{\partial u}{\partial r}\right) \qquad (2)$$

where u and v are the velocities in the longitudinal and radial directions, respectively. The eddy viscosity, ν_t, is much higher than the kinematic viscosity of the fluid, ν.

The equations for the kinetic energy and dissipation rate (k-ϵ model) are as follows in the cylindrical coordinates:

$$u\frac{\partial k}{\partial x} + v\frac{\partial k}{\partial r} = \frac{1}{\sigma_k r}\frac{\partial}{\partial r}\left(\nu_t r\frac{\partial k}{\partial r}\right) + P - \epsilon \qquad (3)$$

and

$$u\frac{\partial \epsilon}{\partial x} + v\frac{\partial \epsilon}{\partial r} = \frac{1}{\sigma_\epsilon r}\frac{\partial}{\partial r}\left(\nu_t r\frac{\partial \epsilon}{\partial r}\right) + \frac{\epsilon}{k}(C_{\epsilon 1}P - C_{\epsilon 2}\epsilon) \quad (4)$$

where k and ϵ are the turbulent kinetic energy and the dissipation rate, respectively. The rate of turbulent kinetic energy production, P, and the eddy viscosity, ν_t, are given by the usual closure equations.

The boundary conditions for this set of equations are: At the symmetry axis ($r = 0$),

$$\frac{\partial u}{\partial r} = \frac{\partial k}{\partial r} = \frac{\partial \epsilon}{\partial r} = v = 0 \qquad (5)$$

and at the jet edge ($r = r_e$),

$$u = k = \epsilon = 0. \qquad (6)$$

Following the usual method of obtaining similarity solutions for jets, we introduce a dimensionless stream function, F:

$$\Psi(x, \eta) = C_\mu u_0(x) x^2 F(\eta) \qquad (7)$$

with the similarity variable, η, defined as:

$$\eta = \frac{r}{C_\mu^{1/2} x}. \qquad (8)$$

The axial and radial velocities, u and v, are obtained from the derivatives of the stream function and the axial centerline velocity is calculated from the momentum conservation condition:

$$u_0(x) = \frac{u_{00}}{(8C_\mu)^{1/2}(x/D)\sqrt{\int_0^\infty \frac{[F'(\eta)]^2}{\eta}\,d\eta}}. \qquad (9)$$

The kinetic energy and the rate of dissipation functions yield the following dimensionless functions, $G(\eta)$ and $H(\eta)$:

$$\frac{k}{u_0^2} = G(\eta) \qquad (10)$$

and

$$\frac{\epsilon x}{u_0^3} = H(\eta) \qquad (11)$$

When the equations obtained from the similarity condition are substituted in the governing and closure equations, we obtain the following set for the self-similar axisymmetric jet:

$$FF' + \frac{G^2}{H}[\eta F'' - F'] = 0, \qquad (12)$$

$$2F'G + FG' + \frac{1}{\sigma_k}\left[\eta\frac{G^2}{H}G'\right]'$$

$$+ \frac{G^2}{H\eta^3}[\eta^2 F''^2 + F'^2 - 2F'F''\eta] - \eta H = 0, \quad (13)$$

and

$$4F'H + FH' + \frac{1}{\sigma_\epsilon}\left[\eta\frac{G^2}{H}H'\right]'$$

$$+ \frac{C_{\epsilon 1}H}{G\eta^3}\left[\frac{G^2}{H}(\eta^2 F''^2 - 2\eta F''F' + F'^2)\right]$$

$$- C_{\epsilon 2}\frac{H^2}{G}\eta = 0 \quad (14)$$

where the prime (′) denotes derivatives with respect to the similarity variable η. The continuity equation is redundant in this set, because it is automatically satisfied by the choice of the stream function, Ψ. The boundary conditions at the axis of symmetry and the jet edge are:

$$F(0) = G'(0) = H'(0) = F'(0) = 0 \qquad (15)$$

and

$$G(\eta_e) = H(\eta_e) = 0, \qquad (16)$$

respectively.

A glance at equations 12 through 16 of the axisymmetric jet, proves that they are markedly different than the corresponding equations of the radial and plane jets, which were derived by Paullay et al. (1985). It also proves that these equations are coupled and highly nonlinear. This causes stability problems in their numerical solution. In addition, the value of η_e is unknown and needs to be determined by iteration, a task which further complicates the problem. These difficulties are avoided by making use of another transformation, which introduces a new dependent variable, U, and a new independent variable, ξ, as follows:

$$U = F_\xi \frac{H}{G^2\eta} \qquad (17)$$

and

$$\frac{d\eta}{d\xi} = \frac{G^2}{H}\eta. \qquad (18)$$

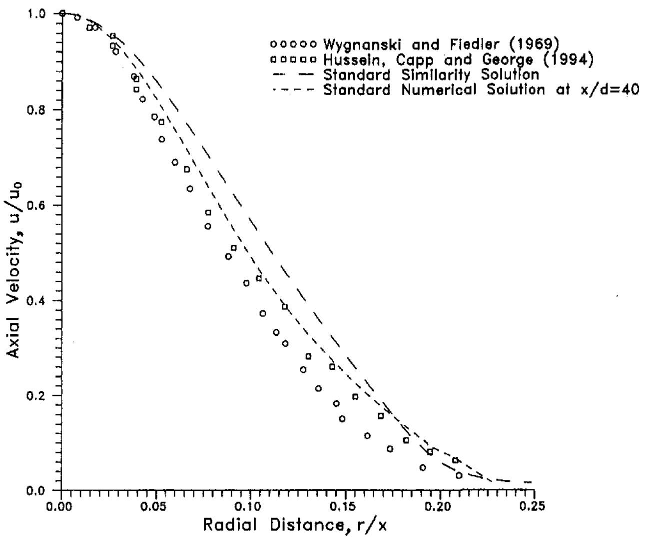

Fig. 1 Radial distribution of axial velocity, u/u_0, obtained with the standard turbulence model

In this case, the subscript ξ denotes an ordinary derivative with respect to this variable.

The boundary condition for Eq. (18) is chosen so that the η to ξ transformation maps $\eta = 0$, the symmetry axis, onto $\xi = 0$. The governing equations of momentum, turbulent kinetic energy and turbulent dissipation function are, hence, reduced to the following set, which is simpler and more convenient to solve numerically:

$$FU + U_\xi - U\frac{G^2}{H} = 0, \qquad (19)$$

$$2GF_\xi + FG_\xi + \frac{G_{\xi\xi}}{\sigma_k} + \frac{F^2U^2}{\eta^2} - \frac{F_\xi H\eta}{U} = 0, \qquad (20)$$

and

$$4F_\xi H + FH_\xi + \frac{H_{\xi\xi}}{\sigma_\epsilon} + \frac{H}{G}\left[\frac{C_{\epsilon1}F^2U^2}{\eta^2} - G^2C_{\epsilon2}\eta^2\right] = 0. \qquad (21)$$

The double subscript ξ denotes the second ordinary derivative with respect to ξ. The transformed boundary conditions for the symmetry axis $\xi = 0$ are:

$$F(0) = G_\xi(0) = H_\xi(0) = U(0) = 0 \qquad (22)$$

and for the jet edge, which is now transformed to $\xi = \infty$:

$$G(\infty) = H(\infty) = 0 \qquad (23)$$

III Results

The advantage of the last transformation (Eqs. (17) and (18)) is that the velocity function U is not multiplied by its derivatives and the jet edge is mapped onto a line at infinity. The transformation renders the system less nonlinear and more robust. We easily solved the system of the resulting equations, by using a Runge-Kutta fourth-order numerical scheme and the standard parameters of the k-ϵ model: $C_\mu = 0.09$, $C_{\epsilon1} = 1.44$, $C_{\epsilon2} = 1.92$, $\sigma_k = 1.0$, and $\sigma_\epsilon = 1.3$. In this case, the results of the similarity solution for the dimensionless axial velocity are shown in Fig. 1, together with the experimental data of Wygnanski and Fiedler, 1969 and Hussein et al., 1994. Also depicted is a numerical solution obtained from a commercial CFD code (Fluent, version 4.2). It is obvious, that the similarity solution with the standard turbulence constants, overestimates the width of the jet. The results of the Fluent code, show better agreement with the sets of data.

Since it is known that the k-ϵ model with the standard set of model constants does not agree well with the experimental data, we have modified the model constants. By relating our results to the data for the confined jet (Wygnanski and Fiedler, 1969), we obtained results for what will be called similarity solution I; and by comparing with the data of the free jet (Hussein et al., 1994) we obtained the results of similarity solution II. The model constants used for the similarity solution I are:

$$C_\mu = 0.09, \quad C_{\epsilon1} = 1.45, \quad C_{\epsilon2} = 1.84,$$
$$\sigma_k = 1.16, \quad \sigma_\epsilon = 0.79 \qquad (24)$$

and for similarity solution II:

$$C_\mu = 0.09, \quad C_{\epsilon1} = 1.45, \quad C_{\epsilon2} = 1.84,$$
$$\sigma_k = 0.849, \quad \sigma_\epsilon = 0.775 \qquad (25)$$

Because the Fluent code consumes a considerable amount of CPU time, it was impossible to perform optimization studies with it, and obtain the model constants, which best agree with the data. For this reason, we used the same constants as with the similarity solution II. Because of this, one should not draw conclusions about the relative merits of the numerical versus the similarity solutions. In the figures that follow, we present the Fluent code results for reference only.

The profile of the dimensionless axial velocity u/u_0, with the optimized model constants, is depicted in Fig. 2. As expected, the results of the similarity solutions compare well with the experimental data of Wygnanski and Fiedler as well as those of Hussein et al. (1994). Similarity Solution I deviates from the data far from the centerline (further than $r/x = 0.1$). We believe that this is due to the difference of the turbulence structure and the inability of the k-ϵ model to simulate eddies of markedly different sizes with one set of parameters. Similarity solution II offers better agreement with the longitudinal velocity data at $r/x > 0.1$.

Figure 3 shows the dimensionless radial velocity, v/u_0. It is obvious that the similarity solution I agrees with the experimental data of Wygnanski and Fiedler for radial distances r/x less than 0.10. The similarity solution II compares better with the

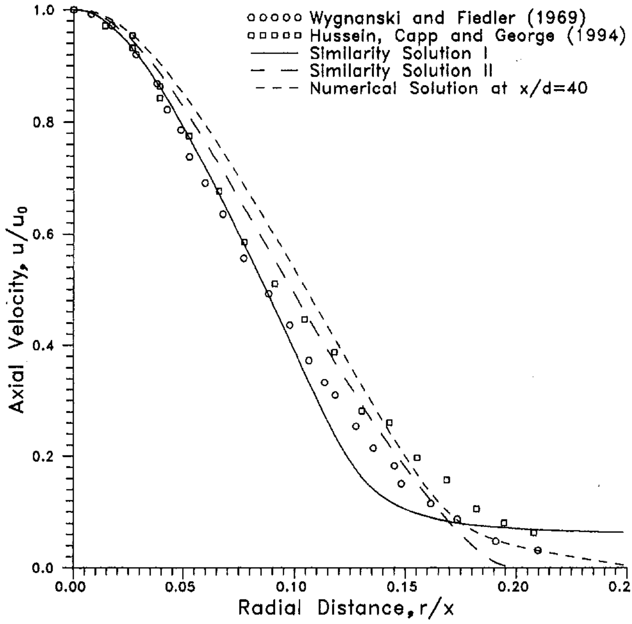

Fig. 2 Radial distribution of axial velocity, u/u_0, obtained with the optimized turbulence model

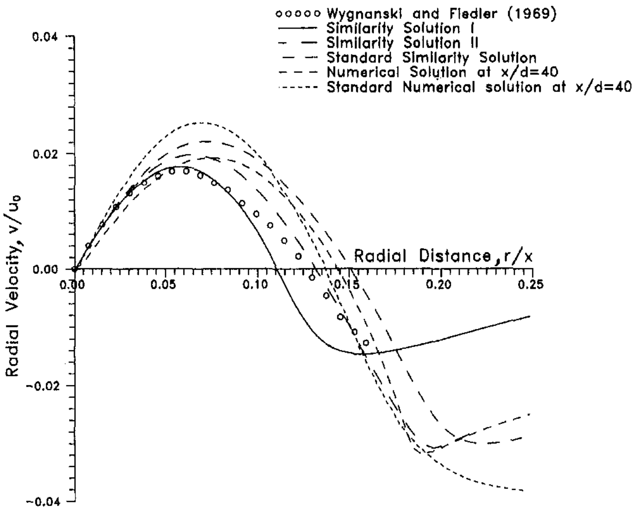

Fig. 3 Radial velocity, v/u_0, obtained with the optimized turbulence model

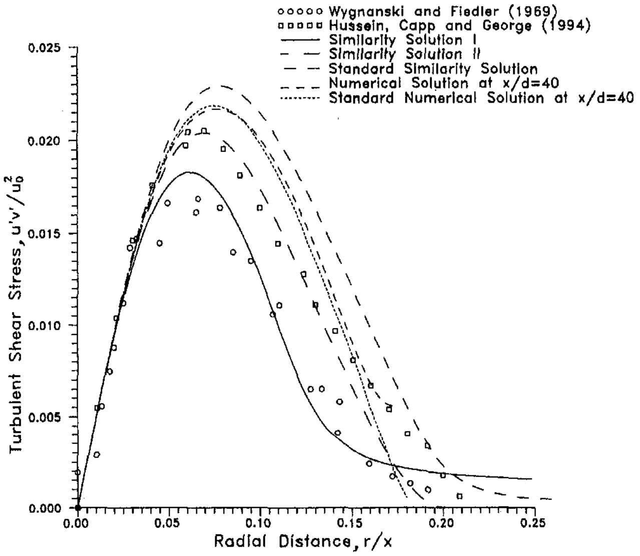

Fig. 4 Radial distribution of turbulent shear stress, $u'v'/u_0^2$, obtained with the optimized turbulence model

data of Hussein et al., 1994, up to $r/x = 0.18$. At the edge of the jet, the results are mixed and any agreement with the similarity or the numerical solutions appears to be coincidental.

The radial profiles of the turbulent shear stress are shown in Fig. 4. The shear stress results of similarity solution I show a close agreement to the experimental data of Wygnanski and Fiedler at the core of the jet as well as in the far field, up to a radial distance $r/x = 0.2$. The similarity solution II agrees better with the experimental data of Hussein et al. (1994).

IV Conclusions

A similarity method has been developed to transform the partial differential equations of a round axisymmetric jet onto ordinary differential equations. The k-ϵ turbulence model equations are also transformed. The results obtained from the optimized similarity solutions agree well with available experimental data of the velocity and the shear stress profiles.

Acknowledgments

The authors are grateful for the partial support provided for this work by grants from NASA, LEQSF, and DOE (through CBR) to Tulane University.

References

Abramovich, G. N., 1963, *The Theory of Turbulent Jets*, MIT Press, Cambridge MA.

George, W. K., 1989, "The Self-Preservation of Turbulent Flows and its Relation to Initial Conditions and Coherent Structures," *Advances in Turbulence*, W. K. George and R.E.A. Arndt, eds., Hemisphere, pp. 39–72.

Hussein J. H., Capp, S. P., and George, W. K., 1994, "Velocity Measurements in a High-Reynolds-Number, Momentum Conserving, Axisymmetric, Turbulent Jet," *Journal of Fluid Mechanics*, Vol. 258, pp. 31–75.

Kumar, S., Nikitopoulos, D. N., and Michaelides, E. E., 1989, "The Effect of Bubbles on the Turbulence of a Liquid Jet," *Experiments in Fluids*, Vol. 7, pp. 484–492.

List, E. J., 1982, *Mechanics of Turbulent Buoyant Jets and Plumes in Turbulent buoyant Jets and Plumes*, W. Rodi, ed., Pergamon Press, Oxford.

Paullay, A. J., Melnik, R. E., Rubel, A., Rudman, S., and Siclari, M. J., 1985, "Similarity Solution for Plane and Radial Jets Using a k-ϵ Turbulent Model," ASME JOURNAL OF FLUIDS ENGINEERING, Vol. 107, pp. 79–85.

So, R. M. C., 1986, "On Similarity Solutions for Turbulent and Heated Round Jets," *ZAMP*, Vol. 37, pp. 625–631.

Townsend, A. A., 1976, *The Structure of Turbulent Shear Flow*, Cambridge Univ. Press.

Wollmers, H. and Rotta, J. C., 1977, "Similar Solutions of the Mean Velocity, Turbulent Energy and Length Scale Equations," *AIAA Journal*, Vol. 15, No. 5, pp. 714–720.

Wygnanski, I. and Fiedler, H. E., 1969, "Some Measurements in the Self-Preserving Jet," *Journal of Fluid Mechanics*, Vol. 38, pp. 577–612.

Flow Measurements Near a Reynolds Ridge

A. Warncke,[1] M. Gharib,[1] and T. Roesgen[2]

Introduction

The Reynolds ridge is a well-known phenomenon first observed in 1854 by Henry David Thoreau. It was then rediscovered by Langton in 1872, but Reynolds was the first to recognize that the surface tension difference was the physical mechanism behind its formation and saw the equality between the case of a spreading film and that of a stagnant film met by oncoming flow. However, it wasn't until McCutchen in 1970 that the prediction of a boundary layer forming beneath the film was introduced as the cause of the surface deformation rise ahead of the film due to the retardation of the flow. The first quantitative theory of the ridge was formed by Harper and Dixon (1974), who stated that the surface tension gradient balances the viscous shear stress generated in the boundary layer. Experimental studies of the ridge so far include Schlieren visualizations by Sellin (1968) as well as by Scott (1982) who measured the surface slope across the ridge and found good comparisons between the theoretical results of Harper and Dixon. Finally, it was Scott who recognized that even at very low levels of surface contamination the Reynolds ridge is found to exist.

The more recent interest in the study of the Reynolds ridge is its application to studying flows on the ocean surface. Naturally occurring soluble and insoluble surfactants abound on the ocean surface. Thus, a study of the effect of surfactant gradients and the consequent production of vorticity in the vicinity of a Reynolds ridge, can provide insight into the overall understanding of the air/water interface of the ocean surface.

---

[1] Graduate Aeronautical Laboratories, California Institute of Technology, Pasadena, CA 91125.

[2] Section WGO ESA-ESTEC, Postbus 299 Keplerlan 1 NL-2200 AG, Noordwijk, Netherlands.

Contributed by the Fluids Engineering Division of THE AMERICAN SOCIETY OF MECHANICAL ENGINEERS. Manuscript received by the Fluids Engineering Division September 12, 1995; revised manuscript received April 16, 1996. Associate Technical Editor: D. P. Telionis.

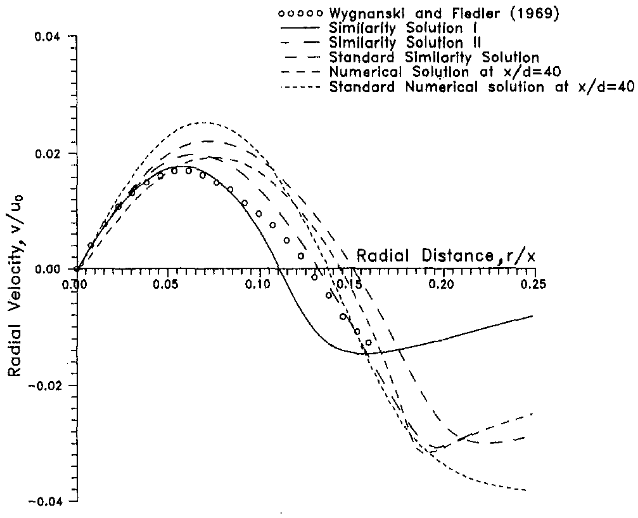

Fig. 3 Radial velocity, v/u_0, obtained with the optimized turbulence model

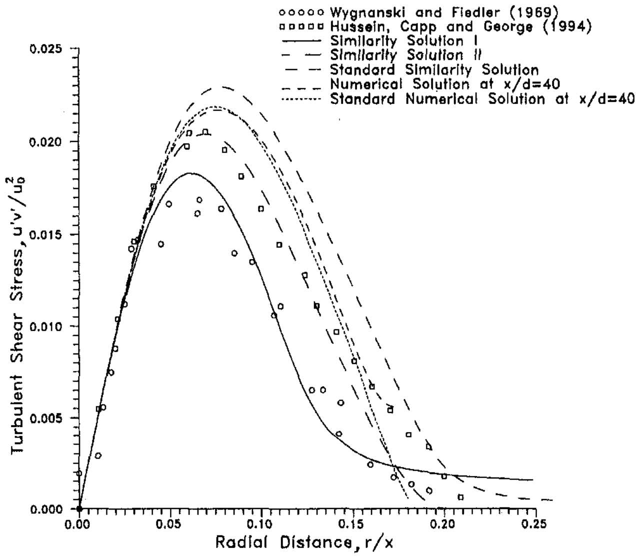

Fig. 4 Radial distribution of turbulent shear stress, $u'v'/u_0^2$, obtained with the optimized turbulence model

data of Hussein et al., 1994, up to $r/x = 0.18$. At the edge of the jet, the results are mixed and any agreement with the similarity or the numerical solutions appears to be coincidental.

The radial profiles of the turbulent shear stress are shown in Fig. 4. The shear stress results of similarity solution I show a close agreement to the experimental data of Wygnanski and Fiedler at the core of the jet as well as in the far field, up to a radial distance $r/x = 0.2$. The similarity solution II agrees better with the experimental data of Hussein et al. (1994).

IV Conclusions

A similarity method has been developed to transform the partial differential equations of a round axisymmetric jet onto ordinary differential equations. The k-ϵ turbulence model equations are also transformed. The results obtained from the optimized similarity solutions agree well with available experimental data of the velocity and the shear stress profiles.

Acknowledgments

The authors are grateful for the partial support provided for this work by grants from NASA, LEQSF, and DOE (through CBR) to Tulane University.

References

Abramovich, G. N., 1963, *The Theory of Turbulent Jets*, MIT Press, Cambridge MA.

George, W. K., 1989, "The Self-Preservation of Turbulent Flows and its Relation to Initial Conditions and Coherent Structures," *Advances in Turbulence*, W. K. George and R.E.A. Arndt, eds., Hemisphere, pp. 39–72.

Hussein J. H., Capp, S. P., and George, W. K., 1994, "Velocity Measurements in a High-Reynolds-Number, Momentum Conserving, Axisymmetric, Turbulent Jet," *Journal of Fluid Mechanics*, Vol. 258, pp. 31–75.

Kumar, S., Nikitopoulos, D. N., and Michaelides, E. E., 1989, "The Effect of Bubbles on the Turbulence of a Liquid Jet," *Experiments in Fluids*, Vol. 7, pp. 484–492.

List, E. J., 1982, *Mechanics of Turbulent Buoyant Jets and Plumes in Turbulent buoyant Jets and Plumes*, W. Rodi, ed., Pergamon Press, Oxford.

Paullay, A. J., Melnik, R. E., Rubel, A., Rudman, S., and Siclari, M. J., 1985, "Similarity Solution for Plane and Radial Jets Using a k-ϵ Turbulent Model," ASME JOURNAL OF FLUIDS ENGINEERING, Vol. 107, pp. 79–85.

So, R. M. C., 1986, "On Similarity Solutions for Turbulent and Heated Round Jets," *ZAMP*, Vol. 37, pp. 625–631.

Townsend, A. A., 1976, *The Structure of Turbulent Shear Flow*, Cambridge Univ. Press.

Wollmers, H. and Rotta, J. C., 1977, "Similar Solutions of the Mean Velocity, Turbulent Energy and Length Scale Equations," *AIAA Journal*, Vol. 15, No. 5, pp. 714–720.

Wygnanski, I. and Fiedler, H. E., 1969, "Some Measurements in the Self-Preserving Jet," *Journal of Fluid Mechanics*, Vol. 38, pp. 577–612.

Flow Measurements Near a Reynolds Ridge

A. Warncke,[1] M. Gharib,[1] and T. Roesgen[2]

Introduction

The Reynolds ridge is a well-known phenomenon first observed in 1854 by Henry David Thoreau. It was then rediscovered by Langton in 1872, but Reynolds was the first to recognize that the surface tension difference was the physical mechanism behind its formation and saw the equality between the case of a spreading film and that of a stagnant film met by oncoming flow. However, it wasn't until McCutchen in 1970 that the prediction of a boundary layer forming beneath the film was introduced as the cause of the surface deformation rise ahead of the film due to the retardation of the flow. The first quantitative theory of the ridge was formed by Harper and Dixon (1974), who stated that the surface tension gradient balances the viscous shear stress generated in the boundary layer. Experimental studies of the ridge so far include Schlieren visualizations by Sellin (1968) as well as by Scott (1982) who measured the surface slope across the ridge and found good comparisons between the theoretical results of Harper and Dixon. Finally, it was Scott who recognized that even at very low levels of surface contamination the Reynolds ridge is found to exist.

The more recent interest in the study of the Reynolds ridge is its application to studying flows on the ocean surface. Naturally occurring soluble and insoluble surfactants abound on the ocean surface. Thus, a study of the effect of surfactant gradients and the consequent production of vorticity in the vicinity of a Reynolds ridge, can provide insight into the overall understanding of the air/water interface of the ocean surface.

---

[1] Graduate Aeronautical Laboratories, California Institute of Technology, Pasadena, CA 91125.

[2] Section WGO ESA-ESTEC, Postbus 299 Keplerlan 1 NL-2200 AG, Noordwijk, Netherlands.

Contributed by the Fluids Engineering Division of THE AMERICAN SOCIETY OF MECHANICAL ENGINEERS. Manuscript received by the Fluids Engineering Division September 12, 1995; revised manuscript received April 16, 1996. Associate Technical Editor: D. P. Telionis.

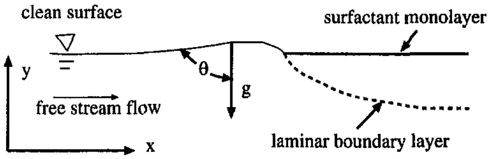

Fig. 1 Flow schematic near a Reynolds ridge

Theory

The equation for surface parallel vorticity, as derived from Lugt (1987, 1988), Lundgren (1988), and shown by Gharib and Weigand (1995), in a two-dimensional curvilinear coordinate system is:

$$\omega_z = -\frac{\tau_{\text{Air}}}{\mu} - \frac{1}{\mu}\frac{\partial \sigma}{\partial s} - 2\frac{u_s}{R} + 2\frac{\partial u_r}{\partial s} \qquad (1)$$

where s is the surface tangential coordinate, r is the surface normal coordinate, z is the coordinate normal to the two dimensional plane defined by r and s, R is the radius of curvature of the free surface, σ is the surface tension, and the shear force due to air is included but most often assumed negligible. From this equation it is obvious that the surface tension gradient plays an important role in the boundary condition at an interface. It will be shown how this boundary condition results in a vorticity flux at the free surface.

So far, as stated above, it is understood that the physical mechanism for the free surface elevation at the leading edge of a surfactant monolayer is due to the retardation of flow within the boundary layer beneath the film. However, this deceleration of the flow ahead of the film, due to the presence of a surface tension gradient, provides a source of vorticity at the free surface. For the case experimentally tested, the Reynolds ridge is stationary in front of a stagnant film met by oncoming flow (see Fig. 1). (Note in Fig. 1 x and y are defined as the surface parallel and normal coordinates respectively to correspond with the presentation of the results.) For this steady-state case, where the normal component of velocity at the free surface is inherently zero and the pressure at the free surface is constant, the equation for the vorticity flux at a free surface as derived by Rood (1995) and Gharib (1992) simplifies to:

$$v\left(\frac{\partial \omega_z}{\partial r}\right)_{r=0} \cong -u_s\frac{\partial u_s}{\partial s} - g\cos\theta \qquad (2)$$

such that θ is the angle between the free surface and g, the direction of gravity. Thus a positive value of the right hand side implies a positive flux of positive vorticity into the flow at the free surface. Also, for this case, it is obvious that the vorticity flux at the free surface can be attributed to two sources: (1) the deceleration of the flow at the free surface and (2) the local slope of the free surface due to a change of θ from ninety degrees. Thus, experimentally measuring these quantities will indicate the dominating source of vorticity generated at the free surface in the presence of a Reynolds ridge.

Experimental Setup

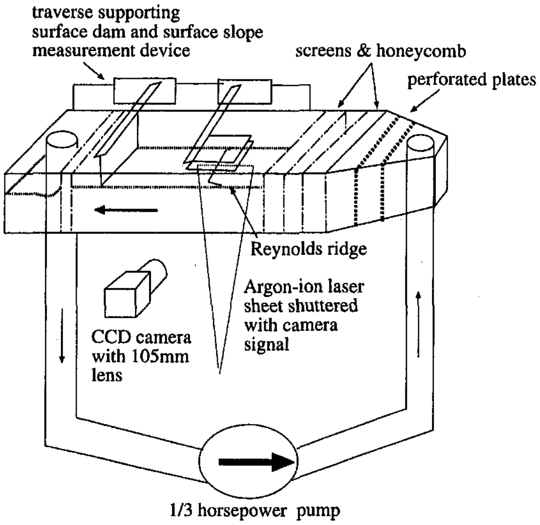

Fig. 2 Experimental setup

A small free surface water tunnel with a 4 in. × 4 in. × 12-in. long test section, as shown in Fig. 2, was constructed to provide the formation of a Reynolds ridge for experimental study. For the results presented, Sodium Dodecyl Sulfate (SDS), a soluble surfactant, was used as a surface contaminant to form the surfactant monolayer behind the Reynolds ridge. First, the surface slope was measured using a new technique developed by Roesgen (1996). In short, it involves measuring the displacement of collimated light, as it travels from below the free surface, through the use of an array of microlenses. By imaging the focal plane of the lenslet array and measuring the displacement of the focal points, one can measure the slope of the free surface at each focal point. Simultaneously, a separate experiment was performed to acquire the Digital Particle Image Velocimetry (DPIV) images of the flow. A CCD camera was set up focusing on a small region of 0.5 cm × 0.3 cm. An argon-ion laser sheet was then shuttered with the camera signal to provide two instantaneous digital images with a known time difference between them. These images were then processed using the DPIV technique as presented by Willert and Gharib (1991) to provide velocity and vorticity fields of the flow.

Results

First, the free surface slope across the Reynolds ridge was measured. Figure 3 displays the data integrated to show the free surface deformation or height profile. This data is found to agree qualitatively with the slope profiles measured by Scott (1982). The velocity field in the vicinity of a Reynolds ridge, displaying the boundary layer beneath the surfactant film, for a free stream flow of 12 cm/s is shown in Fig. 4. (Note that the free surface is located at the top edge of the plots in both Figs. 4 and 6.) Extrapolated from this data, velocity profiles within the boundary layer at various downstream distances are presented in Figure 5. Notice the slight increase in steepness of the slope of the

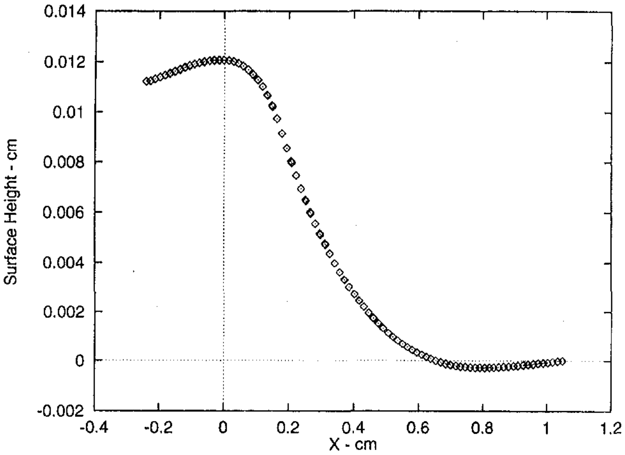

Fig. 3 Free surface height profile integrated from the slope measurement (measurement error <5 percent)

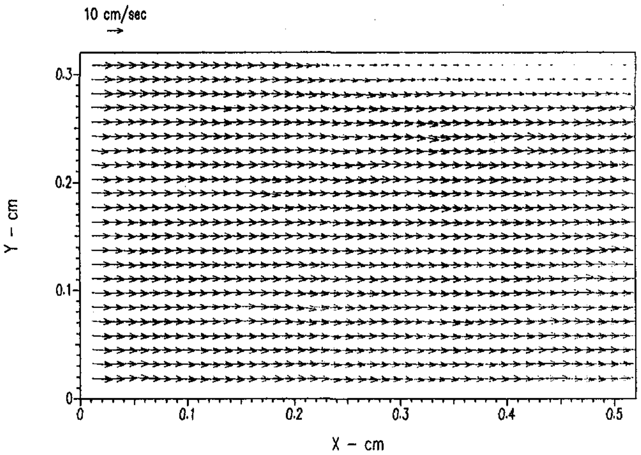

Fig. 4 Velocity field in the vicinity of a Reynolds ridge (measurement error <5 percent)

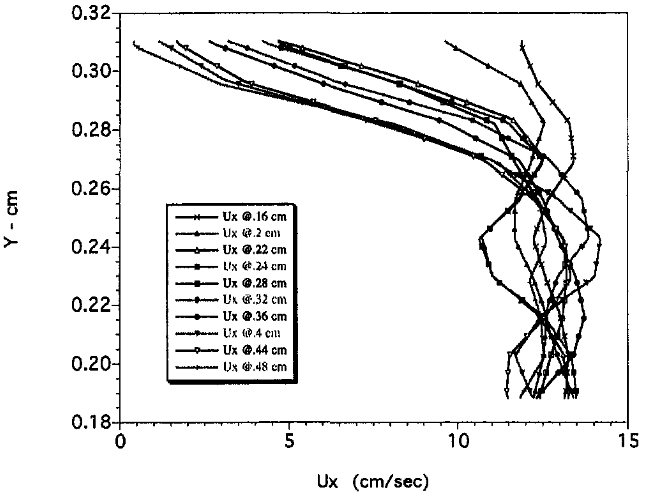

Fig. 5 Boundary layer profiles at various downstream distances (measurement error <5 percent)

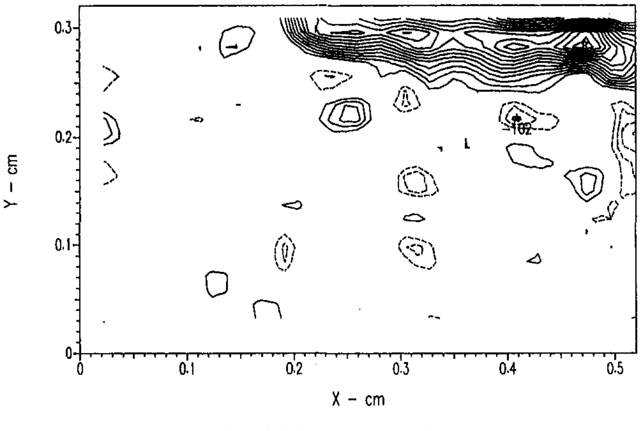

Fig. 6 Vorticity field in the vicinity of a Reynolds ridge (measurement error <10 percent)

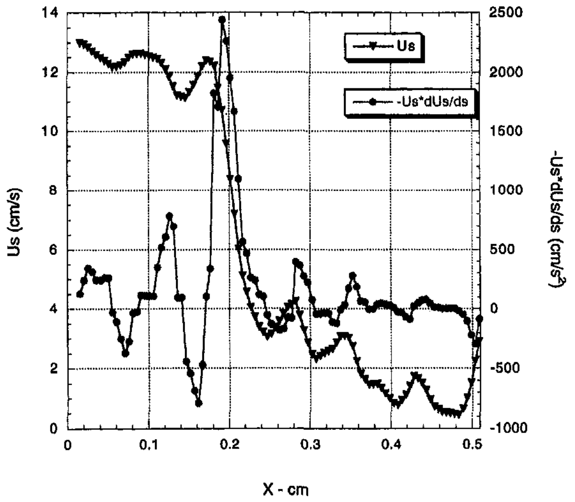

Fig. 7 Velocity and deceleration term (from Eq. (2)) profiles at the free surface (measurement error <5 percent)

profile near the free surface farther downstream. Other data obtained shows this trend to continue farther downstream of the ridge. In addition, the vorticity field calculated from the velocity data is shown in Fig. 6. Also extracted from the velocity data was the velocity profile along the free surface as shown in Fig. 7. From this, the deceleration term of Eq. (2) was calculated and is also presented in Fig. 7. The large fluctuation in the deceleration term upstream of the boundary layer is caused by to small fluctuations in the high velocity in this region. Still, one can see the large vorticity flux that occurs at the free surface because of the drastic drop in velocity that occurs on the ridge. Note how the flow initially decelerates ahead of the boundary layer but the peak in vorticity flux corresponds exactly to the point where the boundary layer begins.

Conclusions

From the above results, the magnitudes of the two terms in Eq. (2) may be estimated. From the theoretical calculations of the free surface profile by Harper and Dixon (1974), as well as the experimental results of Scott (1982) and those presented in Fig. 3, one can see that the angle θ over the deformation profile remains small such that the order of magnitude of the $g \cos \theta$ term is one or less. However, looking at Fig. 7, we see that the deceleration term reaches an order of magnitude of four. Therefore, the dominant source of vorticity in the vicinity of a Reynolds ridge is the deceleration of the flow at the free surface as it approaches the stagnant film. Notice too, it is in a small region of about 0.5 mm that this large vorticity flux occurs at the free surface. In other words it must be within the region where the surface tension gradient is located, as ahead of the film the water is considered clean and within the film itself no large gradients of surface tension subsist. It is interesting to note as well that this region occurs in the vicinity of the inflection point of the height profile of the ridge. It is at this point on the free surface as well that a slight downward component is detected in the velocity field. Thus all flow, but that right at the free surface moves down into the boundary layer beneath the film, while just at the free surface the flow is decelerated accounting for the change in curvature of the free surface. The vorticity generated by this deceleration is then convected downstream to form the boundary layer observed.

Also, the boundary layer profiles show evidence of approaching very small shear stress at the film as exhibited by the steepening of the boundary layer profiles farther downstream of the ridge. This agrees with the fact that there is no longer a large surface tension gradient at the free surface in the film to support that shear stress in the flow. These profiles exhibit a shape similar to those found near a flat plate in the presence of a pressure gradient. In further experiments we hope to gain a better understanding of this free surface boundary layer.

In addition, we plan to acquire simultaneous velocity field, free surface profile, and surface tension measurements near the

Reynolds ridge which will provide even more insight into the unique nature of this flow. But so far it has been determined that it is the boundary condition of the surface tension gradient at the free surface in the vicinity of a Reynolds ridge which causes the flow to dynamically conform, with a rapid deceleration over a small region, resulting in a large vorticity flux at the free surface.

Acknowledgments

We would like to thank Dana Dabiri for his help and advice while performing this work. This work was supported by ONR contract# N00014-94-1-0596. The National Science Foundation, and the Zonta International Amelia Earhart Fellowship Award have supported first author Amy Warncke towards her graduate work.

References

Gharib, M., 1992, "On Some Aspects of Near Surface Vortices,"

Gharib, M., and A. Weigand, 1995, "Experimental Studies of Vortex Disconnection and Connection at a Free Surface," submitted to *Journal of Fluid Mechanics.*

Harper, J. F. and Dixon, J. N., 1974, "The Leading edge of a Surface Film on Contaminated Flowing Water," *Proc. 5th Australian Conf. on Hydraulics and Fluid Mech.*, Christchurch, New Zealand, pp. 499–505.

Lugt, H. J., 1987, "Local Flow Properties at a Viscous Free Surface," *Physics of Fluids*, vol. 30, pp. 3647–3652.

Lugt, H. J., 1988, "Fundamental Viscous Flow Properties at a Free Surface," *Fluid Dynamics Transactions*, vol. 14, pp. 1–20.

Lundgren, T. S., 1988, "A Free Surface Vortex Method with Weak Viscous Effects," Mathematical Aspects of Vortex Dynamics," *Proceedings of the Workshop on Mathematical Aspects of Vortex Dynamics*, Leesburg, VA, pp. 68–79.

Rood, E. P., 1995, "Free-Surface Vorticity," Chapter 17 in *Fluid Vortices*, S. Green, ed., Kluwer Academic Publishing, Norwell, MA.

Roesgen, T., "Dynamic Surface Slope Measurements Using Microlens Arrays," to be published in *Experiment of Fluids.*

Sellin, R. H. J., 1968, *Nature*, Vol. 217, pp. 536–538.

Scott, S. C., 1982, "Flow Beneath a Stagnant Film on Water: the Reynolds ridge," *Journal of Fluid Mechanics*, vol. 116, pp. 283–296.

Willert, C., and M. Gharib, 1991, "Digital Particle Image Velocimetry," *Experiment in Fluids*, Vol. 10, pp. 181–183.

A Novel Pump for MEMS Applications

Mihir Sen,[1] Daniel Wajerski,[1] and Mohamed Gad-el-Hak[1]

We present a novel approach for pumping fluids in micromechanical applications at extremely low Reynolds numbers. It is based on the rotation of a cylinder placed asymmetrically in a narrow duct; the differential viscous resistance between the small and large gaps causes a net flow along the channel. We report on experiments using glycerin and several cm-scale prisms having circular, square, and rectangular cross-sections. The Reynolds number, based on cylinder size and angular velocity, varies in the range of 0.01–10. The flow is visualized using tracer particles. The flow generated depends on the geometrical parameters, but is proportional to the angular velocity of the cylinder. An average flow velocity that is about ten percent of the surface speed of the cylinder has been obtained.

Manufacturing processes that can create extremely small machines have been developed in recent years. Motors, electrostatic actuators, pneumatic actuators, valves, gears, and tweezers of about 10 μm size have been fabricated. These have been used as sensors for pressure, temperature, velocity, mass flow, or sound, and as actuators for linear and angular motions. Current usage ranges from airbags to blood analysis (O'Connor, 1992). There is considerable work under way to include other applications, one example being the micro-steam engine described by Lipkin (1993). Many of these new applications will need fluid to be pumped in a duct; at such small scales this is a challenge.

There have been several studies of microfabricated pumps. Some of them use nonmechanical effects. Ion-drag is used in electrohydrodynamic pumps (Bart et al., 1990; Richter et al., 1991; Fuhr et al., 1992); these rely on the electrical properties of the fluid and are thus not suitable for many applications. Valveless pumping by ultrasound has also been proposed (Moroney et al., 1991), but produces very little pressure difference.

It is important to emphasize that mechanical pumps based on conventional centrifugal or axial turbomachinery will not work at micromachine scales where the Reynolds numbers are typically small. Centrifugal forces are negligible and, furthermore, the Kutta condition through which lift is normally generated is invalid when inertial forces are vanishingly small. In general there are three ways in which mechanical micropumps can work:

(*a*) *Positive-Displacement Pumps.* These are mechanical pumps with a membrane or diaphragm actuated in a reciprocating mode and with unidirectional inlet and outlet valves. They work on the same physical principle as their larger cousins. Micropumps with piezoelectric actuators have been fabricated (Van Lintel et al., 1988; Esashi et al., 1989; Smits, 1990). Other actuators, such as thermopneumatic, electrostatic, electromagnetic or bimetallic, can be used. These exceedingly minute positive-displacement pumps require even smaller valves, seals and mechanisms, a not-too-trivial micromanufacturing challenge. In addition, there are long-term problems associated with wear or clogging and consequent leaking around valves. The pumping capacity of these pumps is also limited by the small displacement and frequency involved. Gear pumps are a different kind of positive-displacement device.

(*b*) *Continuous, Parallel-Axis Rotary Pumps.* A screw-type, three-dimensional device for low Reynolds numbers was proposed by Taylor (1972) for propulsion purposes and shown in his seminal film. It has an axis of rotation parallel to the flow direction implying that the powering motor must be submerged in the flow, the flow turned through an angle, or that complicated gearing would be needed.

(*c*) *Continuous, Transverse-Axis Rotary Pumps.* This is the class of machines that we propose here. We assert that a rotating body, asymmetrically placed within a duct, will produce a net flow due to viscous action. The axis of rotation can be perpendicular to the flow direction and the cylinder can thus be easily powered from outside a duct. A related viscous-flow pump was designed by Odell and Kovasznay (1971) for a water channel with density stratification. However, their design operates at a much higher Reynolds number and is too complicated for microfabrication.

Fluid flow at the micromachine level is complicated by issues such as interfacial forces, slip-flow and Knudsen number effects. To develop an operational viscous-flow micropump one must first demonstrate its working at the macroscale where these special effects are not important. Our purpose here is to show experimentally that viscous forces can indeed be used to pump fluid at low Reynolds numbers. Reynolds numbers representative of micromachine applications in air or water can be obtained with cm-size cylinders and with glycerin as the working

---

[1] Professor, Research Assistant, and Professor, respectively, Department of Aerospace and Mechanical Engineering, University of Notre Dame, Notre Dame, IN 46556. Professor Sen is a Mem. ASME; Professor Gad-el-Hak is a Fellow ASME.

Contributed by the Fluids Engineering Division of THE AMERICAN SOCIETY OF MECHANICAL ENGINEERS. Manuscript received by the Fluids Engineering Division February 26, 1996; revised manuscript received April 24, 1996. Associate Technical Editor: D. P. Telionis.

Reynolds ridge which will provide even more insight into the unique nature of this flow. But so far it has been determined that it is the boundary condition of the surface tension gradient at the free surface in the vicinity of a Reynolds ridge which causes the flow to dynamically conform, with a rapid deceleration over a small region, resulting in a large vorticity flux at the free surface.

Acknowledgments

We would like to thank Dana Dabiri for his help and advice while performing this work. This work was supported by ONR contract# N00014-94-1-0596. The National Science Foundation, and the Zonta International Amelia Earhart Fellowship Award have supported first author Amy Warncke towards her graduate work.

References

Gharib, M., 1992, "On Some Aspects of Near Surface Vortices,"

Gharib, M., and A. Weigand, 1995, "Experimental Studies of Vortex Disconnection and Connection at a Free Surface," submitted to *Journal of Fluid Mechanics.*

Harper, J. F. and Dixon, J. N., 1974, "The Leading edge of a Surface Film on Contaminated Flowing Water," *Proc. 5th Australian Conf. on Hydraulics and Fluid Mech.*, Christchurch, New Zealand, pp. 499–505.

Lugt, H. J., 1987, "Local Flow Properties at a Viscous Free Surface," *Physics of Fluids*, vol. 30, pp. 3647–3652.

Lugt, H. J., 1988, "Fundamental Viscous Flow Properties at a Free Surface," *Fluid Dynamics Transactions*, vol. 14, pp. 1–20.

Lundgren, T. S., 1988, "A Free Surface Vortex Method with Weak Viscous Effects," Mathematical Aspects of Vortex Dynamics," *Proceedings of the Workshop on Mathematical Aspects of Vortex Dynamics*, Leesburg, VA, pp. 68–79.

Rood, E. P., 1995, "Free-Surface Vorticity," Chapter 17 in *Fluid Vortices*, S. Green, ed., Kluwer Academic Publishing, Norwell, MA.

Roesgen, T., "Dynamic Surface Slope Measurements Using Microlens Arrays," to be published in *Experiment of Fluids.*

Sellin, R. H. J., 1968, *Nature*, Vol. 217, pp. 536–538.

Scott, S. C., 1982, "Flow Beneath a Stagnant Film on Water: the Reynolds ridge," *Journal of Fluid Mechanics*, vol. 116, pp. 283–296.

Willert, C., and M. Gharib, 1991, "Digital Particle Image Velocimetry," *Experiment in Fluids*, Vol. 10, pp. 181–183.

A Novel Pump for MEMS Applications

Mihir Sen,[1] Daniel Wajerski,[1] and Mohamed Gad-el-Hak[1]

We present a novel approach for pumping fluids in micromechanical applications at extremely low Reynolds numbers. It is based on the rotation of a cylinder placed asymmetrically in a narrow duct; the differential viscous resistance between the small and large gaps causes a net flow along the channel. We report on experiments using glycerin and several cm-scale prisms having circular, square, and rectangular cross-sections. The Reynolds number, based on cylinder size and angular velocity, varies in the range of 0.01–10. The flow is visualized using tracer particles. The flow generated depends on the geometrical parameters, but is proportional to the angular velocity of the cylinder. An average flow velocity that is about ten percent of the surface speed of the cylinder has been obtained.

Manufacturing processes that can create extremely small machines have been developed in recent years. Motors, electrostatic actuators, pneumatic actuators, valves, gears, and tweezers of about 10 μm size have been fabricated. These have been used as sensors for pressure, temperature, velocity, mass flow, or sound, and as actuators for linear and angular motions. Current usage ranges from airbags to blood analysis (O'Connor, 1992). There is considerable work under way to include other applications, one example being the micro-steam engine described by Lipkin (1993). Many of these new applications will need fluid to be pumped in a duct; at such small scales this is a challenge.

There have been several studies of microfabricated pumps. Some of them use nonmechanical effects. Ion-drag is used in electrohydrodynamic pumps (Bart et al., 1990; Richter et al., 1991; Fuhr et al., 1992); these rely on the electrical properties of the fluid and are thus not suitable for many applications. Valveless pumping by ultrasound has also been proposed (Moroney et al., 1991), but produces very little pressure difference.

It is important to emphasize that mechanical pumps based on conventional centrifugal or axial turbomachinery will not work at micromachine scales where the Reynolds numbers are typically small. Centrifugal forces are negligible and, furthermore, the Kutta condition through which lift is normally generated is invalid when inertial forces are vanishingly small. In general there are three ways in which mechanical micropumps can work:

(*a*) *Positive-Displacement Pumps.* These are mechanical pumps with a membrane or diaphragm actuated in a reciprocating mode and with unidirectional inlet and outlet valves. They work on the same physical principle as their larger cousins. Micropumps with piezoelectric actuators have been fabricated (Van Lintel et al., 1988; Esashi et al., 1989; Smits, 1990). Other actuators, such as thermopneumatic, electrostatic, electromagnetic or bimetallic, can be used. These exceedingly minute positive-displacement pumps require even smaller valves, seals and mechanisms, a not-too-trivial micromanufacturing challenge. In addition, there are long-term problems associated with wear or clogging and consequent leaking around valves. The pumping capacity of these pumps is also limited by the small displacement and frequency involved. Gear pumps are a different kind of positive-displacement device.

(*b*) *Continuous, Parallel-Axis Rotary Pumps.* A screw-type, three-dimensional device for low Reynolds numbers was proposed by Taylor (1972) for propulsion purposes and shown in his seminal film. It has an axis of rotation parallel to the flow direction implying that the powering motor must be submerged in the flow, the flow turned through an angle, or that complicated gearing would be needed.

(*c*) *Continuous, Transverse-Axis Rotary Pumps.* This is the class of machines that we propose here. We assert that a rotating body, asymmetrically placed within a duct, will produce a net flow due to viscous action. The axis of rotation can be perpendicular to the flow direction and the cylinder can thus be easily powered from outside a duct. A related viscous-flow pump was designed by Odell and Kovasznay (1971) for a water channel with density stratification. However, their design operates at a much higher Reynolds number and is too complicated for microfabrication.

Fluid flow at the micromachine level is complicated by issues such as interfacial forces, slip-flow and Knudsen number effects. To develop an operational viscous-flow micropump one must first demonstrate its working at the macroscale where these special effects are not important. Our purpose here is to show experimentally that viscous forces can indeed be used to pump fluid at low Reynolds numbers. Reynolds numbers representative of micromachine applications in air or water can be obtained with cm-size cylinders and with glycerin as the working

---

[1] Professor, Research Assistant, and Professor, respectively, Department of Aerospace and Mechanical Engineering, University of Notre Dame, Notre Dame, IN 46556. Professor Sen is a Mem. ASME; Professor Gad-el-Hak is a Fellow ASME.

Contributed by the Fluids Engineering Division of THE AMERICAN SOCIETY OF MECHANICAL ENGINEERS. Manuscript received by the Fluids Engineering Division February 26, 1996; revised manuscript received April 24, 1996. Associate Technical Editor: D. P. Telionis.

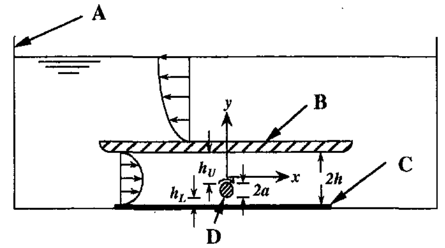

Fig. 1 Schematic of set-up

fluid. Few experiments and many numerical studies of both steady (Ingham and Tang, 1990; Tang and Ingham, 1991; Kimura et al., 1992) and unsteady (Badr et al., 1989; 1990) flow around a rotating circular cylinder are available in the open literature. There has also been work on flow around a square cylinder that is either forced to rotate (Ohba and Kuroda, 1993) or is autorotating (Zaki et al., 1994). However, there is nothing reported on the generation of a flow by rotating a cylinder.

The present laboratory experiments are carried out on the set-up shown schematically in Fig. 1. The interior dimensions of the Plexiglas tank **A** are 48.9 cm length, 15.2 cm width and 14.3 cm depth. A tightly-fitted 15.2 cm square plate **B** of the same material can be moved to any height within the tank. We are interested in the flow within the channel formed by this wall and the floor of the tank. For some of the runs a plastic sheet **C** was laid on the floor to reduce the lower gap h_L. A two-dimensional, stainless-steel cylinder **D** is placed in leak-proof bearings and can be rotated by an external electric motor (not shown). Cylinders of circular (0.898 cm diameter), square (0.898 cm diagonal) and rectangular (0.898 cm × 0.1 cm) cross-sections are tested; unless otherwise mentioned, a circular cylinder is assumed. The tank is filled with glycerin, the relative density and viscosity of which are measured before each run using a Fisher Scientific hydrometer and a Brookfield Synchro-Lectric viscometer, respectively. Due to absorption of atmospheric moisture the viscosity of the glycerin decreased from about 1.1 kg/m.s to just about one-half this value over the period of the experimentation, while the density remained approximately constant at 1260 kg/m^3. Visualization is by means of tracer particles in the fluid illuminated by a sheet of light in the mid-spanwise plane. Each run is videotaped for later analysis.

For a circular cylinder the governing parameters in the problem are: the rotational rate of the cylinder ω, its diameter $2a$, the separation between channel walls $2h$, the eccentricity of the cylinder as measured by $h_U + a - h$, and the sum of the channel lengths upstream and downstream of the cylinder L_l. In here, h_U is the upper gap, and h_L is the lower one. The governing parameters can be nondimensionalized as a Reynolds number $\mathrm{Re} = \omega(2a)^2/\nu$, where ν is the kinematic viscosity of the fluid, relative channel wall separation $s = h/a$, eccentricity $\epsilon = (h_U + a - h)/2a$, and channel length $L_l/2a$. The rotation of the cylinder, its eccentricity, and the position of the plate **B** can be varied in the experiments. Note that the average velocity in the channel is not known a priori and cannot, therefore, be used as a velocity scale. Instead we use the tangential velocity of the cylinder itself to define a Reynolds number, so that Re is not a ratio of inertial to viscous forces in the classical sense. The choice of a characteristic length to define Re is arbitrary; the other length scales in the problem are related to a via the dimensionless wall separation and eccentricity.

In the present experiments, the qualitative nature of the flow field generated by the rotating cylinder depends on the gap between the cylinder and the wall. Close to the cylinder, a primary circulation following the motion of the cylinder is always present. But on the side of the cylinder with the larger gap (normally the upper side in the present arrangement), two qualitatively different secondary flow patterns are observed. For a large h_U there is a single secondary vortex lying directly on top of the cylinder, which rotates counter to the cylinder motion. On the other hand, for a small h_U there are two small co-rotating secondary vortices located to the left and right of the cylinder. For $h_L = 0$ transition between the two patterns is observed to take place when h_U is approximately 12 mm ($s = 2.34$, $\epsilon = 0.67$). These patterns are very similar to the creeping flow eddies observed when a rotating cylinder is placed in the center of a rectangular box (Hellou and Coutanceau, 1992), or placed eccentrically within a larger circular cylinder as in journal bearings (Ottino, 1989; Ghosh et al., 1992).

From the video the time of travel of the tracer particles for a 2 cm distance in the x-direction is measured. Repeating this for different y-positions, the fluid velocity field $u^*(y)$ is determined. The first velocity measurements are made with the channel walls 14 mm apart, and with the cylinder at the lower extreme. Figure 2 shows an example of the measured velocities at four sections of the channel at different values of x, two upstream and two downstream of the cylinder. Parabolic profiles of the form $u^*(y) = U_{\max}(1 - y^2/h^2)$ are fitted to the data at each section using a least-square analysis. In general, the data at the section $x = -4$ cm fits its parabolic profile with the least error. The parabola at this section is also shown in Fig. 2. The flow at this section is almost parallel to the channel walls, while at other sections it is either affected by the inlet or outlet to the channel or is too close to the cylinder. This section is then used for the rest of the velocity measurements. We can determine an average velocity $\bar{u}^* = (1/2h)\int_{-h}^{h} u(y)dy$ at the chosen section which will also be the same at other sections. Though the integration can be done either on the experimental data using a trapezoidal rule or on the fitted parabola, we simply take $\bar{u}^* = \frac{2}{3}U_{\max}$ from now on since the difference is of the order of five percent. We can also show that the free surface of the glycerin does not affect the flow rate if it is far enough from plate **B**. The difference in average velocity in the lower channel is measured to be around one percent on changing the glycerin depth from 42.5 mm to 65 mm.

The next series of measurements are made by changing the rotation of the cylinder, but keeping the eccentricity and channel separation constant. The cylinder is again touching the bottom of the channel wall. Figure 3 shows the measured average velocity in the channel, $\bar{u}^*$, as a function of the surface speed of the cylinder, ωa. The straight line corresponds to a fit of $\bar{u}^* = 0.095\ \omega a$. The nondimensional average velocity defined by $\bar{u} \equiv \bar{u}^*/\omega a = 0.095$ under these conditions. A similar though

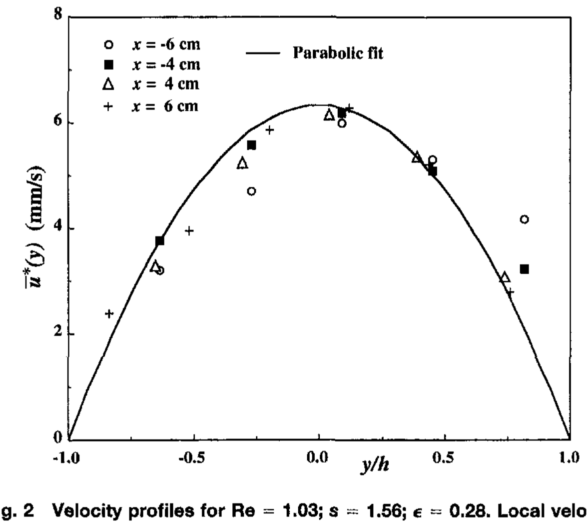

Fig. 2 Velocity profiles for Re = 1.03; s = 1.56; ϵ = 0.28. Local velocity is determined by recording the average time-of-travel of 20 tracer particles. The standard deviation for such measurements is typically ten percent of the mean.

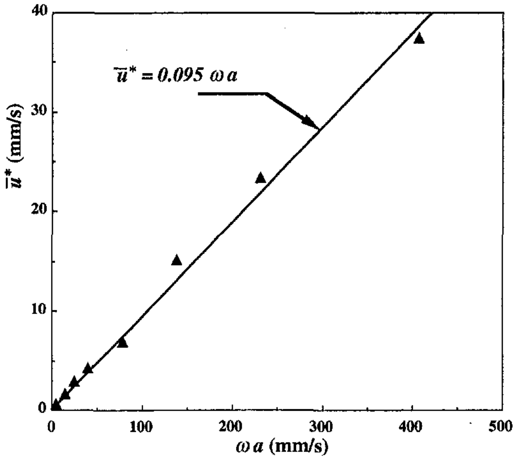

Fig. 3 Average velocity for $s = 1.56$; $\epsilon = 0.28$. Uncertainty in computing the bulk velocity is ± five percent.

slightly different graph is obtained if Re, which is in the 0.1–10 range, is used as the abscissa.

Geometrical parameters like relative eccentricity and channel separation also affect the flow rate. In the present set-up we are unable to vary them independently, but can change both by moving the plate **B**. Measurements are made by changing the gap h_U and keeping Re roughly constant. Figure 4 shows the effect on the average velocity, $\bar{u}^*$, and volume flow rate per unit width, 2 $h\bar{u}^*$. Both these variables are seen to have a maximum, though at slightly different values of h_U. The maximum volume flow rate roughly corresponds to the value of h_U around which the secondary flow pattern changes from a single vortex to two.

Experiments with cylinders of square and rectangular sections are also carried out for comparison. In each case the largest dimension of the section is used to define the Reynolds number. All three cylinders have this dimension the same so that they sweep out the same area. At Re = 1.12, $s = 1.78$, and $\epsilon = 0.17$, the nondimensional average fluid velocity in the channel using the circular cylinder is $\bar{u} = 0.046$, while for the square and the rectangular cylinders it is 64.4 and 31.8 percent of this value, respectively. It appears therefore that the circular cylinder gives the best pumping performance. A weak pulsating motion superimposed on the unidirectional mean flow is observed for the two non-circular cylinders. Although not tried in here, other configurations using the same principle can be used to pump a fluid at low Reynolds numbers. For example, two counter-rotating cylinders placed symmetrically in the channel along the y-axis would perhaps be more efficient than the present asymmetric configuration. However, in a microelectromechanical systems (MEMS) application of the present idea, simplicity of construction and operation would probably be more coveted than a modest improvement in efficiency.

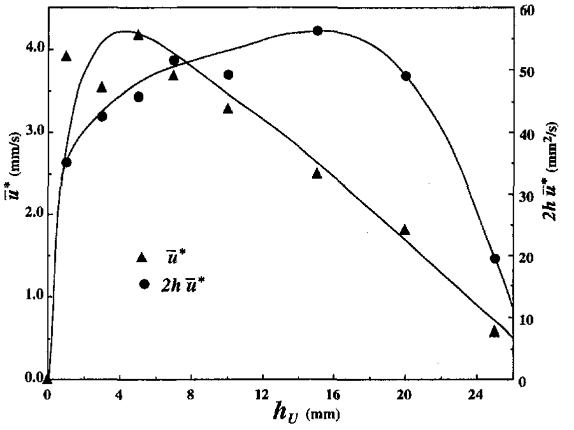

Fig. 4 Average velocity and volume flow rate for $h_L = 0$; Re = 1.05. Uncertainty in computing the bulk velocity is ± five percent.

The experiments reported here show that a two-dimensional, rotating cylinder eccentrically placed within a channel can drive a viscous fluid. We have been able to generate an average flow velocity that is about 10 percent of the surface speed of the cylinder. This proportionality is consistent with what can be expected for the solution of the Navier-Stokes equation in the limit of negligible inertia terms. As the Reynolds number increases, one can expect the slope of the curve in Fig. 3 to level off. It also appears that the low-Reynolds-number viscous effect is reversible in that continuous flow can rotate a cylinder placed eccentrically within channel walls.

The proposed pumping mechanism can be used at very low Reynolds numbers and is suitable for micromachine applications. Further exploration of the operation of this micropump will be numerical, as in the work by Beskok and Karniadakis (1992; 1994), and will be followed by experiments utilizing a microfabricated motor-pump assembly. The latter are obviously difficult to perform not only for the fabrication involved but also for the measurement techniques which are still under development. The proposed pumping configuration can be built using the LIGA microfabrication technique, a German-developed method based on lithography, electrodeposition and plastic molding. Our plan is to fabricate a prototype micropump in cooperation with the Center for Advanced Microstructures and Devices at Louisiana State University. The present device is also ideal for pumping high-viscosity polymers through macrochannels; while conventional pumps can potentially degrade the long-chain molecules, minimum damage would be caused by the envisioned pump.

This work is supported by National Science Foundation SGER grant no. CTS-9521612 and monitored by Drs. Robert L. Powell and Roger E. A. Arndt. We thank Dr. Alain Texier for his help with the photography and image processing.

References

Badr, H. M., Coutanceau, M., and Dennis, S. C. R., 1990, "Unsteady Flow Past a Rotating Circular Cylinder at Reynolds Numbers 103 and 104," *Journal of Fluid Mechanics*, Vol. 220, pp. 459–484.

Badr, H. M., Dennis, S. C. R., and Young, P. J. S., 1989, "Steady and Unsteady Flow Past a Rotating Circular Cylinder at Low Reynolds Numbers," *Computers and Fluids*, Vol. 17, pp. 579–609.

Bart, S. F., Tavrow, L. S., Mehregany, M., and Lang, J. H., 1990, "Microfabricated Electrohydrodynamic Pumps," *Sensors and Actuators A*, Vol. 21–23, pp. 193–197.

Beskok, A., and Karniadakis, G. E., 1992, "Simulation of Slip-Flows in Complex Micro-Geometries," *Micromechanical Systems*, D. Cho, J. P. Peterson, A. P. Pisano and C. Friedrich, eds., ASME DSC-Vol. 40, pp. 355–370.

Beskok, A., and Karniadakis, G. E., 1994, "Simulation of Heat and Momentum Transfer in Complex Micro-Geometries," *Journal of Thermophysics and Heat Transfer*, Vol. 8, pp. 647–655.

Esashi, M., Shoji, S., and Nakano, A., 1989, "Normally Closed Microvalve Fabricated on a Silicon Wafer," *Sensors and Actuators*, Vol. 20, pp. 163–169.

Fuhr, G., Hagedorn, R., Müller, T., Benecke, W., and Wagner, B., 1992, "Microfabricated Electrohydrodynamic (EHD) Pumps for Liquids of Higher Conductivity," *Journal of Microelectromechanical Systems*, Vol. 1, pp. 141–145.

Ghosh, S., Chang, H.-C., and Sen, M., 1992, "Heat-Transfer Enhancement due to Slender Recirculation and Chaotic Transport between Counter-Rotating Eccentric Cylinders," *Journal of Fluid Mechanics*, Vol. 238, pp. 119–154.

Hellou, M., and Coutanceau, M., 1992, "Cellular Stokes Flow Induced by Rotation of a Cylinder in a Closed Channel," *Journal of Fluid Mechanics*, Vol. 236, pp. 557–577.

Ingham, D. B., and Tang, T., 1990, "A Numerical Investigation into the Steady Flow Past a Rotating Circular Cylinder at Low and Intermediate Reynolds Numbers," *Journal of Computational Physics*, Vol. 87, pp. 91–107.

Kimura, T., Tsutahara, M., and Wang, Z.-Y., 1992, "Wake of a Rotating Circular Cylinder," *AIAA Journal*, Vol. 30, pp. 555–556.

Lipkin, R., 1993, "Micro Steam Engine Makes Forceful Debut," *Science News*, Vol. 144, Sept., p. 197.

Moroney, R. M., White, R. M., and Howe, R. T., 1991, ''Ultrasonically Induced Microtransport,'' *Proceedings IEEE MEMS 91* (Nara, Japan), IEEE, New York, pp. 277–282.

O'Connor, L., 1992, ''MEMS: Micromechanical Systems,'' *Mechanical Engineering,* Vol. 114, Feb., pp. 40–47.

Odell, G. M., and Kovasznay, L. S. G., 1971, ''A New Type of Water Channel with Density Stratification,'' *Journal of Fluid Mechanics,* Vol. 50, pp. 535–543.

Ohba, H., and Kuroda, S., 1993, ''Numerical Analysis of Flows around a Rotating Square Cylinder,'' *JSME International Journal, Series B,* Vol. 36, pp. 592–597.

Ottino, J. M., 1989, *The Kinematics of Mixing: Stretching, Chaos, and Transport,* Cambridge University Press, U.K.

Richter, A., Plettner, A., Hofmann, K. A., and Sandmaier, H., 1991, ''A Micromachined Electrohydrodynamic (EHD) Pump,'' *Sensors and Actuators A,* Vol. 29, pp. 159–168.

Smits, J. G., 1990, ''Piezoelectric Micropump with Three Valves Working Peristaltically,'' *Sensors and Actuators A,* Vol. 21–23, pp. 203–206.

Tang, T., and Ingham, D. B., 1991, ''On the Steady Flow Past a Rotating Circular Cylinder at Reynolds Numbers 60 and 100,'' *Computers and Fluids,* Vol. 19, pp. 217–230.

Taylor, Sir G., 1972, ''Low-Reynolds-Number Flows,'' *Illustrated Experiments in Fluid Mechanics,* National Committee for Fluid Mechanics Films, M.I.T. Press, Cambridge, MA, pp. 47–54.

Van Lintel, H. T. G., Van de Pol, F. C. M., and Bouwstra, S., 1988, ''A Piezoelectric Micropump Based on Micromachining of Silicon,'' *Sensors and Actuators,* Vol. 15, pp. 153–167.

Zaki, T. G., Sen, M., and Gad-el-Hak, M., 1994, ''Numerical and Experimental Investigation of Flow Past a Freely Rotatable Square Cylinder,'' *Journal of Fluid Mechanics,* Vol. 8, pp. 555–582.